

# Advances in MRI Techniques and Applications

Guest Editors: Zhengchao Dong, Trevor Andrews, Chuanmiao Xie,  
and Takeshi Yokoo





---

# **Advances in MRI Techniques and Applications**

BioMed Research International

---

## **Advances in MRI Techniques and Applications**

Guest Editors: Zhengchao Dong, Trevor Andrews,  
Chuanmiao Xie, and Takeshi Yokoo



---

Copyright © 2015 Hindawi Publishing Corporation. All rights reserved.

This is a special issue published in “BioMed Research International.” All articles are open access articles distributed under the Creative Commons Attribution License, which permits unrestricted use, distribution, and reproduction in any medium, provided the original work is properly cited.

## Contents

**Advances in MRI Techniques and Applications**, Zhengchao Dong, Trevor Andrews, Chuanmiao Xie, and Takeshi Yokoo  
Volume 2015, Article ID 139043, 2 pages

**Evaluation of Liver Fibrosis Using Texture Analysis on Combined-Contrast-Enhanced Magnetic Resonance Images at 3.0T**, Takeshi Yokoo, Tanya Wolfson, Keiko Iwaisako, Michael R. Peterson, Haresh Mani, Zachary Goodman, Christopher Changchien, Michael S. Middleton, Anthony C. Gamst, Sameer M. Mazhar, Yuko Kono, Samuel B. Ho, and Claude B. Sirlin  
Volume 2015, Article ID 387653, 12 pages

**Correction for Eddy Current-Induced Echo-Shifting Effect in Partial-Fourier Diffusion Tensor Imaging**, Trong-Kha Truong, Allen W. Song, and Nan-kuei Chen  
Volume 2015, Article ID 185026, 12 pages

**Volumetric MR-Guided High-Intensity Focused Ultrasound with Direct Skin Cooling for the Treatment of Symptomatic Uterine Fibroids: Proof-of-Concept Study**, Marlijne E. Ikin, Johanna M. M. van Breugel, Gerald Schubert, Robbert J. Nijenhuis, Lambertus W. Bartels, Chrit T. W. Moonen, and Maurice A. A. J. van den Bosch  
Volume 2015, Article ID 684250, 10 pages

**MRI for Crohn's Disease: Present and Future**, Kichul Yoon, Kyu-Tae Chang, and Hong J. Lee  
Volume 2015, Article ID 786802, 9 pages

**Pretreatment Diffusion-Weighted MRI Can Predict the Response to Neoadjuvant Chemotherapy in Patients with Nasopharyngeal Carcinoma**, Guo-Yi Zhang, Yue-Jian Wang, Jian-Ping Liu, Xin-Han Zhou, Zhi-Feng Xu, Xiang-Ping Chen, Tao Xu, Wei-Hong Wei, Yang Zhang, and Ying Huang  
Volume 2015, Article ID 307943, 8 pages

**Fast Imaging Technique for fMRI: Consecutive Multishot Echo Planar Imaging Accelerated with GRAPPA Technique**, Daehun Kang, Yul-Wan Sung, and Chang-Ki Kang  
Volume 2015, Article ID 394213, 7 pages

**Tracking Transplanted Stem Cells Using Magnetic Resonance Imaging and the Nanoparticle Labeling Method in Urology**, Jae Heon Kim, Hong J. Lee, and Yun Seob Song  
Volume 2015, Article ID 231805, 9 pages

**Exploring Dynamic Brain Functional Networks Using Continuous "State-Related" Functional MRI**, Xun Li, Yu-Feng Zang, and Han Zhang  
Volume 2015, Article ID 824710, 8 pages

**Tumour Relapse Prediction Using Multiparametric MR Data Recorded during Follow-Up of GBM Patients**, Adrian Ion-Margineanu, Sofie Van Caeter, Diana M. Sima, Frederik Maes, Stefaan W. Van Gool, Stefan Sunaert, Uwe Himmelreich, and Sabine Van Huffel  
Volume 2015, Article ID 842923, 13 pages

**MRI for Assessing Response to Neoadjuvant Therapy in Locally Advanced Rectal Cancer Using DCE-MR and DW-MR Data Sets: A Preliminary Report**, Mario Petrillo, Roberta Fusco, Orlando Catalano, Mario Sansone, Antonio Avallone, Paolo Delrio, Biagio Pecori, Fabiana Tatangelo, and Antonella Petrillo  
Volume 2015, Article ID 514740, 8 pages

**Compressed Sensing for fMRI: Feasibility Study on the Acceleration of Non-EPI fMRI at 9.4T,**

Paul Kyu Han, Sung-Hong Park, Seong-Gi Kim, and Jong Chul Ye

Volume 2015, Article ID 131926, 24 pages

**A Window into the Brain: Advances in Psychiatric fMRI,** Xiaoyan Zhan and Rongjun Yu

Volume 2015, Article ID 542467, 12 pages

**Added Value of Assessing Adnexal Masses with Advanced MRI Techniques,** I. Thomassin-Naggara,

D. Balvay, A. Rockall, M. F. Carette, M. Ballester, E. Darai, and M. Bazot

Volume 2015, Article ID 785206, 10 pages

**MRI Guided Brain Stimulation without the Use of a Neuronavigation System,** Ehsan Vaghefi, Peng Cai,

Fang Fang, Winston D. Byblow, Cathy M. Stinear, and Benjamin Thompson

Volume 2015, Article ID 647510, 8 pages

**Resting-State fMRI in MS: General Concepts and Brief Overview of Its Application,** Emilia Sbardella,

Nikolaos Petsas, Francesca Tona, and Patrizia Pantano

Volume 2015, Article ID 212693, 8 pages

**Evaluation of the Contribution of Signals Originating from Large Blood Vessels to Signals of Functionally Specific Brain Areas,** Jun-Young Chung, Yul-Wan Sung, and Seiji Ogawa

Volume 2015, Article ID 234345, 6 pages

## Editorial

# Advances in MRI Techniques and Applications

**Zhengchao Dong,<sup>1</sup> Trevor Andrews,<sup>2</sup> Chuanmiao Xie,<sup>3</sup> and Takeshi Yokoo<sup>4</sup>**

<sup>1</sup>*Division of Translational Imaging and MRI Unit, College of Physicians and Surgeons, Columbia University and New York State Psychiatric Institute, New York, NY, USA*

<sup>2</sup>*MRI Center for Biomedical Imaging, Department of Radiology, University of Vermont, Burlington, VT, USA*

<sup>3</sup>*Department of Medical Imaging and Interventional Radiology, Cancer Center, Sun Yat-Sen University, Guangzhou, Guangdong, China*

<sup>4</sup>*Advanced Imaging Research Center, University of Texas Southwestern Medical Center, Dallas, TX, USA*

Correspondence should be addressed to Zhengchao Dong; [zhengchaodongcu@gmail.com](mailto:zhengchaodongcu@gmail.com)

Received 13 July 2015; Accepted 14 July 2015

Copyright © 2015 Zhengchao Dong et al. This is an open access article distributed under the Creative Commons Attribution License, which permits unrestricted use, distribution, and reproduction in any medium, provided the original work is properly cited.

Magnetic resonance imaging (MRI) has been playing an increasingly important role in biomedical research and in clinical diagnosis. The techniques of MRI have experienced rapid development and found wide applications in recent years. The technical development is marked not only by the improvement and optimization of conventional MR imaging techniques but also by the emergence of new pulse sequences such as CEST-MRI (Chemical Exchange Saturation Transfer MRI) and DWIBS (Diffusion-weighted Whole-body Imaging with Background body signal Suppression) and by new techniques such as compressed sensing MRI and MR fingerprinting. The wide proliferation of MRI techniques has led to ever-increasing applications of MR imaging and enormous new findings in basic biomedical research as well as clinical sciences. This special issue aims at reflecting the advances in MR imaging techniques and applications.

After rigorous review procedures, the selected papers in this special issue demonstrate how broad the field of MRI has become since Paul Lauterbur's classic paper in 1973. The types of papers include review articles as well as original research. Within this issue are papers that study not only data acquisition and reconstruction methods but also specialized analysis methods and new combinations of MR with therapeutic and interventional techniques. The imaging methods cover structural MRI, functional MRI, diffusion-weighted imaging, and diffusion tensor imaging. The applications addressed are similarly wide reaching, containing cancer, liver diseases, brain function, and so forth.

Of particular note, this special issue contains several papers on perhaps the most common use of MRI in MR research centers: functional MRI (fMRI) of the brain. Neuronal activation in the brain results in local increase in the oxygen-enriched blood in capillaries associated with the signal change measured in traditional BOLD-based fMRI. One paper (J. Chung et al.) examines the fusiform face region and the fundamental confoundedness of the signal of blood from large vessels causing a mismatch between the localization of neuronal activation and that of fMRI signal. Once considered to be simply "physiological noise," certain characteristic fluctuations in the fMRI signal during rest have been shown to be associated with specific neuronal networks. Due to the practical appeal of fMRI without tasks, we are including two review papers reflecting the recent great interest in clinical methods for "resting state" fMRI, one for multiple sclerosis (E. Sbardella et al.) and the other for psychiatric disorders (X. Zhan et al.). In a related paper (X. Li et al.), a temporal decomposition method is presented which decomposes a single brain functional network into several modes to explore dynamic brain functional networks in a continuous, "state-related," "finger-force feedback" fMRI experiment. Finally, two papers are included which highlight some of the many ways in which advanced data acquisition (D. Kang et al.) and image reconstruction methods (P. K. Han et al.), such as segmented echo-planar imaging (EPI) and compressed sensing, can help to overcome some of the image quality obstacles of fMRI at high field strength.

Two other neuro-MRI studies are presented as well regarding areas of strong interest in MR: diffusion tensor imaging (DTI) and MR guidance. In the first paper (T.-K. Truong et al.), a new method is presented for the correction of eddy current-induced echo-shifting effect that produces three types of artifacts, namely, the eddy current induced signal loss, the artificial signal modulation due to eddy current-induced erroneous  $T_2^*$  weighting, and artificial signal elevation associated with partial Fourier reconstruction. The second paper (E. Vaghefi et al.) presents an MRI-based technique to guide the noninvasive transcranial brain stimulation without the use of a neuronavigation system.

As MR has matured technically primarily for neuroapplications, it has also proven to be increasingly useful for body imaging. An example is the technique of real-time MR thermometry guidance for ultrasound ablation of uterine fibroids, in which excessive skin heating has been an obstacle. To address this issue, the feasibility and safety of utilizing a water-cooled device in contact with the skin are proposed and examined in a paper (M. Ikink et al.). Another “hot topic” in body MR has been the study of liver fibrosis, using a variety of MR methods (e.g., MR elastography and DWI). In this issue, a paper (T. Yokoo et al.) is included which examines the use of a combined Gd and USPIO contrast agent together with texture analysis to better depict the reticular signal abnormalities associated with fibrosis. In a review of MRI for Crohn’s Disease (K. Yoon et al.), a variety of methods are presented for inflammatory bowel disease including endoluminal and intravenous contrast agents, DWI, dynamic bowel motility imaging, and MR spectroscopy of fecal and urine samples. Finally, MR-based molecular imaging is presented in a review paper (J. H. Kim et al.) focusing on labelling stem cell with nanoparticles in urology to evaluate migration and survival of transplanted stem cells in prostate cancer and bladder dysfunction models.

With the many technical advances in the field, several MR methods have demonstrated their utility in terms of oncology. One paper (I. Thomassin-Naggara et al.) reviews the impact of perfusion and diffusion MRI and a new diagnostic MR scoring system (Adnex MR) upon the preoperative diagnostic accuracy in women with possible ovarian cancer. The utility of combining structural, perfusion, diffusion, and MR spectroscopy data is also presented in this issue for tumour relapse prediction using multiparametric analysis in glioblastoma patients (E. Vaghefi et al.). The use of MR (using diffusion MR and/or dynamic contrast enhancement) to predict the response to neoadjuvant therapy is presented in two papers (G.-Y. Zhang et al. and M. Petrillo et al.) focusing on nasopharyngeal carcinoma and rectal cancer, respectively.

In summary, the papers collected in this special issue cover a wide range of topics that are on the frontier of the MRI techniques and their applications.

### **Authors’ Contribution**

Takeshi Yokoo and Trevor Andrews contributed equally to the editorial.

### **Acknowledgment**

We hereby thank the authors for their work and hope this special issue will find interested readers in biomedical and clinical fields.

*Zhengchao Dong  
Trevor Andrews  
Chuanmiao Xie  
Takeshi Yokoo*

## Research Article

# Evaluation of Liver Fibrosis Using Texture Analysis on Combined-Contrast-Enhanced Magnetic Resonance Images at 3.0T

Takeshi Yokoo,<sup>1,2</sup> Tanya Wolfson,<sup>3</sup> Keiko Iwaisako,<sup>1,4,5</sup> Michael R. Peterson,<sup>6</sup> Haresh Mani,<sup>7</sup> Zachary Goodman,<sup>8</sup> Christopher Changchien,<sup>1</sup> Michael S. Middleton,<sup>1</sup> Anthony C. Gamst,<sup>3</sup> Sameer M. Mazhar,<sup>4</sup> Yuko Kono,<sup>1</sup> Samuel B. Ho,<sup>4,9</sup> and Claude B. Sirlin<sup>1</sup>

<sup>1</sup>Departments of Radiology, University of California, San Diego, CA 92103, USA

<sup>2</sup>Department of Radiology and Advanced Imaging Research Center, University of Texas Southwestern Medical Center, 2201 Inwood Road, NE2.210B, Dallas, TX 75390-9085, USA

<sup>3</sup>Computational and Applied Statistics Laboratory, San Diego Supercomputer Center, University of California, San Diego, CA 92093, USA

<sup>4</sup>Departments of Medicine, University of California, San Diego, CA 92103, USA

<sup>5</sup>Department of Target Therapy Oncology, Kyoto University Graduate School of Medicine, Kyoto, Japan

<sup>6</sup>Departments of Pathology, University of California, San Diego, CA 92103, USA

<sup>7</sup>Department of Pathology, Penn State Hershey Medical Center, Hershey, PA 17033, USA

<sup>8</sup>Center for Liver Diseases, Inova Fairfax Hospital, Falls Church, VA 22042, USA

<sup>9</sup>VA San Diego Healthcare System, San Diego, CA 92161, USA

Correspondence should be addressed to Takeshi Yokoo; [takeshi.yokoo@utsouthwestern.edu](mailto:takeshi.yokoo@utsouthwestern.edu)

Received 29 July 2014; Revised 15 October 2014; Accepted 18 October 2014

Academic Editor: Trevor Andrews

Copyright © 2015 Takeshi Yokoo et al. This is an open access article distributed under the Creative Commons Attribution License, which permits unrestricted use, distribution, and reproduction in any medium, provided the original work is properly cited.

**Purpose.** To noninvasively assess liver fibrosis using combined-contrast-enhanced (CCE) magnetic resonance imaging (MRI) and texture analysis. **Materials and Methods.** In this IRB-approved, HIPAA-compliant prospective study, 46 adults with newly diagnosed HCV infection and recent liver biopsy underwent CCE liver MRI following intravenous administration of superparamagnetic iron oxides (ferumoxides) and gadolinium DTPA (gadopentetate dimeglumine). The image texture of the liver was quantified in regions-of-interest by calculating 165 texture features. Liver biopsy specimens were stained with Masson trichrome and assessed qualitatively (METAVIR fibrosis score) and quantitatively (% collagen stained area). Using  $L_1$  regularization path algorithm, two texture-based multivariate linear models were constructed, one for quantitative and the other for quantitative histology prediction. The prediction performance of each model was assessed using receiver operating characteristics (ROC) and correlation analyses. **Results.** The texture-based predicted fibrosis score significantly correlated with qualitative ( $r = 0.698$ ,  $P < 0.001$ ) and quantitative ( $r = 0.757$ ,  $P < 0.001$ ) histology. The prediction model for qualitative histology had 0.814–0.976 areas under the curve (AUC), 0.659–1.000 sensitivity, 0.778–0.930 specificity, and 0.674–0.935 accuracy, depending on the binary classification threshold. The prediction model for quantitative histology had 0.742–0.950 AUC, 0.688–1.000 sensitivity, 0.679–0.857 specificity, and 0.696–0.848 accuracy, depending on the binary classification threshold. **Conclusion.** CCE MRI and texture analysis may permit noninvasive assessment of liver fibrosis.

## 1. Introduction

The ongoing epidemic of Chronic Liver Disease (CLD) is a major contributor to liver-related mortality and morbidity in

the United States. More than 20,000 Americans die from CLD complications each year [1]. The most common etiologies for CLD are chronic hepatitis C virus (HCV) infection and alcoholic hepatitis [2, 3]. Over 4 million Americans are HCV

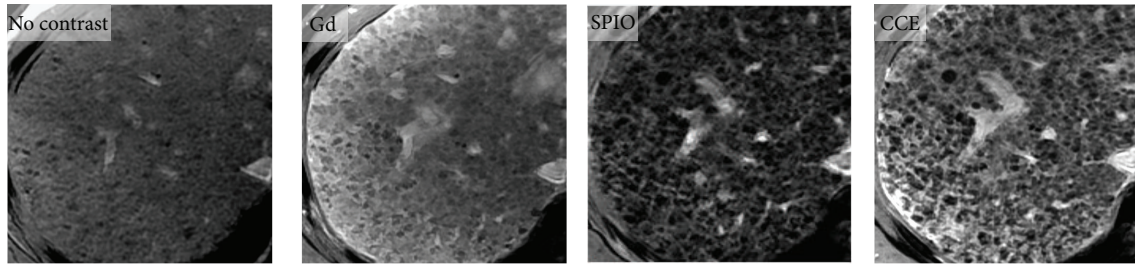


FIGURE 1: MR images of liver in 60-year old man with HCV-related cirrhosis. Noncontrast, Gd-only, SPIO-only, and CCE 2D breath-hold T1-weighted gradient-echo images of cirrhotic liver due to HCV. Abnormal reticular pattern of the liver parenchyma is better visualized on single-contrast-enhanced (Gd or SPIO) images than on unenhanced image and better visualized on CCE images than on single-contrast-enhanced images. Gd: gadolinium; SPIO: superparamagnetic iron oxide, and CCE: combined contrast enhanced.

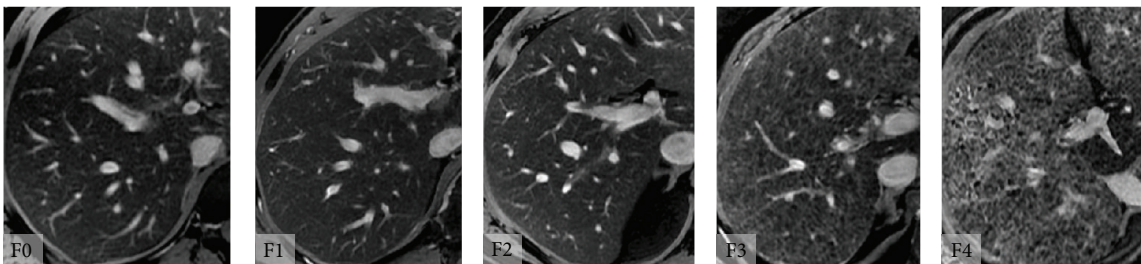


FIGURE 2: Combined contrast enhanced (CCE) MR images at various stages of fibrosis. CCE MR images in adults with chronic HCV infection and histologically determined Metavir fibrosis stages F0, F1, F2, F3, and F4. Subjectively, the reticular texture of the liver parenchyma becomes progressively more pronounced with increasing Metavir fibrosis stage.

carriers, but many are asymptomatic and unaware of their infection [4].

The common pathway in the natural history of CLD, including chronic HCV infection, is progressive liver fibrosis and ultimately cirrhosis [5]. Fibrosis indicates cumulative liver damage, contributes to the development of portal hypertension and hepatic dysfunction, and predicts poor clinical outcome [6, 7]. Most liver-related mortality and morbidity occur in the cirrhotic population [8]. Assessment of liver fibrosis is therefore critical in the management of patients with CLD.

The current gold standard for fibrosis evaluation is liver biopsy. The severity of fibrosis due to HCV infection is often classified using an ordinal scale such as the Metavir system [9]. However, biopsy is invasive and thus problematic for frequent monitoring. Moreover, its interpretation is subjective, leading to inter- and intraobserver variability [10–12]. For these reasons, noninvasive and objective techniques are under investigation, including fibrosis-specific serum markers [13, 14], ultrasound elastography [15, 16], magnetic resonance (MR) elastography [17–19], diffusion weighted MR imaging [20–22], and single-contrast-enhanced MR imaging [23–25].

Another promising MR imaging-based technique is combined-contrast-enhanced (CCE) MR imaging [26]. This technique exploits the complementary effects of positive contrast enhancement by gadolinium-chelates (Gd) and negative enhancement by superparamagnetic iron oxide (SPIO) agents. Compared to noncontrast, Gd-enhanced, or SPIO-enhanced images, CCE images better depict the reticular

signal abnormalities associated with fibrosis as shown in Figure 1 [27]. The conspicuity of this pattern appears to parallel histologic fibrosis severity (Figure 2) suggesting that liver fibrosis can be assessed by the severity of the “texture” abnormality.

The potential role of texture analysis in liver fibrosis assessment was previously explored in retrospective studies using qualitative [26] and quantitative [26, 28–30] texture analysis. The purpose of this prospective study was to provide proof-of-concept that quantitative texture analysis using CCE MR imaging may permit noninvasively assess liver fibrosis in adults with HCV infection using CCE MR imaging.

## 2. Method and Materials

**2.1. Study Design and Subjects.** This prospective, cross-sectional, observational clinical study was approved by an institutional review board and is HIPAA-compliant. Potential eligible subjects were referred for research MR imaging examination from hepatology clinics at our institution. Written informed consents were obtained. Selection criteria are listed in Table 1. Patient recruitment was stratified according to the fibrosis severity at liver biopsy and continued until at least five subjects in each fibrosis severity category (per clinical biopsy reports) were enrolled.

**2.2. Liver Biopsy.** Subjects had a percutaneous 16-gauge needle-core biopsy of the right hepatic lobe for clinical care by the referring hepatologists. Specimens were processed in

TABLE 1: Selection criteria.

Inclusion criteria	Exclusion criteria
(i) Age >18 years	(i) Estimated GFR <60 mL/mL ( $N = 0$ potential subjects)
(ii) Newly diagnosed HCV infection, without clinically overt cirrhosis	(ii) Imaging not performed within 30 days of biopsy ( $N = 2$ )
(iii) Recent or planned biopsy <sup>1</sup>	(iii) Nondiagnostic biopsy or trichrome slide unavailable ( $N = 2$ )
(iv) Willing and able to undergo CCE MRI exam within 30 days of biopsy	(iv) Contraindication to MR exam ( $N = 1$ ) <sup>2</sup>
(v) Willing and able to undergo phlebotomy for estimated GFR determination within 30 days of biopsy	(v) Lack of intravenous access ( $N = 1$ )
	(vi) History of severe allergic reaction or anaphylaxis ( $N = 0$ )
	(vii) History of liver diseases other than HCV including iron overload ( $N = 0$ )
	(viii) Severe claustrophobia ( $N = 0$ )
	(ix) Pregnant or nursing mother ( $N = 0$ )

<sup>1</sup>Biopsies were performed for clinical care. <sup>2</sup>Due to intraorbital shrapnel. GFR: glomerular filtration rate. Parenthesis ( ) contains the number of potential subjects excluded for the criterion.

the pathology department per routine protocol, including Masson-trichrome staining. Clinical biopsy reports were generated by staff pathologists. Each clinical report included assessment of fibrosis severity (none, mild, moderate, severe, and cirrhosis); the clinically reported fibrosis severity was used for the block recruitment but not analyzed.

**2.3. Qualitative and Quantitative Scoring of Histology.** The trichrome-stained slides were further evaluated for research purposes. The entire slides were digitized using an APERIO ScanScope scanner (Aperio Technologies, Inc., Vista, CA). The digitized images were viewed using the Aperio ImageScope software and the fibrosis severity was scored qualitatively by histomorphology and quantitatively by digital image analysis.

Qualitative scoring was performed independently by three pathologists with expertise in liver pathology (MRP, HM, and ZG). Without knowledge of clinical, MR imaging, or quantitative histology findings, each reader reviewed the digitized histology images, subjectively assessed the adequacy of each specimen, and assigned to each specimen a Metavir fibrosis score, F0–F4. The readers were blinded to each other's scores. Other histology features (e.g., necro-inflammation, steatosis, iron) were not recorded. To assess adequacy of specimen, one pathologist (MRP) counted the number of portal triads within each noncirrhotic specimen; portal triads were not counted in cirrhotic specimens due to architectural distortion. The total length of each specimen was recorded.

Quantitative scoring was performed by a hepatology research scientist (KI) using ImageScope software analysis tools, without knowledge of the clinical, MR imaging, or qualitative histology findings. Staining variability was corrected by digitally adjusting color saturation. Total specimen area was manually segmented, and the blue-stained pixels (representing collagen) were segmented using manual intensity thresholding. Percent (%) collagen was calculated as the ratio of blue-stained to total specimen pixels.

**2.4. MR Imaging.** Subjects received SPIO (ferumoxides, Feridex, Bayer HealthCare Pharmaceuticals, Wayne, NJ) continuous intravenous infusion (0.5 mL/kg) diluted in 100 mL of 5% dextrose solution, passed through a 5- $\mu$ m filter at 2–4 mL/min over 30 minutes per manufacturer's instructions.

Thirty minutes after completion of SPIO infusion, subjects were scanned supine in a superconducting MR whole body system at 3T (GE Signa EXCITE HD, GE Medical Systems, Milwaukee, WI), with an 8-channel torso phase-array coil and a dielectric pad centered over the liver. Gadolinium-DTPA (gadopentetate dimeglumine, Magnevist, Bayer HealthCare Pharmaceuticals, Wayne, NJ) was injected intravenously (0.1 mmol/kg). Using a 2D chemically fat-saturated fast spoiled gradient-recalled echo (FSPGR) sequence without parallel imaging, four sets of axial CCE images of the liver were acquired during separate 18–28 second breath-holds, 4–10 minutes after Gd injection. In this 6-minute window, enhancement of the liver by the two agents (SPIO and Gd) is subjectively constant according to our clinical experience of CCE MR imaging in cirrhotic and non-cirrhotic livers; moreover, the T1- and T2\* shortening effects of gadopentetate and ferumoxides in liver may be assumed stable over this period from the known liver clearance rates of these agents [31–33]. The four image sets were acquired to help ensure that at least one set was free of visible motion artifacts. Imaging parameters included TR 100 ms, TE 6 ms, FA 70°, slice thickness 4 mm, interslice gap 4 mm, number of slices 5, and bandwidth 130 Hz/pixel. Two of the four image sets were acquired with 384 × 224 and two with 384 × 256 matrix. Field-of-view was adjusted to accommodate body habitus and breath-hold capacity. These parameters were selected to provide simultaneous T1- and T2\*-weighting to exploit Gd- and SPIO-enhancement, respectively; adequate signal-to-noise ratio; high spatial resolution; and relatively short acquisition time. The Food and Drug Administration (IND number 75,579) approved off-label use of Magnevist-Feridex combined contrast for this research study.

**2.5. Image Processing and Texture Analysis.** A radiology resident (TY) and a trained research assistant (CC) analyzed the CCE images without knowledge of clinical or biopsy findings. From the four CCE image sets, the set with the highest resolution and subjectively least motion artifact was selected. Representative CCE images of the liver (1–5 sections per subject) were exported in DICOM format. Using MATLAB (Mathworks, Natick, MA), a total of five nonoverlapping rectangular regions-of-interest (ROIs) of size >100 mm<sup>2</sup> were placed per subject within areas of subjectively uniform texture

in the right hepatic lobe (Couinaud segments IV–VIII), avoiding artifacts, bile ducts, and vessels. Each ROI image was standardized by rotating to the Cartesian coordinate system with zero tilt-angle, interpolating to 0.5 mm/pixel resolution, removing bilinear spatial trend of signal intensities, and scaling to 0-1 intensity range.

Gradient and Laplacian transformations (1st and 2nd spatial derivatives) were applied to each standardized ROI to generate additional “edge-enhanced” and “zero-crossing” texture patterns. For each untransformed (original) and transformed (gradient, Laplacian) ROI, 55 texture features were calculated as detailed in the supplementary materials available online at <http://dx.doi.org/10.1155/2014/387653>. These texture features represented five texture feature classes: pixel intensity histogram, Gaussian mixture model, autocorrelation, cooccurrence matrices, and Voronoi polygons. These classes were selected based on the expected imaging characteristics of fibrosis texture, as explained in the supplementary materials. For each subject, the texture features were averaged across the five ROI's to generate a set of 165 average texture features.

## 2.6. Statistical Analyses

**2.6.1. Comparison of Histologic Scores.** For each subject, the average, standard deviation (STD), and range of the Metavir scores of the three pathology readers were calculated. The interreader agreement was assessed by intraclass correlation coefficient (ICC, two-way analysis for precise agreement) and their 95% confidence intervals (CIs) were calculated. ICC was also calculated for each pair of readers. The average Metavir scores of the three readers were compared to %-collagen scores using Pearson correlation analysis.

**2.6.2. Comparison of Texture and Histology.** A biostatistician (TW) performed statistical analysis using the 165 texture features to predict qualitative (Metavir) and quantitative (%-collagen) fibrosis scores. A path-following algorithm for  $L_1$  regularized linear model called GLM-path [34] with a Gaussian link (i.e., linear regression) was used to identify the optimal linear model of texture features that minimized the fibrosis prediction error for each number of predictors (i.e., features). The optimal number of predictors was determined by Akaike Information Criterion (AIC) [35]. Using the qualitative and quantitative fibrosis scores as the reference, two texture-based fibrosis prediction models were constructed, respectively. For each subject, the predicted qualitative (Metavir) and quantitative (%-collagen) fibrosis scores were calculated using respective prediction models.

Pearson's correlation was used to evaluate the strength of the relationship between the predicted and histologic scores. Additionally, the performance of each prediction model for dichotomized classification was assessed using receiver-operating-characteristics (ROC) analysis using the average histologically determined Metavir score as the reference standard. At each of four classification thresholds (Metavir F1, F2, F3, and F4 for qualitative scoring; 5, 10, 15, and 20% collagen for quantitative scoring), the classification accuracy,

sensitivity, and specificity (and their CIs) were calculated at the predicted fibrosis score cutoff value that maximized the sum of sensitivity and specificity.

The regularization employed by the GLM-path algorithm is designed to minimize prediction error over independent validation datasets [34]. Therefore no dedicated validation procedure was performed in this proof-of-concept study. However, the algorithm may not necessarily minimize the prediction error of the test dataset itself; thus, some degree of mismatch between the predicted and actual fibrosis scores is expected.

## 3. Results

**3.1. Subjects.** Between August 2007 and March 2009, 52 newly diagnosed HCV-positive adults (age  $51.2 \pm 6.3$  years, 38 male, 12 female) with recent or planned liver biopsy were recruited for CCE imaging. Six subjects were excluded (Table 1). The remaining 46 subjects formed the study group. All subjects completed the MR examination without serious adverse effects. At least one CCE image set was subjectively adequate in quality for further image analyses in each subject.

**3.2. Qualitative versus Quantitative Histology.** Examples of biopsy specimens are shown in Figure 3. The histology specimen's average  $\pm$  STD [range] of the total length and the number of portal triads were  $21.9 \pm 9.8$  mm [6.7–44.2] and  $14.2 \pm 6.0$  [4–28], respectively.

Figure 4(a) shows the histogram of qualitative Metavir scores assigned by the three readers. The 3-reader agreement was good with ICC of 0.772 (95% CI [0.653–0.859]). Pairwise ICCs were 0.727, 0.768, and 0.831, depending on the reader pairs. All readers agreed that all biopsy specimens were adequate.

Figure 4(b) shows the histogram of quantitative %-collagen rounded to the nearest 5%. Over half the subjects had rounded %-collagen  $\leq 5\%$ . As shown in Figure 5 the relationship between the qualitative (average Metavir) and quantitative (%-collagen) scores was curvilinear, as has been observed by others [36, 37]. Log-linear plot of quantitative ( $y$ -axis) and qualitative ( $x$ -axis) scores demonstrated significant linear correlation with Pearson's  $r = 0.81$  ( $P < 0.001$ ).

**3.3. Image Texture versus Histology.** The liver image textures of representative subjects are shown in Figure 6 with their respective qualitative (Metavir) and quantitative (%-collagen) scores.

Using qualitative histology as the reference, GLM-path analysis identified a set of 6 texture features predictive of Metavir fibrosis scores (Table 2). As shown in Figure 7(a), the Metavir score predicted by a 6-feature model linearly correlated with the average Metavir scores of the three readers with  $r = 0.698$  ( $P < 0.001$ ). Table 3 summarizes the ROC analysis results at each classification threshold. AUCs were 0.814–0.976, sensitivities 0.659–1.000, specificities 0.778–0.930, and accuracies 0.674–0.935, depending on the classification threshold.

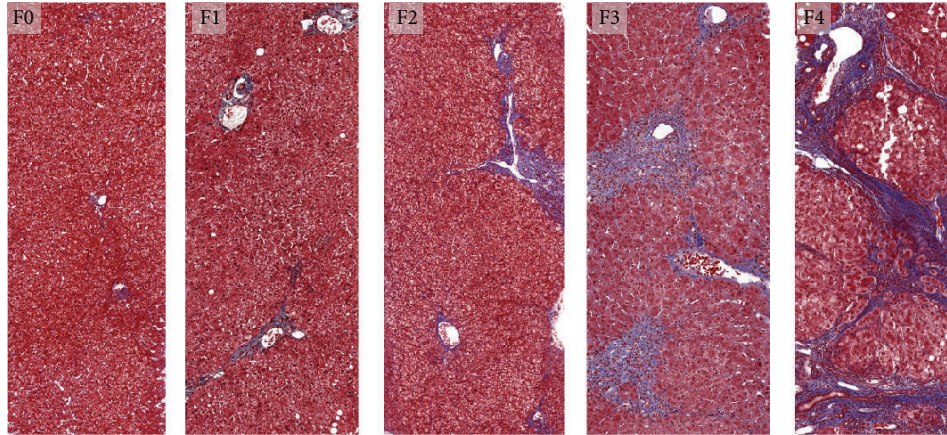


FIGURE 3: Histologic assessment of liver HCV-related fibrosis. Liver biopsy specimen from subjects with chronic HCV infection, stained with Masson-trichrome. F0 (absent fibrosis), F1 (stellate enlargement of portal tracts), F2 (enlarged portal tracts with rare septa), F3 (numerous septa without cirrhosis), and F4 (cirrhosis) according to Metavir scoring system. Trichrome stains fibrosis blue.

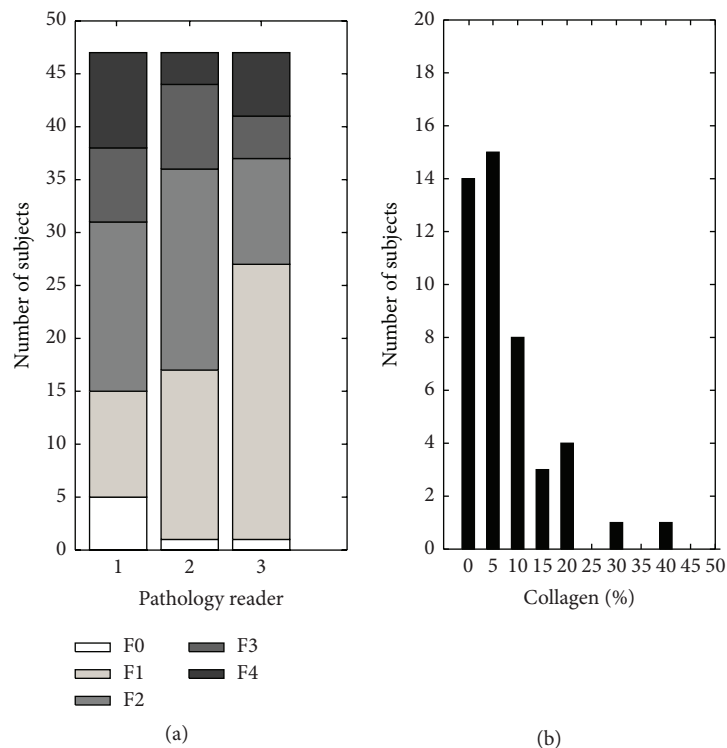


FIGURE 4: Fibrosis severity distribution. The study group’s histograms by Metavir fibrosis score (left) and %-collagen (right). The most common Metavir fibrosis score was F1 or F2 depending on the reader. Nine subjects (19%; 9/46) had a score of F4 (cirrhosis) from at least one reader. %-collagen is rounded to the nearest 5%.

Using quantitative histology as the reference, GLM-path analysis identified another set of 6 texture features predictive of %-collagen scores (Table 4). As shown in Figure 5 (LEFT) the %-collagen score predicted by the 6-feature model linearly correlated with %-collagen score of histology with  $r = 0.757$  ( $P < 0.001$ ). Table 5 summarizes the ROC analysis results at threshold values at 5, 20, 15, and 20% fibrosis. AUCs were 0.742–0.950, sensitivities 0.688–1.000, specificities 0.679–0.857, and accuracies 0.696–0.848, depending on the classification threshold.

Identified texture features were similar but not identical between qualitative and quantitative prediction models (Tables 2 and 4). Two classes of texture features were common to both Gaussian-mixture model and Voronoi polygons. One class of texture features (pixel intensity histogram) was predictive only for qualitative scores. Texture features of both untransformed and transformed ROI images were found to be predictive. For illustration purposes, these texture classes derived from a ROI in a cirrhotic subject are shown in Figure 8.

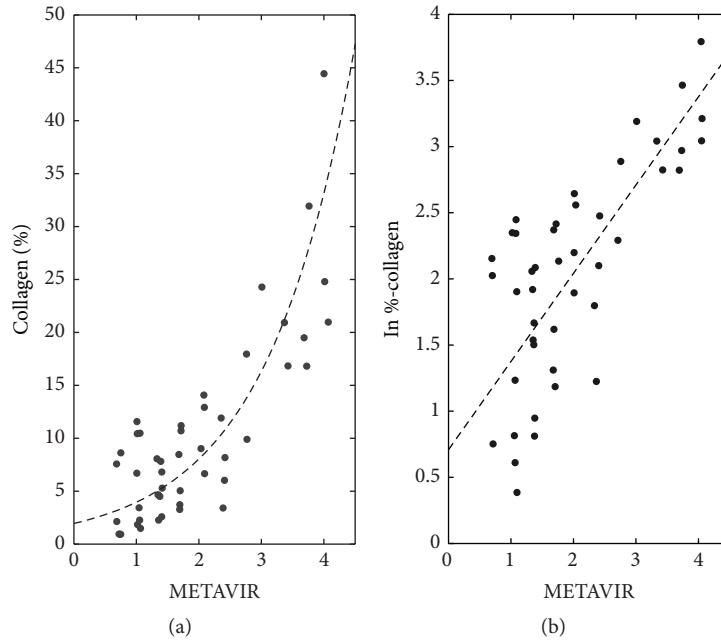


FIGURE 5: Comparison between quantitative versus qualitative histology. Average Metavir of 3 pathology readers versus (a) raw %-collagen (b) and natural logarithm of %-collagen. As shown in (a), the relationship between quantitative and qualitative histology scores is curvilinear. Pearson's correlation coefficient ( $r$ ) of plot B is 0.81, with  $P < 0.001$ .

TABLE 2: Fibrosis prediction model parameters (texture versus Metavir).

	Source image	Texture class	Texture feature
1	Original	Pixel intensity histogram	Mean pixel intensity
2	Original	Gaussian mixture model	STD of the lower intensity pixels
3	Original	Gaussian mixture model	AIC of two-Gaussian fit/AIC of single-Gaussian fit
4	Original	Voronoi polygons	STD of the 1st order inertial moment
5	Gradient	Voronoi polygons	Mean of the 2nd order inertial moment
6	Laplacian	Pixel intensity histogram	Mode/interquartile range

Six most predictive texture features, from strongest to weakest. Keys: STD: standard deviation, AIC: Akaike Information Criterion, inertial moments: mathematical description the shape/area of the Voronoi polygons (see supplementary materials).

TABLE 3: Receiver operating characteristics (texture versus Metavir).

Classification	Cutoff	Area under curve	Sensitivity	Specificity	Accuracy
F <1 versus F $\geq$ 1	1.805	0.814 [0.654 0.975]	0.659 [0.513 0.804]	0.800 [0.449 1.000]	0.674 [0.524 0.797]
F <2 versus F $\geq$ 2	1.916	0.889 [0.783 0.994]	0.895 [0.757 1.000]	0.778 [0.621 0.919]	0.826 [0.686 0.916]
F <3 versus F $\geq$ 3	2.060	0.862 [0.701 1.000]	0.778 [0.506 1.000]	0.784 [0.651 0.916]	0.783 [0.615 0.867]
F <4 versus F = 4	2.174	0.976 [0.855 1.000]	1.000 [0.907 1.000]	0.930 [0.854 1.000]	0.935 [0.788 0.974]

Cutoff: the operating point on the ROC curve closest to (0, 1), the point of maximum sensitivity and specificity. [ ]—95% confidence interval. The mismatch between the texture-based cutoff and the histologic classification threshold is expected (see text).

#### 4. Discussion

This study prospectively assessed liver fibrosis in HCV-infected adults noninvasively using quantitative texture analysis of CCE MR images. Liver biopsy was used as the reference standard. Fibrosis severity was scored qualitatively (Metavir) and quantitatively (%-collagen). The study design closely simulated a typical clinical situation, in which a newly diagnosed HCV-positive patient without clinically overt cirrhosis requires assessment of liver fibrosis.

We utilized a CCE MR imaging technique, in which SPIOs and an extracellular Gd-based agent are administered sequentially. Prior studies suggested complimentary effects of SPIO and Gd for visualizing fibrosis. SPIOs accumulate by phagocytosis in Kupffer cells in the hepatic lobules, causing T2\*-related negative enhancement. Extracellular Gd-based agents such as Gd-DTPA distribute to the interstitial space of the fibrotic perlobular septa, causing T1-related positive enhancement. The result is a linear meshwork of high-signal perlobular septa against a background of low-signal lobules,

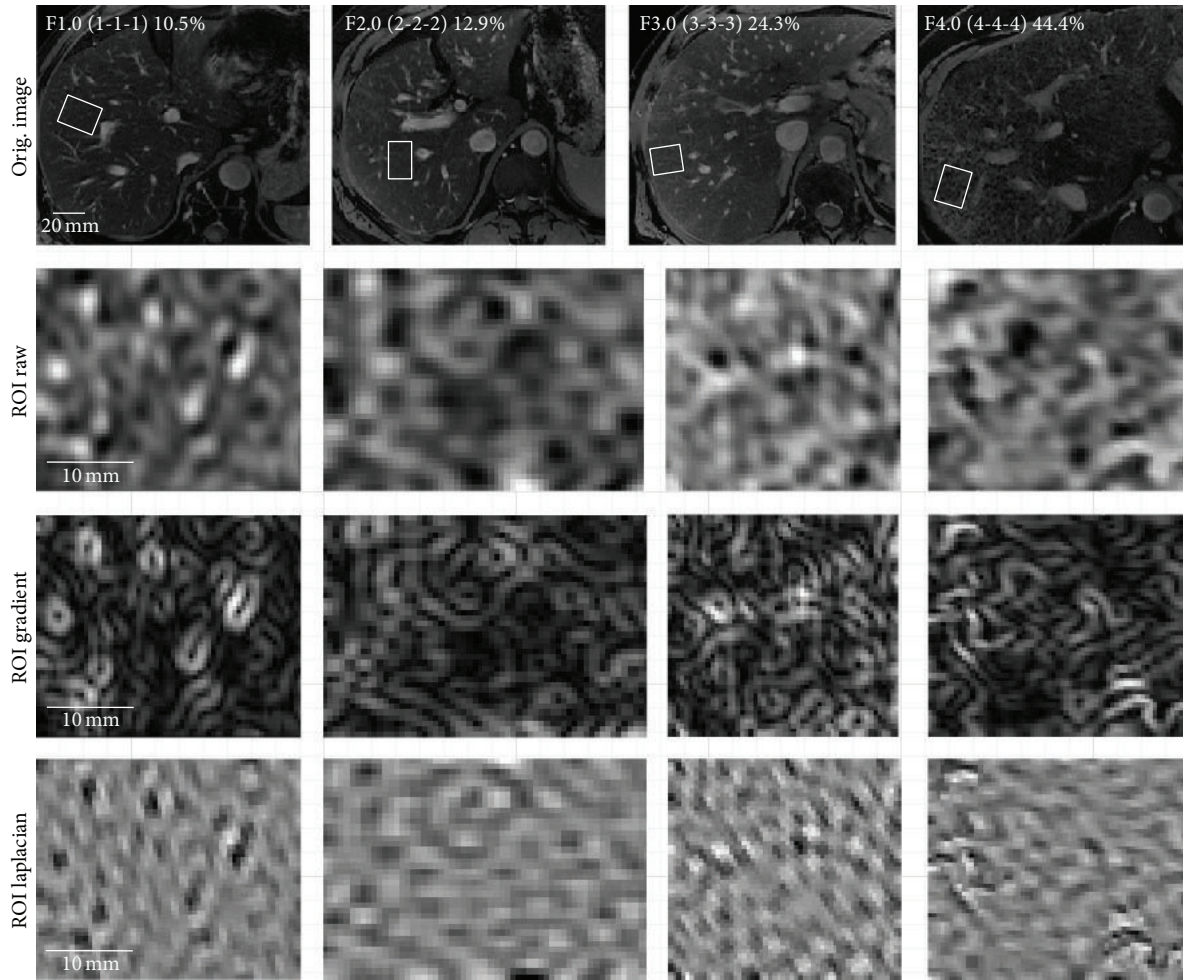


FIGURE 6: Regions-of-interest on CCE MR images in four subjects. Regions-of-interest drawn on CCE MR images in four representative subjects. Average Metavar (and individual reader METAVIR) and %-collagen scores are shown. Subjectively, high-signal reticular texture becomes increasingly conspicuous and disorganized with increasing Metavar and %-collagen scores. CCE: combined contrast enhanced.

TABLE 4: Fibrosis prediction model parameters (texture versus %-collagen).

	Source image	Texture class	Texture feature
1	Original	Gaussian mixture model	STD of the lower intensity pixels
2	Original	Voronoi polygons	Mean of the 2nd order inertial moment
3	Original	Voronoi polygons	STD of the 1st order inertial moment
4	Gradient	Voronoi polygons	Mean of the 2nd order inertial moment
5	Gradient	Gaussian mixture model	STD of the lower intensity pixels
6	Laplacian	Voronoi polygons	Mean of the 3rd order inertial moment

Six most predictive texture features, from strongest to weakest. Keys: STD: standard deviation, AIC: Akaike Information Criterion, inertial moments: mathematical description the shape/area of the Voronoi polygons (see supplementary materials).

TABLE 5: Receiver operating characteristics (texture versus %-collagen).

Classification	Cutoff	Area under curve	Sensitivity	Specificity	Accuracy
<5% versus ≥5%	9.315	0.806 [0.680 0.932]	0.688 [0.527 0.848]	0.857 [0.674 1.000]	0.739 [0.592 0.850]
<10% versus ≥10%	9.807	0.742 [0.589 0.895]	0.722 [0.515 0.929]	0.679 [0.506 0.852]	0.696 [0.547 0.815]
<15% versus ≥15%	10.500	0.894 [0.758 1.000]	0.900 [0.714 1.000]	0.750 [0.609 0.891]	0.783 [0.638 0.884]
<20% versus ≥20%	11.234	0.950 [0.826 1.000]	1.000 [0.907 1.000]	0.825 [0.707 0.943]	0.848 [0.686 0.916]

Cutoff: the operating point on the ROC curve closest to (0, 1), the point of maximum sensitivity and specificity. [ ]—95% confidence interval. The mismatch between the texture-based cutoff and the histologic classification threshold is expected (see text).

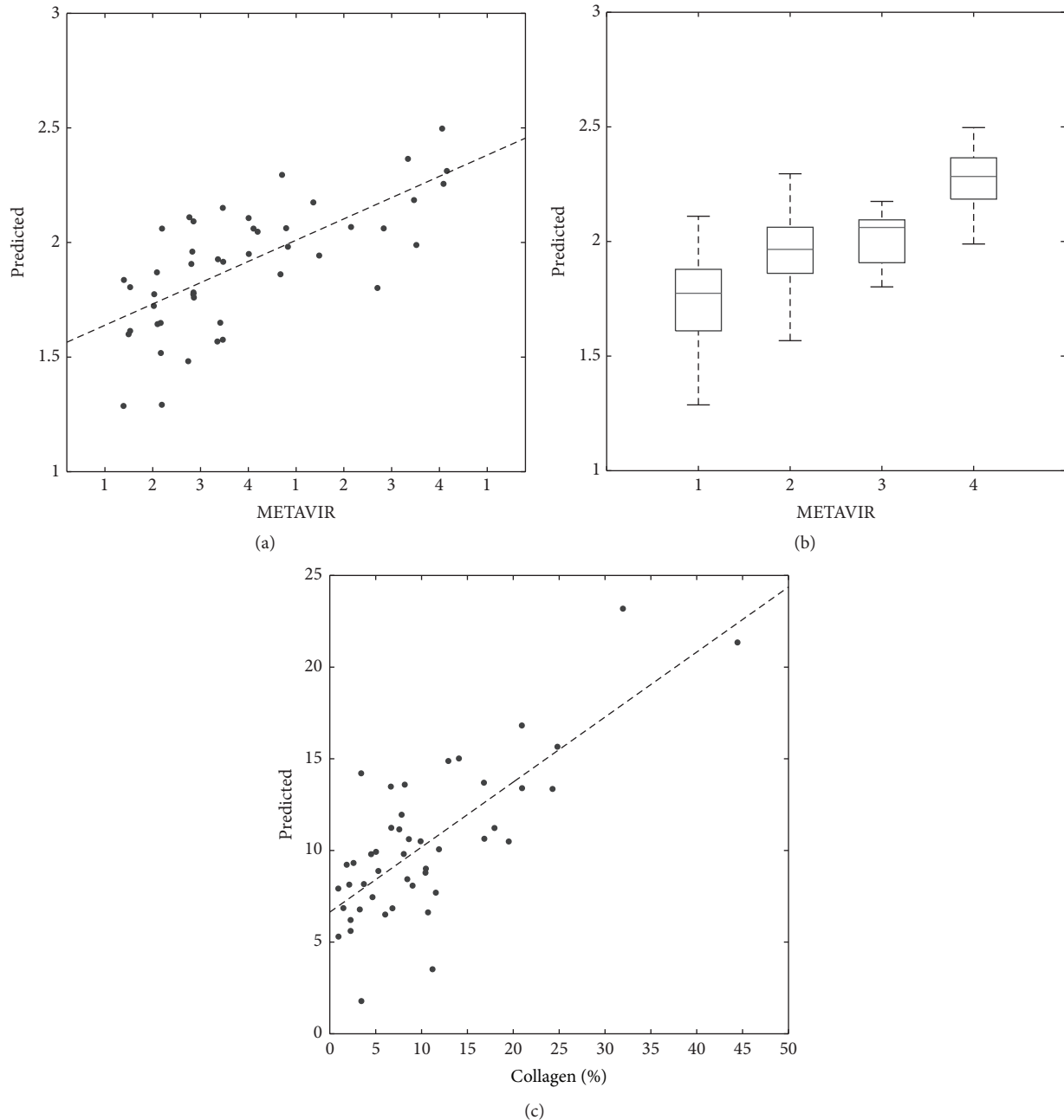


FIGURE 7: Texture versus histologic fibrosis scores. (a) The correlation between the texture and qualitative histology score (average Metavir) is statistically significant with 0.698 ( $P < 0.001$ ) with best-fit line of slope 1.546 and intercept 0.186. (b) Box-plot of texture score versus rounded average Metavir. Spearman's correlation is significant at  $\rho = 0.635$  ( $P < 0.001$ ). (c) The correlation between texture and quantitative histology score (percent-fibrosis) is statistically significant with 0.767 ( $P < 0.001$ ), with best-fit line of slope 0.355 and intercept 6.636. The nonunit slope and nonzero intercept are attributable in part to the regularization procedure employed by the GLM-path algorithm (see text).

producing a reticular texture pattern that subjectively becomes more conspicuous with increasing fibrosis severity [26, 27].

We found that CCE MR image texture of the liver can be objectively quantified to predict fibrosis severity. The abnormal texture was detectable at early fibrosis stage, for example,  $F > 2$  Metavir score or  $>15\%$ -collagen with accuracy of 0.826 and 0.783, respectively. The predicted fibrosis scores

correlated with but did not exactly match the corresponding histologically determined scores. The imperfect agreement between predicted and actual fibrosis scores is likely due to three factors: intrinsic inaccuracy of the texture-based technique used in our study, expected mismatch due to the regularization procedure employed by GLM-path (explained earlier), and intrinsic inaccuracy of liver biopsy as a reference standard (explained later).

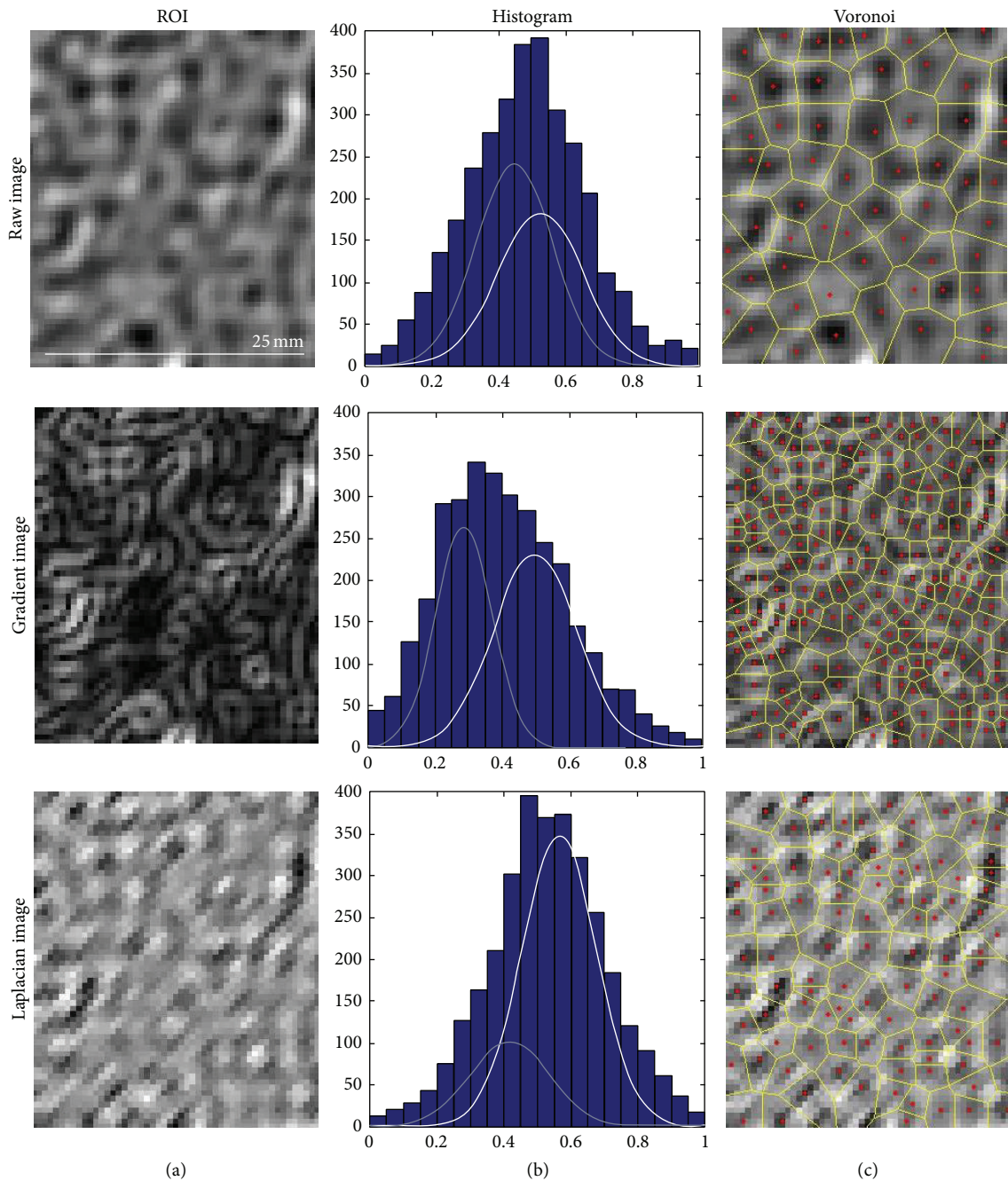


FIGURE 8: Illustrative examples of texture feature classes for fibrosis prediction. A 54 year-old female with cirrhosis. (c) Standardized regions of interest (ROI) images, without transformation (raw), with gradient and Laplacian transformations. (b) Corresponding pixel intensity histogram and its Gaussian mixture model fit with two normal populations. (a) Voronoi polygons constructed on the corresponding ROI images. These texture classes were found to be predictive of liver fibrosis on CCE images (see text). For each texture class (intensity histogram, Gaussian mixture, and Voronoi polygons), relevant statistics were calculated as detailed in supplementary materials and were used for fibrosis prediction.

Gaussian mixture models and Voronoi polygons were found to be predictive texture classes by both qualitative and quantitative histology prediction models. This is consistent with the postulated complimentary effects of SPIO and Gd producing the reticular enhancement pattern in fibrotic livers. A Gaussian mixture model fits two normal distributions,

each with its own mean and variance, to the overall pixel intensity histogram. On a CCE image, the liver contains two populations of pixels, one comprised of low-signal SPIO-containing pixels devoid of fibrosis and the other of high-signal Gd-containing pixels in fibrotic septa. With progression of fibrosis, the proportion of high-signal Gd-containing

pixels (i.e., fibrosis) increases and, therefore, the pixel intensity histogram is better fitted by a mixture of two Gaussian distributions than a single Gaussian. The Voronoi polygon algorithm generates a tessellation of polygons that “carves” the liver parenchyma into low-intensity nodules, thereby objectively modeling the reticular texture seen subjectively in progressive fibrosis.

Another MR-based technique, MR elastography (MRE), is increasing in popularity and availability for noninvasive assessment of liver fibrosis. This technique measures the biomechanical stiffness of the liver, which increases as a consequence of fibrosis [38]. In a retrospective study in HCV-infected population [39], the reported AUC, sensitivity, and specificity of MRE in detecting clinically significant fibrosis ( $F \geq 2$ ) was 0.986, 0.885, and 1.00, respectively, similar to slightly higher than those of the CCE texture method. However, texture-based methods may have a theoretical advantage of more direct visualization of fibrosis while MRE measures the tissue biomechanical sequela of fibrosis. Another practical advantage of texture-based methods is that they can be implemented on any clinical scanner using standard sequences, while MRE requires dedicated hardware (mechanical wave transducer) and sequences. Disadvantages of texture-based methods are the need for intravenous access and injection of contrast agents, including two agents for the CCE technique described here. Also, visualization of subtle reticulations associated with early fibrosis is sensitive to patient motion; consequently we obtained four CCE image sets in separate breath-holds, to ensure that at least one set was motion-free. As motion correction/minimization techniques become more robust and clinically available, it may be possible to acquire images during free breathing with higher signal-to-noise ratio and spatial resolution.

A limitation of this study is the use of single liver biopsy as the reference standard. A typical core biopsy ( $\sim 30 \text{ mm}^3$ ) samples only 1/50,000 of the liver and is significantly smaller than the imaging ROI ( $>400 \text{ mm}^3$ ) used in the texture analysis. Also, biopsied sites are difficult to colocalize with imaging ROIs, which is relevant because the severity of fibrosis can be heterogeneous across the liver. An error frequency of up to 33% has been reported for differences in  $\geq$  one fibrosis stage and cirrhosis may be missed in 10–30% of blind biopsies [40]. Thus even a “perfect” fibrosis prediction method may have only moderate observed accuracy in binary classification if single-biopsy histology is used as the reference. Obtaining multiple biopsies may reduce errors in the reference standard, but increases the complication risk and was not feasible in this study. Considering these limitations, moderate accuracy of CCE MR imaging is appropriate and expected. Determination of the true accuracy of fibrosis imaging may require histologic evaluation of larger specimens than those obtained by percutaneous biopsy. Another consideration for the accuracy of biopsy as the reference standard is observer bias [10]. To minimize the observer bias and increase the accuracy of fibrosis staging, this study used the average Metavir score of three hepatopathologists’ independent interpretations as the reference standard. While averaging of an ordinal fibrosis score is less than ideal, it is arguably the most valid fibrosis severity metric available from

a single biopsy specimen. Such a practice is not uncommon in hepatology literature [41–44]. As average Metavir score is expected to preserve the rank-order relationship of the fibrosis severity, it should be sufficient to mathematically construct a valid fibrosis prediction model.

While this study suggested a promising indication for SPIO agents in liver fibrosis imaging, ferumoxides were withdrawn from the US market in 2009. Recently, another intravenously injectable SPIO-based drug, ferumoxytol (Feraheme, AMAG Pharmaceuticals, Lexington, MA) has been FDA-approved for iron-deficiency therapy and early data on its application as contrast agent for MR imaging are promising [45]. While this new drug likely has similar negative-contrast effects in the liver as ferumoxides, further studies will be necessary to evaluate its effectiveness in CCE imaging.

In summary, this proof-of-concept prospective study showed that CCE MR imaging and quantitative texture analysis may permit noninvasive assessment of liver fibrosis in HCV-infected adults. MR image texture is a potential noninvasive biomarker of liver fibrosis and, with further technical refinement and validation, may provide a new tool in clinical management and research in HCV-infected patients.

## Conflict of Interests

The contents of this work are solely the responsibility of the authors and do not necessarily represent the official views of the funding agencies.

## Acknowledgments

This work was funded in part by grants from the Radiological Society of North America R&E Foundation Research Resident Award no. RR0726, the National Institutes of Health NCMHD EXPORT P60 MD00220, and Bayer Healthcare Grant no. 070525.

## References

- [1] K. D. Kochanek, S. L. Murphy, R. N. Anderson, and C. Scott, “Deaths: final data for 2002,” *National Vital Statistics Reports*, vol. 53, no. 5, pp. 1–115, 2004.
- [2] Y.-S. Lim and W. R. Kim, “The global impact of hepatic fibrosis and end-stage liver disease,” *Clinics in Liver Disease*, vol. 12, no. 4, pp. 733–746, 2008.
- [3] S. Vong and B. P. Bell, “Chronic liver disease mortality in the United States, 1990–1998,” *Hepatology*, vol. 39, no. 2, pp. 476–483, 2004.
- [4] G. L. Armstrong, A. Wasley, E. P. Simard, G. M. McQuillan, W. L. Kuhnert, and M. J. Alter, “The prevalence of hepatitis C virus infection in the United States, 1999 through 2002,” *Annals of Internal Medicine*, vol. 144, no. 10, pp. 705–714, 2006.
- [5] I. M. Arias, *The Liver: Biology and Pathobiology*, John Wiley & Sons, Chichester, UK, 5th edition, 2009.
- [6] L. Peters and J. K. Rockstroh, “Biomarkers of fibrosis and impaired liver function in chronic hepatitis C: how well do they predict clinical outcomes?” *Current Opinion in HIV and AIDS*, vol. 5, no. 6, pp. 517–523, 2010.

- [7] G. Germani, P. Hytioglou, A. Fotiadu, A. K. Burroughs, and A. P. Dhillon, "Assessment of fibrosis and cirrhosis in liver biopsies: an update," *Seminars in Liver Disease*, vol. 31, no. 1, pp. 82–90, 2011.
- [8] P. Marcellin, "Hepatitis B and hepatitis C in 2009," *Liver International*, vol. 29, supplement 1, pp. 1–8, 2009.
- [9] P. Bedossa and T. Poynard, "An algorithm for the grading of activity in chronic hepatitis C," *Hepatology*, vol. 24, no. 2, pp. 289–293, 1996.
- [10] "Intraobserver and interobserver variations in liver biopsy interpretation in patients with chronic hepatitis C. The French METAVIR Cooperative Study Group," *Hepatology*, vol. 20, no. 1, part 1, pp. 15–20, 1994.
- [11] J. Perrault, D. B. McGill, B. J. Ott, and W. F. Taylor, "Liver biopsy: complications in 1000 inpatients and outpatients," *Gastroenterology*, vol. 74, no. 1, pp. 103–106, 1978.
- [12] P. Thampanitchawong and T. Piratvisuth, "Liver biopsy: complications and risk factors," *World Journal of Gastroenterology*, vol. 5, no. 4, pp. 301–304, 1999.
- [13] P. Halfon, F. Imbert-Bismut, D. Messous et al., "A prospective assessment of the inter-laboratory variability of biochemical markers of fibrosis (FibroTest) and activity (ActiTest) in patients with chronic liver disease," *Comparative Hepatology*, vol. 1, article 3, 2002.
- [14] E. Rossi, L. Adams, A. Prins et al., "Validation of the FibroTest biochemical markers score in assessing liver fibrosis in hepatitis C patients," *Clinical Chemistry*, vol. 49, no. 3, pp. 450–454, 2003.
- [15] H. Saito, S. Tada, N. Nakamoto et al., "Efficacy of non-invasive elastometry on staging of hepatic fibrosis," *Hepatology Research*, vol. 29, no. 2, pp. 97–103, 2004.
- [16] A. Ziolkowski, M. Wylezol, M. Kukla et al., "The comparison of scoring scales for liver biopsy assessment in morbidly obese patients undergoing bariatric surgery," *Obesity Surgery*, vol. 15, no. 9, pp. 1309–1314, 2005.
- [17] L. Huwart, F. Peeters, R. Sinkus et al., "Liver fibrosis: non-invasive assessment with MR elastography," *NMR in Biomedicine*, vol. 19, no. 2, pp. 173–179, 2006.
- [18] O. Rouvière, M. Yin, M. A. Dresner et al., "MR elastography of the liver: preliminary results," *Radiology*, vol. 240, no. 2, pp. 440–448, 2006.
- [19] M. Yin, J. A. Talwalkar, K. J. Glaser et al., "Assessment of hepatic fibrosis with magnetic resonance elastography," *Clinical Gastroenterology and Hepatology*, vol. 5, no. 10, pp. 1207.e2–1213.e2, 2007.
- [20] C. Aubé, P. X. Racineux, J. Lebigot et al., "Diagnosis and quantification of hepatic fibrosis with diffusion weighted MR imaging: preliminary results," *Journal de Radiologie*, vol. 85, no. 3, pp. 301–306, 2004.
- [21] M. Koinuma, I. Ohashi, K. Hanafusa, and H. Shibuya, "Apparent diffusion coefficient measurements with diffusion-weighted magnetic resonance imaging for evaluation of hepatic fibrosis," *Journal of Magnetic Resonance Imaging*, vol. 22, no. 1, pp. 80–85, 2005.
- [22] J. A. Talwalkar, M. Yin, J. L. Fidler, S. O. Sanderson, P. S. Kamath, and R. L. Ehman, "Magnetic resonance imaging of hepatic fibrosis: emerging clinical applications," *Hepatology*, vol. 47, no. 1, pp. 332–342, 2008.
- [23] G. Elizondo, R. Weissleder, D. D. Stark et al., "Hepatic cirrhosis and hepatitis: MR imaging enhanced with superparamagnetic iron oxide," *Radiology*, vol. 174, no. 3, pp. 797–801, 1990.
- [24] T. Fujita, K. Ito, K. Honjo, H. Okazaki, T. Matsumoto, and N. Matsunaga, "Hepatic parenchymal enhancement in the cirrhotic liver: evaluation by triple-phase dynamic MRI," *Abdominal Imaging*, vol. 27, no. 1, pp. 29–33, 2002.
- [25] K. M. Vitellas, M. T. Tzalonikou, W. F. Bennett, K. K. Vaswani, and J. G. Bova, "Cirrhosis: spectrum of findings on unenhanced and dynamic gadolinium-enhanced MR imaging," *Abdominal Imaging*, vol. 26, no. 6, pp. 601–615, 2001.
- [26] D. A. Aguirre, C. A. Behling, E. Alpert, T. I. Hassanein, and C. B. Sirlin, "Liver fibrosis: noninvasive diagnosis with double contrast material-enhanced MR imaging," *Radiology*, vol. 239, no. 2, pp. 425–437, 2006.
- [27] F. Hughes-Cassidy, A. D. Chavez, A. Schlang et al., "Superparamagnetic iron oxides and low molecular weight gadolinium chelates are synergistic for direct visualization of advanced liver fibrosis," *Journal of Magnetic Resonance Imaging*, vol. 26, no. 3, pp. 728–737, 2007.
- [28] H. Kato, M. Kanematsu, X. Zhang et al., "Computer-aided diagnosis of hepatic fibrosis: preliminary evaluation of MRI texture analysis using the finite difference method and an artificial neural network," *American Journal of Roentgenology*, vol. 189, no. 1, pp. 117–122, 2007.
- [29] G. Bahl, D. A. Aguirre, G. Motta, A. Fotinos, G. Rescinito, and C. Sirlin, "Quantitative texture analysis of liver fibrosis on double-contrast enhanced gradient recalled echo images," in *Proceedings of the RSNA Annual Meeting*, Chicago, Ill, USA, 2005.
- [30] G. Bahl, I. Cruite, T. Wolfson et al., "Noninvasive classification of hepatic fibrosis based on texture parameters from double contrast-enhanced magnetic resonance images," *Journal of Magnetic Resonance Imaging*, vol. 36, no. 5, pp. 1154–1161, 2012.
- [31] P. F. Hahn and S. Saini, "Liver-specific MR imaging contrast agents," *Radiologic Clinics of North America*, vol. 36, no. 2, pp. 287–297, 1998.
- [32] Y. Gandon, J.-F. Heautot, F. Brunet, D. Guyader, Y. Deugnier, and M. Carsin, "Superparamagnetic iron oxide: clinical time-response study," *European Journal of Radiology*, vol. 12, no. 3, pp. 195–200, 1991.
- [33] S. Aime and P. Caravan, "Biodistribution of gadolinium-based contrast agents, including gadolinium deposition," *Journal of Magnetic Resonance Imaging*, vol. 30, no. 6, pp. 1259–1267, 2009.
- [34] M. Y. Park and T. Hastie, " $L_1$ -regularization path algorithm for generalized linear models," *Journal of the Royal Statistical Society B*, vol. 69, no. 4, pp. 659–677, 2007.
- [35] H. Akaike, "A new look at the statistical model identification," *IEEE Transactions on Automatic Control*, vol. 19, no. 6, pp. 716–723, 1974.
- [36] V. Calvaruso, A. K. Burroughs, R. Standish et al., "Computer-assisted image analysis of liver collagen: relationship to Ishak scoring and hepatic venous pressure gradient," *Hepatology*, vol. 49, no. 4, pp. 1236–1244, 2009.
- [37] M. J. O'Brien, N. M. Keating, S. Elderiny et al., "An assessment of digital image analysis to measure fibrosis in liver biopsy specimens of patients with chronic hepatitis C," *The American Journal of Clinical Pathology*, vol. 114, no. 5, pp. 712–718, 2000.
- [38] S. K. Venkatesh and R. L. Ehman, "Magnetic resonance elastography of liver," *Magnetic Resonance Imaging Clinics of North America*, vol. 22, no. 3, pp. 433–446, 2014.
- [39] S. Ichikawa, U. Motosugi, T. Ichikawa et al., "Magnetic resonance elastography for staging liver fibrosis in chronic hepatitis C," *Magnetic Resonance in Medical Sciences*, vol. 11, no. 4, pp. 291–297, 2012.

- [40] D. S. Manning and N. H. Afdhal, "Diagnosis and quantitation of fibrosis," *Gastroenterology*, vol. 134, no. 6, pp. 1670–1681, 2008.
- [41] M. L. Shiffman, R. T. Stravitz, M. J. Contos et al., "Histologic recurrence of chronic hepatitis C virus in patients after living donor and deceased donor liver transplantation," *Liver Transplantation*, vol. 10, no. 10, pp. 1248–1255, 2004.
- [42] J. C. Hoefs, M. L. Shiffman, Z. D. Goodman, D. E. Kleiner, J. L. Dienstag, and A. M. Stoddard, "Rate of progression of hepatic fibrosis in patients with chronic hepatitis C: results from the HALT-C trial," *Gastroenterology*, vol. 141, no. 3, pp. 900.e2–908.e2, 2011.
- [43] A. Monto, S. Kakar, L. M. Dove, A. Bostrom, E. L. Miller, and T. L. Wright, "Contributions to hepatic fibrosis in HIV-HCV coinfecting and HCV monoinfected patients," *The American Journal of Gastroenterology*, vol. 101, no. 7, pp. 1509–1515, 2006.
- [44] R. Malekzadeh, M. Mohamadnejad, and N. Rakhshani, "Reversibility of cirrhosis in chronic hepatitis B," *Clinical Gastroenterology and Hepatology*, vol. 2, no. 4, pp. 344–347, 2004.
- [45] M. R. Bashir, L. Bhatti, D. Marin, and R. C. Nelson, "Emerging applications for ferumoxytol as a contrast agent in MRI," *Journal of Magnetic Resonance Imaging*, 2014.

## Research Article

# Correction for Eddy Current-Induced Echo-Shifting Effect in Partial-Fourier Diffusion Tensor Imaging

Trong-Kha Truong, Allen W. Song, and Nan-kuei Chen

*Brain Imaging and Analysis Center, Duke University Medical Center, 2424 Erwin Road No. 501, Durham, NC 27705, USA*

Correspondence should be addressed to Nan-kuei Chen; [nankuei.chen@duke.edu](mailto:nankuei.chen@duke.edu)

Received 16 August 2014; Accepted 13 October 2014

Academic Editor: Zhengchao Dong

Copyright © 2015 Trong-Kha Truong et al. This is an open access article distributed under the Creative Commons Attribution License, which permits unrestricted use, distribution, and reproduction in any medium, provided the original work is properly cited.

In most diffusion tensor imaging (DTI) studies, images are acquired with either a partial-Fourier or a parallel partial-Fourier echo-planar imaging (EPI) sequence, in order to shorten the echo time and increase the signal-to-noise ratio (SNR). However, eddy currents induced by the diffusion-sensitizing gradients can often lead to a shift of the echo in  $k$ -space, resulting in three distinct types of artifacts in partial-Fourier DTI. Here, we present an improved DTI acquisition and reconstruction scheme, capable of generating high-quality and high-SNR DTI data without eddy current-induced artifacts. This new scheme consists of three components, respectively, addressing the three distinct types of artifacts. First, a  $k$ -space energy-anchored DTI sequence is designed to recover eddy current-induced signal loss (i.e., Type 1 artifact). Second, a multischeme partial-Fourier reconstruction is used to eliminate artificial signal elevation (i.e., Type 2 artifact) associated with the conventional partial-Fourier reconstruction. Third, a signal intensity correction is applied to remove artificial signal modulations due to eddy current-induced erroneous  $T_2^*$ -weighting (i.e., Type 3 artifact). These systematic improvements will greatly increase the consistency and accuracy of DTI measurements, expanding the utility of DTI in translational applications where quantitative robustness is much needed.

## 1. Introduction

Diffusion tensor imaging (DTI) has proven a powerful tool for characterizing alterations of white matter microstructure [1–4]. DTI has been successfully applied to studies of human brain development [5–13] and various neurological and psychiatric diseases [14–16], including bipolar disorder [17, 18], Creutzfeldt-Jakob disease [19], gliomas [20, 21], depression [22], aphasia [23], Parkinson's disease [24], Alzheimer's disease [24, 25], and schizophrenia [23]. In order to quantify these changes (e.g., in terms of the fractional anisotropy or FA), voxel-wise signal variations across images obtained with different sets of diffusion-sensitizing gradients are fitted with a tensor model. It is also possible to fit the acquired data with alternative models that take non-Gaussian components into consideration, making it possible to resolve crossing fibers [26–29].

Since most of the MRI signal is attenuated by strong diffusion-sensitizing gradients, the signal-to-noise ratio (SNR) is inherently low in DTI data. This issue can be addressed

with several approaches. First, the SNR can be improved by averaging multiple magnitude images from repeated DTI scans, at the expense of a prolonged scan time. Second, high-field systems (e.g., 7 Tesla) may be used to generate DTI data with an inherently higher SNR [30]. However, such systems are not available at the majority of clinical sites. Third, the SNR can be increased by shortening the echo time (TE), based on partial-Fourier echo-planar imaging (EPI), parallel imaging, or the combination of both (see Appendix). Another major benefit of using partial-Fourier EPI, instead of full-Fourier EPI, is that the signal decay within the acquisition window can be reduced and thus the point spread function (PSF) can be improved [31]. In fact, partial-Fourier EPI and parallel partial-Fourier EPI have become the most widely used protocols for DTI studies, because of their higher SNR as compared with full-Fourier EPI.

Even though partial-Fourier EPI and parallel partial-Fourier EPI can generate DTI data with a higher SNR, they are susceptible to various types of artifacts related to the  $k$ -space echo-shifting effect. It has been shown that

the echo-shifting effect caused by intrascan head motion may result in artificial signal variations in DTI [32–34]. We have further used  $k$ -space energy spectrum analysis (KESA) to demonstrate that the echo-shifting-induced artificial signal loss (i.e., Type 1 artifact) in partial-Fourier EPI may not be corrected with postprocessing, while the echo-shifting-induced artificial signal elevation (i.e., Type 2 artifact) may be corrected with a multischeme reconstruction algorithm [35].

In addition to intrascan head motion, hardware-related factors (e.g., eddy currents induced by the diffusion-sensitizing gradients; concomitant fields) also produce a pronounced echo-shifting effect [36], which in turn generates three distinct types of artifacts in partial-Fourier DTI data. Even though the eddy currents may be globally reduced through calibrating the gradient preemphasis [37], this calibration may not effectively remove the spatially inhomogeneous eddy currents in different regions. Furthermore, the preemphasis calibration alone may not effectively address different sources of the echo-shifting effect in DTI data. Therefore, it is highly desirable to develop a new empirical approach to effectively remove the spatially inhomogeneous echo-shifting effects resulting from multiple sources. In this report, we will demonstrate that all three types of artifacts caused by the eddy current-induced echo-shifting effect can be effectively eliminated with a new DTI acquisition and reconstruction scheme. By using this improved and comprehensive methodology, high-quality and high-SNR DTI can be achieved reliably.

Since the eddy currents vary significantly among different MRI scanners, the presence of uncorrected eddy current-induced artifacts makes it difficult to achieve consistent diffusion measures in multicenter DTI studies. We thus expect that the improved acquisition and reconstruction methods proposed in this report will also improve the quantitative consistency of DTI measures for translational applications independent of imaging hardware and sites.

## 2. Theory and Methods

**2.1. Quantification of the Echo-Shifting Effect Associated with Diffusion-Sensitizing Gradients in DTI.** Even though most pulse sequences are designed such that the echo is expected to appear at the center of  $k$ -space, the echo may, in reality, deviate from the  $k$ -space center for different reasons. For example, susceptibility-induced magnetic field gradients may result in an echo displacement or echo-shifting effect in gradient-echo sequences [38–41], whereas intrascan head motion may result in an echo-shifting effect in spin-echo EPI-based DTI [34]. As shown in our previous paper, the echo-shifting effect along the phase-encoding direction resulting from intrascan head motion may result in Type 1 and Type 2 artifacts [35].

Here we will show that, in addition and similar to intrascan head motion, the eddy currents induced by strong diffusion-sensitizing gradients in DTI also produce a pronounced echo-shifting effect. For example, Figure 1(a) shows the central portions ( $16 \times 16$ ) of partial-Fourier DTI  $k$ -space data (with an acquisition matrix size of  $96 \times 76$ ) obtained from a spherical gel phantom on a 3 Tesla MRI scanner

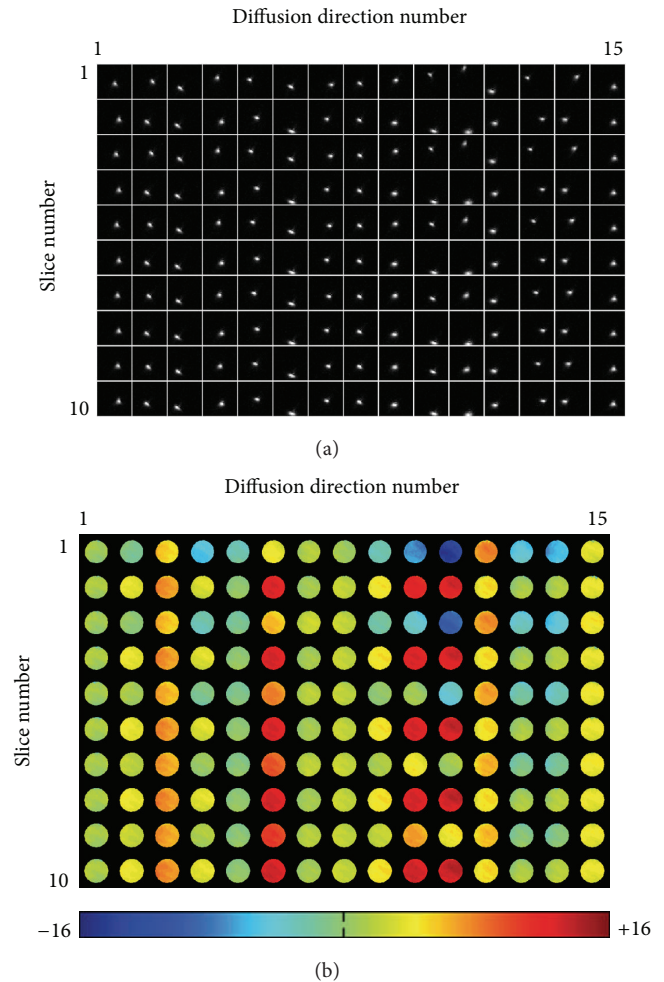


FIGURE 1: (a) The central portion of partial-Fourier DTI  $k$ -space data shows that the eddy current-induced echo-shifting effect varies with the diffusion-encoding direction and slice number. (b) The corresponding echo displacement maps, reflecting the spatially dependent echo-shifting effect along the phase-encoding direction, can be derived from the  $k$ -space energy spectrum analysis.

(General Electric, Waukesha, WI, USA) with 15 diffusion-encoding directions, illustrating the impact of diffusion-sensitizing gradients on the echo-shifting effect along both readout (horizontal) and phase-encoding (vertical) directions. As demonstrated in the subsequent sections, the echo-shifting effect along the phase-encoding direction results in undesirable artifacts. Other scan parameters used in this single-refocused spin-echo DTI scan are listed in Section 2.5 (with only the first 10 slices shown in Figure 1).

Note that Figure 1(a) mainly shows the  $k$ -space echo distribution corresponding to the summed signals from all voxels in an individual slice but does not reveal the spatially dependent echo-shifting effect. In order to quantify the  $k$ -space energy displacement corresponding to different voxels, the KESA method should be employed (as described in [35, 40, 41]). This method can be summarized as a three-step procedure. First,  $N_y$  images are generated from the same  $N_x \times N_y$  2D  $k$ -space data by replacing different numbers

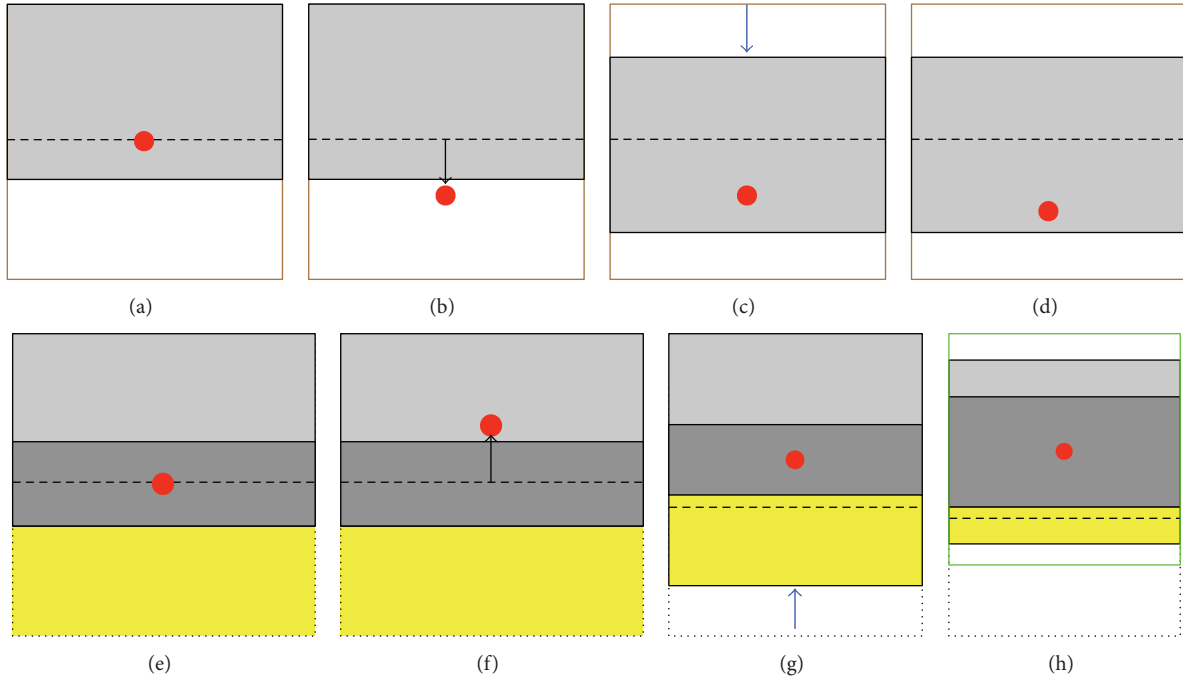


FIGURE 2: (a) The echo energy peak (indicated by the red dot) is expected to appear at the center of the targeted  $k$ -space coverage (enclosed by the solid black and brown lines) for partial-Fourier EPI (with the gray area representing the acquired data). (b) In the presence of an echo-shifting effect, the echo energy peak may be shifted outside the  $k$ -space acquisition area, resulting in signal loss (i.e., Type 1 artifact). (c) By using the proposed  $k$ -space energy-anchored pulse sequence, the  $k$ -space acquisition area (indicated by the gray rectangle) moves along with the eddy current-induced echo-shifting effect, avoiding Type 1 artifacts. (d) Even though the echo-shifting effect corresponding to different voxels within a slice may vary slightly, Type 1 artifacts can still be avoided as long as the echo energy peak remains within the  $k$ -space acquisition area. (e) The central  $k_y$  band (indicated by the dark gray rectangle) can provide phase references to estimate the signals in the omitted region (indicated by a yellow rectangle) in partial-Fourier reconstruction. (f) When the echo energy peak is shifted outside the central  $k_y$  band (while remaining within the  $k$ -space acquisition area), artificial signal elevation (i.e., Type 2 artifact) appears in the reconstructed images. (g) Type 2 artifacts may be reduced or even eliminated in data obtained with the  $k$ -space energy-anchored sequence. (h) Because of the spatially dependent echo-shifting effect, the echo energy peaks corresponding to different voxels within a slice may be shifted variably. In this case, the location of the central  $k_y$  band should be redefined (in postprocessing), according to the spatially dependent echo-shifting effect, to minimize Type 2 artifacts.

$n = 1, 2, 3, \dots, N_y$  of  $k_y$  echo-lines with the values predicted from the remaining  $N_y - n$  lines based on partial-Fourier reconstruction. Second, for a particular voxel, the signal variations across these  $N_y$  images are analyzed to identify the image that has the largest signal difference as compared with its neighboring images. As described in our previous papers, the echo-shifting effect associated with this particular voxel is equal to the number of truncated  $k_y$  lines in the identified image [40]. Third, a  $k$ -space energy displacement map, reflecting the echo-shifting effect for all voxels, can be obtained by repeating the second step for all voxels in the chosen slice.

Figure 1(b) shows the image-domain distribution of the  $k$ -space energy displacement along the phase-encoding direction (i.e.,  $\Delta k_y$  maps) obtained from the phantom DTI data. It can be seen that the echo-shifting effect is relatively uniform within each slice but varies significantly with the diffusion-encoding direction. In addition, for a particular diffusion-encoding direction (e.g., direction number 11), the echo-shifting effect varies more significantly among the odd slices (which were acquired first in this interleaved acquisition)

than among the even slices, likely because the eddy currents have not yet reached a steady-state. Although the echo-shifting effect along the readout direction may also be quantified with the KESA method, it does not result in partial-Fourier DTI artifacts and thus is not quantified in this paper.

**2.2. Correction for Type 1 Artifacts in Partial-Fourier DTI with  $k$ -Space Energy-Anchored Acquisition.** In the absence of an eddy current-induced echo-shifting effect, the  $k$ -space energy peak (as schematically indicated by a red circle in Figure 2(a)) appears at the center of the targeted  $k$ -space coverage, where only a certain portion (gray area in Figure 2(a)) is acquired with partial-Fourier DTI. When there exists a pronounced echo-shifting effect due to eddy currents, the  $k$ -space energy peak may be shifted outside the acquisition window (Figure 2(b)), resulting in unrecoverable signal loss *post hoc*, which is termed Type 1 artifact. Here, we propose to address this issue with a  $k$ -space energy-anchored DTI acquisition approach. With a prior knowledge of the eddy current-induced echo-shifting effect, the prephasing

gradient amplitude along the phase-encoding direction is modified such that the targeted  $k$ -space coverage moves with the  $k$ -space energy displacement (Figure 2(c)), thereby avoiding Type 1 artifacts. Note that different prephasing gradient values are used for different slices and different diffusion-encoding directions according to the corresponding echo-shifting effect. Since the eddy currents are subject-independent, this sequence may be optimized based on infrequently performed phantom calibration scans, where the echo-shifting effect corresponding to different slices and diffusion-encoding directions is quantified with the KESA method. Note that the infrequently performed phantom scan (e.g., once every 6 or 12 months) does not increase the clinical scan time and is thus practical for clinical utilization [42]. The eddy currents are spatially varying, so that the  $k$ -space energy peaks originating from different voxels within a slice may not always be refocused exactly at the center of the targeted  $k$ -space coverage (e.g., Figure 2(d)). Nevertheless, the variation of the echo-shifting effect corresponding to different voxels within an individual slice is insignificant (see Figure 1(b)), and Type 1 artifacts can be avoided as long as the  $k$ -space energy peaks remain within the acquired  $k$ -space.

**2.3. Correction for Type 2 Artifacts in Partial-Fourier DTI with  $k$ -Space Energy-Anchored Acquisition and Multischeme Partial-Fourier Reconstruction.** In partial-Fourier DTI, the intentionally omitted  $k$ -space data (yellow area in Figure 2(e)) can be estimated from the acquired data (light and dark gray areas in Figure 2(e)) by using partial-Fourier reconstruction, where the  $k$ -space data from the central band (dark gray area in Figure 2(e)) provide phase references. However, when the  $k$ -space energy peaks are shifted outside the central band due to eddy currents (Figure 2(f)), the conventional partial-Fourier reconstruction based on these phase references may result in an artificial signal elevation, termed Type 2 artifact. By using a  $k$ -space energy-anchored pulse sequence, Type 2 artifacts can be reduced or even potentially eliminated as schematically shown in Figure 2(g). However, since the eddy currents are spatially varying, the  $k$ -space energy peaks from certain brain regions may be located outside the central band even with a  $k$ -space energy-anchored acquisition, resulting in spatially variable Type 2 artifacts.

To address this issue, we propose to integrate the  $k$ -space energy-anchored acquisition and our previously developed multischeme partial-Fourier reconstruction [35], which can be summarized as a two-step procedure. First, the KESA method is used to identify the  $k$ -space energy peak locations corresponding to different voxels in the human brain DTI data obtained with the  $k$ -space energy-anchored pulse sequence. Second, for a particular voxel, the position and width of the central  $k$ -space band used for phase references in the partial-Fourier reconstruction are chosen based on the corresponding echo-shifting effect (measured from the KESA  $\Delta k_y$  maps derived in the first step) to ensure that the echo peak is located at the center of the central band. Even though the effective spatial resolution along the phase-encoding direction varies spatially as a result of the echo-shifting effect inherent to DTI scans, images obtained from multischeme

partial-Fourier reconstruction may be interpolated to the same spatial resolution. For example, the  $k$ -space data to be reconstructed with the scheme shown in Figure 2(h) can be zero-filled to the area enclosed by the green square.

**2.4. Correction for Type 3 Artifacts in Partial-Fourier DTI with Signal Intensity Correction.** It is well known that the echo-shifting effect in gradient-echo EPI results in variations of the effective TE and  $T_2^*$ -weighting, which in turn produce undesirable signal variations [39]. Similarly, the echo-shifting effect in spin-echo EPI also results in an additional and erroneous  $T_2^*$ -weighting, producing undesirable signal variations. Even though such signal variations may not be very significant in individual diffusion-weighted images, they actually result in severe artifacts when multiple images are combined to derive diffusion measures such as FA maps (as will be shown in the Results section). As schematically illustrated in Figure 3(a) and (1), the signal intensity ( $S_{se}$ ) of spin-echo EPI-based DTI data depends on the TE as a function of a  $T_2$  exponential decay (as indicated by a black dashed line in Figure 3(a)):

$$S_{se} = S_0 \cdot \exp\left(-\frac{TE}{T_2}\right). \quad (1)$$

In the presence of an eddy current-induced echo-shifting effect, the effective TE ( $TE_{eff}$ ) differs from the targeted spin-echo TE and the generated echoes have both  $T_2$ - and  $T_2'$ -weighting (i.e., the spin-echo becomes an asymmetric spin-echo), as schematically shown in Figure 3(b). The asymmetric spin-echo signal intensity ( $S_{ase}$ ) can be represented by either (2) or (3), where  $\Delta TE = TE_{eff} - TE$ , depending on the direction of the echo displacement (see Figure 3(b)):

$$S_{ase;R} = S_0 \cdot \exp\left(-\frac{TE + \Delta TE}{T_2}\right) \cdot \exp\left(-\frac{\Delta TE}{T_2'}\right); \quad (2)$$

for  $\Delta TE > 0$

$$S_{ase;L} = S_0 \cdot \exp\left(-\frac{TE + \Delta TE}{T_2}\right) \cdot \exp\left(\frac{\Delta TE}{T_2'}\right); \quad (3)$$

for  $\Delta TE < 0$ .

Equations (2) and (3) can be reformatted to (4) and (5), respectively:

$$S_{ase;R} = S_{se} \cdot \exp\left(-\Delta TE \left(\frac{1}{T_2} + \frac{1}{T_2'}\right)\right); \quad \text{for } \Delta TE > 0, \quad (4)$$

$$S_{ase;L} = S_{se} \cdot \exp\left(-\Delta TE \left(\frac{1}{T_2} - \frac{1}{T_2'}\right)\right); \quad \text{for } \Delta TE < 0. \quad (5)$$

The signal reduction (from  $S_{se}$  to  $S_{ase}$ ) resulting from the echo-shifting effect in DTI is termed Type 3 artifact and can be corrected by dividing the acquired signal intensity of each voxel by either  $\exp(-\Delta TE/T_2^*)$  for  $\Delta TE > 0$  or  $\exp(-\Delta TE/T_2^-)$  for  $\Delta TE < 0$ , where  $1/T_2^* = 1/T_2 + 1/T_2'$  and  $1/T_2^- = 1/T_2 - 1/T_2'$  [43]. Note that  $\Delta TE$  is spatially variable and is computed as the product of the EPI echo-spacing time and  $\Delta k_y$ , which is measured with the KESA method from the human DTI  $k$ -space data.

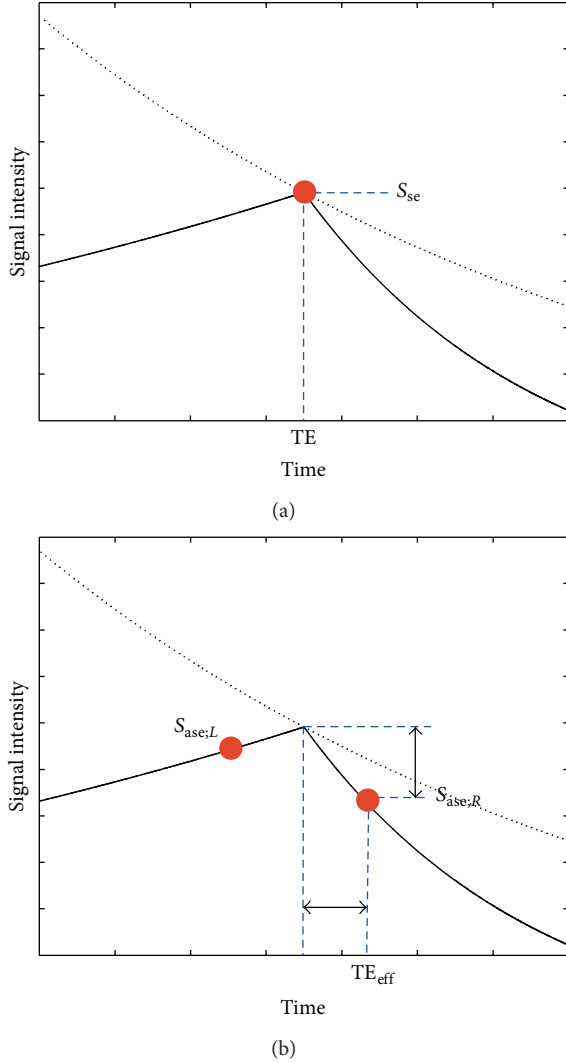


FIGURE 3: (a) The spin-echo DTI signal (indicated by the red dot) varies with the echo time according to a  $T_2$  decay curve (indicated by the dashed curve). (b) In the presence of an echo-shifting effect, the DTI signal is reduced by an additional  $T_2'$ -weighting.  $S_{se}$  = spin-echo signal intensity (1),  $S_{ase,R}$  = asymmetric spin-echo signal intensity for  $\Delta TE > 0$  (4),  $S_{ase,L}$  = asymmetric spin-echo signal intensity for  $\Delta TE < 0$  (5). The horizontal arrow represents  $\Delta TE$  and the vertical arrow represents the signal reduction from Type 3 artifacts (see text for details).

**2.5. Phantom Experiments and Implementation of the  $k$ -Space Energy-Anchored DTI Pulse Sequence.** DTI data were obtained from a spherical gel phantom on a 3 Tesla MRI scanner by using a single-refocused spin-echo partial-Fourier EPI sequence (i.e., with a Stejskal-Tanner diffusion preparation scheme) with the following scan parameters: TR = 4 s, TE = 103 ms, acquisition matrix size =  $96 \times 76$  (i.e., partial-Fourier EPI with 28 overscans), voxel size =  $(2.5 \text{ mm})^3$ ,  $b = 1000 \text{ s/mm}^2$ , diffusion gradient amplitude = 40 mT/m,  $\delta = 22 \text{ ms}$ ,  $\Delta = 26 \text{ ms}$ , inter- $k_y$  echo-spacing time = 0.944 ms, 20 slices, and 15 diffusion-encoding directions. The acquired data were analyzed with the KESA method to quantify

the echo-shifting effect corresponding to different slices and diffusion-encoding directions. Based on the derived KESA  $\Delta k_y$  maps (Figure 1(b)), a  $k$ -space energy-anchored partial-Fourier EPI pulse sequence, with its phase-encoding prephasing gradient appropriately adjusted across slices and diffusion-encoding directions, was then implemented to minimize Type 1 artifacts.

**2.6. Human Data Acquisition and Analysis.** The proposed DTI acquisition and reconstruction methods were evaluated in three healthy volunteers on our 3 Tesla MRI scanner. Participants gave written informed consent for a protocol approved by the institutional review board of Duke University Medical Center. Six sets of DTI data were acquired from each participant by using both the conventional partial-Fourier EPI and the new  $k$ -space energy-anchored partial-Fourier EPI sequences, with three different acquisition matrix sizes:  $96 \times 64$  (i.e., 16 overscans),  $96 \times 60$  (i.e., 12 overscans), and  $96 \times 56$  (i.e., 8 overscans) at TE = 82, 75, and 66 ms, respectively. Other scan parameters were identical to those used in the phantom scan.

The conventional partial-Fourier EPI data were reconstructed with Cuppen's algorithm [44]. The  $k$ -space energy-anchored EPI data (with Type 1 artifacts inherently eliminated) were reconstructed with the KESA-based multischeme partial-Fourier reconstruction method to correct for Type 2 artifacts, and the signal intensity correction was subsequently performed to minimize Type 3 artifacts. The signal intensity correction assumed average values of  $T_2 = 80 \text{ ms}$  and  $T_2^* = 47 \text{ ms}$  for white matter at 3 T [45]. However, note that, even for a  $\pm 5 \text{ ms}$  variation in  $T_2$  and  $T_2^*$  values, the correction factors would only vary by about 3% for the largest eddy current-induced echo shift measured. Even though Cuppen's method was used in the current implementation of the multischeme reconstruction, other types of partial-Fourier reconstruction algorithm (e.g., homodyne reconstruction) can also be used in our multischeme reconstruction.

The consistency in the FA maps derived from the three conventional DTI data sets acquired with different matrix sizes was assessed by calculating the root mean square errors between all three possible pairs of FA maps (i.e., 16 versus 12 overscans; 12 versus 8 overscans; and 16 versus 8 overscans) and by subsequently averaging these three values. This procedure was then repeated for the three  $k$ -space energy-anchored DTI data sets acquired with different matrix sizes to assess the FA consistency in the improved DTI scheme.

We also acquired conventional partial-Fourier DTI data with a larger matrix size of  $96 \times 76$  (i.e., 28 overscans) at TE = 103 ms. Four repeated scans were performed, so that the reconstructed magnitude data could be averaged to improve the SNR. Note that this data set, with a large number of overscans, has inherently low levels of Type 1 and Type 2 artifacts, even when processed with the conventional partial-Fourier reconstruction algorithm. Type 3 artifacts are also inherently lower in this data set acquired at a longer TE. Nevertheless, the very minor residual Type 2 and Type 3 artifacts were corrected with the multischeme partial-Fourier reconstruction and signal intensity correction, respectively, before averaging the four sets of magnitude images. The FA

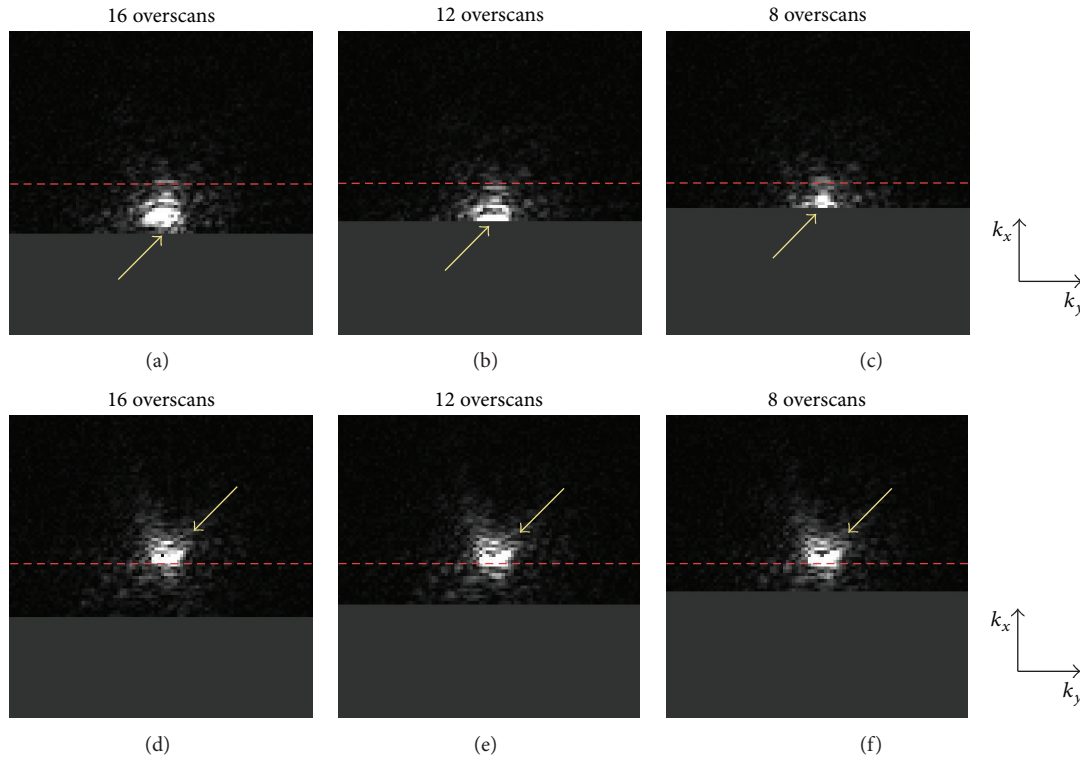


FIGURE 4: (a) to (c) show that the  $k$ -space data obtained with the conventional partial-Fourier DTI sequence, corresponding to different numbers of overscans, may be affected by a truncation artifact (i.e., Type 1 artifact) in the presence of an eddy current-induced echo-shifting effect. (d) to (f) show that this truncation artifact can be avoided in partial-Fourier DTI data obtained with the proposed  $k$ -space energy-anchored pulse sequence, where the  $k$ -space coverage moves with the echo-shifting effect.

map generated from this averaged data set was then used as a reference to assess the accuracy of the other FA maps obtained at shorter TEs.

### 3. Results

Figure 4 compares diffusion-weighted EPI  $k$ -space data obtained from a representative subject using the conventional partial-Fourier acquisition scheme (top row) and the new  $k$ -space energy-anchored partial-Fourier acquisition scheme (bottom row) with different numbers of overscans (shown in three columns). This figure shows that, because of the eddy current-induced echo-shifting effect, the  $k$ -space energy peaks can easily be truncated in conventional partial-Fourier EPI, particularly with fewer overscans. Even though such an undesirable  $k$ -space energy truncation can potentially be avoided by using many overscans (e.g., full-Fourier or near full-Fourier EPI), the resultant SNR would be significantly reduced. On the other hand, by using the proposed  $k$ -space energy-anchored acquisition approach, the  $k$ -space energy peaks are consistently located at the center of the targeted  $k$ -space coverage, so that the  $k$ -space energy truncation can be minimized regardless of the number of overscans to avoid signal losses and ensure a high SNR.

Figure 5 compares diffusion-weighted images obtained with conventional partial-Fourier EPI (top row) and the

improved acquisition and reconstruction methods (middle and bottom rows). Because of the echo-shifting effect in conventional partial-Fourier EPI, the images acquired with fewer overscans are significantly degraded by unrecoverable signal loss (i.e., Type 1 artifacts, as indicated by arrows in the top row). When reconstructing the  $k$ -space energy-anchored EPI data with the conventional Cuppen's algorithm, the resulting images are free from Type 1 artifacts but are still susceptible to artificial signal elevation (i.e., Type 2 artifacts) in several regions, as shown in the orange boxes in the middle row. Both Type 1 and Type 2 artifacts can be effectively eliminated when the  $k$ -space energy-anchored EPI data are reconstructed with the recently developed multischeme partial-Fourier reconstruction algorithm, as shown in the bottom row.

Figure 6 further illustrates the image quality improvement obtained after correcting for Type 3 artifacts, in addition to Type 1 and Type 2 artifacts. The top row of Figure 6 shows FA maps derived from conventional partial-Fourier EPI data acquired with three different numbers of overscans. As expected, the FA map with the fewest overscans has the most pronounced artifacts. As shown in the middle row of Figure 6, the FA maps are much more consistent when Type 1 and Type 2 artifacts are removed with the  $k$ -space energy-anchored acquisition and multischeme partial-Fourier reconstruction, respectively. However, there still exist

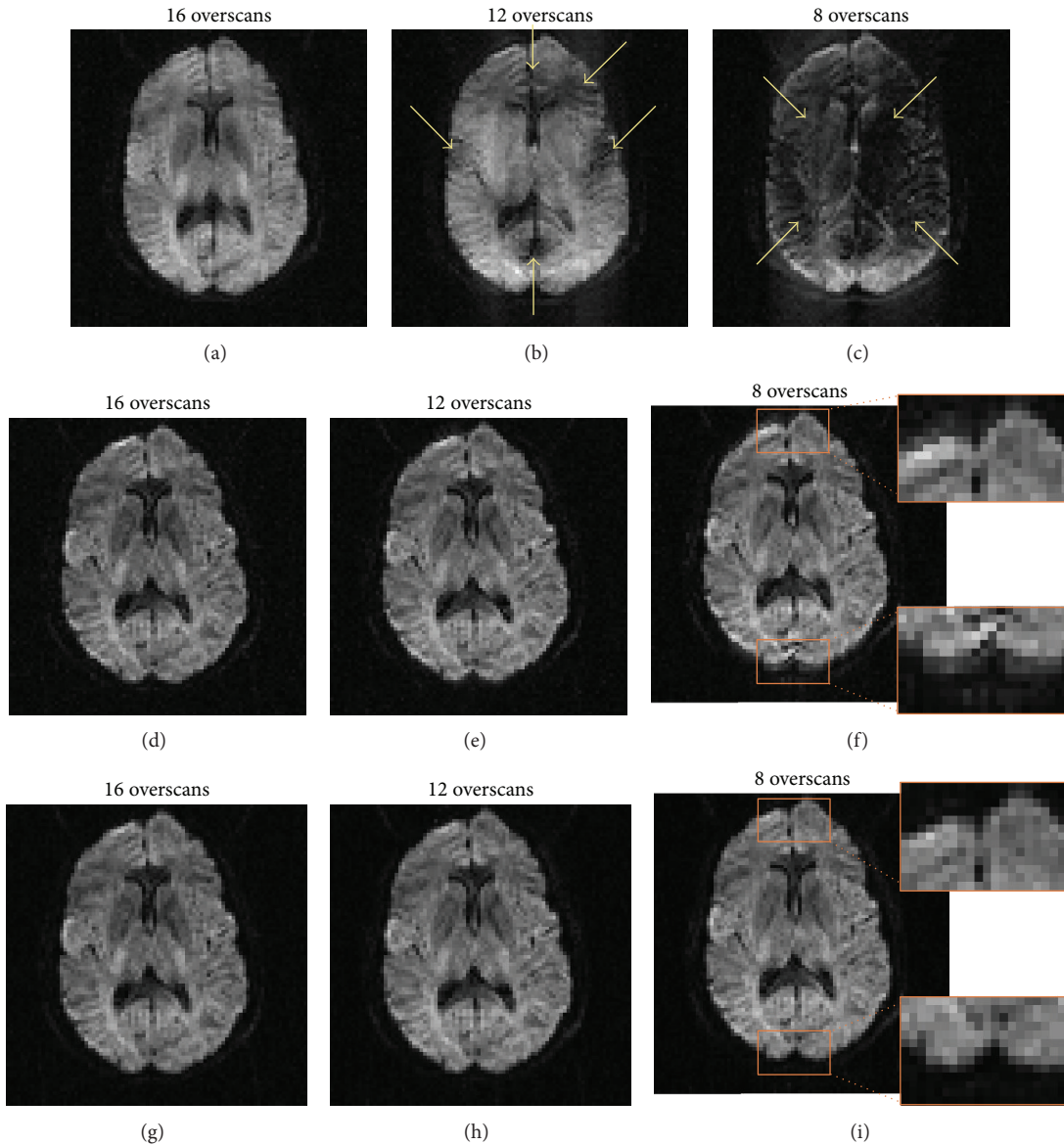


FIGURE 5: (a) to (c) show that the conventional partial-Fourier diffusion-weighted images are degraded by Type 1 artifacts, particularly for data obtained with a smaller number of overscans. (d) to (f) show that Type 1 artifacts can be avoided in data obtained with the *k*-space energy-anchored DTI sequence and reconstructed with the conventional partial-Fourier algorithm. However, artificial signal elevation (i.e., Type 2 artifact) appears in several regions. (g) to (i) show that both Type 1 and Type 2 artifacts can be eliminated when the multischeme partial-Fourier reconstruction algorithm is used to reconstruct the data acquired with the *k*-space energy-anchored pulse sequence.

errors in several areas (e.g., the red color indicated by arrows) due to signal intensity variations across different diffusion-encoding directions (i.e., Type 3 artifacts). After correcting for these residual artifacts, more consistent and accurate FA maps can be obtained from *k*-space energy-anchored EPI data for all numbers of overscans, based on the following assessments.

First, the averaged values of root mean squares, reflecting the FA inconsistency across the data obtained with different numbers of overscans, are 0.31 for conventional DTI (i.e., the top row of Figure 6), 0.13 for *k*-space energy-anchored DTI with Type 1 and Type 2 artifacts removed (i.e., the middle row

of Figure 6), and 0.13 for *k*-space energy-anchored DTI with all three types of artifacts removed (i.e., the bottom row of Figure 6). In other words, as compared with the conventional partial-Fourier DTI, the level of FA consistency is improved by 58% after artifact correction using the developed methods.

Second, the FA inaccuracy in the nine FA maps shown in Figures 6(a) to 6(i), estimated by their root mean square errors relative to the low-artifact reference scan (i.e., with 28 overscans and 4 averages), is (a) 0.19, (b) 0.24, (c) 0.43, (d) 0.19, (e) 0.22, (f) 0.25, (g) 0.18, (h) 0.21, and (i) 0.24. In other words, as compared with the conventional partial-Fourier DTI, the accuracy level can be improved by 5.2%

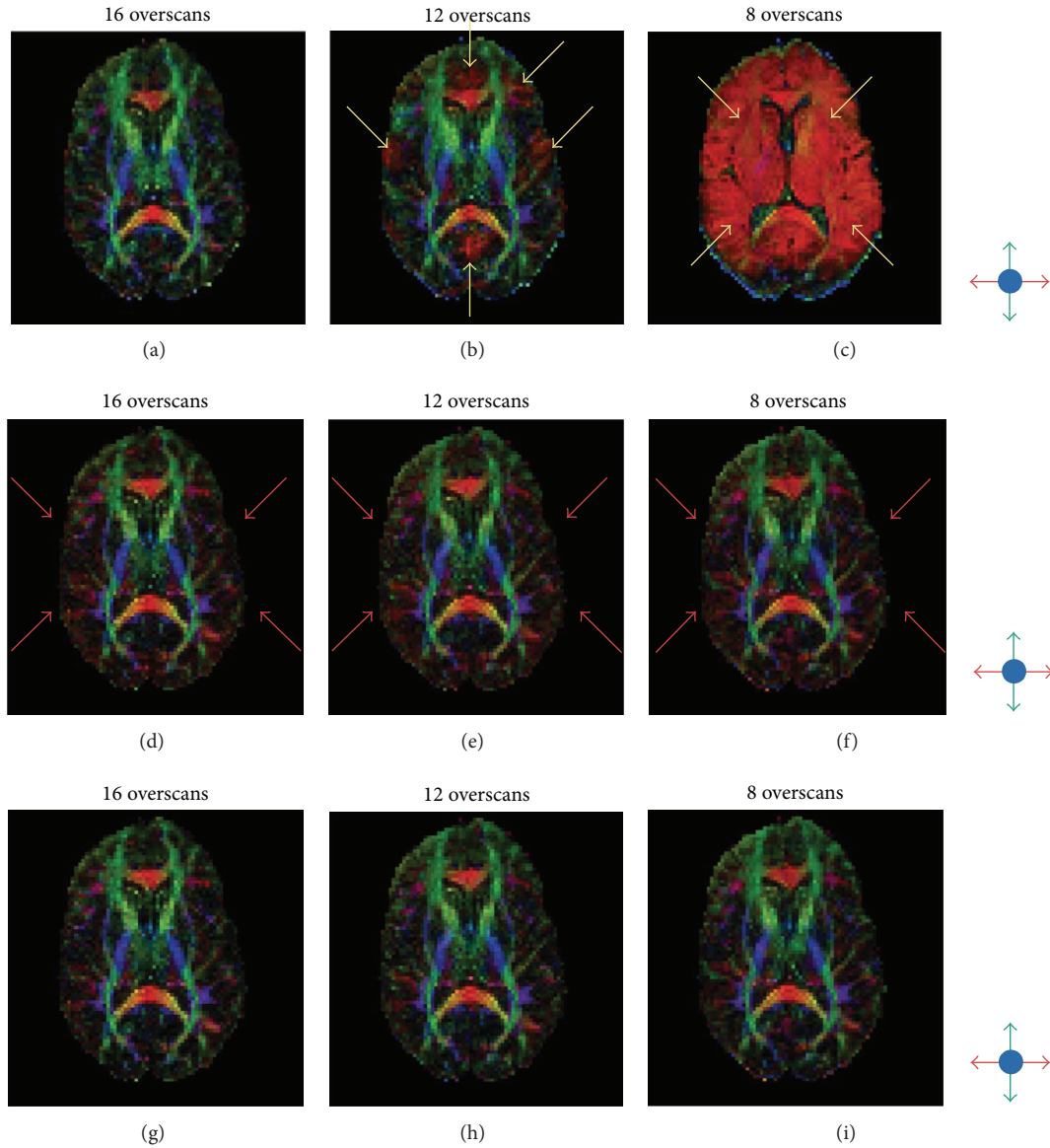


FIGURE 6: (a) to (c) show that the FA maps obtained with conventional partial-Fourier DTI and different numbers of overscans are highly inconsistent, due to the echo-shifting-induced Type 1 and Type 2 artifacts. (d) to (f) show that more consistent FA maps, across data acquired with different numbers of overscans, can be obtained after correcting for Type 1 and Type 2 artifacts. (g) to (i) show that the accuracy, quality, and consistency level can be further improved after correcting for Type 3 artifacts.

(for 16 overscans) to 44.2% (for 8 overscans) by using the improved acquisition and reconstruction scheme.

Third, it can be seen that the FA map obtained at short TE with the proposed DTI scheme (Figure 6(i)) has a higher SNR as compared with the FA maps obtained at long TE (Figures 6(a) and 6(g)), which appear to be more pixelated. Altogether, these results demonstrate that the artifacts caused by the eddy current-induced echo-shifting effect in partial-Fourier DTI can be effectively reduced with the new acquisition and reconstruction scheme, making it possible to simultaneously achieve high-quality and high-SNR DTI scans based on partial-Fourier EPI.

#### 4. Discussion

The eddy currents and resulting DTI artifacts not only change with imaging parameters (e.g., TR, TE, diffusion-sensitizing gradient settings, number of overscans in partial-Fourier DTI), but also vary significantly from scanner to scanner, even when using identical scan parameters. As a result, eddy current-induced artifacts always contribute to the variations in diffusion measures across multiple scanners, making it difficult to design a standardized diagnostic DTI protocol that is consistent across multiple centers if only conventional acquisition and reconstruction methods are used. Here, we report

an improved DTI acquisition and reconstruction scheme to minimize three distinct types of eddy current-induced artifacts existing in conventional partial-Fourier DTI. As demonstrated in this paper, when using the proposed DTI scheme, more consistent and accurate diffusion measures can be obtained from DTI scans acquired with different levels of eddy currents. We believe that the developed methods should prove highly valuable for generating reliable and consistent DTI data for translational applications and in multicenter trials.

Both Type 1 and Type 2 artifacts can inherently be minimized in full-Fourier DTI and conventional partial-Fourier DTI with a large number of overscans, however at the expense of an unavoidably longer TE and thus lower SNR (see Appendix). On the other hand, conventional partial-Fourier DTI data obtained with a smaller number of overscans have a higher SNR but are more susceptible to eddy current-induced artifacts. By using the DTI acquisition and reconstruction scheme presented in this paper, it is feasible to produce high-quality and high-SNR data with minimal eddy current-induced artifacts. Note that the goal of this paper is not to identify a universal set of DTI parameters (e.g., number of overscans) that optimizes both SNR and image quality, as the optimal parameters may vary for different DTI applications. The purpose of this paper is to demonstrate that it is feasible to minimize eddy current-induced artifacts in high-SNR partial-Fourier EPI with an improved acquisition and reconstruction scheme, rather than choosing a conventional full-Fourier or near full-Fourier DTI protocol that produces data with a lower SNR.

The  $k$ -space energy-anchored DTI pulse sequence, designed to eliminate Type 1 artifacts, relies on calibration data measured from a phantom scan. Since the eddy currents are relatively reproducible, these phantom calibration scans can be performed very infrequently (e.g., once every 6 or 12 months). Type 2 and Type 3 artifacts, on the other hand, are removed in postprocessing based on the information derived with the KESA method from the human brain DTI data. In addition to Type 1, Type 2, and Type 3 artifacts, eddy currents also result in geometric distortions and blurring artifacts, which we did not address in this work (e.g., the edge artifacts in the FA maps shown in Figure 6). However, additional distortion correction procedures may be incorporated to further remove such artifacts [46].

In this initial implementation, we used a phantom calibration with the same parameters (slice orientation, b-factor, diffusion-encoding directions, etc.) as the DTI scans to measure the eddy current-induced echo shifts. However, to avoid the need for a protocol-specific calibration and to increase the practical utility of the proposed method, future implementations may potentially use a single calibration to model the eddy currents and to compute the resulting echo shifts for different DTI protocols, as recently proposed for the correction of eddy current-induced distortions [47, 48].

It has been shown that the eddy currents can be reduced with a twice-refocused spin-echo DTI sequence [49, 50]. In this sequence, the diffusion-sensitizing gradient waveforms are designed to minimize eddy currents with intermediate decay rates, which contribute the most to temporal phase

variations within the acquisition window and thus to geometric distortions in EPI [49]. However, eddy currents with short and long decay rates, which contribute significantly to the phase error accumulated prior to the EPI acquisition window and thus to the echo-shifting effect, may not always be nulled in twice-refocused spin-echo EPI. In this case, the improved DTI methods presented in this paper can also be applied to effectively remove the echo-shifting-induced artifacts in twice-refocused spin-echo DTI.

Finally, in this report, we only demonstrate artifact removal in partial-Fourier EPI data as a proof of concept. The proposed  $k$ -space energy-anchored acquisition and improved reconstruction procedures can be readily extended to parallel partial-Fourier EPI, where eddy currents produce the same three distinct types of artifacts.

## 5. Conclusions

In conclusion, we have developed an improved DTI acquisition and reconstruction methodology to effectively remove three distinct types of eddy current-induced artifacts commonly observed in conventional partial-Fourier DTI. We have also demonstrated that this new methodology can simultaneously achieve high-SNR and high-quality partial-Fourier DTI with a small number of overscans. This method is expected to greatly improve the quantitative consistency of DTI measures across subjects and sites, thereby extending the utility of DTI in translational applications at large.

## Appendix

We have performed a numerical analysis to compare the SNR per unit scan time corresponding to different acquisition schemes and to illustrate the need for using either partial-Fourier or parallel partial-Fourier EPI to improve the SNR per unit scan time, particularly for imaging tissues with short  $T_2$  components (e.g., myelin) [51]. Our analysis was performed based on actual imaging parameters obtained from our 3T GE system, using a well-known principle that the SNR per unit scan time in 2D imaging mainly depends on three factors: (1) the effective TE, (2) the number of phase-encoding steps, and (3) the minimally allowed TR. Basically, the SNR decays exponentially with the effective TE and is proportional to the square root of the number of acquired  $k_y$ -lines (for a fixed voxel size). The SNR per unit scan time can then be subsequently estimated according to the minimal TR allowed, which is always much longer than the tissue  $T_1$  value for whole-brain DTI scans.

We have performed numerical simulations with different combinations of commonly used DTI scan parameters and have observed similar benefits of using partial-Fourier scans. For example, for whole-brain DTI scans with in-plane matrix size  $128 \times 128$ , FOV  $24 \times 24$  cm,  $b$ -value  $1000 \text{ s/mm}^2$ , and slice thickness 2 mm, the relative SNR per unit scan time achieved with partial-Fourier EPI with different numbers of overscans (in reference to full-Fourier DTI, i.e., to the data point with 64 overscans) is shown by the blue curve in Figure 7(a), where the white matter  $T_2$  value is assumed to be 80 ms. The SNR

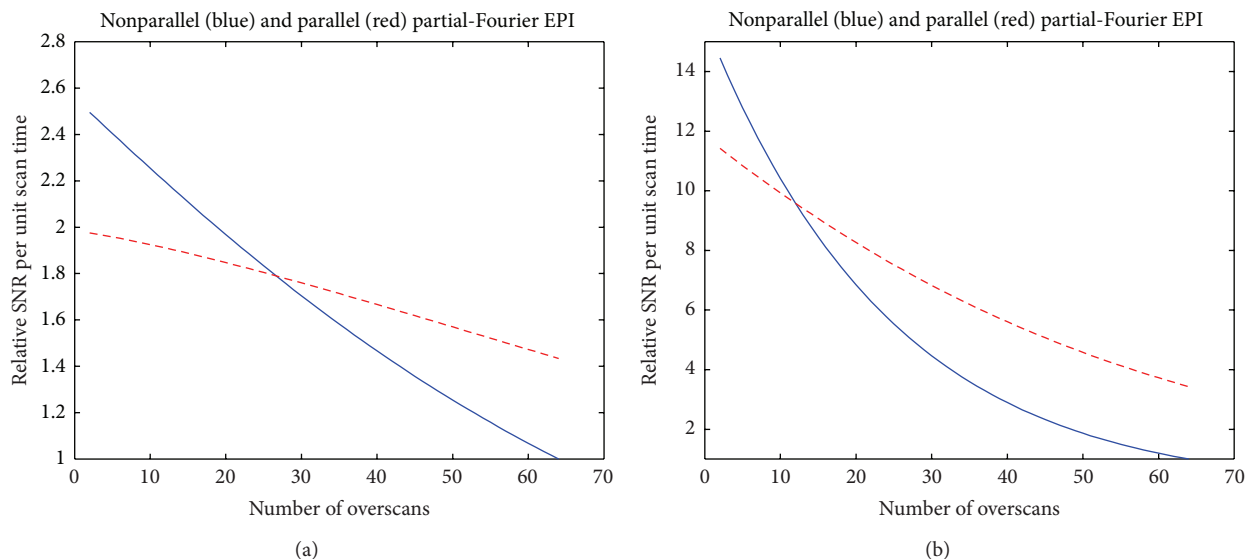


FIGURE 7: (a) The dependence of the relative SNR per unit scan time on the number of overscans for partial-Fourier EPI (blue curve) and parallel partial-Fourier EPI (red curve) of white-matter tissue ( $T_2 = 80$  ms). (b) The dependence of the relative SNR per unit scan time on the number of overscans for partial-Fourier EPI (blue curve) and parallel partial-Fourier EPI (red curve) of myelin ( $T_2 = 30$  ms).

per unit scan time can be improved by more than 2-fold when using a small number of overscans (e.g., <10). The SNR per unit scan time achieved with parallel partial-Fourier DTI (with an acceleration factor of 2) corresponding to different numbers of overscans is shown by the red dashed curve in Figure 7(a) (also in reference to nonparallel full-Fourier DTI), illustrating that it is also beneficial to use a smaller number of overscans for parallel DTI.

Our numerical analysis further shows that the benefit of using DTI with a smaller number of overscans is even more pronounced for detecting the myelin signals (with  $T_2$  value < 35 ms). When assuming the tissue  $T_2$  value to be 30 ms, the SNRs per unit scan time for partial-Fourier DTI and parallel partial-Fourier DTI are shown by the blue and red curves in Figure 7(b), respectively. The SNR per unit scan time can be improved by more than 10-fold (in reference to full-Fourier DTI) when choosing a smaller number of overscans (e.g., <10) for imaging myelin.

### Conflict of Interests

The authors (Trong-Kha Truong, Allen W. Song, and Nan-kuei Chen), being the inventors of a patent application “MRI data acquisition, reconstruction and correction methods for diffusion weighted imaging (DWI) and diffusion tensor imaging (DTI) and related systems” (WO2012088031: PCT/US2011/066019; US20130249555: 13/992,537), have proprietary interest in some of the reported acquisition and reconstruction methods.

### Acknowledgments

This work was supported by NIH Grants R01NS074045, R01EB012586, R01EB009483, and R01NS075017 from the

National Institute of Neurological Disorders and Stroke (NINDS) and the National Institute of Biomedical Imaging and Bioengineering (NIBIB). The content is solely the responsibility of the authors and does not necessarily represent the official views of the NINDS, the NIBIB, or the NIH.

### References

- [1] P. J. Basser, J. Mattiello, and D. LeBihan, “MR diffusion tensor spectroscopy and imaging,” *Biophysical Journal*, vol. 66, no. 1, pp. 259–267, 1994.
- [2] C. Pierpaoli, P. Jezzard, P. J. Basser, A. Barnett, and G. Di Chiro, “Diffusion tensor MR imaging of the human brain,” *Radiology*, vol. 201, no. 3, pp. 637–648, 1996.
- [3] S. Mori and J. Zhang, “Principles of diffusion tensor imaging and its applications to basic neuroscience research,” *Neuron*, vol. 51, no. 5, pp. 527–539, 2006.
- [4] Y. Assaf and O. Pasternak, “Diffusion tensor imaging (DTI)-based white matter mapping in brain research: a review,” *Journal of Molecular Neuroscience*, vol. 34, no. 1, pp. 51–61, 2008.
- [5] J. Dubois, G. Dehaene-Lambertz, S. Kulikova, C. Poupon, P. S. Hüppi, and L. Hertz-Pannier, “The early development of brain white matter: a review of imaging studies in fetuses, newborns and infants,” *Neuroscience*, vol. 276, pp. 48–71, 2014.
- [6] M. M. Herting, J. B. Colby, E. R. Sowell, and B. J. Nagel, “White matter connectivity and aerobic fitness in male adolescents,” *Developmental Cognitive Neuroscience*, vol. 7, pp. 65–75, 2014.
- [7] M. Lamar, X. J. Zhou, R. A. Charlton, D. Dean, D. Little, and S. C. Deoni, “In vivo quantification of white matter microstructure for use in aging: a focus on two emerging techniques,” *The American Journal of Geriatric Psychiatry*, vol. 22, no. 2, pp. 111–121, 2014.
- [8] K. L. Mills and C. K. Tamnes, “Methods and considerations for longitudinal structural brain imaging analysis across development,” *Developmental Cognitive Neuroscience*, vol. 9, pp. 172–190, 2014.

- [9] A. Paydar, E. Fieremans, J. I. Nwankwo et al., "Diffusional kurtosis imaging of the developing brain," *American Journal of Neuroradiology*, vol. 35, no. 4, pp. 808–814, 2014.
- [10] M. Rovaris, G. Iannucci, M. Cercignani et al., "Age-related changes in conventional, magnetization transfer, and diffusion-tensor MR imaging findings: study with whole-brain tissue histogram analysis," *Radiology*, vol. 227, no. 3, pp. 731–738, 2003.
- [11] S. M. Bruijn, A. van Impe, J. Duysens, and S. P. Swinnen, "White matter microstructural organization and gait stability in older adults," *Frontiers in Aging Neuroscience*, vol. 6, article 104, 2014.
- [12] D. J. Simmonds, M. N. Hallquist, M. Asato, and B. Luna, "Developmental stages and sex differences of white matter and behavioral development through adolescence: a longitudinal diffusion tensor imaging (DTI) study," *NeuroImage*, vol. 92, pp. 356–368, 2014.
- [13] M. Wu, L. H. Lu, A. Lowes et al., "Development of superficial white matter and its structural interplay with cortical gray matter in children and adolescents," *Human Brain Mapping*, vol. 35, no. 6, pp. 2806–2816, 2014.
- [14] H.-P. Müller and J. Kassubek, "Diffusion tensor magnetic resonance imaging in the analysis of neurodegenerative diseases," *Journal of Visualized Experiments*, no. 77, 2013.
- [15] P. C. Sundgren, M. Petrou, R. E. Harris et al., "Diffusion-weighted and diffusion tensor imaging in fibromyalgia patients: a prospective study of whole brain diffusivity, apparent diffusion coefficient, and fraction anisotropy in different regions of the brain and correlation with symptom severity," *Academic Radiology*, vol. 14, no. 7, pp. 839–846, 2007.
- [16] T. Zhu, R. Hu, W. Tian et al., "SPatial REgression Analysis of Diffusion tensor imaging (SPREAD) for longitudinal progression of neurodegenerative disease in individual subjects," *Magnetic Resonance Imaging*, vol. 31, no. 10, pp. 1657–1667, 2013.
- [17] M. Barysheva, N. Jahanshad, L. Foland-Ross, L. L. Altschuler, and P. M. Thompson, "White matter microstructural abnormalities in bipolar disorder: a whole brain diffusion tensor imaging study," *NeuroImage: Clinical*, vol. 2, no. 1, pp. 558–568, 2013.
- [18] M. Wessa, J. Houenou, M. Leboyer et al., "Microstructural white matter changes in euthymic bipolar patients: a whole-brain diffusion tensor imaging study," *Bipolar Disorders*, vol. 11, no. 5, pp. 504–514, 2009.
- [19] E. Caverzasi, R. G. Henry, P. Vitali et al., "Application of quantitative DTI metrics in sporadic CJD," *NeuroImage: Clinical*, vol. 4, pp. 426–435, 2014.
- [20] M. Inglese, S. Brown, G. Johnson, M. Law, E. Knopp, and O. Gonen, "Whole-brain N-acetylaspartate spectroscopy and diffusion tensor imaging in patients with newly diagnosed gliomas: a preliminary study," *American Journal of Neuroradiology*, vol. 27, no. 10, pp. 2137–2140, 2006.
- [21] E. A. Steffen-Smith, J. E. Sarlls, C. Pierpaoli et al., "Diffusion tensor histogram analysis of pediatric diffuse intrinsic pontine glioma," *BioMed Research International*, vol. 2014, Article ID 647356, 9 pages, 2014.
- [22] M. S. Korgaonkar, N. J. Cooper, L. M. Williams, and S. M. Grieve, "Mapping inter-regional connectivity of the entire cortex to characterize major depressive disorder: a whole-brain diffusion tensor imaging tractography study," *NeuroReport*, vol. 23, no. 9, pp. 566–571, 2012.
- [23] M. L. Mandelli, E. Caverzasi, R. J. Binney et al., "Frontal white matter tracts sustaining speech production in primary progressive aphasia," *The Journal of Neuroscience*, vol. 34, no. 29, pp. 9754–9767, 2014.
- [24] R. D. Perea, R. C. Rada, J. Wilson et al., "A comparative white matter study with Parkinson's disease, Parkinson's disease with dementia and Alzheimer's disease," *Journal of Alzheimer's Disease & Parkinsonism*, vol. 3, article 123, 2013.
- [25] S. J. Teipel, M. J. Grothe, M. Filippi et al., "Fractional anisotropy changes in Alzheimer's disease depend on the underlying fiber tract architecture: a multiparametric DTI study using joint independent component analysis," *Journal of Alzheimer's Disease*, vol. 41, no. 1, pp. 69–83, 2014.
- [26] M. D. King, J. Houseman, S. A. Roussel, N. van Bruggen, S. R. Williams, and D. G. Gadian, "q-Space imaging of the brain," *Magnetic Resonance in Medicine*, vol. 32, no. 6, pp. 707–713, 1994.
- [27] L. R. Frank, "Anisotropy in high angular resolution diffusion-weighted MRI," *Magnetic Resonance in Medicine*, vol. 45, no. 6, pp. 935–939, 2001.
- [28] V. J. Wedeen, R. P. Wang, J. D. Schmahmann et al., "Diffusion spectrum magnetic resonance imaging (DSI) tractography of crossing fibers," *NeuroImage*, vol. 41, no. 4, pp. 1267–1277, 2008.
- [29] C. Liu, S. C. Mang, and M. E. Moseley, "In vivo generalized diffusion tensor imaging (GDTI) using higher-order tensors (HOT)," *Magnetic Resonance in Medicine*, vol. 63, no. 1, pp. 243–252, 2010.
- [30] G. Soria, M. De Notaris, R. Tudela et al., "Improved assessment of ex vivo brainstem neuroanatomy with high-resolution MRI and DTI at 7 Tesla," *Anatomical Record*, vol. 294, no. 6, pp. 1035–1044, 2011.
- [31] J. S. Hyde, B. B. Biswal, and A. Jesmanowicz, "High-resolution fMRI using multislice partial k-space GR-EPI with cubic voxels," *Magnetic Resonance in Medicine*, vol. 46, no. 1, pp. 114–125, 2001.
- [32] A. W. Anderson and J. C. Gore, "Analysis and correction of motion artifacts in diffusion weighted imaging," *Magnetic Resonance in Medicine*, vol. 32, no. 3, pp. 379–387, 1994.
- [33] R. J. Ordidge, J. A. Helpert, Z. X. Qing, R. A. Knight, and V. Nagesh, "Correction of motional artifacts in diffusion-weighted MR images using navigator echoes," *Magnetic Resonance Imaging*, vol. 12, no. 3, pp. 455–460, 1994.
- [34] P. Storey, F. J. Frigo, R. S. Hinks et al., "Partial k-space reconstruction in single-shot diffusion-weighted echo-planar imaging," *Magnetic Resonance in Medicine*, vol. 57, no. 3, pp. 614–619, 2007.
- [35] N.-K. Chen, K. Oshio, and L. P. Panych, "Improved image reconstruction for partial fourier gradient-echo echo-planar imaging (EPI)," *Magnetic Resonance in Medicine*, vol. 59, no. 4, pp. 916–924, 2008.
- [36] C. Meier, M. Zwanger, T. Feiweier, and D. Porter, "Concomitant field terms for asymmetric gradient coils: consequences for diffusion, flow, and echo-planar imaging," *Magnetic Resonance in Medicine*, vol. 60, no. 1, pp. 128–134, 2008.
- [37] V. J. Schmithorst and B. J. Dardzinski, "Automatic gradient preemphasis adjustment: a 15-minute journey to improved diffusion-weighted echo-planar imaging," *Magnetic Resonance in Medicine*, vol. 47, no. 1, pp. 208–212, 2002.
- [38] S. Posse, "Direct imaging of magnetic field gradients by group spin-echo selection," *Magnetic Resonance in Medicine*, vol. 25, no. 1, pp. 12–29, 1992.
- [39] R. Deichmann, O. Josephs, C. Hutton, D. R. Corfield, and R. Turner, "Compensation of susceptibility-induced bold sensitivity losses in echo-planar fMRI imaging," *NeuroImage*, vol. 15, no. 1, pp. 120–135, 2002.

- [40] N.-K. Chen, K. Oshio, and L. P. Panych, "Application of k-space energy spectrum analysis to susceptibility field mapping and distortion correction in gradient-echo EPI," *NeuroImage*, vol. 31, no. 2, pp. 609–622, 2006.
- [41] T.-K. Truong, N.-K. Chen, and A. W. Song, "Application of k-space energy spectrum analysis for inherent and dynamic  $B_0$  mapping and deblurring in spiral imaging," *Magnetic Resonance in Medicine*, vol. 64, no. 4, pp. 1121–1127, 2010.
- [42] N. G. Papadakis, T. Smponias, J. Berwick, and J. E. W. Mayhew, "k-space correction of eddy-current-induced distortions in diffusion-weighted echo-planar imaging," *Magnetic Resonance in Medicine*, vol. 53, no. 5, pp. 1103–1111, 2005.
- [43] D. L. Thomas, M. F. Lythgoe, D. G. Gadian, and R. J. Ordidge, "Rapid simultaneous mapping of T2 and T2\* by Multiple acquisition of spin and gradient echoes using interleaved echo planar imaging (MASAGE-IEPI)," *NeuroImage*, vol. 15, no. 4, pp. 992–1002, 2002.
- [44] J. J. Cuppen, J. P. Groen, and J. Konijn, "Magnetic resonance fast Fourier imaging," *Medical Physics*, vol. 13, no. 2, pp. 248–253, 1986.
- [45] J. P. Wansapura, S. K. Holland, R. S. Dunn, and W. S. Ball Jr., "NMR relaxation times in the human brain at 3.0 tesla," *Journal of Magnetic Resonance Imaging*, vol. 9, no. 4, pp. 531–538, 1999.
- [46] T.-K. Truong, N.-K. Chen, and A. W. Song, "Dynamic correction of artifacts due to susceptibility effects and time-varying eddy currents in diffusion tensor imaging," *NeuroImage*, vol. 57, no. 4, pp. 1343–1347, 2011.
- [47] K. O'Brien, A. Daducci, N. Kickler et al., "3-D residual eddy current field characterisation: applied to diffusion weighted magnetic resonance imaging," *IEEE Transactions on Medical Imaging*, vol. 32, no. 8, pp. 1515–1525, 2013.
- [48] D. Xu, J. K. Maier, K. F. King et al., "Prospective and retrospective high order eddy current mitigation for diffusion weighted echo planar imaging," *Magnetic Resonance in Medicine*, vol. 70, no. 5, pp. 1293–1305, 2013.
- [49] O. Heid, "Eddy current-nulled diffusion weighting," in *Proceedings of the Annual Meeting of the International Society for Magnetic Resonance in Medicine (ISMRM '00)*, Denver, Colo, USA, 2000.
- [50] T. G. Reese, O. Heid, R. M. Weisskoff, and V. J. Wedeen, "Reduction of eddy-current-induced distortion in diffusion MRI using a twice-refocused spin echo," *Magnetic Resonance in Medicine*, vol. 49, no. 1, pp. 177–182, 2003.
- [51] A. V. Avram, A. Guidon, and A. W. Song, "Myelin water weighted diffusion tensor imaging," *NeuroImage*, vol. 53, no. 1, pp. 132–138, 2010.

## Clinical Study

# Volumetric MR-Guided High-Intensity Focused Ultrasound with Direct Skin Cooling for the Treatment of Symptomatic Uterine Fibroids: Proof-of-Concept Study

Marlijne E. Ikink,<sup>1</sup> Johanna M. M. van Breugel,<sup>1</sup> Gerald Schubert,<sup>2</sup> Robbert J. Nijenhuis,<sup>1</sup> Lambertus W. Bartels,<sup>3</sup> Chrit T. W. Moonen,<sup>3</sup> and Maurice A. A. J. van den Bosch<sup>1</sup>

<sup>1</sup> Department of Radiology, University Medical Center Utrecht, Heidelberglaan 100, 3584 CX Utrecht, The Netherlands

<sup>2</sup> Philips Healthcare, Philips Medical Systems MR, Äyritie 4, 01511 Vantaa, Finland

<sup>3</sup> Department of Radiology and Image Sciences Institute, University Medical Center Utrecht, Heidelberglaan 100, 3584 CX Utrecht, The Netherlands

Correspondence should be addressed to Marlijne E. Ikink; [m.ikink@umcutrecht.nl](mailto:m.ikink@umcutrecht.nl)

Received 11 July 2014; Accepted 18 August 2014

Academic Editor: Trevor Andrews

Copyright © 2015 Marlijne E. Ikink et al. This is an open access article distributed under the Creative Commons Attribution License, which permits unrestricted use, distribution, and reproduction in any medium, provided the original work is properly cited.

**Objective.** To prospectively assess the safety and technical feasibility of volumetric magnetic resonance-guided high-intensity focused ultrasound (MR-HIFU) ablation with direct skin cooling (DISC) during treatment of uterine fibroids. **Methods.** In this proof-of-concept study, eight patients were consecutively selected for clinical MR-HIFU ablation of uterine fibroids with the use of an additional DISC device to maintain a constant temperature ( $T \approx 20^\circ\text{C}$ ) at the interface between the HIFU table top and the skin. Technical feasibility was verified by successful completion of MR-HIFU ablation. Contrast-enhanced T1-weighted MRI was used to measure the treatment effect (nonperfused volume (NPV) ratio). Safety was evaluated by recording of adverse events (AEs) within 30 days' follow-up. **Results.** All MR-HIFU treatments were successfully completed in an outpatient setting. The median NPV ratio was 0.56 (IQR [0.27–0.72]). Immediately after treatment, two patients experienced coldness related discomfort which resolved at the same day. No serious (device-related) AEs were reported. Specifically, no skin burns, cold injuries, or subcutaneous edema were observed. **Conclusion.** This study showed that it is safe and technically feasible to complete a volumetric MR-HIFU ablation with DISC. This technique may reduce the risk of thermal injury to the abdominal wall during MR-HIFU ablation of uterine fibroids. This trial is registered with NTR4189.

## 1. Introduction

Over the last decade, minimally or noninvasive treatment options have gained popularity and continue to evolve and expand with developments in technology and with growing experience. Numerous technological advances have been driven by the observed benefits of the minimally invasive approach, including less side effects, shorter recovery time, and favorable cosmetic results. Since the first feasibility report in 2003 [1], magnetic resonance-guided high-intensity focused ultrasound (MR-HIFU) has been successfully employed to treat symptomatic uterine fibroids in a clinical setting. Although not all uterine fibroids are

symptomatic, they are in at least 25% of the Caucasian women in their reproductive years associated with significant morbidity, including abnormal menstrual bleeding, pelvic discomfort, and reproductive dysfunction [2, 3]. An increasing number of symptomatic patients demand less invasive treatment methods in order to achieve symptom relief and a better quality of life. MR-HIFU offers the advantage to perform completely noninvasive thermal ablation because the ultrasound transducer is located outside the abdomen and steers high-intensity focused ultrasound energy into the targeted area through the intact skin.

Since 2010, a volumetric MR-HIFU system has been available for routine clinical treatments of uterine fibroids [4].

The volumetric ablation approach utilizes the accumulation of heat by electronically steering the focus along outward-moving concentric circles, producing well-defined regions of protein denaturation, irreversible cell damage, and coagulative necrosis. However, the treatment of larger ablation volumes requires more thermal energy which may lead to a temperature increase along the ultrasound beam axis in the near field (i.e., intermediate layers located between the ultrasound transducer and the target region, such as epidermis, dermis, subcutaneous tissue, and deeper abdominal layers) [5]. During periods of thermal stress, the rate of heat transfer through the skin surface depends primarily on the heat capacity (or ability to absorb heat) and the thermal conductivity (or ability to transfer heat) of the skin to facilitate heat loss [6]. This heat flux may be enhanced through blood circulation by carrying the heat to adjacent tissues [7, 8]. Temperature rise within the skin layers will mainly occur in the subcutaneous tissue due to its lower specific heat capacity [6], insulator properties [6, 7, 9], and its lower blood supply [10–12] than that of other tissues in the abdominal wall. Additionally, reflections at boundaries between different media (e.g., air-skin and/or skin-fat) can occur because of differences in the acoustic impedance of various media [13]. The transmission losses from reflection at the skin interface and attenuation through the skin layers might lead to hot spots and skin overheating. Although MR-HIFU ablation of uterine fibroids is related to a low complication rate, skin toxicity and abdominal discomfort have been described by several groups [1, 14–21]. Undesired heat accumulation in the near field and target area is moderated by enforcing conservative cooling times between the subsequent energy depositions (sonications) to prevent irreversible thermal tissue damage [22, 23], such as skin burns, subcutaneous edema formation, or fat necrosis [24]. The cooling time is chosen to ensure return of the heated tissue layers to body temperature, and cooling ranges typically a few minutes per energy delivery. This leads to undesirably long delays between the sonications, which contributes to prolonged overall treatment times. It would therefore be valuable to regulate the temperature of the skin layers at a constant (room) temperature to reduce thermal tissue damage during MR-HIFU ablation, and accordingly, speed up the treatment procedure.

In this study we demonstrate the concept for the clinical use of a direct skin cooling (DISC) device added to an MR-HIFU system during volumetric ablation of uterine fibroids. The purpose of this study was to evaluate the feasibility and safety of uterine fibroid treatments using this DISC system as additional buffer against potential adverse events related to skin heating.

## 2. Materials and Methods

**2.1. Patients and Lesions.** This prospective nonrandomized proof-of-concept study (NL45458.041.13) was approved by the Institutional Review Board and was conducted in accordance with the rules for international good clinical practice. Patients who participated in this study were already selected for clinical MR-HIFU ablation of uterine fibroids based on

their history, physical examination, and diagnostic pelvic MRI examination. Routine inclusion and exclusion were carried out; eligible patients met the following inclusion criteria [21]: (1) 18 years or older, (2) clinically diagnosed with symptomatic uterine fibroids, (3) referred by their gynecologists with an absolute indication for intervention, (4) premenopausal or perimenopausal, (5) not currently pregnant or breastfeeding, (6) no general contraindications for magnetic resonance imaging (MRI) and MR contrast agents, and (7) able to undergo the MR-HIFU procedure based on a diagnostic pelvic MRI examination in prone position (Achieva 1.5-T, Philips Healthcare, Best, The Netherlands). Exclusion criteria were (1) the presence of other pelvic diseases, (2) unavoidable extensive scar tissue in the lower abdomen (in some cases alternate ultrasound beam paths were possible to avoid scar tissue, e.g., via beam shaping or beam angulation), (3) interposition of the bowel between the anterior abdominal wall and the dominant uterine fibroid, (4) excessive fibroid size ( $\geq 12$  cm), and (5) too many lesions ( $\geq 10$  uterine fibroids). All patients gave written informed consent for conducting an MR-HIFU procedure with the presence of the direct skin cooling (DISC) device.

**2.2. MR-HIFU System.** All treatments were performed on a modified clinical MR-HIFU fibroid therapy system (Sonalleve, Philips Healthcare, Vantaa, Finland) integrated into a 1.5-T MRI scanner (Achieva, Philips Healthcare, Best, The Netherlands). MR images were used for treatment localization, feedback control (beam guidance), real-time temperature mapping with the proton resonance frequency shift (PRFS) thermometry method, and posttreatment verification of the ablated tissue. The curved patient MR table top incorporated a phased-array 256-channel HIFU transducer (radius of curvature: 14 cm, operating at 1.2 MHz) housed in an electromechanical positioning system to deliver spatially and temporally controlled heating. The DISC device consisted of a liquid (water) cooling reservoir which was mounted on top of the standard clinical MR-HIFU table top, between the degassed liquid (oil) bath—in which the HIFU transducer is immersed—and the patients' skin. A schematic illustration of the clinical volumetric MR-HIFU system with and without the presence of the investigational DISC device is shown in Figure 1. The water cooling reservoir was connected to a water pump, cooling element, temperature regulator, degasser, and a bubble-trap to assure that air bubbles were extracted from the DISC system. The temperature of the water cooling reservoir was regulated at a constant room temperature ( $T \approx 20^\circ\text{C}$ ), such that the temperature was well tolerated on bare skin. The DISC system was filled with degassed water and turned on (10 minutes) before the start of the MR-HIFU treatment to establish the target temperature of the water cooling reservoir. By the active displacement of water through the liquid cooling reservoir (circuit) a stable temperature could be guaranteed. The temperatures in the water cooling reservoir were measured using a fiber-optical temperature sensor (Soft-Sens, Opsens Inc., Québec, QC, Canada), which was placed in the water between the two Mylar (polyethylene terephthalate) membranes outside the immediate acoustic beam path. Since the skin is in direct contact with the cooled water reservoir

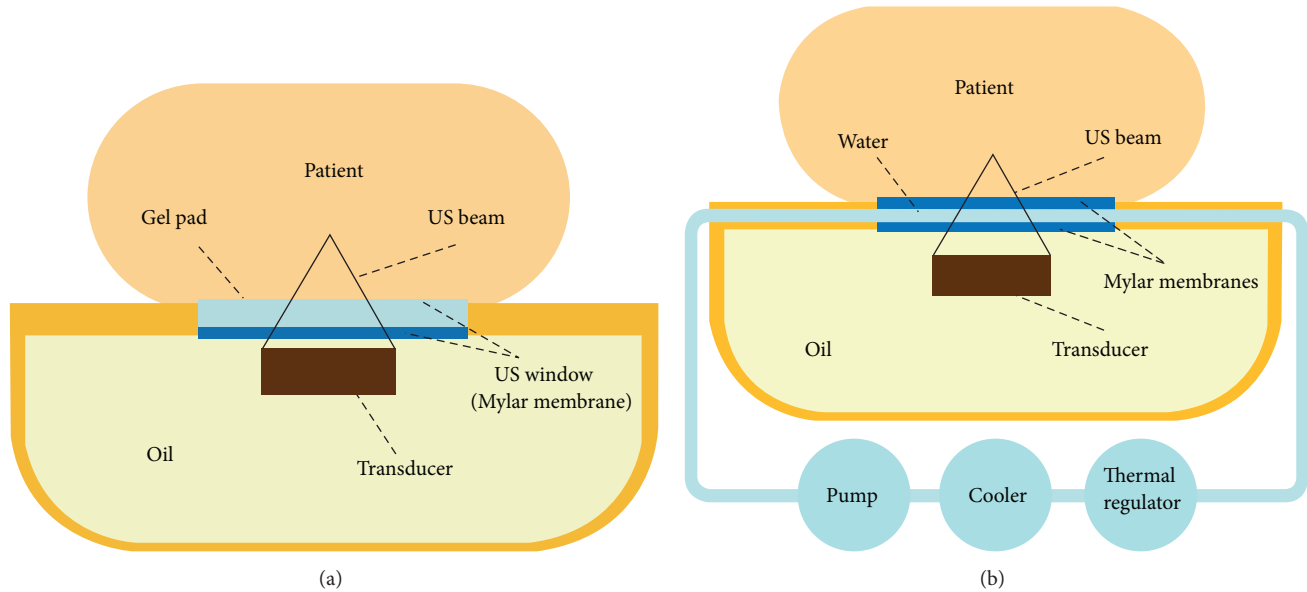


FIGURE 1: Schematic illustration of the differences between the clinical volumetric MR-HIFU system with (b) and without (a) the presence of the investigational DISC device.

(separated only by a  $50\ \mu\text{m}$  thick membrane), the measured water temperature directly reflects the patient's skin temperature throughout the MR-HIFU ablation. Local hotspots on skin level that appear during individual sonications are equilibrated on timescales of some tens of seconds. During acquisition of diagnostic MR images, the flow within the water cooling reservoir was stopped to prevent artifacts on the MR data.

**2.3. MR-HIFU Procedure.** All patients were treated in an outpatient setting. Patient preparation on the day of the MR-HIFU procedure (i.e., hair removal of the lower abdomen; insertion of an intravenous line and Foley catheter), treatment planning, and the volumetric ablation protocol have been described in previous publications [19, 21]. Cooling times were enforced as in normal MR-HIFU treatments, so that the DISC device was used as an additional safety buffer against potential adverse events related to skin heating. The required cooling times of at least 90 seconds were respected as suggested by the feedback MR-HIFU system. A standardized preprocedural pain management protocol was used with paracetamol 1,000 mg intravenous (Paracetamol Kabi, 10 mg/mL, Fresenius Kabi Nederland B.V., Schelle, Belgium), diclofenac 75 mg intravenous (Voltaren, 25 mg/mL, Novartis Pharma B.V., Arnhem, The Netherlands), and oxycodone 5 mg capsules (OxyNorm, 5 mg, Mundipharma Pharmaceuticals B.V., Hoevelaken, The Netherlands). In this study, patients were asked to lie down in prone position (feet first) on the patient MR table top with the integrated DISC device. A wetted ultrasound gel pad (7.5 mm) or a thin mixture (10:1) of degassed water and ultrasound gel (gel film) was used as coupling agents to provide adequate direct contact for the ultrasound waves to penetrate the patients' skin. Two different types of acoustic couplers were evaluated, in order to assess whether treatment could also be carried out without the commonly used gel pad. Standard MR images

were acquired to detect any obstacles in the ultrasound beam path and the contact surface to ensure that MR-HIFU ablation was safe with respect to heating in unwanted locations due to the presence of air bubbles, scars, bowel, bone, and/or implants. A typical representation of the MR images in the MR-HIFU user interface is shown in Figure 2. The following MR sequences were used: coronal membrane bubble scan (three-dimensional (3D) spoiled gradient echo (FFE) with repetition time [TR], 5.8 milliseconds [ms]; echo time [TE], 4.0 ms; flip angle [FA],  $6^\circ$ ; field of view [FOV],  $260\ \text{mm} \times 260\ \text{mm}$ ; acquired [ACQ] voxel size,  $1.00 \times 1.00 \times 2.00\ \text{mm}^3$ ; reconstructed [REC] voxel size,  $0.49 \times 0.49 \times 1.00\ \text{mm}^3$ ; number of averages [NSA], 6; acquisition time, 00:39 minutes), coronal skin bubble scan (multislice single-echo FFE with TR, 150 ms; TE, 15 ms; FA,  $55^\circ$ ; FOV,  $280\ \text{mm} \times 280\ \text{mm}$ ; ACQ voxel size,  $1.25 \times 1.25 \times 2.50\ \text{mm}^3$ ; REC voxel size,  $0.31 \times 0.31 \times 2.50\ \text{mm}^3$ ; NSA, 2; acquisition time, 00:38 minutes), coronal scar scan (single-echo 3D FFE with TR, 21 ms; TE, 6.0 ms; FA,  $15^\circ$ ; FOV,  $200\ \text{mm} \times 200\ \text{mm}$ ; ACQ voxel size,  $0.89 \times 0.89 \times 2.00\ \text{mm}^3$ ; REC voxel size,  $0.31 \times 0.31 \times 1.00\ \text{mm}^3$ ; NSA, 3; acquisition time, 02:06.5 minutes), and anatomical 3D T2-weighted (T2w) turbo spin echo (TSE) with TR, 1425 ms; TE, 130 ms; FA,  $90^\circ$ ; FOV,  $250\ \text{mm} \times 250\ \text{mm}$ ; ACQ voxel size,  $1.20 \times 1.39 \times 3.00\ \text{mm}^3$ ; REC voxel size,  $0.49 \times 0.49 \times 1.50\ \text{mm}^3$ ; NSA, 2; acquisition time, 03:50.8 minutes, and 3D T1-weighted (T1w) FFE with TR, 3.6 ms; TE, 1.90 ms; FA,  $7^\circ$ ; FOV,  $220\ \text{mm} \times 240\ \text{mm}$ ; ACQ voxel size,  $1.25 \times 1.53 \times 2.50\ \text{mm}^3$ ; REC voxel size,  $0.47 \times 0.47 \times 1.25\ \text{mm}^3$ ; NSA, 8; acquisition time, 01:57.3 minutes. During the treatment procedure, patients received conscious sedation (propofol-ketamine combination) to reduce and control pain or discomfort and involuntary movements. Monitored anesthesia care (MAC) was provided by the anesthesiologist (procedural sedation specialist), which included preprocedural screening, intraoperative support of vital functions

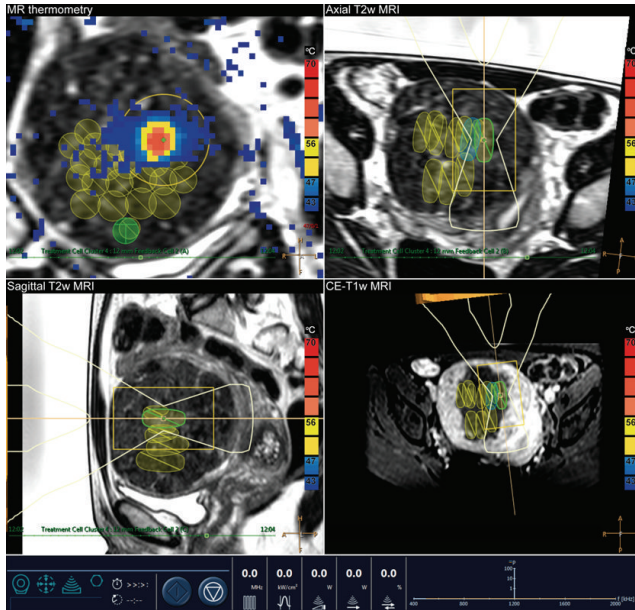


FIGURE 2: Typical representation of the MR images in the MR-HIFU user interface during treatment of uterine fibroids. The patient was lying in prone position (feet first) on the MR table top with the integrated direct skin cooling (DISC) device. The uterine fibroid was positioned directly above the MR-HIFU transducer. The ultrasound beam path was planned using T2-weighted MRI in three orthogonal planes, that is, coronal (top left), axial (top right), and sagittal (bottom left) plane. During each sonication, color temperature maps were computed by the MR-HIFU system using the proton resonance frequency shift (PRFS) thermometry method and shown on top of the anatomical images (top left). Immediately after MR-HIFU treatment, the volume that was successfully treated was defined as the nonenhancing part of the fibroid on contrast-enhanced T1-weighted MRI (bottom right).

and administration of anesthetic agents, and postprocedural anesthesia management. After completion of the MR-HIFU procedure, a set of MR images of the target region was obtained including a contrast-enhanced (gadobutrol, Gadovist, 0.1 mmol/kg, Bayer Schering Pharma) T1-weighted (CE-T1w) TFE sequence (with TR, 5.4 ms; TE, 2.6 ms; FA,  $10^\circ$ ; FOV, 250 mm  $\times$  250 mm; ACQ voxel size,  $1.49 \times 1.89 \times 3.00$  mm<sup>3</sup>; REC voxel size,  $0.49 \times 0.49 \times 1.50$  mm<sup>3</sup>; NSA, 4; acquisition time, 02:14.5 minutes) to allow a sum-of-slice measurement of the nonperfused volume (NPV), indicating the volume of fibroid tissue that is nonviable. Following this, patients were conducted to the recovery room for medical supervision before being discharged from the hospital on the same day.

**2.4. Data Collection.** The primary endpoint of this study was the technical feasibility of clinical MR-HIFU fibroid treatments with direct skin cooling, as determined by recording the successfully completed treatments using the investigational DISC device. Treatment completion was judged by an experienced operating physician (M.v.d.B.). If a treatment was aborted before the desired ablation volume was achieved and the backup CE-labelled MR-HIFU system had to be

used, the treatment was counted as a failure. The extent of treatment was reported by measuring the NPV ratios, defined as the nonenhancing part of the fibroid divided by the fibroid volume. The achieved NPV ratios were compared to data from the literature to assess whether the performed treatments represent typical MR-HIFU ablations. In order to determine the effectiveness of the MR-HIFU treatments with the DISC device, the energy deposition rate (in kilojoule per hour [kJ/h]) was calculated by dividing the deposited treatment energy [kJ] by the total treatment time (1/[h]). The treatment time was defined as the time from the start of the first to the end of the last sonication.

The secondary endpoint of this study was to gain insights into factors influencing the safety. Safety was assessed by recording (serious) adverse events and whether they were related to the investigational DISC device, in particular by inspection of patients' skin immediately after MR-HIFU treatment. All adverse events (AEs) were recorded and classified following the 14155:2011 standard for Good Clinical Practice in clinical investigation of medical devices for human subjects issued by the International Organization for Standardization (ISO). Any AEs observed during or after MR-HIFU treatment were followed and documented until they had abated or until a stable situation had been reached. Patients were contacted by telephone 3 days, 7 days, and 30 days after the MR-HIFU procedure to determine whether any AEs had occurred. A pain assessment scale was obtained using the visual analogue scale (VAS) from 0 (no pain) to 10 (worst pain possible). The flow chart in Figure 3 shows the patients' progress through the study.

**2.5. Statistical Analysis.** Data were prospectively collected and analyzed to evaluate the safety and feasibility of performing MR-HIFU treatment of uterine fibroids in a volumetric MR-HIFU system equipped with a DISC device. The sample size calculation was based on the two-sided Agresti-Coull 95% confidence interval (95% CI) [25]. The Agresti-Coull interval is known to provide optimal coverage for binominal proportions when the sample size is small and the success probability approaches 0 or 1 [26, 27]. The estimate of the Agresti-Coull 95% CI showed that 8 successfully treated patients would be needed to detect a therapy success rate of at least 63%. Estimations for different proportions of successful therapy completion are presented in Table 1. Descriptive statistics were used to describe the distribution of the patients' demographic and lesion characteristics. The treatment data of each patient was subsequently summarized and reported. Categorical data are presented in number and percentage, whereas continuous data are given in median and interquartile range (IQR). Statistical analyses were performed using IBM SPSS Statistics, version 20.0 (Armonk, New York, USA).

### 3. Results

Eight Caucasian patients with nine treatable uterine fibroids were consecutively enrolled in this study. One patient was treated for two uterine fibroids during the same MR-HIFU treatment. Three patients had a scar in the lower abdomen:

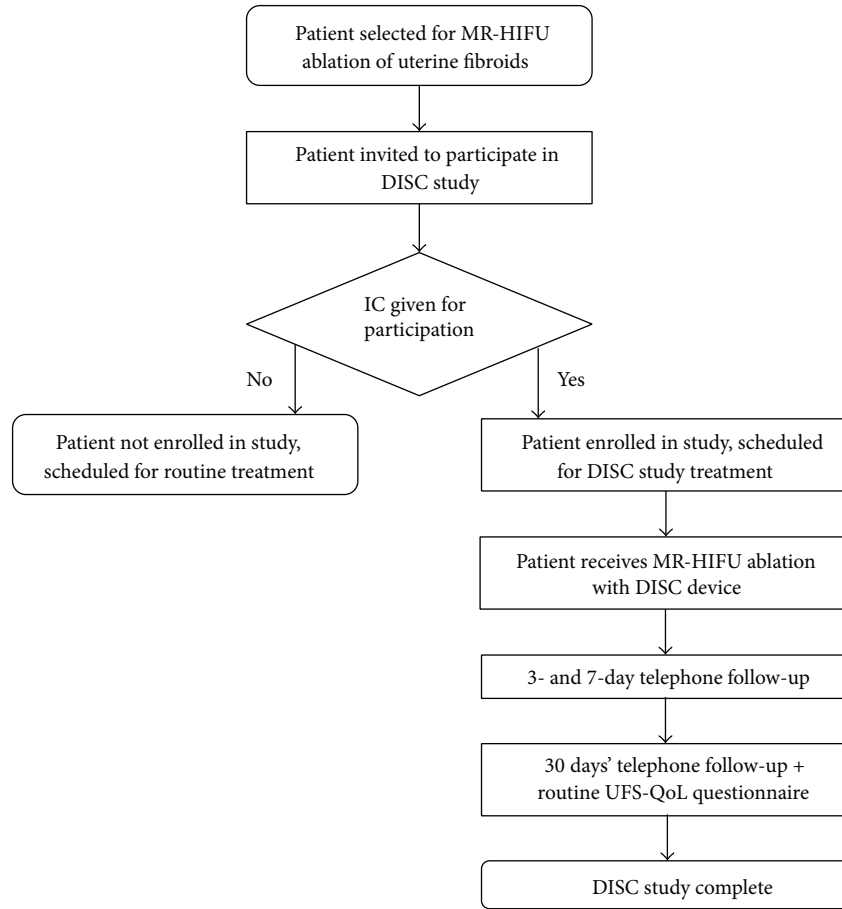


FIGURE 3: Flowchart shows the patients’ progress ( $n = 8$ ) through the DISC study. MR-HIFU: magnetic resonance-guided high-intensity focused ultrasound; DISC: direct skin cooling; IC: informed consent; UFS-QoL: uterine fibroid symptom and health-related quality of life.

TABLE 1: Estimated binominal proportion confidence intervals using the Agresti-Coull (adjusted Wald) method [25].

Sample size <sup>a</sup>	Observed outcome		$\hat{p}$	Estimation	
	Successes <sup>a</sup>	Failures <sup>a</sup>		Lower	Upper
8	8	0	0.84	0.63	1.00
8	7	1	0.75	0.51	1.00
8	6	2	0.67	0.40	0.94
8	5	3	0.58	0.30	0.87

<sup>a</sup>Values are expressed in numbers;  $\hat{p}$ : sample proportion of success; CI: confidence interval.

one patient (ID number 4) had undergone an abdominal myomectomy (Pfannenstiell incision), one patient (ID number 1) underwent an open appendectomy (McBurney incision), and one patient (ID number 2) had minor laparoscopic scars after a diagnostic laparoscopy due to chronic abdominal pain. In patient 4, urinary bladder filling (with a saline solution) was used to avoid the surgical scar in the ultrasound beam path. Baseline data collected for each patient at the beginning of the study are presented in Table 2. All MR-HIFU treatments were successfully completed using the investigational DISC device; no technical failure was observed. The use of the backup CE-labeled MR-HIFU system was not necessary. The median treatment time was 192 minutes (IQR

[180–225]), with a median energy deposition rate of 67 kJ/h (IQR [55–92]). The median volume of the uterine fibroids was 147 cm<sup>3</sup> (IQR [49–338]); the median maximum fibroid diameter was 7.7 cm (IQR [5.1–8.8]). A median nonperfused volume of 56 cm<sup>3</sup> (IQR [14–91]) was achieved, and a median NPV ratio of 0.56 (IQR [0.27–0.72]) was found. In one patient (ID number 7), no NPV could be achieved due to insufficient heating probably as a result of the tissue characteristics of the uterine fibroid (type 3) [28]. Table 3 shows an overview of the treatment data of each patient treated in this study.

No serious (device-related) adverse events were observed within 30 days’ follow-up. No patient required prolonged observation before discharge or readmission after hospital

TABLE 2: Baseline characteristics and MRI findings ( $n = 8$ ).

Patient characteristics	
Age (years) <sup>a</sup>	42.5 (38.8–47.8)
BMI (kg/m <sup>2</sup> ) <sup>a</sup>	23.1 (19.9–28.1)
Symptoms <sup>b</sup>	
Menorrhagia	3 (38%)
Bulky symptoms	4 (50%)
Infertility	1 (12%)
tSSS <sup>a</sup>	57.9 (38.3–79.0)
Total HRQoL <sup>a</sup>	48.7 (28.9–80.4)
Lesion characteristics	
Number of fibroids <sup>b</sup>	
Solitary fibroid	2 (25%)
Multiple fibroids	6 (75%)
2–5 fibroids	4 (67%)
6–10 fibroids	2 (33%)
Location of fibroids <sup>b</sup>	
Intramural	6 (67%)
Submucosal	3 (33%)
Type of fibroid <sup>b</sup>	
Type 1	4 (45%)
Type 2	3 (33%)
Type 3	2 (22%)
Maximum fibroid diameter (cm) <sup>a</sup>	7.7 (5.1–8.8)
Uterine fibroid volume (cm <sup>3</sup> ) <sup>a</sup>	147 (49–338)

<sup>a</sup>Median (interquartile range); <sup>b</sup>number (percentage); MR-HIFU: MR-guided high-intensity focused ultrasound; tSSS: transformed symptom severity score (range 0–100); high scores indicate more severe symptoms; HRQoL: health-related quality of life (range 0–100); high scores indicate better quality of life; type 1: low signal intensity on T2-weighted imaging; type 2: intermediate signal intensity on T2-weighted imaging; type 3: high signal intensity on T2-weighted imaging; NPV: nonperfused volume.

discharge. In particular, no skin burns, cold injuries, or subcutaneous edema (determined by increased signal intensity on T2w images) was observed in patients treated with the DISC device. Several mild AEs were reported, such as abdominal pain or cramping ( $n = 3$ ), back pain ( $n = 3$ ), abdominal tenderness ( $n = 2$ ), ergonomic problems ( $n = 2$ ), namely, fibular compression neuropathy due to external pressure at the right fibular head during a long treatment procedure of 230 minutes (ID number 3) and pressure marks due to the curved patient table top, dyspepsia and constipation ( $n = 2$ ), dizziness ( $n = 3$ ), and lethargy ( $n = 4$ ). One mild device-related AE occurred, namely, coldness-related discomfort which was rapidly resolved with a hot water bottle on the day of treatment ( $n = 2$ ). At the moment of hospital discharge, the median VAS score was 1.5 (IQR [0.25–3.0], range [0–7]). Typically, AEs resolved within 7 days' follow-up and patients were able to resume their daily activities again. However, after 30 days, two patients were still recovering from ongoing AEs (constipation and lethargy), both probably related to the administration of anaesthetic agents.

#### 4. Discussion

During MR-HIFU treatments, undesired heating outside of the targeted ablation area may occur, in particular in the near field region of the HIFU beam. Currently, the risk of near field damage is mitigated by the time-consuming enforcement of cooling periods between ultrasound sonications. Introduction of a cooled interface which allows direct cooling of the patients' skin may further mitigate undesired heating (by shifting the baseline temperature), potentially increasing treatment efficacy and providing an additional buffer. In this proof-of-concept study we have demonstrated the safety and feasibility of using a direct skin cooling (DISC) device added to a volumetric MR-HIFU system for uterine fibroid treatments. To the best of our knowledge, this concept had not yet been investigated in a clinical setting. Our results showed that it is technically feasible and safe to complete an MR-HIFU treatment with a DISC device. No thermal damage to the near field, due to temperature increase of the ultrasound energy emitted from the HIFU transducer, was observed in this study. All eight patients (100%) could be treated as in normal clinical practice, representing a typical case series of uterine fibroid MR-HIFU treatments. No clinical or technical problems have occurred preventing MR-HIFU treatments using the DISC device to be successfully completed. No serious (device-related) AEs occurred after treatment and the achieved median NPV ratio (0.56 (IQR [0.27–0.72])) was comparable to data previously published. Reported NPV ratios ranged from 0.40 to 0.70 with a median NPV ratio of 0.56 [21, 29–33]. Specifically, no skin redness and/or irritation of the abdominal wall—either related to skin heating or skin cooling—were seen. As known, cutaneous microvascular reactivity (namely, thermoregulatory reflex) is essential to maintain the human core temperature during challenges to thermal hemostasis [34, 35]. Prolonged exposure of direct cooling of the skin will eventually lead to cutaneous vasoconstriction [36–38], which may induce ischemia. Extended exposure to localized cold-induced vasoconstriction may cause various injuries to the patients' skin that typically fall within the domain termed nonfreezing cold injury (NFCI) [39, 40]. However, these injuries (e.g., chilblains or immersion foot) are most commonly reported to the body's lower extremities, such as the legs and feet [41, 42]. In addition, the literature evidence indicates that no serious thermal tissue damage is to be expected within several hours until freezing occurs [43, 44]. In general, NFCI occurs at temperatures of 0°C to 15°C. Considering the temperatures and exposure times relevant for patients during an MR-HIFU procedure, it can be concluded that the probability of occurrence for this specific low temperature event was indeed very unlikely.

It should be noted that this is a technical feasibility study with a small number of patients ( $n = 8$ ). Despite the promising preliminary results, the current study was not designed to measure the efficacy of the cooling system. Therefore, further research is needed to assess the clinical efficacy of this investigational DISC device as add-on to the volumetric MR-HIFU system. In a future step, a clinical

TABLE 3: Summary of treatment data of each patient treated with the DISC device.

ID	Patient		Patient geometry		Type	Fibroid		Treatment			Patient condition			
	Age [years]	BMI [kg/m <sup>2</sup> ]	Subcut. fat [mm]	Abdominal scars		Volume [cm <sup>3</sup> ]	NPV [cm <sup>3</sup> ]	NPV ratio [%]	Energy [kJ]	Time [min]	Energy deposition rate [kJ/h]	Skin temp. [°C]	Skin redness	Subcut. edema
1	43	28.4	18-21	Yes	2	408	249	61	368	223	99	23.0	no	no
2	48	28.1	28-33	Yes	1	25	15	60	169	163	62	21.5	no	no
3	42	22.1	8-14	No	3	268	67	25	331	230	86	22.0	no	no
4	48	24.2	12-14	Yes	2	77	56	72	155	189	49	21.5	no	no
5	47	19.7	8-10	No	1	73	52	71	234	191	74	21.5	no	no
6	38	28.0	14-20	No	1+1	17+147	14+66	82+45	240	225	64	20.5	no	no
7	31	20.3	7-15	No	3	200	0	0	294	177	100	21.0	no	no
8	41	18.4	2-4	No	2	415	115	28	183	193	63	20.5	no	no

ID: identification number; temp.: equilibrium temperature as measured in the water reservoir; subcut.: subcutaneous.

follow-up study will investigate to which extent the DISC system allows for speeding up uterine fibroid MR-HIFU treatments by benefiting from reduced cooling times. After each sonication, the cooling effect in the subcutaneous tissue layers will be systematically monitored using the T2-based thermometry as recently described by Baron et al. [45]. The acquired temperature (cool-down) information in the near field can be used to provide thermal feedback to the MR-HIFU system and use this to adjust the cooling periods between the subsequent energy depositions in real time. This novel technique may result in some advantages for the patient and their treating physician: (1) ablation of larger volumes of (fibroid) tissue in the shortest period of time that is safely possible and (2) more efficient treatment of type 3 uterine fibroids with a high signal intensity on T2w imaging [28, 46]. The fact that it is technically feasible to produce thermal lesions safely in the present study highlights the potential of this DISC system in the future MR-HIFU ablations of uterine fibroids. Another practical advantage of using DISC is that it seems sufficient to use a gel film (water-gel mixture) for acoustic coupling between the table top membrane and the depilated skin of the patient. Previously, it was easy to trap air bubbles between the commonly used (15 mm) gel pad and the patients' skin in the process of patient positioning. Since air bubbles may reflect the ultrasound energy—due to their low acoustic impedance [47]—they can cause abdominal pain or discomfort and skin burns. This restriction appears alleviated now by the use of a gel film, because we did not observe any air bubbles after positioning. Furthermore, without the insulating gel pad, the patient profits directly from the cooling effect without dissipation. Finally, the DISC system with gel-film has the same thickness as the old gel pads (Figure 1). This means that it is possible to reach targets as deep in the patient body as before. Consequently, the use of a gel film will potentially reduce risks and offers opportunities to speed up the patient preparation and overall treatment time.

Several limitations to the present study need to be acknowledged. First, we did not analyze the patient-reported outcomes of symptom severity (tSSS) and health-related quality of life (HRQoL) as measure of the treatment effect. The focus of the current study was to verify that the use of the DISC device did not affect the performance of the volumetric MR-HIFU system. The upcoming studies will require a larger patient cohort, larger ablation volumes, longer follow-up, and careful evaluation of the treatment efficacy using this DISC system. This information could be used to develop targeted interventions aimed at specific subgroups of patients, such as patients with hyperintense uterine fibroids on pretreatment T2w MRI [28] with the use of targeted vessel ablation [48]. Another limitation of our study is that we did the postdischarge follow-up by telephone interviewing. While this may not give us always an objective evaluation (due to absence of nonverbal cues), it provided us with the required information about the safety outcome.

In conclusion, in this proof-of-concept study we successfully performed clinical volumetric MR-HIFU ablation of uterine fibroids using an additional DISC device for reducing the risk of thermal damage to the abdominal wall. On the basis of the small number of patients studied, using the

additional DISC device in this trial appears to be safe. No serious (device-related) adverse events occurred.

## Conflict of Interests

The authors declare that there is no conflict of interests regarding the publication of this paper.

## Acknowledgments

This work was supported in part by Philips Healthcare (Philips Medical Systems MR, Finland). One author (Gerald Schubert) is an employee of Philips Healthcare; however the first two authors (Marlijn E. Ikin and Johanna M. M. van Breugel) in control of the study data and data analysis are not employees of Philips Healthcare.

## References

- [1] C. M. Tempany, E. A. Stewart, N. McDannold, B. J. Quade, F. A. Jolesz, and K. Hynynen, "MR imaging-guided focused ultrasound surgery of uterine leiomyomas: a feasibility study," *Radiology*, vol. 226, no. 3, pp. 897–905, 2003.
- [2] S. F. Cramer and A. Patel, "The frequency of uterine leiomyomas," *The American Journal of Clinical Pathology*, vol. 94, no. 4, pp. 435–438, 1990.
- [3] V. C. Buttram Jr. and R. C. Reiter, "Uterine leiomyomata: etiology, symptomatology, and management," *Fertility and Sterility*, vol. 36, no. 4, pp. 433–445, 1981.
- [4] M. O. Köhler, C. Mougenot, B. Quesson et al., "Volumetric HIFU ablation under 3D guidance of rapid MRI thermometry," *Medical Physics*, vol. 36, no. 8, pp. 3521–3535, 2009.
- [5] X. Fan and K. Hynynen, "Ultrasound surgery using multiple sonications: treatment time considerations," *Ultrasound in Medicine and Biology*, vol. 22, no. 4, pp. 471–482, 1996.
- [6] F. C. Henriques and A. R. Moritz, "Studies of thermal injury: I. The conduction of heat to and through skin and the temperatures attained therein. A theoretical and an experimental investigation," *American Journal of Pathology*, vol. 23, pp. 530–549, 1947.
- [7] G. S. Anderson, "Human morphology and temperature regulation," *International Journal of Biometeorology*, vol. 43, no. 3, pp. 99–109, 1999.
- [8] D. L. Kellogg and P. Pérgola, "Skin responses to exercise and training," in *Exercise and Sport Science*, W. E. Garrett and D. T. Kirkendall, Eds., pp. 239–250, Lippincott Williams & Wilkins, Philadelphia, Pa, USA, 1st edition, 2000.
- [9] M. L. Cohen, "Measurement of the thermal properties of human skin. A review," *Journal of Investigative Dermatology*, vol. 69, no. 3, pp. 333–338, 1977.
- [10] M. Rowland and T. N. Tozer, "Membranes and distribution table 4-4," in *Clinical Pharmacokinetics and Pharmacodynamics: Concepts and Applications*, pp. 73–110, Wolters Kluwer Health/Lippincott William & Wilkins, Philadelphia, Pa, USA, 4th edition, 2010.
- [11] I. Heinonen, J. Kemppainen, K. Kaskinoro, J. Knuuti, R. Boushel, and K. K. Kalliokoski, "Capacity and hypoxic response of subcutaneous adipose tissue blood flow in humans," *Circulation Journal*, vol. 78, no. 6, pp. 1501–1506, 2014.

- [12] J. M. Johnson, G. L. Brengelmann, J. R. S. Hales, P. M. Vanhoutte, and C. B. Wenger, "Regulation of the cutaneous circulation," *Federation Proceedings*, vol. 45, no. 13, pp. 2841–2850, 1986.
- [13] R. Williams, "Production and transmission of ultrasound," *Physiotherapy*, vol. 73, no. 3, pp. 113–116, 1987.
- [14] E. A. Stewart, W. M. W. Gedroyc, C. M. C. Tempany et al., "Focused ultrasound treatment of uterine fibroid tumors: safety and feasibility of a noninvasive thermoablative technique," *The American Journal of Obstetrics and Gynecology*, vol. 189, no. 1, pp. 48–54, 2003.
- [15] E. A. Stewart, J. Rabinovici, C. M. C. Tempany et al., "Clinical outcomes of focused ultrasound surgery for the treatment of uterine fibroids," *Fertility and Sterility*, vol. 85, no. 1, pp. 22–29, 2006.
- [16] J. Rabinovici, Y. Inbar, A. Revel et al., "Clinical improvement and shrinkage of uterine fibroids after thermal ablation by magnetic resonance-guided focused ultrasound surgery," *Ultrasound in Obstetrics & Gynecology*, vol. 30, no. 5, pp. 771–777, 2007.
- [17] J. Leon-Villapalos, M. Kaniorou-Larai, and P. Dziewulski, "Full thickness abdominal burn following magnetic resonance guided focused ultrasound therapy," *Burns*, vol. 31, no. 8, pp. 1054–1055, 2005.
- [18] G. K. Hesley, K. R. Gorny, T. L. Henrichsen, D. A. Woodrum, and D. L. Brown, "A clinical review of focused ultrasound ablation with magnetic resonance guidance: an option for treating uterine fibroids," *Ultrasound Quarterly*, vol. 24, no. 2, pp. 131–139, 2008.
- [19] M. J. Voogt, H. Trillaud, Y. S. Kim et al., "Volumetric feedback ablation of uterine fibroids using magnetic resonance-guided high intensity focused ultrasound therapy," *European Radiology*, vol. 22, no. 2, pp. 411–417, 2012.
- [20] R. MacHtinger, Y. Inbar, S. Cohen-Eylon, D. Admon, A. Alagem-Mizrachi, and J. Rabinovici, "MR-guided focus ultrasound (MRgFUS) for symptomatic uterine fibroids: predictors of treatment success," *Human Reproduction*, vol. 27, no. 12, pp. 3425–3431, 2012.
- [21] M. E. Ikink, M. J. Voogt, H. M. Verkooijen et al., "Mid-term clinical efficacy of a volumetric magnetic resonance-guided high-intensity focused ultrasound technique for treatment of symptomatic uterine fibroids," *European Radiology*, vol. 23, no. 11, pp. 3054–3061, 2013.
- [22] C. Damianou and K. Hynynen, "Focal spacing and near-field heating during pulsed high temperature ultrasound therapy," *Ultrasound in Medicine and Biology*, vol. 19, no. 9, pp. 777–787, 1993.
- [23] K. Hynynen, A. Darkazanli, E. Unger, and J. F. Schenck, "MRI-guided noninvasive ultrasound surgery," *Medical Physics*, vol. 20, no. 1, pp. 107–115, 1993.
- [24] Y.-S. Kim, B. Keserci, A. Partanen et al., "Volumetric MR-HIFU ablation of uterine fibroids: role of treatment cell size in the improvement of energy efficiency," *European Journal of Radiology*, vol. 81, no. 11, pp. 3652–3659, 2012.
- [25] A. Agresti and B. A. Coull, "Approximate is better than "exact" for interval estimation of binomial proportions," *The American Statistician*, vol. 52, no. 2, pp. 119–126, 1998.
- [26] D. L. Brown, T. T. Cai, and A. DasGupta, "Confidence intervals for a binomial proportion and asymptotic expansions," *The Annals of Statistics*, vol. 30, no. 1, pp. 160–201, 2002.
- [27] J. Sauro and J. R. Lewis, "Estimating completion rates from small samples using binominal confidence intervals: comparisons and recommendations," in *Proceedings of the Human Factors and Ergonomics Society Annual Meeting*, vol. 49, pp. 2100–2103, 2005.
- [28] K. Funaki, H. Fukunishi, T. Funaki, K. Sawada, Y. Kaji, and T. Maruo, "Magnetic resonance-guided focused ultrasound surgery for uterine fibroids: relationship between the therapeutic effects and signal intensity of preexisting T2-weighted magnetic resonance images," *The American Journal of Obstetrics and Gynecology*, vol. 196, no. 2, pp. e184–e186, 2007.
- [29] M. J. Park, Y.-S. Kim, H. Rhim, and H. K. Lim, "Safety and therapeutic efficacy of complete or near-complete ablation of symptomatic uterine fibroid tumors by MR imaging-guided high-intensity focused US Therapy," *Journal of Vascular and Interventional Radiology*, vol. 25, no. 2, pp. 231–239, 2014.
- [30] Y.-S. Kim, M. J. Park, B. Keserci et al., "Uterine fibroids: postsonication temperature decay rate enables prediction of therapeutic responses to MR imaging-guided high-Intensity focused ultrasound ablation," *Radiology*, vol. 270, no. 2, pp. 589–600, 2014.
- [31] S.-W. Yoon, S. H. Cha, Y. G. Ji, H. C. Kim, M. H. Lee, and J. H. Cho, "Magnetic resonance imaging-guided focused ultrasound surgery for symptomatic uterine fibroids: estimation of treatment efficacy using thermal dose calculations," *European Journal of Obstetrics Gynecology & Reproductive Biology*, vol. 169, no. 2, pp. 304–308, 2013.
- [32] M. J. Park, Y.-S. Kim, B. Keserci, H. Rhim, and H. K. Lim, "Volumetric MR-guided high-intensity focused ultrasound ablation of uterine fibroids: treatment speed and factors influencing speed," *European Radiology*, vol. 23, no. 4, pp. 943–950, 2013.
- [33] S.-W. Yoon, S. J. Seong, S.-G. Jung, S. Y. Lee, H. S. Jun, and J. T. Lee, "Mitigation of abdominal scars during MR-guided focused ultrasound treatment of uterine leiomyomas with the use of an energy-blocking scar patch," *Journal of Vascular and Interventional Radiology*, vol. 22, no. 12, pp. 1747–1750, 2011.
- [34] N. Charkoudian, "Skin blood flow in adult human thermoregulation: how it works, when it does not, and why," *Mayo Clinic Proceedings*, vol. 78, no. 5, pp. 603–612, 2003.
- [35] J. M. Johnson and D. L. Kellogg Jr., "Thermoregulatory and thermal control in the human cutaneous circulation," *Frontiers in Bioscience—Scholar*, vol. 2, no. 3, pp. 825–853, 2010.
- [36] S. Khoshnevis, N. K. Craik, and K. R. Diller, "Cold-induced vasoconstriction may persist long after cooling ends: an evaluation of multiple cryotherapy units," *Knee Surgery, Sports Traumatology, Arthroscopy*, 2014.
- [37] G. J. Hodges, K. Zhao, W. A. Kosiba, and J. M. Johnson, "The involvement of nitric oxide in the cutaneous vasoconstrictor response to local cooling in humans," *Journal of Physiology*, vol. 574, no. 3, pp. 849–857, 2006.
- [38] C. T. Minson, "Thermal provocation to evaluate microvascular reactivity in human skin," *Journal of Applied Physiology*, vol. 109, no. 4, pp. 1239–1246, 2010.
- [39] C. H. E. Imray, P. Richards, J. Greeves, and J. W. Castellani, "Nonfreezing cold-induced injuries," *Journal of the Royal Army Medical Corps*, vol. 157, no. 1, pp. 79–84, 2011.
- [40] W. B. Long III, R. F. Edlich, K. L. Winters, and L. D. Britt, "Cold injuries," *Journal of Long-Term Effects of Medical Implants*, vol. 15, no. 1, pp. 67–78, 2005.
- [41] B. J. Ingram and T. J. Raymond, "Recognition and treatment of freezing and nonfreezing cold injuries," *Current Sports Medicine Reports*, vol. 12, no. 2, pp. 125–130, 2013.
- [42] R. Sallis and C. M. Chassay, "Recognizing and treating common cold-induced injury in outdoor sports," *Medicine & Science in Sports & Exercise*, vol. 31, no. 10, pp. 1367–1373, 1999.

- [43] J. A. McMahon and A. Howe, "Cold weather issues in sideline and event management," *Current Sports Medicine Reports*, vol. 11, no. 3, pp. 135–141, 2012.
- [44] B. E. Tloutan, A. J. Mancini, J. A. Mandell, D. E. Cohen, and M. R. Sanchez, "Skin conditions in figure skaters, ice-hockey players and speed skaters: part II cold-induced, infectious and inflammatory dermatoses," *Sports Medicine*, vol. 41, no. 11, pp. 967–984, 2011.
- [45] P. Baron, M. Ries, R. Deckers et al., "In vivo T<sub>2</sub>-based MR thermometry in adipose tissue layers for high-intensity focused ultrasound near-field monitoring," *Magnetic Resonance in Medicine*, vol. 72, no. 4, pp. 1057–1064, 2013.
- [46] Z. M. Lénárd, N. J. McDannold, F. M. Fennessy et al., "Uterine leiomyomas: MR imaging-guided focused ultrasound surgery-imaging predictors of success 1," *Radiology*, vol. 249, no. 1, pp. 187–194, 2008.
- [47] P. N. T. Wells, "Absorption and dispersion of ultrasound in biological tissue," *Ultrasound in Medicine & Biology*, vol. 1, no. 4, pp. 369–376, 1975.
- [48] M. J. Voogt, M. Van Stralen, M. E. Ikin et al., "Targeted vessel ablation for more efficient magnetic resonance-guided high-intensity focused ultrasound ablation of uterine fibroids," *CardioVascular and Interventional Radiology*, vol. 35, no. 5, pp. 1205–1210, 2012.

## Review Article

# MRI for Crohn's Disease: Present and Future

Kichul Yoon,<sup>1,2</sup> Kyu-Tae Chang,<sup>3</sup> and Hong J. Lee<sup>2</sup>

<sup>1</sup>Department of Internal Medicine, Korea University, Seoul 136-705, Republic of Korea

<sup>2</sup>Biomedical Research Institute, Chung-Ang University College of Medicine, Seoul 156-756, Republic of Korea

<sup>3</sup>National Primate Research Center (NPRC), Korea Research Institute of Bioscience and Biotechnology (KRIBB), Ochang 363-883, Republic of Korea

Correspondence should be addressed to Kyu-Tae Chang; changkt@kribb.re.kr and Hong J. Lee; leehj71@gmail.com

Received 18 August 2014; Revised 9 October 2014; Accepted 11 December 2014

Academic Editor: Takeshi Yokoo

Copyright © 2015 Kichul Yoon et al. This is an open access article distributed under the Creative Commons Attribution License, which permits unrestricted use, distribution, and reproduction in any medium, provided the original work is properly cited.

Crohn's disease (CD) is a chronic inflammatory condition with relapsing-remitting behavior, often causing strictures or penetrating bowel damage. Its lifelong clinical course necessitates frequent assessment of disease activity and complications. Computed tomography (CT) enterography has been used as primary imaging modality; however, the concern for radiation hazard limits its use especially in younger population. Magnetic resonance (MR) imaging has advantages of avoiding radiation exposure, lower incidence of adverse events, ability to obtain dynamic information, and good soft-tissue resolution. MR enterography (MRE) with oral contrast agent has been used as primary MR imaging modality of CD with high sensitivity, specificity, and interobserver agreement. The extent of inflammation as well as transmural ulcers and fibrostenotic diseases can be detected with MRE. Novel MR techniques such as diffusion-weighted MRI (DWI), motility study, PET-MRI, and molecular imaging are currently investigated for further improvement of diagnosis and management of CD. MR spectroscopy is a remarkable molecular imaging tool to analyze metabolic profile of CD with human samples such as plasma, urine, or feces, as well as colonic mucosa itself.

## 1. Introduction

Inflammatory bowel disease (IBD) includes two major forms of chronic intestinal disorder: Crohn's disease (CD) and ulcerative colitis (UC) [1, 2]. CD is a chronic inflammatory condition characterized by relapsing-remitting clinical behavior, potentially affecting any portion of the gastrointestinal tract from mouth to anus. It can occur at any age but most often in second or third decade [3]. A systematic review revealed that the highest annual incidence of CD was 12.7 per 100,000 person-years in Europe, 5.0 person-years in Asia and the Middle East, and 20.2 per 100,000 person-years in North America [4]. According to an extensive review of natural course for CD [5], at the time of diagnosis one-third of the patients had ileitis, colitis, or ileocolitis, up to one-third of the patients had evidence of a stricturing or penetrating intestinal complication. Half of all patients had experienced an intestinal complication within 20 years after diagnosis. The combined effects of genetic, environmental, and/or epithelial barrier dysfunction cause activation of mucosal immune

responses, which in turn lead to inflammatory response [1]. It is not unusual to find intestinal inflammation leading to progressive bowel damage, increasing disability, and an impaired quality of life [5].

The diagnosis of CD is made from patient's history and physical examination supported by laboratory, endoscopic, radiologic, and pathologic findings. The European Crohn's and Colitis Organisation (ECCO) grouped clinical disease activity into mild, moderate, and severe but these are not precisely defined entities. Most clinical trials in patients with active Crohn's disease recruit patients with a Crohn's Disease Activity Index (CDAI) of >220 [6]. This index is a point score and comprises eight items (stool frequency, abdominal pain, subjective general wellbeing, presence of complications and abdominal mass, use of antidiarrheal medications, hematocrit, and weight deviation) [7]. Treatment of Crohn's disease aims to achieve sustained clinical and endoscopic remission and to interrupt the disease course that ends in intestinal failure and complications [8].

## 2. MRI for CD: Present

*2.1. Diagnostic Tools for CD.* The gold standard diagnostic tools for CD are ileocolonoscopy and gastroduodenoscopy, providing direct and reliable image of mucosal surface. They have advantage of getting the tissue sample and even treating bleeding complication. However, they only cover proximal small bowel or terminal ileum, requiring other modalities for small bowel evaluation. Transabdominal ultrasound is used as initial imaging modality but it lacks both sensitivity and specificity with high interobserver variability [2]. Capsule endoscopy provides mucosal imaging of small bowel but can only be used when stricture is excluded. Patients with extensive small bowel CD are at higher risk of capsule retention, limiting its clinical use [9, 10]. There have been several radiologic approaches to assess small bowel in CD. The small-bowel follow-through (SBFT) has been the standard modality; however, several studies have shown that SBFT is not accurate and feasible study over other modalities such as computed tomography (CT), enterography, or capsule endoscopy [11, 12]. Among them, CT enterography has been the most commonly used cross-sectional imaging modality to evaluate CD patients. However, due to its potential hazard from ionizing radiation, its repetitive use can be of concern especially in CD, a disease with early onset and frequent relapses [13, 14].

Magnetic resonance (MR) imaging is being preferred because it lacks radiation exposure with validated sensitivity and specificity in both adults and children [15–18]. MR imaging has many advantages other than the lack of radiation, such as provision of static and dynamic three-dimensional information of small bowel, improved soft-tissue contrast resolution, and lower incidence of adverse events compared with CT with iodinated contrast agent. On the contrary, it also has limitations such as higher cost, variations in image quality, and lower spatial and temporal resolution [17, 19–22].

### 2.2. MR Enterography (MRE)

*2.2.1. Intraluminal Contrast Agents: Type of Contrast.* Use of MRI for bowel has not been popular until recently because it needed long acquisition time, making the imaging of the primarily peristaltic organ difficult. Furthermore, lack of proper contrast for bowel had also limited its use. Imaging of small bowel needs luminal distension because even large lesion can be undetected if the bowel is evaluated in collapsed state [23, 24]. According to these signal properties, agents can be classified as positive (“bright” lumen), negative (“dark” lumen), or biphasic agents (“bright” lumen on T1 and “dark” on T2 or conversely “dark” lumen on T2 and “bright” on T1) [23]. There are a number of hyperosmolar T1 hypointense/T2 hyperintense biphasic oral contrast agents currently available. Water is cheap, safe, and readily available agent. However, its rapid absorption limits its role of proper distension of small bowel [25]. So it is mixed with other agents to improve luminal distension. Lactose delays the absorption of the water in contrast material effectively, obtaining conspicuity of the bowel [26]. Diatrizoic acid (gastrografin) can achieve very good distention, homogeneity, and delineation in the central

segments from the ileum to the left colon flexure in majority of cases, due to the adequate contrast media supply in these regions. Diarrhea is a major problem affecting nearly all patients [27]. Recent report showed that 3% sorbitol and a psyllium based bulk fiber showed no significant difference at distending the small bowel [28]. Other groups reported that novel mixture containing methylcellulose powder with water, low-concentration (4.9%) barium, and sorbitol allowed good-quality enterographic images and patient tolerance [29].

*2.2.2. Intraluminal Contrast Agents: Methods of Delivery.* Enteroclysis has been employed as one of the useful MR techniques for evaluation of CD. However, administration of 1.5 to 2 L of isosmotic water solution through nasojejunal catheter causes patient discomfort. In contrast, MR enterography (MRE) takes the cross-sectional images targeting small bowel after administration of large volume of oral enteric contrast without nasojejunal intubation [20, 30]. Several studies have shown that MRE has better patient compliance than enteroclysis and similar diagnostic efficacy to the method in evaluating CD [31, 32]. It assesses not only the bowel but also the surrounding perienteric structures such as mesentery or adjacent organs [19, 20, 22, 33]. Therefore, proper use of aforementioned contrast agents does allow MR imaging evaluation of small bowel CD.

*2.3. Conventional Techniques.* Antiperistaltic agents are commonly used these days in practice as recent studies have shown benefits in using antiperistaltic (IV glucagon), improving visualization of the bowel wall, mainly because they suppress peristalsis to reduce motion-related blurring and ghosting artifacts [34].

Although there is no definite consensus or guideline on oral contrast regimen, the agents described above are generally administered 10 to 15 minutes before the scanning. The scout imaging assesses the progression of oral contrast and distension. If the contrast has not reached terminal ileum, the further imaging can be postponed. Patients can be scanned in the prone or supine position in multichannel torso or body phased array coil on a 1.5- or 3-tesla (T) magnet [18]. The sequences of the MRE examination include axial and coronal T2-weighted single-shot fast spin echo (SSFSE) sequences and balanced steady state free precession (SSFP) sequences. SSFSE acquires all the necessary data for reconstruction with one excitation [35]. It is excellent for visualizing edema, wall thickening, and fluid in bowel wall and mesentery [18]. Balanced SSFP is characterized by two unique features, a very high signal-to-noise ratio and a T2/T1-weighted image contrast [36]. The recent development of faster pulse sequences provides an opportunity to provide a movie of cine images [37]. Cine imaging confers the ability to observe the motion of intestinal segments over a relatively short period and in real time. It provides high temporal, spatial, and contrast resolution for monitoring bowel contractions [38]. After administration of IV gadolinium-containing contrast material (0.1-0.2 mmol/kg), dynamic coronal 3D T1-weighted gradient echo (GRE) sequences with fat suppression are obtained in time intervals of 45 to 55, 70, and 180 seconds. These intervals are institutionally specific. Delayed axial and

coronal postcontrast 2D or 3D T1-weighted sequences with fat suppression are acquired following dynamic imaging [18]. Although rapid transit to the right colon is seen in some patients, most patients require a delay of at least 40–60 minutes from contrast material ingestion to imaging [39, 40].

The field strength of the MRI magnet will affect the rate at which images may be obtained [37]. For 1.5 T systems, the MRI technologist selects 5 to 7 representative coronal slices of the abdomen using the sagittal localizer image. Each slice is obtained during a 30-second period with a total of 50 images obtained during that time period. With newer 3 T systems, it is possible to obtain up to 110 images per location during the same 30-second time period. The presence of “banding” artifact inherent to the SSFP sequence is of concern for 3 T imaging. It is pronounced particularly at air/soft tissue interfaces [37]. Imaging at higher field strength has a greater signal-to-noise ratio and also has the potential of reducing scan times. A retrospective study of 46 children with biopsy-proven CD reported that, with appropriate attention to technique and with optimal distension and control of movement, high-quality 3 T assessment of the abdomen, pelvis, and perineum is possible [41].

**2.4. Diffusion-Weighted MRI (DWI).** Like other abdominal applications, DWI benefits from increased signal-to-noise ratio at 3 T with improved sensitivity compared with 1.5 T. However, image distortion from increased magnetic susceptibility often results in a loss of image quality at 3 T. Magnetic susceptibility artifacts may be limited by using parallel imaging techniques such as sensitivity encoding, integrated parallel acquisition, generalized autocalibrating partially parallel acquisition, and array spatial sensitivity encoding [42].

Diffusion-weighted MRI (DWI) has long been used in other parts of body such as brain. Although application of DWI to assess bowel is a relatively new trend, DWI may yield comparable performances for detecting and assessing ileal inflammation in CD [43]. A high signal intensity in DWI and restricted diffusion of the bowel wall also have been related to acute inflammation [44–46].

A review with 18 patients having active CD of terminal ileum showed that DWI can provide quantitative measures of small bowel inflammation that can differentiate actively inflamed small bowel segments from normal small bowel in CD. It showed better sensitivity compared with dynamic contrast-enhanced MR [46]. An observational prospective study with 130 CD patients reported that, at certain apparent diffusion coefficient, sensitivity and specificity of discriminating active from nonactive CD were 96.9% and 98.1%, respectively, for the colon/rectum, and 85.9% and 81.6%, respectively, for ileum. They also reported high interobserver agreement [47]. A recent study involved 31 CD patients with ileal involvement to compare DWI with conventional MRE in estimating inflammation in small bowel CD. DWI hyperintensity was highly correlated with disease activity evaluated using conventional MRE [43]. DWI also showed additional value to T2-weighted imaging for diagnosis of internal fistula and sinus tracts, according to a retrospective study reviewing the 25 fistulous lesions [48].

**2.5. MRE Findings in CD.** Patients with CD can be classified by Montreal or Paris classification regarding age of onset, localization, behavior, and growth. The behavior is subdivided into B1 (nonstricturing/nonpenetrating), B2 (stricturing), and B3 (penetrating). Perianal penetrating diseases are considered separately, as they show different prognosis than other penetrating patterns of CD [49]. Although there is no exact definition or consensus, disease activity is usually grouped into mild, moderate, and severe. CDAI comprises relatively complex clinical and laboratory data, limiting its clinical use [2]. Differentiation between the subtypes is clinically important because active inflammation is usually treated medically unless there are extramural complications, while fibrostenotic disease characterized by obstructive symptoms often requires surgery [50].

Maglante et al. suggested an imaging-based classification of small bowel CD subtypes. They radiologically classified CD into four groups: active inflammatory, fibrostenotic, fistulizing/perforating, and reparative or regenerative subtype. They reasonably correlate with the clinical classifications [22].

**2.6. Active Inflammatory Subtype.** Active inflammatory subtype of CD is characterized by local inflammation, aphthoid and deep ulcers, frequent transmural inflammation with lymphoid aggregates, and granuloma formation. Different morphological and functional parameters are used to assess disease activity in MRE. They are thickness of wall, the degree of wall gadolinium- (Gd-) enhancement, T2 mural signal intensity, enhancement of local lymph nodes, pattern of wall Gd-enhancement, increased mesenteric vascularity, and time-enhancement curves of Gd-wall enhancement. Each of these parameters has proved to be statistically correlated with the biological, endoscopic, or histological activity [21, 51–53].

Mesenteric edema is present in some patients with advanced active disease, and it tracks along the adjacent mesentery from an inflamed bowel loop [40]. The degree of thickening has been proven to be correlated with Crohn's Disease Activity Index. A wall thickness greater than 3 mm in a distended small bowel loop can be regarded as abnormal. In patients with small bowel CD, wall thickness usually ranges between 5 and 10 mm. Thickened wall without edema has low to moderate signal intensity on SSFP and HASTE images [40, 54]. Stratified contrast enhancement with avid enhancement of the mucosa relative to the submucosa and muscular layers helps confirm active Crohn's disease [40]. Signal hyperintensity in the bowel wall in T2-weighted images (T2WIs), especially in fat-suppressed sequences, indicates wall edema and is a sign of acute inflammation [55]. Increased intravenous contrast enhancement of the bowel wall also indicates acute inflammation. Mucosal increased enhancement with submucosal edema is so-called “stratified type of bowel enhancement” and has been especially related to acute disease [30]. Full-thickness nonstratified enhancement of intestinal wall can represent transmural acute inflammation as well [56].

On high-resolution SSFP image with fat suppression, aphthoid ulcers are seen as a nidus of high signal intensity surrounded by moderate signal intensity [57]. Transmural ulcers are outlined by luminal contrast material and seen as linear high-signal intensity into the bowel wall. Images obtained in

a plane perpendicular to the bowel allow accurate assessment of transmural and peri-intestinal inflammatory changes [57].

**2.7. Fibrostenotic/Fistulizing Subtype.** Small bowel obstruction is the chief clinical manifestation of fibrostenotic disease. A fixed narrowing of the affected segment is seen on MRE. Chronic fibrotic strictures typically are hypointense on both T1- and T2-weighted images and show inhomogeneous contrast enhancement, with no evidence of edema or surrounding inflammation of mesentery [20, 57]. Large sinus tracts and fistulas may be outlined by enteral contrast material and are seen as high-signal intensity linear features. Solitary internal fistulas present as tubular tracts, star-shaped bowel loops, indicating a complex internal fistula [58].

A recent study with MRE evaluating 76 CD patients showed high  $\kappa$  value and Lin's concordance correlation coefficient between the intraoperative and radiological assessments. The diagnosis of a stricture had highest sensitivity and the detection of inflammatory mass showed the lowest sensitivity. Abscesses had the lowest positive predictive value in that study, while fistulae were found to have the best correlation between the surgical and MRE-based diagnoses [59]. Various efforts have been made to improve diagnostic value of MRE. A study comparing MRE with or without water enema showed that MRE with enema was statistically superior to MRE without enema in detecting inflammation in the terminal ileum, ascending colon, and rectum [60]. Further improvement of imaging quality, sensitivity, and specificity of MRE is expected with technical developments.

**2.8. MRI for Motility.** Many studies have shown that gut motility at MRI is decreased in active or chronic CD. The bowel segments affected by CD show significantly increased number of lesions in individual patient as well as overall patients with CD [61–64]. The sequence for small bowel motility is a fast cine sequence using fast T2-weighted SSFP or echo planar imaging sequences with a maximum repetition time of 1 second. The images must be acquired before the application of a spasmolytic drug [61]. There was a study correlating MR-detectable motility alterations of the terminal ileum with biopsy-documented active and chronic changes in CD. It analyzed 43 patients who underwent both MRE and terminal ileum biopsy. Histopathology correlated with presence of hypomotility or complete arrest and grade of motility alterations [63]. Another study measured contraction frequency, amplitude, amplitude diameter ratio, and luminal diameter via MRI as well as the blood levels of CRP and fecal levels of calprotectin. A significant inverse linear correlation was found between the contraction frequency and both the level of CRP and calprotectin [64]. In addition, a study with healthy volunteers assessing software-quantified small bowel motility captured with MRI and testing the ability to detect changes in motility induced by pharmacologic agents showed that the repeatability between baseline measurements of motility was high. The measured motility with neostigmine was significantly higher than that with placebo, whereas that with butylscopolamine was significantly lower than that with placebo [65].

### 3. MRI for CD: Future

**3.1. PET-MRI.** There are novel MRI-related techniques not yet easily available or cost-effective but have potential application to CD. Both positron emission tomography (PET) with fluorodeoxyglucose (FDG) and MRI have been shown to be useful for diagnostic evaluation of a variety of inflammatory processes. However, only a few PET-MRI units are operational around the world and mostly only for research use. CD could be a candidate target of the novel technique PET-MRI but it currently has no clearly established role [66].

#### 3.2. MR Spectroscopy

**3.2.1. Introduction of MRS.** Genomics and proteomics have emerged to explain biological phenomenon. However, they do not provide dynamic metabolic status of tissue and whole organism [67]. MR molecular imaging and MR spectroscopy (MRS) are still experimental but promising, because they are some of the leading technologies in metabolomics and have possibility to analyze and characterize the molecular composition of inflamed bowel wall [51]. As MRS has more accurate quantitation and better reproducibility than mass spectrometry, MRS is already routinely used in many malignant conditions such as brain, breast, and prostate cancer [68]. The essential goal of MRS is to determine the distribution of metabolites associated with the relevant pathology. Their presence, absence, or relative amount compared with other metabolites is analyzed [69]. The MR signal produces varying but predictive pattern of resonant frequencies corresponding to molecular arrangements of some atomic nuclei susceptible to perturbations, typically protons. The structural or chemical information regarding the reaction of the nuclei can be obtained. After the examination is performed the data are usually presented in a one-dimensional NMR (nuclear MR) frequency spectrum [69, 70]. There are a number of biologically relevant MR-visible isotopes in vivo. The most common nuclei used are those that do not require exogenous label such as  $^{31}\text{P}$ ,  $^1\text{H}$ , and  $^{23}\text{Na}$  which generate spectra from endogenous metabolites [71].

**3.2.2. MRS Techniques in CD.**  $^1\text{H}$ NMR is most commonly employed in MRS for inflammatory bowel disease. On a one-dimensional NMR spectrum, the peak shows signal from a particular chemical configuration of the nucleus (e.g.,  $^1\text{H}$ ) and the intensity is also noted. Area under a peak relates to the number of nuclei that have identical chemical bonding configuration [69]. Recently, two-dimensional J-resolved (JRES) NMR spectroscopy has been introduced. It additionally disperses the overlapping resonances into a second dimension. It has advantages such as increased spectral dispersion, confidence in metabolite identification, and reduced batch-to-batch variation. It also has some disadvantages like longer acquisition times, higher technical variability, and phase-twisted lineshapes [72].

Chemometric analysis and comparison of  $^1\text{H}$ NMR are commonly hampered by intersample peak position and line width variation due to matrix effects. To mitigate this problem, "targeted profiling" method was introduced. Individual

NMR resonances of interest are mathematically modeled from pure compound spectra. This database is then interrogated to identify and quantify metabolites in complex spectra of mixtures, such as biofluids. The method is highly stable in PCA-based pattern recognition, insensitive to water suppression, relaxation times, and scaling factors. Hence, direct comparison of data acquired under varying conditions is made possible [73].

The feasibility of metabonomics in clinical studies was first suggested using  $^1\text{H}$  NMR based metabonomic analysis on plasma and urine samples obtained from healthy subjects. The  $^1\text{H}$  NMR spectra obtained for urine and plasma samples were analysed using principal components analysis (PCA) in order to generate metabonomic data [74, 75].  $^1\text{H}$  NMR-based metabonomic approach has been suggested as a quantitative measurement of metabolic response in CD [76].

A recent study tried to find metabolic biomarkers and the correlation between serum zinc in CD patients performed  $^1\text{H}$  NMR spectroscopy experiments on a 500 MHz spectrometer and five-millimeter NMR tubes. Deuterium oxide ( $\text{D}_2\text{O}$ ) 100  $\mu\text{L}$  provided NMR lock signal for NMR spectrometer. Broad resonances caused from combination of high molecular weight components were suppressed by Carr-Purcell-Meiboom-Gill (CPMG) experiment. It enhanced visualization of superimposed sharper resonances from low molecular weight (amino acids and carboxylic acids). CPMG spin echo pulse sequent was used to record ID  $^1\text{H}$  NMR spectra, which were recorded at 298 K. Peaks in the serum spectra were referenced to the chemical shift of lactate. The integral values of each spectrum were normalized to a constant sum of all integrals [77].

Biochemical analysis of fecal extracts has been studied by several institutions because it is cost-effective and reflects biochemical changes of bowel disease. Characterization of fecal extracts obtained from patients with CD and UC by employing  $^1\text{H}$  NMR spectroscopy and multivariate pattern recognition techniques was reported to differentiate two IBDs. The 400  $\mu\text{L}$  of fecal extract was added to 200  $\mu\text{L}$  of water containing  $\text{D}_2\text{O}$  and a chemical shift reference sodium 3-(trimethylsilyl)propionate-2,2,3,3- $\text{d}_4$ . After centrifuge, the supernatant was pipetted into 5 mm NMR tube and  $^1\text{H}$  NMR spectra were acquired for each sample at 600.13 MHz for  $^1\text{H}$  equipped with a 5 mm triple resonance probe with an inverse detection [78].

**3.3. MRS Findings in IBD.** There have been several studies on MRS findings in IBD. Most of them included both UC and CD for analysis, showing similarities and differences between them. A study using *in vitro*  $^1\text{H}$  NMR reported that patients with IBD showed similar metabolic profile in macroscopically involved and uninvolved colonic mucosa compared with that of controls [76]. The past few years have seen an increase in studies of experimental and human IBD focusing on the search for small metabolites, such as amino acids, bases, and tricarboxylic acid (TCA) cycle intermediates. Experimental methods for the screening of metabolites in serum, urine, fecal extracts, and colon tissue include  $^1\text{H}$  NMR spectroscopy [79]. A very recent study tried to

search for metabolic biomarkers and the correlation with serum zinc in Crohn's disease patients. The result suggested valine and isoleucine as differentiating metabolites for CD diagnosis [77]. The authors have previously proposed that  $^1\text{H}$  NMR could be used as part of metabonomics to diagnose CD, as the disease shows signs and symptoms similar to other medical problems. Applications of NMR and supervised pattern recognition in the field of metabonomics were also reviewed in recent years [80].

According to an analysis of the fecal extracts of both CD and UC patients, they were characterized by reduced levels of butyrate, acetate, methylamine, and trimethylamine, reflecting changes in the gut microbiota. Quantities of amino acids were elevated in the feces from CD and UC, implying malabsorption. Metabolic differences in fecal profiles were more marked in the CD group, indicating more extensive inflammation in the specific study. They reported that glycerol resonances were a dominant feature of fecal spectra from patients with CD [78]. A basic research also supports the metabonomic approach to IBD. Metabolic profiling of the fecal extracts of dextran sulfate sodium- (DSS-) induced colitis mice with  $^1\text{H}$  NMR was reported. It was carried out to assess the effects of probiotics on colonic inflammation. Mice treated with probiotic lactic acid bacteria showed increased short chain fatty acids levels in the feces [81].

Quantitative metabonomic profiling of serum, plasma, and urine from human subjects with active CD and UC was also performed, employing  $^1\text{H}$  NMR and "targeted analysis." In serum and plasma of IBD patients, methanol, mannose, formate, 3-methyl-2-oxovalerate, and amino acids such as isoleucine were prominently increased. In urine, maximal increases were observed for mannitol, allantoin, xylose, and carnitine. Both serum and plasma of UC and CD patients showed significant decreases in urea and citrate, whereas, in urine, decreases were observed, among others, for betaine and hippurate. The metabolic differences between the CD and UC cohorts are less pronounced [82].

To identify tissue-specific markers associated with CD, a metabonomic approach to monitor events associated with the gradual development of CD-like ileitis in the TNF( $\Delta\text{ARE}/\text{WT}$ ) mouse model was done using  $^1\text{H}$  NMR. The approach showed shifts in the intestinal lipid metabolism concomitant to the histological onset of inflammation. The advanced disease was characterized by a significantly altered metabolism of cholesterol, triglycerides, phospholipids, plasmalogens, and sphingomyelins in the inflamed ileal tissue and the adjacent proximal colon. Modifications of the general cell membrane composition, alteration of energy homeostasis, and the generation of inflammatory lipid mediators could explain the result [83].

Metabolism of the colonic mucosa itself of patients with IBD was also reported using  $^1\text{H}$  NMR. In the active phase of UC and CD, significantly lower concentration of amino acids (isoleucine, leucine, valine, alanine, glutamate, and glutamine), membrane components (choline, glycerophosphorylcholine, and myoinositol), lactate, and succinate was observed compared to normal mucosa of controls. Patients in the active phase of UC and CD also showed increased

level of alpha-glucose compared to normal mucosa. In contrast to active disease, altered level of metabolites indicated decreased protein and carbohydrate metabolism in patients with chronic inflammation. Decreased energy status and deterioration of mucosa integrity during chronic inflammation could explain these findings [84]. In a study based on urinary metabolomics, individuals with IBD could be differentiated from healthy ones. Major differences between IBD and healthy included TCA cycle intermediates, amino acids, and gut microflora metabolites [85].

NMR has shown possibilities to differentiate between UC and CD, which is not always easy on clinical practice. Interestingly, formate was significantly lower in colonic mucosa of patients with active UC compared to patients with the active colonic CD, suggesting the potential of in vitro MRS in the differentiation of these two diseases [84]. NMR of urine samples also revealed that hippurate levels were lowest in CD patients and differed significantly between the three cohorts (UC, CD, and healthy control). Urine formate levels were higher and 4-cresol sulfate levels were lower in CD patients than in UC patients or controls. PCA also revealed clustering of the groups; PLS-DA modeling was able to distinguish the cohorts [86].

**3.4. Nanoparticles.** Imaging of inflammatory sites can be achieved by making use of several different characteristics of affected tissues. A relatively new and promising application of lipidic nanoparticles is their use as multimodal MR contrast agents. The imaging of inflammatory sites has been studied mainly in cardiovascular diseases such as atherosclerosis or myocardial infarction. Nanoparticles are employed not only for diagnosis but also for monitoring of drug delivery [87, 88]. As many inflammatory conditions have distinct molecular features in the diseased tissues, lipid-based nanoparticles could be another possibility to evaluate CD.

Imaging of inflammatory sites can be achieved by making use of several different characteristics of affected tissues. Specific overexpression of endothelial adhesion molecules caused by the inflammatory cytokines can be used as a target for contrast agents. Ongoing angiogenic response could also be used by injection of a nonspecific contrast agent which would accumulate at the inflamed site. Magnetic nanoparticles have frequently been used as MRI contrast agents as they disturb the relaxation of nearby protons, thus darkening T2-weighted MRIs. Depending on their size, nanoparticles can be used to detect vascular leak. There was a report on development of a noninvasive method using ferumoxtran-10 nanoparticles to visualize type 1 diabetes at the target organ level in patients with active insulinitis. Ferumoxtran-10 has a dextran coating and it is readily taken up by macrophages without provoking activation or inducing proinflammatory cytokines. It has been used in the noninvasive detection of clinically occult cancer metastatic to lymph nodes. All participants underwent at least 3 MRI scans: a premagnetic nanoparticle (MNP) series, an immediate post-MNP series, an indicator of vascular volume and useful for pancreas volume estimates, and a delayed post-MNP series, which likely reflects leakage of MNPs and retention by phagocytic cells [89, 90].

In addition, migration of cells involved in inflammation can be followed after labeling the cells with an appropriate contrast material when cells are labeled outside the body and subsequently injected [91, 92]. Currently, much effort is being put into research on the targeted imaging of cell adhesion molecules involved in inflammation. Targeting of the adhesion molecule could be done with antibodies, proteins, peptides, or small molecules conjugated to an MRI contrast agent. Lipid-based contrast agents have been used for those strategies. However, there have not been enough studies to apply this strategy specific to CD [93, 94].

Using fluorescent magnetic nanoparticles, a group of researchers screened the library against different cell lines and discovered a series of nanoparticles with high specificity for endothelial cells, activated human macrophages, or pancreatic cancer cells [95]. Currently the studies using nanoparticles particularly for CD have been scarce. It could be a topic for researchers; however it currently has no clearly established role in CD.

## 4. Conclusion

In recent years, MRE has become a part of standard diagnostic modality in CD. Novel MRI techniques such as DWI, motility studies, PET-MRI, and molecular imaging might further contribute to diagnosis and management of this chronic inflammatory disease.

## Conflict of Interests

The authors declare that there is no conflict of interests regarding the publication of this paper.

## Acknowledgment

This research was supported by grants from the KRIBB Research Initiative Program (KGM4611411), Republic of Korea.

## References

- [1] D. Corridoni, K. O. Arseneau, and F. Cominelli, "Inflammatory bowel disease," *Immunology Letters*, vol. 161, no. 2, pp. 231–235, 2014.
- [2] M. W. Laass, D. Roggenbuck, and K. Conrad, "Diagnosis and classification of Crohn's disease," *Autoimmunity Reviews*, vol. 13, no. 4-5, pp. 467–471, 2014.
- [3] R. D'Iincà and R. Caccaro, "Measuring disease activity in Crohn's disease: what is currently available to the clinician," *Clinical and Experimental Gastroenterology*, vol. 7, no. 1, pp. 151–161, 2014.
- [4] N. A. Molodecky, I. S. Soon, D. M. Rabi et al., "Increasing incidence and prevalence of the inflammatory bowel diseases with time, based on systematic review," *Gastroenterology*, vol. 142, no. 1, pp. 46.e42–54.e42, 2012.
- [5] L. Peyrin-Biroulet, E. V. Loftus, J.-F. Colombel, and W. J. Sandborn, "The natural history of adult crohn's disease in population-based cohorts," *The American Journal of Gastroenterology*, vol. 105, no. 2, pp. 289–297, 2010.

- [6] G. van Assche, A. Dignass, J. Panes et al., "The second European evidence-based consensus on the diagnosis and management of Crohn's disease: definitions and diagnosis," *Journal of Crohn's and Colitis*, vol. 4, no. 1, pp. 7–27, 2010.
- [7] W. R. Best, J. M. Bechtel, J. W. Singleton, and F. Kern Jr., "Development of a Crohn's disease activity index. National cooperative Crohn's disease study," *Gastroenterology*, vol. 70, no. 3, pp. 439–444, 1976.
- [8] D. C. Baumgart and W. J. Sandborn, "Crohn's disease," *The Lancet*, vol. 380, no. 9853, pp. 1590–1605, 2012.
- [9] R. Sidhu, D. S. Sanders, A. J. Morris, and M. E. McAlindon, "Guidelines on small bowel enteroscopy and capsule endoscopy in adults," *Gut*, vol. 57, no. 1, pp. 125–136, 2008.
- [10] B. Hall, G. Holleran, D. Costigan, and D. McNamara, "Capsule endoscopy: high negative predictive value in the long term despite a low diagnostic yield in patients with suspected Crohn's disease," *United European Gastroenterology Journal*, vol. 1, no. 6, pp. 461–466, 2013.
- [11] P. B. Wold, J. G. Fletcher, C. D. Johnson, and W. J. Sandborn, "Assessment of small bowel Crohn disease: noninvasive peroral CT enterography compared with other imaging methods and endoscopy—feasibility study," *Radiology*, vol. 229, no. 1, pp. 275–281, 2003.
- [12] S. L. Triester, J. A. Leighton, G. I. Leontiadis et al., "A meta-analysis of the yield of capsule endoscopy compared to other diagnostic modalities in patients with obscure gastrointestinal bleeding," *American Journal of Gastroenterology*, vol. 100, no. 11, pp. 2407–2418, 2005.
- [13] T. Fujii, M. Naganuma, Y. Kitazume et al., "Advancing magnetic resonance imaging in crohn's disease," *Digestion*, vol. 89, no. 1, pp. 24–30, 2014.
- [14] D. J. Brenner and E. J. Hall, "Computed tomography—an increasing source of radiation exposure," *The New England Journal of Medicine*, vol. 357, no. 22, pp. 2277–2284, 2007.
- [15] T. Bosemani, A. Ozturk, A. Tekes, M. O. Hemker, and T. A. G. M. Huisman, "Feasibility of an optimized MR enterography protocol in the evaluation of pediatric inflammatory bowel disease," *JBR-BTR*, vol. 96, no. 4, pp. 196–202, 2013.
- [16] I. Absah, D. H. Bruining, J. M. Matsumoto et al., "MR enterography in pediatric inflammatory bowel disease: retrospective assessment of patient tolerance, image quality, and initial performance estimates," *American Journal of Roentgenology*, vol. 199, no. 3, pp. W367–W375, 2012.
- [17] J. L. Fidler, L. Guimaraes, and D. M. Einstein, "MR imaging of the small bowel," *Radiographics*, vol. 29, no. 6, pp. 1811–1825, 2009.
- [18] S. A. Anupindi, O. Terreblanche, and J. Courtier, "Magnetic resonance enterography: inflammatory bowel disease and beyond," *Magnetic Resonance Imaging Clinics of North America*, vol. 21, no. 4, pp. 731–750, 2013.
- [19] B. C. Allen and J. R. Leyendecker, "MR enterography for assessment and management of small bowel crohn disease," *Radiologic Clinics of North America*, vol. 52, no. 4, pp. 799–810, 2014.
- [20] M. M. Al-Hawary, E. M. Zimmermann, and H. K. Hussain, "MR imaging of the small bowel in crohn disease," *Magnetic Resonance Imaging Clinics of North America*, vol. 22, no. 1, pp. 13–22, 2014.
- [21] J. Rimola, S. Rodriguez, O. Garcia-Bosch et al., "Magnetic resonance for assessment of disease activity and severity in ileocolonic Crohn's disease," *Gut*, vol. 58, no. 8, pp. 1113–1120, 2009.
- [22] D. D. T. Maglinte, N. Gourtsoyiannis, D. Rex, T. J. Howard, and F. M. Kelvin, "Classification of small bowel Crohn's subtypes based on multimodality imaging," *Radiologic Clinics of North America*, vol. 41, no. 2, pp. 285–303, 2003.
- [23] A. Laghi, P. Paolantonio, F. Iafrate, F. Altomari, C. Miglio, and R. Passariello, "Oral contrast agents for magnetic resonance imaging of the bowel," *Topics in Magnetic Resonance Imaging*, vol. 13, no. 6, pp. 389–396, 2002.
- [24] M. Chalian, A. Ozturk, M. Oliva-Hemker, S. Pryde, and T. A. G. M. Huisman, "MR enterography findings of inflammatory bowel disease in pediatric patients," *The American Journal of Roentgenology*, vol. 196, no. 6, pp. W810–W816, 2011.
- [25] O. Minowa, Y. Ozaki, S. Kyogoku, N. Shindoh, Y. Sumi, and H. Katayama, "MR imaging of the small bowel using water as a contrast agent in a preliminary study with healthy volunteers," *American Journal of Roentgenology*, vol. 173, no. 3, pp. 581–582, 1999.
- [26] H. Arslan, Ö. Etlik, M. Kayan, M. Harman, Ý. Tuncer, and O. Temizöz, "Peroral CT enterography with lactulose solution: preliminary observations," *American Journal of Roentgenology*, vol. 185, no. 5, pp. 1173–1179, 2005.
- [27] A. S. Borthne, J. B. Dormagen, K. I. Gjesdal, T. Storaas, I. Lygren, and J. T. Geitung, "Bowel MR imaging with oral Gastrografin: an experimental study with healthy volunteers," *European Radiology*, vol. 13, no. 1, pp. 100–106, 2003.
- [28] S. Saini, E. Colak, S. Anthwal, P. A. Vlachou, A. Raikhlina, and A. Kirpalani, "Comparison of 3% sorbitol vs psyllium fibre as oral contrast agents in MR enterography," *The British Journal of Radiology*, vol. 87, no. 1042, p. 20140100, 2014.
- [29] O. Algin, S. Evrimler, E. Ozmen et al., "A novel biphasic oral contrast solution for enterographic studies," *Journal of Computer Assisted Tomography*, vol. 37, no. 1, pp. 65–74, 2013.
- [30] D. J. Grand, M. Beland, and A. Harris, "Magnetic resonance enterography," *Radiologic Clinics of North America*, vol. 51, no. 1, pp. 99–112, 2013.
- [31] A. G. Schreyer, A. Geissler, H. Albrich et al., "Abdominal MRI after enteroclysis or with oral contrast in patients with suspected or proven Crohn's disease," *Clinical Gastroenterology and Hepatology*, vol. 2, no. 6, pp. 491–497, 2004.
- [32] A. Negaard, L. Sandvik, A. E. Berstad et al., "MRI of the small bowel with oral contrast or nasojejunal intubation in Crohn's disease: randomized comparison of patient acceptance," *Scandinavian Journal of Gastroenterology*, vol. 43, no. 1, pp. 44–51, 2008.
- [33] K. P. Murphy, P. D. McLaughlin, O. J. O'Connor, and M. M. Maher, "Imaging the small bowel," *Current Opinion in Gastroenterology*, vol. 30, no. 2, pp. 134–140, 2014.
- [34] J. R. Dillman, E. A. Smith, S. Khalatbari, and P. J. Strouse, "IV glucagon use in pediatric MR enterography: effect on image quality, length of examination, and patient tolerance," *American Journal of Roentgenology*, vol. 201, no. 1, pp. 185–189, 2013.
- [35] A. Nozaki, "Single shot fast spin echo (SSFSE)," *Nihon Rinsho*, vol. 56, no. 11, pp. 2792–2797, 1998.
- [36] K. Scheffler and S. Lehnhardt, "Principles and applications of balanced SSFP techniques," *European Radiology*, vol. 13, no. 11, pp. 2409–2418, 2003.
- [37] J. Courtier, M. Ohliger, S. J. Rhee, O. Terreblanche, M. B. Heyman, and J. D. Mackenzie, "Shooting a moving target: use of real-time cine magnetic resonance imaging in assessment of the small bowel," *Journal of Pediatric Gastroenterology and Nutrition*, vol. 57, no. 4, pp. 426–431, 2013.

- [38] M. Wakamiya, A. Furukawa, S. Kanasaki, and K. Murata, "Assessment of small bowel motility function with cine-MRI using balanced steady-state free precession sequence," *Journal of Magnetic Resonance Imaging*, vol. 33, no. 5, pp. 1235–1240, 2011.
- [39] D. Lohan, C. Cronin, C. Meehan, A. N. Alhajeri, C. Roche, and J. Murphy, "MR small bowel enterography: optimization of imaging timing," *Clinical Radiology*, vol. 62, no. 8, pp. 804–807, 2007.
- [40] D. J. M. Tolan, R. Greenhalgh, I. A. Zealley, S. Halligan, and S. A. Taylor, "MR enterographic manifestations of small bowel crohn disease," *Radiographics*, vol. 30, no. 2, pp. 367–384, 2010.
- [41] C. Dagia, M. Ditchfield, M. Kean, and A. Catto-Smith, "Feasibility of 3-T MRI for the evaluation of Crohn disease in children," *Pediatric Radiology*, vol. 40, no. 10, pp. 1615–1624, 2010.
- [42] K. J. Chang, I. R. Kamel, K. J. Macura, and D. A. Bluemke, "3.0-T MR imaging of the Abdomen: comparison with 1.5 T," *Radiographics*, vol. 28, no. 7, pp. 1983–1998, 2008.
- [43] A. Buisson, A. Joubert, P.-F. Montoriol et al., "Diffusion-weighted magnetic resonance imaging for detecting and assessing ileal inflammation in Crohn's disease," *Alimentary Pharmacology and Therapeutics*, vol. 37, no. 5, pp. 537–545, 2013.
- [44] A. Oto, F. Zhu, K. Kulkarni, G. S. Karczmar, J. R. Turner, and D. Rubin, "Evaluation of diffusion-weighted MR imaging for detection of bowel inflammation in patients with Crohn's disease," *Academic Radiology*, vol. 16, no. 5, pp. 597–603, 2009.
- [45] S. Kiryu, K. Dodanuki, H. Takao et al., "Free-breathing diffusion-weighted imaging for the assessment of inflammatory activity in crohn's disease," *Journal of Magnetic Resonance Imaging*, vol. 29, no. 4, pp. 880–886, 2009.
- [46] A. Oto, A. Kayhan, J. T. B. Williams et al., "Active Crohn's disease in the small bowel: evaluation by diffusion weighted imaging and quantitative dynamic contrast enhanced MR imaging," *Journal of Magnetic Resonance Imaging*, vol. 33, no. 3, pp. 615–624, 2011.
- [47] C. Hordonneau, A. Buisson, J. Scanzi et al., "Diffusion-weighted magnetic resonance imaging in ileocolonic Crohn's disease: validation of quantitative index of activity," *The American Journal of Gastroenterology*, vol. 109, no. 1, pp. 89–98, 2014.
- [48] C. Schmid-Tannwald, G. Agrawal, F. Dahi, I. Sethi, and A. Oto, "Diffusion-weighted MRI: role in detecting abdominopelvic internal fistulas and sinus tracts," *Journal of Magnetic Resonance Imaging*, vol. 35, no. 1, pp. 125–131, 2012.
- [49] J. Satsangi, M. S. Silverberg, S. Vermeire, and J.-F. Colombel, "The Montreal classification of inflammatory bowel disease: controversies, consensus, and implications," *Gut*, vol. 55, no. 6, pp. 749–753, 2006.
- [50] N. Griffin, L. A. Grant, S. Anderson, P. Irving, and J. Sanderson, "Small bowel MR enterography: problem solving in Crohn's disease," *Insights into Imaging*, vol. 3, no. 3, pp. 251–263, 2012.
- [51] F. Maccioni, "Introduction to the feature section on "crohn's disease activity: MRI assessment and clinical implications"" *Abdominal Imaging*, vol. 37, no. 6, pp. 917–920, 2012.
- [52] G. A. J. Sempere, V. M. Sanjuan, E. M. Chulia et al., "MRI evaluation of inflammatory activity in Crohn's disease," *American Journal of Roentgenology*, vol. 184, no. 6, pp. 1829–1835, 2005.
- [53] R. del Vescovo, I. Sansoni, R. Caviglia et al., "Dynamic contrast enhanced magnetic resonance imaging of the terminal ileum: differentiation of activity of Crohn's disease," *Abdominal Imaging*, vol. 33, no. 4, pp. 417–424, 2008.
- [54] M. Zappa, C. Stefanescu, D. Cazals-Hatem et al., "Which magnetic resonance imaging findings accurately evaluate inflammation in small bowel Crohn's disease? A retrospective comparison with surgical pathologic analysis," *Inflammatory Bowel Diseases*, vol. 17, no. 4, pp. 984–993, 2011.
- [55] S. Punwani, M. Rodriguez-Justo, A. Bainbridge et al., "Mural inflammation in Crohn disease: location-matched histologic validation of MR imaging features," *Radiology*, vol. 252, no. 3, pp. 712–720, 2009.
- [56] P. Rodriguez, R. Mendez, F. Matute, P. Hernandez, and J. L. Mendoza, "Imaging crohn disease: MR enterography," *Journal of Computer Assisted Tomography*, vol. 38, no. 2, pp. 219–227, 2014.
- [57] R. Sinha, P. Rajiah, P. Murphy, P. Hawker, and S. Sanders, "Utility of high-resolution MR imaging in demonstrating transmural pathologic changes in Crohn disease," *Radiographics*, vol. 29, no. 6, pp. 1847–1867, 2009.
- [58] K. A. Herrmann, H. J. Michaely, C. J. Zech, J. Seiderer, M. F. Reiser, and S. O. Schoenberg, "Internal fistulas in Crohn disease: magnetic resonance enteroclysis," *Abdominal Imaging*, vol. 31, no. 6, pp. 675–687, 2006.
- [59] G. Schill, I. Iesalnieks, M. Haimerl et al., "Assessment of disease behavior in patients with crohn's disease by MR enterography," *Inflammatory Bowel Diseases*, vol. 19, no. 5, pp. 983–990, 2013.
- [60] C. Friedrich, A. Fajfar, M. Pawlik et al., "Magnetic resonance enterography with and without biphasic contrast agent enema compared to conventional ileocolonoscopy in patients with Crohn's disease," *Inflammatory Bowel Diseases*, vol. 18, no. 10, pp. 1842–1848, 2012.
- [61] F. Maccioni, M. A. Patak, A. Signore, and A. Laghi, "New frontiers of MRI in Crohn's disease: motility imaging, diffusion-weighted imaging, perfusion MRI, MR spectroscopy, molecular imaging, and hybrid imaging (PET/MRI)," *Abdominal Imaging*, vol. 37, no. 6, pp. 974–982, 2012.
- [62] S. Bickelhaupt, J. M. Froehlich, R. Cattin et al., "Software-assisted small bowel motility analysis using free-breathing MRI: feasibility study," *Journal of Magnetic Resonance Imaging*, vol. 39, no. 1, pp. 17–23, 2014.
- [63] J. L. Cullmann, S. Bickelhaupt, J. M. Froehlich et al., "MR imaging in Crohn's disease: correlation of MR motility measurement with histopathology in the terminal ileum," *Neurogastroenterology and Motility*, vol. 25, no. 9, pp. e749–e577, 2013.
- [64] S. Bickelhaupt, S. Pazahr, N. Chuck et al., "Crohn's disease: Small bowel motility impairment correlates with inflammatory-related markers C-reactive protein and calprotectin," *Neurogastroenterology and Motility*, vol. 25, no. 6, pp. 467–473, 2013.
- [65] A. Menys, S. A. Taylor, A. Emmanuel et al., "Global small bowel motility: assessment with dynamic MR imaging," *Radiology*, vol. 269, no. 2, pp. 443–450, 2013.
- [66] H. Jadvar and P. M. Colletti, "Competitive advantage of PET/MRI," *European Journal of Radiology*, vol. 83, no. 1, pp. 84–94, 2014.
- [67] J. K. Nicholson, J. C. Lindon, and E. Holmes, "Metabonomics": understanding the metabolic responses of living systems to pathophysiological stimuli via multivariate statistical analysis of biological NMR spectroscopic data," *Xenobiotica*, vol. 29, no. 11, pp. 1181–1189, 1999.
- [68] K. Pinker, A. Stadlbauer, W. Bogner, S. Gruber, and T. H. Helbich, "Molecular imaging of cancer: MR spectroscopy and beyond," *European Journal of Radiology*, vol. 81, no. 3, pp. 566–577, 2012.
- [69] M. E. Mullins, "MR spectroscopy: truly molecular imaging; past, present and future," *Neuroimaging Clinics of North America*, vol. 16, no. 4, pp. 605–618, 2006.

- [70] A. W. J. M. Glaudemans, F. Maccioni, L. Mansi, R. A. J. O. Dierckx, and A. Signore, "Imaging of cell trafficking in Crohn's disease," *Journal of Cellular Physiology*, vol. 223, no. 3, pp. 562–571, 2010.
- [71] R. J. Gillies and D. L. Morse, "In vivo magnetic resonance spectroscopy in cancer," *Annual Review of Biomedical Engineering*, vol. 7, pp. 287–326, 2005.
- [72] C. Ludwig and M. R. Viant, "Two-dimensional J-resolved NMR spectroscopy: review of a key methodology in the metabolomics toolbox," *Phytochemical Analysis*, vol. 21, no. 1, pp. 22–32, 2010.
- [73] A. M. Weljie, J. Newton, P. Mercier, E. Carlson, and C. M. Slupsky, "Targeted profiling: quantitative analysis of  $^1\text{H}$  NMR metabolomics data," *Analytical Chemistry*, vol. 78, no. 13, pp. 4430–4442, 2006.
- [74] E. M. Lenz, J. Bright, I. D. Wilson, S. R. Morgan, and A. F. P. Nash, "A  $^1\text{H}$  NMR-based metabolomic study of urine and plasma samples obtained from healthy human subjects," *Journal of Pharmaceutical and Biomedical Analysis*, vol. 33, no. 5, pp. 1103–1115, 2003.
- [75] E. M. Lenz, J. Bright, I. D. Wilson et al., "Metabonomics, dietary influences and cultural differences: a  $^1\text{H}$  NMR-based study of urine samples obtained from healthy British and Swedish subjects," *Journal of Pharmaceutical and Biomedical Analysis*, vol. 36, no. 4, pp. 841–849, 2004.
- [76] U. Sharma, R. R. Singh, V. Ahuja, G. K. Makharia, and N. R. Jagannathan, "Similarity in the metabolic profile in macroscopically involved and un-involved colonic mucosa in patients with inflammatory bowel disease: an *in vitro* proton ( $^1\text{H}$ ) MR spectroscopy study," *Magn Reson Imaging*, vol. 28, no. 7, pp. 1022–1029, 2010.
- [77] F. Fathi, L. Majari-Kasmaee, A. Mani-Varnosfaderani et al., " $^1\text{H}$  NMR based metabolic profiling in crohn's disease by random forest methodology," *Magnetic Resonance in Chemistry*, vol. 52, no. 7, pp. 370–376, 2014.
- [78] J. R. Marchesi, E. Holmes, F. Khan et al., "Rapid and noninvasive metabolomic characterization of inflammatory bowel disease," *Journal of Proteome Research*, vol. 6, no. 2, pp. 546–551, 2007.
- [79] M. Storr, H. J. Vogel, and R. Schicho, "Metabonomics: is it useful for inflammatory bowel diseases?" *Current Opinion in Gastroenterology*, vol. 29, no. 4, pp. 378–383, 2013.
- [80] F. Fathi, F. Ektefa, M. Hagh-Azali, and H. A. Aghdaie, "Metabonomics exposes metabolic biomarkers of Crohn's disease by  $^1\text{H}$ NMR," *Gastroenterology and Hepatology from Bed to Bench*, vol. 6, supplement 1, pp. S19–S22, 2013.
- [81] Y.-S. Hong, Y.-T. Ahn, J.-C. Park et al., " $^1\text{H}$  NMR-based metabolomic assessment of probiotic effects in a colitis mouse model," *Archives of Pharmacal Research*, vol. 33, no. 7, pp. 1091–1101, 2010.
- [82] R. Schicho, R. Shaykhtudinov, J. Ngo et al., "Quantitative metabolomic profiling of serum, plasma, and urine by  $^1\text{H}$  NMR spectroscopy discriminates between patients with inflammatory bowel disease and healthy individuals," *Journal of Proteome Research*, vol. 11, no. 6, pp. 3344–3357, 2012.
- [83] P. Baur, F.-P. Martin, L. Gruber et al., "Metabolic phenotyping of the Crohn's disease-like IBD etiopathology in the  $\text{TNF}^{\Delta\text{ARE}/\text{WT}}$  mouse model," *Journal of Proteome Research*, vol. 10, no. 12, pp. 5523–5535, 2011.
- [84] K. Balasubramanian, S. Kumar, R. R. Singh et al., "Metabolism of the colonic mucosa in patients with inflammatory bowel diseases: an *in vitro* proton magnetic resonance spectroscopy study," *Magnetic Resonance Imaging*, vol. 27, no. 1, pp. 79–86, 2009.
- [85] N. S. Stephens, J. Siffledeen, X. Su, T. B. Murdoch, R. N. Fedorak, and C. M. Slupsky, "Urinary NMR metabolomic profiles discriminate inflammatory bowel disease from healthy," *Journal of Crohn's and Colitis*, vol. 7, no. 2, pp. e42–e48, 2013.
- [86] H. R. T. Williams, I. J. Cox, D. G. Walker et al., "Characterization of inflammatory bowel disease with urinary metabolic profiling," *The American Journal of Gastroenterology*, vol. 104, no. 6, pp. 1435–1444, 2009.
- [87] B. C. te Boekhorst, G. A. van Tilborg, G. J. Strijkers, and K. Nicolay, "Molecular MRI of inflammation in atherosclerosis," *Current Cardiovascular Imaging Reports*, vol. 5, no. 1, pp. 60–68, 2012.
- [88] L. E. Paulis, T. Geelen, M. T. Kuhlmann et al., "Distribution of lipid-based nanoparticles to infarcted myocardium with potential application for MRI-monitored drug delivery," *Journal of Controlled Release*, vol. 162, no. 2, pp. 276–285, 2012.
- [89] S. A. Sargsyan and J. M. Thurman, "Molecular imaging of autoimmune diseases and inflammation," *Molecular Imaging*, vol. 11, no. 3, pp. 251–264, 2012.
- [90] J. L. Gaglia, A. R. Guimaraes, M. Harisinghani et al., "Noninvasive imaging of pancreatic islet inflammation in type 1A diabetes patients," *Journal of Clinical Investigation*, vol. 121, no. 1, pp. 442–445, 2011.
- [91] M. E. Kool, V. C. Cappendijk, K. B. J. M. Cleutjens et al., "Accumulation of ultrasmall superparamagnetic particles of iron oxide in human atherosclerotic plaques can be detected by *in vivo* magnetic resonance imaging," *Circulation*, vol. 107, no. 19, pp. 2453–2458, 2003.
- [92] M. F. Kircher, J. R. Allport, E. E. Graves et al., "In vivo high resolution three-dimensional imaging of antigen-specific cytotoxic T-lymphocyte trafficking to tumors," *Cancer Research*, vol. 63, no. 20, pp. 6838–6846, 2003.
- [93] J. Barkhausen, W. Ebert, C. Heyer, J. F. Debatin, and H.-J. Weimann, "Detection of atherosclerotic plaque with gadofluorine-enhanced magnetic resonance imaging," *Circulation*, vol. 108, no. 5, pp. 605–609, 2003.
- [94] W. J. M. Mulder, G. J. Strijkers, G. A. F. van Tilborg, A. W. Griffioen, and K. Nicolay, "Lipid-based nanoparticles for contrast-enhanced MRI and molecular imaging," *NMR in Biomedicine*, vol. 19, no. 1, pp. 142–164, 2006.
- [95] R. Weissleder, K. Kelly, E. Y. Sun, T. Shtatland, and L. Josephson, "Cell-specific targeting of nanoparticles by multivalent attachment of small molecules," *Nature Biotechnology*, vol. 23, no. 11, pp. 1418–1423, 2005.

## Clinical Study

# Pretreatment Diffusion-Weighted MRI Can Predict the Response to Neoadjuvant Chemotherapy in Patients with Nasopharyngeal Carcinoma

Guo-Yi Zhang,<sup>1</sup> Yue-Jian Wang,<sup>1</sup> Jian-Ping Liu,<sup>2</sup> Xin-Han Zhou,<sup>2</sup> Zhi-Feng Xu,<sup>2</sup>  
Xiang-Ping Chen,<sup>1</sup> Tao Xu,<sup>1</sup> Wei-Hong Wei,<sup>1</sup> Yang Zhang,<sup>1</sup> and Ying Huang<sup>3</sup>

<sup>1</sup>Cancer Center, Cancer Research Institute, Foshan Hospital, Sun Yat-sen University, Foshan, Guangdong 528000, China

<sup>2</sup>Imaging Diagnosis Center, Foshan Hospital, Sun Yat-sen University, Foshan, Guangdong 528000, China

<sup>3</sup>Department of Radiation Oncology, State Key Laboratory of Oncology in Southern China, Collaborative Innovation Center of Cancer Medicine, Cancer Center, Sun Yat-sen University, Guangzhou, Guangdong 510060, China

Correspondence should be addressed to Ying Huang; [huangying@sysucc.org.cn](mailto:huangying@sysucc.org.cn)

Received 22 August 2014; Revised 31 March 2015; Accepted 1 April 2015

Academic Editor: Zhengchao Dong

Copyright © 2015 Guo-Yi Zhang et al. This is an open access article distributed under the Creative Commons Attribution License, which permits unrestricted use, distribution, and reproduction in any medium, provided the original work is properly cited.

**Purpose.** To explore the potential of diffusion-weighted (DW) magnetic resonance imaging (MRI) using apparent diffusion coefficient (ADC) for predicting the response to neoadjuvant chemotherapy in nasopharyngeal carcinoma (NPC). **Methods and Materials.** Ninety-two consecutive patients with NPC who underwent three cycles of neoadjuvant chemotherapy were retrospectively analyzed. DW and anatomical MRI were performed before and after neoadjuvant chemotherapy prior to radiotherapy. Pretreatment ADCs and percentage increases in ADC after chemotherapy were calculated for the primary lesions and metastatic adenopathies. Receiver operating characteristic curve analysis was used to select optimal pretreatment ADCs. **Results.** Pretreatment mean ADCs were significantly lower for responders than for nonresponders (primary lesions,  $P = 0.012$ ; metastatic adenopathies,  $P = 0.013$ ). Mean percentage increases in ADC were higher for responders than for nonresponders (primary lesions,  $P = 0.008$ ; metastatic adenopathies,  $P < 0.001$ ). The optimal pretreatment primary lesion and metastatic adenopathy ADCs for differentiating responders from nonresponders were  $0.897 \times 10^{-3} \text{ mm}^2/\text{sec}$  and  $1.031 \times 10^{-3} \text{ mm}^2/\text{sec}$ , respectively. **Conclusions.** NPC patients with low pretreatment ADCs tend to respond better to neoadjuvant chemotherapy. Pretreatment ADCs could be used as a new pretreatment imaging biomarker of response to neoadjuvant chemotherapy.

## 1. Introduction

Nasopharyngeal carcinoma (NPC) is one of the most common malignancies in Southeast Asia, especially in the southern provinces of China [1]. In patients with advanced NPC, neoadjuvant chemotherapy has been established as an alternative treatment for reducing tumor size, thereby facilitating local control and improving the disease-free survival rate, but not the overall survival rate, after administration of subsequent concurrent chemoradiotherapy [2–7]. However, not all patients respond to neoadjuvant chemotherapy, so identification of nonresponders at the time of pretreatment staging would allow the treatment regimens of individual patients to be modified or altered to concurrent chemoradiotherapy.

Currently, anatomical magnetic resonance imaging (MRI) is normally used to assess the tumor response after neoadjuvant chemotherapy in NPC [8, 9], though changes in the morphologically based measures of tumor diameter and volume occur relatively late during the treatment course. Furthermore, anatomical MRI cannot be used to predict the tumor response to neoadjuvant chemotherapy prior to treatment. The value of <sup>18</sup>F-fluorodeoxyglucose positron emission tomography (FDG-PET) with respect to predicting tumor response is often hampered by its false-positive and expensive check cost [10, 11]. Therefore, it would be advantageous to identify novel imaging biomarkers that could predict the response to neoadjuvant chemotherapy prior to treatment in patients with NPC.

Diffusion-weighted (DW) MRI measures the diffusivity of water molecules within tissue extracellular spaces, which is quantified using apparent diffusion coefficients (ADCs). In general, intratumoral cell death induced by treatment increases water diffusion and leads to an increase in the ADC. Some early studies showed that DW MRI is helpful for predicting or detecting the response to chemoradiotherapy or radiosensitivity in head and neck carcinoma [12–19]. However, the efficacy of pretreatment ADCs obtained by DW MRI for predicting the response to neoadjuvant chemotherapy in NPC, or other head and neck carcinomas, has not been reported. The purpose of this study was to evaluate the potential of DW MRI using ADCs for predicting the response to neoadjuvant chemotherapy in patients with NPC.

## 2. Materials and Methods

**2.1. Patients.** This retrospective study was approved by the institutional review board and written informed consent was obtained from all participating patients or their next of kin. This study comprised 98 ethnic Chinese patients who were newly diagnosed with untreated and nonmetastatic NPC and who underwent both DW MRI and anatomical MRI before (baseline MRI) and after neoadjuvant chemotherapy but before radiotherapy (follow-up MRI) between March 2010 and April 2014. Median time between baseline MRI and the start of chemotherapy was 8 days (range, 2–21 days). Median time between the completion of chemotherapy and follow-up MRI was 16 days (range, 6–21 days). All 98 patients underwent the same neoadjuvant chemotherapeutic regimen and subsequently received intensity-modulated radiotherapy (IMRT). Six patients were later excluded from the study for the following reasons: four failed to complete three cycles of neoadjuvant chemotherapy, and two had inadequate DW MRI image quality due to excessive susceptibility or motion artifacts. The remaining 92 patients included 70 males (mean age, 46.5 years; range, 21–73 years) and 22 females (mean age, 44.3 years; range, 20–71 years). The World Health Organization (WHO) histologic type distribution was as follows: type I ( $n = 1$ ), type II ( $n = 9$ ), and type III ( $n = 82$ ). According to the 2010 American Joint Committee on Cancer (AJCC) tumor-node-metastases (TNM) staging system [20], the prechemotherapy clinical stage distribution was as follows: stage III, 52 patients; IVA, 29; and IVB, 11.

Neoadjuvant chemotherapy consisted of docetaxel ( $60 \text{ mg/m}^2$  or  $65 \text{ mg/m}^2$  d1), cisplatin ( $60 \text{ mg/m}^2$  or  $65 \text{ mg/m}^2$  d1), and fluorouracil ( $600 \text{ mg/m}^2$  or  $650 \text{ mg/m}^2$  d1–5) via intravenous infusion, repeated every 21 days for 3 cycles. After neoadjuvant chemotherapy, all patients were treated with definitive IMRT followed by concomitant chemotherapy ( $30\text{--}40 \text{ mg/m}^2$  cisplatin or nedaplatin weekly).

**2.2. Imaging Protocol.** All patients underwent MRI using a 1.5 Tesla system (Signa CV/i, GE Healthcare, Milwaukee, WI, USA). The region from the suprasellar cistern to the inferior margin of the sternal end of the clavicle was examined using a head and neck combined coil. A T2-weighted fast spin-echo (FSE) sequence in the axial plane with a matrix of  $512 \times 512$  and repetition time (TR)/echo time (TE) = 2889 ms/70.8 ms,

a T1-weighted FSE sequence in the axial, coronal, and sagittal planes with a matrix of  $560 \times 560$  and TR/TE = 627 ms/8.6 ms, and an echo-planar DWI sequence with a matrix of  $224 \times 224$ , TR/TE = 1360 ms/89.8 ms, and  $b$ -values of 0, 100, 500, and  $1,000 \text{ s/mm}^2$  were obtained before injection of contrast material. After intravenous injection of Gd-DTPA at a dose of  $0.1 \text{ mmol/kg}$  body weight, T1-weighted axial and sagittal sequences and T1-weighted fat-suppressed coronal sequences were performed sequentially, with parameters similar to those applied before the Gd-DTPA injection. The section thickness and interslice gap were 5 mm and 0 mm, respectively.

**2.3. Image Assessment.** The MRI scans were evaluated independently on a work station (Medi-PACS, Vancouver, Canada) by two radiologists, each with over 10 years of experience interpreting NPC MR images; any differences were resolved by consensus. Both radiologists were blinded to the therapeutic responses to neoadjuvant chemotherapy and other clinical findings.

Regions of interest (ROIs) were placed on the primary lesions and metastatic adenopathies on the images acquired using a  $b$ -value of  $0 \text{ s/mm}^2$  (excluding any necrotic regions identified with the aid of the T2-weighted and T1-weighted postcontrast MR images), and then the ROIs were automatically copied to the other  $b$ -value images by the software. Subsequently, all ROIs were merged per lesion for each  $b$ -value, and the average SI was calculated for the entire lesion. ADCs were derived using the following equation:  $\text{ADC} = -\ln[\text{SI}(b)/\text{SI}(0)]/b$ , where  $b$  is the diffusion weighting factor and  $\text{SI}(b)$  and  $\text{SI}(0)$  are the signal intensities with and without diffusion-sensitizing gradients, respectively [19]. Percentage increases in ADC (ADC%) were calculated as follows:  $\text{ADC\%} = (\text{ADC}_{\text{post}} - \text{ADC}_{\text{pre}})/\text{ADC}_{\text{pre}} \times 100$ , where  $\text{ADC}_{\text{pre}}$  and  $\text{ADC}_{\text{post}}$  are the pre- and posttreatment ADCs, respectively.

For each lesion, contours were drawn around the lesion border at each slice position based on anatomical MRI. Subsequently, the volume of each lesion was calculated using the following equation:  $(\sum \text{surface at each slice position}) * (\text{slice thickness} + \text{interslice gap})$ . Percentage increases in volume (V%) were calculated as follows:  $V\% = (V_{\text{post}} - V_{\text{pre}})/V_{\text{pre}} \times 100$ , where  $V_{\text{pre}}$  and  $V_{\text{post}}$  are the pre- and posttreatment tumor volume, respectively.

The Response Evaluation Criteria in Solid Tumors (RECIST) guidelines were used to classify patients as responders or nonresponders on the basis of anatomical MRI [21]. A patient was considered to be a responder if all assessable lesions (both primary lesion and metastatic adenopathies) completely disappeared or partially reduced ( $\geq 30\%$  in the sum of the maximal diameters) on the follow-up MRI. A patient was considered to be a nonresponder if measurable lesions were stable ( $< 30\%$  reduction or  $< 20\%$  increase in the sum of the maximal diameters) or progressed ( $\geq 20\%$  increase in the area(s) of the original lesion(s) or the appearance of new lesions) on the follow-up MRI.

**2.4. Statistical Analysis.** Interreader agreement was evaluated with Cohen  $K$  coefficient for the image assessment. A  $K$  value of 0.4–0.6 indicated moderate agreement; 0.6–0.8, good

agreement; and above 0.8, very good agreement [22]. The independent-samples *t*-test was used to compare the responders and nonresponders with respect to tumor volume (mean tumor volume of primary lesions and metastatic adenopathies before and after chemotherapy), pre- and post-treatment mean ADCs, and percentage increases in ADCs after chemotherapy. Fisher’s exact test was used to compare age, sex, tumor pathology, and clinical stage between responders and nonresponders. Spearman’s rank correlation was performed to evaluate the correlation between (a) the changes in ADCs and change in tumor volume on follow-up MRI and (b) pretreatment tumor ADCs and percentage change in tumor volume after chemotherapy.

To determine the optimal pretreatment ADC cutoff values with which to differentiate responders from nonresponders, receiver operating characteristic (ROC) curves and the areas under the curve (AUCs) were to evaluate the effectiveness of different criteria. The optimal cutoff value was defined as the value corresponding to the highest average sensitivity and specificity. The overall accuracy was represented by the AUC: the larger the area, the better the test. Sensitivity, specificity, and accuracy were calculated using the standard definitions [23]. SPSS version 16.0 (IBM, Armonk, NY, USA) was used for all data analyses, except for Fisher’s exact test and ROC curve analysis that were performed using MedCalc software version 10.3.0.0 (MedCalc software, Mariakerke, Belgium). *P*-values < 0.05 were considered significant.

### 3. Results

**3.1. Interobserver Agreement.** In the per-lesion analysis, there was excellent agreement for the image assessment between observers 1 and 2, with *K* coefficients of 0.930 and 0.932 for pre- and posttreatment volume of primary lesions, 0.937 and 0.934 for pre- and posttreatment volume of metastatic adenopathies, 0.927 and 0.924 for pre- and posttreatment ADCs of primary lesions, and 0.931 and 0.928 for pre- and posttreatment ADCs of metastatic adenopathies. Any differences between observers 1 and 2 were resolved by consensus.

**3.2. Treatment Outcomes.** After completion of neoadjuvant chemotherapy, the primary tumor treatment responses were distributed as follows: complete resolution, 24 (26.1%) patients; partial resolution, 55 (59.8%) patients; and stability, 13 (14.1%) patients. The treatment responses of the metastatic cervical lymph nodes were distributed as follows: complete resolution, 44 (55.0%) patients; partial resolution, 26 (32.5%) patients; and stability, 10 (12.5%) patients. When the treatment responses of the primary tumor and metastatic cervical lymph nodes were considered together, 76 (82.6%) of the 92 patients were categorized as responders, and 16 (17.4%) were categorized as nonresponders (Table 1). No significant differences were observed between responders and nonresponders with respect to age, sex, tumor histology, or clinical stage (Table 2).

**3.3. DW MRI and Tumor Volume.** The mean tumor volumes of the primary lesions and metastatic adenopathies at prechemotherapy MRI were 37.2 cm<sup>3</sup> (median, 36.6 cm<sup>3</sup>;

TABLE 1: Response to neoadjuvant chemotherapy in 92 patients with NPC.

Response	Number of patients		
	NP ( <i>n</i> = 92)	LN ( <i>n</i> = 80)*	Combination (NP + LN)
<b>Responders</b>			
Complete response	24 (26.1%)	44 (55.0%)	20 (21.7%)
Partial response	55 (59.8%)	26 (32.5%)	56 (60.9%)
<b>Nonresponders</b>			
Stable disease	13 (14.1%)	10 (12.5%)	16 (17.4%)
Progressive disease	0 (0%)	0 (0%)	0 (0%)

NP = nasopharynx; LN = regional neck lymph nodes.  
\*12 patients with N0 disease were not included in the analysis.

TABLE 2: Clinicopathologic features of the responders and nonresponders.

Characteristic	Number of patients		<i>P</i> -value
	Responders ( <i>n</i> = 76)	Nonresponders ( <i>n</i> = 16)	
<b>Sex</b>			
Male	58	12	1.000
Female	18	4	
<b>Age</b>			
≥50 years	26	6	0.802
<50 years	50	10	
<b>WHO pathologic type</b>			
Type 1	1	0	0.834
Type 2	7	2	
Type 3	68	14	
<b>Clinical stage (2010)</b>			
III	43	9	0.997
IVA	24	5	
IVB	9	2	

WHO = World Health Organization.

range, 3.8–96.5 cm<sup>3</sup>) and 18.4 cm<sup>3</sup> (median, 16.2 cm<sup>3</sup>; range, 1.3–49 cm<sup>3</sup>), respectively. No significant difference was observed between responders and nonresponders in terms of the mean pretreatment tumor volume (primary lesions, 36.6 cm<sup>3</sup> ± 2.7 (standard error) versus 40.4 cm<sup>3</sup> ± 6.7, *P* = 0.770; metastatic adenopathies, 18.6 cm<sup>3</sup> ± 1.7 versus 19.5 cm<sup>3</sup> ± 4.5, *P* = 0.906). However, after completion of neoadjuvant chemotherapy, responders had a smaller mean tumor volume than nonresponders (primary lesions, 9.2 cm<sup>3</sup> ± 1.2 versus 28.0 cm<sup>3</sup> ± 4.7, *P* = 0.014; metastatic adenopathies, 2.6 cm<sup>3</sup> ± 0.5 versus 12.6 cm<sup>3</sup> ± 2.9, *P* = 0.003) (Table 3).

Before neoadjuvant chemotherapy, the mean ADCs of responders were significantly lower than that of nonresponders (primary lesions: [0.798 ± 0.007] × 10<sup>-3</sup> mm<sup>2</sup>/sec versus [0.964 ± 0.010] × 10<sup>-3</sup> mm<sup>2</sup>/sec, *P* = 0.012; metastatic adenopathies: [0.964 ± 0.010] × 10<sup>-3</sup> mm<sup>2</sup>/sec versus [1.135 ± 0.042] × 10<sup>-3</sup> mm<sup>2</sup>/sec, *P* = 0.013). After completion of neoadjuvant chemotherapy,

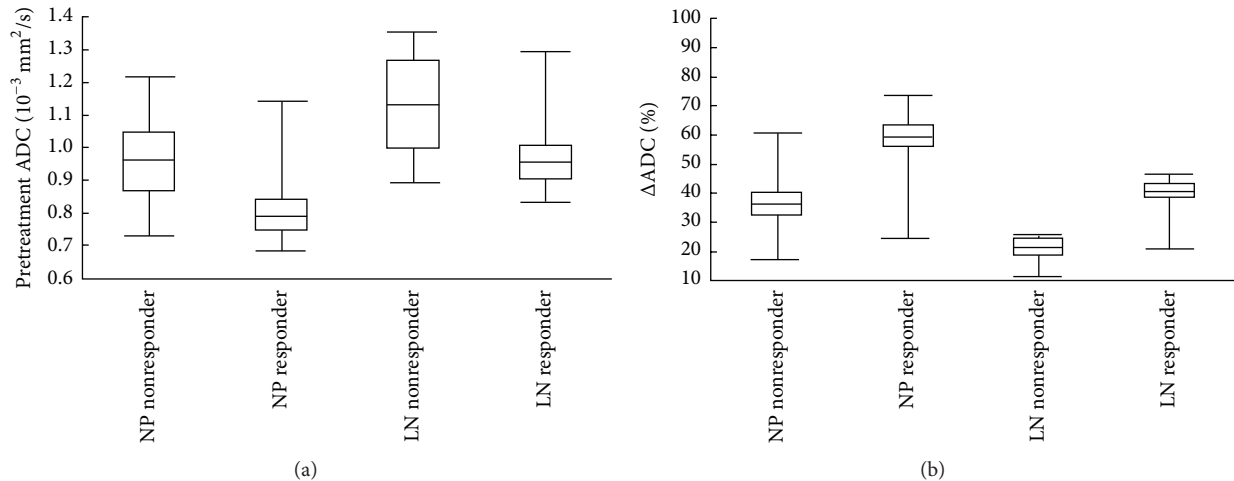


FIGURE 1: (a) Comparison of pretreatment ADCs for responders and nonresponders in patients with NPC. Responders had significantly lower pretreatment ADCs (primary lesions,  $P = 0.012$ ; metastatic adenopathies,  $P = 0.013$ ). (b) Comparison of  $\Delta$ ADCs for responders and nonresponders. Responders had significantly higher  $\Delta$ ADCs (primary lesions,  $P = 0.008$ ; metastatic adenopathies,  $P < 0.001$ ). Box-whisker plots are presented with median (-), interquartile range (box), and minima/maxima (-). NP = nasopharynx; LN = regional neck lymph nodes.

TABLE 3: Tumor volume and ADCs of the primary tumor and metastatic adenopathies in 92 patients with NPC.

Characteristic	Number of patients		P-value
	Responders ( $n = 76$ )	Nonresponders ( $n = 16$ )	
Tumor volume (cm <sup>3</sup> )			
NP pretreatment	37.3 ± 2.7	36.2 ± 7.0	0.884
NP posttreatment	9.1 ± 1.2	23.7 ± 4.7	0.010
LN pretreatment	18.2 ± 1.7	20.0 ± 4.6	0.708
LN posttreatment	2.4 ± 0.5	14.3 ± 3.1	0.004
ADC ( $\times 10^{-3}$ mm <sup>2</sup> /sec)			
NP pretreatment	0.809 ± 0.009	0.953 ± 0.038	0.003
NP posttreatment	1.276 ± 0.007	1.306 ± 0.033	0.182
LN pretreatment	0.966 ± 0.010	1.121 ± 0.045	0.007
LN posttreatment	1.354 ± 0.009	1.355 ± 0.045	0.983
Increase in ADC (%)			
NP	58.5 ± 1.0	38.2 ± 3.1	<0.001
LN	40.4 ± 0.5	21.2 ± 1.3	<0.001

NP = nasopharynx; LN = regional neck lymph nodes.

no significant difference in the mean ADCs was observed between responders and nonresponders (primary lesions:  $[1.274 \pm 0.011] \times 10^{-3}$  mm<sup>2</sup>/sec versus  $[1.366 \pm 0.020] \times 10^{-3}$  mm<sup>2</sup>/sec,  $P = 0.526$ ; metastatic adenopathies:  $[1.354 \pm 0.013] \times 10^{-3}$  mm<sup>2</sup>/sec versus  $[1.427 \pm 0.031] \times 10^{-3}$  mm<sup>2</sup>/sec,  $P = 0.217$ ). However, the mean percentage increases in the ADCs were significantly greater in responders than in nonresponders (primary lesions,  $60.0\% \pm 2.4$  versus  $34.8\% \pm 3.2$ ,  $P = 0.008$ ; metastatic adenopathies,  $40.7\% \pm 2.7$  versus  $26.5\% \pm 3.3$ ,  $P < 0.001$ ) (Figures 1 and 2) (Table 3). Additionally, the changes in the ADCs correlated with the change in tumor volume at follow-up MRI (primary lesions:  $r = 0.611$ ,  $P < 0.001$ ;

metastatic adenopathies:  $r = 0.676$ ,  $P < 0.001$ ). Furthermore, a strong negative correlation was observed between the mean pretreatment tumor ADC and percentage change in tumor volume after chemotherapy (primary lesions:  $r = -0.570$ ,  $P < 0.001$ ; metastatic adenopathies:  $r = -0.423$ ,  $P < 0.001$ ).

**3.4. ROC Curve Analysis.** The optimal pretreatment primary tumor ADC for differentiating responders from nonresponders using ROC curve analysis was  $0.897 \times 10^{-3}$  mm<sup>2</sup>/sec; this cutoff value had a sensitivity of 89.9% (71/79; 95% confidence interval: 81.0–95.5%), specificity of 76.9% (10/13; 95% confidence interval: 46.2–95.0%), and area under the empirical ROC curve of 0.821 (95% confidence interval: 0.727–0.893). The optimal pretreatment metastatic adenopathy ADC cutoff value for differentiating responders from nonresponders was  $1.031 \times 10^{-3}$  mm<sup>2</sup>/sec, which yielded a sensitivity of 85.7% (60/70; 95% confidence interval: 75.3–92.9%), specificity of 80.0% (8/10; 95% confidence interval: 44.4–97.5%), and area under the empirical ROC curve of 0.830 (95% confidence interval: 0.730–0.905) (Figure 3).

## 4. Discussion

This study demonstrated that, in patients with NPC, responders to neoadjuvant chemotherapy have significantly lower pretreatment ADCs than nonresponders, and a strong negative correlation exists between the mean pretreatment ADCs and percentage change in tumor volume on follow-up MRI. The patients with lower pretreatment ADCs had a better response to neoadjuvant chemotherapy compared to those with higher pretreatment ADCs, in accordance with other clinical studies [24–27]. In rectal cancer [24, 25] and breast cancer [26, 27], responders had lower ADCs before neoadjuvant chemotherapy than nonresponders. Therefore, we suggest that pretreatment ADCs could be used as a novel imaging biomarker to predict the response before neoadjuvant

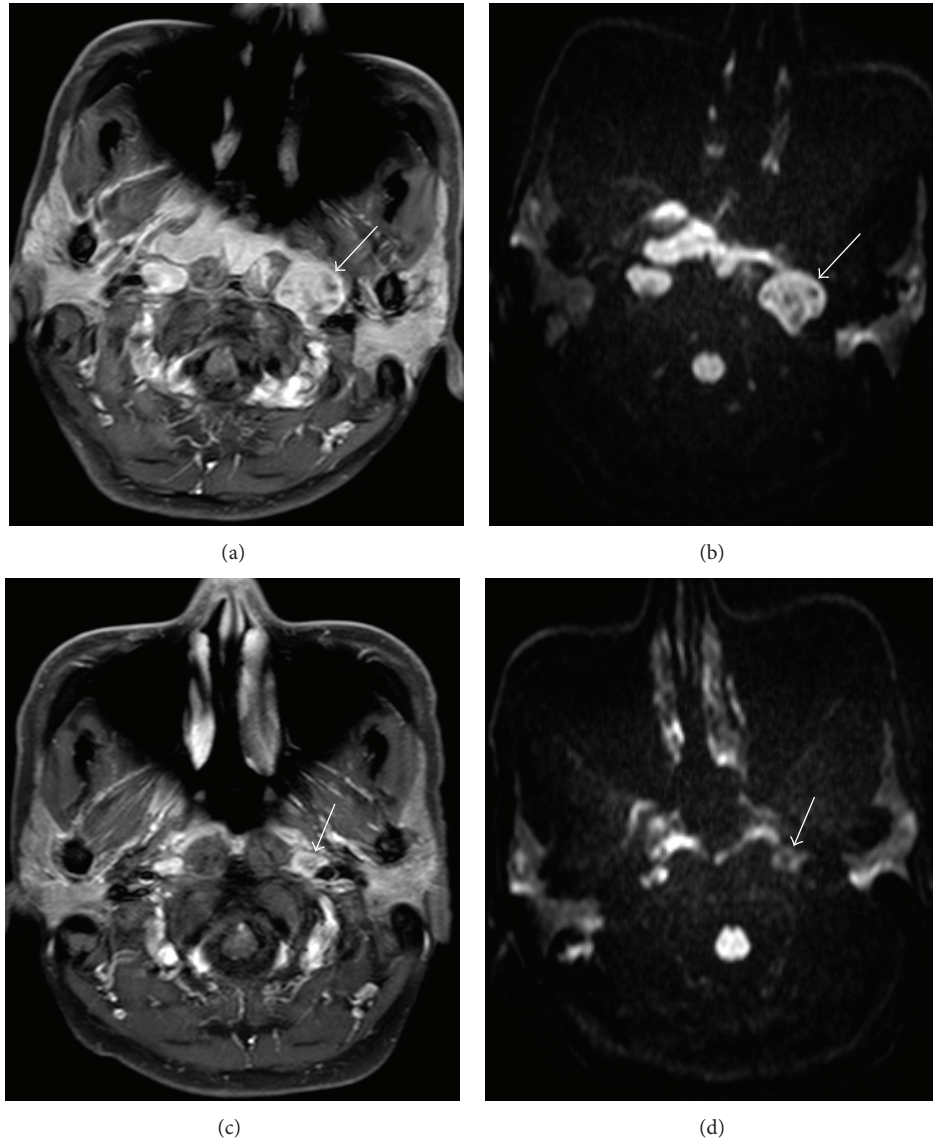


FIGURE 2: DW MRI findings in a 48-year-old female patient with NPC who responded to neoadjuvant chemotherapy. Pretreatment (a) axial contrast-enhanced T1-weighted image and (b) ADC maps showing an enlarged lymph node in the left retropharyngeal space (arrow). The mean pretreatment ADC of this lesion was  $0.993 \times 10^{-3} \text{ mm}^2/\text{sec}$ . Posttreatment (c) axial contrast-enhanced T1-weighted image and (d) ADC maps showing that the formerly enlarged right lymph node partially resolved; the volume of this lesion reduced by 83%. Neoadjuvant chemotherapy increased the mean ADC of this lesion to  $1.383 \times 10^{-3} \text{ mm}^2/\text{sec}$ .

chemotherapy in patients with NPC. This could facilitate tailored therapeutic approaches in NPC, with some patients spared from ineffective and unnecessary treatment toxicities.

After completion of neoadjuvant chemotherapy, the percentage increases in the ADCs of responders were significantly greater than that of nonresponders, and the changes in the ADCs correlated with the change in tumor volume at follow-up MRI. Previous studies have shown that low pretreatment ADCs indicate viable tumor tissue with a high cellularity, whereas high ADCs reflect less metabolic tumor tissue with a low cellularity [28, 29]. Tumor tissue with a high rate of cellular proliferation is more sensitive to chemotherapy or radiotherapy, which acts by inducing cellular damage

and lysis in proliferating cells followed by a reduction in cellular volume, thereby enhancing the diffusion of water molecules and increasing the ADCs values on DW MRI. However, tumors with a low cellularity are likely to be in a situation of hypoxia and ischemia, which reduces the delivery of chemotherapeutic agents to the tumor. Furthermore, cancer cells that have a slow rate of metabolism are less sensitive to cytotoxic chemotherapy or radiotherapy [28]. Therefore the changes in the ADCs of tumors with a low cellularity after completion of chemotherapy or radiotherapy will always be lower than the changes in the ADCs of tumors with a high cellularity. Interestingly, some studies have shown that large changes in ADCs during the early stages of treatment

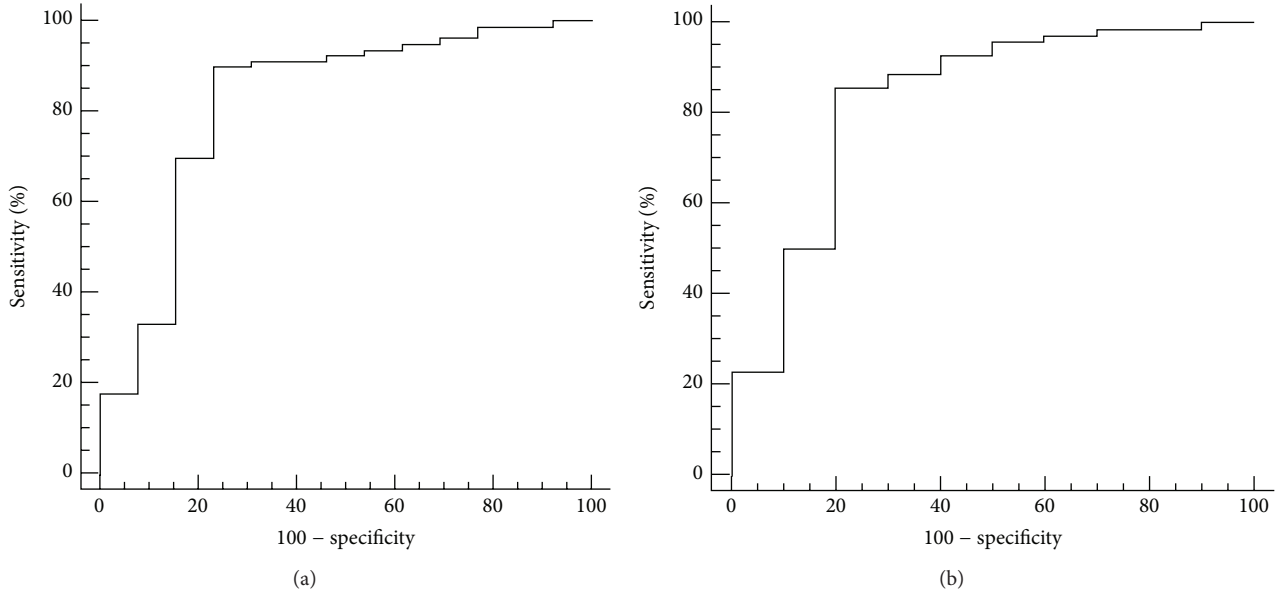


FIGURE 3: ROC curves of the ability of pretreatment primary tumor ADC (a) or metastatic adenopathy ADC (b) to predict the response to neoadjuvant chemotherapy in patients with nasopharyngeal carcinoma. The optimal pretreatment ADC cutoff values for the primary tumor and metastatic adenopathy were  $0.897 \times 10^{-3} \text{ mm}^2/\text{sec}$  and  $1.031 \times 10^{-3} \text{ mm}^2/\text{sec}$ , with areas under the ROC curves of 0.830 and 0.821, respectively.

(after the first or second cycle of neoadjuvant chemotherapy or 1-2 weeks after the start of radiotherapy), which occur prior to changes in tumor diameter or volume, indicate a better response to treatment [12, 18, 30]. Therefore, in most malignant tumors, an obvious increase in the ADC is regarded as an important imaging biomarker of successful treatment [12-19, 24-27].

Over the last 10 years or so, DW MRI has been successfully employed in head and neck cancer to distinguish between residual disease or tumor recurrence and inflammation or necrosis after completion of (chemo)radiotherapy [31]. Additionally, pretreatment ADCs or changes in ADCs during (chemo)radiotherapy have been reported as useful markers for predicting locoregional failure or progression-free survival in head and neck carcinoma [17, 32]. Some early studies indicated the potential of ADCs for evaluating treatment response in head and neck carcinoma [12, 14, 18]. King et al. [14] reported that a large change in ADCs within two weeks of treatment was predictive of a better response to (chemo)radiotherapy. Kim et al. [18] observed that low pretreatment ADCs or a significant increase in ADCs within one week of treatment was indicative of a higher rate of locoregional remission after concurrent chemoradiation. Recently, a study of 31 patients with NPC showed that high ADCs and early large increases in ADCs after initiation of neoadjuvant chemotherapy were indicative of a better response to subsequent concurrent chemoradiotherapy [12]. However, to our knowledge, the use of pretreatment ADCs for predicting the response to neoadjuvant chemotherapy in patients with NPC or other head and neck carcinomas has not yet been reported. This study showed that patients with NPC and low pretreatment ADCs were more likely to respond to neoadjuvant chemotherapy, and large increases in ADCs after

completion of neoadjuvant chemotherapy correlated with a better response to neoadjuvant chemotherapy. Therefore, assessment of ADCs may help identify patients who will fail to respond to neoadjuvant chemotherapy, thereby enabling individualized treatment planning and allowing some patients to avoid unnecessary chemotherapy and the associated toxicities.

It should be stressed that DW MRI was not performed after each cycle of neoadjuvant chemotherapy in this study. Other studies reported that changes in ADCs after the first cycle of neoadjuvant chemotherapy could provide more detailed information on tumor response [30]. Furthermore, the sample size in this study was relatively small, and most of the patients with NPC responded to neoadjuvant chemotherapy, which could result in statistical bias. Thus, one should be wary of applying the ADC cutoff values defined in this population for defining responders and nonresponders. In addition, pathologic confirmation of imaging findings is not possible in patients with NPC, who are typically treated with radiotherapy rather than surgery. Thus, determining the treatment response to chemotherapy based on anatomical MRI may be inaccurate. Therefore, we acknowledge that prospective, large cohort, and multicentre studies are necessary to confirm our findings and recommendations.

## 5. Conclusions

In NPC, patients with low pretreatment ADCs tended to respond better to neoadjuvant chemotherapy. Pretreatment ADCs have potential as a novel imaging marker to predict the response to neoadjuvant chemotherapy, which could facilitate individual therapeutic approaches and allow some

patients with NPC to avoid ineffective chemotherapy and unnecessary treatment toxicities.

## Disclaimer

The authors alone are responsible for the content and writing of the paper.

## Conflict of Interests

The authors report no conflict of interests.

## Authors' Contribution

Guo-Yi Zhang and Yue-Jian Wang contributed equally to this work.

## Acknowledgments

This work was supported by grants from the Natural Science Foundation of China (no. 81402244), the Natural Science Foundation of Guangdong Province (Grant S2011040004296), the Science and Technology Planning Program of Guangdong Province (Grant 20120318050), and the Science and Technology Key Project of Foshan City (Grant 201008051).

## References

- [1] E. T. Chang and H.-O. Adami, "The enigmatic epidemiology of nasopharyngeal carcinoma," *Cancer Epidemiology Biomarkers and Prevention*, vol. 15, no. 10, pp. 1765–1777, 2006.
- [2] E. P. Hui, B. B. Ma, S. F. Leung et al., "Randomized phase II trial of concurrent cisplatin-radiotherapy with or without neoadjuvant docetaxel and cisplatin in advanced nasopharyngeal carcinoma," *Journal of Clinical Oncology*, vol. 27, no. 2, pp. 242–249, 2009.
- [3] E. Cvitkovic, F. Eschwege, M. Raha et al., "Preliminary results of a randomized trial comparing neoadjuvant chemotherapy (cisplatin, epirubicin, bleomycin) plus radiotherapy vs. radiotherapy alone in stage IV ( $\geq N_2, M_0$ ) undifferentiated nasopharyngeal carcinoma: a positive effect on progression-free survival," *International Journal of Radiation Oncology, Biology, Physics*, vol. 35, no. 3, pp. 463–469, 1996.
- [4] D. T. T. Chua, J. S. T. Sham, D. Choy et al., "Preliminary report of the Asian-Oceanian Clinical Oncology Association randomized trial comparing cisplatin and epirubicin followed by radiotherapy versus radiotherapy alone in the treatment of patients with locoregionally advanced nasopharyngeal carcinoma," *Cancer*, vol. 83, no. 11, pp. 2270–2283, 1998.
- [5] J. Ma, H.-Q. Mai, M.-H. Hong et al., "Results of a prospective randomized trial comparing neoadjuvant chemotherapy plus radiotherapy with radiotherapy alone in patients with locoregionally advanced nasopharyngeal carcinoma," *Journal of Clinical Oncology*, vol. 19, no. 5, pp. 1350–1357, 2001.
- [6] D. T. T. Chua, J. Ma, J. S. T. Sham et al., "Long-term survival after cisplatin-based induction chemotherapy and radiotherapy for nasopharyngeal carcinoma: a pooled data analysis of two phase III trials," *Journal of Clinical Oncology*, vol. 23, no. 6, pp. 1118–1124, 2005.
- [7] L. Xu, J. Pan, J. Wu et al., "Factors associated with overall survival in 1706 patients with nasopharyngeal carcinoma: significance of intensive neoadjuvant chemotherapy and radiation break," *Radiotherapy & Oncology*, vol. 96, no. 1, pp. 94–99, 2010.
- [8] G.-Y. Zhang, L.-Z. Liu, W.-H. Wei, Y.-M. Deng, Y.-Z. Li, and X. W. Liu, "Radiologic criteria of retropharyngeal lymph node metastasis in nasopharyngeal carcinoma treated with radiation therapy," *Radiology*, vol. 255, no. 2, pp. 605–612, 2010.
- [9] X.-B. Liao, Y.-P. Mao, L.-Z. Liu et al., "How does magnetic resonance imaging influence staging according to AJCC staging system for nasopharyngeal carcinoma compared with computed tomography?" *International Journal of Radiation Oncology Biology Physics*, vol. 72, no. 5, pp. 1368–1377, 2008.
- [10] V. Lai and P. L. Khong, "Updates on MR imaging and  $^{18}F$ -FDG PET/CT imaging in nasopharyngeal carcinoma," *Oral Oncology*, vol. 50, no. 6, pp. 539–548, 2014.
- [11] S.-C. Chan, W.-H. Kuo, H.-M. Wang et al., "Prognostic implications of post-therapy  $^{18}F$ -FDG PET in patients with locoregionally advanced nasopharyngeal carcinoma treated with chemoradiotherapy," *Annals of Nuclear Medicine*, vol. 27, no. 8, pp. 710–719, 2013.
- [12] Y. Chen, X. Liu, D. Zheng et al., "Diffusion-weighted magnetic resonance imaging for early response assessment of chemoradiotherapy in patients with nasopharyngeal carcinoma," *Magnetic Resonance Imaging*, vol. 32, no. 6, pp. 630–637, 2014.
- [13] S. Chawla, S. Kim, L. Dougherty et al., "Pretreatment diffusion-weighted and dynamic contrast-enhanced MRI for prediction of local treatment response in squamous cell carcinomas of the head and neck," *American Journal of Roentgenology*, vol. 200, no. 1, pp. 35–43, 2013.
- [14] A. D. King, K.-K. Chow, K.-H. Yu et al., "Head and neck squamous cell carcinoma: diagnostic performance of diffusion-weighted MR imaging for the prediction of treatment response," *Radiology*, vol. 266, no. 2, pp. 531–538, 2013.
- [15] V. Vandecaveye, P. Dirix, F. de Keyzer et al., "Diffusion-weighted magnetic resonance imaging early after chemoradiotherapy to monitor treatment response in head-and-neck squamous cell carcinoma," *International Journal of Radiation Oncology Biology Physics*, vol. 82, no. 3, pp. 1098–1107, 2012.
- [16] M. Lambrecht, P. Dirix, V. Vandecaveye, F. de Keyzer, R. Hermans, and S. Nuyts, "Role and value of diffusion-weighted MRI in the radiotherapeutic management of head and neck cancer," *Expert Review of Anticancer Therapy*, vol. 10, no. 9, pp. 1451–1459, 2010.
- [17] V. Vandecaveye, P. Dirix, F. de Keyzer et al., "Predictive value of diffusion-weighted magnetic resonance imaging during chemoradiotherapy for head and neck squamous cell carcinoma," *European Radiology*, vol. 20, no. 7, pp. 1703–1714, 2010.
- [18] S. Kim, L. Loevner, H. Quon et al., "Diffusion-weighted magnetic resonance imaging for predicting and detecting early response to chemoradiation therapy of squamous cell carcinomas of the head and neck," *Clinical Cancer Research*, vol. 15, no. 3, pp. 986–994, 2009.
- [19] A. D. King, F. K. F. Mo, K.-H. Yu et al., "Squamous cell carcinoma of the head and neck: diffusion-weighted MR imaging for prediction and monitoring of treatment response," *European Radiology*, vol. 20, no. 9, pp. 2213–2220, 2010.
- [20] S. B. Edge, D. R. Byrd, C. C. Compton, A. G. Fritz, F. L. Greene, and A. Trotti, Eds., *AJCC Cancer Staging Handbook From the AJCC Cancer Staging Manual*, Springer, New York, NY, USA, 7th edition, 2010.

- [21] P. Therasse, S. G. Arbuck, E. A. Eisenhauer et al., "New guidelines to evaluate the response to treatment in solid tumors," *Journal of the National Cancer Institute*, vol. 92, no. 3, pp. 205–216, 2000.
- [22] J. Cohen, "A coefficient of agreement for nominal scales," *Educational and Psychological Measurement*, vol. 20, pp. 37–46, 1960.
- [23] R. S. Galen, "Predictive value of laboratory tests," *The American Journal of Cardiology*, vol. 36, no. 4, pp. 536–538, 1975.
- [24] A. Dzik-Jurasz, C. Domenig, M. George et al., "Diffusion MRI for prediction of response of rectal cancer to chemoradiation," *The Lancet*, vol. 360, no. 9329, pp. 307–308, 2002.
- [25] A. F. DeVries, C. Kremser, P. A. Hein et al., "Tumor microcirculation and diffusion predict therapy outcome for primary rectal carcinoma," *International Journal of Radiation Oncology Biology Physics*, vol. 56, no. 4, pp. 958–965, 2003.
- [26] S. H. Park, W. K. Moon, N. Cho et al., "Diffusion-weighted MR imaging: pretreatment prediction of response to neoadjuvant chemotherapy in patients with breast cancer," *Radiology*, vol. 257, no. 1, pp. 56–63, 2010.
- [27] L. Nilsen, A. Fangberget, O. Geier, D. R. Olsen, and T. Seierstad, "Diffusion-weighted magnetic resonance imaging for pretreatment prediction and monitoring of treatment response of patients with locally advanced breast cancer undergoing neoadjuvant chemotherapy," *Acta Oncologica*, vol. 49, no. 3, pp. 354–360, 2010.
- [28] P. D. Humphries, N. J. Sebire, M. J. Siegel, and O. E. Olsen, "Tumors in pediatric patients at diffusion-weighted MR imaging: apparent diffusion coefficient and tumor cellularity," *Radiology*, vol. 245, no. 3, pp. 848–854, 2007.
- [29] A. C. Guo, T. J. Cummings, R. C. Dash, and J. M. Provenzale, "Lymphomas and high-grade astrocytomas: comparison of water diffusibility and histologic characteristics," *Radiology*, vol. 224, no. 1, pp. 177–183, 2002.
- [30] U. Sharma, K. K. A. Danishad, V. Seenu, and N. R. Jagannathan, "Longitudinal study of the assessment by MRI and diffusion-weighted imaging of tumor response in patients with locally advanced breast cancer undergoing neoadjuvant chemotherapy," *NMR in Biomedicine*, vol. 22, no. 1, pp. 104–113, 2009.
- [31] D. W. Tshering Vogel, P. Zbaeren, A. Geretschlaeger, P. Vermathen, F. De Keyzer, and H. C. Thoeny, "Diffusion-weighted MR imaging including bi-exponential fitting for the detection of recurrent or residual tumour after (chemo)radiotherapy for laryngeal and hypopharyngeal cancers," *European Radiology*, vol. 23, no. 2, pp. 562–569, 2013.
- [32] S. Berrak, S. Chawla, S. Kim et al., "Diffusion weighted imaging in predicting progression free survival in patients with squamous cell carcinomas of the head and neck treated with induction chemotherapy," *Academic Radiology*, vol. 18, no. 10, pp. 1225–1232, 2011.

## Research Article

# Fast Imaging Technique for fMRI: Consecutive Multishot Echo Planar Imaging Accelerated with GRAPPA Technique

Daehun Kang,<sup>1,2</sup> Yul-Wan Sung,<sup>1</sup> and Chang-Ki Kang<sup>3</sup>

<sup>1</sup> Kansei Fukushi Research Institute, Tohoku Fukushi University, Sendai 989-3201, Japan

<sup>2</sup> Graduate School of Information Science, Tohoku University, Sendai 980-8579, Japan

<sup>3</sup> Neuroscience Research Institute and Department of Radiological Science, Gachon University, 1198 Kuwol-dong, Namdong-gu, Incheon 405-760, Republic of Korea

Correspondence should be addressed to Chang-Ki Kang; [changkik@gmail.com](mailto:changkik@gmail.com)

Received 18 August 2014; Revised 13 October 2014; Accepted 3 November 2014

Academic Editor: Trevor Andrews

Copyright © 2015 Daehun Kang et al. This is an open access article distributed under the Creative Commons Attribution License, which permits unrestricted use, distribution, and reproduction in any medium, provided the original work is properly cited.

This study was to evaluate the proposed consecutive multishot echo planar imaging (cmsEPI) combined with a parallel imaging technique in terms of signal-to-noise ratio (SNR) and acceleration for a functional imaging study. We developed cmsEPI sequence using both consecutively acquired multishot EPI segments and variable flip angles to minimize the delay between segments and to maximize the SNR, respectively. We also combined cmsEPI with the generalized autocalibrating partially parallel acquisitions (GRAPPA) method. Temporal SNRs were measured at different acceleration factors and number of segments for functional sensitivity evaluation. We also examined the geometric distortions, which inherently occurred in EPI sequence. The practical acceleration factors,  $R = 2$  or  $R = 3$ , of the proposed technique improved the temporal SNR by maximally 18% in phantom test and by averagely 8.2% in in vivo experiment, compared to cmsEPI without parallel imaging. The data collection time was decreased in inverse proportion to the acceleration factor as well. The improved temporal SNR resulted in better statistical power when evaluated on the functional response of the brain. In this study, we demonstrated that the combination of cmsEPI with the parallel imaging technique could provide the improved functional sensitivity for functional imaging study, compensating for the lower SNR by cmsEPI.

## 1. Introduction

In functional magnetic resonance imaging (fMRI) studies, echo planar imaging (EPI) technique has been widely used for investigating brain functions in which the signal is based on blood-oxygen-level-dependent (BOLD) contrast, reflecting the relationship between neuronal activity and concentration of deoxyhemoglobin in a blood vessel [1, 2]. Since EPI is one of the fastest imaging techniques, it has been suitable for observing functional dynamic changes of the brain. For high-resolution functional imaging, a segmented EPI, that is, multishot EPI (msEPI), has been employed as an alternative to a typical single-shot EPI (ssEPI) [2–5], because ssEPI image showed severe geometrical distortion and signal loss caused by accumulated magnetic susceptibility or field inhomogeneity. Also, the effective spatial resolution became

worse by  $T_2^*$  filter effect of a tissue, as a readout period in ssEPI increases [3, 6, 7].

In the previous study [4], the authors suggested msEPI to be performed by the acquisition of all the segments in a single slice before continuing on to the next slices in turn. The study demonstrated that optimum contrast sensitivity in BOLD-based fMRI experiments using msEPI could be achieved by using the short repetition time (TR) values between segments and the long echo train length. The short TR between segments was achievable with minimized intersegment delay. The other studies suggested variable flip angles (VFA) to maximize signal-to-noise ratio (SNR) for a short duration of a segment, rather than the Ernst angle [5, 8]. Thus, both the minimum intersegment delay and VFA were employed to optimize msEPI for functional imaging. This technique was named as interleaved or snapshot EPI in the previous

studies [5, 8]. To avoid confusing with other multishot EPI techniques, we called it as consecutive multishot EPI (cmsEPI).

In the meantime, the advance of RF multicoil arrays and their encoding capability has made the parallel imaging acquisition possible, which was associated with the significant scan time reduction in many clinical applications. Many parallel imaging reconstruction methods such as sensitivity encoding (SENSE) [9], simultaneous acquisition of spatial harmonics (SMASH) [10], and generalized autocalibrating partially parallel acquisitions (GRAPPA) [11] have been suggested. However, they also come with a nonuniform noise enhancement and then with a nonuniform loss in SNR compared to nonaccelerated images as presented in the previous studies [9, 12, 13]. Nevertheless, the utilization of the parallel imaging acquisitions became essential due to the enhancement of imaging speed and sensitivity, especially at high field MRI above 3T [14].

The combined technique, however, of cmsEPI with a parallel imaging has not been reported in ultrahigh field 7T MRI. In this study, therefore, we investigated cmsEPI with GRAPPA technique to improve SNR and evaluated the functional sensitivity of the proposed technique.

## 2. Materials and Methods

**2.1. Sequence Design.** Each segment of cmsEPI pulse sequence consisted of a fat-saturating RF pulse, a slice-selective RF pulse, navigators, and a data acquisition as plotted in Figure 1(a). The minimized interval between the segments required VFA for the slice-selective RF pulses, which allowed the segments to have an equivalent transverse magnetization theoretically. A typical Cartesian k-space was filled with k-space trajectories as many as the number of segments without overlapping. The relative size of a blip along a phase-encoding direction of each segment was also the same as the number of segments.

For the accelerated acquisition, the number of segments to be measured was reduced by the factor of  $1/R$ , in which  $R$  denoted the reduction or acceleration factor. The corresponding modified VFA were also adjusted to the reduced number of segments, which was defined as the following:

$$\theta_n = \sin^{-1} \left( \frac{1}{\sqrt{N/R - n + 1}} \right), \quad (1)$$

where  $\theta_n$ ,  $N$ , and  $n$  denote the  $n$ th flip angle, the number of segments, and an integer in range between 1 and  $N/R$ , respectively.

For 6 segments, for example, a sequence of flip angles was  $24^\circ$ ,  $26^\circ$ ,  $30^\circ$ ,  $35^\circ$ ,  $45^\circ$ , and  $90^\circ$  in order, as shown in Figure 1(b). In a reduction factor of 2 ( $R = 2$ ), only three flip angles were required, that is,  $35^\circ$ ,  $45^\circ$ , and  $90^\circ$ , in order. In a k-space with a reduction factor of 2, three segments were chosen to make a trajectory with a constant interval along phase-encoding direction. Two measurements were conducted for the reference lines, each of which had 3 segments (1st, 3rd, and 5th segments or 2nd, 4th, and 6th segments) as described in Figures 1(c) and 1(d). Parallel imaging reconstruction was

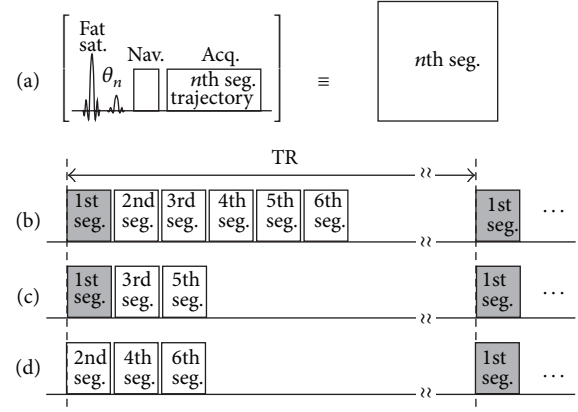


FIGURE 1: Simplified pulse sequence diagram. (a) The definition of a segment in multishot EPI, which consists of a fat-saturating RF pulse, a slice-selective RF pulse, navigators, and a data acquisition. Timing diagrams of (b) cmsEPI for 6 segments and (c) accelerated cmsEPI with reduction factor of  $R = 2$  for 6 segments. For the reference data of  $R = 2$ , all six segments need to be acquired but in two sets: one includes 1st, 3rd, and 5th segments and the other 2nd, 4th, and 6th segments as described in (d). Fat Sat.: fat saturation; FA: flip angle; Nav.: navigation echo; Seg.: segment; TR: repetition time or time for acquisition of one slice.

conducted with the autocalibration of a GRAPPA reconstruction kernel [11, 15].

At the same time, the navigator echoes following the excitation pulse were used for correcting not only the misalignment between alternating echoes along readout direction but also the intersegment amplitude discontinuities along phase-encoding direction [5]. A varying timing gap, namely, echo time shifting, was also inserted prior to data acquisition for preventing phase discontinuities of intersegment [16, 17].

**2.2. Data Acquisition.** For investigating the effect of parallel imaging on cmsEPI, we obtained images with different segments and acceleration factors, that is, 8 segments with  $R = 1$ , 2, and 4 or 6 segments with  $R = 1$ , 2, and 3. The acquisitions were performed three times on different days for reproducibility. The data with  $R = 8$  in 8 segments and  $R = 6$  in 6 segments were excluded, because the image reconstruction failed. Each dataset consisted of 50 volumes with which the temporal SNR (tSNR) was calculated. This experiment was performed with a spherical phantom filled with water.

Functional in vivo experiments consisted of two protocols: one was performed without any stimulus in order to analyze tSNR with the acquired 50 volumes during a resting state and the other was performed with visual stimulus, in which a flickering checker board of 8 Hz was utilized. A dummy period of 18 seconds was given prior to the initial session. A stimulus session of 18 seconds and a resting session of 18 seconds were repeated 4 times. Hence, each functional experiment was conducted for 162 seconds and 54 volumes were acquired. In functional in vivo experiment, only two conditions of 6 segments with  $R = 1$  and  $R = 3$  were acquired for comparison. The functional data were preprocessed and

analyzed with SPM8 (The Wellcome Department of Imaging Neuroscience, London, UK).

All imaging was performed in 7T MRI (MAGNETOM, SIEMENS, Erlangen). Data acquisition parameters were as follows: field of view (FOV)  $220 \times 220 \text{ mm}^2$ , in-plane resolution  $1.0 \times 1.0 \text{ mm}^2$ , partial Fourier factor 6/8, slice thickness 1.0 mm, TE 30 ms, TR 3000 ms, 5 slices, and 3.0 mm interslice gap. Note that TR 3000 ms means the time interval between subsequent volumes. The actual TR between segments was about 55 ms per segment per slice. For the acceleration factor  $R = 3$ , only 2 segments were acquired with an additional temporal gap of 220 ms between slices, which corresponds to the duration of 4 segments.

**2.3. Image Reconstruction.** Based on the reference data, the images were reconstructed by using multicolumn multiline interpolation (MCMLI) with a kernel of  $5 \times 4 (k_x \times k_y)$ , resulting in nonaliased images. Both nearest acquired line ( $k_y$ ) and column ( $k_x$ ) neighboring points were interpolated to reconstruct each missing data in the k-spaces from multiple channels [15].

To compensate for the error of intersegment, the acquired navigators were used to determine the amplitude gains of segments, in which each navigator's energy, that is, sum of square of navigator, was calculated. Then, the intersegment amplitude discontinuity was corrected by the gains. The accelerated data were recovered by GRAPPA algorithm implemented on MATLAB program (The MathWorks, Inc., Natick, Massachusetts, USA).

**2.4. Data Analysis.** Datasets for tSNR analysis were handled with a voxel-based analysis by the following equation [18, 19]:

$$\text{tSNR}(r) = \frac{\text{mean}_{k=1 \dots K}(S_N(r, k))}{\text{stdev}_{k=1 \dots K}(S_N(r, k))}, \quad (2)$$

where  $S_N$ ,  $r$ , and  $K$  denoted a noised (measured) signal, a voxel position, and the number of measurements.

For in vivo dataset, region-of-interest (ROI) was determined within the gray matters chosen by threshold of the magnitude of a mean image. The threshold was selected to determine a midrange between representative intensities of CSF and white matter, which played a role in making a mask. The ROI was divided to three regions along a phase-encoding direction in order to evaluate the nonuniform loss in tSNR, and the mean and the standard deviation of voxels of each ROI or all the ROIs were evaluated.

### 3. Results

Figure 2 showed the normalized tSNRs at different acceleration factors of cmsEPI in a phantom test. Comparing with  $R = 1$ , the mean tSNR in  $R = 2$  increased by 18% and 12% in 6 and 8 segments, respectively. After that, with the acceleration factors of 3 and 4, the tSNR was decreased as acceleration factor increased. The mean tSNR with 6 segments and  $R = 3$  was similar to that of  $R = 1$ .

In in vivo experiment, Figures 3(a) and 3(b) showed the tSNR maps of cmsEPI with  $R = 3$  and  $R = 1$ , respectively.

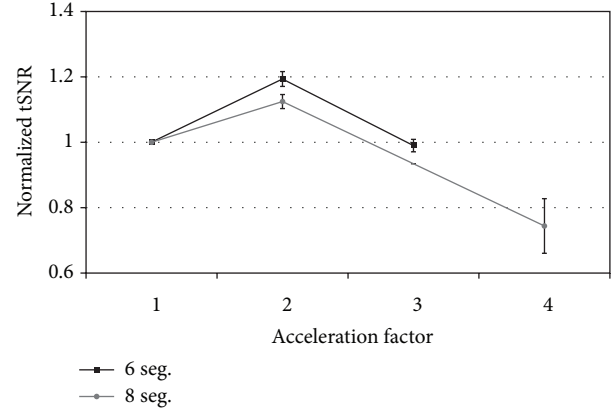


FIGURE 2: Comparison of temporal SNR at different conditions in phantom test. All of data were normalized to  $R = 1$ .

TABLE 1: Comparison of averaged tSNRs on ROIs selected from the gray matter compartment.

	$R = 1$	$R = 3$	Gain (%)
ROI 1	$33.7 \pm 7.6$	$38.5 \pm 9.0$	+14.2
ROI 2	$34.1 \pm 7.9$	$34.3 \pm 7.9$	+0.6
ROI 3	$30.4 \pm 6.9$	$32.2 \pm 7.5$	+6.0
Whole ROIs	$33.1 \pm 7.7$	$35.8 \pm 8.7$	+8.2

Basically, voxels including CSF tended to have a relatively high tSNR and voxels around brain ventricle had the highest tSNR. The tSNR difference between reduction factors was plotted in Figure 3(c). The most brain area of cmsEPI with  $R = 3$  had a higher tSNR than that with  $R = 1$  in in vivo experiment, although only the small portion of the image, especially at the midline of an image, had a decreased tSNR. For quantitatively evaluating the gain in tSNR, a mean and a standard deviation of voxels at ROIs were calculated from the tSNR difference map, and the result was presented in Table 1. The tSNR of each ROI of cmsEPI with  $R = 3$  was equal to or larger than  $R = 1$ , and an average gain of the tSNR was about 8.2% up to 14.2%.

In functional experiments, the visual stimulus was utilized in order to observe the activations on the primary visual area of the brain. As a result, Figures 4(a) and 4(b) showed the activation maps obtained by cmsEPI with  $R = 3$  and  $R = 1$ , respectively. To compare the two statistical values, they were displayed in the same range of  $t$ -value. The result of cmsEPI with  $R = 3$  had larger activated areas and higher  $t$ -values than that of  $R = 1$ . Figure 4(c) showed activation profiles in white lines on Figures 4(a) and 4(b), which showed similar patterns to each other. The profile of  $R = 3$ , however, provided better statistical power for activation than that of  $R = 1$ .

Figure 5 showed the distortion comparison between cmsEPI and ssEPI. Images in cmsEPI had almost the same degree of distortion, regardless of acceleration factors, while ssEPI showed explicit geometric distortion.

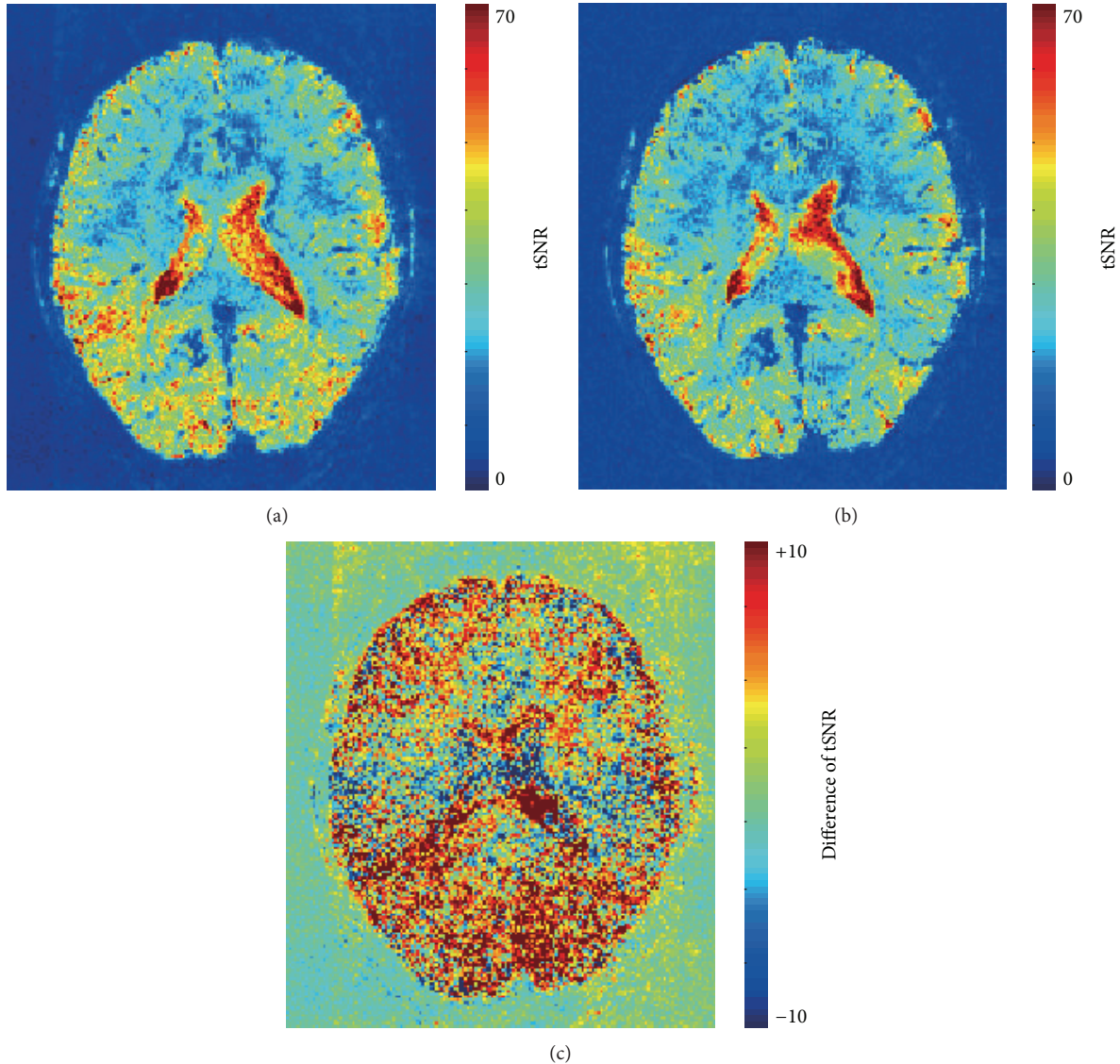


FIGURE 3: tSNR maps with/without parallel acquisition. (a) tSNR map with parallel acquisition. (b) tSNR map without parallel acquisition. (c) Difference of temporal SNR. In (c), the difference map was derived by subtraction of both maps ( $tSNR_{R=3} - tSNR_{R=1}$ ).

#### 4. Discussion

In this study, we demonstrated that cmsEPI combined with GRAPPA reconstruction provided increased tSNR compared to cmsEPI without acceleration. The image quality of the accelerated image such as signal deformation and geometrical distortion was preserved similarly to or better than the nonaccelerated image. The functional experiment to prove the functional effectiveness showed the increased functional sensitivity, in which the activated area was much broader and  $t$ -values were higher than in the nonaccelerated cmsEPI.

According to the previous study [20], better tSNR resulted from improved static SNR within some boundaries. Similarly, the static SNR mainly improved by the modified VFA in the parallel imaging acquisition could lead to increased tSNR. With employing acceleration acquisition, VFA were

increased, leading to gain of a magnitude of transverse magnetization for each segment. When a longitudinal magnetization of  $M_0$  was given, the transverse magnetization of  $M_0/\sqrt{n/R}$  will be applied to each segment of cmsEPI by the modified VFA. For instance, 6 segments with  $R = 1$  or  $R = 3$ , would lead to the applied transverse magnetization of  $0.4 \cdot M_0$  ( $\approx M_0/\sqrt{6}$ ) or  $0.7 \cdot M_0$  ( $\approx M_0/\sqrt{6/3}$ ), respectively. Hence, the modified VFA by parallel imaging acquisition could produce higher strength of signal.

It should be noted that the improved tSNR seems to mitigate the disadvantage of parallel imaging reconstruction such as noise enhancement. Typically, parallel imaging such as GRAPPA resulted in a loss in tSNR by a factor of  $g\sqrt{R}$ , where  $g$  denoted nonuniform loss in tSNR based on coil geometry. With considering the transverse magnetization

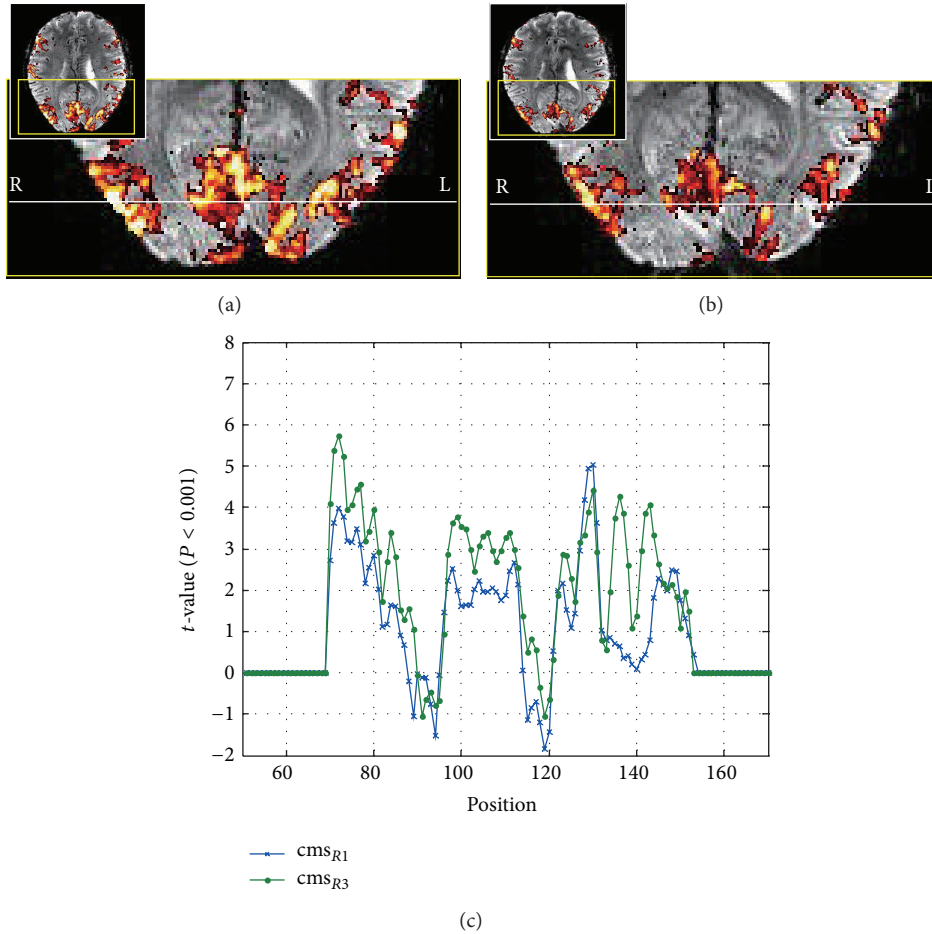


FIGURE 4: fMRI activation maps with/without parallel acquisition. (a) fMRI activation map with parallel acquisition. (b) fMRI activation map without parallel acquisition. (c) Comparison of  $t$ -values with/without parallel acquisition, in which  $t$ -values came from the white lines of (a) and (b). The improved tSNR led to entirely increased  $t$ -value (statistical power) to functional responses.

and the effect of parallel imaging, the tSNRs can be estimated as follows:

$$\begin{aligned}
 \text{tSNR}^{\text{non}} &\propto \left(\frac{M_0}{\sqrt{n}}\right)^2 = \frac{M_0^2}{n}, \\
 \text{tSNR}^{\text{acc}} &\propto \left(\frac{M_0}{\sqrt{n/R}}\right)^2 \cdot \frac{1}{g\sqrt{R}} = \frac{\sqrt{R}}{g} \cdot \frac{M_0^2}{n}.
 \end{aligned}
 \tag{3}$$

In (3), the superscripts of “non” and “acc” denoted a nonaccelerated and an accelerated cmsEPI, respectively. According to the equations, the tSNR of the accelerated cmsEPI entirely increased by a square root of a reduction factor but still could be decreased locally and nonuniformly by  $g$ -factor. Here, the variable of  $\sqrt{R}$  at the equation led to improvement of the tSNR, when implemented with modified VFA described in (1). It was a contrast from the original VFA consistently decreasing the tSNR as shown in the supplementary figure, in Supplementary Material available online at <http://dx.doi.org/10.1155/2015/394213>, where the original

VFA was in a condition without taking account of the acceleration factor of  $R$  in (1). Therefore, the modified VFA could essentially increase the tSNR in accelerated acquisitions.

In functional study, acceleration factor  $R = 3$  was selected instead of  $R = 2$ , although  $R = 2$  provided higher tSNR than  $R = 3$ . Since tSNR of  $R = 3$  was similar to  $R = 1$  in phantom test, the physiological effect of  $R = 3$  could be investigated and compared with  $R = 1$  in vivo test. And the acceleration factor of  $R = 3$  or 4 has been used in most of functional experiments as well as  $R = 2$  in ssEPI. In comparison of  $R = 1$  and  $R = 3$ , tSNR difference between phantom and in vivo tests was observed due to the possible existence of physiological noise. It showed that images in  $R = 3$  were less affected by physiological noise due to the shorter acquisition time so that tSNR in  $R = 3$  might be better than expected in in vivo test.

It was not performed to directly compare the tSNR of the proposed method with the tSNR of ssEPI. The tSNR in ssEPI has been known to decrease with the acceleration factor, which is typically proportional to  $M_0^2/g\sqrt{R}$ . However, the accelerated acquisition in ssEPI could additionally provide the shorter TE due to the reduced echo train length.

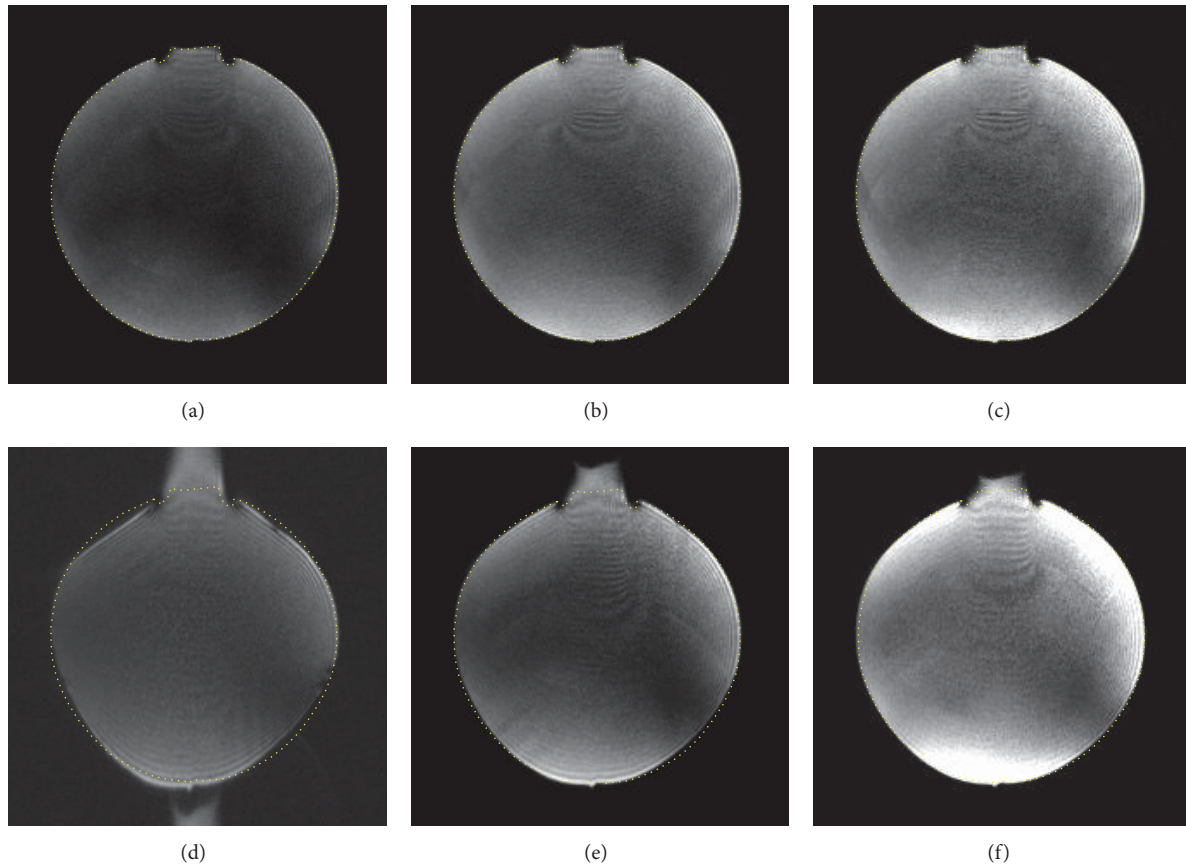


FIGURE 5: Comparison with single-shot EPI. Images were acquired by cmsEPI with 6 segments and (a, b, and c)  $R = 1, 2,$  and  $3$  and single-shot EPI with (d, e, and f)  $R = 1, 2,$  and  $3$ , respectively. The yellow dotted line was drawn from the outline of (a).

The reduced TE would have more influence on tSNR than the acceleration factor and the  $g$ -factor. In practical cases, possibly minimal TEs of ssEPI having the in-plane resolution of  $1.0 \text{ mm}^2$  were 68 ms and 29 ms in  $R = 1$  and  $R = 3$ , respectively. Considering a voxel with  $T_2^*$  of 60 ms, the signal intensity in TE of 29 ms would apparently be about 1.9 times higher than in TE of 68 ms. Thus, since the tSNR was determined by imaging parameters, the direct comparison of the tSNR would not be necessary. As the same TE was given, the proposed method would provide lower tSNR than ssEPI.

Artifacts on the image could occur by intersegment modulations arising from VFA, which would occur in both magnitude and phase. The magnitude modulation would be caused by a nonideal shape in a slice-selective RF profile and different sensitivities of a RF coil to various flip angles, but it could be almost compensated by the comparison of navigators of segments. The intersegment phase modulation would be also caused by B1 field differences of various flip angles, that is, signal phase difference between practical excitation RF pulses with  $45^\circ$  and  $90^\circ$ . In contrast to the magnitude modulation described above, the level of the artifact by the phase modulation could be changed in the region where B1 significantly deviates from the nominal one. Further study will be needed for handling these artifacts.

The proposed method has the similar image contrast with conventional ssEPI, because cmsEPI with parallel imaging can preserve the image contrast given by the same TR and TE as ssEPI. The image contrast of a typical msEPI, however, includes the different T1 recovery effect as well as the  $T_2^*$  relaxation effect due to a time interval between excitation RF pulses, compared with ssEPI.

In addition, the proposed method with the shorter echo time and the echo train length could function as an alternative and controllable geometrical distortion correction technique, leading to reduction in the geometrical distortion inherently and preventing of the signal loss by field inhomogeneity. Though the postprocessing distortion correction techniques such as PSF-mapping can produce a distortion-corrected image similar to the distortion-free gradient-recalled echo image (GRE) [21], the information loss by a fast  $T_2^*$  decay is hard to be recovered completely. Therefore, the proposed method is possible to be easily implemented with other postprocessing correction techniques.

The proposed method also has the potential capability of further improving the imaging coverage. The future extension of the proposed method for imaging coverage can be achieved by multiband (MB) or simultaneous multislice (SMS) techniques based on 2D imaging [22]. However, direct

3D approach using multiple excitations should be carefully applied to the proposed method, because minimum intersegment can be conflicted by multiple excitations with constant interval or too many segments can cause the decrease in static SNR of an image.

## 5. Conclusions

This study proposed an advanced technique of cmsEPI for functional study. We demonstrated that the combination of cmsEPI with parallel imaging acquisition could provide a synergic effect to improve functional sensitivity.

## Conflict of Interests

The authors declare that there is no conflict of interests regarding the publication of this paper.

## Acknowledgments

The authors acknowledge JSPS KAKENHI Grant nos. 26350995 and 25330173 and MEXT-Supported Program for the Strategic Research Foundation at Private Universities, 2014–2018.

## References

- [1] S. Ogawa, T. M. Lee, A. R. Kay, and D. W. Tank, "Brain magnetic resonance imaging with contrast dependent on blood oxygenation," *Proceedings of the National Academy of Sciences of the United States of America*, vol. 87, no. 24, pp. 9868–9872, 1990.
- [2] N. K. Logothetis, J. Pauls, M. Augath, T. Trinath, and A. Oeltermann, "Neurophysiological investigation of the basis of the fMRI signal," *Nature*, vol. 412, no. 6843, pp. 150–157, 2001.
- [3] F. G. C. Hoogenraad, P. J. W. Pouwels, M. B. M. Hofman et al., "High-resolution segmented EPI in a motor task fMRI study," *Magnetic Resonance Imaging*, vol. 18, no. 4, pp. 405–409, 2000.
- [4] R. S. Menon, C. G. Thomas, and J. S. Gati, "Investigation of BOLD contrast in fMRI using multi-shot EPI," *NMR in Biomedicine*, vol. 10, no. 4-5, pp. 179–182, 1997.
- [5] S.-G. Kim, X. Hu, G. Adriany, and K. Ugurbil, "Fast interleaved echo-planar imaging with navigator: high resolution anatomic and functional images at 4 tesla," *Magnetic Resonance in Medicine*, vol. 35, no. 6, pp. 895–902, 1996.
- [6] F. Farzaneh, S. J. Riederer, and N. J. Pelc, "Analysis of  $T_2$  limitations and off-resonance effects on spatial resolution and artifacts in echo-planar imaging," *Magnetic Resonance in Medicine*, vol. 14, no. 1, pp. 123–139, 1990.
- [7] A. Jesmanowicz, P. A. Bandettini, and J. S. Hyde, "Single-shot half k-space high-resolution gradient-recalled EPI for fMRI at 3 Tesla," *Magnetic Resonance in Medicine*, vol. 40, no. 5, pp. 754–762, 1998.
- [8] D. N. Guilfoyle and J. Hrabe, "Interleaved snapshot echo planar imaging of mouse brain at 7.0 T," *NMR in Biomedicine*, vol. 19, no. 1, pp. 108–115, 2006.
- [9] K. P. Pruessmann, M. Weiger, M. B. Scheidegger, and P. Boesiger, "SENSE: sensitivity encoding for fast MRI," *Magnetic Resonance in Medicine*, vol. 42, pp. 952–962, 1999.
- [10] D. K. Sodickson and W. J. Manning, "Simultaneous acquisition of spatial harmonics (SMASH): fast imaging with radiofrequency coil arrays," *Magnetic Resonance in Medicine*, vol. 38, no. 4, pp. 591–603, 1997.
- [11] M. A. Griswold, P. M. Jakob, R. M. Heidemann et al., "Generalized autocalibrating partially parallel acquisitions (GRAPPA)," *Magnetic Resonance in Medicine*, vol. 47, no. 6, pp. 1202–1210, 2002.
- [12] D. K. Sodickson, M. A. Griswold, P. M. Jakob, R. R. Edelman, and W. J. Manning, "Signal-to-noise ratio and signal-to-noise efficiency in SMASH imaging," *Magnetic Resonance in Medicine*, vol. 41, pp. 1009–1022, 1999.
- [13] F. A. Breuer, S. A. R. Kannengiesser, M. Blaimer, N. Seiberlich, P. M. Jakob, and M. A. Griswold, "General formulation for quantitative G-factor calculation in GRAPPA reconstructions," *Magnetic Resonance in Medicine*, vol. 62, no. 3, pp. 739–746, 2009.
- [14] K. P. Pruessmann, "Parallel imaging at high field strength: synergies and joint potential," *Topics in Magnetic Resonance Imaging*, vol. 15, no. 4, pp. 237–244, 2004.
- [15] Z. Wang, J. Wang, and J. A. Detre, "Improved data reconstruction method for GRAPPA," *Magnetic Resonance in Medicine*, vol. 54, no. 3, pp. 738–742, 2005.
- [16] F. Hennel, "Multiple-shot echo-planar imaging," *Concepts in Magnetic Resonance*, vol. 9, no. 1, pp. 43–57, 1997.
- [17] D. A. Feinberg and K. Oshio, "Phase errors in multi-shot echo planar imaging," *Magnetic Resonance in Medicine*, vol. 32, no. 4, pp. 535–539, 1994.
- [18] O. Dietrich, J. G. Raya, S. B. Reeder, M. F. Reiser, and S. O. Schoenberg, "Measurement of signal-to-noise ratios in MR images: influence of multichannel coils, parallel imaging, and reconstruction filters," *Journal of Magnetic Resonance Imaging*, vol. 26, no. 2, pp. 375–385, 2007.
- [19] C. Triantafyllou, R. D. Hoge, G. Krueger et al., "Comparison of physiological noise at 1.5 T, 3 T and 7 T and optimization of fMRI acquisition parameters," *NeuroImage*, vol. 26, no. 1, pp. 243–250, 2005.
- [20] C. Triantafyllou, R. D. Hoge, G. Krueger et al., "Comparison of physiological noise at 1.5 T, 3 T and 7 T and optimization of fMRI acquisition parameters," *NeuroImage*, vol. 26, no. 1, pp. 243–250, 2005.
- [21] M.-H. In and O. Speck, "Highly accelerated PSF-mapping for EPI distortion correction with improved fidelity," *Magnetic Resonance Materials in Physics, Biology and Medicine*, vol. 25, no. 3, pp. 183–192, 2012.
- [22] S. Moeller, E. Yacoub, C. A. Olman et al., "Multiband multislice GE-EPI at 7 tesla, with 16-fold acceleration using partial parallel imaging with application to high spatial and temporal whole-brain fMRI," *Magnetic Resonance in Medicine*, vol. 63, no. 5, pp. 1144–1153, 2010.

## Review Article

# Tracking Transplanted Stem Cells Using Magnetic Resonance Imaging and the Nanoparticle Labeling Method in Urology

Jae Heon Kim,<sup>1</sup> Hong J. Lee,<sup>2</sup> and Yun Seob Song<sup>1</sup>

<sup>1</sup>Department of Urology, Soonchunhyang University Hospital, College of Medicine, Soonchunhyang University, Seoul, Republic of Korea

<sup>2</sup>Biomedical Research Institute, Chung-Ang School of Medicine, Seoul, Republic of Korea

Correspondence should be addressed to Hong J. Lee; leehj71@gmail.com and Yun Seob Song; yssong@schmc.ac.kr

Received 4 September 2014; Revised 10 March 2015; Accepted 17 March 2015

Academic Editor: Zhengchao Dong

Copyright © 2015 Jae Heon Kim et al. This is an open access article distributed under the Creative Commons Attribution License, which permits unrestricted use, distribution, and reproduction in any medium, provided the original work is properly cited.

A reliable *in vivo* imaging method to localize transplanted cells and monitor their viability would enable a systematic investigation of cell therapy. Most stem cell transplantation studies have used immunohistological staining, which does not provide information about the migration of transplanted cells *in vivo* in the same host. Molecular imaging visualizes targeted cells in a living host, which enables determining the biological processes occurring in transplanted stem cells. Molecular imaging with labeled nanoparticles provides the opportunity to monitor transplanted cells noninvasively without sacrifice and to repeatedly evaluate them. Among several molecular imaging techniques, magnetic resonance imaging (MRI) provides high resolution and sensitivity of transplanted cells. MRI is a powerful noninvasive imaging modality with excellent image resolution for studying cellular dynamics. Several types of nanoparticles including superparamagnetic iron oxide nanoparticles and magnetic nanoparticles have been used to magnetically label stem cells and monitor viability by MRI in the urologic field. This review focuses on the current role and limitations of MRI with labeled nanoparticles for tracking transplanted stem cells in urology.

## 1. Introduction

Molecular imaging technologies have evolved recently and facilitate functional monitoring and evaluation of genes and organs for their roles in health and disease [1, 2]. Stem cell transplantation has good prospects for clinical application. However, the challenges in molecular imaging are to develop effective imaging strategies with a combination of imaging modalities, labeling reporter systems, and probes. Several studies have used magnetic resonance imaging (MRI) to trace transplanted stem cells in animal models [3, 4].

Several molecular imaging modalities including positron emission tomography (PET), MRI, and newer modalities are based on transmitting light through tissues, such as *in vivo* bioluminescence imaging and fluorescence imaging. Among them, MRI is the most popular imaging modality. MRI used in conjunction with magnetically labeling is a powerful technique for noninvasively detecting and tracking transplanted cells in longitudinal animal studies [1, 2, 5].

Labeling materials have great importance in the field of molecular imaging. Labeling stem cells makes merged cells

distinguishable from host cells to follow transplanted stem cells.

Molecular materials for labeling should first reveal cellular and molecular processes throughout the entire study period. Secondly, the probes should be highly sensitive to small changes in cell function and distribution. Finally, they should not significantly alter the labeled biological process itself [1, 2, 5].

Gadolinium and ferric oxide are two common cell labeling contrast media used during MRI [6]. New technologies with tumor targeting and drug delivery are being conceptualized. Developments in nanotechnology have provided more innovative and effective approaches in various areas of clinical research, such as diagnosis [7], monitoring [8, 9], and therapy [10–12]. Labeling with nanoparticles is an emerging trend, particularly in oncology such as “cancer nanotheranostics,” which includes simultaneous imaging and treating cancer cells by applying nanoparticles [13].

Although many studies have investigated the efficiency of molecular imaging using MRI with labeled nanoparticles, few studies are available in the urologic field. The aim of

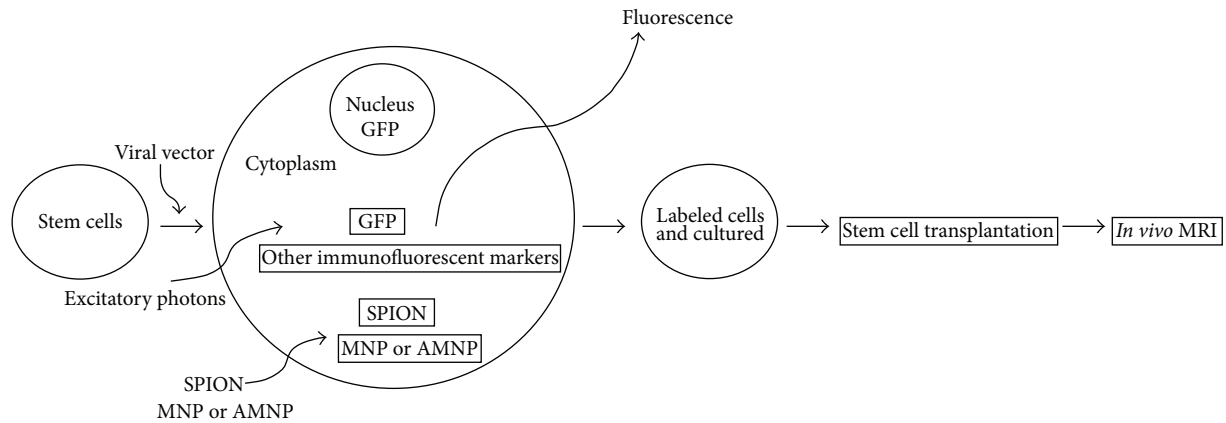


FIGURE 1: Schematic imaging of stem cell tracking using magnetic resonance imaging (MRI) combined with nanoparticle labeling.

this study was to review MRI and labeling techniques for tracking transplanted stem cells (physiological labeling) in the urologic field and to review the characteristics and limitations of current nanoparticle labeling methods.

## 2. Stem Cell Labeling

Cell labeling can be divided into physical cell labeling and reporter gene imaging. Physical cell labeling is completed before cell administration and can be accomplished with superparamagnetic iron oxide (SPIO) particles for MRI [14, 15] and radionuclide labeling for single-photon emission computed tomography [16] and PET [17]. In reporter gene imaging, a gene coding synthesis of a detectable protein is introduced into a target cell line or tissue via viral or nonviral vectors. As a result, changes in signals following cell administration can be used as indicators of cell proliferation and death [18].

Many labeling techniques involve incubating cells and use of transfection agents. The different magnetic labeling techniques result in a considerable increase in the cellular iron content [26], which is 100 times greater than physiological levels [27]. The largest amount of intracellular iron oxide particles and the use of high-resolution gradient echo sequences allow for highly sensitive *in vivo* MRI methods for detecting viability and efficiency of transplanted stem cells.

Most studies have tracked physically labeled transplanted stem cells (Figure 1). Migration of lymphocytes [28], hematopoietic stem cells [29], mesenchymal stromal cells (MSCs) [30], neuronal precursor cells [31], and tumor cells [32] has been demonstrated in different disease models using *in vivo* MRI. Specific cancer stem cell antigens or receptors have been detected by reporter gene imaging.

Application of conventional GFP-like fluorescent proteins, including eGFP, DsRed, and mCherry, has limitations due to the penetration depths of visible light in the body [33]. To overcome this limitation, near-infrared fluorescent protein (IFP) has been developed from the DrBpHP bacterial phytochrome of *Deinococcus radiodurans* and showed

the possibility in the application of IFPs for protein labeling and *in vivo* tracking imaging [5].

## 3. Iron Oxide Nanoparticles

The original iron oxide nanoparticles were developed in 1995 and were Dextran-coated iron oxide nanoparticle with a 100–150 nm hydrodynamic radius and contained a 5–10 nm iron oxide core [34]. These standard, well-characterized iron oxide nanoparticles have been used widely, but low labeling amounts and efficiencies were shortcomings [35]. To overcome this weak point, simple transfection agents were combined with ferumoxides enabling robust labeling of a number of cell types [36].

Most recently, a nanomaterial consisting of a mixture of ferumoxytol, heparin sulfate, and protamine sulfate has been reported and can be used to safely label various types of cells for tracking by MRI [8]. Ferumoxytol, heparin sulfate, and a protamine sulfate conjugate is currently the most popular material for physical cell labeling in urology [37]. Dextran-coated superparamagnetic iron oxide nanoparticles (SPIONs) and micron-sized iron oxide particles were developed for MRI-based cell tracking [26, 38]. The size of iron oxide particles for cell labeling ranges from very small particles to micron-sized particles, and SPIO is a medium-sized particle [39–41].

Among the different types of nanoparticles, SPIONs are promising candidates for use with molecular imaging modalities due to their superparamagnetic behavior and surface-modification properties. One of the important features of SPIONs is that they lose their magnetism and become highly dispersed when the magnetic field is switched off, which prevents easy recognition and engulfment by macrophages [42].

As SPIONs are biodegradable and biocompatible, they can be applied in various biomedical fields, such as magneto-transfection [43], gene therapy [44], and cell and biological material separation [45]. SPIONs are mostly magnetite ( $\text{Fe}_3\text{O}_4$ ), and they convert to maghemite when exposed to oxygen.

They can be metabolized easily and transported by proteins, such as ferritin, transferrin, and hemosiderin, and they can be stored in endogenous iron reserves of the body for later use [1, 2].

The advantage of applying a magnetic field to guide nanoparticles to their target is to reduce stem cell waste, lower the frequency of stem cell administration, and avoid unwanted side effects [1, 2]. SPIONs are very promising materials for biomedical applications due to their increased ability to covalently attach to various receptors, peptides, antibodies, or ligands [46]. Furthermore, SPIO particles have no adverse effects on viability or proliferation of labeled cells [40, 47].

#### 4. Non-SPION Nanoparticles

Most magnetic labeling procedures depend on Dextran-coated magnetic nanoparticles. Several magnetic cell labeling methods have been developed but the most commonly used one is cocultivating Dextran-coated nanoparticles with a transfection agent [48].

However, these materials follow a low-efficiency fluid-phase endocytosis pathway and require long incubation times or the use of transfection agents to achieve substantial iron uptake. Moreover, the complexes formed by the nanoparticles and transfection agents are not easily controlled.

Anionic magnetic nanoparticles (AMNPs) have negative surface charges, are free of a Dextran coating, adsorb readily to cell membranes, and are internalized without the need for transfection agents or long incubation times [20, 49, 50]. AMNPs permit controlled uptake by various cell types [20, 51–53]. AMNPs have advantages of easy and rapid absorption and subsequent internalization by endocytosis [50, 54, 55]. AMNP biocompatibility has been demonstrated in many preclinical studies, including local cell grafts for tissue regeneration [20, 56] and immune cell trafficking after systemic injection [52, 57, 58].

Fluorescent magnetic nanoparticles (MNPs) contain rhodamine B isothiocyanate within a silica shell to overcome the negative surface charge. This tagging material does not require a transfection agent during cell labeling, the MNP core is composed of ferrite, and the inner silica shell portion contains fluorescent materials [59]. It has both magnetic and optical features, and Prussian blue staining is not necessary to detect viability and efficiency of transplanted stem cells within tissue. *In vivo* tracking of transplanted MSCs labeled with fluorescent MNPs in a liver cirrhosis rat model by MRI has been reported [60].

Among the six studies that used MRI and physical labeling, three used SPIONs, two used MNPs, and one used AMNPs (Table 1).

Gadolinium (Gd) based contrast agents are normally used to reduce  $T_1$  period and to give positive contrast in MR images. Available agents are different kinds of gadolinium ion based chelates which are relatively stable molecules. To date, Gd based contrast agent has evolved to be more efficient contrast agents including Gd<sup>3+</sup> based agents with higher molecular weight like Gd-DTPA functionalized polymers,

Gd-DTPA terminated dendrimers, and Gd complex loaded liposomes as well as high density lipoprotein nanoparticles or micelles [61]. Recently, several new nanoparticles are introduced for *in vivo* imaging including Fe<sub>3</sub>O<sub>4</sub>@SiO<sub>2</sub> nanoparticles and Gd-DOTA-peptides [62–64].

#### 5. Ideal Features of Labeled Nanoparticles

Nanoparticles for any biological application must be biocompatible, nontoxic, and stable at physiological pH. The ideal features are high magnetization and a narrow size distribution. The nanoparticles should have contrast enhancement properties for imaging and tracking of malignant cells/tissues, and their surfaces should be coated with biodegradable material. They should have the ability to conjugate with a range of receptors with high targeting and drug-delivery efficiencies. The half-life should be long, and the zeta-potential should be optimized [1, 5, 9].

#### 6. Current Uses for MRI Techniques in Urology

MRI is a widely used powerful imaging technique that provides high resolution in the field of urology. It is used to evaluate stem cells transplanted to urologic organs. MRI alone or MRI with a physical labeling method has been used to monitor the efficiency of cell transplantation, cellular homing, and targeting. MRI has been used in prostate cancer research, bladder dysfunction research, urethral sphincter studies, and a penis study (Table 1).

**6.1. Prostate Cancer.** Molecular imaging combined with a labeling technique has been used to detect specific prostate cancer antigens. Two studies showed the efficiency of MRI for detecting transplanted stem cells as a vector for prodrug therapy. Abrate et al. [21] reported that MRI can be used to follow orthotopic tumor progression. Although those authors did not apply a physical labeling method, they demonstrated that intravenous injections of CD-MSC cells, followed by intraperitoneal administration of 5-fluorocytosine, caused tumor regression in transgenic adenocarcinoma of the mouse prostate model, which develops aggressive and spontaneous prostate cancer.

Lee et al. [19] reported monitoring the migration of genetically modified stem cells by MRI after labeling the cells with fluorescent MNPs. Human neural stem cells encoding CD (HB1.F3.CD) were prepared and labeled with MNPs (Figure 2). HB1.F3.CD stem cells systemically transplanted into tumor-bearing C57B mice migrated toward the tumor, and tumor implant volume decreased significantly in combination with the prodrug 5-FC.

**6.2. Bladder.** Traditionally, many studies showed the efficacy of stem cell treatment in bladder dysfunction [65–67]; however only several studies introduced molecular imaging techniques. Yun and Ja [24] showed similar viability of MSCs loaded with SPIONs compared to unlabeled cells. SPIO-labeled MSCs underwent normal chondrogenic, adipogenic,

TABLE 1: Studies using stem cell-based gene therapy for prostate cancer.

Study	Stem cell	Animal	Organ	Nanoparticle	Labeling viability	Labeling efficiency	Iron quantification	In vivo MRI	In vitro MRI	Labeling dose
Lee et al. [19]	Human NSC	C57BL/6 mice	Metastatic prostate cancer	MNP	Immunofluorescence microscope, X-gal staining	None	None	T2-weighted gradient-echo	None	100 $\mu\text{g}/\text{mL}$ MNP
Rivière et al. [20]	Pig MPC	Pig	Urethral sphincter	AMNP	Indirect antidesmin immunofluorescence	Prussian blue staining and electron microscopic imaging	Magnetophoresis, electron spin resonance	T1-weighted gradient-echo	T1, T2-weighted gradient-echo	$4.5 \times 10^9$ AMNPs
Abrate et al. [21]	Human MSC	C57BL/6 mice	Metastatic prostate cancer	None	None	Prussian blue staining and electron microscopic imaging	None	T2-weighted RARE images	None	None
Lee et al. [22]	Human MSC	Rat	Bladder	SPION	Trypan blue staining	Prussian blue staining	None	T1-weighted gradient-echo	None	25 $\mu\text{g}/\text{mL}$ SPION
Song et al. [23]	Human MSC	Rat, rabbit	Penis	SPION	Trypan blue staining	Prussian blue staining and electron microscopic imaging	None	T2-weighted gradient-echo	T1-weighted gradient-echo	25 $\mu\text{g}/\text{mL}$ SPION
Yun and Ja [24]	Human MSC	Rat, rabbit	Bladder	SPION	Trypan blue staining	Prussian blue staining and electron microscopic imaging	None	T2-weighted gradient-echo	T2-weighted gradient-echo	25 $\mu\text{g}/\text{mL}$ SPION
Lee et al. [25]	Human NSC	Rat	Bladder	MNP	Immunofluorescence microscope	None	None	T2-weighted gradient-echo	None	100 $\mu\text{g}/\text{mL}$ MNP

NSC: neural stem cell; MNP: magnetic nanoparticle; MPC: myogenic precursor cell; MSC: mesenchymal stem cell; SPION: super paramagnetic iron oxide nanoparticle.

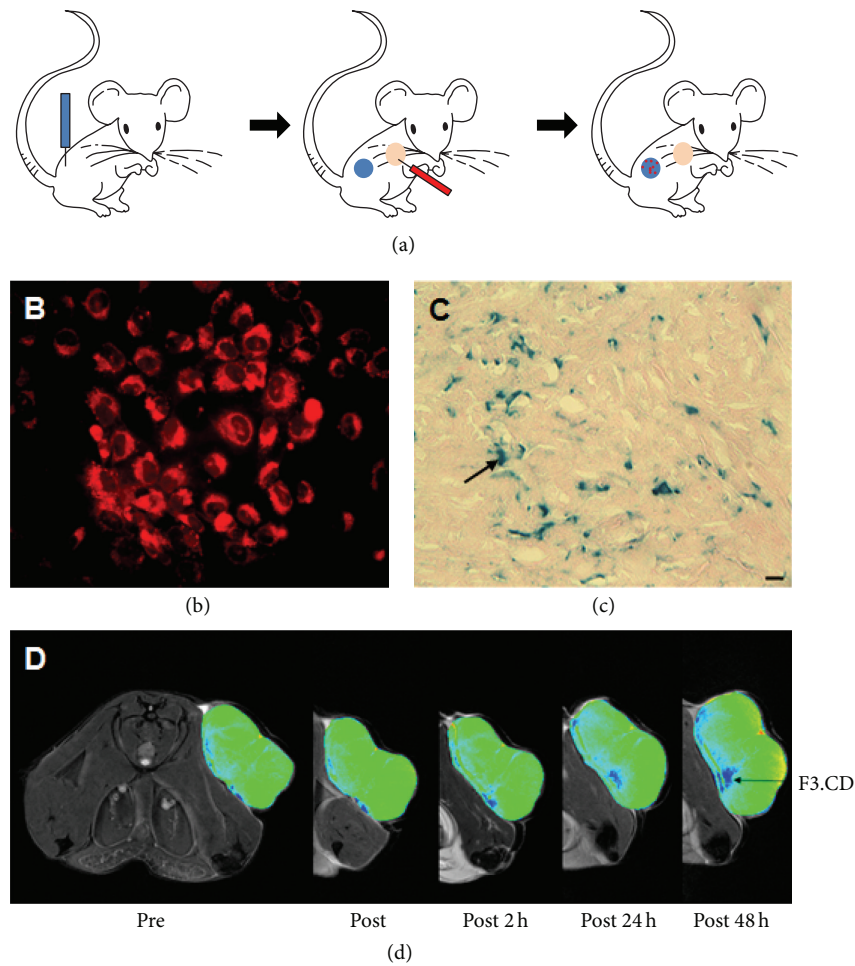


FIGURE 2: Intravascular delivery of stem cells (HB1.F3.CD) targeting prostate cancer. (a) Schematic illustration of inducing prostate cancer using TRAMPC2, a systemic injection of HB1.F3.CD cells, and migration of the gene-modified stem cells toward the prostate cancer. Blue = TRAMPC2; red = HB1.F3.CD cells. (b) X-gal staining of induced prostate cancer 2 days after injecting HB1.F3.CD cells. Arrow indicates the cells. (c) Magnetic resonance imaging (MRI) of prostate cancer 48 hr after injecting HB1.F3.CD cells into mice. Arrow indicates the cells (scale bar, 100  $\mu$ m). HB1.F3, neural stem cells; CD, cytosine deaminase.

and osteogenic differentiation. MRI signal intensity in the areas of SPION-labeled MSCs in rat and rabbit bladders decreased and was confined locally. MRI demonstrated that SPION-labeled MSCs injected into the bladder could be seen for at least 12 weeks.

Lee et al. [22] reported that MRI images were useful to track transplanted MSCs in bladder outlet obstruction induced bladder dysfunction. Serial T2-weighted MRI images were taken immediately after transplant of SPION-labeled MSCs and at 4 weeks after transplantation. T2-weighted MRI showed a clear hypointense signal induced by the SPION-labeled MSCs. Collagen and transforming growth factor- $\beta$  expression protein increased after bladder outlet obstruction, and the expression of both returned to original levels after MSC transplantation.

Lee et al. [25] reported the efficiency of MRI for tracking transplanted MSCs in a spinal cord injury-induced bladder dysfunction model. MNP-labeled B10 cells were injected into the bladder wall 4 weeks after the spinal cord injury. Serial

MRI was taken immediately after MNP-B10 injection and at 4 weeks after transplantation.

6.3. *Penis*. Song et al. [23] suggested that MRI can be used to investigate the long-term therapeutic potential of MSCs to treat erectile dysfunction. SPION-labeled MSCs injected into the corpus cavernosa of rats and rabbits were evaluated noninvasively by molecular MRI. MRI signal intensity at the areas of SPION-labeled MSCs in the rat and rabbit corpus cavernosa decreased and was confined locally. MRI demonstrated that the MSCs could be observed for at least 12 weeks after injection into the corpus cavernosum.

6.4. *Urethral Sphincter*. Rivière et al. [20] magnetically labeled muscle implants with AMNPs. They evaluated the biocompatibility of the labeling procedure and its utility for noninvasive MRI follow-up of cell therapy in a female pig model. AMNPs were adsorbed onto the implant surface of myogenic precursor cells and were magnetically labeled

within the implants. Magnetic labeling did not affect cell proliferation or differentiation. Autograft detection *in vivo* by 0.3-T MRI was possible for up to 1 month.

## 7. Discussion

Although molecular imaging techniques have evolved significantly during the last decade, no single imaging modality can provide all the information required to track transplanted stem cells and monitor their functional effects. Each imaging modality used for stem cell tracing has its advantages and disadvantages [54, 68]. PET has high sensitivity for tracking biomarkers *in vivo* but lacks the ability to provide detailed anatomic structure. Optical imaging has high molecular sensitivity but provides less anatomical localization and is mainly used in small animals. MRI coupled with physical labeling has high resolution and the capabilities of three-dimensional anatomical imaging. However, MRI has low sensitivity for cell tracing. Moreover, it cannot detect cell number or location by cell division because cell division may dilute intracellular markers with the shedding of iron particles [69]. Hence, it is necessary to combine complementary imaging methodologies as with multimodality imaging approaches.

Some nonspecific signal problems occur with different imaging modalities as a result of dead transplanted cells. For example, dead transplanted cells containing iron oxide nanoparticles may result in MRI signals representing macrophage phagocytosis of labeled cell debris [1, 2, 5]. Limitations continue in the basic knowledge about the pivotal biological characters of transplanted stem cells, such as survival, integration, and migration, and the influence of the host microenvironment. Despite the potential for biomedical applications, SPIONs face some targeting and imaging limitations. The proportion of SPIONs that reach the target through surface-bound antibodies is low, thereby limiting their application for imaging and drug delivery.

MRI is a commonly used imaging modality and it could be used in a large animal model. To detect successful delivery and subsequent migration using iron oxide-based agents, *ex vivo* labeling of the stem cells are required [1]. The robust negative contrast image generated by iron oxide agents has shown efficient cell labeling. Studies have also reported successful tracking at near single-cell resolution [70]. However, to assess the viability additional techniques are needed such as using promoter genes, engineering cells to overexpress transferrin receptors, and nongenomic technique using manganese-enhanced MRI.

To date, the important pitfalls of MRI with SPIO labeled cells or luciferase-based bioluminescent imaging are that these modalities could provide the information about cell survival, anatomical coregistration of engrafted cells together with real time, and image-guided delivery. To overcome these limitations, chemical exchange saturation transfer is an emerging MRI contrast mechanism based on the use of radiofrequency saturation pulses to detect agents containing protons that exchange rapidly with water [27]. Chan et al. [9] reported that pH nanosensor-based MRI technique can monitor cell death *in vivo* noninvasively. They demonstrated that specific MRI parameters related with cell death

of microencapsulated hepatocytes are associated with the measured bioluminescence imaging radiance.

To overcome this problem, classic physical labeling must be upgraded with a reporter gene imaging technique. In fact, this combined modality is being investigated in cancer stem cell studies. SPIONs with specific tumor-targeting ligands and sensitive imaging probes must be developed [71]. To date, most *in vivo* imaging studies showed the limitations in detecting the engraftment of stem cells [72].

Another major problem facing drug delivery using nanoparticles is the burst effect. When drug-coated nanoparticles are injected into a system, a significant quantity of the drug is liberated suddenly due to alterations in the physiological host environment, which can be dangerous to the patient [1, 2, 5]. To overcome this effect, nanoparticles must be cross-linked with polymers or incorporated into a polymer matrix that provides more rigidity and helps provide sustained drug delivery under *in vivo* conditions for longer times [1, 2, 5]. Mahmoudi and Laurent [73] demonstrated increased stability of drug-loaded SPIONs under *in vivo* conditions using a PEG-cofumarate cross linking agent. Other issues that must be solved regarding nanoparticles include toxicity, gene alternations, penetration of the blood-brain barrier, and colloidal stability [1, 2, 5].

Molecular imaging combined with a nanoparticle labeling method is useful not only for physical labeling to monitor stem cells but also to detect prostate cancer antigens. Recent preclinical studies on multimodal molecular imaging methods have the potential to be helpful for noninvasive prostate cancer diagnosis and image-guided immunotherapy [74, 75]. Multiple groups are actively pursuing the development of imaging probes for cellular and molecular MRI [75–79]. More studies are needed to develop various molecular markers, including ligands, antibodies, and peptides that can easily bind MRO probes.

*In vivo* imaging represents a dedicated platform to evaluate and quantify molecular and cellular events related to cellular engraftment. This integrative approach should be more developed with validation for systematic translation of stem cell therapy.

## 8. Conclusions

Molecular imaging is a new discipline that allows for *in vivo* cellular and molecular imaging of pathophysiological processes and the results of therapeutic interventions. MRI is a contending and complementing modality for stem cell studies in urology. MRI can be used to evaluate migration and survival of transplanted stem cells in prostate cancer and bladder dysfunction models. It has also shown potential utility for use on erectile dysfunction and urethral sphincter dysfunction. Noninvasive imaging methods using MRI have the advantage of longitudinal monitoring of transplanted stem cells in animals.

## Conflict of Interests

The authors declare that they have no conflict of interests.

## Acknowledgment

This research was supported by the Research Program through the National Research Foundation of Korea (NRF) funded by the Ministry of Education, Science, and Technology (2010-0011678) and by the Soonchunhyang University Research Fund.

## References

- [1] L. Josephson, C.-H. Tung, A. Moore, and R. Weissleder, "High-efficiency intracellular magnetic labeling with novel superparamagnetic-Tat peptide conjugates," *Bioconjugate Chemistry*, vol. 10, no. 2, pp. 186–191, 1999.
- [2] L. Tong, M. Zhao, S. Zhu, and J. Chen, "Synthesis and application of superparamagnetic iron oxide nanoparticles in targeted therapy and imaging of cancer," *Frontiers of Medicine in China*, vol. 5, no. 4, pp. 379–387, 2011.
- [3] L. E. Gonzalez-Lara, X. Xu, K. Hofstetrova, A. Pniak, A. Brown, and P. J. Foster, "In vivo magnetic resonance imaging of spinal cord injury in the mouse," *Journal of Neurotrauma*, vol. 26, no. 5, pp. 753–762, 2009.
- [4] J. Guenoun, A. Ruggiero, G. Doeswijk et al., "In vivo quantitative assessment of cell viability of gadolinium or iron-labeled cells using MRI and bioluminescence imaging," *Contrast Media & Molecular Imaging*, vol. 8, no. 2, pp. 165–174, 2013.
- [5] D. Yu, W. C. Gustafson, C. Han et al., "An improved monomeric infrared fluorescent protein for neuronal and tumour brain imaging," *Nature Communications*, vol. 5, article 4626, 2014.
- [6] L. Yan, Y. Han, Y. He et al., "Cell tracing techniques in stem cell transplantation," *Stem Cell Reviews*, vol. 3, no. 4, pp. 265–269, 2007.
- [7] M. V. Yigit, A. Moore, and Z. Medarova, "Magnetic nanoparticles for cancer diagnosis and therapy," *Pharmaceutical Research*, vol. 29, no. 5, pp. 1180–1188, 2012.
- [8] J. E. Rosen, L. Chan, D.-B. Shieh, and F. X. Gu, "Iron oxide nanoparticles for targeted cancer imaging and diagnostics," *Nanomedicine: Nanotechnology, Biology, and Medicine*, vol. 8, no. 3, pp. 275–290, 2012.
- [9] K. W. Y. Chan, G. Liu, X. Song et al., "MRI-detectable pH nanosensors incorporated into hydrogels for in vivo sensing of transplanted-cell viability," *Nature Materials*, vol. 12, no. 3, pp. 268–275, 2013.
- [10] S. Balivada, R. S. Rachakatla, H. Wang et al., "A/C magnetic hyperthermia of melanoma mediated by iron(0)/iron oxide core/shell magnetic nanoparticles: a mouse study," *BMC Cancer*, vol. 10, article 119, 2010.
- [11] F. Dilnawaz, A. Singh, C. Mohanty, and S. K. Sahoo, "Dual drug loaded superparamagnetic iron oxide nanoparticles for targeted cancer therapy," *Biomaterials*, vol. 31, no. 13, pp. 3694–3706, 2010.
- [12] A. Z. Wang, V. Bagalkot, C. C. Vassiliou et al., "Superparamagnetic iron oxide nanoparticle-aptamer bioconjugates for combined prostate cancer imaging and therapy," *ChemMedChem*, vol. 3, no. 9, pp. 1311–1315, 2008.
- [13] P. Zou, Y. Yu, Y. A. Wang et al., "Superparamagnetic iron oxide nanotheranostics for targeted cancer cell imaging and pH-dependent intracellular drug release," *Molecular Pharmaceutics*, vol. 7, no. 6, pp. 1974–1984, 2010.
- [14] E. Syková and P. Jendelová, "Magnetic resonance tracking of transplanted stem cells in rat brain and spinal cord," *Neurodegenerative Diseases*, vol. 3, no. 1-2, pp. 62–67, 2006.
- [15] V. Vanecek, V. Zablotskii, S. Forostyak et al., "Highly efficient magnetic targeting of mesenchymal stem cells in spinal cord injury," *International Journal of Nanomedicine*, vol. 7, pp. 3719–3730, 2012.
- [16] A. S. Arbab, C. Thiffault, B. Navia et al., "Tracking of In-111-labeled human umbilical tissue-derived cells (hUTC) in a rat model of cerebral ischemia using SPECT imaging," *BMC Medical Imaging*, vol. 12, article 33, 2012.
- [17] J. K. Jaiswal, H. Mattoussi, J. M. Mauro, and S. M. Simon, "Long-term multiple color imaging of live cells using quantum dot bioconjugates," *Nature Biotechnology*, vol. 21, no. 1, pp. 47–51, 2003.
- [18] N. Sun, A. Lee, and J. C. Wu, "Long term non-invasive imaging of embryonic stem cells using reporter genes," *Nature Protocols*, vol. 4, no. 8, pp. 1192–1201, 2009.
- [19] H. J. Lee, S. W. Doo, D. H. Kim et al., "Cytosine deaminase-expressing human neural stem cells inhibit tumor growth in prostate cancer-bearing mice," *Cancer Letters*, vol. 335, no. 1, pp. 58–65, 2013.
- [20] C. Rivière, F. P. Boudghène, F. Gazeau et al., "Iron oxide nanoparticle-labeled rat smooth muscle cells: cardiac MR imaging for cell graft monitoring and quantitation," *Radiology*, vol. 235, no. 3, pp. 959–967, 2005.
- [21] A. Abrate, R. Buono, T. Canu et al., "Mesenchymal stem cells expressing therapeutic genes induce autochthonous prostate tumour regression," *European Journal of Cancer*, vol. 50, no. 14, pp. 2478–2488, 2014.
- [22] H. J. Lee, J. H. Won, S. H. Doo et al., "Inhibition of collagen deposit in obstructed rat bladder outlet by transplantation of superparamagnetic iron oxide-labeled human mesenchymal stem cells as monitored by molecular magnetic resonance imaging (MRI)," *Cell Transplantation*, vol. 21, no. 5, pp. 959–970, 2012.
- [23] Y.-S. Song, J.-H. Ku, E.-S. Song et al., "Magnetic resonance evaluation of human mesenchymal stem cells in corpus cavernosa of rats and rabbits," *Asian Journal of Andrology*, vol. 9, no. 3, pp. 361–367, 2007.
- [24] S. S. Yun and H. K. Ja, "Monitoring transplanted human mesenchymal stem cells in rat and rabbit bladders using molecular magnetic resonance imaging," *Neurourology and Urodynamics*, vol. 26, no. 4, pp. 584–593, 2007.
- [25] H. J. Lee, J. An, S. W. Doo et al., "Improvement in spinal cord injury-induced bladder fibrosis using mesenchymal stem cell transplantation into the bladder wall," *Cell Transplantation*, 2014.
- [26] E. M. Shapiro, S. Skrtic, and A. P. Koretsky, "Sizing it up: cellular MRI using micron-sized iron oxide particles," *Magnetic Resonance in Medicine*, vol. 53, no. 2, pp. 329–338, 2005.
- [27] R. Sun, J. Dittrich, M. Le-Huu et al., "Physical and biological characterization of superparamagnetic iron oxide- and ultra-small superparamagnetic iron oxide-labeled cells: a comparison," *Investigative Radiology*, vol. 40, no. 8, pp. 504–513, 2005.
- [28] S. A. Anderson, J. Shukaliak-Quandt, E. K. Jordan et al., "Magnetic resonance imaging of labeled T-cells in a mouse model of multiple sclerosis," *Annals of Neurology*, vol. 55, no. 5, pp. 654–659, 2004.
- [29] A. S. Arbab, V. Frenkel, S. D. Pandit et al., "Magnetic resonance imaging and confocal microscopy studies of magnetically labeled endothelial progenitor cells trafficking to sites of tumor angiogenesis," *Stem Cells*, vol. 24, no. 3, pp. 671–678, 2006.
- [30] C. Bos, Y. Delmas, A. Desmoulière et al., "In vivo MR imaging of intravascularly injected magnetically labeled mesenchymal

- stem cells in rat kidney and liver," *Radiology*, vol. 233, no. 3, pp. 781–789, 2004.
- [31] E. M. Shapiro, O. Gonzalez-Perez, J. Manuel García-Verdugo, A. Alvarez-Buylla, and A. P. Koretsky, "Magnetic resonance imaging of the migration of neuronal precursors generated in the adult rodent brain," *NeuroImage*, vol. 32, no. 3, pp. 1150–1157, 2006.
- [32] C. Heyn, J. A. Ronald, S. S. Ramadan et al., "In vivo MRI of cancer cell fate at the single-cell level in a mouse model of breast cancer metastasis to the brain," *Magnetic Resonance in Medicine*, vol. 56, no. 5, pp. 1001–1010, 2006.
- [33] J. Lecoq and M. J. Schnitzer, "An infrared fluorescent protein for deeper imaging," *Nature Biotechnology*, vol. 29, no. 8, pp. 715–716, 2011.
- [34] J. W. M. Bulte and D. L. Kraitchman, "Iron oxide MR contrast agents for molecular and cellular imaging," *NMR in Biomedicine*, vol. 17, no. 7, pp. 484–499, 2004.
- [35] A. S. Arbab, L. A. Bashaw, B. R. Miller, E. K. Jordan, J. W. M. Bulte, and J. A. Frank, "Intracytoplasmic tagging of cells with ferumoxides and transfection agent for cellular magnetic resonance imaging after cell transplantation: methods and techniques," *Transplantation*, vol. 76, no. 7, pp. 1123–1130, 2003.
- [36] J. A. Frank, H. Zywicke, E. K. Jordan et al., "Magnetic intracellular labeling of mammalian cells by combining (FDA-approved) superparamagnetic iron oxide MR contrast agents and commonly used transfection agents," *Academic Radiology*, vol. 9, supplement 2, pp. S484–S487, 2002.
- [37] M. Gutova, J. A. Frank, M. D'Apuzzo et al., "Magnetic resonance imaging tracking of ferumoxytol-labeled human neural stem cells: studies leading to clinical use," *Stem Cells Translational Medicine*, vol. 2, no. 10, pp. 766–775, 2013.
- [38] K. A. Hinds, J. M. Hill, E. M. Shapiro et al., "Highly efficient endosomal labeling of progenitor and stem cells with large magnetic particles allows magnetic resonance imaging of single cells," *Blood*, vol. 102, no. 3, pp. 867–872, 2003.
- [39] J. W. M. Bulte, I. D. Duncan, and J. A. Frank, "In vivo magnetic resonance tracking of magnetically labeled cells after transplantation," *Journal of Cerebral Blood Flow & Metabolism*, vol. 22, no. 8, pp. 899–907, 2002.
- [40] L. Kostura, D. L. Kraitchman, A. M. Mackay, M. F. Pittenger, and J. W. M. Bulte, "Feridex labeling of mesenchymal stem cells inhibits chondrogenesis but not adipogenesis or osteogenesis," *NMR in Biomedicine*, vol. 17, no. 7, pp. 513–517, 2004.
- [41] L. Matuszewski, T. Persigehl, A. Wall et al., "Cell tagging with clinically approved iron oxides: feasibility and effect of lipofection, particle size, and surface coating on labeling efficiency," *Radiology*, vol. 235, no. 1, pp. 155–161, 2005.
- [42] L.-S. Wang, M.-C. Chuang, and J.-A. A. Ho, "Nanotheranostics—a review of recent publications," *International Journal of Nanomedicine*, vol. 7, pp. 4679–4695, 2012.
- [43] S. Prijic, L. Prosen, M. Cemazar et al., "Surface modified magnetic nanoparticles for immuno-gene therapy of murine mammary adenocarcinoma," *Biomaterials*, vol. 33, no. 17, pp. 4379–4391, 2012.
- [44] H. J. Lee, Y. T. C. Nguyen, M. Muthiah et al., "MR traceable delivery of p53 tumor suppressor gene by PEI-functionalized superparamagnetic iron oxide nanoparticles," *Journal of Biomedical Nanotechnology*, vol. 8, no. 3, pp. 361–371, 2012.
- [45] H. Xu, Z. P. Aguilar, L. Yang et al., "Antibody conjugated magnetic iron oxide nanoparticles for cancer cell separation in fresh whole blood," *Biomaterials*, vol. 32, no. 36, pp. 9758–9765, 2011.
- [46] C. Fang, F. M. Kievit, O. Veiseh et al., "Fabrication of magnetic nanoparticles with controllable drug loading and release through a simple assembly approach," *Journal of Controlled Release*, vol. 162, no. 1, pp. 233–241, 2012.
- [47] J. W. M. Bulte, T. Douglas, B. Witwer et al., "Magnetodendrimers allow endosomal magnetic labeling and in vivo tracking of stem cells," *Nature Biotechnology*, vol. 19, no. 12, pp. 1141–1147, 2001.
- [48] J. A. Frank, B. R. Miller, A. S. Arbab et al., "Clinically applicable labeling of mammalian and stem cells by combining superparamagnetic iron oxides and transfection agents," *Radiology*, vol. 228, no. 2, pp. 480–487, 2003.
- [49] C. Wilhelm and F. Gazeau, "Universal cell labelling with anionic magnetic nanoparticles," *Biomaterials*, vol. 29, no. 22, pp. 3161–3174, 2008.
- [50] C. Wilhelm, F. Gazeau, J. Roger, J. N. Pons, and J.-C. Bacri, "Interaction of anionic super-paramagnetic nanoparticles with cells: kinetic analyses of membrane adsorption and subsequent internalization," *Langmuir*, vol. 18, no. 21, pp. 8148–8155, 2002.
- [51] A. Naveau, P. Smirnov, C. Ménager et al., "Phenotypic study of human gingival fibroblasts labeled with superparamagnetic anionic nanoparticles," *Journal of Periodontology*, vol. 77, no. 2, pp. 238–247, 2006.
- [52] P. Smirnov, F. Gazeau, M. Lewin et al., "In vivo cellular imaging of magnetically labeled hybridomas in the spleen with a 1.5-T clinical MRI system," *Magnetic Resonance in Medicine*, vol. 52, no. 1, pp. 73–79, 2004.
- [53] C. Wilhelm, L. Bal, P. Smirnov et al., "Magnetic control of vascular network formation with magnetically labeled endothelial progenitor cells," *Biomaterials*, vol. 28, no. 26, pp. 3797–3806, 2007.
- [54] M. Modo, M. Hoehn, and J. W. M. Bulte, "Cellular MR imaging," *Molecular Imaging*, vol. 4, no. 3, pp. 143–164, 2005.
- [55] C. Wilhelm, C. Billotey, J. Roger, J. N. Pons, J.-C. Bacri, and F. Gazeau, "Intracellular uptake of anionic superparamagnetic nanoparticles as a function of their surface coating," *Biomaterials*, vol. 24, no. 6, pp. 1001–1011, 2003.
- [56] J.-F. Deux, J. Dai, C. Rivière et al., "Aortic aneurysms in a rat model: in vivo MR imaging of endovascular cell therapy," *Radiology*, vol. 246, no. 1, pp. 185–192, 2008.
- [57] C. Billotey, C. Asford, O. Beuf et al., "T-cell homing to the pancreas in autoimmune mouse models of diabetes: in vivo MR imaging," *Radiology*, vol. 236, no. 2, pp. 579–587, 2005.
- [58] P. Smirnov, E. Lavergne, F. Gazeau et al., "In vivo cellular imaging of lymphocyte trafficking by MRI: a tumor model approach to cell-based anticancer therapy," *Magnetic Resonance in Medicine*, vol. 56, no. 3, pp. 498–508, 2006.
- [59] J. S. Kim, T. J. Yoon, K. N. Yu et al., "Toxicity and tissue distribution of magnetic nanoparticles in mice," *Toxicological Sciences*, vol. 89, no. 1, pp. 338–347, 2006.
- [60] T. H. Kim, J. K. Kim, W. Shim, S. Y. Kim, T. J. Park, and J. Y. Jung, "Tracking of transplanted mesenchymal stem cells labeled with fluorescent magnetic nanoparticle in liver cirrhosis rat model with 3-T MRI," *Magnetic Resonance Imaging*, vol. 28, no. 7, pp. 1004–1013, 2010.
- [61] J.-L. Bridot, A.-C. Faure, S. Laurent et al., "Hybrid gadolinium oxide nanoparticles: multimodal contrast agents for in vivo imaging," *Journal of the American Chemical Society*, vol. 129, no. 16, pp. 5076–5084, 2007.

- [62] L. Cao, B. Li, P. Yi et al., "The interplay of  $T_1$ - and  $T_2$ -relaxation on  $T_1$ -weighted MRI of hMSCs induced by Gd-DOTA-peptides," *Biomaterials*, vol. 35, no. 13, pp. 4168–4174, 2014.
- [63] F. Tian, G. Chen, P. Yi et al., "Fates of  $\text{Fe}_3\text{O}_4$  and  $\text{Fe}_3\text{O}_4/\text{SiO}_2$  nanoparticles in human mesenchymal stem cells assessed by synchrotron radiation-based techniques," *Biomaterials*, vol. 35, no. 24, pp. 6412–6421, 2014.
- [64] P. Yi, G. Chen, H. Zhang et al., "Magnetic resonance imaging of  $\text{Fe}_3\text{O}_4/\text{SiO}_2$ -labeled human mesenchymal stem cells in mice at 11.7 T," *Biomaterials*, vol. 34, no. 12, pp. 3010–3019, 2013.
- [65] J. H. Kim, S. R. Shim, S. W. Doo et al., "Bladder recovery by stem cell based cell therapy in the bladder dysfunction induced by spinal cord injury: systematic review and meta-analysis," *PLoS ONE*, vol. 10, no. 3, Article ID e0113491, 2015.
- [66] J. H. Kim, H. J. Lee, and Y. S. Song, "Treatment of bladder dysfunction using stem cell or tissue engineering technique," *Korean Journal of Urology*, vol. 55, no. 4, pp. 228–238, 2014.
- [67] J. H. Kim, S. R. Lee, Y. S. Song, and H. J. Lee, "Stem cell therapy in bladder dysfunction: where are we? and where do we have to go?" *BioMed Research International*, vol. 2013, Article ID 930713, 10 pages, 2013.
- [68] J. C. Sipe, M. Filippi, G. Martino et al., "Method for intracellular magnetic labeling of human mononuclear cells using approved iron contrast agents," *Magnetic Resonance Imaging*, vol. 17, no. 10, pp. 1521–1523, 1999.
- [69] Y. Takahashi, O. Tsuji, G. Kumagai et al., "Comparative study of methods for administering neural stem/progenitor cells to treat spinal cord injury in mice," *Cell Transplantation*, vol. 20, no. 5, pp. 727–739, 2011.
- [70] P. Foster-Gareau, C. Heyn, A. Alejski, and B. K. Rutt, "Imaging single mammalian cells with a 1.5 T clinical MRI scanner," *Magnetic Resonance in Medicine*, vol. 49, no. 5, pp. 968–971, 2003.
- [71] T. Koyama, M. Shimura, Y. Minemoto et al., "Evaluation of selective tumor detection by clinical magnetic resonance imaging using antibody-conjugated superparamagnetic iron oxide," *Journal of Controlled Release*, vol. 159, no. 3, pp. 413–418, 2012.
- [72] C. Toma, W. R. Wagner, S. Bowry, A. Schwartz, and F. Villanueva, "Fate of culture-expanded mesenchymal stem cells in the microvasculature: in vivo observations of cell kinetics," *Circulation Research*, vol. 104, no. 3, pp. 398–402, 2009.
- [73] M. Mahmoudi and S. Laurent, "Controlling the burst effect of a drug by introducing starch in the structure of magnetic polyurethane microspheres containing superparamagnetic iron oxide nanoparticles," *IEEE Transactions on Nanotechnology*, vol. 17, pp. 43–51, 2010.
- [74] M. Beissert, R. Lorenz, and E. W. Gerharz, "Rational imaging in locally advanced prostate cancer," *Der Urologe—Ausgabe A*, vol. 47, no. 11, pp. 1405–1416, 2008.
- [75] B. Turkbey, P. S. Albert, K. Kurdziel, and P. L. Choyke, "Imaging localized prostate cancer: current approaches and new developments," *The American Journal of Roentgenology*, vol. 192, no. 6, pp. 1471–1480, 2009.
- [76] E. Eyal, B. N. Bloch, N. M. Rofsky et al., "Principal component analysis of dynamic contrast enhanced mri in human prostate cancer," *Investigative Radiology*, vol. 45, no. 4, pp. 174–181, 2010.
- [77] H.-C. Huang, P.-Y. Chang, K. Chang et al., "Formulation of novel lipid-coated magnetic nanoparticles as the probe for in vivo imaging," *Journal of Biomedical Science*, vol. 16, no. 1, article 86, 2009.
- [78] S. E. Lapi, H. Wahnische, D. Pham et al., "Assessment of an  $^{18}\text{F}$ -labeled phosphoramidate peptidomimetic as a new prostate-specific membrane antigen-targeted imaging agent for prostate cancer," *Journal of Nuclear Medicine*, vol. 50, no. 12, pp. 2042–2048, 2009.
- [79] Z. Li, L. Jian, H. Wang, and Y. Cui, "Flow injection chemiluminescent determination of clenbuterol using GoldMag particles as carrier," *Food Additives and Contaminants*, vol. 24, no. 1, pp. 21–25, 2007.

## Research Article

# Exploring Dynamic Brain Functional Networks Using Continuous “State-Related” Functional MRI

Xun Li,<sup>1,2</sup> Yu-Feng Zang,<sup>1,2</sup> and Han Zhang<sup>1,2</sup>

<sup>1</sup>Center for Cognition and Brain Disorders, Hangzhou Normal University, Hangzhou 311121, China

<sup>2</sup>Zhejiang Key Laboratory for Research in Assessment of Cognitive Impairments, Hangzhou 310015, China

Correspondence should be addressed to Han Zhang; [napoleon1982@gmail.com](mailto:napoleon1982@gmail.com)

Received 21 August 2014; Revised 17 January 2015; Accepted 25 February 2015

Academic Editor: Zhengchao Dong

Copyright © 2015 Xun Li et al. This is an open access article distributed under the Creative Commons Attribution License, which permits unrestricted use, distribution, and reproduction in any medium, provided the original work is properly cited.

We applied a “temporal decomposition” method, which decomposed a single brain functional network into several “modes”; each of them dominated a short temporal period, on a continuous, “state-” related, “finger-force feedback” functional magnetic resonance imaging experiment. With the hypothesis that attention and internal/external information processing interaction could be manipulated by different (real and sham) feedback conditions, we investigated functional network dynamics of the “default mode,” “executive control,” and sensorimotor networks. They were decomposed into several modes. During real feedback, the occurrence of “default mode-executive control competition-related” mode was higher than that during sham feedback ( $P = 0.0003$ ); the “default mode-visual facilitation-related” mode more frequently appeared during sham than real feedback ( $P = 0.0004$ ). However, the dynamics of the sensorimotor network did not change significantly between two conditions ( $P > 0.05$ ). Our results indicated that the visual-guided motor feedback involves higher cognitive functional networks rather than primary motor network. The dynamics monitoring of inner and outside environment and multisensory integration could be the mechanisms. This study is an extension of our previous region-specific and static-styled study of our brain functional architecture.

## 1. Introduction

Many studies have suggested that our brain is an intricate system [1, 2]. Understanding the spatial and temporal organization of this complex system is of great importance to both basic and clinical neuroscience. Various studies have demonstrated the complexity of the human brain using functional magnetic resonance imaging (fMRI) based on spatiotemporal characteristics with methods such as independent component analysis (ICA) [3] and complex network analysis [4].

Nowadays, a new characteristic of the brain functional networks has been catching researchers’ eyes. It is the dynamic functional networks or time-varied functional connectivity which treats the brain functioning as a nonstationary process. Dedicated analysis methods have been proposed. Among various methods, “temporal decomposition” [5–7] does not rely on statistical hypothesis, and it is simple, intuitive, and straightforward. The main idea of this method is that only a small proportion of the time frames corresponding

to “suprathreshold signal” of a seed region are utilized and classified into different subgroups or “modes” depending on the spatial similarity of these frames. The modes were interpreted to reflect the intermittent or brief interaction between the seed region and other different brain regions at different time [5–7].

However, in their original paper [7], the analysis was only performed on resting-state fMRI data. The interpretation and the biological meaning of their findings have only been simply discussed because the resting-state brain activity and its functions have been still an elusive concept [8]. In their latter paper [5, 6], they made a methodological alteration in which the fMRI data was totally blindly decomposed without a priori seed region definition. The total data-driven method, in addition to passive resting-state experimental design, has hindered us from further interpretation of the biological meaning and underlying mechanism of this method. To our best knowledge, there has been no study utilizing this method in a task-related experiment. Hence, the resultant dynamic modes could not be compared between different states which

are manipulated by researchers. In turn, one could not understand the specific function of the dynamic modes.

In the current study, we applied this method to a continuous, “state-related” task fMRI experiment and sought to discover different dynamic characteristics during different conditions. We hypothesized that, through such an experimental manipulation, the dynamic feature of some modes could be modulated. We specifically conducted a continuous finger force feedback experiment on a group of healthy volunteers. The manipulation was finger force control with true pressure data shown via a visual feedback “real feedback” or with false pressure feedback data “sham feedback.” Previous fMRI studies using the similar experiment have found task activation differences [9] and fractional amplitude of low-frequency fluctuation (fALFF) differences [10] in the DMN between different feedback conditions. Besides, block-designed fMRI studies have reported differences in activation in the contralateral motor cortex during various motor feedback tasks [11, 12]. Neurofeedback can also improve executive functioning in children [13], indicating the alternation of the executive control network (ECN) [14]. Therefore, we chose the PCC, left motor cortex (LMC), and dorsolateral prefrontal cortex (DLPFC) as seed regions, which are key nodes of the DMN, sensorimotor network (SMN) [15], and ECN, respectively.

The first goal was to investigate dynamic characteristics of these brain networks under continuous feedback condition, which could reveal the competition or cooperation among different brain networks during brief time period. The second goal was to investigate the difference in participation of these networks between the real and sham feedback conditions, to further understand the biological mechanisms of the dynamic brain functional organization.

## 2. Materials and Methods

**2.1. Subjects.** There were totally forty-three healthy right-handed adults ( $22.7 \pm 1.6$  years, range 19–25; 23 females) participating in this study. Each subject gave written informed consent. The entry criteria included no history of brain injury, neurological illness, and psychiatric disorders. Data from five subjects were excluded due to technical problems or excessive head motion. The remaining 38 subjects (mean age  $22.3 \pm 1.6$  years; 19 females) were further analyzed. All experiments were approved by the Ethics Committee of the National Key Laboratory of Cognitive Neuroscience and Learning, Beijing Normal University, and were conducted in accordance with the Declaration of Helsinki.

**2.2. Experimental Design.** Each participant underwent three 8-minute fMRI scans during resting state, the real feedback state (RF), and the sham feedback state (SF). During resting state, subjects were instructed to keep their eyes closed, remain still, and stay relaxed. The purpose of this session was to allow the subjects to adapt to the fMRI scanning environment. The order of RF and SF sessions was counterbalanced across subjects. In the RF state, the subjects were asked to grip a pressure sensor using the right index finger and thumb. This

sensor is one module of an MRI-compatible physiological multichannel analyzer (model MPI50, BIOPAC Systems, Inc., Goleta, CA, USA). The sampling frequency was 250 Hz and the pressure sensitivity was  $0.01 \text{ cmH}_2\text{O}$ . The sensor recorded the pressure in real time via an airtight tube. The pressure was synchronously presented to the participant on a screen. The target force was set at  $20 \text{ mmH}_2\text{O}$ , which is small enough to reduce the possibility of muscular fatigue. The subjects were asked to continuously maintain the pinch force at the target level. In the SF state, the subjects were also asked to maintain the pinch force at the same level, but with a video of another participant’s performance during RF presented. Before the experiment, all the subjects had a short training session. For more details please refer to our previous paper [10].

**2.3. Image Acquisition.** MR images were collected using a Siemens Trio 3-Tesla scanner in the imaging center at Beijing Normal University. The participants lied supine with the head snugly fixed by foam pads to minimize head movement. After localization scanning, three fMRI sessions were conducted using echo-planar imaging sequence with the same parameters: 33 axial slices, repetition time (TR) = 2000 ms, echo time (TE) = 30 ms, flip angle =  $90^\circ$ , thickness/gap = 3.5/0.7 mm, field of view (FOV) =  $200 \times 200 \text{ mm}^2$ , and matrix =  $64 \times 64$ . Then a 3D T1 magnetization-prepared rapid gradient echo (MPRAGE) image was acquired (128 sagittal slices, thickness/gap = 1.33/0 mm, in-plane resolution =  $256 \times 192$ , TR/TE = 2530/3.39 ms, inversion time = 1100 ms, flip angle =  $7^\circ$ , and FOV =  $256 \times 256 \text{ mm}^2$ ).

**2.4. Image Preprocessing.** The fMRI data was preprocessed using DPARSFA v2.3 [16] and REST v1.8 [17] based on SPM8 (<http://www.fil.ion.ucl.ac.uk/spm/>) and Matlab 2013a (the MathWorks, Inc., Natick, MA, USA). Major steps included removal of the first four time points, slice timing correction, head motion correction, spatial normalization to Montreal Neurological Institute (MNI) space, spatial smoothing with a Gaussian kernel (FWHM = 6 mm), temporal filtering (0.01–0.08 Hz), removal of linear and quadratic trends, and regression of covariates, including the global signal, the time series of the white matter and cerebrospinal fluid, and six affine motion parameters [7]. The exclusion criterion for excessive head motion was  $>2 \text{ mm}$  translation or  $>2^\circ$  rotation in any direction. We also calculated framewise displacement (FD) as another measure of head motion which could identify possible “bad” frames [18]. These bad frames might affect the following temporal decomposition result. To rule out such an effect, we conducted the following analyses with and without removing the bad frames.

**2.5. Temporal Decomposition.** We chose the PCC, LMC, and DLPFC as regions of interest (ROIs), which are the major nodes of the DMN, SMN, and ECN. Seed regions were 12 mm diameter spheres centered at (0, -53, 26), (-38, -22, 56), and (44, 36, 20) in MNI coordinates, respectively, which were chosen based on previous studies [19–21]. The average time series in each ROI was extracted. A 15% threshold was applied on the time series extracted from the PCC, LMC,

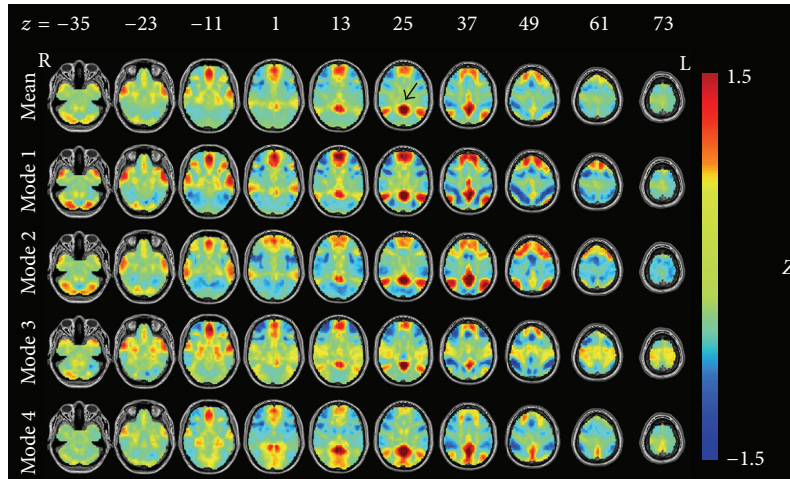


FIGURE 1: The posterior cingulate cortex- (PCC-) related modes after temporal decomposition. All results were converted to Z-maps and arranged by the occurrence frequency. The first line represents the average pattern of the four modes. Black arrow in the first row points out the seed region approximately.

and DLPFC; that is, only time frames with BOLD intensity exceeding that threshold were selected for following analysis [7]. This threshold can be set manually, but here we only follow parameter setting of Liu et al. The fMRI frames for all subjects and both RF and SF sessions were chosen and put together and then sorted by *k*-means clustering method [22] based on their spatial similarities. The fMRI frames sorted into the same cluster were averaged and transformed to Z-statistical maps by dividing the SE. In paper by Liu et al., after inspection of a series of results with different cluster numbers, the one which showed the best balance between richness and redundancy was reserved. Several automatic cluster number estimation methods were also used but the results were suboptimal [5, 6]. Following their method, we also set this number to be 4, 6, and 8 and then inspected the clustering results separately. We found that the resultant “modes” were clearer when the number of clusters was 4. Therefore, we only showed this result in this paper.

**2.6. Characterizing Participation of Each Mode and Comparing It between Different States.** If a specific mode is dominant, it will show more frequently. We used the occurrence of a specific mode to characterize participation of each mode in the task. We hypothesized that the occurrence of the same modes should be different between real and sham feedback states. We calculated the number of suprathreshold time frames of the four modes for every subject and for RF and SF sessions separately and used the ratio between this number and the total time frames as the occurrence of modes. Paired *t*-tests were performed on the ratios between the real and sham feedback states.

### 3. Results

**3.1. Dynamic Modes of PCC, LMC, and DLPFC.** The temporal decomposition results based on the seed regions of the PCC, LMC, and DLPFC are shown in Figures 1–3. They were

ranked by the occurrence of modes despite the task state (i.e., overall occurrence for both RF and SF sessions). The DMN, SMN, and ECN were dominant in these three results. Besides this, several other brain networks also took part in the feedback process. In Figure 1, the average map of the four modes matched well with the DMN, while the spatial pattern of the four modes differed from each other. Mode 1 showed activation of the DMN as well as deactivation of the regions in dorsal attention network (DAN) and ECN [19], which were typical anticorrelated networks demonstrated by Fox and his colleagues [23]. Mode 2 also showed activation of the DMN, but without obvious anticorrelated networks. Besides DMN, the activation of the frontoparietal control network (FCN) [24] was also found in a few upper slices. Mode 3 showed the coactivation of the SMN and DMN, with deactivation of the DAN and ECN. Mode 4 showed the coactivation of the DMN and the visual areas. With all bad frames removed, reanalyses of the temporal decomposition produced similar results (see Figure S1 in Supplementary Material available online at <http://dx.doi.org/10.1155/2015/824710>). A quantitative differentiation of these modes was further conducted using Dice coefficient to measure the dissimilarity among them, indicating a fundamental difference in spatial pattern between each other (see Supplementary Material and Figure S2).

In Figure 2, the averaged map shows an obvious pattern of sensorimotor network. However, Mode 1 looked like the combination of the DAN and ECN, with the decreased activity of the DMN. Mode 2 showed the activation mainly in the SMN. Modes 3 and 4 both showed activation of the SMN, but in Mode 3 we also found the pattern of DMN, while in Mode 4 we could have found the decreased activity in visual areas.

The averaged map in Figure 3 shows ECN dominance. Mode 1 shows the anticorrelation between the ECN and the DMN. From Mode 2, we could find the activation of the ECN and FCN and the deactivation of the visual areas. Mode 3

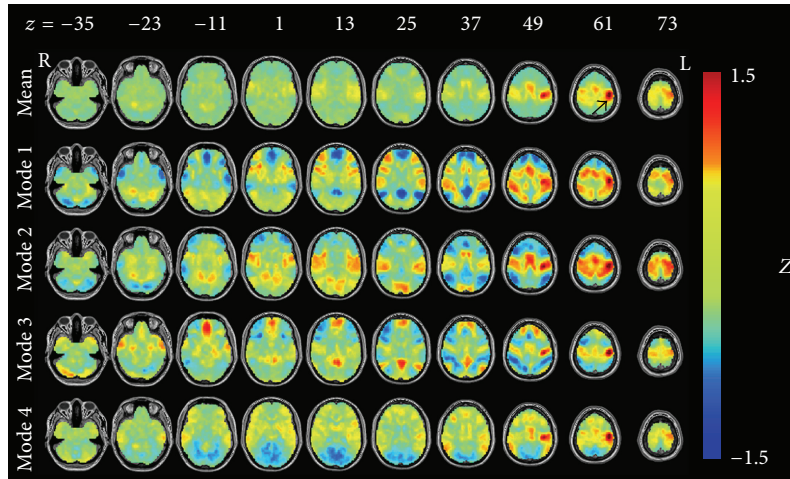


FIGURE 2: The left motor cortex- (LMC-) related modes after temporal decomposition. All results were converted to Z-maps and arranged by occurrence frequency. The first line represents the average result of the four modes. Black arrow in the first row points out the seed region approximately.

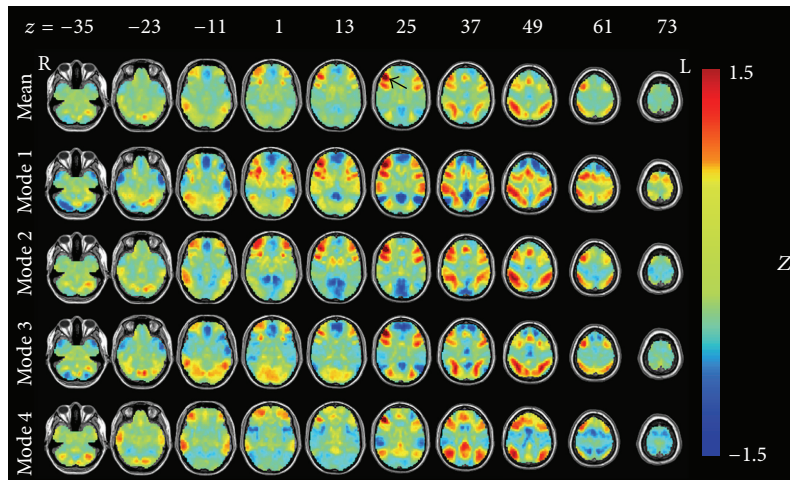


FIGURE 3: The dorsal lateral prefrontal cortex- (DLPFC-) related modes after temporal decomposition. All results were converted to Z-maps and arranged by occurrence frequency. The first line represents the average result of the four modes. Black arrow in the first row points out the seed region approximately.

showed the coactivation of the ECN and the visual areas. Mode 4 showed the coactivation of the FCN and DMN.

**3.2. Different Occurrence Frequency under Different Feedback States.** Figure 4 shows the occurrence frequency of the different modes derived from three different seed regions under real and sham feedback states. The paired  $t$ -test was performed on occurrence frequency between the two states for every mode. As we performed totally 12 times (3 seed regions  $\times$  four modes) of paired  $t$ -tests, we divided a significant  $P$  value of 0.05 by 12 to perform multiple comparison correction (i.e., use  $P < 0.0042$  to achieve the corrected  $P$  value of 0.05).

We found that PCC-related Mode 1 (real  $>$  sham,  $P = 0.0003$ ) and Mode 4 (sham  $>$  real,  $P = 0.0004$ ) were significantly modulated by different feedback states. However, for

LMC-related modes, no difference was found. For DLPFC-related modes, Mode 1 (real  $>$  sham,  $P = 0.0011$ ) and Mode 3 (sham  $>$  real,  $P = 0.0031$ ) were found to have different occurrence between two states. The surface view of these modes as well as their occurrence frequency for all subjects under RF and SF states is plotted in Figures 5 and 6.

## 4. Discussion

In this study, we performed a new method, investigated the dynamic characteristics of brain networks on finger force feedback fMRI data, and had two main findings. Firstly, we found that the DMN, SMN, and ECN did not act independently. Instead, several other networks or brain regions are coactivated or competed with them, which formulated different modes from a brief time period. Secondly, different

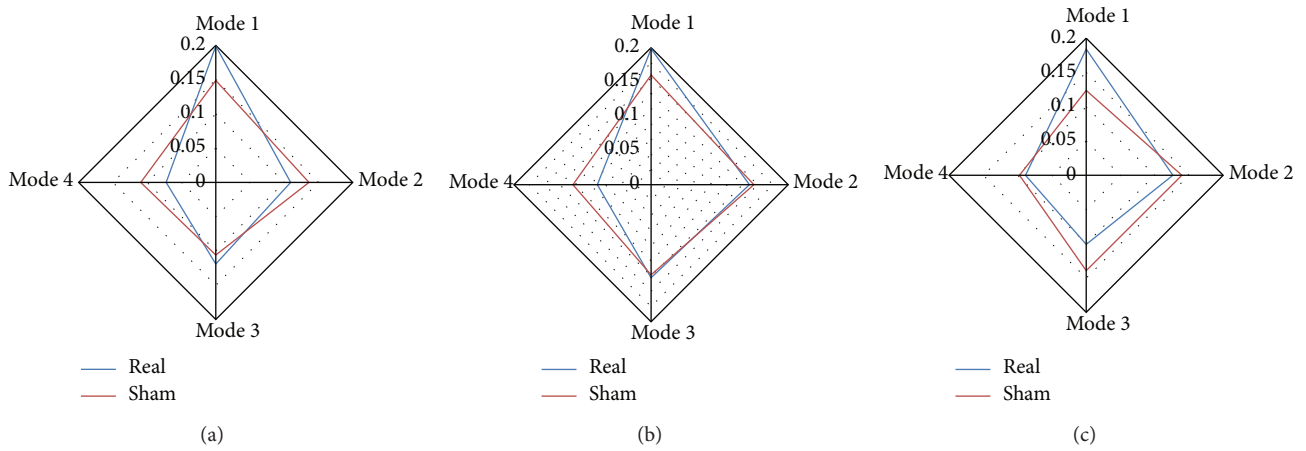


FIGURE 4: The occurrence frequency of different modes for three seed regions under real and sham conditions. (a) PCC-related modes, (b) LMC-related modes, and (c) DLPPFC-related modes.

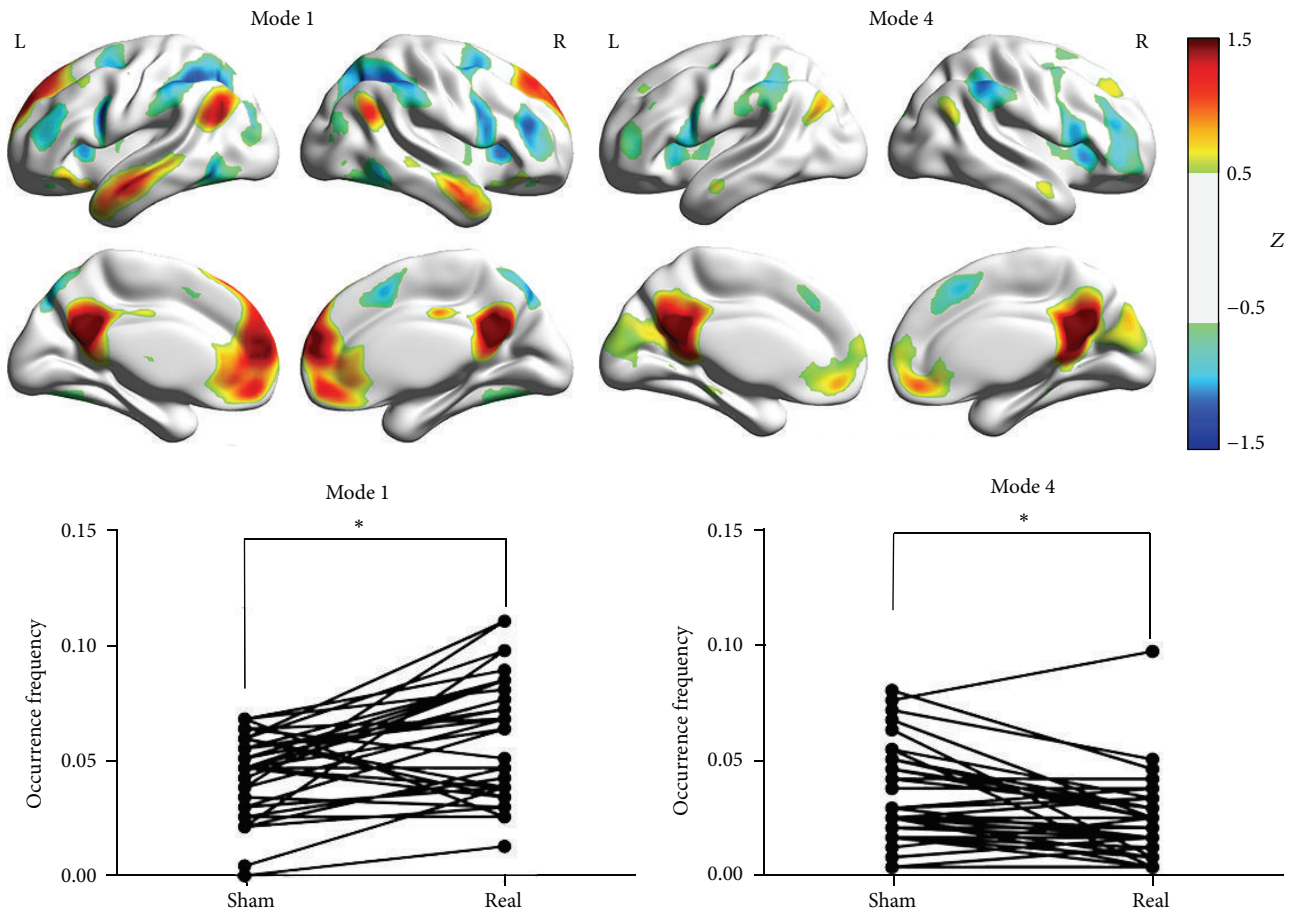


FIGURE 5: The brain surface view of the PCC-related Mode 1 and Mode 4. For a better view, we set a threshold of  $Z = 0.5$  here to separate the brain regions. The paired  $t$ -test results of these two modes are shown at the bottom.  $x$ -axis represents two states, while  $y$ -axis represents the occurrence frequency. The sign of  $*$  represents the  $P$  value lower than 0.05 (corrected).

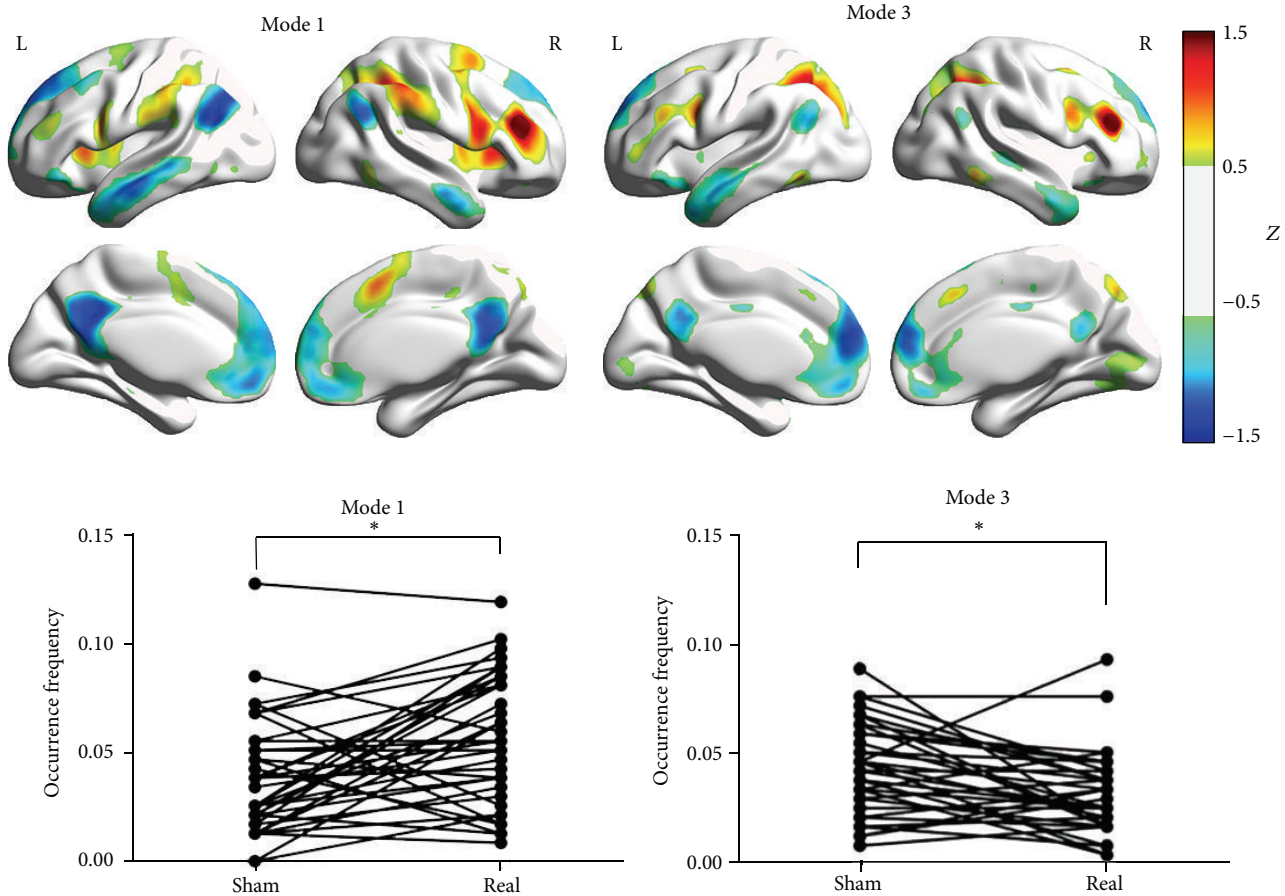


FIGURE 6: The brain surface view of the DLPFC-related Mode 1 and Mode 3. For a better view, we set a threshold of  $Z = 0.5$  here to separate the brain regions. The paired  $t$ -test results of these two modes are shown at the bottom.  $x$ -axis represents two states, while  $y$ -axis represents the occurrence frequency. The sign of \* represents the  $P$  value lower than 0.05 (corrected).

modes participated differently during RF and SF states. Such a difference was not in spatial pattern but in temporal information (i.e., occurrence frequency).

**4.1. Biological Meaning of Different Modes.** We found that different modes did not represent different brain networks; they were more likely to be combinations of several networks [25]. Previous study has already shown a complex and dynamic functional architecture of the PCC [26]. This may explain the variety of the modes derived from the time frames when PCC was active. From PCC-related Mode 1 and DLPFC-related Mode 1, we found an obvious competition between the DMN and ECN. This might reflect the reciprocal relationship between internal monitoring or self-reference and high-order cognition-related functions. Interestingly, though this competition occupied most of the time, PCC-related Mode 2 and DLPFC-related Mode 4 indicated that these two networks could be coactivated sometimes. PCC-related Mode 2 validated the finding from Spreng et al. [24] in which they found that the FCN acted as regional convergence zones that functionally interact with both default and dorsal attention regions during cognitive tasks [24]. Another interesting finding is that, for all seed regions, there

were always several modes having a close relationship with the visual areas. Although such a relationship was not predominant throughout the time course, it occurred at some brief time period as discovered by the dynamic analysis method we used. This might be due to the intensive visual feedback during the tasks. We also compared the temporal decomposition result with that derived from a widely used functional connectivity analysis method, ICA, using MICA toolbox (<http://www.nitrc.org/projects/cogicat/>, [27]). The two results were quite different (see Supplementary Material and Figure S3), indicating that conventional stationary analysis method could not find dynamically interacted brain networks.

**4.2. Different Occurrence of the Modes under Different Feedback States.** We found all of the modes based on both RF and SF feedback fMRI data. However, the same modes did not mean the same occurrence. The paired  $t$ -test results showed significant differences in occurrence frequency of the PCC-related Modes 1 and 4 as well as the DLPFC-related Modes 1 and 3. The PCC-related Mode 1 and the DLPFC-related Mode 1 (they both reflected “default mode-executive control competition”) appeared more frequently during RF,

while the other two modes (“default mode-visual facilitation” or “executive control-visual facilitation”) appeared more frequently during SF. The “default mode-executive control competition” might be the basis of finger force feedback, since this type of feedback involves both self-monitoring and executive controlling. The “default mode/executive control-visual facilitation” might be caused by the unmatched self-produced finger force and visual feedback. We should note that although subjects had realized that the finger force curve shown in the screen was not produced by themselves, they might still try to follow the curve in some instant. This speculation was further validated by inquiring the subjects after the experiments. No significant difference in occurrence frequency was found for the SMN-related modes. We speculated that, for motor network, there was no difference in task demand between RF and SF states, since both tasks required similar continuous finger force pressure holding.

**4.3. Limitations.** Our study has several limitations. First, the RF and SF data were put together into temporal decomposition, which has to be based on a hypothesis that the spatial pattern of the modes should be similar during two states. However, we had no direct evidence to support this point. Second, the combination and competition of different brain networks need to be extensively investigated, together with integration of other data, such as behavioral performance and physiological signal recording, to facilitate the interpretation. Third, we only simply averaged the time frames in the same category and this may eliminate the information of the occurrence orders (i.e., precise timing information). Such information may be more informative, which needs further investigation. Fourth, as the intersubject differences or variability is of great importance in neuroscience specially resting-state studies, we also did the temporal decomposition for a randomly selected subject. However, with blurred patterns (result not shown here), the four modes derived from this subject had no correspondence with those derived from all the subjects. We admitted that the application of this method at individual level is currently not applicable. High individual variability should be expected. However, such an individual variability could be an interesting topic for correlation with individual behavior data. Finally, the spatial and temporal resolution will affect the result, especially for dynamic functional connectivity studies like ours. As clustering is based on spatial similarity, the higher spatial resolution is the more accurate spatial clustering result that can be achieved. Besides, the increase of temporal resolution will produce more frames for the following clustering, and one might detect much more transient functional connectivity patterns. In the future, an imaging sequence with both high spatial and temporal resolution should be used, that is, multiband echo-planar imaging [28].

## 5. Conclusions

In this study, we performed temporal decomposition analysis on a group of subjects who performed finger force feedback tasks and revealed different modes combined by various

brain networks. The occurrence frequency of several modes showed difference between two feedback states. These findings could help us better understand the dynamics of the functional integration of our brain.

## Conflict of Interests

The authors declare that there is no conflict of interests regarding the publication of this paper.

## Acknowledgments

This work is partially supported by the National Natural Science Foundation of China (nos. 81201156, 81271652). Dr. Zang is partly supported by “Qian Jiang Distinguished Professor” Program. The authors thank Mr. Zhang-Ye Dong and Mr. Zhen-Xiang Zang for data collection and Dr. Hang Zhang for his valuable suggestions during preparation of this paper.

## References

- [1] J. D. Power, A. L. Cohen, S. M. Nelson et al., “Functional network organization of the human brain,” *Neuron*, vol. 72, no. 4, pp. 665–678, 2011.
- [2] X.-N. Zuo, A. Di Martino, C. Kelly et al., “The oscillating brain: complex and reliable,” *NeuroImage*, vol. 49, no. 2, pp. 1432–1445, 2010.
- [3] M. J. McKeown and T. J. Sejnowski, “Independent component analysis of fMRI data: examining the assumptions,” *Human Brain Mapping*, vol. 6, no. 5-6, pp. 368–372, 1998.
- [4] M. Rubinov and O. Sporns, “Complex network measures of brain connectivity: uses and interpretations,” *NeuroImage*, vol. 52, no. 3, pp. 1059–1069, 2010.
- [5] D. Liu, Z. Dong, X. Zuo, J. Wang, and Y. Zang, “Eyes-open/eyes-closed dataset sharing for reproducibility evaluation of resting state fMRI data analysis methods,” *Neuroinformatics*, vol. 11, no. 4, pp. 469–476, 2013.
- [6] X. Liu, C. Chang, and J. H. Duyn, “Decomposition of spontaneous brain activity into distinct fMRI co-activation patterns,” *Frontiers in Systems Neuroscience*, vol. 7, article 101, 2013.
- [7] X. Liu and J. H. Duyn, “Time-varying functional network information extracted from brief instances of spontaneous brain activity,” *Proceedings of the National Academy of Sciences of the United States of America*, vol. 110, no. 11, pp. 4392–4397, 2013.
- [8] A. A. Fingelkurts, A. A. Fingelkurts, and S. Kähkönen, “Functional connectivity in the brain—is it an elusive concept?” *Neuroscience & Biobehavioral Reviews*, vol. 28, no. 8, pp. 827–836, 2005.
- [9] P. Halder, S. Brem, K. Bucher et al., “Electrophysiological and hemodynamic evidence for late maturation of hand power grip and force control under visual feedback,” *Human Brain Mapping*, vol. 28, no. 1, pp. 69–84, 2007.
- [10] Z.-Y. Dong, D.-Q. Liu, J. Wang et al., “Low-frequency fluctuation in continuous real-time feedback of finger force: a new paradigm for sustained attention,” *Neuroscience Bulletin*, vol. 28, no. 4, pp. 456–467, 2012.
- [11] B. Keisker, M.-C. Hepp-Reymond, A. Blickenstorfer, and S. S. Kollias, “Differential representation of dynamic and static

- power grip force in the sensorimotor network,” *European Journal of Neuroscience*, vol. 31, no. 8, pp. 1483–1491, 2010.
- [12] J. P. Kuitz-Buschbeck, R. Gilster, S. Wolff, S. Ulmer, H. Siebner, and O. Jansen, “Brain activity is similar during precision and power gripping with light force: an fMRI Study,” *NeuroImage*, vol. 40, no. 4, pp. 1469–1481, 2008.
- [13] M. E. J. Kouijzer, J. M. H. de Moor, B. J. L. Gerrits, M. Congedo, and H. T. van Schie, “Neurofeedback improves executive functioning in children with autism spectrum disorders,” *Research in Autism Spectrum Disorders*, vol. 3, no. 1, pp. 145–162, 2009.
- [14] T. A. Niendam, A. R. Laird, K. L. Ray, Y. M. Dean, D. C. Glahn, and C. S. Carter, “Meta-analytic evidence for a superordinate cognitive control network subserving diverse executive functions,” *Cognitive, Affective & Behavioral Neuroscience*, vol. 12, no. 2, pp. 241–268, 2012.
- [15] C. F. Beckmann, M. DeLuca, J. T. Devlin, and S. M. Smith, “Investigations into resting-state connectivity using independent component analysis,” *Philosophical Transactions of the Royal Society B: Biological Sciences*, vol. 360, no. 1457, pp. 1001–1013, 2005.
- [16] C.-G. Yan and Y.-F. Zang, “DPARF: a MATLAB toolbox for ‘pipeline’ data analysis of resting-state fMRI,” *Frontiers in Systems Neuroscience*, vol. 4, article 13, 2010.
- [17] X.-W. Song, Z.-Y. Dong, X.-Y. Long et al., “REST: a Toolkit for resting-state functional magnetic resonance imaging data processing,” *PLoS ONE*, vol. 6, no. 9, Article ID e25031, 2011.
- [18] J. D. Power, K. A. Barnes, A. Z. Snyder, B. L. Schlaggar, and S. E. Petersen, “Spurious but systematic correlations in functional connectivity MRI networks arise from subject motion,” *NeuroImage*, vol. 59, no. 3, pp. 2142–2154, 2012.
- [19] W. W. Seeley, V. Menon, A. F. Schatzberg et al., “Dissociable intrinsic connectivity networks for salience processing and executive control,” *Journal of Neuroscience*, vol. 27, no. 9, pp. 2349–2356, 2007.
- [20] K. R. A. van Dijk, T. Hedden, A. Venkataraman, K. C. Evans, S. W. Lazar, and R. L. Buckner, “Intrinsic functional connectivity as a tool for human connectomics: theory, properties, and optimization,” *Journal of Neurophysiology*, vol. 103, no. 1, pp. 297–321, 2010.
- [21] L. Wang, C.-S. Yu, H. Chen et al., “Dynamic functional reorganization of the motor execution network after stroke,” *Brain*, vol. 133, no. 4, pp. 1224–1238, 2010.
- [22] A. Mezer, Y. Yovel, O. Pasternak, T. Gorfine, and Y. Assaf, “Cluster analysis of resting-state fMRI time series,” *NeuroImage*, vol. 45, no. 4, pp. 1117–1125, 2009.
- [23] M. D. Fox, A. Z. Snyder, J. L. Vincent, M. Corbetta, D. C. Van Essen, and M. E. Raichle, “The human brain is intrinsically organized into dynamic, anticorrelated functional networks,” *Proceedings of the National Academy of Sciences of the United States of America*, vol. 102, no. 27, pp. 9673–9678, 2005.
- [24] R. N. Spreng, W. D. Stevens, J. P. Chamberlain, A. W. Gilmore, and D. L. Schacter, “Default network activity, coupled with the frontoparietal control network, supports goal-directed cognition,” *NeuroImage*, vol. 53, no. 1, pp. 303–317, 2010.
- [25] L. Cocchi, A. Zalesky, A. Fornito, and J. B. Mattingley, “Dynamic cooperation and competition between brain systems during cognitive control,” *Trends in Cognitive Sciences*, vol. 17, no. 10, pp. 493–501, 2013.
- [26] R. Leech, R. Braga, and D. J. Sharp, “Echoes of the brain within the posterior cingulate cortex,” *Journal of Neuroscience*, vol. 32, no. 1, pp. 215–222, 2012.
- [27] H. Zhang, X.-N. Zuo, S.-Y. Ma, Y.-F. Zang, M. P. Milham, and C.-Z. Zhu, “Subject order-independent group ICA (SOI-GICA) for functional MRI data analysis,” *NeuroImage*, vol. 51, no. 4, pp. 1414–1424, 2010.
- [28] S. M. Smith, K. L. Miller, S. Moeller et al., “Temporally-independent functional modes of spontaneous brain activity,” *Proceedings of the National Academy of Sciences of the United States of America*, vol. 109, no. 8, pp. 3131–3136, 2012.

## Research Article

# Tumour Relapse Prediction Using Multiparametric MR Data Recorded during Follow-Up of GBM Patients

Adrian Ion-Margineanu,<sup>1,2</sup> Sofie Van Caeter,<sup>3</sup> Diana M. Sima,<sup>1,2</sup> Frederik Maes,<sup>2,4</sup>  
Stefaan W. Van Gool,<sup>5</sup> Stefan Sunaert,<sup>3</sup> Uwe Himmelreich,<sup>6</sup> and Sabine Van Huffel<sup>1,2</sup>

<sup>1</sup>Department of Electrical Engineering (ESAT), STADIUS Center for Dynamical Systems, Signal Processing and Data Analytics, KU Leuven, Kasteelpark Arenberg 10, P.O. Box 2446, 3001 Leuven, Belgium

<sup>2</sup>iMinds Medical IT, 3000 Leuven, Belgium

<sup>3</sup>Department of Radiology, University Hospitals of Leuven, Herestraat 49, 3000 Leuven, Belgium

<sup>4</sup>Department of Electrical Engineering (ESAT), PSI Center for Processing Speech and Images, KU Leuven, Kasteelpark Arenberg 10, 3001 Leuven, Belgium

<sup>5</sup>Department of Pediatric Neuro-Oncology, University Hospitals Leuven, Herestraat 49, 3000 Leuven, Belgium

<sup>6</sup>Biomedical MRI/MoSAIC, Department of Imaging and Pathology, KU Leuven, 3000 Leuven, Belgium

Correspondence should be addressed to Adrian Ion-Margineanu; [adrian@esat.kuleuven.be](mailto:adrian@esat.kuleuven.be)

Received 5 September 2014; Accepted 16 December 2014

Academic Editor: Zhengchao Dong

Copyright © 2015 Adrian Ion-Margineanu et al. This is an open access article distributed under the Creative Commons Attribution License, which permits unrestricted use, distribution, and reproduction in any medium, provided the original work is properly cited.

*Purpose.* We have focused on finding a classifier that best discriminates between tumour progression and regression based on multiparametric MR data retrieved from follow-up GBM patients. *Materials and Methods.* Multiparametric MR data consisting of conventional and advanced MRI (perfusion, diffusion, and spectroscopy) were acquired from 29 GBM patients treated with adjuvant therapy after surgery over a period of several months. A 27-feature vector was built for each time point, although not all features could be obtained at all time points due to missing data or quality issues. We tested classifiers using LOPO method on complete and imputed data. We measure the performance by computing BER for each time point and wBER for all time points. *Results.* If we train random forests, LogitBoost, or RobustBoost on data with complete features, we can differentiate between tumour progression and regression with 100% accuracy, one time point (i.e., about 1 month) earlier than the date when doctors had put a label (progressive or responsive) according to established radiological criteria. We obtain the same result when training the same classifiers solely on complete perfusion data. *Conclusions.* Our findings suggest that ensemble classifiers (i.e., random forests and boost classifiers) show promising results in predicting tumour progression earlier than established radiological criteria and should be further investigated.

## 1. Introduction

GBM is the most common and malignant intracranial tumor [1], representing as much as 30% of primary brain tumors with increasing incidence in some geographic regions [2]. The patients have a median survival of only 10 to 14 months after diagnosis with only 3 to 5% of patients surviving more than three years. Recurrence is universal, and, at the time of relapse, the median survival is only five to seven months despite therapy [3].

The current standard of care is surgical resection followed by radiotherapy and concomitant and adjuvant temozolomide (TMZ) chemotherapy [4].

Magnetic resonance imaging (MRI) is the most widely used medical imaging technique for identifying the location and size of brain tumours. However, conventional MRI has a limited specificity in determining the underlying type of brain tumour and tumour grade [5, 6]. More advanced MR techniques like diffusion-weighted MRI, perfusion-weighted MRI, and chemical shift imaging (CSI) are promising in the

characterization of brain tumours as they give potentially more physiological information [7–9].

Diffusion-weighted imaging (DWI) and diffusion kurtosis imaging (DKI) visualize the tissue structure and are useful for assessing tumour cellularity, because they give information about the movement of the water inside different tissues including biological barriers. Typical parameters related to diffusion are apparent diffusion coefficient (ADC), mean diffusivity (MD), mean kurtosis (MK), and fractional anisotropy (FA). MD is a general parameter that accounts for the mean diffusivity in all directions, MK might be a specific parameter for tissue structure [10], and FA is a general index of anisotropy, with a value of zero corresponding to isotropic diffusion and a value of one corresponding to diffusion only in one direction.

Perfusion-weighted MRI (PWI) provides measurements that reflect changes in blood flow, volume, and angiogenesis. Hypervascularity due to glioma-induced neovascularization may show up as high relative cerebral blood volume (rCBV) while necrosis of different tissues may show up as low rCBV [11].

MR spectroscopy provides information about metabolites present in normal and abnormal tissues [12]. This information can be represented as metabolite maps using CSI.

We have studied patients with GBM that had the tumour surgically removed and afterwards were treated according to two different protocols developed for evaluating dendritic cell immunotherapy: HGG-IMMUNO-2003 [13–16] and HGG-IMMUNO-2010 [13].

The focus of our paper is finding a map between the multiparametric MR data acquired during the follow-up of the patients and the relapse of the brain tumour after surgery, as described by the clinically accepted RANO criteria [17]. In order to do this, we test different families of classifiers on multiparametric MR data, starting from simple ones, for example,  $k$ -nearest neighbours ( $k$ -NN) and linear discriminant analysis (LDA), and moving to nonlinear classifiers, for example, random forests and neural networks, using a total of 27 features extracted from PWI, DKI, and CSI data.

## 2. Materials and Methods

**2.1. Study Setup.** There are 29 patients included in this study, out of which 16 patients were treated according to the HGG-IMMUNO-2003 protocol [13–16] and 13 patients according to the HGG-IMMUNO-2010 protocol [13].

Patients that were treated according to the HGG-IMMUNO-2003 protocol are patients with relapsed GBM that received immune therapy as the sole treatment strategy.

Patients that were treated according to the HGG-IMMUNO-2010 protocol are patients with primary GBM that had surgery. For the follow-up treatment after surgery the patients were split into two groups. The first group consisting of 6 patients who received radiochemotherapy and the immune therapy vaccine. The second group consisting of the remaining 7 patients who received just radiochemotherapy for the first six months after surgery, and after those six months all 7 patients received radiochemotherapy plus the

immune therapy vaccine. We refer to the first group as “HGG-IMMUNO-2010 vaccine” and to the second group as “HGG-IMMUNO-2010 placebo.”

All 29 patients were offered monthly MRI follow-up, but after six months under immune therapy all patients switched to a three-monthly schedule.

The local ethics committee approved this study and informed consent was obtained from every patient before the first imaging time point.

Based on radiological evaluation of the follow-up MRI scans using the current guidelines for response assessment of high grade glioma [17], each patient was assigned to one of two clinical groups:

- (i) patients with *progressive disease* during follow-up which exhibit an increase of  $\geq 25\%$  in the sum of the products of perpendicular diameter of enhancing lesions compared to the smallest tumour measurement obtained either at baseline or best response,
- (ii) patients with *complete response* with disappearance of all measurable and nonmeasurable disease sustained for at least 4 weeks.

Based on this assessment, each MRI time point for each patient was considered to be labeled or unlabeled as follows: labeled as “responsive” for all time points at and after the moment when the patient was considered as “complete response”; labeled as “progressive” for all time points at and after the moment when the patient was considered as “progressive disease”; or “unlabeled” for all time points preceding the decision moment.

**2.2. MRI Acquisition and Processing.** Magnetic resonance imaging was performed on a clinical 3 Tesla MR imaging system (Philips Achieva, Best, Netherlands), using a body coil for transmission and a 32-channel head coil for signal reception. The imaging protocol consisted of diffusion kurtosis imaging, dynamic susceptibility weighted contrast-MRI (DSC-MRI), and MR spectroscopy, combined with standard anatomical imaging (T1-weighted MRI after contrast administration, T2-weighted MRI, and FLAIR (fluid attenuated inversion recovery) MR images).

**2.2.1. Anatomical Magnetic Resonance Imaging.** MR images were acquired as previously described [9, 18, 19]. In brief, an axial spin echo T2-weighted MR image (TR/TE: 3000/80 msec, slice/gap: 4/1 mm, field of view (FOV):  $230 \times 184 \text{ mm}^2$ , turbo factor (TF): 10, and acquisition matrix:  $400 \times 300$ ), an axial fluid-attenuated inversion recovery (FLAIR) image (TR/TE/IR: 11000/120/2800 msec, slice/gap: 4/1 mm, and acquisition matrix:  $240 \times 134$ ), and a T1-weighted 3D spoiled gradient echo scan (fast field echo-FFE, TR/TE: 9.7/4.6 msec, flip angle:  $8^\circ$ , turbo field echo factor: 180, acquisition voxel size:  $0.98 \times 0.98 \times 1 \text{ mm}^3$ , 118 contiguous partitions, and inversion time: 900 msec) after contrast administration were acquired as high-resolution anatomical reference images.

Regions of interest (ROI) were manually drawn around the solid contrast-enhancing region if present, avoiding areas

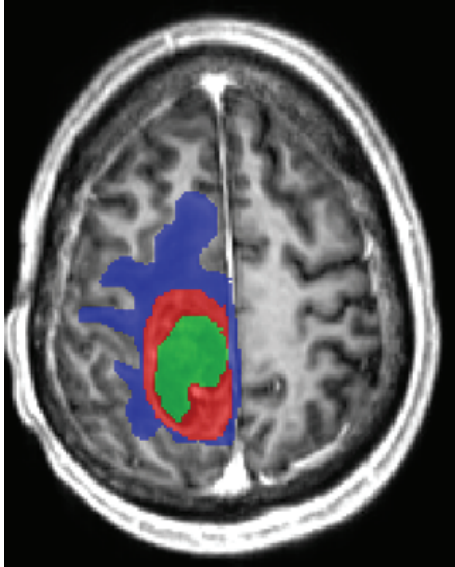


FIGURE 1: Delineations on T1 MR image postcontrast. Green—necrosis, red—CE, and blue—ED.

of necrosis (N) or cystic components such as the surgical cavity. A second ROI was manually drawn around the entire lesion (TO), that is, contrast enhancement (CE) and perilesional oedema (ED). The ROI containing the perilesional oedema was obtained by extracting the contrast-enhancing portion from the total lesion. Finally, a separate ROI was drawn around the contralateral normal appearing white matter (NAWM) to standardize the hemodynamic measurements of DSC-MRI.

The manual delineations were drawn by a radiologist (SVC) with 5 years experience of MR imaging of brain tumours. An example of delineations on T1 post contrast image can be seen in Figure 1, where green is the necrosis, red is CE, and blue is ED.

**2.2.2. Magnetic Resonance Spectroscopy.** A 2D-CSI short echo time protocol was used as validated in [20]. The volume of interest (VOI) is positioned on the slice of the transverse reconstruction of the T1-weighted 3D-FFE sequence with the largest section of contrast enhancement. The slice thickness of the VOI is 10 mm and the VOI is  $80 \times 80 \times 10 \text{ mm}^3$ , with each voxel being  $5 \times 5 \times 10 \text{ mm}^3$  ( $16 \times 16$  voxels in total). If the contrast-enhancing lesion was smaller than  $2 \text{ cm}^3$  or the contrast enhancement is located in areas with large susceptibility differences, for example, the basal forebrain or the anterior temporal lobes, a single voxel (SV) technique was performed (TR/TE: 2000/35 msec, minimal volume:  $1 \text{ cm}^3$ ).

MR spectra were processed using the MATLAB 2010b environment (MathWorks, MA, USA) with SPID graphical user interface [21] as described in detail in [20].

Nine metabolites were quantified using the AQSES-MRSI quantification method [22]: N-acetyl aspartate (NAA), glutamine (Gln), glutamate (Glu), total creatine (Cre), phosphorylcholine (PCh), glycerophosphorylcholine (GPC), myo-inositol (Myo), and lipids (Lips) at 0.9 and 1.3 ppm, referred to

as Lip1 and Lip2, respectively. Glu + Gln and PCh + GPC were reported as Glx and tCho (total choline), respectively. For each metabolite, AQSES-MRSI reported metabolite concentrations in institutional units and their error estimates as Cramer-Rao lower bounds (CRLBs) [23]. After quantification, good quality voxels were selected based on the CRLBs and spectral quality assessment as recommended by Kreis (FWHM of metabolites  $<0.07\text{--}0.1$  ppm, no unexplained features in the residuals, no doubled peaks or evidence for movement artifacts, symmetric line shape, no outer volume ghosts or other artifacts present) [24]. CRLB lower than 20% for tCho, NAA, Glx, Cre, and Lips and CRLB lower than 50% for Myo were considered sufficient. From these representative voxels, the mean metabolite ratios as proposed by Kounelakis et al. were calculated [25] over the CE region: NAA/tCho, NAA/sum, tCho/sum, NAA/Cre, Lips/tCho, tCho/Cre, Myo/sum, Cre/sum, Lips/Cre and Glx/sum (10 parameters). The sum represents the sum of the concentrations of all quantified metabolites.

Sixty-six percent (66%) of all spectroscopic time points are not included in this study. There are two reasons for this: (1) quantification was not possible for all time points (MR spectroscopy data was not acquired for all patients due to patient movement) and (2) the rest of them did not pass the quality control recommended by Kreis [24].

**2.2.3. Dynamic Susceptibility Weighted Imaging (DSC-MRI).** Perfusion images were obtained using a standard DSC perfusion MR imaging protocol consisting of a gradient echo-EPI sequence, TR/TE: 1350/30 msec, section thickness/gap: 3/0 mm, dynamic scans: 60, FOV:  $200 \times 200 \text{ mm}^2$ , matrix:  $112 \times 109$ , number of slices: 23, and scan time: 1 minute 26 seconds. EPI data were acquired during the first pass following a rapid injection of a 0.1 mmol/kg body weight bolus of megluminegadoterat (Dotarem, Guerbet, Villepinte, France) via a mechanical pump at a rate of 4 mL/sec, followed by a 20 mL bolus of saline. Preload dosing was performed according to Hu et al. in order to correct for T1-weighted leakage (preload dose 0.1 mmol/kg megluminegadoterat, incubation time 10 min) [26].

DSC data were analyzed using DPTools (<http://www.fmrtools.org>), as described in [18].

The mean values of the considered perfusion parameters were retrieved in the CE, ED, and NAWM regions. We report relative rCBV (rrCBV), relative rCBF (rrCBF), and relative DR (rDR) of tumoural tissue by using the corresponding parameter value in the contralateral NAWM as internal reference.

Although quantification was possible for all time points, after quality assessment done by visual inspection by SVC, 30% of them were not included in this study.

**2.2.4. Diffusion Kurtosis Imaging (DKI).** DKI data were acquired according to the previously described protocol in [18, 19] (SE-EPI-DWI sequence with TR/TE: 3200/90 msec,  $\delta/\Delta$ : 20/48.3 msec; FOV:  $240 \times 240 \text{ mm}^2$ , matrix:  $96 \times 96$ , number of slices: 44, 1 signal average acquired, section thickness/gap: 2.5/0 mm, and *b*-values: 700, 1000, and

2800 sec/mm<sup>2</sup> in 25, 40, and 75 uniformly distributed directions, resp.) [27]. The DKI data were processed as described in [18]. Fractional anisotropy (FA), mean diffusivity (MD), and mean kurtosis (MK) were derived from the tensors [10, 28]. A nonlinear registration of the parameter maps to the anatomical MR imaging data was performed to minimize the local misalignment between the EPI distorted DKI data and the anatomical data on which the ROIs were manually positioned. MK, MD, and FA were determined in the CE and ED regions.

Although quantification was possible for all time points, after quality control according to [27], 44% of them were not included in this study.

*2.2.5. Summary of MRI Acquisition and Processing.* In total, from 29 patients, we have 178 data points of follow-up MR imaging sessions, and each of these ones has 27 features:

- (i) 3 volumes, contrast enhancement (CE), oedema (ED), and necrosis (N)
- (ii) 6 perfusion features, rrCBV, rrCBF, and rDR for CE and ED
- (iii) 6 diffusion features, MK, MD, and FA for CE and ED
- (iv) 10 spectroscopic features, from CE—NAA/tCho, NAA/sum, tCho/sum, NAA/Cre, Lips/tCho, tCho/Cre, Myo/sum, Cre/sum, Lips/Cre, and Glx/sum
- (v) a parameter (0 or 1) for total resection of the tumour
- (vi) a parameter (0, 1, or 2) to describe the group of the patient, HGG-IMMUNO-2003, HGG-IMMUNO-2010 placebo, or HGG-IMMUNO-2010 vaccine.

Out of all 178 measurements, if we extract just the ones with complete features, it will result in a subset of 18 patients with 45 measurements. This implies that more than 75% of the measurements have at least one feature missing. Five features are always present: the three volumes, the parameter for tumour resection, and the parameter for different groups.

*2.3. Classifiers.* We have used several supervised and semisupervised classifiers, as presented in Table 1, with the goal of testing whether the unlabeled data could have been reliably labeled before the actual labeling was performed in the clinic according to the RANO criteria.

The list of classifiers in Table 1 is representative for the most important families of classification methods, starting from simple classical methods such as linear discriminant analysis (LDA) and  $k$ -nearest neighbour ( $k$ -NN) up to more complex nonlinear classifiers such as random forests and neural networks.

Each classifier is based on a mathematical model, which needs to be optimised on the basis of a training dataset. The training set consists here of labeled data, that is, data at and after a clinical decision has been made. The test set on which we compare classifiers consists of data that have no label, that is, time points before the decision of “progressive” or “responsive” has been made.

All classifiers are implemented in MATLAB R2013a (MathWorks, MA, USA). All classifiers except least squares

TABLE 1: Supervised and semisupervised classifiers tested in this paper.

Supervised classifiers	Handles missing values
Random forests	✓
Classification tree	✓
Boost ensembles	✓
Neural networks	—
SVM	—
LSSVM	—
$k$ -NN	—
dLDA	—
Semisupervised classifiers	
LDS	—
SMIR	—
S4VM	—

support vector machines (LSSVMs) and the semisupervised ones are part of the Statistics Toolbox and Neural Networks Toolbox of MATLAB R2013a.

$k$ -NN [29] is one of the basic classifiers in machine learning. The class label of a new testing point is given by the most common class among its  $k$  neighbours. We used the default MATLAB R2013a (Statistics Toolbox) function “*knnclassify*” to run a grid search for the best combination of number of neighbours ( $k$ ) and type of distance. We varied  $k$  between 1 and 11 and the distance was either “euclidean,” “cityblock,” “cosine,” or “correlation.” We found the best results for the combination of 3 neighbours and the “correlation” distance.

Diagonal LDA (dLDA [30]) is a simple modification of linear discriminant analysis, which implies that we use the pseudoinverse of the covariance matrix instead of the actual inverse. We used the default MATLAB R2013a implementation “*classify*” from the Statistics Toolbox.

SVMs [31, 32] are among the most popular machine learning models because they are easy to understand: given a training set with points that belong to two classes, we try to find the best hyperplane to differentiate between the two types of points. We can try this in the original space or we can map the points to another space by using the kernel trick. We used the default MATLAB R2013a (Statistics Toolbox) implementations “*svmtrain*” and “*svmclassify*.” We used different types of kernel: linear, polynomial, radial basis function, and multilevel perceptron.

Classification tree [33] is an algorithm commonly used in machine learning. Like in a real tree there are leaves which represent class labels and branches. At each node of a tree a single feature is used to discriminate between different branches. We used the default MATLAB R2013a (Statistics Toolbox) implementation “*classregtree*.”

Neural networks [34–37] are built on interconnected layers of artificial “neurons” that try to map an input vector to its specific output. There are three types of layers: input, hidden, and output. The weights between different neurons are trained until a maximum number of iterations or a minimum error is reached. We used the default MATLAB R2013a (Neural Network Toolbox) implementation “*net*” with 10

hidden neurons. We tested four types of neural networks: pattern net, feed forward net, cascade forward net, and fit net.

Random forests [38, 39] are part of the ensemble methods for classification that use a collection of decision trees. Each decision tree learns a rule and then it can classify a new point. The new point is assigned to the class voted by the majority of the decision trees. We used the default MATLAB R2013a (Statistics Toolbox) implementation “TreeBagger” with 100 trees.

Boosting algorithms [40–43] start with a collection of weak classifiers (e.g., decision trees) and with each iteration they try to improve the overall classification by learning what was misclassified at the previous step. We used the default MATLAB R2013a (Statistics Toolbox) implementation “fitensemble” with 100 trees. We tested seven types of boosting algorithms: AdaBoost, LogitBoost, GentleBoost, RobustBoost, LPBoost, TotalBoost, and RUSBoost.

LSSVMs [44, 45] are a powerful machine learning technique. We downloaded LSSVMlab from [46] and followed the instructions from [47] to tune the parameters. We used different types of kernel: linear, polynomial, radial basis function, and also the Bayesian approach on LSSVM.

The semisupervised classifiers used in this paper are low density separation (LDS [48]), squared-loss mutual information regularization (SMIR [49]), and safe semisupervised support vector machine (S4VM [50, 51]). In the last years there has been a steady increase in the use and development of semisupervised classifiers, as they take into account information from unlabeled data also, not just from labeled data. This makes them powerful machine learning tools. The implementation for semisupervised classifiers was downloaded from [52–54].

Classifiers were tested first with all features described in Section 2.2.5 taken as input, but then also by selecting subsets of the available features as input, that is, only the features pertaining to a single modality (perfusion, diffusion, and spectroscopy). Additionally, classifiers were tested first on the smaller dataset containing 45 time points with a complete set of features and then on the larger dataset containing 178 time points where missing values have been imputed according to Section 2.4, presented below.

**2.4. In-House Imputation Method.** Some classifiers have built-in strategies of handling missing values, but other classifiers do not handle missing values (see Table 1). This is why we developed our own in-house imputation method, so the handling of missing values will be the same for all classifiers.

Our method is based on the volumes of contrast enhancement and oedema regions, in the sense that if the volume of a tumour region is zero, that missing tissue is considered healthy tissue. If we have values of any modality (perfusion, diffusion, and spectroscopy) that are missing from CE or ED, and the volume of CE or ED corresponding to that measurement is zero, and then we assume that those missing values belong to a normal type of tissue. For perfusion, because we normalize every parameter to the normal appearing white matter value, the missing values will be replaced by 1's. For diffusion and spectroscopy, the missing values will be

replaced by the average of the features taken over the measurements which were labeled as responsive, because we consider that these measurements are recorded from a healthy tissue. If we have missing values without association to zero volume for CE or ED, they will be replaced by the average taken over all the labeled measurements.

## 2.5. Performance Indices

**Leave One Patient Out (LOPO).** Classifiers are trained on labeled data from all patients except one who is the test patient. Each patient in turn is selected as test patient. All time points that belong to the test patient are classified independently. Results for each classifier are averaged per time point over all patients relative to the time point at which the clinical decision was made.

This way of testing is intuitive from a medical point of view and provides us with information about how good is the classification when we approach the decision time. In this way we can look at the temporal evolution of the classification for each patient.

We compute the balanced error rate (BER) at each time point before and after the decision, using the clinical decision assigned to each patient as expected label for all time points of this patient. BER is computed as

$$BER_i = \frac{ERR_i^{resp} + ERR_i^{prog}}{2}, \quad (1)$$

where

$$\begin{aligned} ERR_i^{resp} &= (\text{Number of responsive patients} \\ &\quad \text{misclassified as progressive}) \\ &\quad \times (\text{Total number of responsive patients})^{-1}, \\ ERR_i^{prog} &= (\text{Number of progressive patients} \\ &\quad \text{misclassified as responsive}) \\ &\quad \times (\text{Total number of progressive patients})^{-1}. \end{aligned} \quad (2)$$

For each classifier we have a grand total of 17 time points, due to the fact that there are patients with up to 6 time points after the decision time point and there are others with up to 11 time points before the decision. In order to compare the classifiers by using just one error number instead of 17, we compute a weighted average for each classifier's time response. This performance measurement is denoted by “weighted BER (wBER)” in the Results section.

We use two sets of weights:

- (i) one for the temporal response—the classifier should perform better when we approach the labeling time point and after it:

$$\begin{aligned} W_i^t &= 1, \quad \text{if } i \geq \text{decision time point}, \\ W_i^t &= 1 - \frac{0.5}{11} \cdot i, \quad \text{if } i < \text{decision time point} \end{aligned} \quad (3)$$

TABLE 2: Detailed BER results for each time point for the best 6 classifiers when using the leave-one-patient-out method on complete features for all MR modalities. The decision moment marked by bold font. Some time points do not have results because there were no complete measurements.

BER	Random forests	dLDA	SVM-lin	LogitBoost	RobustBoost	SVM-mlp
$L + 5$	—	—	—	—	—	—
$L + 4$	—	—	—	—	—	—
$L + 3$	0	0	0	0	0	0
$L + 2$	0	0	0	0	0	0
$L + 1$	0	0	0	0	0	0
<b>L</b>	<b>0</b>	<b>0.1</b>	<b>0.217</b>	<b>0</b>	<b>0</b>	<b>0.1</b>
$L - 1$	0	0.125	0	0	0	0.125
$L - 2$	0.25	0.25	0.5	0.25	0.25	0.25
$L - 3$	0.5	0.5	1	0.5	0.5	0.25
$L - 4$	1	1	1	1	1	0.5
$L - 5$	0.25	0.25	0.25	0.25	0.25	0.25
$L - 6$	0.5	0	0	0.5	0.5	0
$L - 7$	1	0	1	1	1	0
$L - 8$	—	—	—	—	—	—
$L - 9$	0	0	0	0	0	0
$L - 10$	—	—	—	—	—	—
$L - 11$	0	0	1	0	0	0
wBER	0.148	0.172	0.276	0.148	0.148	0.136

TABLE 3: Detailed BER results for each time point for the best 6 supervised classifiers when using the leave-one-patient-out method on imputed features for all MR modalities. The decision moment marked by bold font.

BER	Random forests	dLDA	SVM-lin	LogitBoost	RobustBoost	SVM-mlp
$L + 5$	0	0	0	0	0	0
$L + 4$	0	0	0	0	0	0
$L + 3$	0	0	0	0	0	0
$L + 2$	0.125	0.25	0.125	0.125	0.125	0
$L + 1$	0.171	0.071	0.071	0.171	0.171	0.071
<b>L</b>	<b>0.105</b>	<b>0.022</b>	<b>0.149</b>	<b>0.188</b>	<b>0.105</b>	<b>0.359</b>
$L - 1$	0.214	0.065	0.130	0.3	0.192	0.192
$L - 2$	0.444	0.417	0.194	0.444	0.472	0.5
$L - 3$	0.418	0.382	0.282	0.418	0.418	0.482
$L - 4$	0.475	0.413	0.388	0.475	0.413	0.475
$L - 5$	0.688	0.438	0.563	0.688	0.688	0.688
$L - 6$	0.368	0.467	0.3	0.567	0.567	0.567
$L - 7$	0.375	0.375	0.75	0.5	0.75	0.625
$L - 8$	0.5	0.333	0.583	0.5	0.75	0.333
$L - 9$	0.333	0.333	0.833	0.333	0.833	0.5
$L - 10$	0.5	0.75	0.75	0.5	1	0.75
$L - 11$	0.5	0.5	1	0.5	0.5	0.5
wBER	0.294	0.216	0.242	0.335	0.325	0.352

TABLE 4: Weighted BER for the best 6 supervised classifiers when using the leave-one-patient-out method with complete features for each MR modality separately.

Weighted BER	Random forests	dLDA	SVM-lin	LogitBoost	RobustBoost	SVM-mlp
Perfusion	0.148	0.256	0.220	0.148	0.148	0.193
Diffusion	0.358	0.259	0.255	0.367	0.367	0.349
Spectroscopy	0.571	0.561	0.600	0.609	0.623	0.629

TABLE 5: Weighted BER for the best 6 supervised classifiers trained on imputed features from each MR modality separately.

Weighted BER	Random forests	dLDA	SVM-lin	LogitBoost	RobustBoost	SVM-mlp
Perfusion	0.294	0.311	0.275	0.289	0.265	0.282
Diffusion	0.277	0.327	0.322	0.277	0.277	0.380
Spectroscopy	0.412	0.401	0.423	0.423	0.408	0.415

TABLE 6: wBER comparison between our in-house method of imputing missing values and built-in imputation strategy of different supervised classifiers.

Weighted BER	Our method	Built-in method
Random forests	0.294	0.423
AdaBoost	0.324	0.333
LogitBoost	0.335	0.241
GentleBoost	0.308	0.245
RobustBoost	0.325	0.296
LPBoost	0.256	0.369
TotalBoost	0.289	0.323
RUSBoost	0.308	0.361
Decision tree	0.346	0.651

TABLE 7: Weighted BER for supervised and semisupervised classifiers trained on complete and imputed data. We marked the best 6 classifiers by bold font.

Weighted BER	Complete features	Imputed features	Average
dLDA	<b>0.172</b>	<b>0.216</b>	<b>0.194</b>
SVM-lin	<b>0.276</b>	<b>0.242</b>	<b>0.259</b>
SVM-poly	0.285	0.334	0.310
SVM-rbf	0.493	0.520	0.507
SVM-mlp	<b>0.136</b>	<b>0.352</b>	<b>0.244</b>
Bayesian LSSVM	0.371	0.469	0.420
LSSVM-lin	0.452	0.280	0.366
LSSVM-poly	0.462	0.362	0.412
LSSVM-rbf	0.408	0.320	0.364
Random forests	<b>0.148</b>	<b>0.294</b>	<b>0.221</b>
AdaBoost	0.505	0.324	0.415
LogitBoost	<b>0.148</b>	<b>0.335</b>	<b>0.242</b>
GentleBoost	0.296	0.308	0.302
RobustBoost	<b>0.148</b>	<b>0.325</b>	<b>0.237</b>
LPBoost	0.505	0.256	0.381
TotalBoost	0.505	0.289	0.397
RUSBoost	0.281	0.308	0.295
Classification tree	0.268	0.346	0.307
3-NN (correlation)	0.357	0.428	0.392
Pattern net	0.449	0.288	0.366
Feed forward net	0.399	0.411	0.405
Cascade forward net	0.586	0.485	0.535
Fit net	0.535	0.350	0.443
LDS	0.442	0.534	0.488
SMIR	0.278	0.436	0.357
S4VM	0.456	0.473	0.465

(ii) one for patient population—the time points with more patients get a higher weight (see Table 14 from the Appendix):

$$W_i^p = \frac{\text{Number of patients at time point } i}{\text{Total number of patients}}. \quad (4)$$

The equation of wBER is

$$\text{wBER} = \frac{\sum W_i^p \cdot W_i^t \cdot \text{BER}_i}{\sum W_i^p \cdot W_i^t}. \quad (5)$$

### 3. Results and Discussion

#### 3.1. Results

3.1.1. *LOPO When Using All Modalities.* Table 7 from the Appendix shows how different classifiers perform on complete and on imputed features when using all MR modalities.

We selected the best 6 classifiers (marked by bold font in Table 7) and present their detailed BER results for each time point in Table 2.

Table 3 shows the detailed BER results for each time point for the best 6 classifiers (marked by bold font in Table 7) when using data with imputed features.

3.1.2. *LOPO When Using Each Modality.* Table 4 shows how the best 6 supervised classifiers (marked by bold font in Table 7) perform on complete features when using each MR modality separately.

Tables 8, 9, and 10 from the Appendix list the performance of the best supervised classifiers (marked by bold font in Table 7) when using, respectively, perfusion, diffusion, or spectroscopy data separately, considering complete features only.

Table 5 shows how the best 6 classifiers (marked by bold font in Table 7) perform on imputed features when using each MR modality separately.

Tables 11, 12, and 13 from the Appendix list the performance of the best supervised classifiers (marked by bold font in Table 7) when using, respectively, perfusion, diffusion, or spectroscopy data separately, considering imputed features only.

TABLE 8: Detailed BER results for each time point for the best 6 supervised classifiers when using the leave-one-patient-out method on complete perfusion features. The decision moment marked by bold font. Some time points do not have results because there were no complete perfusion measurements.

BER on perfusion	Random forests	dLDA	SVM-lin	LogitBoost	RobustBoost	SVM-mlp
$L + 5$	—	—	—	—	—	—
$L + 4$	—	—	—	—	—	—
$L + 3$	0	0	0	0	0	0
$L + 2$	0	0	1	0	0	0
$L + 1$	0	0	1	0	0	0
<b>L</b>	<b>0</b>	<b>0.217</b>	<b>0.05</b>	<b>0</b>	<b>0</b>	<b>0.05</b>
$L - 1$	0	0.187	0.187	0	0	0.187
$L - 2$	0.25	0.25	0.375	0.25	0.25	0.25
$L - 3$	0.5	0.5	0.5	0.5	0.5	0.5
$L - 4$	1	1	1	1	1	0.5
$L - 5$	0.25	0.25	0.25	0.5	0.5	0.5
$L - 6$	0.5	0.5	0.5	0.5	0.5	0.5
$L - 7$	1	1	1	1	1	1
$L - 8$	—	—	—	—	—	—
$L - 9$	0	0	0	0	0	0
$L - 10$	—	—	—	—	—	—
$L - 11$	0	0	0	0	0	0

TABLE 9: Detailed BER results for each time point for the best 6 supervised classifiers when using the leave-one-patient-out method on complete diffusion features. The decision moment marked by bold font. Some time points do not have results because there were no complete diffusion measurements.

BER on diffusion	Random forests	dLDA	SVM-lin	LogitBoost	RobustBoost	SVM-mlp
$L + 5$	—	—	—	—	—	—
$L + 4$	—	—	—	—	—	—
$L + 3$	0	0	0	0	0	1
$L + 2$	0	0.25	0	0	0	0.5
$L + 1$	0	0	0	0	0	0
<b>L</b>	<b>0.217</b>	<b>0.1</b>	<b>0.1</b>	<b>0.217</b>	<b>0.217</b>	<b>0.267</b>
$L - 1$	0.562	0.25	0.125	0.562	0.562	0.562
$L - 2$	0.5	0.25	0.5	0.5	0.5	0.375
$L - 3$	0.5	0.75	0.75	0.5	0.5	0.25
$L - 4$	0.5	1	0.5	0.5	0.5	0.5
$L - 5$	0.25	0.25	0.5	0.5	0.5	0
$L - 6$	0.5	0	0.5	0.5	0.5	0
$L - 7$	0	0	0	0	0	0
$L - 8$	—	—	—	—	—	—
$L - 9$	1	1	1	1	1	0
$L - 10$	—	—	—	—	—	—
$L - 11$	1	1	1	1	1	0

3.1.3. *In-House Imputation Strategy versus Built-In Imputation Strategy.* Table 6 shows how different classifiers perform with our in-house imputation of missing values (Section 2.4) versus the built-in imputation strategy of missing values for the classifiers marked in Table 1.

3.2. *Discussion.* A first conclusion that we can draw from a comparative analysis of the different classifiers is that we

obtain the lowest error when training classifiers on data with complete features and not on data with imputed features, no matter the imputation method (our in-house method or the built-in method). In order to improve the performance of classifiers, improving the quality of the data would help.

The lowest error when using complete features is around 0.14 (SVM-mlp—0.136), while if we use imputed features the lowest error is 0.216 (dLDA). The best classifiers on complete

TABLE 10: Detailed BER results for each time point for the best 6 supervised classifiers when using the leave-one-patient-out method on complete spectroscopy features. The decision moment marked by bold font. Some time points do not have results because there were no complete spectroscopy measurements.

BER on spectroscopy	Random forests	dLDA	SVM-lin	LogitBoost	RobustBoost	SVM-mlp
$L + 5$	—	—	—	—	—	—
$L + 4$	—	—	—	—	—	—
$L + 3$	0	0	0	0	0	0
$L + 2$	1	0.75	0.75	1	1	1
$L + 1$	1	1	1	1	1	0
<b>L</b>	<b>0.55</b>	<b>0.583</b>	<b>0.632</b>	<b>0.6</b>	<b>0.55</b>	<b>0.583</b>
$L - 1$	0.562	0.562	0.813	0.5	0.562	0.687
$L - 2$	0.625	0.625	0.25	0.625	0.75	0.875
$L - 3$	0.25	0.5	0.25	0.5	0.5	0.25
$L - 4$	0.5	0.5	1	0.5	0.5	1
$L - 5$	0.5	0.5	0	1	1	1
$L - 6$	0.5	0	0.5	0.5	0.5	0.5
$L - 7$	0	0	1	0	0	0
$L - 8$	—	—	—	—	—	—
$L - 9$	1	1	1	1	1	0
$L - 10$	—	—	—	—	—	—
$L - 11$	1	1	1	1	1	0

TABLE 11: Detailed BER results for each time point for the best 6 supervised classifiers when using the leave-one-patient-out method on imputed perfusion features. The decision moment marked by bold font.

BER on perfusion	Random forests	dLDA	SVM-lin	LogitBoost	RobustBoost	SVM-mlp
$L + 5$	0	0	0	0	0	0
$L + 4$	0	0	0	0	0	0
$L + 3$	0	0.25	0	0	0	0.25
$L + 2$	0.125	0	0	0.125	0	0.125
$L + 1$	0.171	0.071	0.071	0.171	0.071	0
<b>L</b>	<b>0.127</b>	<b>0.109</b>	<b>0.043</b>	<b>0.127</b>	<b>0.043</b>	<b>0.109</b>
$L - 1$	0.130	0.196	0.152	0.214	0.130	0.279
$L - 2$	0.444	0.528	0.472	0.389	0.444	0.417
$L - 3$	0.418	0.464	0.418	0.373	0.418	0.281
$L - 4$	0.475	0.475	0.475	0.412	0.475	0.512
$L - 5$	0.687	0.687	0.687	0.625	0.687	0.562
$L - 6$	0.567	0.567	0.567	0.567	0.567	0.567
$L - 7$	0.5	0.5	0.5	0.5	0.5	0.5
$L - 8$	0.5	0.5	0.5	0.5	0.5	0.5
$L - 9$	0.333	0.5	0.5	0.333	0.333	0.333
$L - 10$	0.5	0.5	0.5	0.5	0.5	0.25
$L - 11$	0.5	0.5	0.5	0.5	0.5	0

features are ensemble classifiers (random forests and boosting algorithms), dLDA, and SVM, while the best classifiers on imputed features are dLDA, SVM-lin, and random forests.

If we compare the results of single MR modalities when training classifiers on data with complete features, we can say that the use of spectroscopy only leads to the worst results with a minimum error of 0.561. The single use of perfusion generates better results than using only diffusion data, especially when using ensemble methods (random forests, LogitBoost, and RobusBoost), with a minimum error of 0.148 compared to 0.255. When using imputed features, the minimum error almost doubles.

An interesting aspect when looking at detailed measurements on complete features (Table 2) is the fact that we have error equal to zero (perfect classification), one time point before the actual labeling according to the RANO criteria, when using random forests, LogitBoost, or RobustBoost. This means that we can predict the patient outcome (progressive, responsive) with 100% accuracy one time point (i.e., about 1 month in our study) earlier than the actual clinical decision was made. When looking at each MR modality separately (Tables 8, 9, and 10) we notice that the same result could have been obtained by using solely the perfusion data. This is a very important finding, mainly because perfusion is very fast to

TABLE 12: Detailed BER results for each time point for the best 6 supervised classifiers when using the leave-one-patient-out method on imputed diffusion features. The decision moment marked by bold font.

BER on diffusion	Random forests	dLDA	SVM-lin	LogitBoost	RobustBoost	SVM-mlp
$L + 5$	0	0	0	0	0	0
$L + 4$	0	0	0	0	0	0
$L + 3$	0	0	0	0	0	0.25
$L + 2$	0	0.125	0	0	0	0
$L + 1$	0.1	0.243	0.243	0.1	0.1	0.314
<b>L</b>	<b>0.105</b>	<b>0.297</b>	<b>0.192</b>	<b>0.105</b>	<b>0.105</b>	<b>0.420</b>
$L - 1$	0.254	0.257	0.257	0.254	0.254	0.424
$L - 2$	0.361	0.25	0.25	0.361	0.361	0.278
$L - 3$	0.282	0.473	0.473	0.282	0.282	0.436
$L - 4$	0.45	0.637	0.637	0.45	0.45	0.387
$L - 5$	0.562	0.5	0.562	0.562	0.562	0.437
$L - 6$	0.433	0.367	0.533	0.433	0.433	0.433
$L - 7$	0.5	0.5	0.5	0.5	0.5	0.75
$L - 8$	0.667	0.167	0.667	0.667	0.667	0.667
$L - 9$	0.667	0.667	0.667	0.667	0.667	0.5
$L - 10$	0.75	0.75	0.75	0.75	0.75	0.75
$L - 11$	1	0.5	1	1	1	1

TABLE 13: Detailed BER results for each time point for the best 6 supervised classifiers when using the leave-one-patient-out method on imputed spectroscopy features. The decision moment marked by bold font.

BER on spectroscopy	Random forests	dLDA	SVM-lin	LogitBoost	RobustBoost	SVM-mlp
$L + 5$	0	0	0	0	0	0
$L + 4$	0	0	0	0	0	0
$L + 3$	0	0	0	0	0	0.25
$L + 2$	0.25	0.25	0.125	0.25	0.25	0.25
$L + 1$	0	0	0	0	0	0
<b>L</b>	<b>0.562</b>	<b>0.504</b>	<b>0.609</b>	<b>0.587</b>	<b>0.543</b>	<b>0.569</b>
$L - 1$	0.293	0.337	0.380	0.315	0.293	0.359
$L - 2$	0.389	0.389	0.389	0.389	0.389	0.389
$L - 3$	0.436	0.436	0.381	0.436	0.436	0.336
$L - 4$	0.55	0.55	0.612	0.55	0.55	0.55
$L - 5$	0.687	0.687	0.562	0.687	0.687	0.687
$L - 6$	0.433	0.433	0.533	0.6	0.433	0.433
$L - 7$	0.75	0.75	0.875	0.75	0.75	0.75
$L - 8$	0.667	0.667	0.667	0.667	0.667	0.667
$L - 9$	0.667	0.167	0.667	0.667	0.667	0.667
$L - 10$	0.75	0.75	0.25	0.75	0.75	0.75
$L - 11$	1	1	1	0.5	1	1

measure (2-3 minutes) and it has the lowest rate of missing data, which makes it reliable. Our study is not the only one that shows that perfusion parameters are very reliable when it comes to differentiating between tumour tissues and other tissues. Multiple studies (among others Barajas Jr. et al. [55] and Hu et al. [56]) prove that perfusion parameters are strongly correlated with tumour progression and overall survival. The main reason behind this strong correlation is the fact that tumours grow very fast, so they require large amounts of nutrients to develop, which is reflected in the angiogenesis of the tumour. This increase in angiogenesis is visualised and measured using perfusion imaging.

When comparing the two methods of imputing missing values, our in-house method (Section 2.4), and the classifier-dependent built-in strategies, the difference between them is not important with respect to the performance of the classifiers.

Using machine learning for classification of brain tumoral tissue is a field with an increasing amount of work.

In [57] Hu et al. use a support vector machine approach on multiparametric MRI (perfusion, diffusion, and anatomical MRI) to automatically differentiate between radiation necrosis voxels and progressive tumour voxels coming from patients with resected GBM. They optimize a one-class SVM

TABLE 14: Number of samples for each time point. The decision moment marked by bold font.

	Number of complete samples	Number of imputed samples
$L + 5$	0	2
$L + 4$	0	2
$L + 3$	1	3
$L + 2$	3	8
$L + 1$	1	12
<b>L</b>	<b>13</b>	<b>29</b>
$L - 1$	9	29
$L - 2$	6	24
$L - 3$	3	16
$L - 4$	2	13
$L - 5$	2	12
$L - 6$	2	8
$L - 7$	1	6
$L - 8$	0	5
$L - 9$	1	4
$L - 10$	0	3
$L - 11$	1	2

based on the area under receiver operator curve from 6000 training voxels manually delineated from 8 patients and then tested on manually delineated voxels from 8 new patients. Their results show that perfusion and diffusion have a high discrimination rate between radiation necrosis and tumour progression.

In [55] Barajas Jr. et al. use perfusion MR imaging to investigate which parameters can be used to differentiate between recurrent GBM and radiation necrosis. Their study was based on 57 patients, they used Welch  $t$  test to compare measurements between groups, and they found that all perfusion parameters (relative CBV, peak height, and percentage of signal intensity recovery) are strongly correlated with tumour progression.

In [56] Hu et al. use perfusion metrics on contrast enhancement lesions (CBV mean, mode, maximum, width, and a new thresholding metric called fractional tumor burden (FTB)) to see how they correlate to overall survival (OS). Their study was based on 25 patients with recurrent GBM and found that all parameters are strongly correlated with OS.

In [58] Weybright et al. used chemical shift imaging (CSI) to differentiate voxels with tumour recurrence and radiation injury. Their study was based on 29 patients and they had high quality data for 28 of them (97%). They found that the Cho/NAA and Cho/Cr ratios may be the best numerical discriminators between tumour recurrence and radiation injury.

Although we cannot compare our results directly to the ones from the studies presented before due to different approaches on classifying different tissues, it is becoming more obvious that a learning algorithm based on multiparametric MR data will evolve in the near future and will

help clinicians in differentiating between progressive tumoral tissue and other types (necrotic or normal).

## 4. Conclusions

In this paper we compare different supervised and semisupervised classifiers. We train them on multiparametric MR data with complete and imputed features. The data was acquired from 29 patients selected from follow-up studies of GBM. We investigate the leave-one-patient-out testing method and come to the conclusion that the same label according to the RANO criteria could have been put earlier with at least one month with 100% accuracy, if we train random forests, LogitBoost, or RobustBoost on data with complete features. More interesting is the fact that the same result is achieved by the same classifiers using only complete perfusion data.

For future work we plan on using the temporal evolution of the features when classifying different MR sessions and also allow updating the class labels in time. Moreover, we are going to try new methods of processing the raw MR data to improve the quality of it.

## Appendix

In Tables 7–14 we use balanced error rate (BER) and weighted balanced error rate (wBER) to present the performance of the classifiers. BER and wBER are numbers between 0 and 1, 0 being perfect classification and 1 being total misclassification.

## Conflict of Interests

The authors declare that there is no conflict of interests regarding the publication of this paper.

## Acknowledgments

This work has been funded by the following projects: Flemish Government FWO project G.0869.12N (tumor imaging); Belgian Federal Science Policy Office: IUAP P7/19/(DYSCO, “dynamical systems, control, and optimization,” 2012–2017); and EU: the research leading to these results has received funding from the European Research Council under the European Union’s Seventh Framework Programme (FP7/2007–2013). This paper reflects only the authors’ views and the Union is not liable for any use that may be made of the contained information. Other EU fundings: EU MC ITN TRANSACT 2012 (no. 316679).

## References

- [1] P. C. Burger, F. S. Vogel, S. B. Green, and T. A. Strike, “Glioblastoma multiforme and anaplastic astrocytoma: pathologic criteria and prognostic implications,” *Cancer*, vol. 56, no. 5, pp. 1106–1111, 1985.
- [2] M. Dobs, V. G. Khurana, B. Shadbolt et al., “Increasing incidence of glioblastoma multiforme and meningioma, and decreasing incidence of Schwannoma (2000–2008): findings of a multicenter Australian study,” *Surgical Neurology International*, vol. 2, p. 176, 2011.

- [3] A. M. Rulseh, J. Keller, J. Klener et al., "Long-term survival of patients suffering from glioblastoma multiforme treated with tumor-treating fields," *World Journal of Surgical Oncology*, vol. 10, article 220, 2012.
- [4] R. Stupp, W. P. Mason, M. J. van den Bent et al., "Radiotherapy plus concomitant and adjuvant temozolomide for glioblastoma," *The New England Journal of Medicine*, vol. 352, no. 10, pp. 987–996, 2005.
- [5] B. L. Dean, B. P. Drayer, C. R. Bird et al., "Gliomas: classification with MR imaging," *Radiology*, vol. 174, no. 2, pp. 411–415, 1990.
- [6] F. Earnest IV, P. J. Kelly, B. W. Scheithauer et al., "Cerebral astrocytomas: histopathologic correlation of MR and CT contrast enhancement with stereotactic biopsy," *Radiology*, vol. 166, no. 3, pp. 823–827, 1988.
- [7] S. J. Nelson and S. Cha, "Imaging glioblastoma multiforme," *The Cancer Journal*, vol. 9, no. 2, pp. 134–145, 2003.
- [8] J. Rees, "Advances in magnetic resonance imaging of brain tumours," *Current Opinion in Neurology*, vol. 16, no. 6, pp. 643–650, 2003.
- [9] M. Vrabec, S. Van Cauter, U. Himmelreich et al., "MR perfusion and diffusion imaging in the follow-up of recurrent glioblastoma treated with dendritic cell immunotherapy: a pilot study," *Neuroradiology*, vol. 53, no. 10, pp. 721–731, 2011.
- [10] J. H. Jensen, J. A. Helpers, A. Ramani, H. Lu, and K. Kaczynski, "Diffusional kurtosis imaging: the quantification of non-Gaussian water diffusion by means of magnetic resonance imaging," *Magnetic Resonance in Medicine*, vol. 53, no. 6, pp. 1432–1440, 2005.
- [11] R. Lund, S. Rand, H. Krouwer, C. Schultz, and K. Schmainda, "Using rCBV to distinguish radiation necrosis from tumor recurrence in malignant gliomas," *International Journal of Radiation Oncology, Biology, Physics*, vol. 63, supplement 1, pp. S65–S66, 2005, Proceedings of the 47th Annual Meeting of the American Society for Therapeutic Radiology and Oncology.
- [12] W. Möller-Hartmann, S. Herminghaus, T. Krings et al., "Clinical application of proton magnetic resonance spectroscopy in the diagnosis of intracranial mass lesions," *Neuroradiology*, vol. 44, no. 5, pp. 371–381, 2002.
- [13] S. van Gool, W. Maes, H. Ardon, T. Verschuere, S. van Cauter, and S. de Vleeschouwer, "Dendritic cell therapy of high-grade gliomas," *Brain Pathology*, vol. 19, no. 4, pp. 694–712, 2009.
- [14] S. de Vleeschouwer, F. van Calenbergh, P. Demaerel et al., "Transient local response and persistent tumor control in a child with recurrent malignant glioma: treatment with combination therapy including dendritic cell therapy: case report," *Journal of Neurosurgery*, vol. 100, no. 5, pp. 492–497, 2004.
- [15] S. Rutkowski, S. de Vleeschouwer, E. Kaempgen et al., "Surgery and adjuvant dendritic cell-based tumour vaccination for patients with relapsed malignant glioma, a feasibility study," *British Journal of Cancer*, vol. 91, no. 9, pp. 1656–1662, 2004.
- [16] S. de Vleeschouwer, S. Fieuws, S. Rutkowski et al., "Post-operative adjuvant dendritic cell-based immunotherapy in patients with relapsed glioblastoma multiforme," *Clinical Cancer Research*, vol. 14, no. 10, pp. 3098–3104, 2008.
- [17] P. Y. Wen, D. R. Macdonald, D. A. Reardon et al., "Updated response assessment criteria for high-grade gliomas: response assessment in neuro-oncology working group," *Journal of Clinical Oncology*, vol. 28, no. 11, pp. 1963–1972, 2010.
- [18] S. Van Cauter, F. De Keyser, D. Sima et al., "Integrating diffusion kurtosis imaging, dynamic susceptibility-weighted contrast-enhanced MRI, and short echo time chemical shift imaging for grading gliomas," *Neuro-Oncology*, vol. 16, no. 7, pp. 1010–1021, 2014.
- [19] S. Van Cauter, J. Veraart, J. Sijbers et al., "Gliomas: diffusion kurtosis MR imaging in grading," *Radiology*, vol. 263, no. 2, pp. 492–501, 2012.
- [20] S. van Cauter, D. M. Sima, J. Luts et al., "Reproducibility of rapid short echo time CSI at 3T for clinical applications," *Journal of Magnetic Resonance Imaging*, vol. 37, no. 2, pp. 445–456, 2013.
- [21] SPID, <http://homes.esat.kuleuven.be/~biomed/software.php#SpidGUI>.
- [22] A. R. Croitor Sava, D. M. Sima, J.-B. Poulet, A. J. Wright, A. Heerschap, and S. van Huffel, "Exploiting spatial information to estimate metabolite levels in two-dimensional MRSI of heterogeneous brain lesions," *NMR in Biomedicine*, vol. 24, no. 7, pp. 824–835, 2011.
- [23] S. Cavassila, S. Deval, C. Huegen, D. van Ormondt, and D. Graveron-Demilly, "Cramér-Rao bounds: an evaluation tool for quantitation," *NMR in Biomedicine*, vol. 14, no. 4, pp. 278–283, 2001.
- [24] R. Kreis, "Issues of spectral quality in clinical  $^1H$ -magnetic resonance spectroscopy and a gallery of artifacts," *NMR in Biomedicine*, vol. 17, no. 6, pp. 361–381, 2004.
- [25] M. G. Kounelakis, I. N. Dimou, M. E. Zervakis et al., "Strengths and weaknesses of 1.5T and 3T MRS data in brain glioma classification," *IEEE Transactions on Information Technology in Biomedicine*, vol. 15, no. 4, pp. 647–654, 2011.
- [26] L. S. Hu, L. C. Baxter, D. S. Pinnaduwaage et al., "Optimized prelude leakage-correction methods to improve the diagnostic accuracy of dynamic susceptibility-weighted contrast-enhanced perfusion MR imaging in posttreatment gliomas," *American Journal of Neuroradiology*, vol. 31, no. 1, pp. 40–48, 2010.
- [27] D. H. J. Poot, A. J. den Dekker, E. Achten, M. Verhoye, and J. Sijbers, "Optimal experimental design for diffusion kurtosis imaging," *IEEE Transactions on Medical Imaging*, vol. 29, no. 3, pp. 819–829, 2010.
- [28] E. S. Hui, M. M. Cheung, L. Qi, and E. X. Wu, "Towards better MR characterization of neural tissues using directional diffusion kurtosis analysis," *NeuroImage*, vol. 42, no. 1, pp. 122–134, 2008.
- [29] T. Cover and P. Hart, "Nearest neighbor pattern classification," *IEEE Transactions on Information Theory*, vol. 13, no. 1, pp. 21–27, 1967.
- [30] G. A. Seber, *Multivariate Observations*, vol. 252, John Wiley & Sons, New York, NY, USA, 2009.
- [31] C. Cortes and V. Vapnik, "Support-vector networks," *Machine Learning*, vol. 20, no. 3, pp. 273–297, 1995.
- [32] N. Cristianini and J. Shawe-Taylor, *An Introduction to Support Vector Machines and Other Kernel-Based Learning Methods*, Cambridge University Press, Cambridge, UK, 2000.
- [33] L. Breiman, J. Friedman, C. J. Stone, and R. A. Olshen, *Classification and Regression Trees*, CRC Press, Boca Raton, Fla, USA, 1984.
- [34] K. Hornik, M. Stinchcombe, and H. White, "Multilayer feedforward networks are universal approximators," *Neural Networks*, vol. 2, no. 5, pp. 359–366, 1989.
- [35] M. T. Hagan and M. B. Menhaj, "Training feedforward networks with the Marquardt algorithm," *IEEE Transactions on Neural Networks*, vol. 5, no. 6, pp. 989–993, 1994.
- [36] F. Rosenblatt, *Principles of Neurodynamics; Perceptrons and the Theory of Brain Mechanisms*, Spartan Books, Washington, DC, USA, 1962.

- [37] R. P. Lippmann, "An introduction to computing with neural nets," *IEEE ASSP magazine*, vol. 4, no. 2, pp. 4–22, 1987.
- [38] L. Breiman, "Random forests," *Machine Learning*, vol. 45, no. 1, pp. 5–32, 2001.
- [39] L. Breiman, "Bagging predictors," *Machine Learning*, vol. 24, no. 2, pp. 123–140, 1996.
- [40] Y. Freund and R. E. Schapire, "A decision-theoretic generalization of on-line learning and an application to boosting," in *Computational Learning Theory*, pp. 23–37, Springer, 1995.
- [41] J. Friedman, T. Hastie, R. Tibshirani et al., "Additive logistic regression: a statistical view of boosting (with discussion and a rejoinder by the authors)," *The Annals of Statistics*, vol. 28, no. 2, pp. 337–407, 2000.
- [42] Y. Freund, "A more robust boosting algorithm," <http://arxiv.org/abs/0905.2138>.
- [43] C. Seiffert, T. M. Khoshgoftaar, J. Van Hulse, and A. Napolitano, "RUSBoost: improving classification performance when training data is skewed," in *Proceedings of the 19th International Conference on Pattern Recognition (ICPR '08)*, pp. 1–4, Tampa, Fla, USA, 2008.
- [44] J. A. K. Suykens and J. Vandewalle, "Least squares support vector machine classifiers," *Neural Processing Letters*, vol. 9, no. 3, pp. 293–300, 1999.
- [45] J. A. Suykens, T. Van Gestel, J. De Brabanter et al., *Least Squares Support Vector Machines*, vol. 4, World Scientific, 2002.
- [46] ESAT, <http://www.esat.kuleuven.be/sista/lssvmlab/>.
- [47] K. de Brabanter, P. Karsmakers, F. Ojeda et al., "Ls-svmlab toolbox users guide," ESAT-SISTA Technical Report, 2011.
- [48] O. Chapelle and A. Zien, *Semi-Supervised Classification by Low Density Separation*, 2004.
- [49] G. Niu, W. Jitkrittum, B. Dai, H. Hachiya, and M. Sugiyama, "Squared-loss mutual information regularization: a Novel information-theoretic approach to semi-supervised learning," in *Proceedings of the 30th International Conference on Machine Learning (ICML '13)*, pp. 1047–1055, June 2013.
- [50] Y.-F. Li and Z.-H. Zhou, "Towards making unlabeled data never hurt," *IEEE Transactions on Pattern Analysis and Machine Intelligence*, vol. 37, no. 1, pp. 175–188, 2011.
- [51] X. Zhu and A. B. Goldberg, *Introduction to Semi-Supervised Learning*, vol. 3 of *Synthesis Lectures on Artificial Intelligence and Machine Learning*, Morgan & Claypool, 2009.
- [52] M. Sugiyama, 2014, <http://www.ms.k.u-tokyo.ac.jp/software.html>.
- [53] LAMDA, <http://lamda.nju.edu.cn/Data.ashx>.
- [54] O. Chapelle, <http://olivier.chapelle.cc/lds/>.
- [55] R. F. Barajas Jr., J. S. Chang, M. R. Segal et al., "Differentiation of recurrent glioblastoma multiforme from radiation necrosis after external beam radiation therapy with dynamic susceptibility-weighted contrast-enhanced perfusion MR imaging," *Radiology*, vol. 253, no. 2, pp. 486–496, 2009.
- [56] L. S. Hu, J. M. Eschbacher, J. E. Heiserman et al., "Reevaluating the imaging definition of tumor progression: perfusion MRI quantifies recurrent glioblastoma tumor fraction, pseudoprogression, and radiation necrosis to predict survival," *Neuro-Oncology*, vol. 14, no. 7, pp. 919–930, 2012.
- [57] X. Hu, K. K. Wong, G. S. Young, L. Guo, and S. T. Wong, "Support vector machine multiparametric MRI identification of pseudoprogression from tumor recurrence in patients with resected glioblastoma," *Journal of Magnetic Resonance Imaging*, vol. 33, no. 2, pp. 296–305, 2011.
- [58] P. Weybright, P. C. Sundgren, P. Maly et al., "Differentiation between brain tumor recurrence and radiation injury using MR spectroscopy," *The American Journal of Roentgenology*, vol. 185, no. 6, pp. 1471–1476, 2005.

## Clinical Study

# MRI for Assessing Response to Neoadjuvant Therapy in Locally Advanced Rectal Cancer Using DCE-MR and DW-MR Data Sets: A Preliminary Report

**Mario Petrillo,<sup>1</sup> Roberta Fusco,<sup>1</sup> Orlando Catalano,<sup>1</sup> Mario Sansone,<sup>2</sup> Antonio Avallone,<sup>3</sup> Paolo Delrio,<sup>4</sup> Biagio Pecori,<sup>5</sup> Fabiana Tatangelo,<sup>6</sup> and Antonella Petrillo<sup>1</sup>**

<sup>1</sup>Division of Radiology, Department of Diagnostic Imaging, Radiant and Metabolic Therapy, Istituto Nazionale Tumori-IRCCS “Fondazione Giovanni Pascale”, Via Mariano Semmola, 80131 Naples, Italy

<sup>2</sup>Department of Electrical Engineering and Information Technologies, University of Naples Federico II, Via Claudio 21, 80125 Naples, Italy

<sup>3</sup>Division of Gastrointestinal Medical Oncology, Department of Abdominal Oncology, Istituto Nazionale Tumori-IRCCS “Fondazione Giovanni Pascale”, Via Mariano Semmola, 80131 Naples, Italy

<sup>4</sup>Division of Gastrointestinal Surgical Oncology, Department of Abdominal Oncology, Istituto Nazionale Tumori-IRCCS “Fondazione Giovanni Pascale”, Via Mariano Semmola, 80131 Naples, Italy

<sup>5</sup>Division of Radiotherapy, Department of Diagnostic Imaging, Radiant and Metabolic Therapy, Istituto Nazionale Tumori-IRCCS “Fondazione Giovanni Pascale”, Via Mariano Semmola, 80131 Naples, Italy

<sup>6</sup>Division of Diagnostic Pathology, Department of Diagnostic and Laboratory Pathology, Istituto Nazionale Tumori-IRCCS “Fondazione Giovanni Pascale”, Via Mariano Semmola, 80131 Naples, Italy

Correspondence should be addressed to Antonella Petrillo; [a.petrillo@istitutotumori.na.it](mailto:a.petrillo@istitutotumori.na.it)

Received 9 July 2014; Revised 8 May 2015; Accepted 13 May 2015

Academic Editor: Zhengchao Dong

Copyright © 2015 Mario Petrillo et al. This is an open access article distributed under the Creative Commons Attribution License, which permits unrestricted use, distribution, and reproduction in any medium, provided the original work is properly cited.

To evaluate MRI for neoadjuvant therapy response assessment in locally advanced rectal cancer (LARC) using dynamic contrast enhanced-MRI (DCE-MRI) and diffusion weighted imaging (DWI), we have compared magnetic resonance volumetry based on DCE-MRI ( $V(DCE)$ ) and on DWI ( $V(DWI)$ ) scans with conventional T2-weighted volumetry ( $V(C)$ ) in LARC patients after neoadjuvant therapy. Twenty-nine patients with LARC underwent MR examination before and after neoadjuvant therapy. A manual segmentation was performed on DCE-MR postcontrast images, on DWI ( $b$ -value 800 s/mm<sup>2</sup>), and on conventional T2-weighted images by two radiologists. DCE-MRI, DWI, and T2-weighted volumetric changes before and after treatment were evaluated. Nonparametric sample tests, interobserver agreement, and receiver operating characteristic curve (ROC) were performed. Diagnostic performance linked to DCE-MRI volumetric change was superior to T2-w and DW-MRI volumetric changes performance (specificity 86%, sensitivity 93%, and accuracy 93%). Area Under ROC (AUC) of  $V(DCE)$  was greater than AUCs of  $V(C)$  and  $V(DWI)$  resulting in an increase of 15.6% and 11.1%, respectively. Interobserver agreement between two radiologists was 0.977, 0.864, and 0.756 for  $V(C)$ ,  $V(DCE)$ , and  $V(DWI)$ , respectively.  $V(DCE)$  seems to be a promising tool for therapy response assessment in LARC. Further studies on large series of patients are needed to refine technique and evaluate its potential value.

## 1. Introduction

Rectal cancer is a frequent malignancy in both men and women, accounting for 40,290 new cases in the USA in 2012 [1]. Despite the efforts done to introduce screening programs, most patients are diagnosed in a locally advanced stage of the disease (T3-T4, Nx, and Mx). Total mesorectal excision

(TME) combined with preoperative radiation therapy and concurrent chemotherapy (pCRT) is the current standard for locally advanced rectal cancer (LARC) [2]. TME is associated with significant morbidity and functional complications, evolving conservative treatment strategies are being developed for patients with early rectal cancer at diagnosis and patients with significant/complete tumor regression after

pCRT. A further conservative strategy has been to adopt a “wait and see” policy, omitting surgery when a complete clinical response is obtained after pCRT. This strategy has the advantage of reducing morbidity and provides a “true” organ-sparing approach, considering that sphincter preservation without adequate function has questionable benefit. CRT induces tumor downstaging and complete or partial pathologic responses through vascular changes and cell death [3]: a pathologic complete response (pCR) was verified in up to 24% of patients. A pCR is known to be associated with a favorable oncologic outcome, with regard to both recurrence and survival [4, 5]. Morphological MRI evaluation (mMRI) is considered the best available tool for LARC staging, allowing an accurate evaluation of the disease extent, up to and beyond and over the mesorectal fascia, and of the lymph node involvement [6]. However, there are some limitations in depicting the changes after CRT through morphological MRI alone. A favorable tumor response may not correspond to an appreciable tumor size reduction. MR imaging, like other morphologic imaging techniques (endorectal ultrasonography and computed tomography) is hampered by interpretation difficulties in assessing the presence of residual tumor within areas of radiation-induced fibrosis [6]. Studies are therefore focusing on the potential added benefit of functional and/or quantitative methods of MR image evaluation. Functional MRI visualizes underlying biological characteristics of tumors, adding a new dimension to the morphological information from conventional MRI. The combination of objective MRI biomarkers with detailed morphological MRI makes MRI a potentially powerful response measurement tool that provides comprehensive information on tumor heterogeneity and changes in heterogeneity as a result of treatment. Dynamic contrast-enhanced MRI (DCE-MRI) has proven useful in detecting residual tumor after CRT [7]. Previous studies have been investigated functional parameters derived by DCE-MRI dataset for noninvasive response assessment in various malignancies, including rectal cancer [8, 9]. Moreover, in various oncology fields, researchers have recently suggested that diffusion-weighted imaging (DWI) can potentially be used to identify biomarkers of treatment response [3]. These assertions are based on the fact that DWI could provide individual tumor apparent diffusion coefficient (ADC) increase rates during the course of CRT, which could reflect biological tumor changes.

DCE and DW MR imaging after CRT were shown to be more valuable than morphologic MR imaging to recognize pathological response from residual tumor, because on DCE and DW images, viable tumor remnants are more easily recognized, as they appear hyperintense compared with the low signal intensity (SI) of the surrounding non neoplastic tissue. Hence, it can be hypothesized that volumetry of the tumor that is based on SI characteristics on DCE or DW images may be more accurate than conventional MR volumetry to distinguish between complete and noncomplete responders.

With this study, we aim to determine the diagnostic performance of DCE and DW imaging for the assessment of a pathological response after CRT in patients with LARC by means of volumetric SI measurements ( $V(DCE)$  and  $V(DWI)$ , resp.) and to compare the performance of DCE and

DW imaging with volumetry on conventional T2-weighted MR images.

## 2. Materials and Methods

**2.1. Patient Selection.** Twenty-nine consecutive patients with a median age of 62 years (range 29–76 years) were enrolled in this prospective study, from March 2010 to November 2013. All patients had a biopsy-proven rectal adenocarcinoma. Endorectal ultrasonography, MRI of the liver and pelvis, CT of the abdomen and pelvis, and chest X-ray were used as staging procedures. Inclusion criteria were patients with clinical T4, nodal involvement, or T3 N0 with a tumor location of  $\leq 5$  cm from the anal verge, or a circumferential resection margin of  $\leq 5$  mm, defined by MRI. Exclusion criteria were inability to give informed consent, previous rectal surgery, and contraindications to MRI or to MR contrast media. All patients were enrolled within the phase I-II prospective trial described in [10] which was approved by the Independent Ethical Committee of our institution. They all gave written informed consent to participate in the trial.

**2.2. Neoadjuvant Therapy.** External radiation therapy was performed using a 3-field technique (one posteroanterior and two lateral fields). Standard fractions of 1.8 Gy/day to the reference point were given, 5 times a week up to a total dose of 45 Gy. All patients received biweekly bevacizumab at 5 mg/kg plus three biweekly cycles of oxaliplatin at 100 mg/m<sup>2</sup> and raltitrexed at 2.5 mg/m<sup>2</sup>, on day 1, and levo-folinic acid at 250 mg/m<sup>2</sup>, and 5-Fluorouracil at 800 mg/m<sup>2</sup> on day 2 [2, 10].

**2.3. MRI Data Acquisitions.** All patients underwent DCE-MRI examination before and after pCRT (90 days on average, range 86–94 days between the two MRI evaluations). Imaging was performed with a 1.5 T scanner (Magnetom Symphony, Siemens Medical System, Erlangen, Germany) equipped with a phased-array body coil. Patients were placed in a supine, head-first position. Mild rectal lumen distension was achieved with 60–90 mL of nondiluted ferumoxil (Lumirem, Guerbet, RoissyCdGCedex, France) suspension introduced per rectum [11]. Precontrast coronal T1w 2D turbo spin-echo images and sagittal and axial T2w 2D turbo spin-echo images of the pelvis were obtained. After that, axial DWIs were acquired (spin-echo diffusion-weighted echo-planar imaging [SE-DW-EPI]) at three  $b$ -values of 0, 400, and 800 sec/mm<sup>2</sup>. Subsequently, axial, dynamic, contrast-enhanced T1w, FLASH 3D gradient-echo images were acquired. We obtained one sequence before and ten sequences, without any delay, after IV injection of 2 mL/kg of a positive, gadolinium-based paramagnetic contrast medium (Gd-DOTA, Dotarem, Guerbet, RoissyCdGCedex, France). The contrast medium was injected using Spectris Solaris EP MR (MEDRAD Inc., Indianola, PA), with a flow rate of 2 mL/s, followed by a 10 mL saline flush at the same rate. Temporal resolution was 0.58 minutes, corresponding to 35 seconds (as reported in Table 1). Total acquisition time for precontrast and ten postcontrast sequences was 6.4 minutes. Then, sagittal, axial, and coronal postcontrast T1w 2D turbo spin-echo images,

TABLE 1: Pulse sequence parameters on MR studies.

Sequence	Orientation	TR/TE/FA (ms/ms/deg.)	AT (min)	FOV (mm × mm)	Acquisition matrix	ST/Gap (mm/mm)	TF
T1w 2D TSE	Coronal	499/13/150	2.36	450 × 450	256 × 230	3/0	3
T2w 2D TSE	Sagittal	4820/98/150	4.17	260 × 236	256 × 139	3/0	13
T2w 2D TSE	Axial	3970/98/150	3.48	270 × 236	256 × 157	3/0	13
SE-DW-EPI	Axial	2700/83	6.37	136 × 160	160 × 102	4/0	/
T1w FLASH 3D	Axial	9.8/4.76/25	0.58	330 × 247	256 × 192	3/0	/
T1w FLASH 3D	Axial	9.8/4.76/25	0.58 × 10	330 × 247	256 × 192	3/0	/
T1w 2D TSE	Sagittal	538/13/150	2.35	250 × 250	256 × 230	3/0	5
T1w 2D TSE	Coronal	538/13/150	2.52	250 × 250	256 × 230	3/0	5
T1w 2D TSE	Axial	450/12/150	2.31	270 × 236	256 × 202	3/0	5

Note: TR = repetition time, TE = echo time, FOV = field of view, FA = flip angle, ST = slice thickness, TF = turbo factor, and AT = acquisition time.

with and without fat saturation were obtained (Table 1). The axial images were acquired without any angulation. Axial T1-w pre- and postcontrast sequences were acquired at the same position as the T2-w sequence. MRI total acquisition time was around 40 minutes. Patients did not receive bowel preparation, antispasmodic medication, or rectal distention before any of the MR examinations.

**2.4. Image Data Analysis.** The MR images were evaluated on a picture archiving and communication system and were independently analyzed by two radiologists with years of specific expertise reading pelvic MR images. The observers were blinded to each other's results, the clinical patient data, and pathology reports. The readers calculated tumor volumes by manually tracing the tumor boundaries slice by slice on DCE-MRI derived images obtained subtracting the basal and the 5th post-contrastographic series ( $V(DCE)$ ), on diffusion weighted image a  $b$ -value of  $800 \text{ s/mm}^2$  ( $V(DWI)$ ) and on conventional T2-weighted images ( $V(C)$ ).

Whole-tumor volume was then calculated considering the total number of pixel (slice by slice) and multiplying this by pixel size in  $\text{mm}^2$ . On the T2-weighted images, tumor was defined as areas of isointense signal as compared with the relatively lower hypointense signal of the normal adjacent muscular rectal wall. On post-CRT T2-weighted MR images, areas of markedly low SI at the location of the primary tumor bed were interpreted as fibrosis. As the risk for residual tumor in these fibrotic areas is known to be  $\pm 50\%$ , they were also included in the volumetric measurements [12]. On DCE-MRI data sets, measurements were performed on subtraction images considering basal signal and 5th postcontrastographic series. Area of hyper-intense signal compared with normal bowel wall or background of lower SI tissue, were considered as tumor. On the DW images, measurements were performed on high  $b$  value ( $800 \text{ sec/mm}^2$ ) images and were based on a visual analysis. To avoid errors due to T2 shine effect only areas with high SI on high- $b$  value images and low SI on ADC maps, when compared with the normal bowel wall or background of lower SI tissue on high- $b$  value images, were considered tumor.

For each data sets (DCE, DWI, and T2-weighted), the readers determined (a) pre-CRT tumor volume; (b) post-CRT

tumor volume (TV); and (c) the tumor volume reduction ratio ( $\Delta$  volume), which was calculated as follows:  $(TV_{\text{pre}} - TV_{\text{post}}) \times 100 / TV_{\text{pre}}$ , where  $TV_{\text{pre}}$  is pre-CRT tumor volume and  $TV_{\text{post}}$  is post-CRT tumor volume.

### 2.5. Surgical Approach and Evaluation of Pathologic Response.

All patients underwent total mesorectal excision after completing pCRT. An anterior resection or an abdominoperineal resection was performed on the basis of the results of post-CRT restaging. The surgical specimens containing the tumor were processed and evaluated by a single pathologist who was not aware of the clinical and MRI findings. Specimens were examined according to the Sixth American Joint Committee on Cancer TNM staging system. The tumor regression grade (TRG) was evaluated according to the method of Mandard et al. [13, 14]. TRG 1 means a complete response with absence of residual cancer and fibrosis extending through the wall. TRG 2 is the presence of residual cancer cells scattered through the fibrosis. TRG 3 corresponds to the presence of fibrosis and tumor cells, with predominancy of fibrosis. TRG 4 indicates as fibrosis and tumor cells, with predominancy of tumor cells. TRG 5 is the absence of regressive changes. Patients with a TRG 1 or 2 score were considered as responders, whereas the remaining patients (TRG 3, 4, or 5) were classified as not responders [9].

**2.6. Statistical Analysis.** Tumor volume percentage changes of the responder and nonresponder groups were analyzed using the Mann-Whitney test. A Wilcoxon signed-rank test was used to compare pre- and post-CRT volumes. Receiver Operating Characteristic (ROC) curves were also used to compare the diagnostic performance of  $V(DCE)$ ,  $V(DWI)$  and  $V(C)$  reduction rates after pCRT. Area Under ROC Curve (AUC) were calculated [15] and optimal thresholds were obtained maximizing the Youden index [16]. Sensitivity, specificity, positive predictive value and negative predictive value were performed considering optimal cut-off values. Fischer exact tests were used to investigate if results were statistically significant. Interobserver agreement was also obtained using interobserver correlation coefficient (ICC) for continuous variables (0–0.20, poor agreement; 0.21–0.40, fair agreement; 0.41–0.60, moderate agreement; 0.61–0.80, good agreement; and 0.81–1.00, excellent agreement).

A  $p$  value  $< 0.05$  was considered significant for all tests. All analyses were performed using Statistics Toolbox of Matlab R2007a (The Math-Works Inc., Natick, MA).

### 3. Results

Histopathologic analysis of the surgical specimen yielded the following findings: 5 patients had T0, 6 had T1, 14 had T2, 3 had T3, and 1 had T4 tumor. Five patients had TRG 1, 9 patients had TRG 2, 7 patients had TRG 3, and 8 patients had TRG 4.

Table 2 shows patient characteristics and volume changes assessed by the three volumetric methods: T2-w volumetric change, DCE-MRI volumetric change and DW-MRI volumetric change. Table 3 shows median and standard deviation values of volumes assessed by three volumetric approaches before and after treatment. Wilcoxon's test findings reported significant decreases in volumetric measures, between pre- and posttreatment, assessed with all methods (Table 3):  $V(C)$  median value decreased from  $36.9 \text{ cm}^3$  to  $16.7 \text{ cm}^3$ ;  $V(DCE)$  median value decreased from  $30.9 \text{ cm}^3$  to  $16.5 \text{ cm}^3$ ;  $V(DWI)$  median value decreased from  $14.59 \text{ cm}^3$  to  $6.0 \text{ cm}^3$  ( $p < 0.01$ ).

Statistically significant differences between responders and not responders, in the volumetric percentage changes were obtained by Mann-Whitney test for all volumetric approaches (Table 3) and these were visualized in boxplots (Figure 1). Table 4 reports the performance of three volumetric methods in terms of sensitivity, specificity, and area under ROC. Optimal cut-off values were also reported. The results are statistically significant (Fisher test  $p < 0.01$ ).

According to TRG, DCE-MRI volume estimations change after pCRT showed best results in terms of specificity, sensitivity, and accuracy, respectively, of 86%, 93%, and 93%.  $V(C)$  showed a significant correlation between response and TRG with a sensitivity, a specificity and an accuracy, respectively, of 86%, 73%, and 79% (37% cut-off, AUC 0.76), and  $V(DWI)$  showed a sensitivity, a specificity and an accuracy, respectively, of 64%, 94%, and 76% (39% cut-off, AUC 0.81). Figure 2 shows ROCs for three volumetric approaches. AUC of  $V(DCE)$  change is superior of AUCs of  $V(C)$  change and  $V(DWI)$  change resulting an increase of 15.6% and of 11.1%, respectively.

Interobserver agreement was 0.977 (95% confidence interval (CI) 0.954–0.989), 0.864 (95% CI 0.835–0.884), and 0.756 (95% CI 0.705–0.780) for  $V(C)$ ,  $V(DCE)$ , and  $V(DWI)$ .

### 4. Discussion

**4.1. Synopsis of New Findings.** The focus of this study was to clarify the association between manual tumor volume estimations obtained by T2-weighted imaging, DWI, DCE-MRI images, and TRG to predict LARC response after pCRT. This study shows that manual tumor volume estimation using DCE-MRI can furnish better performance in terms of sensitivity, specificity, and accuracy. To the best of our knowledge, no prior studies have compared the performances of manual tumor volume measurements on T2-weighted (T2-w), DWI, and DCE-MRI images to predict LARC response after pCRT.

TABLE 2: Patient characteristics with volumetric change for individual patient.

Patient number	Age	pT	pN	TRG	V(C) change [%]	V(DCE) change [%]	V(DWI) change [%]
1	74	2	0	4	37,10	33,28	38,86
2	50	1	0	2	70,76	91,34	61,08
3	75	1	0	3	-96,50	29,88	36,67
4	54	1	0	2	61,22	67,40	-5,60
5	50	2	0	2	77,65	35,07	81,40
6	58	0	0	1	52,36	46,52	7,69
7	57	1	0	3	53,18	-3,71	62,42
8	67	0	0	1	80,34	70,57	72,33
9	70	1	1	2	59,99	39,59	46,72
10	75	2	0	2	77,81	78,21	22,49
11	78	2	1	3	8,85	-38,50	1,51
12	68	2	0	3	20,20	27,42	18,58
13	48	0	0	1	92,84	86,56	92,89
14	44	2	1	3	2,37	21,72	3,00
15	59	4	0	4	94,93	8,51	24,50
16	60	1	0	2	-4,52	28,52	39,50
17	63	2	0	3	21,73	13,52	-86,38
18	58	2	0	4	35,39	-2,57	43,52
19	44	2	0	4	66,01	34,08	22,63
20	63	3	1	4	28,05	3,26	-77,05
21	69	2	1	2	48,51	44,32	64,58
22	76	2	1	2	42,17	68,19	25,73
23	72	0	0	1	85,58	79,34	84,50
24	61	2	0	4	14,12	-83,35	-45,41
25	64	3	1	4	-45,75	20,64	21,25
26	58	3	0	3	44,51	18,94	28,28
27	76	2	0	2	50,72	60,61	36,40
28	77	2	0	4	13,16	75,04	-16,52
29	57	0	1	1	-23,73	12,45	49,65

Note: pT = pathological T stage; pN = pathological N stage;  $V(C)$  = conventional T2-weighted volumetry;  $V(DWI)$  = diffusion-weighted imaging volumetry;  $V(DCE)$  = dynamic contrast enhanced volumetry.

**4.2. Comparisons with Other Studies.** Tumor volume has been proven to be an important prognostic indicator for a variety of tumors, although the extra workload necessary to perform manual tumor volume measurements on MRI images have limited its applications in clinical routine. The goal to be achieved after pCRT for LARC is pathologic complete response. The latter could be assessed using the TRG, a pathological score widely considered as a potential tool to guide therapy in patients with LARC being an independent predictor of the likelihood of local recurrence, distant metastasis, and overall and disease-free survival [5]. Many approaches using MRI have been investigated to compare response after pCRT with TRG. The correlation shown between MR tumor volume estimation on T2-w images and the pCR has been the subject of many reports

TABLE 3: Volume measures assessed by the three volumetric methods (V(C), V(DCE), and V(DWI)).

Tool	All ( <i>n</i> = 29)	Responders ( <i>n</i> = 14)	Nonresponders ( <i>n</i> = 15)	<i>p</i> value
V(C)				
Pre-CRT [cm <sup>3</sup> ]	36.9 ± 34.4	30.6 ± 22.6	38.4 ± 26.6	
Post-CRT [cm <sup>3</sup> ]	16.7 ± 8.8	12.4 ± 6.9	20.6 ± 9.5	
Volume change [%]	44.5 ± 43.0	60.6 ± 33.2	21.7 ± 46.6	<0.001*
V(DCE)				
Pre-CRT [cm <sup>3</sup> ]	30.9 ± 29.1	31.4 ± 23.7	33.9 ± 25.4	
Post-CRT [cm <sup>3</sup> ]	18.5 ± 8.1	11.1 ± 6.7	24.7 ± 10.8	
Volume change [%]	33.3 ± 38.4	64.0 ± 23.7	19.0 ± 36.9	<0.001*
V(DWI)				
Pre-CRT [cm <sup>3</sup> ]	14.6 ± 12.6	12.5 ± 10.1	15.8 ± 9.3	
Post-CRT [cm <sup>3</sup> ]	9.0 ± 5.1	6.4 ± 4.4	7.9 ± 5.5	
Volume change [%]	28.3 ± 43.1	48.2 ± 30.0	21.2 ± 44.0	<0.001*

Note: results are expressed as median value ± standard deviation.

\*Wilcoxon signed-rank test.

CRT, chemoradiation therapy; V(C), conventional T2-weighted volumetry; V(DWI), diffusion-weighted imaging volumetry; V(DCE), dynamic contrast enhanced volumetry.

TABLE 4: Performance of volumetric approaches (V(C), V(DCE), and V(DWI)).

	Sensitivity [%]	Specificity [%]	Accuracy [%]	Cut-off [%]	AUC
V(C) change	0.86	0.73	0.79	37.4	0.76
V(DCE) change	0.86	0.93	0.93	34.2	0.90
V(DWI) change	0.64	0.94	0.76	39.1	0.81

Note: V(C), conventional T2-weighted volumetry; V(DWI), diffusion-weighted imaging volumetry; V(DCE), dynamic contrast enhanced volumetry; AUC, area under ROC.

[17–19], even if conflicting results were reported: Kang et al. [20] showed a significant association with pCR for patients with a tumor volume reduction rate of more than 75%, whilst Kim et al. [21] observed no significant difference between patient with a pCR and those with residual disease. DW-MRI is an alternative technique potentially able to overcome part of V(C) limits, being capable of showing viable neoplastic tissue due to its reliability in detecting the restricted proton diffusion in hypercellular tissues with high nucleocytoplasmic ratio. According to some authors, the volume measurements obtained on post-CRT DW MR images were significantly more accurate than those obtained on post-CRT T2-w MR images to assess pathological complete response [22–25]. DCE-MRI is another technique that can provide functional information on tumor viability deriving tumoral neoangiogenic changes linked to contrast medium kinetics. Many authors described its potential advantages in predict response to therapy in different tumors [5–7], where neoformed tumor capillaries, being leaky, can determine a rapid gadolinium uptake, an early wash-out and overall shorter first pass, especially if compared with healthy tissues. Moreover, this kinetic behavior of contrast agent in DCE-MRI has been observed as correlated with some biomarkers expressed by highly vascularized tumoral tissues, such as the vascular endothelial growth factor expression and the microvessel density [7–9, 26]. Volumetric measure could be utilized in association with functional quantitative MRI parameters to increase their accuracy for tumor response

therapy assessment. In fact, a recent study of Bajpai et al. [27] reported that apparent diffusion coefficient obtained on DW-MRI did not correlate with necrosis after chemotherapy in osteosarcoma but on adjusting for volume (apparent diffusion coefficient per unit volume); significant correlation was found and this appears to be a sensitive substitute for response evaluation in osteosarcoma. Future investigations could be done using these recent findings.

However, few authors have proposed a tumor volume estimation based on DCE-MRI images, using a manual or an automatic segmentation, mainly focusing their works on breast cancer [27, 28]. Moreover, to the best of our knowledge, no study has investigated the association between these volumes measured by DCE-MRI and TRG in LARC.

**4.3. Study Limitations.** V(C) showed a significant correlation between response and TRG with a sensitivity, a specificity and an accuracy, respectively, of 86%, 73%, and 79% (37% cut-off, AUC 0.76). Despite the excellent agreement between observers (0.977), understaging was present in 5 patients in which were assessed a decrease in volume >38% and a TRG of 3 or 4, confirming that T2-w volume assessment alone is not sufficiently accurate, being not able to identify between the persistence of viable tissue and the peritumoral fibrosis present after radiation therapy. Moreover, according to observers, was difficult to decide which fibrotic areas, remaining suspicious for tumor on T2-w images, should be included in the volume measurements and which should not.

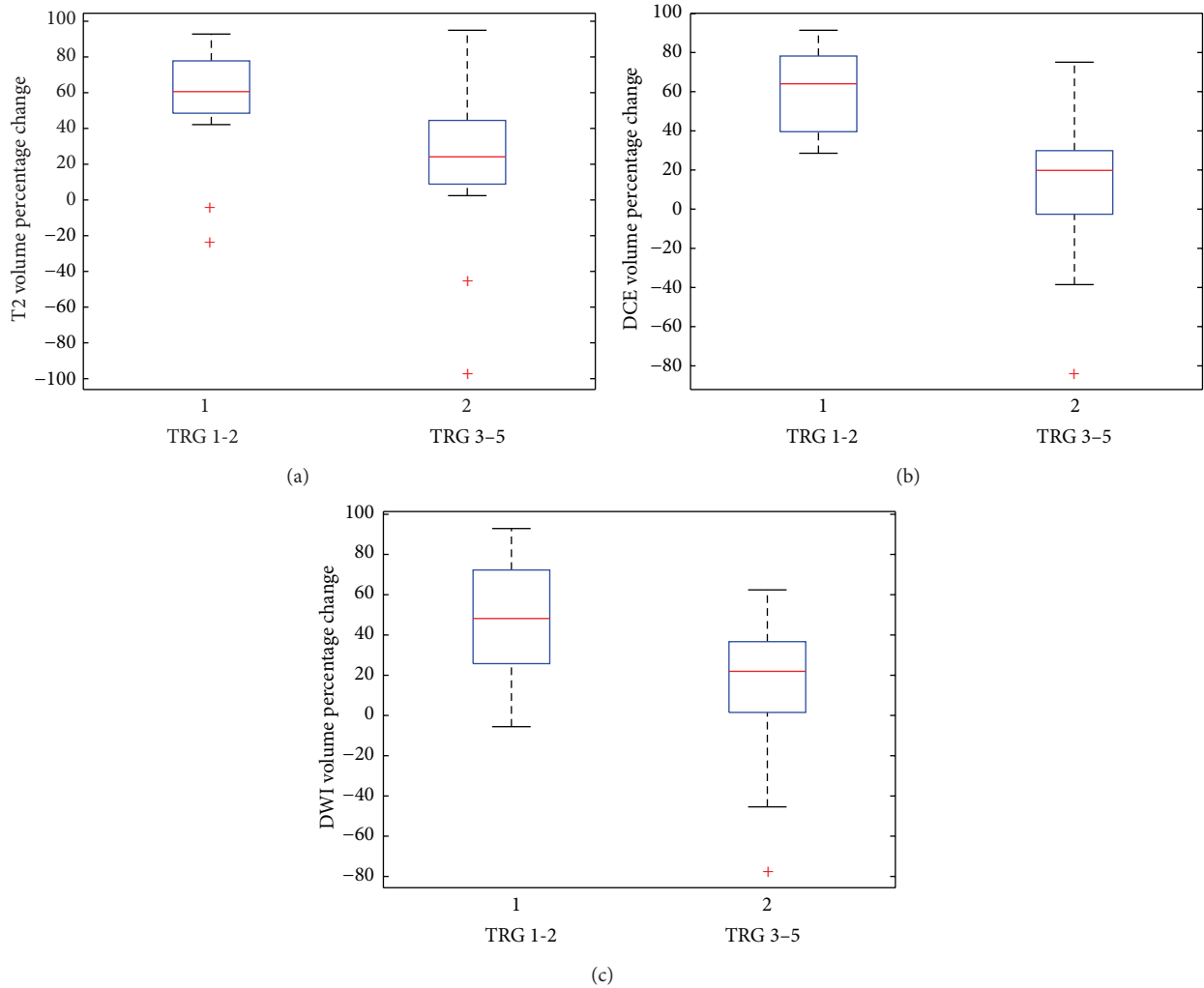


FIGURE 1: Boxplots of three volumetric approaches: (a) shows  $V(C)$  boxplot, (b) shows  $V(DCE)$  boxplot, and (c) shows  $V(DWI)$  boxplot. The middle line is the median value. The inferior and superior extremes of the box correspond to the first and third quartiles, respectively. The whiskers lines correspond to values within 1.5 times the interquartile range from the ends of the box. Outlier data beyond the ends of the whiskers are displayed with a + sign.

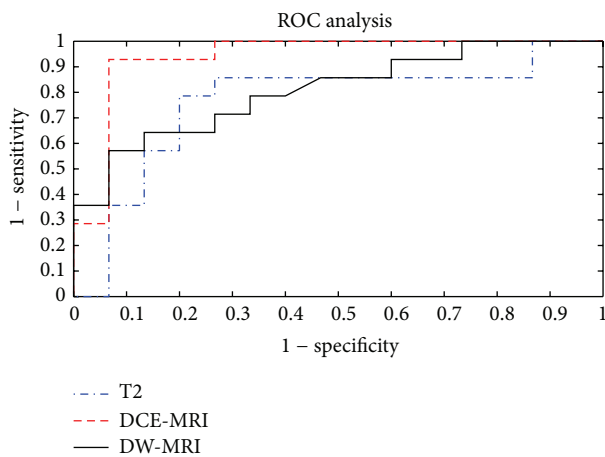


FIGURE 2: ROCs of three volumetric approaches ( $V(C)$ ,  $V(DCE)$ , and  $V(DWI)$ ).

$V(DWI)$  showed a sensitivity, a specificity, and an accuracy, respectively, of 64%, 94%, and 76% (39% cut-off, AUC 0.81) confirming the ability of  $V(DWI)$  in reducing the understaging observed with  $V(C)$  estimations. The agreement between observers was good (0.756) and both observers during segmentation easily and quickly recognized high-SI areas of “viable tumor” thus avoiding the inclusion of fibrotic areas that, due to their poor water content coupled with lower nucleocytoplasmic ratio, were not visible on either high  $b$ -value images and ADC maps. However, the low sensitivity of 64% obtained in our series reflects some intrinsic limits of  $V(DWI)$  measurements: during evaluation it is mandatory to remember that small bleedings or friable haemorrhagic/necrotic tissues can impact negatively on DW evaluations, causing field inhomogeneity due to susceptibility artefacts that, causing “enlargement” and “distortion” of “bright” areas on  $b$ -800 images, can make the tumor segmentation not accurate; the low spatial resolution with relative

“small voxels” obtained, despite the large Field of View (FOV) used, can be a source of wide differences in estimated volumes causing tumor overestimation on post-CRT scans. Moreover, to reduce potential sources of false negative due to overestimation of residual tumor, a comparative evaluation with ADC maps is mandatory when areas of necrosis are identified and can be wrongly included in tumor being recognised like bright areas on images acquired with high  $b$ -values ( $\geq b=800$ ) due to the “T2 shine effect” [29].  $V(DCE)$  showed best results with a sensitivity, a specificity, and an accuracy, respectively, of 86%, 93%, and 93% (34% cut-off, AUC 0.90) coupled with an excellent agreement between observers (0.864). Under staging, only in 1 patient was present that, although showing a great decrease in volume >37% on pCRT scan (75%), showed a TRG of 4. This false negative was probably due to the tumor appearance, which was mainly vegetant, with a great decrease in volume on  $V(DCE)$  measurements particularly on lumen side, whilst the persisting extramural viable tumor tissue was more easily detectable on T2-w and DW scans (as large spiculae in mesorectal fat-pad or high intensity areas on  $b=800$  images). Only 2 patients were false positive: these patients constituted the main limit of  $V(DCE)$  segmentation. The choice of segmenting tumor on subtracted images obtained after 140s from contrast agent administration led to an inclusion of those areas in which inflammation phenomena were prominent (areas characterized by a continuous rise in SI followed by a stable intensity over the time) with an intrinsic potential overestimation, mainly on after pCRT scans. However, being  $V(DCE)$  focussed to identify “not effective” neoadjuvant treatments a false positive could be more tolerated than a false negative.

**4.4. Clinical Applicability of the Study.** Despite interesting results in terms of overall performance of  $V(DCE)$ , currently, standard methods for tumor volume assessment based on manual delineation of volumes are time consuming. The mean time required to perform a volume measurement using multiple ROIs was approximately 10–15 minutes when pre- and post-CRT scans were considered and experienced radiologists employed, which is impractical. Therefore, semi-automated segmentation is needed.

## 5. Conclusions

In literature comparative studies between DCE-MRI, DW-MRI, and conventional MR volumetry are not present to assess therapy response evaluation after pCRT in LARC. In our series, manual segmentation of tumor volumes, made on DCE-MRI subtracted images, showed the best results in terms of sensitivity, specificity, and accuracy. When these results are validated in a larger prospective study and semiautomated software will be available they could be implemented in routine practice.

## Conflict of Interests

The authors declare that there is no conflict of interests regarding the publication of this paper.

## References

- [1] R. Siegel, D. Naishadham, and A. Jemal, “Cancer statistics, 2012,” *CA Cancer Journal for Clinicians*, vol. 62, no. 1, pp. 10–29, 2012.
- [2] A. Avallone, P. Delrio, C. Guida et al., “Biweekly oxaliplatin, raltitrexed, 5-fluorouracil and folinic acid combination chemotherapy during preoperative radiation therapy for locally advanced rectal cancer: a phase I-II study,” *British Journal of Cancer*, vol. 94, no. 12, pp. 1809–1815, 2006.
- [3] D. Jennings, B. N. Hatton, J. Guo et al., “Early response of prostate carcinoma xenografts to docetaxel chemotherapy monitored with diffusion MRI,” *Neoplasia*, vol. 4, no. 3, pp. 255–262, 2002.
- [4] N. A. Janjan, C. Crane, B. W. Feig et al., “Improved overall survival among responders to preoperative chemoradiation for locally advanced rectal cancer,” *American Journal of Clinical Oncology: Cancer Clinical Trials*, vol. 24, no. 2, pp. 107–112, 2001.
- [5] M. Maas, P. J. Nelemans, V. Valentini et al., “Long-term outcome in patients with a pathological complete response after chemoradiation for rectal cancer: a pooled analysis of individual patient data,” *The Lancet Oncology*, vol. 11, no. 9, pp. 835–844, 2010.
- [6] R. G. H. Beets-Tan and G. L. Beets, “Rectal cancer: review with emphasis on MR imaging,” *Radiology*, vol. 232, no. 2, pp. 335–346, 2004.
- [7] M. O. Leach, K. M. Brindle, J. L. Evelhoch et al., “The assessment of antiangiogenic and antivascular therapies in early-stage clinical trials using magnetic resonance imaging: issues and recommendations,” *British Journal of Cancer*, vol. 92, no. 9, pp. 1599–1610, 2005.
- [8] C. Hayes, A. R. Padhani, and M. O. Leach, “Assessing changes in tumour vascular function using dynamic contrast-enhanced magnetic resonance imaging,” *NMR in Biomedicine*, vol. 15, no. 2, pp. 154–163, 2002.
- [9] M. Z. Xiao, D. Yu, L. Z. Hong et al., “3D dynamic contrast-enhanced MRI of rectal carcinoma at 3T: correlation with microvascular density and vascular endothelial growth factor markers of tumor angiogenesis,” *Journal of Magnetic Resonance Imaging*, vol. 27, no. 6, pp. 1309–1316, 2008.
- [10] A. Avallone, P. Delrio, B. Pecori et al., “Oxaliplatin plus dual inhibition of thymidilate synthase during preoperative pelvic radiotherapy for locally advanced rectal carcinoma: long-term outcome,” *International Journal of Radiation Oncology, Biology, Physics*, vol. 79, no. 3, pp. 670–676, 2011.
- [11] A. Petrillo, O. Catalano, P. Delrio et al., “Post-treatment fistulas in patients with rectal cancer: MRI with rectal superparamagnetic contrast agent,” *Abdominal Imaging*, vol. 32, no. 3, pp. 328–331, 2007.
- [12] R. F. A. Vliegen, G. L. Beets, G. Lammering et al., “Mesorectal fascia invasion after neoadjuvant chemotherapy and radiation therapy for locally advanced rectal cancer: accuracy of MR imaging for prediction,” *Radiology*, vol. 246, no. 2, pp. 454–462, 2008.
- [13] A.-M. Mandard, F. Dalibard, J.-C. Mandard et al., “Pathologic assessment of tumor regression after preoperative chemoradiotherapy of esophageal carcinoma: clinicopathologic correlations,” *Cancer*, vol. 73, no. 11, pp. 2680–2686, 1994.
- [14] C. A. M. Marijnen, I. D. Nagtegaal, E. Kapiteijn et al., “Radiotherapy does not compensate for positive resection margins in rectal cancer patients: report of a multicenter randomized trial,” *International Journal of Radiation Oncology Biology Physics*, vol. 55, no. 5, pp. 1311–1320, 2003.

- [15] E. R. DeLong, D. M. DeLong, and D. L. Clarke-Pearson, "Comparing the areas under two or more correlated receiver operating characteristic curves: a nonparametric approach," *Biometrics*, vol. 44, no. 3, pp. 837–845, 1988.
- [16] E. F. Schisterman, N. J. Perkins, A. Liu, and H. Bondell, "Optimal cut-point and its corresponding Youden index to discriminate individuals using pooled blood samples," *Epidemiology*, vol. 16, no. 1, pp. 73–81, 2005.
- [17] M. R. Torkzad, J. Lindholm, A. Martling, B. Cedermark, B. Glimelius, and L. Blomqvist, "MRI after preoperative radiotherapy for rectal cancer; correlation with histopathology and the role of volumetry," *European Radiology*, vol. 17, no. 6, pp. 1566–1573, 2007.
- [18] V. R. Muthusamy and K. J. Chang, "Optimal methods for staging rectal cancer," *Clinical Cancer Research*, vol. 13, no. 22, pp. 6877–6884, 2007.
- [19] MERCURY Study Group, "Diagnostic accuracy of preoperative magnetic resonance imaging in predicting curative resection of rectal cancer: prospective observational study," *The British Medical Journal*, vol. 333, no. 7572, pp. 779–784, 2006.
- [20] J. H. Kang, Y. C. Kim, H. Kim et al., "Tumor volume changes assessed by three-dimensional magnetic resonance volumetry in rectal cancer patients after preoperative chemoradiation: the impact of the volume reduction ratio on the prediction of pathologic complete response," *International Journal of Radiation Oncology Biology Physics*, vol. 76, no. 4, pp. 1018–1025, 2010.
- [21] Y. H. Kim, D. Y. Kim, T. H. Kim et al., "Usefulness of magnetic resonance volumetric evaluation in predicting response to preoperative concurrent chemoradiotherapy in patients with resectable rectal cancer," *International Journal of Radiation Oncology, Biology, Physics*, vol. 62, no. 3, pp. 761–768, 2005.
- [22] L. Curvo-Semedo, D. M. J. Lambregts, M. Maas et al., "Rectal cancer: assessment of complete response to preoperative combined radiation therapy with chemotherapy—conventional MR volumetry versus diffusion-weighted MR imaging," *Radiology*, vol. 260, no. 3, pp. 734–743, 2011.
- [23] S. F. Carbone, L. Pirtoli, V. Ricci et al., "Assessment of response to chemoradiation therapy in rectal cancer using MR volumetry based on diffusion-weighted data sets: a preliminary report," *Radiologia Medica*, vol. 117, no. 7, pp. 1112–1124, 2012.
- [24] S. F. Carbone, L. Pirtoli, V. Ricci et al., "Diffusion-weighted MR volumetry for assessing the response of rectal cancer to combined radiation therapy with chemotherapy," *Radiology*, vol. 263, no. 1, article 311, 2012.
- [25] Y. C. Kim, J. S. Lim, K. C. Keum et al., "Comparison of diffusion-weighted MRI and MR volumetry in the evaluation of early treatment outcomes after preoperative chemoradiotherapy for locally advanced rectal cancer," *Journal of Magnetic Resonance Imaging*, vol. 34, no. 3, pp. 570–576, 2011.
- [26] J. Bajpai, S. Gamanagatti, M. C. Sharma et al., "Noninvasive imaging surrogate of angiogenesis in osteosarcoma," *Pediatric Blood and Cancer*, vol. 54, no. 4, pp. 526–531, 2010.
- [27] J. Bajpai, S. Gamanagatti, R. Kumar et al., "Role of MRI in osteosarcoma for evaluation and prediction of chemotherapy response: correlation with histological necrosis," *Pediatric Radiology*, vol. 41, no. 4, pp. 441–450, 2011.
- [28] A. Yi, N. Cho, S.-A. Im et al., "Survival outcomes of breast cancer patients who receive neoadjuvant chemotherapy: association with dynamic contrast-enhanced MR imaging with computer-aided evaluation," *Radiology*, vol. 268, no. 3, pp. 662–672, 2013.
- [29] Q. Liu, J.-M. Ye, L. Xu, X.-N. Duan, J.-X. Zhao, and Y.-H. Liu, "Correlation between dynamic contrast-enhanced MRI and histopathology in the measurement of tumor and breast volume and their ratio in breast cancer patients: a prospective study," *Chinese Medical Journal*, vol. 125, no. 21, pp. 3856–3860, 2012.

## Research Article

# Compressed Sensing for fMRI: Feasibility Study on the Acceleration of Non-EPI fMRI at 9.4T

Paul Kyu Han,<sup>1,2</sup> Sung-Hong Park,<sup>2</sup> Seong-Gi Kim,<sup>3,4</sup> and Jong Chul Ye<sup>1</sup>

<sup>1</sup>Bio Imaging and Signal Processing Lab, Department of Bio and Brain Engineering, Korea Advanced Institute of Science and Technology (KAIST), 373-1 Guseong-dong, Yuseong-gu, Daejeon 305-701, Republic of Korea

<sup>2</sup>Magnetic Resonance Imaging Lab, Department of Bio and Brain Engineering, Korea Advanced Institute of Science and Technology (KAIST), 373-1 Guseong-dong, Yuseong-gu, Daejeon 305-701, Republic of Korea

<sup>3</sup>Center for Neuroscience Imaging Research, Institute for Basic Science (IBS), Suwon 440-746, Republic of Korea

<sup>4</sup>Department of Biomedical Engineering, Sungkyunkwan University (SKKU), Suwon 440-746, Republic of Korea

Correspondence should be addressed to Sung-Hong Park; [sunghongpark@kaist.ac.kr](mailto:sunghongpark@kaist.ac.kr) and Jong Chul Ye; [jong.ye@kaist.ac.kr](mailto:jong.ye@kaist.ac.kr)

Received 22 August 2014; Accepted 5 November 2014

Academic Editor: Zhengchao Dong

Copyright © 2015 Paul Kyu Han et al. This is an open access article distributed under the Creative Commons Attribution License, which permits unrestricted use, distribution, and reproduction in any medium, provided the original work is properly cited.

Conventional functional magnetic resonance imaging (fMRI) technique known as gradient-recalled echo (GRE) echo-planar imaging (EPI) is sensitive to image distortion and degradation caused by local magnetic field inhomogeneity at high magnetic fields. Non-EPI sequences such as spoiled gradient echo and balanced steady-state free precession (bSSFP) have been proposed as an alternative high-resolution fMRI technique; however, the temporal resolution of these sequences is lower than the typically used GRE-EPI fMRI. One potential approach to improve the temporal resolution is to use compressed sensing (CS). In this study, we tested the feasibility of  $k$ - $t$  FOCUSS—one of the high performance CS algorithms for dynamic MRI—for non-EPI fMRI at 9.4T using the model of rat somatosensory stimulation. To optimize the performance of CS reconstruction, different sampling patterns and  $k$ - $t$  FOCUSS variations were investigated. Experimental results show that an optimized  $k$ - $t$  FOCUSS algorithm with acceleration by a factor of 4 works well for non-EPI fMRI at high field under various statistical criteria, which confirms that a combination of CS and a non-EPI sequence may be a good solution for high-resolution fMRI at high fields.

## 1. Introduction

Functional magnetic resonance imaging (fMRI) has had a wide impact in both the research and clinical community since its development. In conventional fMRI studies, positive blood oxygen level-dependent (BOLD) response signal is used as a measure to map neural activity in the brain [1], and the most common MR pulse sequence for acquiring BOLD fMRI images has been gradient-recalled echo (GRE) echo-planar imaging (EPI) due to its fast acquisition speed and high sensitivity to BOLD effect. However, this technique is susceptible to local magnetic field inhomogeneity and becomes sensitive to image distortion and degradation especially at high magnetic fields. Non-EPI sequences such as spoiled gradient echo or balanced steady-state free precession (bSSFP) can be used as an alternative tool for fMRI [2–9]; however, the major drawback of using these sequences for

fMRI studies is the low temporal resolution compared to the typically used GRE-EPI.

One solution to overcome the low temporal resolution of non-EPI sequences is to adopt parallel imaging technique [10–12]. Although proven useful, the usage of parallel imaging results in reduced signal-to-noise ratio (SNR) due to the acceleration factor, the geometric factor of the different coil elements, and the  $k$ -space filling trajectory. The other solution to improve the temporal resolution of non-EPI sequences is to use compressed sensing (CS) [13–15]. CS theory states that it is possible to reconstruct an aliasing-free image even at sampling rates dramatically lower than the Nyquist sampling limit, as long as the nonzero signal is sparse and sampled incoherently. These requirements can be well satisfied in dynamic MRI, since arbitrary trajectories can be implemented to incoherently sample data and dynamic MR images can be sparsified due to high temporal redundancy [16, 17].

Recently, CS theory was successfully applied to dynamic MRI in a new algorithm called *k-t* FOCUSS by employing random sampling pattern in *k-t* space and by using various sparsifying temporal transforms such as Fourier transform (FT) and Karhunen-Loève transform (KLT) to utilize the temporal redundancies [16, 18].

Though CS theory has gained attraction for its vast potential for MRI application, CS had been successfully applied to fMRI in only a few studies in the past. In most of the studies, CS was applied to GRE-EPI fMRI: ordinary GRE-EPI [19, 20] and spiral scan GRE-EPI [21]. Despite its application, GRE-EPI is generally known to suffer from the contribution of magnetic field inhomogeneity, which can degrade the performance of CS algorithms. Recently, it has been reported that application of CS to GRE-fMRI may increase statistical performance of activation detection [22]. Non-EPI sequences such as bSSFP or GRE may work better with CS algorithms than GRE-EPI, since the sequences utilize different RF excitations for each TR.

The signal dynamics of steady-state sequences such as bSSFP are known to be more complicated than other conventional sequences and may need careful examination prior to the application of CS to real data. Also, due to the large degree of freedom in CS application, it is important to understand the artifacts and effects related to CS reconstruction without any confounding factors from true physical artifacts. Thus, an extensive simulation study prior to actual CS application is required to reconstruct data appropriately, preserve fMRI signal details, and eventually create a general CS framework.

In this study, we tested the feasibility of CS for non-EPI fMRI at 9.4T using the model of rat somatosensory stimulation. Fully sampled data with high-resolution spoiled gradient echo and 4 independent pass-band bSSFP fMRI each with different phase-cycling angles ( $0^\circ$ ,  $90^\circ$ ,  $180^\circ$ , and  $270^\circ$ ) underwent retrospective downsampling and reconstruction using *k-t* FOCUSS algorithm. Various sampling patterns and sparsifying transforms such as temporal FT and KLT were employed to systematically study the effects of different *k*-space sampling pattern and the effects of choosing a different CS reconstruction algorithm in high field CS fMRI. The baseline image quality and sensitivity and specificity of activation maps from data with CS reconstruction were compared to those from the original full-sampled data. The potential for improving the temporal resolution of non-EPI fMRI at high magnetic fields without sacrificing quality of fMRI activation maps is demonstrated in this paper.

## 2. Methods

**2.1. Animal Preparation and Data Acquisition.** Three male Sprague-Dawley rats weighing 250~450 g (Charles River Laboratories, Wilmington, MA, USA) were used with the approval from the Institutional Animal Care and Use Committee (IACUC) at University of Pittsburgh. Animal preparation was the same as previously published [7]. Briefly, the rats were intubated for mechanical ventilation (RSP-1002, Kent Scientific, CT, USA). The catheters were inserted in

the femoral artery and femoral vein for blood gas sampling and fluid administration (5% dextrose in saline infused at 0.4 mL/hr), respectively. Once the surgery was finished, the isoflurane level was maintained at 1.4%. Ventilation rate and volume were adjusted based on blood gas analysis results (Stat profile pHox; Nova Biomedical, MA, USA).

Electrical stimulation was applied to either the right or left forepaw using two needle electrodes inserted under the skin between digits 2 and 4 [23]. Stimulation parameters for activation studies were as follows: current = 1.2~1.6 mA, pulse duration = 3 ms, repetition rate = 6 Hz, stimulation duration = 15 s, and interstimulation period = 3 min.

All experiments were carried out on a Varian 9.4T/31 cm MRI system (Palo Alto, CA) with an actively shielded gradient coil of 12 cm inner diameter, which operates at a maximum gradient strength of 40 G/cm and rise time of 120  $\mu$ s. A homogeneous coil and a surface coil (Nova Medical, Wilmington, MA) were used for RF excitation and reception, respectively. Localized shimming was performed with point resolved spectroscopy [24] over a coronal slab ( $\sim 12 \times 6 \times 6$  mm<sup>3</sup>) covering forelimb somatosensory cortex to yield a water spectral linewidth of 20~30 Hz. Spoiled gradient echo (which is denoted by GRE throughout this paper) and pass-band bSSFP studies were performed with TR/TE = 20/10 ms and 10/5 ms, respectively. The bSSFP fMRI studies were performed with four different phase-cycling angles ( $\theta$ ) of  $0^\circ$ ,  $90^\circ$ ,  $180^\circ$ , and  $270^\circ$  (which are denoted by PC 0, PC 1, PC 2, and PC 3, resp., throughout this paper). The resolution parameters were the same for all studies: matrix size =  $256 \times 192$ , FOV =  $2.4 \times 2.4$  cm<sup>2</sup>, number of slice = 1, and slice thickness = 2 mm. Flip angles for all the bSSFP and GRE fMRI studies were  $16^\circ$  and  $8^\circ$ , respectively. Forty-eight measurements were acquired for each bSSFP fMRI study: 16 during prestimulus baseline, 8 during stimulation, and 24 during the poststimulus period. These numbers of measurements were reduced by half for GRE fMRI study, in order to maintain the same spatial resolution. Four bSSFP and one GRE fMRI studies composed one full set and each full set was repeated 15 to 25 times for averaging per subject rat.

**2.2. *k*-Space Sampling Patterns.** The initial data to undergo CS reconstruction is important to guarantee high performance of CS algorithms. All fMRI studies in this work were conducted with block design paradigm; thus downsampling was considered in the *k-t* (i.e., *k*-space-temporal) domain to utilize CS algorithms optimized for exploiting temporal redundancy in dynamic MRI. In order to determine the optimal sampling pattern for CS application on fMRI data acquired at high field, four different sampling patterns were considered (Figures 1(b)–1(e)): sampling masks were generated using uniform random sampling (Figure 1(b)), Gaussian random sampling (Figure 1(c)), a mixture of Gaussian and uniform random sampling (Figure 1(d)), and a mixture of Gaussian and uniform random sampling with full sampling of *k*-space center 1 line (Figure 1(e)). The generated sampling masks were applied to each full-sampled *k*-space dataset for retrospective downsampling before the CS reconstruction procedure.

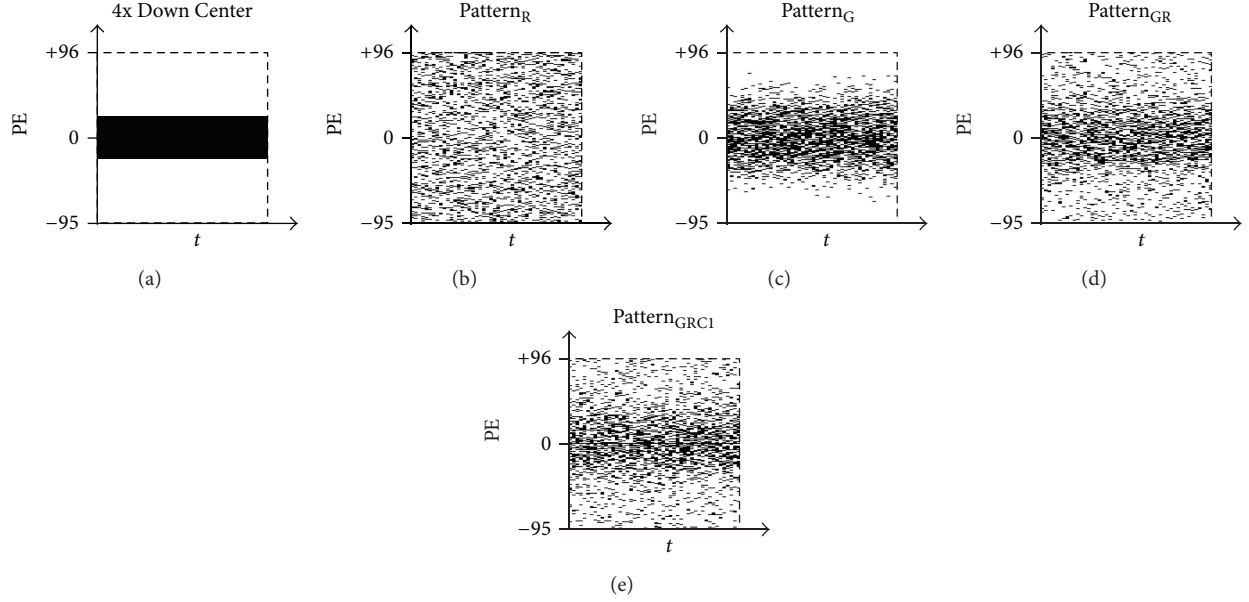


FIGURE 1: Masks of five different sampling patterns with downsampling factor of 4. Patterns of (a) full sampling of  $k$ -space center, (b) uniform random sampling, (c) Gaussian random sampling, (d) mixture of Gaussian and uniform random sampling, and (e) mixture of Gaussian and uniform random sampling with full sampling of center 1 line are shown. All masks are generated to sample only a quarter of the total data (total size of the data indicated by dashed box). Notice that no  $k$ -space high frequency information is included in (a) and (c).

In this study, a fixed downsampling factor of 4 was applied to all datasets: only a quarter of the original  $k$ -space data was used for CS reconstruction. Each 2D sampling mask was generated for each time frame and a fixed number of  $N_{PE}/4$  lines were sampled along the phase-encoding (PE) direction to maintain the downsampling factor of 4 (where  $N_{PE}$  indicates the total number of PE lines). Note that bSSFP or GRE sequences utilize different RF excitations for each TR; thus the acceleration factor depends on the total number of PE lines sampled. The uniform random sampling mask was generated by sampling the PE lines according to a uniform probability distribution. The Gaussian random sampling mask was generated by sampling the PE lines according to a Gaussian probability distribution of  $P(k_y) = Ae^{-(k_y)^2/2\sigma^2}$ , with  $\sigma = N_{PE}/9$  (where  $k_y$  indicates  $k$ -space PE line number index in the range of  $-95$  to  $96$ ,  $\sigma$  indicates standard deviation, and  $A$  indicates the weighting factor which was adjusted to make the equation a valid probability density function). The mixture of Gaussian and uniform random sampling mask was generated by sampling  $N_{PE}/6$  number of PE lines according to the above Gaussian probability distribution and subsequently sampling  $N_{PE}/12$  number of PE lines according to a uniform random probability distribution ( $N_{PE}/6 + N_{PE}/12 = N_{PE}/4$  lines were sampled in total). The mixture of Gaussian and uniform random sampling with full sampling of  $k$ -space center 1 line was generated similarly, but with continuous sampling of the  $k$ -space center 1 line (i.e.,  $k_y = 0$ ) for each time frame along the temporal dimension. Pseudocodes for generation of the sampling patterns are provided as follows.

*Pseudocode for Generation of  $k$ -Space Downsampling Pattern on 2D Time-Series MRI Data.*

For downsampling factor ( $D$ ), one has the following.

#### (A) Uniform Random Sampling Mask

- (1) Generate uniform probability distribution along the PE dimension of  $k$ -space data.
- (2) Sample  $N_{PE}/D$  number of PE lines according to the uniform probability distribution.
- (3) Repeat steps (1)-(2) for each time frame.

#### (B) Gaussian Random Sampling Mask

- (1) Define  $\sigma$  in relation to  $N_{PE}$ .
- (2) Generate Gaussian probability distribution  $P(k_y) = Ae^{-(k_y)^2/2\sigma^2}$  along the PE dimension of  $k$ -space data.
- (3) Sample  $N_{PE}/D$  number of PE lines according to the Gaussian probability distribution.
- (4) Repeat steps (1)-(3) for each time frame.

#### (C) Mixture of Gaussian and Uniform Random Sampling Mask (Gaussian : Random = $a : b$ )

- (1) Define  $\sigma$  in relation to  $N_{PE}$ .
- (2) Generate Gaussian probability distribution  $P(k_y) = Ae^{-(k_y)^2/2\sigma^2}$  along the PE dimension of  $k$ -space data.
- (3) Sample  $(N_{PE}/D) \times (a/(a+b))$  number of PE lines according to the Gaussian probability distribution.
- (4) Generate uniform probability distribution along the PE dimension for the remaining PE lines.
- (5) Sample  $(N_{PE}/D) \times (b/(a+b))$  number of PE lines according to the uniform probability distribution.
- (6) Repeat steps (1)-(5) for each time frame.

(1) **for**  $k = 1, \dots, N_{\text{FOCI}}$  **do**

(2) Compute the weighting matrix  $\mathbf{W}^{(k)}$

$$\mathbf{W}^{(k)} = \begin{pmatrix} |q_1^{(k-1)}|^P & 0 & \dots & 0 \\ 0 & |q_2^{(k-1)}|^P & \dots & 0 \\ \vdots & \vdots & \ddots & \vdots \\ 0 & 0 & \dots & |q_N^{(k-1)}|^P \end{pmatrix}. \quad (*)$$

(3) Perform  $N_{\text{CG1}}$  iterations of CG to obtain  $\mathbf{q}^{(n)}$  from the following minimization problem:

$$\mathbf{q}^{(k)} = \arg \min_{\mathbf{q}} \left\{ \|\mathbf{y} - \mathbf{A}\mathbf{x}^{(0)} - \mathbf{A}\mathbf{W}^{(k)}\mathbf{q}\|_2^2 + \lambda \|\mathbf{q}\|_2^2 \right\} \quad (**)$$

(4) Set  $\mathbf{x}^{(k)} = \mathbf{x}^{(0)} + \mathbf{W}^{(k)}\mathbf{q}^{(k)}$ .

(5) **end for**

(6) Set  $\mathbf{X}^{(k)} = \text{unvec}(\mathbf{x}^{(k)})$ .

(7) Set  $\widehat{\mathbf{U}} = \mathbf{X}^{(k)}\Phi^H$ .

ALGORITHM 1:  $\widehat{\mathbf{U}} = \text{ktFOCUSS}(p_1, \lambda_1, N_{\text{CG1}}, N_{\text{FOCI}}, \Phi, \mathbf{x}^{(0)})$ .

Inputs:  $p, \lambda, N_{\text{CG}}, N_{\text{FOCI}}$ , and  $\mathbf{x}^{(0)}$ .

(1) Set  $\Phi$  as temporal Fourier Transform.

(2) Set  $\widehat{\mathbf{U}} = \text{ktFOCUSS}(p_1, \lambda_1, N_{\text{CG1}}, N_{\text{FOCI}}, \Phi, \mathbf{x}^{(0)})$ .

(3) **for**  $k = 1, \dots, N_{\text{KLT}}$  **do**

(4) Set  $\Phi \leftarrow \text{eig}(\widehat{\mathbf{U}}^H \widehat{\mathbf{U}})$ .

(5) Set  $\widehat{\mathbf{U}} = \text{ktFOCUSS}(p_2, \lambda_2, N_{\text{CG2}}, N_{\text{FOCI}}, \Phi, \mathbf{x}^{(0)})$ .

(6) **end for**

ALGORITHM 2:  $k$ - $t$  FOCUSS with Karhunen-Loéve transform.

(D) Mixture of Gaussian and Uniform Random Sampling Mask with Full Sampling of Center 1 Line (Gaussian : Random =  $a : b$ )

- (1) Sample 1 PE line from the  $k$ -space center (e.g.,  $k_y = 0$ ).
- (2) Repeat all steps from (C) with  $N_{\text{PE}}/D-1$  number of PE lines.

The Gaussian probability distribution was considered as a derivative form of  $k$ -space center-weighted downsampling pattern, with stronger weighting on  $k$ -space low-frequency information. Sampling using a mixture of Gaussian and uniform random probability distributions was considered as a further variation preserving information at both high and low frequencies. The inclusion of  $k$ -space center 1 line was considered as an option to preserve the lowest frequency information, since the center of  $k$ -space contains most of the contrast information for an MR image. For comparison analysis, original full-sampled data was used as the ground truth to study the effect of CS reconstruction, and a simple quarter downsampled mask with full sampling of  $k$ -space center (Figure 1(a)) was used as a control. Throughout the paper, uniform random sampling pattern, Gaussian random sampling pattern, mixture of Gaussian and uniform random sampling pattern, and mixture of Gaussian and uniform random sampling pattern with full sampling of center 1

line will be denoted by Pattern<sub>R</sub>, Pattern<sub>G</sub>, Pattern<sub>GR</sub>, and Pattern<sub>GRC1</sub>, respectively.

**2.3. CS Algorithms.** Two variations of  $k$ - $t$  FOCUSS algorithms, temporal FT and KLT (which will be further denoted by Algorithms 1 and 2, resp.), were used in this study (see the Appendix for detailed description of  $k$ - $t$  FOCUSS algorithms) [16]. The covariance matrix for Algorithm 2 was defined to be constructed from an initial reconstruction using Algorithm 1 with preliminary parameter of  $N_{\text{FOCI}} = 2$  for each dataset:

$$\mathbf{C} = \widehat{\mathbf{U}}^H \widehat{\mathbf{U}}, \quad (1)$$

where  $\widehat{\mathbf{U}} = [\widehat{\mathbf{u}}_1, \widehat{\mathbf{u}}_2, \dots, \widehat{\mathbf{u}}_T]$  indicates the reconstruction from Algorithm 1 (please refer to the Appendix for detailed definition of  $\widehat{\mathbf{U}}$ ). The eigenvectors of the covariance matrix were further used as the KL transform ( $\Phi$ ) and  $N_{\text{KLT}} = 1$  was used to update  $\Phi$  once.

**2.4.  $k$ - $t$  FOCUSS Parameters.** For both algorithms, weighting matrix power factor ( $p$ ) of 0.5 was used to find the sparse solution equivalent to the  $l_1$  solution of CS [16]. Conjugate gradient (CG) iteration number ( $N_{\text{CG}}$ ) of 30 was considered sufficient and was used for both Algorithm 1 ( $N_{\text{CG1}}$ ) and Algorithm 2 ( $N_{\text{CG2}}$ ), based on previous application with  $k$ - $t$  FOCUSS [25]. Regularization factor ( $\lambda$ ) of 0.1 was used for Algorithm 1 ( $\lambda_1$ ) [16] and 0.01 was used for Algorithm 2 ( $\lambda_2$ ) [22].

Both Algorithms 1 and 2 were optimized based on variation in the FOCUSS iteration number ( $N_{\text{FOC}}$ ) parameters (i.e.,  $N_{\text{FOC}1}$  and  $N_{\text{FOC}2}$ , resp.). The following stopping criterion is used to determine the optimal  $N_{\text{FOC}}$  value from each dataset in training phase:

$$\frac{\|\widehat{\mathbf{U}}^{(k)} - \widehat{\mathbf{U}}^{(k-1)}\|_F}{\|\widehat{\mathbf{U}}^{(k)}\|_F} < 0.1, \quad (2)$$

where  $\widehat{\mathbf{U}}^{(k)}$  denotes the CS reconstruction of the spatiotemporal fMRI data at  $k$ th FOC iteration,  $\widehat{\mathbf{U}}^{(k-1)}$  denotes the CS reconstruction of the spatiotemporal fMRI data at  $(k-1)$ th FOC iteration, and  $\|\cdot\|_F$  denotes the Frobenius norm. The performance of  $k$ - $t$  FOCUSS algorithms with the proposed stopping criterion for  $N_{\text{FOC}}$  parameters was evaluated via subject-based leave-one-out cross-validation (i.e., the  $N_{\text{FOC}}$  value for data from each subject was determined based on a training set consisting of data from the other subjects).

The effects of  $N_{\text{CG}}$  and  $\lambda$  were investigated separately for verification with the determined optimal  $N_{\text{FOC}}$  value (i.e., value found during the training phase) for each subject data. The reconstruction of phase-cycled bSSFP and GRE data was used for investigation with all cases of sampling patterns as follows. Residual error  $\|\mathbf{y} - \widehat{\mathbf{y}}\|_2^2$  was used as a measure to observe data fitting and convergence in each  $k$ - $t$  FOCUSS algorithm with increase in  $N_{\text{CG}}$ , where  $\mathbf{y}$  denotes the  $k$ -space time-series data of the sampled  $k$ -space lines and  $\widehat{\mathbf{y}}$  denotes the CS reconstruction of the  $k$ -space time-series data for the corresponding  $k$ -space lines. Average mean square error (MSE) of the whole time-series data was used as a measure to observe the noise level in the reconstructed image with variation in  $\lambda$ , which was calculated as follows:

$$\text{Average MSE} = \frac{\sum_{t=1}^T \|\mathbf{u}_t - \widehat{\mathbf{u}}_t\|_2^2}{TN}, \quad (3)$$

where  $\mathbf{u}_t$  denotes the original full-sampled spatiotemporal fMRI data at time frame  $t$ ,  $\widehat{\mathbf{u}}_t$  denotes the CS reconstructed spatiotemporal fMRI data at time frame  $t$ ,  $T$  denotes the total number of time frames, and  $N$  denotes the total number of image pixels at each time frame.

**2.5. Region of Interest Selection.** A region of interest (ROI) was selected to help compare the effects of different sampling patterns and CS algorithms. The regions determined to be functionally active (i.e., rejecting the null hypothesis  $H_0$ ) according to the  $t$ -statistics map of the original full-sampled data were chosen as the ROI for further analysis. New ROIs were defined for each dataset.

**2.6. Quantitative Analysis.** Frame-by-frame normalized MSE,  $t$ -statistics functional map, ROI time course plot, and receiver operating characteristics (ROC) curve were calculated for further investigation of the applicability of CS for fMRI data at high field. These analyses were performed on the bSSFP data with PC2 for clear evaluation of the effect of CS application, since the sequence corresponds to the conventional bSSFP sequence (i.e.,  $180^\circ$  phase-cycling

displaying a fairly uniform signal contrast without any significant banding artifacts and showed clear activation foci in the full-sampled data.

The frame-by-frame normalized MSE calculation at time  $t$  was performed using the following equation:

$$\text{Frame-by-frame normalized MSE}(t) = \frac{\|\mathbf{u}_t - \widehat{\mathbf{u}}_t\|_2^2}{\|\mathbf{u}_t\|_2^2}. \quad (4)$$

Student's  $t$ -test was performed for each dataset to statistically analyze fMRI data and generate the  $t$ -statistics functional map. The  $T$ -score is calculated on a pixel by pixel basis over time as follows:

$$T\text{-score} = \frac{\bar{x} - \bar{y}}{\sqrt{s_x^2/n_x + s_y^2/n_y}}, \quad (5)$$

where  $\bar{\cdot}$  denote the mean,  $s_{\cdot}$  denote the standard deviation, and  $n_{\cdot}$  denote the length of the baseline time-series  $x$  and activation time-series  $y$ , respectively. The  $t$ -statistics functional map was generated for a significance level of 0.05, and clusters less than 6 pixels were rejected. ROI time course was plotted as the mean ROI value.

The ROC curve was generated to provide standardized and statistically meaningful means for comparing fMRI signal-detection accuracy [26]. For each dataset, the  $t$ -statistics map generated from the original full-sampled data with significance level of 0.05 was used as the ground truth. True positive fraction (TPF) and false positive fraction (FPF) were calculated over various significance levels to generate the ROC curve. The performance was measured by the area under the curve (AUC) ranging from 0 to 1, with 1 representing better performance. The TPF and FPF were calculated using the following equations:

$$\begin{aligned} \text{TPF} &= (\text{Number of True-Positive Activation Voxels}) \\ &\quad \times (\text{Number of Truly Activated Voxels from} \\ &\quad \text{Ground Truth})^{-1}, \\ \text{FPF} &= (\text{Number of False-Positive Activation Voxels}) \\ &\quad \times (\text{Number of Truly Non-Activated Voxels} \\ &\quad \text{from Ground Truth})^{-1}, \end{aligned} \quad (6)$$

where TPF relates to sensitivity and  $1 - \text{FPF}$  relates to specificity.

### 3. Results

**3.1. Determination of  $N_{\text{FOC}}$ .**  $N_{\text{FOC}}$  values determined via subject-based leave-one-out cross-validation for Algorithm 1 were 4, 3, 3, and 3 for Pattern<sub>R</sub>, Pattern<sub>G</sub>, Pattern<sub>GR</sub>, and Pattern<sub>GRCl</sub>, respectively, and those for Algorithm 2 were 5, 4, 4, and 4 for Pattern<sub>R</sub>, Pattern<sub>G</sub>, Pattern<sub>GR</sub>, and Pattern<sub>GRCl</sub>, respectively. Identical  $N_{\text{FOC}}$  values were found regardless of

the pulse sequence type (i.e., GRE and bSSFP PC0, PC1, PC2, and PC3) in all the subjects. All further analyses were performed with the determined  $N_{\text{FOC}}$  values for each subject data, to evaluate the performance of  $k$ - $t$  FOCUSS algorithms with the proposed stopping criterion.

**3.2. Original Data: High Field bSSFP.** Different phase-cycling angles in the fMRI maps of full-sampled bSSFP data showed shifting in activation foci (i.e., the activation foci were located around the cortical surface area for PC1 and 2, while they were located in the middle cortical regions for PC0 and 3, as indicated by white arrows in Figure 2(b)). This spatial shift of activation foci as a function of PC angle implies that the high field phase-cycled bSSFP maps are spatially heterogeneous due to magnetic field inhomogeneity and was used in this study to confirm that CS with an appropriate downsampling scheme can preserve the details of the spatial pattern of the functional activation.

**3.3. Reconstruction with Algorithm 1:  $k$ - $t$  FOCUSS with Temporal FT.** Visually the original baseline images became blurred with artifacts after downsampling was applied (Figure 3). Despite the distortion and degradation after downsampling, the baseline images were well reconstructed using Algorithm 1 regardless of sampling pattern (Figures 4(a)–4(d)). Visually the image contrast and resolution were well preserved for CS reconstructed images from all sampling patterns compared to the original baseline image (Figure 2(a)) and downsampled baseline image with only  $k$ -space low-frequency information (Figure 2(c)). The frame-by-frame normalized MSE values from all the CS sampling patterns were significantly lower than those from downsampling with only  $k$ -space low-frequency information (Figure 5), indicating high reconstruction performance of Algorithm 1. In particular, the mixture of Gaussian and uniform random sampling scheme (i.e., Pattern<sub>GR</sub> and Pattern<sub>GRC1</sub>) showed the lowest frame-by-frame normalized MSE values across all time frames. Overall, all Gaussian-weighted sampling patterns showed increased spatial resolution and SNR (Figures 4(b), 4(c), and 4(d)) with reduction of artifacts (indicated by yellow arrow in Figure 2(a)) for all phase-cycled bSSFP data, while downsampling with only  $k$ -space low-frequency information showed increase of artifacts (Figure 2(c)).

The fMRI maps were also reconstructed well from all Gaussian-weighted sampling patterns using Algorithm 1 (Figures 6(b), 6(c), and 6(d)), while those from Pattern<sub>R</sub> did not show any meaningful functional activations (Figure 6(a)). The fMRI maps from downsampling with only  $k$ -space low-frequency information showed significant blurring in the activation region (Figure 2(d)). The fMRI maps from Pattern<sub>GR</sub> (Figure 6(c)) and Pattern<sub>GRC1</sub> (Figure 6(d)) were closer to the original fMRI maps than those from Pattern<sub>G</sub> (Figure 6(b)) in terms of preserving details in activation foci shift, presumably due to the inclusion of appropriate high frequency  $k$ -space information.

The time course of the mean ROI value was also relatively well preserved in images from all Gaussian-weighted sampling patterns (Figures 7(b), 7(c), and 7(d)), while those

from Pattern<sub>R</sub> differed from the original with significantly increased temporal fluctuation (Figure 7(a)). Mean ROI time courses of images from all Gaussian-weighted sampling patterns resembled those of the original data; even with only (1/4)th of the whole data, the mean ROI time course followed the trend of the original time course with slightly reduced mean amplitude difference, percent signal change, and also signal fluctuation. These observations were applicable regardless of acquisition method and different PC angles for bSSFP. The AUC value of ROC curves indicated overall high sensitivity and specificity of all Gaussian-weighted sampling patterns using Algorithm 1 (Table 1). Pattern<sub>GRC1</sub> displayed the highest ROC performance than other sampling patterns including downsampling with only  $k$ -space low-frequency information.

The reconstruction times of the  $k$ - $t$  FOCUSS algorithms are shown for bSSFP PC2 and GRE in Table 2. Only one representative case is shown for each bSSFP and GRE data since similar results were obtained regardless of bSSFP PC angle, sampling pattern, and subject rats, despite the difference in total time due to the usage of different  $N_{\text{FOC}}$  parameter values. The reconstruction time for the bSSFP data was approximately twice as long as that of the GRE data, since the speed of reconstruction is largely dependent on the size of the matrix and number of time frames (recall that the number of time frames of GRE data was half of that of bSSFP data).

**3.4. Reconstruction with Algorithm 2:  $k$ - $t$  FOCUSS with KLT.** Results of Algorithm 2 in terms of baseline images, frame-by-frame normalized MSE plot, fMRI maps, ROI time course, and AUC values in ROC curve are shown in Figures 8, 9, 10, and 11 and Table 1, respectively. Overall the results were similar to those of Algorithm 1. Slight differences were observed between algorithms in the view points of sensitivity and specificity depending on sampling pattern. The images from all sampling patterns for Algorithm 2 showed slightly lower sensitivity and specificity than those for Algorithm 1. The reconstruction time of Algorithm 2 was longer than that of Algorithm 1, mainly due to the calculation of covariance matrix requiring the preliminary estimation (Table 2).

**3.5. Investigation of  $N_{\text{CG}}$  and  $\lambda$  Effect.** Representative results from CS reconstruction of Pattern<sub>GRC1</sub> using Algorithms 1 and 2 are shown in Figures 12, 13, 14, and 15, and similar results were obtained regardless of acquisition method and sampling patterns. Based on the results from Figures 12 and 14, the  $N_{\text{CG}}$  value of 30 (i.e., value used for both Algorithms 1 and 2 throughout the paper) seems to be sufficient to ensure data fitting and error convergence. As shown in Figures 13 and 15, the reconstruction error of  $k$ - $t$  FOCUSS algorithms was relatively insensitive to  $\lambda$  variation and minimal error was achieved with small values of  $\lambda$  (e.g., less than 1).

## 4. Discussion

To our knowledge, it is the first study to apply CS to high field bSSFP fMRI and to systematically evaluate effects of CS sparsity schemes on non-EPI fMRI. The CS sampling

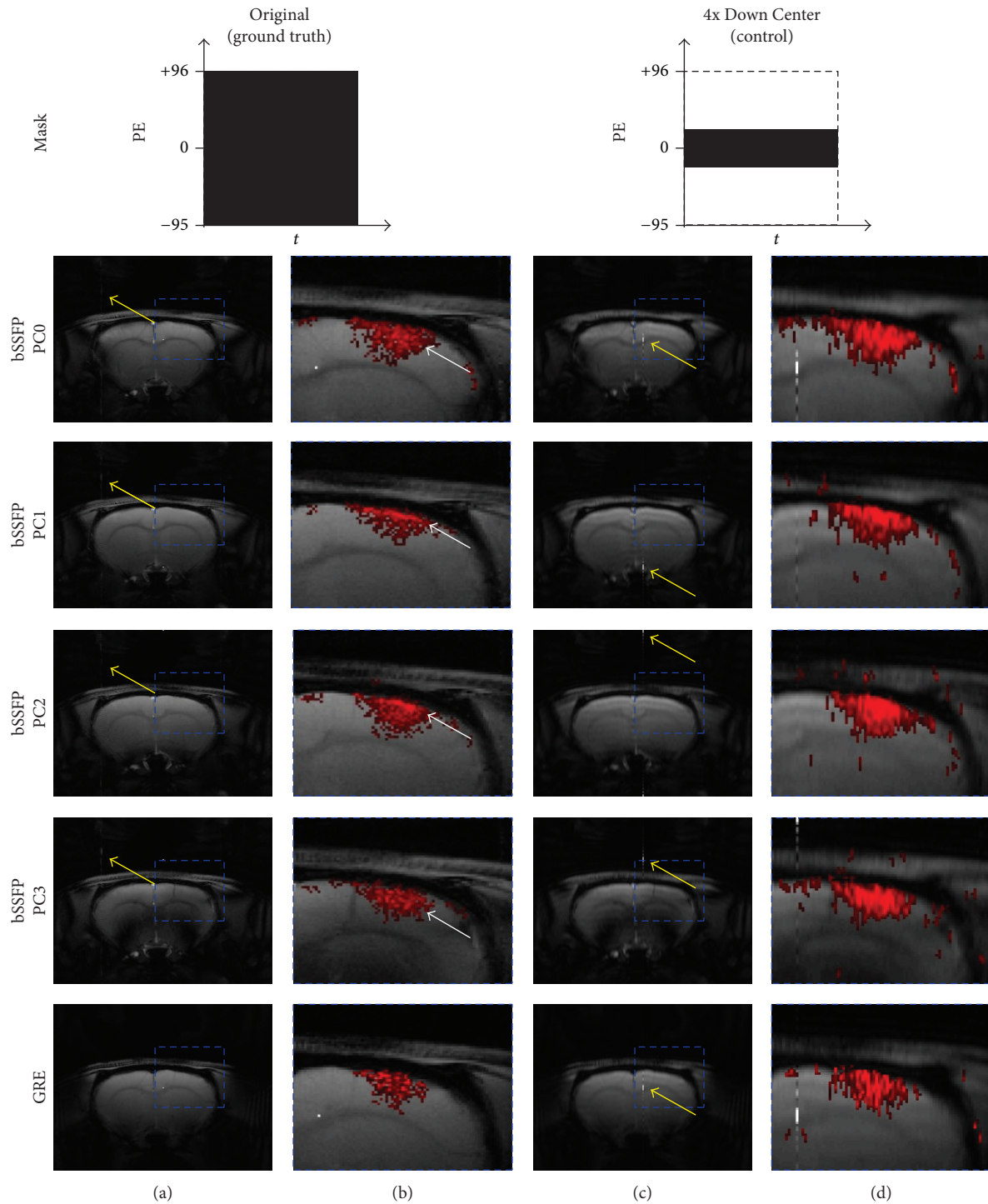


FIGURE 2: Baseline and fMRI images of original and control. (a) Baseline images and (b) fMRI maps of full-sampled data and (c) baseline images and (d) fMRI maps of downsampled data with full acquisition of  $k$ -space center are shown. The 20th and 10th time frame of bSSFP and GRE is shown for baseline images, respectively. The fMRI maps are shown for significance level of 0.05. Downsampling pattern and acquisition method are shown on the top and left-hand side of the images, respectively. The DC artifact is indicated by yellow arrow and the enlarged fMRI activation region is indicated by blue dashed box. Notice the activation foci shift (white arrow) in the phase-cycled bSSFP data. The case from a representative rat is shown since similar results were obtained for different subject rats.

TABLE 1: ROC curve AUC values from fMRI maps of bSSFP time-series data with PC angle of  $180^\circ$  of a representative rat.

4x Down Center (control)		CS			
		Pattern <sub>R</sub>	Pattern <sub>G</sub>	Pattern <sub>GR</sub>	Pattern <sub>GRCl</sub>
0.9794	Algorithm 1	0.8943	0.9800	0.9795	0.9827
	Algorithm 2	0.8639	0.9726	0.9714	0.9825

TABLE 2: Reconstruction speed of  $k$ - $t$  FOCUSS algorithms on downsampled time-series data using Pattern<sub>GRCl</sub> of a representative rat.

	Algorithm 1		Covariance calculation	Algorithm 2	
	Single FT-CG iteration	Total time		Single KLT-CG iteration	Total time
bSSFP PC2	0.46 s	41.35 s	27.81 s	0.64 s	77.26 s
GRE	0.24 s	21.29 s	14.27 s	0.29 s	34.98 s

\*FT: Fourier transform, CG: conjugate gradient method, and KLT: Karhunen-Loève transform.

\*\*Calculated on PC (Windows 7), CPU: 3.30 GHz, RAM: 4.00 GB.

scheme should be determined in relation to the CS algorithm to preserve detailed image information appropriately. Dense sampling in  $k$ -space center region such as Gaussian-weighting or inclusion of  $k$ -space center 1 line was better for CS, due to the fact that most energy is located in the  $k$ -space center region and also due to incoherent aliasing effects from variable-density sampling [13, 16]. The reconstruction results from Pattern<sub>GR</sub> and Pattern<sub>GRCl</sub> also verify that a variation in sampling scheme with more  $k$ -space high frequency information leads to better reconstruction performance preserving signal details (e.g., activation foci shifting phenomenon in bSSFP), which may become critical for applications such as fMRI studies. Inclusion of more  $k$ -space low-frequency information implies less  $k$ -space high frequency information which may lead to an enlargement or blurring of the activation foci in fMRI maps (e.g., Figures 2(d), 6(b), and 10(b)). Thus, both  $k$ -space center and edge regions are important, and methods that achieve a certain balance between them need to be exploited for correct reconstruction of non-EPI fMRI data using CS. Overall the mixture of Gaussian and uniform random sampling scheme reconstructed both the baseline images and fMRI maps well while preserving the signal details and thus seems to be an ideal sampling scheme for CS applied to non-EPI fMRI.

The two algorithms of  $k$ - $t$  FOCUSS with temporal FT and KLT showed similar performances overall. The slight differences in their results are presumed to be due to the utilization of different transformation domains for each iteration. Interestingly,  $k$ - $t$  FOCUSS with temporal FT performed slightly better than  $k$ - $t$  FOCUSS with KLT in terms of ROC performance in this study, despite the fact that KLT is known as an efficient spectral decorrelator [27, 28]. Several factors may account for this. First, the fMRI studies were performed with block design paradigm in this work, and temporal redundancy from the spatial-temporal frequency domain may have been exploited better for such data type. Since KLT is a data-driven transform,  $k$ - $t$  FOCUSS with KLT may potentially perform better in cases of rapid event-related paradigms. Second, the decorrelation of nonperiodic noise might not have been noticeable in the image, since bSSFP sequence is known to provide the highest SNR per

unit time [29, 30] and the simulation studies were performed on datasets with enough averaging (e.g., 15 to 25 times). Recently, it has been reported that application of CS to fMRI can increase FPF in real acquisition settings, and  $k$ - $t$  FOCUSS with KLT has shown to reconstruct fMRI maps with reduced false activations [22]. Thus, the effectiveness of both algorithms needs verification with real fMRI studies. Nonetheless, results from the current study indicate that both algorithms are potentially good solutions for acceleration of high field non-EPI fMRI.

Appropriate choice of CS reconstruction parameters is one of the main concerns of the application of CS. The optimal parameters may vary depending on noise level, temporal resolution, and other possible factors in actual data acquisition environment. In general, reconstruction parameters are found with known noise level [31] or alternatively are selected via cross-validation [32–34]. There are multiple parameters involved for the case of  $k$ - $t$  FOCUSS algorithm, which requires hyperparameter optimization and thus increases the computation burden [16]. Therefore, the effect of two different  $k$ - $t$  FOCUSS parameters,  $\lambda$  and  $N_{CG}$ , is additionally investigated in this study. Considering the physical meaning of each parameter, two different metrics were used for evaluation. Since the regularization parameter  $\lambda$  is a tuning parameter used to find the solution with best improvement in SNR, average MSE was used to show its effect on the noise level in the reconstructed image. Since the CG method is employed to iteratively find the solution to the unknown signal (i.e., denoted by  $\mathbf{x}$  in (A.9) of the Appendix), residual error was used to investigate data fitting and convergence with decreases in measurement error (i.e., difference between sampled  $k$ -space measurements  $\mathbf{y}$  and estimation  $\hat{\mathbf{y}}$ ) as number of CG iterations increases (note that the signal-measurement relationship is defined in (A.4) of the Appendix and can be used to find  $\hat{\mathbf{y}}$  from  $\mathbf{x}$ ). Based on the results from Figures 12 and 14, fixation of  $N_{CG}$  to a sufficient value (e.g., 30 in case of our study) and  $\lambda$  to a small value is preferred to reduce parameter variability and to simplify the usage of  $k$ - $t$  FOCUSS algorithms on high field non-EPI fMRI studies. These results agree with previous applications of  $k$ - $t$  FOCUSS where a sufficient value of  $N_{CG}$

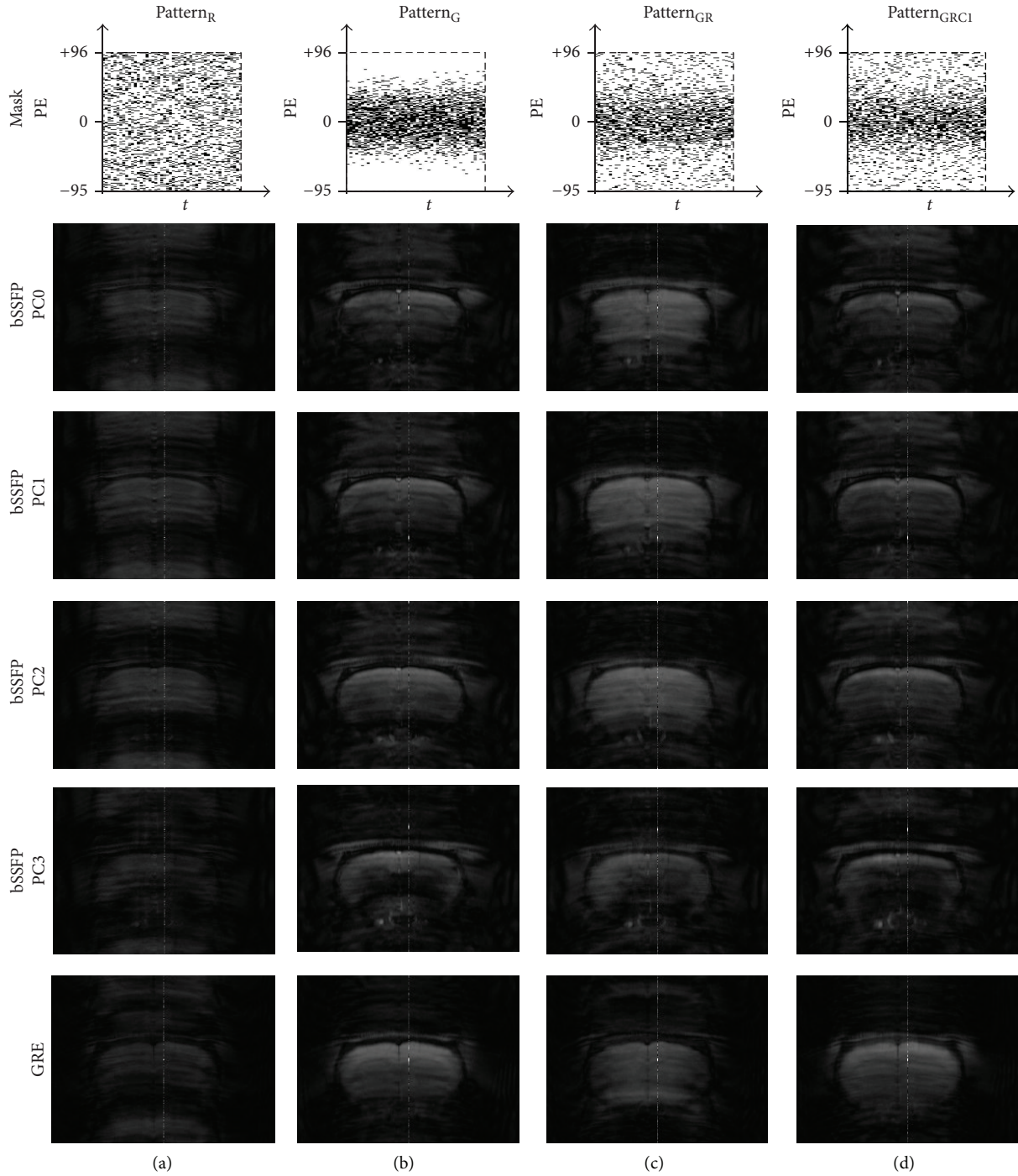


FIGURE 3: Baseline images after downsampling. Baseline images of downsampled data using (a)  $\text{Pattern}_R$ , (b)  $\text{Pattern}_G$ , (c)  $\text{Pattern}_{GR}$ , and (d)  $\text{Pattern}_{GRCl}$  are shown. The 20th and 10th time frame of bSSFP and GRE is shown, respectively. Downsampling pattern and acquisition method are shown on the top and left-hand side of the images, respectively. Notice the blurring and artifacts in the downsampled images. The case from a representative rat is shown since similar results were obtained for different subject rats.

and a small value of  $\lambda$  are used and are proven to perform well in high-quality fMRI studies from real scanner acquisitions [16, 22]. However, care should be taken for extrapolation of these parameters for data types different from those of the current studies. With fixation of  $N_{CG}$  and  $\lambda$ , the only issue for the application of  $k$ - $t$  FOCUSS algorithms for high

field bSSFP fMRI data lies in the choice of  $N_{FOC}$ . The  $N_{FOC}$  parameters found from the current study need to be tested in the context of real CS application for verification and general usage. The choice of a high  $N_{FOC}$  value may ensure minimal error for most cases of applications; however, this also leads to increased number of calculations required for CS

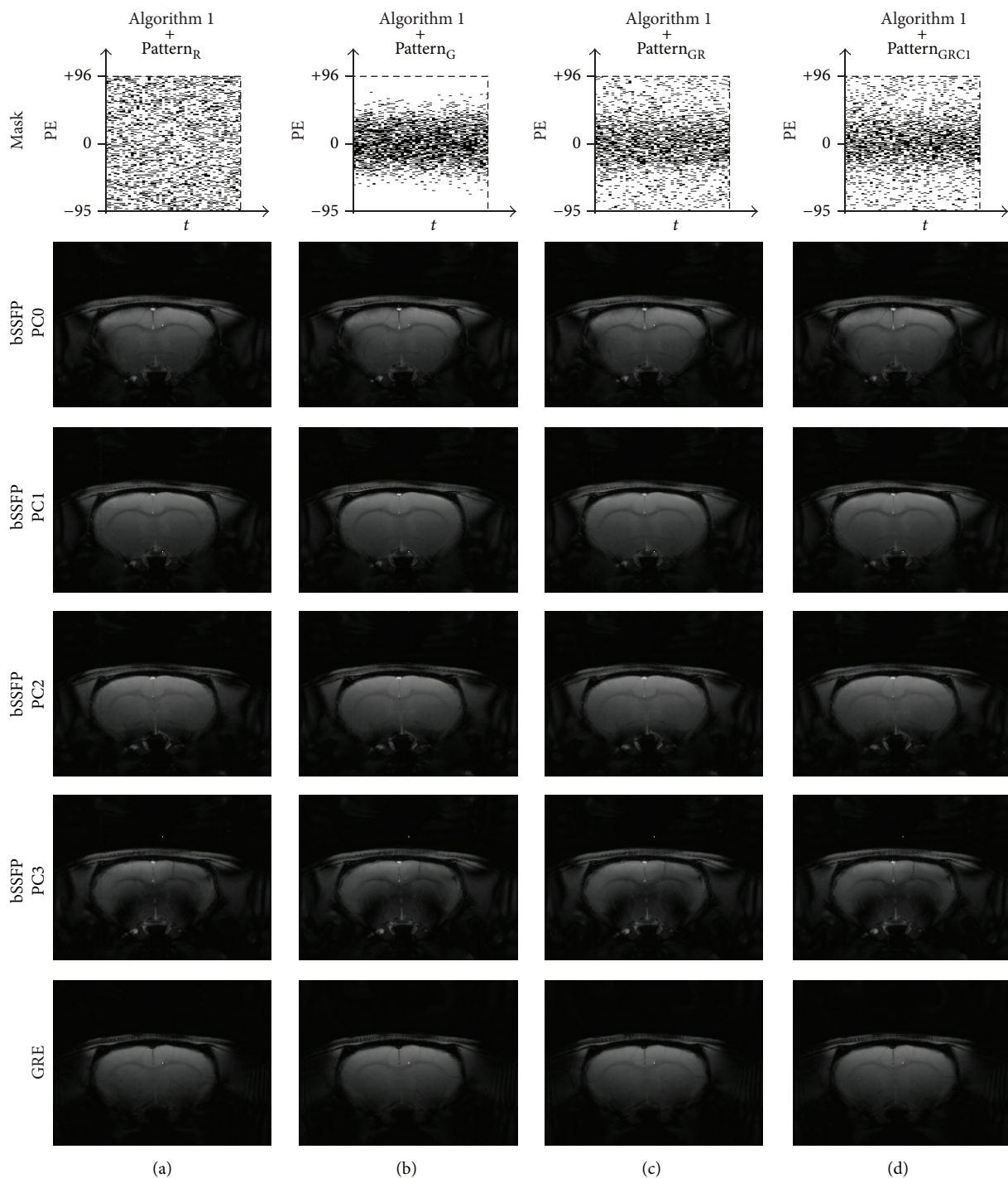


FIGURE 4: Comparison of baseline images reconstructed using Algorithm 1 ( $k$ - $t$  FOCUSS with temporal FT). Baseline images of CS reconstructed data using Algorithm 1 and (a)  $\text{Pattern}_R$ , (b)  $\text{Pattern}_G$ , (c)  $\text{Pattern}_{GR}$ , and (d)  $\text{Pattern}_{GRCI}$  are shown. The 20th and 10th time frame of bSSFP and GRE is shown, respectively. Downsampling pattern and acquisition method are shown on the top and left-hand side of the images, respectively. The case from a representative rat is shown since similar results were obtained for different subject rats.

reconstruction. Thus, the trade-off between minimization of error and increase in postprocessing time must be considered appropriately before choosing the  $N_{\text{FOC}}$  value for future studies.

Eddy currents can cause problems in bSSFP imaging with nonlinear phase-encoding orders. The problems may become noticeable when the sparsity schemes tested in this study are implemented in real acquisition settings. Previously Bieri et

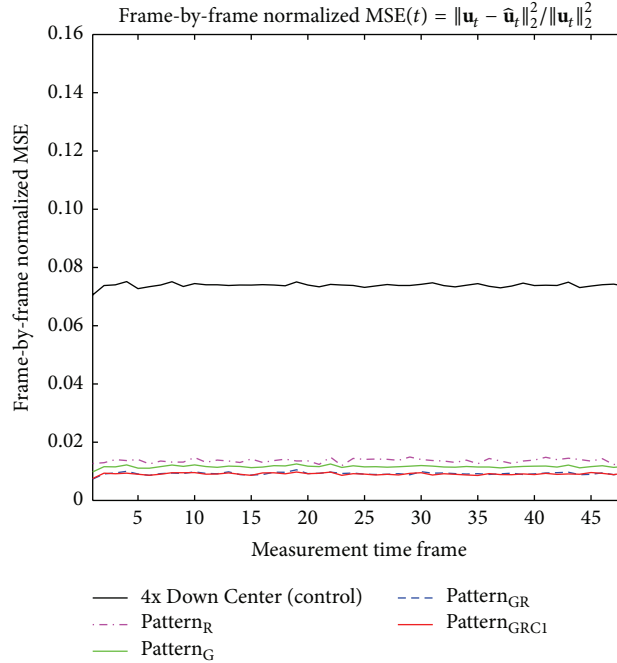


FIGURE 5: Comparison of frame-by-frame normalized MSE plots from reconstructed baseline images using Algorithm 1 ( $k$ - $t$  FOCUSS with temporal FT). The frame-by-frame normalized MSE plots of bSSFP time-series data with PC angle of  $180^\circ$  are shown. The case from a representative rat is shown since similar results were obtained for different subject rats.

TABLE 3: ROC curve AUC values from reconstructed fMRI maps using  $k$ - $t$  FOCUSS algorithms and pairwise sampling of PE lines with  $\text{Pattern}_{\text{GRC1}}$  on bSSFP time-series data with PC angle of  $180^\circ$  of a representative rat.

	Algorithm 1	Algorithm 2
Pairwise PE $\text{Pattern}_{\text{GRC1}}$	0.9810	0.9736

al. [35] discovered a simple method to suppress the eddy current effect by pairing two consecutive  $k$ -space lines. By incorporating this idea, a simulation study was performed to see the effect of pairwise downsampling scheme. A paired  $\text{Pattern}_{\text{GRC1}}$  was generated with a downsampling factor of 4. The downsampling scheme and reconstructed fMRI maps from each  $k$ - $t$  FOCUSS algorithm are shown in Figure 16, and the ROC performance of the reconstructed data is shown in Table 3. The employment of pairwise sampling scheme showed maintenance of activation foci shift but decrease in both activation detection sensitivity and specificity compared to the results without pairwise sampling (Figures 6(d) and 10(d)), regardless of PC angle and  $k$ - $t$  FOCUSS algorithm. Overall, these results indicate that the pairwise sampling scheme may be used to suppress eddy current artifacts in bSSFP fMRI with CS, but there exists trade-off between the suppression of eddy current effect and fMRI sensitivity as well as specificity.

Application of CS to high field non-EPI fMRI can be meaningful for high-resolution fMRI studies, since conventional GRE-EPI fMRI is sensitive to image distortion and degradation caused by local magnetic field inhomogeneity

at high magnetic fields. Although the temporal resolution of non-EPI sequences is lower than the typically used GRE-EPI, it is shown through the study that the temporal resolution or the spatial coverage can be improved using CS. Several potential advantages of CS can be derived for fMRI studies in this regard. First, better temporal resolution increases the number of time frames within a given time and can in turn improve the statistical power of BOLD activations [22, 36]. Second, the weighted-norm process of the CS algorithm can reduce artifacts from scanner-related drifts, respiratory-induced noise, cardiac pulsation, and subject motion [37–39] and can also improve the activation detection sensitivity in  $t$ -statistics [22]. Lastly, CS can improve spatial coverage which is essential for many fMRI studies that require a big ROI or ROIs from multiple brain regions. Thus, the application of CS in fMRI has great potential in practice.

One negative aspect of CS in fMRI studies is the addition of postprocessing time related to CS reconstruction. The reconstruction time of  $k$ - $t$  FOCUSS algorithms is largely affected by the iteration parameters and the size of the data (e.g., matrix size, number of slices, number of time frames, etc.). The results from Table 2 imply that the temporal resolution or spatial coverage of non-EPI sequence fMRI studies can be improved using CS at the cost of reasonable addition of postprocessing time (i.e., several minutes). Therefore, depending on applications, the trade-off between reconstruction time and temporal resolution (and/or spatial coverage) must be investigated before applying CS algorithms to fMRI studies.

In the past, there have been many dynamic MRI studies other than fMRI with acceleration factor of 8 or higher using

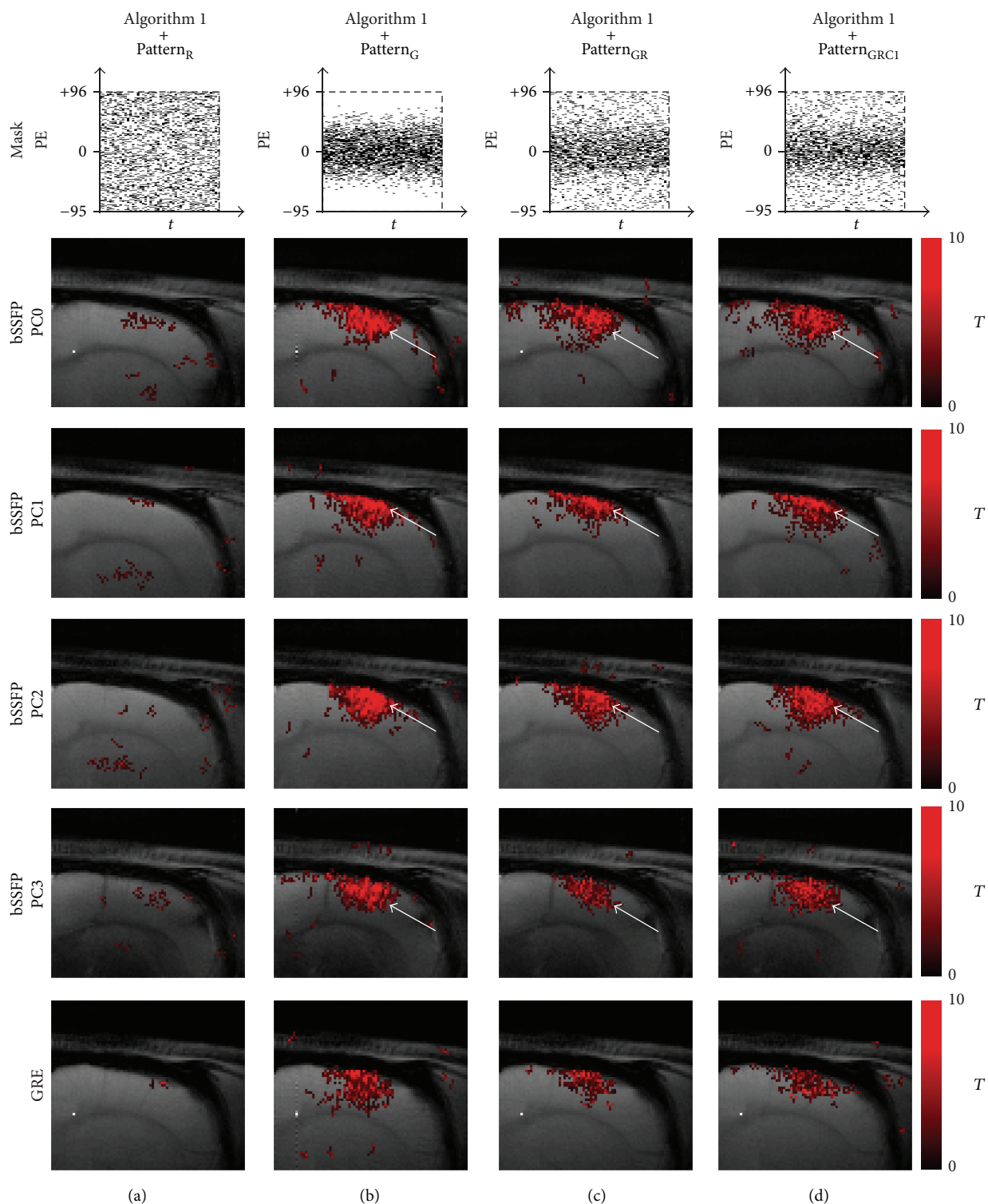


FIGURE 6: Comparison of fMRI maps reconstructed using Algorithm 1 ( $k$ - $t$  FOCUSS with temporal FT). The fMRI maps of CS reconstructed data using Algorithm 1 and (a)  $\text{Pattern}_R$ , (b)  $\text{Pattern}_G$ , (c)  $\text{Pattern}_{GR}$ , and (d)  $\text{Pattern}_{GRCI}$  are shown for significance level of 0.05. Downsampling pattern and acquisition method are shown on the top and left-hand side of the images, respectively. Notice the activation foci shift (white arrow) in the phase-cycled bSSFP data. The case from a representative rat is shown since similar results were obtained for different subject rats.

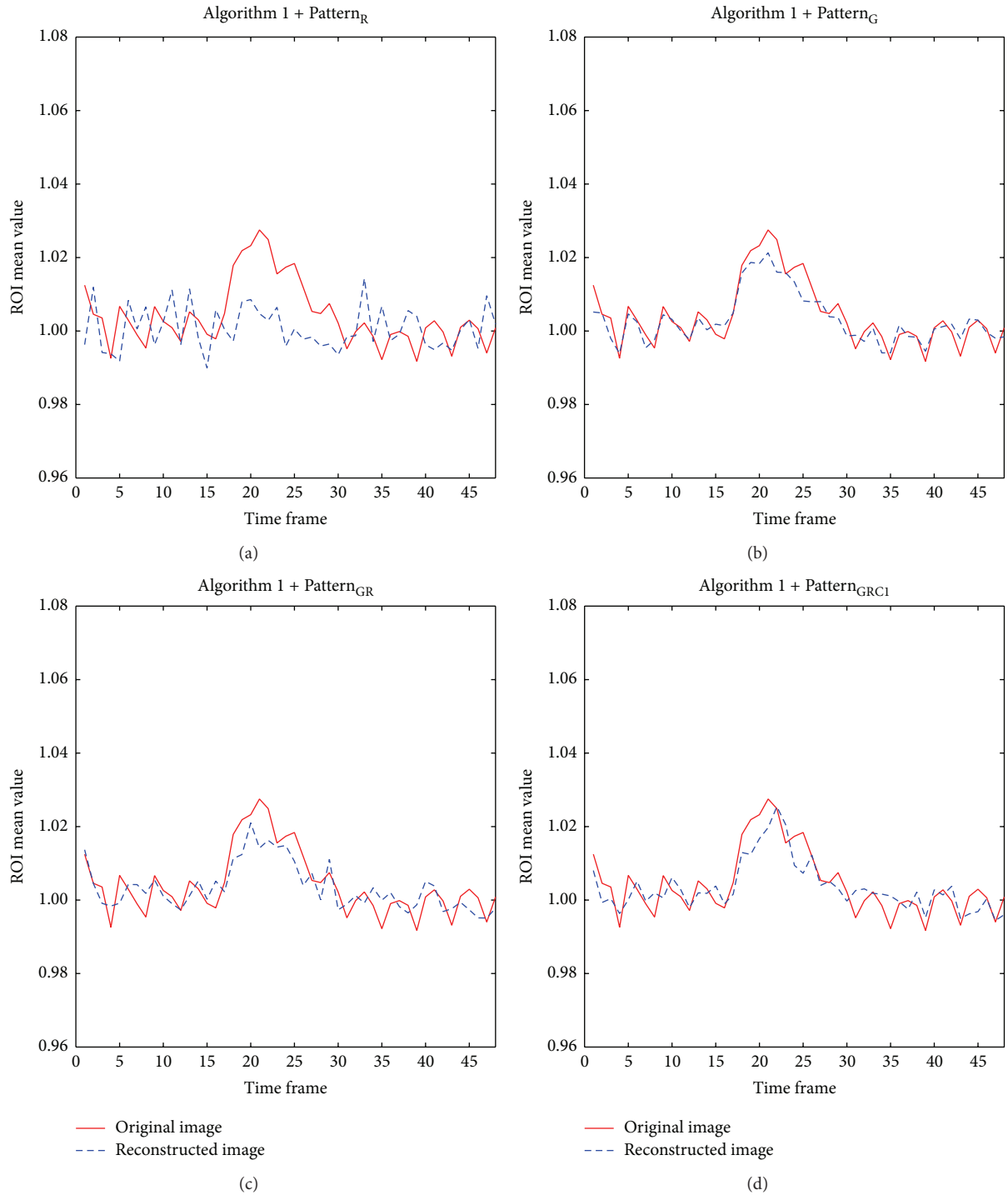


FIGURE 7: Comparison of mean ROI time course plots between full-sampled original data and CS reconstructed data using Algorithm 1 ( $k$ - $t$  FOCUSS with temporal FT). The time course of mean ROI from CS reconstructed data using Algorithm 1 and (a)  $\text{Pattern}_R$ , (b)  $\text{Pattern}_G$ , (c)  $\text{Pattern}_{GR}$ , and (d)  $\text{Pattern}_{GRCI}$  is shown. Mean ROI is calculated from bSSFP time-series data with PC angle of  $180^\circ$ . The case from a representative rat is shown since similar results were obtained for different subject rats.

CS [18, 40–42]. However, CS has been applied to fMRI in a limited number of studies and acceleration factor up to 4 was used in most of the truly accelerated fMRI studies [21, 22]. Decrease in image quality has also been reported

in some pilot studies after CS reconstruction even with 2-fold acceleration [21]. This may be attributed to the fact that distinct from other dynamic MRI studies fMRI requires detection of fine signal changes, which can be achieved by

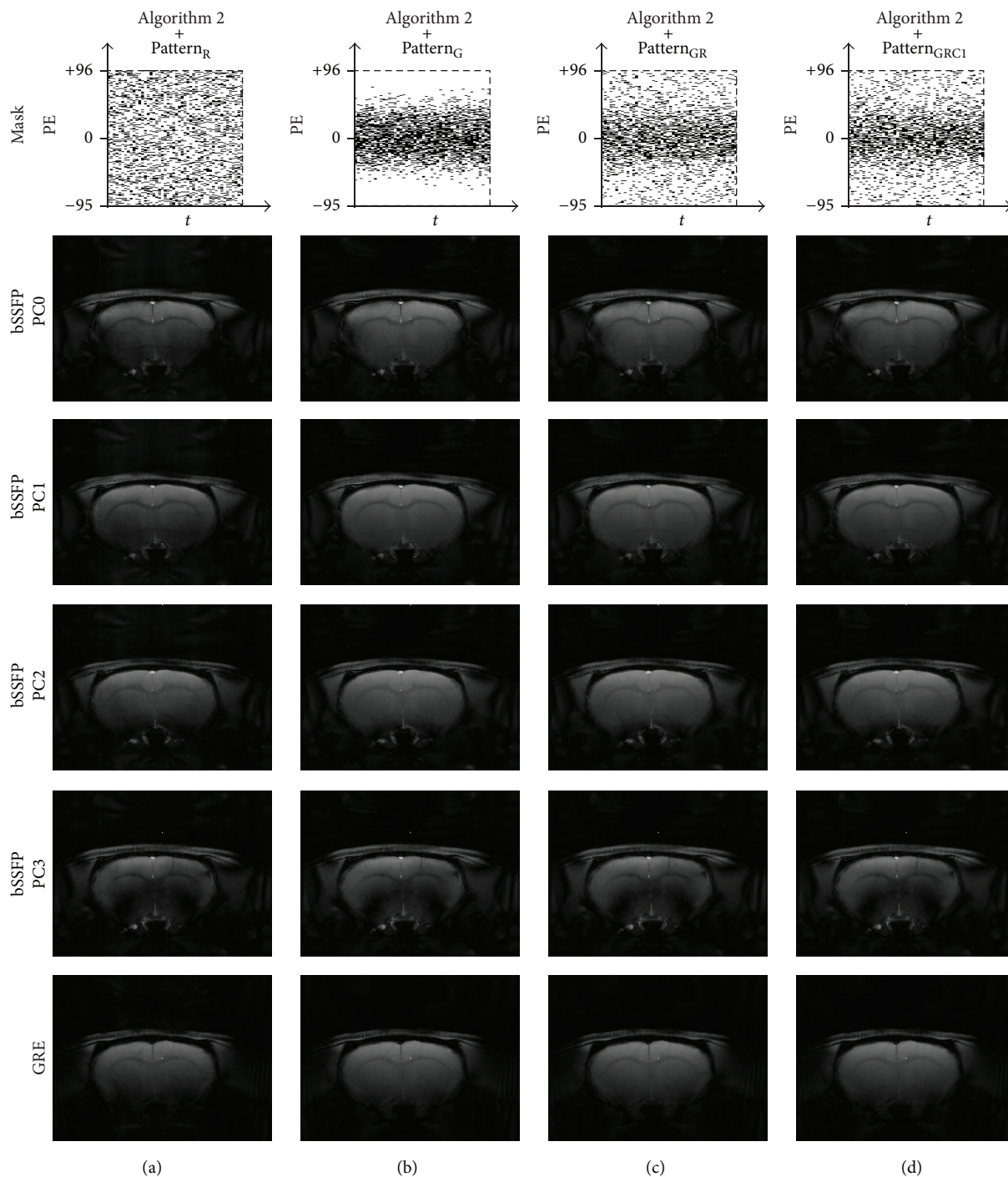


FIGURE 8: Comparison of baseline images reconstructed using Algorithm 2 ( $k$ - $t$  FOCUSS with KLT). Baseline images of CS reconstructed data using Algorithm 2 and (a)  $\text{Pattern}_R$ , (b)  $\text{Pattern}_G$ , (c)  $\text{Pattern}_{GR}$ , and (d)  $\text{Pattern}_{GRC1}$  are shown. The 20th and 10th time frame of bSSFP and GRE is shown, respectively. Downsampling pattern and acquisition method are shown on the top and left-hand side of the images, respectively. The case from a representative rat is shown since similar results were obtained for different subject rats.

preserving high frequency information. Based on the results from our studies, acceleration factor of 4 seems sufficient for CS application on high field non-EPI fMRI studies. For example, for a bSSFP fMRI experiment with matrix size =  $128 \times 128$  and TR = 5 ms, the temporal resolution becomes 0.64 s for a single slice. Thus, the 4-fold acceleration can improve

the temporal resolution up to 0.16 s (i.e., close to the temporal resolution of EPI) or the spatial coverage up to 24 slices (i.e., near whole brain coverage) with temporal resolution less than 4 s (note that although TR was 10 ms in this study, bSSFP with TR  $\leq$  10 ms has been successfully applied to fMRI at high field  $\geq 7$ T). Nonetheless, improvements can be made to

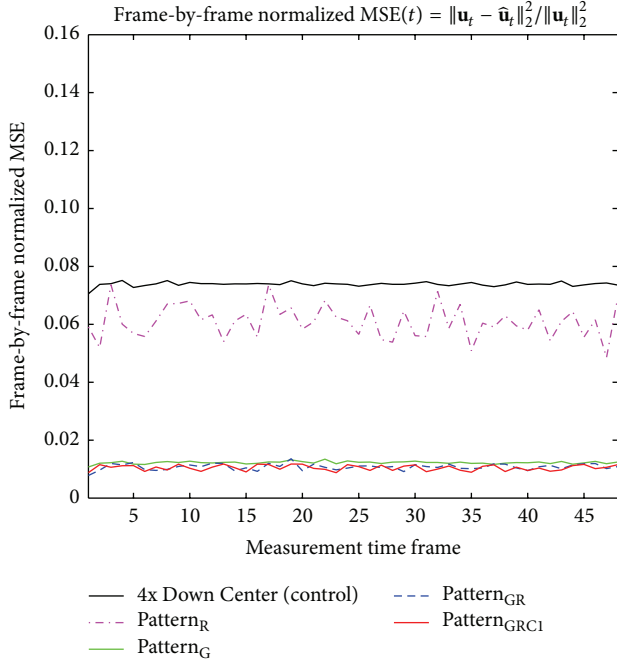


FIGURE 9: Comparison of frame-by-frame normalized MSE plots from reconstructed baseline images using Algorithm 2 ( $k$ - $t$  FOCUSS with KLT). The frame-by-frame normalized MSE plots of bSSFP time-series data with PC angle of  $180^\circ$  are shown. The case from a representative rat is shown since similar results were obtained for different subject rats.

increase the acceleration factor above 4 and the quality may depend on the scan condition (e.g., scan resolution, SNR). A systematic study for different acceleration factors may need to be conducted to further improve application of CS on high field non-EPI fMRI studies.

In this paper, the effect of CS is investigated through retrospective downsampling of full-sampled fMRI data. Therefore, further works are necessary to verify the downsampling schemes that were retrospectively evaluated in this study, by implementing them and performing real fMRI studies, which is beyond the scope of this paper.

## 5. Conclusion

The CS reconstruction of fMRI data acquired at high field using  $k$ - $t$  FOCUSS varies greatly with sampling scheme and thus the sampling scheme must be selected appropriately. Information in both  $k$ -space low and high frequency regions is important for better reconstruction performance and preservation of signal details, respectively, and thus sampling schemes that achieve a certain balance between the two must be selected for the application of CS to non-EPI fMRI data. The two  $k$ - $t$  FOCUSS algorithms, temporal FT and KLT, showed good reconstruction results overall with effective suppression of downsampling artifacts and improved spatial resolution and thus are good candidates for CS in high field non-EPI fMRI studies. The application of CS to fMRI has great potential in practice for improvement of temporal resolution and/or spatial coverage.

## Appendix

### Review of $k$ - $t$ FOCUSS

$k$ - $t$  FOCUSS with Temporal Fourier Transform.  $k$ - $t$  FOCUSS is a recent CS algorithm developed for the reconstruction of dynamic image data [16, 18]. As the name indicates, it is based on FOCal Underdetermined System Solver (FOCUSS) algorithm and utilizes random sampling in the  $k$ - $t$  domain [16, 43, 44]. Here, the basic structure of the algorithm will be speculated. For simplicity, only the case of Cartesian  $k$ -space trajectory will be discussed, with downsampling only in the phase-encoding direction and full sampling in the frequency-encoding direction.

In a discrete setup, the measurement-signal relationship at time  $t$  is

$$\mathbf{y}_t = \mathbf{F}\mathbf{u}_t, \quad t = 1, \dots, T, \quad (\text{A.1})$$

where  $\mathbf{F} \in \mathbb{C}^{m \times n}$  denotes a *downsampled* Fourier transform (FT) along the phase-encoding direction,  $\mathbf{y}_t \in \mathbb{C}^m$  denotes the  $k$  space measurement vectors,  $\mathbf{u}_t \in \mathbb{C}^n$  denotes the image vector at time  $t$ , and  $T$  denotes the number of time frames. If image content varies periodically over time, we can sparsify its temporal variation using  $T \times T$  FT matrix  $\Phi$  such that the corresponding coefficients  $\{\mathbf{x}_t\}$  become sparse:

$$\mathbf{U} \triangleq [\mathbf{u}_1, \mathbf{u}_2, \dots, \mathbf{u}_T] = [\mathbf{x}_1, \mathbf{x}_2, \dots, \mathbf{x}_T] \Phi^H = \mathbf{X}\Phi^H, \quad (\text{A.2})$$

where  $\mathbf{X} \triangleq [\mathbf{x}_1, \mathbf{x}_2, \dots, \mathbf{x}_T]$ .

Then, the measurement-signal relationship becomes

$$\mathbf{Y} \triangleq [\mathbf{y}_1, \mathbf{y}_2, \dots, \mathbf{y}_T] = \mathbf{F}\mathbf{X}\Phi^H. \quad (\text{A.3})$$

Using the property  $\text{vec}(\mathbf{ABC}) = (\mathbf{A} \otimes \mathbf{C}^H) \text{vec}(\mathbf{B})$ , where  $\text{vec}(\cdot)$  denotes columnwise vectorization operation, we have

$$\mathbf{y} = (\mathbf{F} \otimes \Phi) \mathbf{x} = \mathbf{A}\mathbf{x}, \quad (\text{A.4})$$

where  $\mathbf{y} = \text{vec}(\mathbf{Y}) \in \mathbb{C}^{mT}$  and  $\mathbf{x} = \text{vec}(\mathbf{X}) \in \mathbb{C}^{nT}$ . In  $k$ - $t$  FOCUSS, the unknown signal  $\mathbf{x}$  is further decomposed as

$$\mathbf{x} = \mathbf{x}_0 + \Delta\mathbf{x}, \quad (\text{A.5})$$

where  $\mathbf{x}_0$  denotes a predicted signal (such as temporal mean) and  $\Delta\mathbf{x}$  denotes residual signal that needs to be reconstructed using CS. Accordingly, the CS formulation is given by

$$\min \|\Delta\mathbf{x}\|_1 \quad \text{s.t.} \quad \|\mathbf{y} - \mathbf{A}\mathbf{x}_0 - \mathbf{A}\Delta\mathbf{x}\|_2 \leq \epsilon. \quad (\text{A.6})$$

As an optimization method for (A.6),  $k$ - $t$  FOCUSS employs weighted- $l_2$  minimization or FOCUSS algorithm by converting  $\Delta\mathbf{x} = \mathbf{W}\mathbf{q}$ , which provides the following unconstrained form of cost function:

$$C(\mathbf{q}) = \|\mathbf{y} - \mathbf{A}\mathbf{x}_0 - \mathbf{A}\mathbf{W}\mathbf{q}\|_2^2 + \lambda \|\mathbf{q}\|_2^2, \quad (\text{A.7})$$

where

$$\mathbf{W} = \begin{pmatrix} |\bar{q}_1|^p & 0 & \cdots & 0 \\ 0 & |\bar{q}_2|^p & \cdots & 0 \\ \vdots & \vdots & \ddots & \vdots \\ 0 & 0 & \cdots & |\bar{q}_N|^p \end{pmatrix}, \quad \frac{1}{2} \leq p \leq 1. \quad (\text{A.8})$$

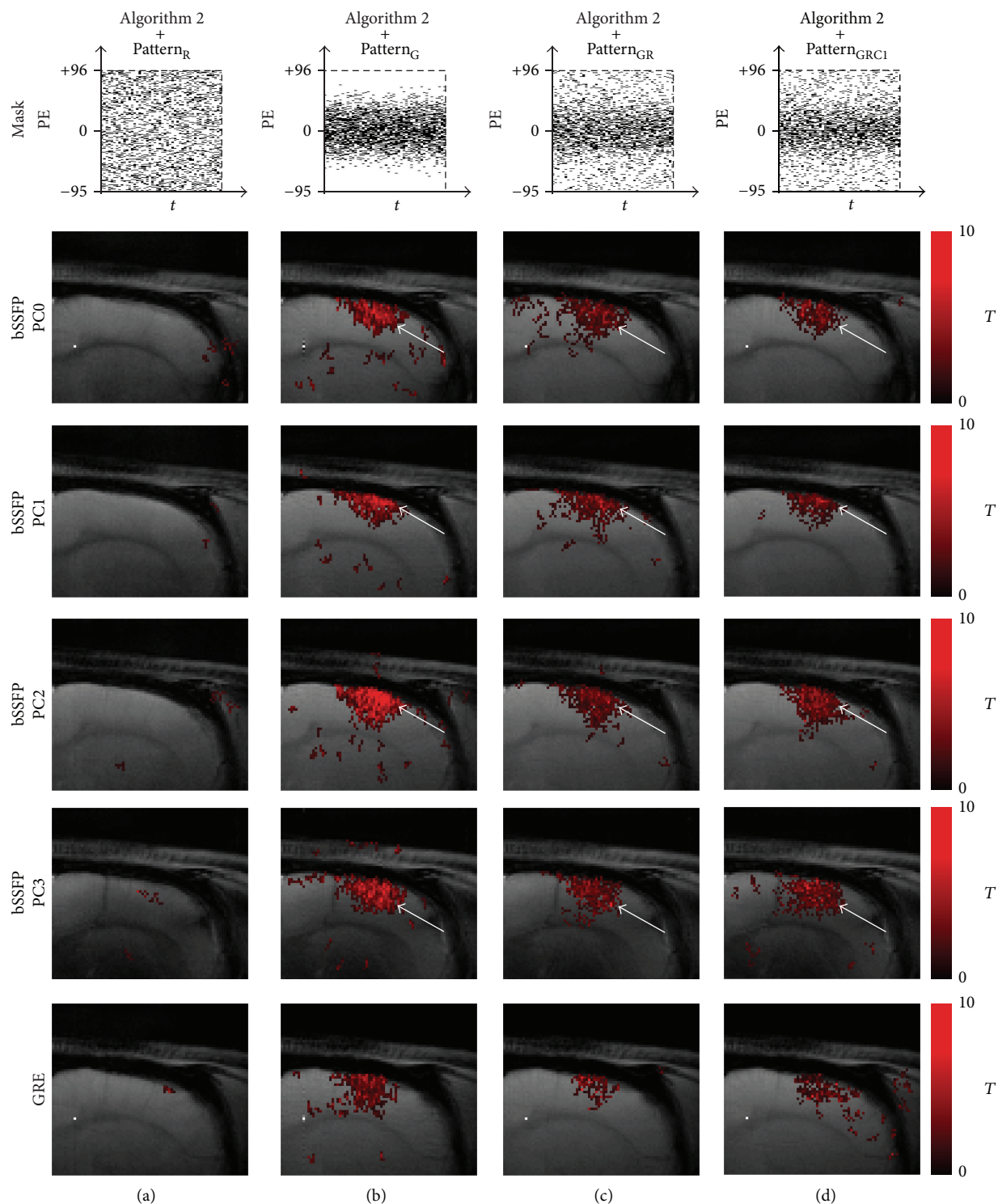


FIGURE 10: Comparison of fMRI maps reconstructed using Algorithm 2 ( $k$ - $t$  FOCUSS with KLT). fMRI maps of CS reconstructed data using Algorithm 2 and (a) Pattern<sub>R</sub>, (b) Pattern<sub>G</sub>, (c) Pattern<sub>GR</sub>, and (d) Pattern<sub>GRCI</sub> are shown for significance level of 0.05. Downsampling pattern and acquisition method used are shown on the top and left-hand side of the images, respectively. Notice the activation foci shift (white arrow) in the phase-cycled bSSFP data. The case from a representative rat is shown since similar results were obtained for different subject rats.

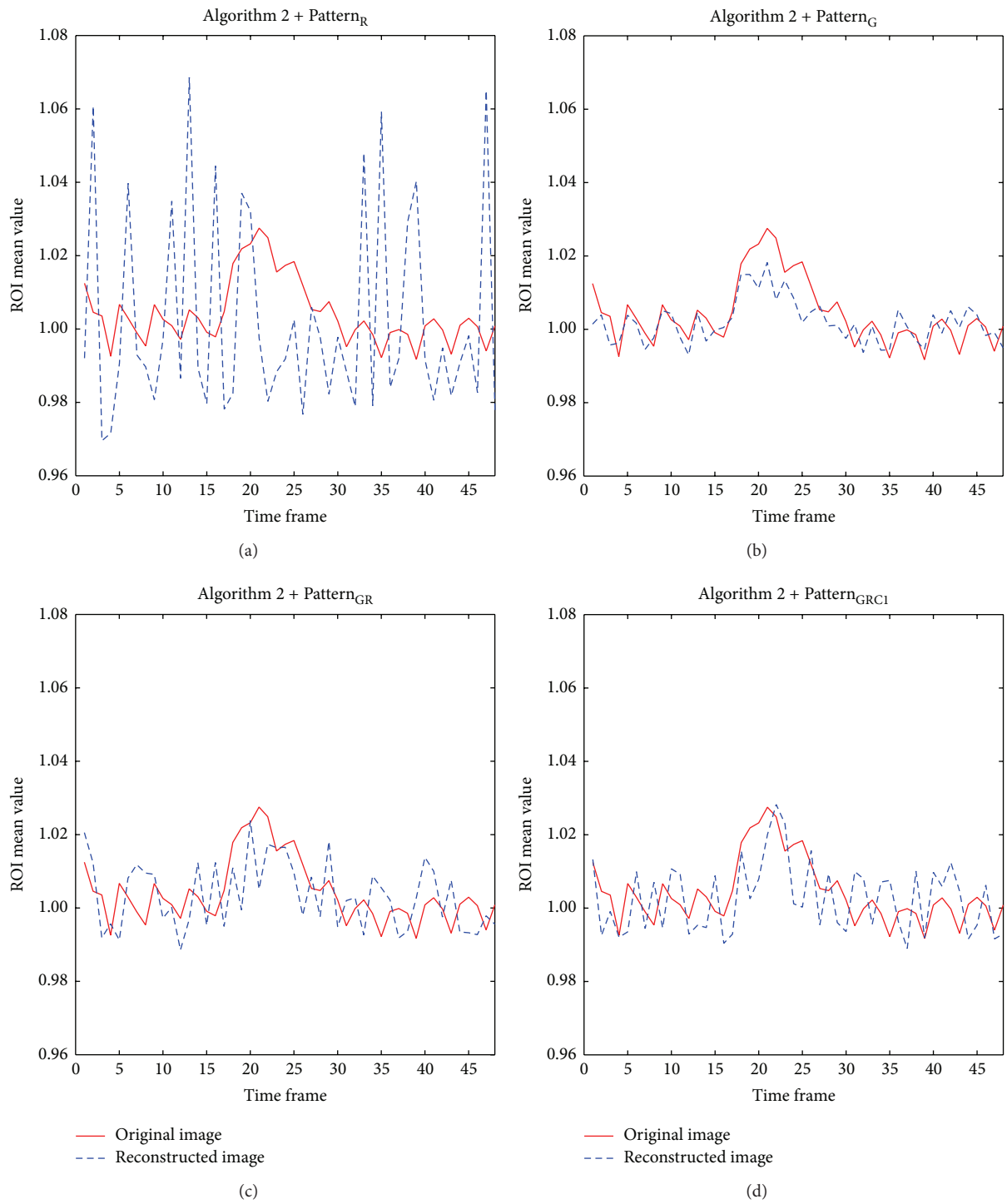


FIGURE 11: Comparison of mean ROI time course plots between full-sampled original data and CS reconstructed data using Algorithm 2 ( $k$ - $t$  FOCUSS with KLT). The time course of mean ROI from CS reconstructed data using Algorithm 2 and (a)  $\text{Pattern}_R$ , (b)  $\text{Pattern}_G$ , (c)  $\text{Pattern}_{GR}$ , and (d)  $\text{Pattern}_{GRC1}$  is shown. Mean ROI is calculated from bSSFP time-series data with PC angle of  $180^\circ$ . The case from a representative rat is shown since similar results were obtained for different subject rats.

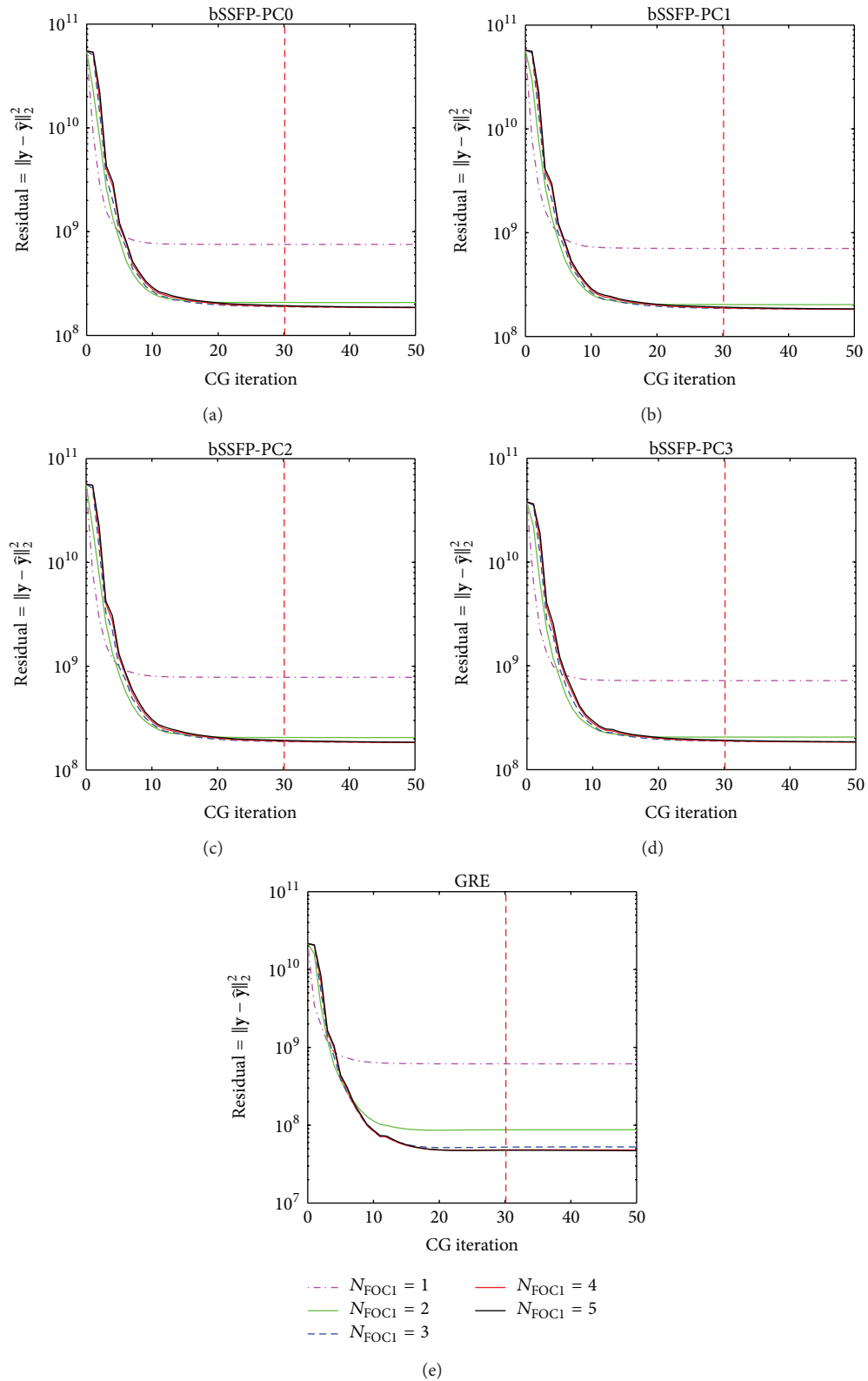


FIGURE 12: Example showing the effect of  $N_{CG1}$  on reconstruction using Algorithm 1 ( $k$ - $t$  FOCUSS with temporal FT). Residual error with  $N_{CG1}$  variation using Algorithm 1 on (a) bSSFP PC0, (b) bSSFP PC1, (c) bSSFP PC2, (d) bSSFP PC3, and (e) GRE data is shown for each different  $N_{FOC1}$ . Plots are obtained from reconstruction of downsampled data using  $\text{Pattern}_{GRC1}$  during testing phase of a representative rat, and similar results were obtained from different sampling patterns and different subject rats. Notice that residual error reaches convergence as  $N_{CG1}$  increases. The chosen  $N_{CG1}$  value of 30 is represented in each plot as a red dashed line.

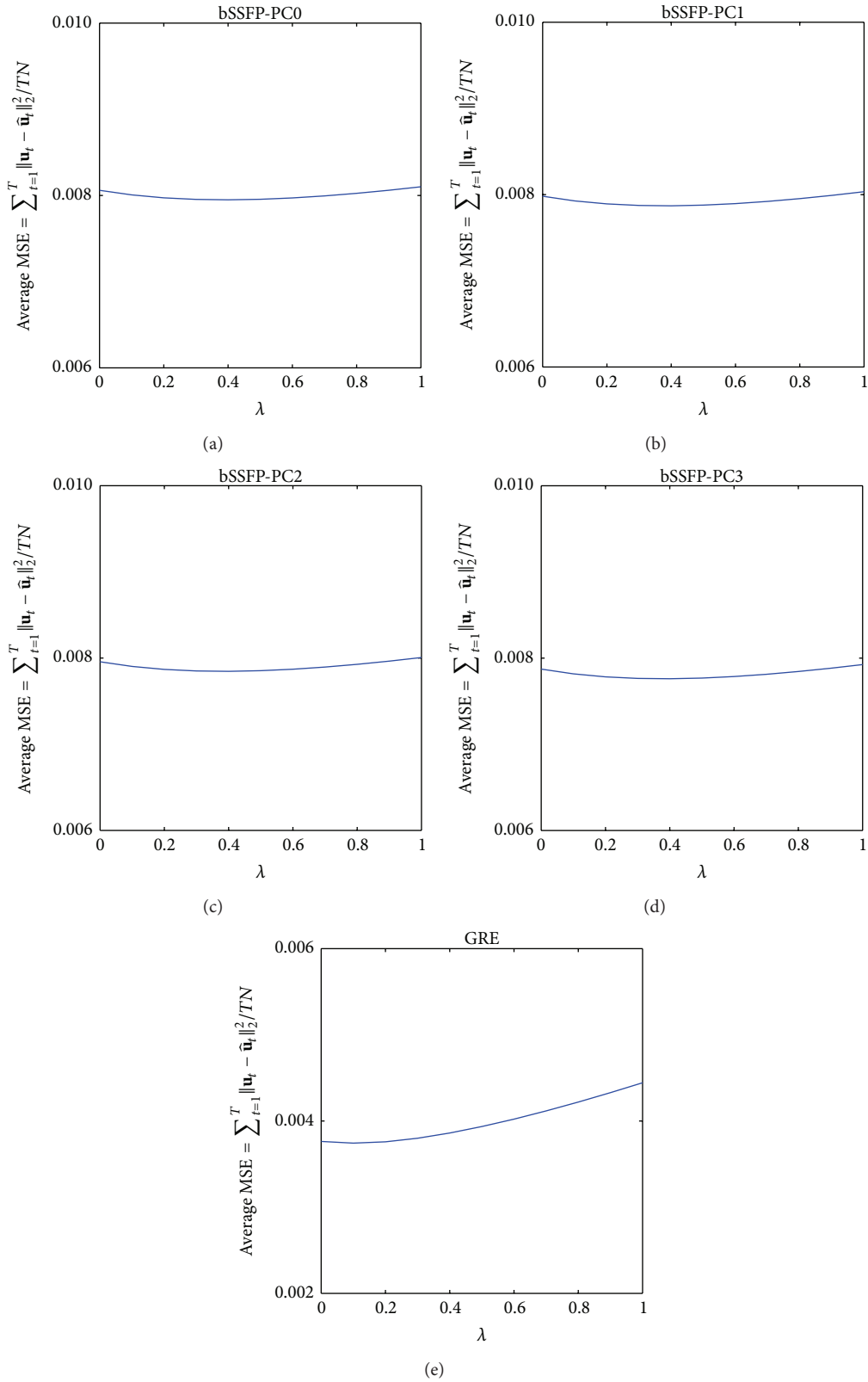


FIGURE 13: Example showing the effect of  $\lambda_1$  on reconstruction using Algorithm 1 ( $k$ - $t$  FOCUSS with temporal FT). Average MSE with  $\lambda_1$  variation using Algorithm 1 on (a) bSSFP PC0, (b) bSSFP PC1, (c) bSSFP PC2, (d) bSSFP PC3, and (e) GRE data is shown. Plots are obtained from reconstruction of downsampled data using  $\text{Pattern}_{\text{GRCI}}$  and optimal  $N_{\text{FOCI}}$  found during testing phase of a representative rat, and similar results were obtained from different sampling patterns and different subject rats. Notice that reconstruction error is relatively invariant to  $\lambda_1$  variation and minimal error is achieved with small values of  $\lambda_1$ .

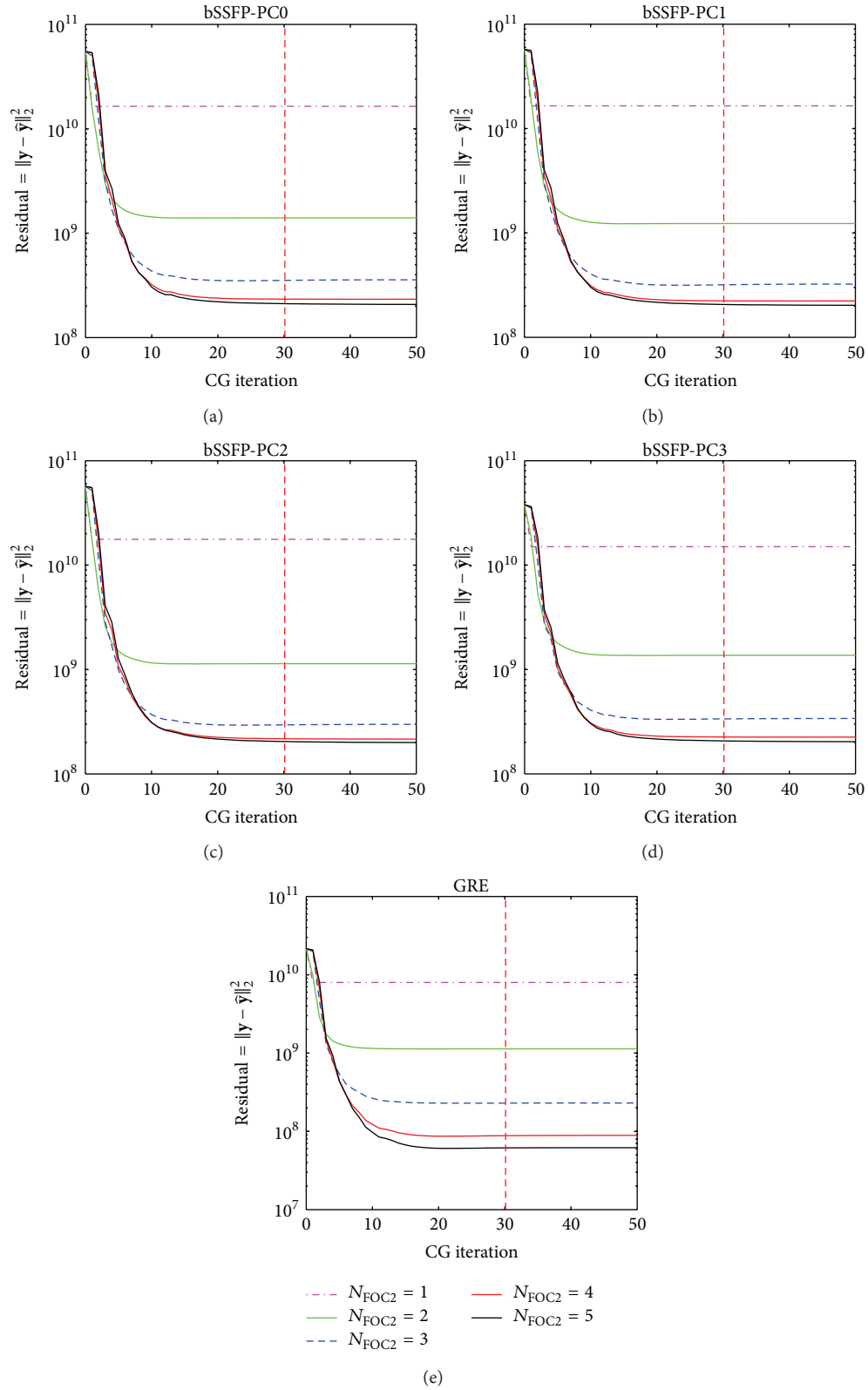


FIGURE 14: Example showing the effect of  $N_{\text{CG2}}$  on reconstruction using Algorithm 2 ( $k$ - $t$  FOCUSS with KLT). Residual error with  $N_{\text{CG2}}$  variation using Algorithm 2 on (a) bSSFP PC0, (b) bSSFP PC1, (c) bSSFP PC2, (d) bSSFP PC3, and (e) GRE data is shown for each different  $N_{\text{FOC2}}$ . Plots are obtained from reconstruction of downsampled data using  $\text{Pattern}_{\text{GRCl}}$  during testing phase of a representative rat, and similar results were obtained from different sampling patterns and different subject rats. Notice that residual error reaches convergence as  $N_{\text{CG2}}$  increases. The chosen  $N_{\text{CG2}}$  value of 30 is represented in each plot as a red dashed line.

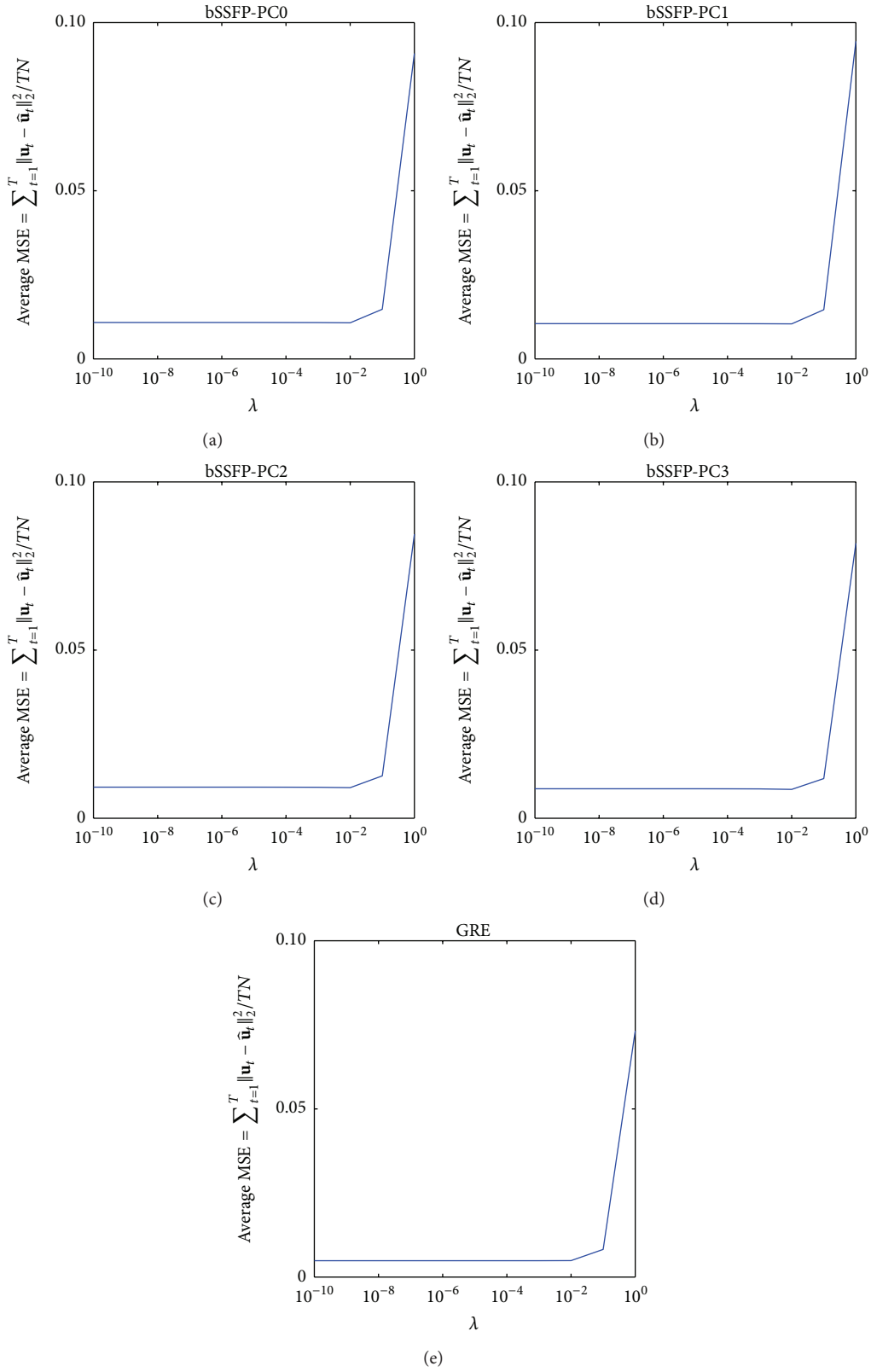


FIGURE 15: Example showing the effect of  $\lambda_2$  on reconstruction using Algorithm 2 ( $k$ - $t$  FOCUSS with KLT). Average MSE with  $\lambda_2$  variation using Algorithm 2 on (a) bSSFP PC0, (b) bSSFP PC1, (c) bSSFP PC2, (d) bSSFP PC3, and (e) GRE data is shown. Plots are obtained from reconstruction of downsampled data using  $\text{Pattern}_{\text{GRC1}}$  and optimal  $N_{\text{FOC2}}$  found during testing phase of a representative rat, and similar results were obtained from different sampling patterns and different subject rats. Notice that reconstruction error is relatively invariant to  $\lambda_2$  variation and minimal error is achieved with small values of  $\lambda_2$ .

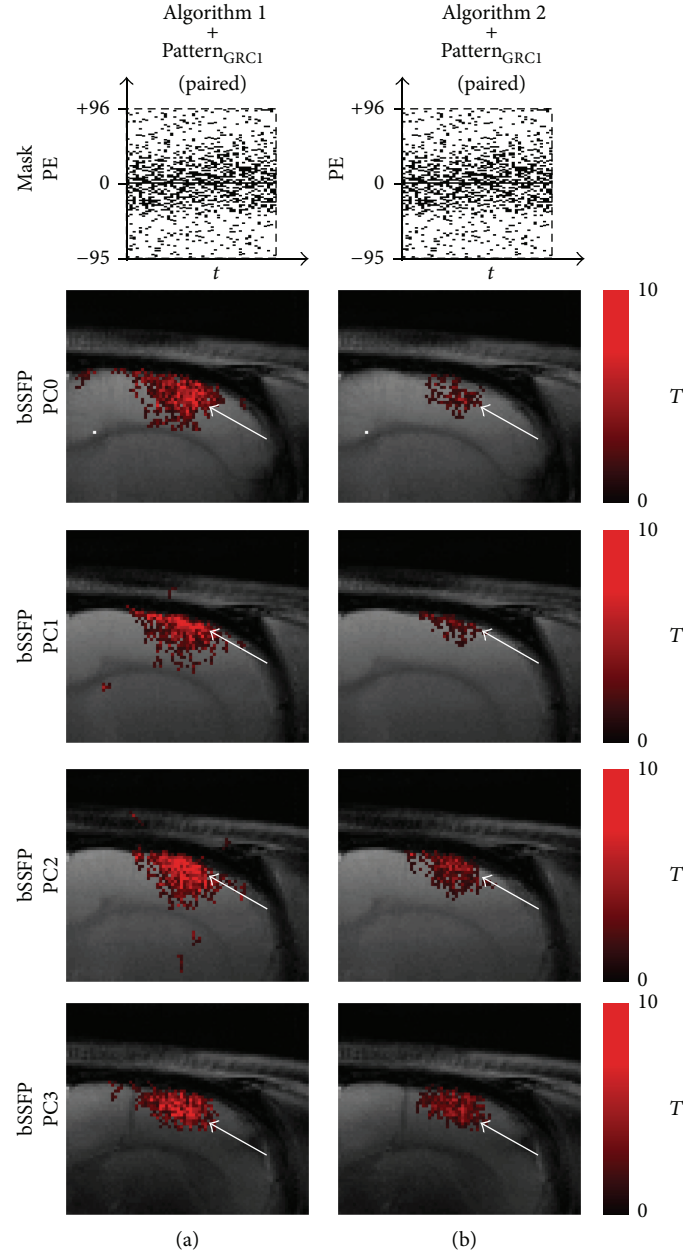


FIGURE 16: Presumed effect of paired random sampling scheme in the reconstruction of fMRI map using  $k$ - $t$  FOCUSS algorithms. The fMRI maps of CS reconstructed data using (a) Algorithm 1 and pairwise sampling of  $\text{Pattern}_{\text{GRC1}}$  and (b) Algorithm 2 and pairwise sampling of  $\text{Pattern}_{\text{GRC1}}$  are shown for significance level of 0.05. Downsampling pattern and acquisition method used are shown on the top and left-hand side of the images, respectively. Notice the decrease in activation sensitivity with the inclusion of pairwise sampling scheme.

Here,  $\bar{\mathbf{q}} = [\bar{q}_1, \dots, \bar{q}_N]$  denotes the estimated signal  $\mathbf{x}$  from the previous iteration with  $N = nT$ . Then, the optimal solution of the problem is found by calculating the following:

$$\mathbf{x} = \mathbf{x}_0 + \Theta \mathbf{A}^H (\mathbf{A} \Theta \mathbf{A}^H + \lambda \mathbf{I})^{-1} (\mathbf{y} - \mathbf{A} \mathbf{x}_0), \quad (\text{A.9})$$

where  $\Theta = \mathbf{W} \mathbf{W}^H$ . Since the direct calculation of (A.9) is computationally demanding due to the matrix inversion of a large size matrix, conjugate gradient (CG) method is used to minimize the cost function (A.7).

A generic form of the implementation of  $k$ - $t$  FOCUSS that utilizes temporal FT  $\Phi$  is summarized in Algorithm 1.

*k-t FOCUSS with KLT.* Even though  $k$ - $t$  FOCUSS has been developed as above utilizing temporal FT as  $\Phi$  in (A.3), other temporal transformations could also be used to efficiently sparsify the signal [16]. One example is the utilization of Karhunen-Loève transform (KLT), which is also known as principal component analysis (PCA) [45].

KLT or PCA is a data-dependent mathematical procedure that uses an orthogonal transformation to convert possibly correlated elements of the data into a set of linearly uncorrelated components called “principal components.” The transformation leads to a result in which the first principal component accounts for the largest possible variance of the data, and each succeeding component has the next largest variance possible under the restriction that it is orthogonal (i.e., uncorrelated) to the preceding components. The transform is known to compact most of the energy into a small number of expansion coefficients [45] and thus is ideal in CS perspective [16].

The application of KLT within  $k$ - $t$  FOCUSS requires calculation of a covariance matrix from a trained dataset. In this paper, the result from  $k$ - $t$  FOCUSS that utilizes temporal FT using Algorithm 1 is used for the calculation of covariance matrix. Once the training dataset is defined, the covariance matrix is constructed as follows:

$$\mathbf{C} = \widehat{\mathbf{U}}^H \widehat{\mathbf{U}}. \quad (\text{A.10})$$

Then, the eigenvectors of  $\mathbf{C}$  can be used for the KL transform; that is,

$$\Phi \leftarrow \text{eig}(\mathbf{C}). \quad (\text{A.11})$$

After updating  $\Phi$ , we can perform additional  $k$ - $t$  FOCUSS iterations. The algorithm is summarized in Algorithm 2.

## Conflict of Interests

The authors declare that there is no conflict of interests regarding the publication of this paper.

## Acknowledgments

This work was supported by the National Research Foundation (NRF) of Korea under project number NRF-2013M3-A9B2076548 and Samsung Research Funding Center of Samsung Electronics under project number SRFC-IT1401-05.

## References

- [1] S. Ogawa, T. M. Lee, A. R. Kay, and D. W. Tank, “Brain magnetic resonance imaging with contrast dependent on blood oxygenation,” *Proceedings of the National Academy of Sciences of the United States of America*, vol. 87, no. 24, pp. 9868–9872, 1990.
- [2] C. Bowen, R. Menon, and J. Gati, “High field balanced-SSFP fMRI: a BOLD technique with excellent tissue sensitivity and superior large vessel suppression,” in *Proceedings of the 13th Annual Meeting of ISMRM*, p. 119, Miami Beach, Fla, USA, 2005.
- [3] J. Frahm, H. Bruhn, K. D. Merboldt, and W. Hänicke, “Dynamic MR imaging of human brain oxygenation during rest and photic stimulation,” *Journal of Magnetic Resonance Imaging*, vol. 2, no. 5, pp. 501–505, 1992.
- [4] R. I. Henkin and L. M. Levy, “Lateralization of brain activation to imagination and smell of odors using functional magnetic resonance imaging (fMRI): left hemispheric localization of pleasant and right hemispheric localization of unpleasant odors,” *Journal of Computer Assisted Tomography*, vol. 25, no. 4, pp. 493–514, 2001.
- [5] H. L. Jin, S. O. Dumoulin, E. U. Saritas et al., “Full-brain coverage and high-resolution imaging capabilities of passband b-SSFP fMRI at 3T,” *Magnetic Resonance in Medicine*, vol. 59, no. 5, pp. 1099–1110, 2008.
- [6] K. L. Miller, S. M. Smith, P. Jezzard, G. C. Wiggins, and C. J. Wiggins, “Signal and noise characteristics of SSFP fMRI: a comparison with GRE at multiple field strengths,” *NeuroImage*, vol. 37, no. 4, pp. 1227–1236, 2007.
- [7] S.-H. Park, T. Kim, P. Wang, and S.-G. Kim, “Sensitivity and specificity of high-resolution balanced steady-state free precession fMRI at high field of 9.4T,” *NeuroImage*, vol. 58, no. 1, pp. 168–176, 2011.
- [8] B. Wowk, M. C. McIntyre, and J. K. Saunders, “k-Space detection and correction of physiological artifacts in fMRI,” *Magnetic Resonance in Medicine*, vol. 38, no. 6, pp. 1029–1034, 1997.
- [9] K. Zhong, J. Leupold, J. Hennig, and O. Speck, “Systematic investigation of balanced steady-state free precession for functional MRI in the human visual cortex at 3 Tesla,” *Magnetic Resonance in Medicine*, vol. 57, no. 1, pp. 67–73, 2007.
- [10] M. A. Griswold, P. M. Jakob, R. M. Heidemann et al., “Generalized autocalibrating partially parallel acquisitions (GRAPPA),” *Magnetic Resonance in Medicine*, vol. 47, no. 6, pp. 1202–1210, 2002.
- [11] K. Pruessmann, M. Weiger, M. Scheidegger, and P. Boesiger, “SENSE: sensitivity encoding for fast MRI,” *Magnetic Resonance in Medicine*, vol. 42, no. 5, pp. 952–962, 1999.
- [12] D. K. Sodickson and W. J. Manning, “Simultaneous acquisition of spatial harmonics (SMASH): fast imaging with radiofrequency coil arrays,” *Magnetic Resonance in Medicine*, vol. 38, no. 4, pp. 591–603, 1997.
- [13] M. Lustig, D. Donoho, and J. M. Pauly, “Sparse MRI: the application of compressed sensing for rapid MR imaging,” *Magnetic Resonance in Medicine*, vol. 58, no. 6, pp. 1182–1195, 2007.
- [14] E. J. Candès, J. Romberg, and T. Tao, “Robust uncertainty principles: exact signal reconstruction from highly incomplete frequency information,” *IEEE Transactions on Information Theory*, vol. 52, no. 2, pp. 489–509, 2006.
- [15] D. L. Donoho, “Compressed sensing,” *IEEE Transactions on Information Theory*, vol. 52, no. 4, pp. 1289–1306, 2006.
- [16] H. Jung, J. C. Ye, and E. Y. Kim, “Improved  $k$ - $t$  BLAST and  $k$ - $t$  SENSE using FOCUSS,” *Physics in Medicine and Biology*, vol. 52, no. 11, pp. 3201–3226, 2007.
- [17] U. Gamper, P. Boesiger, and S. Kozerke, “Compressed sensing in dynamic MRI,” *Magnetic Resonance in Medicine*, vol. 59, no. 2, pp. 365–373, 2008.
- [18] H. Jung, K. Sung, K. S. Nayak, E. Y. Kim, and J. C. Ye, “k-t FOCUSS: a general compressed sensing framework for high resolution dynamic MRI,” *Magnetic Resonance in Medicine*, vol. 61, no. 1, pp. 103–116, 2009.
- [19] O. Jeromin, M. S. Pattichis, and V. D. Calhoun, “Optimal compressed sensing reconstructions of fMRI using 2D deterministic and stochastic sampling geometries,” *BioMedical Engineering Online*, vol. 11, article 25, 2012.
- [20] H. Jung and J. Ye, “Performance evaluation of accelerated functional MRI acquisition using compressed sensing,” in *Proceedings of the IEEE International Symposium on Biomedical Imaging: From Nano to Macro (ISBI '09)*, pp. 702–705, 2009.

- [21] D. J. Holland, C. Liu, X. Song et al., "Compressed sensing reconstruction improves sensitivity of variable density spiral fMRI," *Magnetic Resonance in Medicine*, vol. 70, no. 6, pp. 1634–1643, 2013.
- [22] X. Zong, J. Lee, A. John Poplowsky, S. G. Kim, and J. C. Ye, "Compressed sensing fMRI using gradient-recalled echo and EPI sequences," *NeuroImage*, vol. 92, pp. 312–321, 2014.
- [23] A. C. Silva, S.-P. Lee, G. Yang, C. Ladecola, and S.-G. Kim, "Simultaneous blood oxygenation level-dependent and cerebral blood flow functional magnetic resonance imaging during forepaw stimulation in the rat," *Journal of Cerebral Blood Flow and Metabolism*, vol. 19, no. 8, pp. 871–879, 1999.
- [24] P. A. Bottomley, "Spatial localization in NMR spectroscopy *in vivo*," *Annals of the New York Academy of Sciences*, vol. 508, no. 1, pp. 333–348, 1987.
- [25] L. Chen, A. Samsonov, and E. V. R. Dibella, "A Framework for generalized reference image reconstruction methods including HYPR-LR, PR-FOCUSS, and k-t FOCUSS," *Journal of Magnetic Resonance Imaging*, vol. 34, no. 2, pp. 403–412, 2011.
- [26] J. A. Sorenson and X. Wang, "ROC methods for evaluation of fMRI techniques," *Magnetic Resonance in Medicine*, vol. 36, no. 5, pp. 737–744, 1996.
- [27] Q. Du and J. E. Fowler, "Hyperspectral image compression using JPEG2000 and principal component analysis," *IEEE Geoscience and Remote Sensing Letters*, vol. 4, no. 2, pp. 201–205, 2007.
- [28] B. Penna, T. Tillo, E. Magli, and G. Olmo, "Transform coding techniques for lossy hyperspectral data compression," *IEEE Transactions on Geoscience and Remote Sensing*, vol. 45, no. 5, pp. 1408–1421, 2007.
- [29] K. Scheffler and S. Lehnhardt, "Principles and applications of balanced SSFP techniques," *European Radiology*, vol. 13, no. 11, pp. 2409–2418, 2003.
- [30] K. L. Miller, R. H. N. Tijssen, N. Stikov, and T. W. Okell, "Steady-state MRI: methods for neuroimaging," *Imaging in Medicine*, vol. 3, no. 1, pp. 93–105, 2011.
- [31] S. S. Chen, D. L. Donoho, and M. A. Saunders, "Atomic decomposition by basis pursuit," *SIAM Journal on Scientific Computing*, vol. 20, no. 1, pp. 33–61, 1998.
- [32] P. Boufounos, M. F. Duarte, and R. G. Baraniuk, "Sparse signal reconstruction from noisy compressive measurements using cross validation," in *Proceedings of the IEEE/SP 14th Workshop on Statistical Signal Processing (SSP '07)*, pp. 299–303, Madison, Wis, USA, August 2007.
- [33] R. Ward, "Compressed sensing with cross validation," *IEEE Transactions on Information Theory*, vol. 55, no. 12, pp. 5773–5782, 2009.
- [34] D. Angelosante, G. B. Giannakis, and E. Grossi, "Compressed sensing of time-varying signals," in *Proceedings of the 16th International Conference on Digital Signal Processing*, pp. 1–8, IEEE, 2009.
- [35] O. Bieri, M. Markl, and K. Scheffler, "Analysis and compensation of eddy currents in balanced SSFP," *Magnetic Resonance in Medicine*, vol. 54, no. 1, pp. 129–137, 2005.
- [36] H. M. Nguyen and G. H. Glover, "A modified generalized series approach: application to sparsely sampled fMRI," *IEEE Transactions on Biomedical Engineering*, vol. 60, no. 10, pp. 2867–2877, 2013.
- [37] K. J. Friston, P. Jezzard, and R. Turner, "Analysis of functional MRI time-series," *Human Brain Mapping*, vol. 1, no. 2, pp. 153–171, 1993.
- [38] G. M. Boynton, S. A. Engel, G. H. Glover, and D. J. Heeger, "Linear systems analysis of functional magnetic resonance imaging in human V1," *The Journal of Neuroscience*, vol. 16, no. 13, pp. 4207–4221, 1996.
- [39] M. W. Woolrich, B. D. Ripley, M. Brady, and S. M. Smith, "Temporal autocorrelation in univariate linear modeling of FMRI data," *NeuroImage*, vol. 14, no. 6, pp. 1370–1386, 2001.
- [40] S. G. Lingala, Y. Hu, E. Dibella, and M. Jacob, "Accelerated dynamic MRI exploiting sparsity and low-rank structure: k-t SLR," *IEEE Transactions on Medical Imaging*, vol. 30, no. 5, pp. 1042–1054, 2011.
- [41] M. S. Asif, L. Hamilton, M. Brummer, and J. Romberg, "Motion-adaptive spatio-temporal regularization for accelerated dynamic MRI," *Magnetic Resonance in Medicine*, vol. 70, no. 3, pp. 800–812, 2013.
- [42] H. Yoon, K. Kim, D. Kim, Y. Bresler, and J. Ye, "Motion adaptive patch-based low-rank approach for compressed sensing cardiac cine MRI," *IEEE Transactions on Medical Imaging*, vol. 33, no. 11, pp. 2069–2085, 2014.
- [43] I. F. Gorodnitsky, J. S. George, and B. D. Rao, "Neuromagnetic source imaging with FOCUSS: a recursive weighted minimum norm algorithm," *Electroencephalography and Clinical Neurophysiology*, vol. 95, no. 4, pp. 231–251, 1995.
- [44] I. Gorodnitsky and B. Rao, "Sparse signal reconstruction from limited data using FOCUSS: a re-weighted minimum norm algorithm," *IEEE Transactions on Signal Processing*, vol. 45, no. 3, pp. 600–616, 1997.
- [45] H. V. Poor, *An Introduction to Signal Detection and Estimation*, Springer, New York, NY, USA, 1988.

## Review Article

# A Window into the Brain: Advances in Psychiatric fMRI

**Xiaoyan Zhan<sup>1</sup> and Rongjun Yu<sup>1,2</sup>**

<sup>1</sup>*School of Psychology and Center for Studies of Psychological Application, South China Normal University, 55 West Zhongshan Avenue, Tianhe District, Guangzhou 510631, China*

<sup>2</sup>*School of Economics & Management and Scientific Laboratory of Economic Behaviors, South China Normal University, 55 West Zhongshan Avenue, Tianhe District, Guangzhou 510631, China*

Correspondence should be addressed to Rongjun Yu; [rongjun.yu@gmail.com](mailto:rongjun.yu@gmail.com)

Received 23 August 2014; Revised 16 December 2014; Accepted 17 December 2014

Academic Editor: Zhengchao Dong

Copyright © 2015 X. Zhan and R. Yu. This is an open access article distributed under the Creative Commons Attribution License, which permits unrestricted use, distribution, and reproduction in any medium, provided the original work is properly cited.

Functional magnetic resonance imaging (fMRI) plays a key role in modern psychiatric research. It provides a means to assay differences in brain systems that underlie psychiatric illness, treatment response, and properties of brain structure and function that convey risk factor for mental diseases. Here we review recent advances in fMRI methods in general use and progress made in understanding the neural basis of mental illness. Drawing on concepts and findings from psychiatric fMRI, we propose that mental illness may not be associated with abnormalities in specific local regions but rather corresponds to variation in the overall organization of functional communication throughout the brain network. Future research may need to integrate neuroimaging information drawn from different analysis methods and delineate spatial and temporal patterns of brain responses that are specific to certain types of psychiatric disorders.

## 1. Introduction

The human brain is the most mysterious and vital organ. Recent neuroimaging techniques, including functional magnetic resonance imaging (fMRI), electroencephalography (EEG), and magnetoencephalography (MEG), now allow us to probe the brain at unprecedentedly high temporal or spatial resolution without the use of invasive techniques. Since the first fMRI brain scans of the 1980s, scientists have achieved great progress not only in technical procedures employed to acquire brain imaging data but also in data processing methods which subsequently reveal an inspiring understanding of the brain drawn from various data perspectives. fMRI has become the dominant technique in neuroimaging due to its noninvasiveness, lack of radiation exposure, a relatively good spatial and temporal resolution, and relative ease to acquire.

In this paper, we will review popular data processing methods used in task-based fMRI and resting-state fMRI (see Figure 1 for a summary of mainstream fMRI methods). Some methods introduced in task-based fMRI, such as MVPA, are also applied in the case of resting-state fMRI data. Different

analysis methods probe specific brain activity patterns. The application of these methods to investigating psychiatric disorders will be discussed in great detail. We also point out here that within neuropsychology there is an ongoing paradigm shift from identifying foci of abnormalities to delineating the functional connectivity among several brain regions, towards developing a global understanding of aberrations at the level of large-scale, whole brain networks. The advantages and disadvantages of each neuroimaging method are discussed and compared in order to help researchers select the methods most appropriate to their purposes.

## 2. Task-Based fMRI

Due to the great sensitivity of fMRI signals to event-related changes in neuronal blood flow, we can compare the BOLD signal differences between patients with psychiatric disorders and normal subjects when performing different kinds of tasks in order to elucidate how a brain in a state of disorder functions differently from a normal one. In this section, we will introduce several methods frequently used in task-related fMRI analyses and discuss the advantages and disadvantages

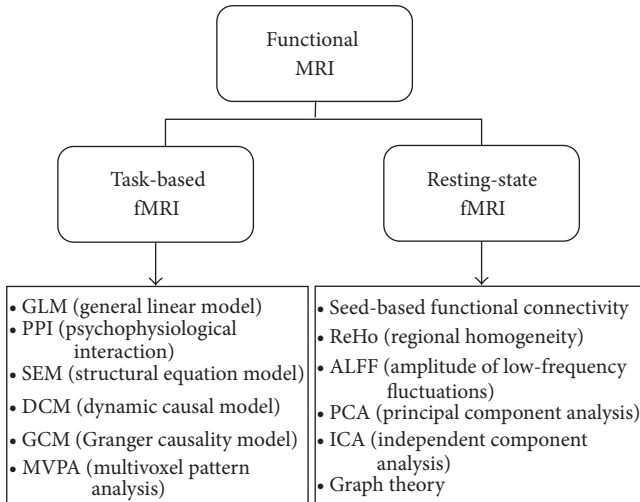


FIGURE 1: A summary of mainstream fMRI neuroimaging methods.

of each method (see Table 1). Also note that these techniques are not mutually exclusive, such that two or more of them may be applied to the same dataset according to the quality of the dataset and the purpose of the study. Of importance, we discussed how these analyses can inform each other and some caveats in using these methods, such as choosing the frequency bands in resting-state fMRI (R-fMRI).

**2.1. Subtraction and Correlation.** The general linear model (GLM) has gained growing popularity in task-related fMRI analysis since its introduction into the neuroimaging community by Friston et al. [1] in 1994, due to its easy interpretability and fast computability. GLM provides a framework for most kinds of data modeling and can minimize confounding factors, such as head motions or respiration from the subject, provided that these data are modeled. The aim of the general linear model is to explain the variation of the time course,  $y_1, \dots, y_i, \dots, y_n$ , in terms of a linear combination of explanatory variables plus a Gaussian error term. The general linear model in matrix form can be written as

$$Y = X\beta + \varepsilon, \quad (1)$$

where  $Y$  is the vector of observed pixel values,  $\beta$  is the vector of parameters, and  $\varepsilon$  is the vector of error terms. The matrix  $X$  is known as the design matrix (Figure 2(a)). It has one row for every time point in the original data and one column for every explanatory variable in the model. In the GLM, the columns of  $X$  contain vectors corresponding to the “on” and “off” elements of the stimulus presented. By finding the magnitude of the parameter in  $\beta$  corresponding to these vectors, the presence or absence of activation can be detected. The aim of GLM analysis is to identify the brain regions that show significant signal change in response to the experimental conditions. Each pixel is assigned a value dependent on the likelihood of the null hypothesis being false. The null hypothesis is that the observed signal changes can be explained purely by random variation in the data.

The brain image containing such information for all voxels is called a statistical parametric map [1]. One of the simplest methods for obtaining results from an fMRI experiment is to perform a simple subtraction on two experimental conditions. By averaging together all the images acquired during the “on” phase of the task and subtracting the average of all the “off” images, brain regions that are activated during the “on” phase of the task can be drawn out of the data pool and identified. Using parametric design, researchers can also examine parametric correlation with behavior in the brain. GLM is also the base of the majority of functional/effective connectivity estimation techniques which will be introduced in the following sections.

GLM is the dominant method used in task-based fMRI. Studies on psychiatric disorders have used this method to compare brain activities induced by certain experimental manipulations in the patient group and in the control group. For example, Juckel et al. [2] scanned patients with schizophrenia and healthy subjects using fMRI while they performed a “monetary incentive delay” task, in which they anticipated potential monetary gain, loss, or neutral outcomes. Following preprocessing, the fMRI data was modeled by GLM with three explanatory variables (“gain,” “loss,” and “neutral outcome,” indicating experimental cues) convolved with Cohen’s gamma-function. Activations of different experimental conditions can be compared based on the BOLD response differences which can be assessed using linear combinations of the estimated GLM parameters ( $\beta$  values). Within-group activation (e.g., “gain versus neutral outcome”) and intergroup differences can be compared by including the BOLD response variations of all subjects in each group in a second-level random effects analysis. However, GLM has also undergone some criticism focusing primarily on the assumptions the model makes [3]. Greater attention should be paid to checking the model’s assumptions when applying GLM as a tool to analyze task-related fMRI data. This approach is the main method used in task-based fMRI in psychiatric research.

**2.2. Psychophysiological Interaction (PPI).** One important goal of neuroimaging research is to describe the pattern of brain connectivity among different regions. Functional connectivity refers to undirected associations between brain regions while effective connectivity reveals a directed and causal relationship. Psychophysiological interaction, in a clever use of the GLM, measures how functional connectivity is affected by psychological variables without specifying the directions of such influences [4]. It examines how brain activity can be explained by the interaction between an experimental variable (e.g., level of attention) and the coupling between signals from a particular brain area (the source area) and signals from voxels in the rest of the entire brain (Figure 2(b)). A psychophysiological interaction means that the contribution of one area to another changes significantly with the experimental or psychological context. In other words, regional responses in the source area to an experimental or psychological factor are modulated by signals from a distal brain region. Das et al. [5] used a behavioral

TABLE 1: Comparisons among different task-based fMRI analysis methods.

Methods	Purposes	Strengths	Limitations
General linear model	Estimating to what extent each known predictor contributes to the variability observed in the voxel's BOLD signal time course	(i) Mathematically simple, easily interpreted, and readily available in standard packages (e.g., the SPM software) (ii) Flexible to incorporate multiple quantitative and qualitative independent variables, such as low-frequency drifts and head motion	(i) Relies on assumptions such as appropriate regressors in the matrix and normality of the fMRI noise which are difficult to check
Psychophysiological interaction	“Searching” for regions that correlate differently with a particular region under certain experimental context	(i) Can explore the connectivity of the source area to the rest of the brain and how it interacts with the psychological variables	(i) Only involves one region of interest in one model (ii) Limited in the extent to which you can infer a causal relationship
Structural equation model	Estimating the degree to which the activity between different brain regions is connected and how this connectivity is affected by an experimental variable	(i) Can examine interactions of several regions of interest simultaneously and offer estimations of causal relationships (ii) Predetermined connections are based on prior anatomical or functional knowledge	(i) Causality is predetermined, and this might overlook several aspects of neural activity (ii) Assumes the interactions are linear (i.e., structural equation models are not time-series) (iii) Lacks temporal information
Dynamic causal model	Estimating and making inferences about the coupling among brain regions and how this coupling is affected by changes in experimental context at the neuronal level	(i) Biologically more accurate and realistic than other methods because DCM models interactions at the neuronal rather than the hemodynamic level and complex connectivity patterns between regions can be arbitrarily postulated	(i) Prespecified models are needed (ii) Requires much longer time to estimate parameters than SEM (iii) Neurodynamics in each region are characterized by a single state variable (“neuronal activity”)
Granger causality model	Measuring the predictability of one neural time-series from another	(i) No a priori specification of a model is needed. Thus this model can complement the hypothesis-driven methods and help to form directed graph models of regions and their interactions	(i) The causal relationship may be caused by the differences in hemodynamic latencies in different parts of the brain if long repetition times (TR) are used
Multivoxel pattern analysis	Applying pattern-classification algorithms to demonstrate the relationship between measures of brain activity and a perceptual state and provide an information-theoretic framework for the isolation of regions that uniquely represent a behavior	(i) Simultaneously examines the disparate signals carried within a set of voxels rather than examining individual voxels in parallel (ii) Can decode more complex information due to improved sensitivity and use of spatial information	(i) The possibility of overfitting increases as the classifier becomes more complex, which may result in poor performance in tests of generalization

task in which schizophrenia patients and healthy participants were asked to identify the emotions displayed on a series of facial images presented either supraliminally or subliminally during scanning. Subtraction analyses of fMRI data showed that, compared to healthy controls, schizophrenia patients showed reduced activity in the right amygdala and MPFC during conscious perception of fear (relative to neutral) and also in the bilateral amygdala and rostral ACC of the MPFC during subliminal perception of fear. PPI analyses revealed reduced neural activity in schizophrenia patients, relative to control subjects, in the pathway from the amygdala and its projection to the medial prefrontal cortex (MPFC) in response to fear perception. In another fMRI study, Wang et al. [6] applied PPI analysis to explore how abnormal functional connectivity in mPFC in schizophrenics altered as a result of psychological context or variables. They found

that schizophrenic patients showed higher mPFC-LSTG connectivity under self-generated conditions than under other-generated conditions.

**2.3. Structural Equation Model (SEM).** The structural equation model, which was developed in the field of econometrics and first applied to neuroimaging data in 1991 [7], is another way to measure effective connectivity. Like PPI, SEM is also used to describe how effective connectivity is affected by experimental context. But, compared to PPI, SEM is better at identifying causal relationships and it combines covariances in activity between different brain areas with anatomical models of these brain areas' connections [8, 9]. SEM contains a group of regions and a group of directed connections and these connections are presumed to represent

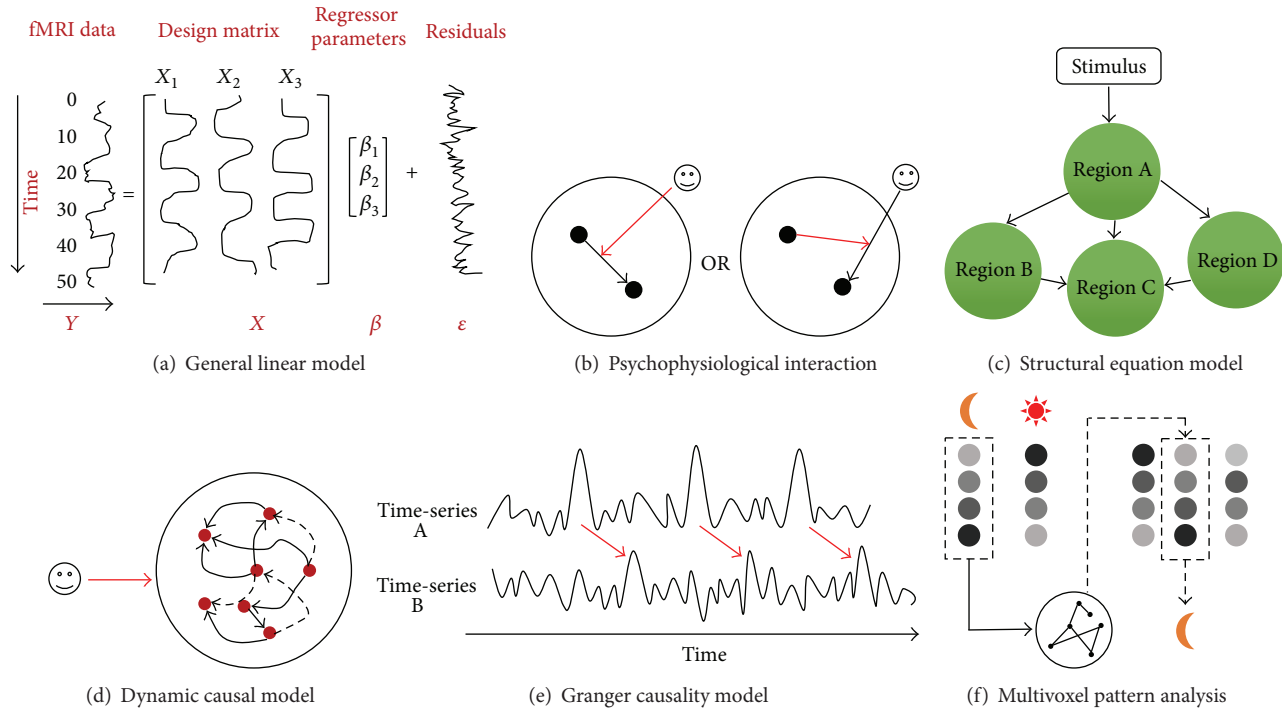


FIGURE 2: A summary of task-related fMRI analysis methods. (a) An example of the general linear model containing the BOLD signal time-series  $Y$  within a particular voxel, the design matrix  $X$  including three regressors of interest, the regressor parameters  $\beta$ , and the unexplained residuals  $\epsilon$ . (b) Psychophysiological interaction can identify how the connectivity between two particular brain regions is modulated by an experimental variable or how a specified region modulates the relationship between an experimental variable and another brain region. (c) Structural equation model includes the stimulus to have an influence on all variables without input within the model. (d) An illustration of the dynamic causal model. (e) An illustration of the Granger causality model. Time-series A can be said to cause time-series B because the pattern of B is similar to A and A has temporal precedence. (f) An example of multivoxel pattern analysis. A specific classifier is chosen to identify the pattern of a certain mental state, whereafter the accuracy of the classifier will be tested using a new dataset.

causal relationships (Figure 2(c)). SEM requires an a priori assumption of causality without inference from the data and from this basis subsequently builds a model about how the regions are connected to each other. Free parameters in these models are “path coefficients”—representing the strength of connections. This approach offers a move from correlational analysis (inherently bidirectional) to unidirectional connections (paths) which imply causality. One well-known strength of SEM is the method’s ability to specify latent variable models that provide separate estimates of relations among latent constructs and their manifest indicators (the measurement model) and of the relations among constructs (the structural model) [10]. Another strength of SEM is the availability of measures of global fit that can provide a summary evaluation of even complex models that involve a large number of linear equations [10]. It has proved useful in distinguishing a patient’s neural network from a normal subject’s neural network in one fMRI simulation study [11]. In another fMRI study, schizophrenic patients were scanned while performing a “2-back” working memory task. SEM was used to assess effective connectivity within a cortical-subcortical-cerebellar network for mnemonic information processing and comparison of group differences [12].

2.4. *Dynamic Causal Model (DCM)*. Similar to SEM, the dynamic causal model is also an approach to estimate effective connectivity and how this connectivity is influenced by experimental variables. However, underlying SEM and DCM are two very distinct generative models (see [10] for a comprehensive comparison of DCM and SEM). DCM treats the brain as a deterministic, dynamic system with a nonlinear and dynamic nature in which the observed BOLD signal recorded by fMRI results from changes in neuronal activity caused by external inputs [6, 13, 14], while SEM does not distinguish “neuronal” levels from “hemodynamic” levels and changes in effective connection lead directly to changes in the covariance structure of the observed hemodynamics in this method. Considering changes in effective connectivity in the brain occur at a neuronal level, DCM is a better method for fMRI analysis.

The goal of DCM is to estimate and make inferences about the coupling among brain areas and how that coupling is influenced by changes in experimental context by building a reasonably realistic neuronal model of interacting brain regions. This model is then supplemented with a forward model of how neuronal or synaptic activity is transformed into a measured response such as the BOLD signal [13]. This

enables estimation of the parameters of effective connectivity from observed data. With DCM, a causal model is built in which neuronal activity in a certain region causes changes in neuronal activity in other regions through interregional connections and self-connections that can be modulated by experimental variables (Figure 2(d)). Effective connectivity is parameterized in terms of coupling among unobserved brain states (e.g., neuronal activity in different regions). The objective is to estimate these parameters by perturbing the system and measuring the response. In brief, the core of DCM distinguished from conventional approaches such as SEM and GCM is that it attempts to model neuronal interactions instead of signals [15] and explore the estimation problem according to the designed perturbations that accommodate experimental inputs. DCM has been broadly used in psychiatric fMRI. For example, in a stroke patient's fMRI study, Grefkes et al. [14] applied DCM of a bilateral network comprising MI, the lateral premotor cortex, and the supplementary motor area (SMA) to assess changes in the endogenous and task-dependent effective connectivity between the cortical motor areas activated by a hand movement task at baseline, following vertex stimulation and contralesional MI stimulation with repetitive transcranial magnetic stimulation (rTMS). In another fMRI study, Roebroek et al. [16] used DCM to examine the effects of Parkinson's disease and dopaminergic therapy and concluded that the DCM model selection is robust and sensitive enough to study clinical populations and their pharmacological treatment.

**2.5. Granger Causality Model (GCM).** GCM is another popular method of estimating effective connectivity [16–18], based on the reasoning that one time-series can be considered to cause another if using the past information of the former can help forecast the latter better than only using the past information of the latter [19]. GCM can provide an estimate of connection directionality when one time-series resembles a time-shifted version of the other, supposing that one with temporal precedence caused the other [20] (Figure 2(e)). This method does not depend upon an a priori assumption of a structural model that contains preselected ROIs and connections between them, which differs from SEM with the goal of contrasting the predefined causal model with real datasets. Furthermore, GCM defines the causal relationship between two stochastic time-series relying purely on temporal precedence in their interdependency. Demirci et al. [21] scanned schizophrenic patients and healthy subjects with fMRI while performing a Sternberg item recognition paradigm (SIRP) and auditory oddball (AOD) tasks. The fMRI data were then decomposed into maximally independent spatial components and corresponding time courses by applying ICA. The time courses for each of the components that were most related to the cognitive task with the most important and meaningful activation patterns were then used as inputs to a Granger causality test that investigated group differences in causal relationships between independent components over a frequency spectrum. Granger causality can also be applied to resting-state fMRI data to infer instantaneous correlation and causal influences. Hamilton et al. [22] measured BOLD

signals of patients suffering from major depressive disorder during resting state and found that hippocampal and vACC activation in depressed participants predicted subsequent decreases in dorsal cortical activity by applying GCM.

**2.6. Multivoxel Pattern Analysis (MVPA).** MVPA is gaining increasing interest in the neuroimaging community because it allows us to detect differences between conditions with higher sensitivity than conventional univariate analysis by focusing on the analysis and comparison of distributed patterns of activity (Figure 2(f)). In such a multivariate approach, data from individual voxels within a region are jointly analyzed. MVPA applies pattern-classification algorithms like support vector machines (SVM) [23–27], neural networks [28–30], or linear discriminant analysis (LDA) [31, 32] as classifiers to distinguish spatial patterns of different mental states and decode the perceptual or cognitive states of an individual. In the analysis of fMRI data, the features that are descriptive of the objects are first chosen, whereafter a subset of these features to be used for classification is selected. The data is divided into two parts: a “training set” and a “testing set.” The pattern-classification algorithm utilizes the training set to train the classifier with the features and the prespecified classes of objects. The classifier thus “learns” a functional relationship between the features and the classes. Finally, the classification algorithm is tested for its generalization capabilities with the testing set. The percentage of correct classifications can be measured.

Like other multivariate approaches (e.g., PCA and ICA), MVPA takes into account multivoxel patterns of brain activity or connectivity. Information contained in these patterns can then be decoded by applying powerful pattern-classification algorithms. This method thus incorporates spatially distributed patterns of activity into the analysis, unlike univariate methods which treat every brain voxel independently. MVPA is often presented in the context of “brain reading” applications reporting that specific mental states or representational content can be decoded from fMRI activity patterns after performing a “training” or “learning phase.”

MVPA has been successfully applied to identify functional connectivity difference between males and females [23], patterns in perception of pain [33], moral intentions [34], consciousness [35, 36], and brain maturity [37]. In a study on subjects with autism spectrum disorder (ASD) conducted by Coutanche et al. [38], reliable correlations between MVPA classification performance and standardized measures of symptom severity that exceeded those observed using a univariate measure were found, which indicated MVPA had the potential to predict clinical symptom severity.

### 3. Resting-State fMRI Analyses

Brain regions which are active when our minds wander may hold a key to understanding neurological disorders and even consciousness itself. Resting-state fMRI, which measures spontaneous low-frequency fluctuations (<0.1 Hz) in the BOLD signal, is a relatively new pathway for evaluating regional interactions in the absence of tasks [39–41]. For a

TABLE 2: Comparisons among resting-state fMRI analysis methods.

Methods	Purposes	Strengths	Limitations
Seed-based FC analysis	Estimating correlations between the predefined voxel or regions and the rest of the brain voxels	(i) Easy to calculate and understand	(i) Requires a priori selection of ROI, which may lead to potential biases
Regional homogeneity	Using Kendall's coefficient concordance to measure the similarity of a given voxel with its nearest neighbors based on the BOLD time-series	(i) Easy to calculate and understand	(i) Potential biases attached to prior seed selection
Amplitude of low-frequency fluctuations	Estimating the intensity of regional spontaneous brain activity by calculating the voxel-wise magnitude within a defined low-frequency range	(i) Can serve as a potential confounding variable when investigating functional connectivity and network	(i) Sensitive to physiological noise, which makes fractional ALFF (fALFF) approach a better choice
Principal component analysis	Finding spatial and temporal components that capture as much of the variability of the data based on decorrelation as possible	(i) Can verify the facticity of difference in the activations between conditions or groups without specifying any prior knowledge of the form of BOLD response or the structure of the experimental design	(i) Based on strong assumptions like linearity, orthogonal principal components, and high signal noise ratio
Independent component analysis	Separating distinct resting-state networks that are spatially or temporally independent of each other and identifying noise within the BOLD signal	(i) Can generate spatially or temporally distributed DM functional connectivity patterns with relatively few a priori assumptions	(i) May be less sensitive to interindividual variation in the composition of such networks and may be more likely to produce errors at the group level if a network is presented across multiple components in some subjects.
Graph theory	Describing the topology of the functional brain networks by calculating connectional characteristics of the graph comprised of nodes (voxels) and edges (connections between voxels)	(i) Directly describes and compares different brain networks utilizing topological parameters	(i) Difficult to interpret

long time neuroscientists have thought that the brain enters a “quiet” state while a person is not doing anything but remaining still. However, the recent studies of resting-state fMRI reveal that there is a persistent level of background activity in the brain during rest, which is called “the default mode” (DM) [8, 11, 41–43]. Some neuroscientists believe that the default mode network (DMN) may be critical in uncovering the neural mechanism of psychiatric disorders ranging from Alzheimer's disease to depression [44–51]. On the other hand, due to its capacity for exploring individual differences, as well as its ease of acquisition, resting-state fMRI has become one of the most popular techniques in neuroimaging. In this section we will introduce several popular resting-state fMRI analysis methods and compare their advantages and disadvantages (see Table 2).

**3.1. Seed-Based FC Analysis.** The seed-based approach extracts BOLD time-series data from a “seed”—a priorly selected voxel or ROI—and assesses the correlation between the average BOLD signal of the seed and the time course of all other brain voxels (Figure 3(a)). Seed-based analysis has been

applied in resting-state fMRI to explore the relationships between resting-state brain activity and motor response regions [39], intelligence [52], descent into sleep [53], cognitive decline in normal aging [54], memory [55], task-related activation correlated with schizophrenia [56], and task-positive and task-negative networks [57]. In an fMRI study conducted by Zhou et al. [58], to investigate patients with paranoid schizophrenia, the right dorsolateral prefrontal cortex and the posterior cingulate cortex were selected as two seed regions. Then, the investigators computed a correlation map by computing the correlation coefficients between the reference time-series in the seed region and the time-series from all other brain voxels from which they found abnormal interregional connectivity in the intrinsic organization in patients with paranoid schizophrenia. Parkinson's disease (PD) is characterized by motor symptoms resulting from the death of dopamine-generating cells. Previous studies on PD have been associated with abnormal task-related brain activation in sensory and motor regions as well as reward related network. In order to study corticostriatal skeletomotor circuit dysfunction in Parkinson's disease, in a recent resting-state fMRI

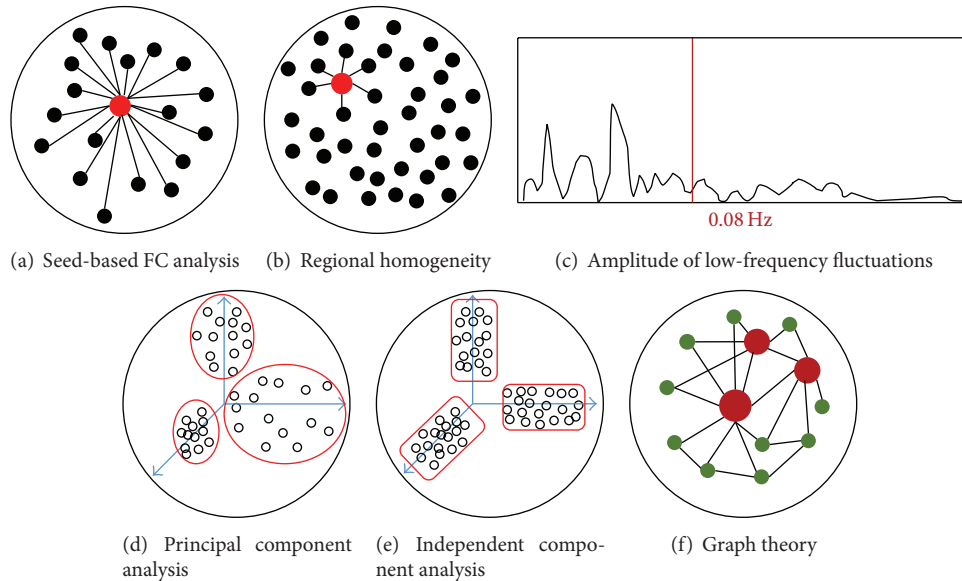


FIGURE 3: A summary of research analysis methods applied to resting-state functional MRI. (a) With seed-based functional connectivity analysis, a voxel or region is predefined and correlations are estimated between the selected “seed” and the remaining brain voxels. (b) An illustration of regional homogeneity (ReHo). (c) An illustration of amplitude of low-frequency fluctuations (ALFF). (d) Principal component analysis (PCA) transforms the original data into a new coordinate system where orthogonal variables are identified while retaining most of their variance. (e) Independent component analysis (ICA) is useful for searching a set of underlying sources of resting-state signals that are maximally independent of each other which can explain the resting-state patterns. (f) Graph theory views ROIs as nodes and correlations between them as the connectivity of the edges and then computes the connectional features of the graph.

study, the putamen and supplementary motor area (SMA) were selected as seed regions due to their roles in reward processing and motor control [59]. Enhanced putamen-SMA functional connectivity was also found in the PD group. Similarly, the periaqueductal gray (PAG) plays a key role in the descending modulation of pain and its functional connectivity has been intensively examined in chronic pain patients [60]. While seed-based FC analysis has the advantage of statistical transparency and comprehensible results, seed-based analysis also suffers from the potential biases attached to prior seed selection. For example, to examine the default network, researchers have used a variety of seeds and generated different versions of the default mode network [61].

**3.2. Regional Homogeneity (ReHo).** ReHo is another straightforward technique that uses Kendall’s coefficient concordance (KCC) to measure the similarity of a given voxel with its nearest neighbors based on the BOLD time-series [62] (Figure 3(b)). Multiple studies which applied ReHo to resting-state fMRI data processing have shown diminished ReHo of specific regions in heavy male smokers [63], patients with Alzheimer’s disease [64], patients with depression [65, 66], patients with schizophrenia [67], patients with Parkinson’s disease [68], children with ASD [69, 70], adults with ADHD [49], and normal aging people [68]. On the contrary, a positive correlation has also been found between ReHo of certain regions and intelligence [71], early blindness [72], and internet addiction disorder [73]. ReHo is very useful in identifying regional abnormality in psychiatric disorders, which may guide further network based analysis. For example,

a recent study found that ReHo changes in schizophrenia are widespread [74], leading to brain-wide network analysis in schizophrenia [75, 76].

**3.3. Amplitude of Low-Frequency Fluctuations (ALFF).** ALFF is an index that reflects the intensity of regional spontaneous brain activity by calculating the voxel-wise magnitude within a defined low-frequency range (Figure 3(c)). In order to reduce ALFF’s sensitivity to physiological noise, Zou et al. [77] proposed a fractional ALFF (fALFF) approach calculating the ratio of power spectrum of low-frequency (0.01–0.08 Hz) to that of the entire frequency range. A number of resting-state fMRI studies have observed higher ALFF in the DMN areas than other areas [77–79]. Applications of ALFF in studies of conditions like depression [80], ADHD [81], PTSD [82], normal aging [83], and schizophrenia [84] have also revealed some exciting findings. Recently, by decomposing R-fMRI low-frequency (typically 0.01–0.1 Hz) oscillations (LFOs) into two distinct frequency bands [slow-5 (0.01–0.027 Hz), slow-4 (0.027–0.073 Hz)], researchers found that LFO amplitudes in the slow-4 band were higher than those in the slow-5 in many brain regions [85, 86]. Yu et al. (2014) further demonstrated that the abnormalities of LFOs in schizophrenia are dependent on the frequency band and suggest that future studies should take the different frequency bands into account when measuring intrinsic brain activity [85].

**3.4. Principal Component Analysis (PCA).** PCA is a data-driven method that does not require the input of any prior

information about the connectivity pattern. It has been found useful in estimating whether there are functional regions with correlated signal responses in human brain mapping [87]. It was first formulated by Pearson [88] and then developed as a useful technique for reducing the dimensionality of complex data sets and for extracting new orthogonal variables identified as principal components [89]. The basic idea of PCA is to find a set of orthogonal bases that can maximize the variance of data and to separate out the most meaningful information from the noise so as to uncover the hidden structure (Figure 3(d)). For fMRI data, PCA has the advantage of verifying the facticity of differences in the activations between conditions or groups without specifying any prior knowledge of the form of BOLD response or the structure of the experimental design [90]. It is often applied in psychiatric fMRI analysis combined with other techniques such as ICA and MVPA. For example, Shen et al. [91] aimed at classifying individuals into schizophrenic and healthy control groups by a quantitative method. They collected fMRI data from patients with schizophrenia and healthy subjects and reduced the data size by using PCA decomposition. Then ICA was employed to extract data on the functionally connected networks in the brain, yielding less noisy components, which would be used as input to the classifier algorithm. However, the effectiveness of PCA is based on strong assumptions like linearity, orthogonal principal components, and high signal noise ratio (SNR) [92]. Sometimes data sets cannot be said to fit within these assumptions.

**3.5. Independent Component Analysis (ICA).** As an extension of PCA, ICA is likewise a data-driven method that has been successfully used in describing fMRI data [93–96]. With the identical goal of finding a new set of variables with lesser redundancy that would provide the best possible representation of observed phenomena, ICA measures redundancy by the much richer concept of independence (Figure 3(e)) and only requires relatively weak assumptions about the independence of source signals compared with PCA, which extracts interested variables based on decorrelation and requires some stringent assumptions [97]. The independent components are assumed statistically independent in ICA. One of the most useful applications of ICA is reducing the negative effects of artifacts for standard GLM-based analysis by using decomposition information [98, 99]. Another useful application of ICA is in detecting the resting-state functional connectivity and identifying RSNs (resting-state networks) [39, 94, 96, 100, 101]. Besides, ICA is also used in task-related fMRI group analysis called FENICA [102]. ICA has been widely applied to the study of brain diseases, such as Alzheimer's disease [20, 44], schizophrenia [21, 22], bipolar disorder [2, 103], and epilepsy [2].

**3.6. Graph Theory.** A hot recent method used in resting-state fMRI is graph theory. Graph theory is a mathematical theory and approach to studying graphs made up of nodes and edges and how these nodes connected by edges interact with each other [58, 104] (Figure 3(f)). The brain network can be described as being analogous to a graph in which voxels can

be viewed as nodes and connections between voxels as edges [105]. In fMRI studies, graph theory has been used by some ambitious researchers seeking to present a comprehensive map of how the brain is organized. The unique characteristic of graph theory compared with the more traditional univariate fMRI methods is that graph theory can serve as a tool to directly describe and compare different brain networks utilizing topological parameters such as clustering-coefficient, characteristic path length, degree of connectivity, centrality, and modularity [106]. Evidence from graph theory in fMRI studies has shown that the brain is structured in a highly efficient organization with both a small-world topology achieved through the presence of hubs and a scale-free topology [107, 108]. Graph theory has been applied not only to resting-state fMRI and task-based fMRI so as to analyze the topology of functional brain networks [105, 109] but also to studies of cortical thickness [110, 111], surface area, and diffusion weighted imaging data [91, 112, 113] so as to analyze the topology of structural brain networks. These studies have illustrated an alteration of arrangements in structural and functional brain networks associated with normal aging [114, 115], multiple sclerosis [116, 117], Alzheimer's disease [118–120], schizophrenia [121–123], depression [124, 125], and epilepsy [110, 126].

## 4. Conclusion

Over the past decades, the development of fMRI techniques has made great contributions to our understanding of the neural mechanism underlying psychiatric disorder. In the present review, we summarize several major MRI methods widely used in psychiatric neuroimaging. Some methods such as ReHo and VBM focus on regional changes, whereas others take a systematic approach and emphasize the whole brain network. These methods together can reveal the abnormalities in brain structures and functions in psychiatric disorders. However, the functional significance of many measures such as ReHo and ALFF is still not well understood. Psychiatric disorders may be associated with very subtle changes in the brain. One single method may not be enough to fully capture the nature of such alternations. A systematic approach using multimodal neuroimaging and a variety of analysis methods has the potential to identify reliable biomarkers for specific psychiatric disorders. With ongoing progress being made in neuroimaging methods, neuroimaging holds clear promise in helping to diagnose and quantify psychiatric diseases.

## Disclosure

The funders had no role in study design, decision to publish, or preparation of the paper.

## Conflict of Interests

The authors declare that there is no conflict of interests regarding the publication of this paper.

## Acknowledgments

The authors acknowledge the Foundation for High-Level Talents in Higher Education of Guangdong (no. C10454) and the National Natural Science Foundation of China (no. 31371128) for financial support.

## References

- [1] K. J. Friston, A. P. Holmes, K. J. Worsley, J. P. Poline, C. D. Frith, and R. S. J. Frackowiak, "Statistical parametric maps in functional imaging: a general linear approach," *Human Brain Mapping*, vol. 2, no. 4, pp. 189–210, 1994.
- [2] G. Juckel, F. Schlagenhauf, M. Koslowski et al., "Dysfunction of ventral striatal reward prediction in schizophrenia," *NeuroImage*, vol. 29, no. 2, pp. 409–416, 2006.
- [3] M. M. Monti, "Statistical analysis of fMRI time-series: a critical review of the GLM approach," *Frontiers in Human Neuroscience*, vol. 5, article 28, 2011.
- [4] K. J. Friston, C. Buechel, G. R. Fink, J. Morris, E. Rolls, and R. J. Dolan, "Psychophysiological and modulatory interactions in neuroimaging," *NeuroImage*, vol. 6, no. 3, pp. 218–229, 1997.
- [5] P. Das, A. H. Kemp, G. Flynn et al., "Functional disconnections in the direct and indirect amygdala pathways for fear processing in schizophrenia," *Schizophrenia Research*, vol. 90, no. 1–3, pp. 284–294, 2007.
- [6] L. Wang, P. D. Metzack, and T. S. Woodward, "Aberrant connectivity during self-other source monitoring in schizophrenia," *Schizophrenia Research*, vol. 125, no. 2–3, pp. 136–142, 2011.
- [7] A. R. McIntosh and F. Gonzalez-Lima, "Structural modeling of functional neural pathways mapped with 2-deoxyglucose: effects of acoustic startle habituation on the auditory system," *Brain Research*, vol. 547, no. 2, pp. 295–302, 1991.
- [8] M. E. Raichle, A. M. MacLeod, A. Z. Snyder, W. J. Powers, D. A. Gusnard, and G. L. Shulman, "A default mode of brain function," *Proceedings of the National Academy of Sciences of the United States of America*, vol. 98, no. 2, pp. 676–682, 2001.
- [9] C. Büchel and K. J. Friston, "Modulation of connectivity in visual pathways by attention: cortical interactions evaluated with structural equation modelling and fMRI," *Cerebral Cortex*, vol. 7, no. 8, pp. 768–778, 1997.
- [10] W. D. Penny, K. E. Stephan, A. Mechelli, and K. J. Friston, "Modelling functional integration: a comparison of structural equation and dynamic causal models," *NeuroImage*, vol. 23, supplement 1, pp. S264–S274, 2004.
- [11] P. Fransson, "How default is the default mode of brain function? Further evidence from intrinsic BOLD signal fluctuations," *Neuropsychologia*, vol. 44, no. 14, pp. 2836–2845, 2006.
- [12] R. Schlösser, T. Gesierich, B. Kaufmann et al., "Altered effective connectivity during working memory performance in schizophrenia: a study with fMRI and structural equation modeling," *NeuroImage*, vol. 19, no. 3, pp. 751–763, 2003.
- [13] K. J. Friston, L. Harrison, and W. Penny, "Dynamic causal modelling," *NeuroImage*, vol. 19, no. 4, pp. 1273–1302, 2003.
- [14] C. Grefkes, D. A. Nowak, L. E. Wang, M. Dafotakis, S. B. Eickhoff, and G. R. Fink, "Modulating cortical connectivity in stroke patients by rTMS assessed with fMRI and dynamic causal modeling," *NeuroImage*, vol. 50, no. 1, pp. 233–242, 2010.
- [15] K. Friston, "Causal modelling and brain connectivity in functional magnetic resonance imaging," *PLoS Biology*, vol. 7, no. 2, Article ID e1000033, 2009.
- [16] A. Roebroeck, E. Formisano, and R. Goebel, "Mapping directed influence over the brain using Granger causality and fMRI," *NeuroImage*, vol. 25, no. 1, pp. 230–242, 2005.
- [17] R. Goebel, A. Roebroeck, D.-S. Kim, and E. Formisano, "Investigating directed cortical interactions in time-resolved fMRI data using vector autoregressive modeling and Granger causality mapping," *Magnetic Resonance Imaging*, vol. 21, no. 10, pp. 1251–1261, 2003.
- [18] W. Liao, D. Mantini, Z. Zhang et al., "Evaluating the effective connectivity of resting state networks using conditional Granger causality," *Biological Cybernetics*, vol. 102, no. 1, pp. 57–69, 2010.
- [19] C. W. Granger, "Some recent developments in a concept of causality," *Journal of Econometrics*, vol. 39, no. 1–2, pp. 199–211, 1988.
- [20] M. Kamiński, M. Ding, W. A. Truccolo, and S. L. Bressler, "Evaluating causal relations in neural systems: Granger causality, directed transfer function and statistical assessment of significance," *Biological Cybernetics*, vol. 85, no. 2, pp. 145–157, 2001.
- [21] O. Demirci, M. C. Stevens, N. C. Andreasen et al., "Investigation of relationships between fMRI brain networks in the spectral domain using ICA and Granger causality reveals distinct differences between schizophrenia patients and healthy controls," *NeuroImage*, vol. 46, no. 2, pp. 419–431, 2009.
- [22] J. P. Hamilton, G. Chen, M. E. Thomason, M. E. Schwartz, and I. H. Gotlib, "Investigating neural primacy in major depressive disorder: multivariate Granger causality analysis of resting-state fMRI time-series data," *Molecular Psychiatry*, vol. 16, no. 7, pp. 763–772, 2011.
- [23] L. Wang, H. Shen, F. Tang, Y. Zang, and D. Hu, "Combined structural and resting-state functional MRI analysis of sexual dimorphism in the young adult human brain: an MVPA approach," *NeuroImage*, vol. 61, no. 4, pp. 931–940, 2012.
- [24] S. LaConte, S. Strother, V. Cherkassky, J. Anderson, and X. Hu, "Support vector machines for temporal classification of block design fMRI data," *NeuroImage*, vol. 26, no. 2, pp. 317–329, 2005.
- [25] J. Mourão-Miranda, E. Reynaud, F. McGlone, G. Calvert, and M. Brammer, "The impact of temporal compression and space selection on SVM analysis of single-subject and multi-subject fMRI data," *NeuroImage*, vol. 33, no. 4, pp. 1055–1065, 2006.
- [26] J. T. Serences, E. F. Ester, E. K. Vogel, and E. Awh, "Stimulus-specific delay activity in human primary visual cortex," *Psychological Science*, vol. 20, no. 2, pp. 207–214, 2009.
- [27] Z. Wang, "Support vector machine learning-based cerebral blood flow quantification for arterial spin labeling MRI," *Human Brain Mapping*, vol. 35, no. 7, pp. 2869–2875, 2014.
- [28] S. J. Hanson, T. Matsuka, and J. V. Haxby, "Combinatorial codes in ventral temporal lobe for object recognition: Haxby (2001) revisited: is there a 'face' area?" *NeuroImage*, vol. 23, no. 1, pp. 156–166, 2004.
- [29] S. M. Polyn, V. S. Natu, J. D. Cohen, and K. A. Norman, "Category-specific cortical activity precedes retrieval during memory search," *Science*, vol. 310, no. 5756, pp. 1963–1966, 2005.
- [30] J. D. Johnson, S. G. R. McDuff, M. D. Rugg, and K. A. Norman, "Recollection, familiarity, and cortical reinstatement: a multivoxel pattern analysis," *Neuron*, vol. 63, no. 5, pp. 697–708, 2009.
- [31] T. A. Carlson, P. Schrater, and S. He, "Patterns of activity in the categorical representations of objects," *Journal of Cognitive Neuroscience*, vol. 15, no. 5, pp. 704–717, 2003.

- [32] R. D. S. Raizada, F.-M. Tsao, H.-M. Liu, I. D. Holloway, D. Ansari, and P. K. Kuhl, "Linking brain-wide multivoxel activation patterns to behaviour: examples from language and math," *NeuroImage*, vol. 51, no. 1, pp. 462–471, 2010.
- [33] K. H. Brodersen, K. Wiech, E. I. Lomakina et al., "Decoding the perception of pain from fMRI using multivariate pattern analysis," *NeuroImage*, vol. 63, no. 3, pp. 1162–1170, 2012.
- [34] J. Koster-Hale, R. Saxe, J. Dungan, and L. L. Young, "Decoding moral judgments from neural representations of intentions," *Proceedings of the National Academy of Sciences of the United States of America*, vol. 110, no. 14, pp. 5648–5653, 2013.
- [35] A. Vanhaudenhuyse, Q. Noirhomme, L. J.-F. Tshibanda et al., "Default network connectivity reflects the level of consciousness in non-communicative brain-damaged patients," *Brain*, vol. 133, part 1, pp. 161–171, 2010.
- [36] R. S. Weil and G. Rees, "Decoding the neural correlates of consciousness," *Current Opinion in Neurology*, vol. 23, no. 6, pp. 649–655, 2010.
- [37] N. U. F. Dosenbach, B. Nardos, A. L. Cohen et al., "Prediction of individual brain maturity using fMRI," *Science*, vol. 329, no. 5997, pp. 1358–1361, 2010.
- [38] M. N. Coutanche, S. L. Thompson-Schill, and R. T. Schultz, "Multi-voxel pattern analysis of fMRI data predicts clinical symptom severity," *NeuroImage*, vol. 57, no. 1, pp. 113–123, 2011.
- [39] B. Biswal, F. Z. Yetkin, V. M. Haughton, and J. S. Hyde, "Functional connectivity in the motor cortex of resting human brain using echo-planar MRI," *Magnetic Resonance in Medicine*, vol. 34, no. 4, pp. 537–541, 1995.
- [40] M. J. Lowe, B. J. Mock, and J. A. Sorenson, "Functional connectivity in single and multislice echoplanar imaging using resting-state fluctuations," *NeuroImage*, vol. 7, no. 2, pp. 119–132, 1998.
- [41] M. D. Greicius, B. Krasnow, A. L. Reiss, and V. Menon, "Functional connectivity in the resting brain: a network analysis of the default mode hypothesis," *Proceedings of the National Academy of Sciences of the United States of America*, vol. 100, no. 1, pp. 253–258, 2003.
- [42] P. Fransson, "Spontaneous low-frequency BOLD signal fluctuations: an fMRI investigation of the resting-state default mode of brain function hypothesis," *Human Brain Mapping*, vol. 26, no. 1, pp. 15–29, 2005.
- [43] M. E. Raichle and A. Z. Snyder, "A default mode of brain function: a brief history of an evolving idea," *NeuroImage*, vol. 37, no. 4, pp. 1083–1090, 2007.
- [44] M. D. Greicius, G. Srivastava, A. L. Reiss, and V. Menon, "Default-mode network activity distinguishes Alzheimer's disease from healthy aging: Evidence from functional MRI," *Proceedings of the National Academy of Sciences of the United States of America*, vol. 101, no. 13, pp. 4637–4642, 2004.
- [45] R. Bluhm, P. Williamson, R. Lanius et al., "Resting state default-mode network connectivity in early depression using a seed region-of-interest analysis: decreased connectivity with caudate nucleus," *Psychiatry and Clinical Neurosciences*, vol. 63, no. 6, pp. 754–761, 2009.
- [46] X. Zhu, X. Wang, J. Xiao et al., "Evidence of a dissociation pattern in resting-state default mode network connectivity in first-episode, treatment-naïve major depression patients," *Biological Psychiatry*, vol. 71, no. 7, pp. 611–617, 2012.
- [47] W. Koch, S. Teipel, S. Mueller et al., "Diagnostic power of default mode network resting state fMRI in the detection of Alzheimer's disease," *Neurobiology of Aging*, vol. 33, no. 3, pp. 466–478, 2012.
- [48] F. Agosta, M. Pievani, C. Geroldi, M. Copetti, G. B. Frisoni, and M. Filippi, "Resting state fMRI in Alzheimer's disease: beyond the default mode network," *Neurobiology of Aging*, vol. 33, no. 8, pp. 1564–1578, 2012.
- [49] L. Q. Uddin, A. M. C. Kelly, B. B. Biswal et al., "Network homogeneity reveals decreased integrity of default-mode network in ADHD," *Journal of Neuroscience Methods*, vol. 169, no. 1, pp. 249–254, 2008.
- [50] M. Assaf, K. Jagannathan, V. D. Calhoun et al., "Abnormal functional connectivity of default mode sub-networks in autism spectrum disorder patients," *NeuroImage*, vol. 53, no. 1, pp. 247–256, 2010.
- [51] M. D. Greicius, B. H. Flores, V. Menon et al., "Resting-state functional connectivity in major depression: abnormally increased contributions from subgenual cingulate cortex and thalamus," *Biological Psychiatry*, vol. 62, no. 5, pp. 429–437, 2007.
- [52] M. Song, Y. Zhou, J. Li et al., "Brain spontaneous functional connectivity and intelligence," *NeuroImage*, vol. 41, no. 3, pp. 1168–1176, 2008.
- [53] L. J. Larson-Prior, J. M. Zempel, T. S. Nolan, F. W. Prior, A. Snyder, and M. E. Raichle, "Cortical network functional connectivity in the descent to sleep," *Proceedings of the National Academy of Sciences of the United States of America*, vol. 106, no. 11, pp. 4489–4494, 2009.
- [54] J. R. Andrews-Hanna, A. Z. Snyder, J. L. Vincent et al., "Disruption of large-scale brain systems in advanced aging," *Neuron*, vol. 56, no. 5, pp. 924–935, 2007.
- [55] C. Ranganath, A. Heller, M. X. Cohen, C. J. Brozinsky, and J. Rissman, "Functional connectivity with the hippocampus during successful memory formation," *Hippocampus*, vol. 15, no. 8, pp. 997–1005, 2005.
- [56] S. Whitfield-Gabrieli, H. W. Thermenos, S. Milanovic et al., "Hyperactivity and hyperconnectivity of the default network in schizophrenia and in first-degree relatives of persons with schizophrenia," *Proceedings of the National Academy of Sciences of the United States of America*, vol. 106, no. 4, pp. 1279–1284, 2009.
- [57] M. D. Fox, A. Z. Snyder, J. L. Vincent, M. Corbetta, D. C. van Essen, and M. E. Raichle, "The human brain is intrinsically organized into dynamic, anticorrelated functional networks," *Proceedings of the National Academy of Sciences of the United States of America*, vol. 102, no. 27, pp. 9673–9678, 2005.
- [58] Y. Zhou, M. Liang, L. Tian et al., "Functional disintegration in paranoid schizophrenia using resting-state fMRI," *Schizophrenia Research*, vol. 97, no. 1–3, pp. 194–205, 2007.
- [59] R. Yu, B. Liu, L. Wang, J. Chen, and X. Liu, "Enhanced functional connectivity between putamen and supplementary motor area in Parkinson's disease patients," *PLoS ONE*, vol. 8, no. 3, Article ID e59717, 2013.
- [60] R. Yu, R. L. Gollub, R. Spaeth, V. Napadow, A. Wasan, and J. Kong, "Disrupted functional connectivity of the periaqueductal gray in chronic low back pain," *NeuroImage: Clinical*, vol. 6, pp. 100–108, 2014.
- [61] D. M. Cole, S. M. Smith, and C. F. Beckmann, "Advances and pitfalls in the analysis and interpretation of resting-state FMRI data," *Frontiers in Systems Neuroscience*, vol. 4, 2010.
- [62] Y. Zang, T. Jiang, Y. Lu, Y. He, and L. Tian, "Regional homogeneity approach to fMRI data analysis," *NeuroImage*, vol. 22, no. 1, pp. 394–400, 2004.
- [63] R. Yu, L. Zhao, J. Tian et al., "Regional homogeneity changes in heavy male smokers: a resting-state functional magnetic

- resonance imaging study," *Addiction Biology*, vol. 18, no. 4, pp. 729–731, 2013.
- [64] Z. Zhang, Y. Liu, T. Jiang et al., "Altered spontaneous activity in Alzheimer's disease and mild cognitive impairment revealed by Regional Homogeneity," *NeuroImage*, vol. 59, no. 2, pp. 1429–1440, 2012.
- [65] Z. Yao, L. Wang, Q. Lu, H. Liu, and G. Teng, "Regional homogeneity in depression and its relationship with separate depressive symptom clusters: a resting-state fMRI study," *Journal of Affective Disorders*, vol. 115, no. 3, pp. 430–438, 2009.
- [66] Z. Liu, C. Xu, Y. Xu et al., "Decreased regional homogeneity in insula and cerebellum: a resting-state fMRI study in patients with major depression and subjects at high risk for major depression," *Psychiatry Research: Neuroimaging*, vol. 182, no. 3, pp. 211–215, 2010.
- [67] H. Liu, Z. Liu, M. Liang et al., "Decreased regional homogeneity in schizophrenia: a resting state functional magnetic resonance imaging study," *NeuroReport*, vol. 17, no. 1, pp. 19–22, 2006.
- [68] T. Wu, X. Long, Y. Zang et al., "Regional homogeneity changes in patients with parkinson's disease," *Human Brain Mapping*, vol. 30, no. 5, pp. 1502–1510, 2009.
- [69] D. K. Shukla, B. Keehn, and R. A. Müller, "Regional homogeneity of fMRI time series in autism spectrum disorders," *Neuroscience Letters*, vol. 476, no. 1, pp. 46–51, 2010.
- [70] J.-J. Paakki, J. Rahko, X. Long et al., "Alterations in regional homogeneity of resting-state brain activity in autism spectrum disorders," *Brain Research*, vol. 1321, pp. 169–179, 2010.
- [71] L. Wang, M. Song, T. Jiang, Y. Zhang, and C. Yu, "Regional homogeneity of the resting-state brain activity correlates with individual intelligence," *Neuroscience Letters*, vol. 488, no. 3, pp. 275–278, 2011.
- [72] C. Liu, Y. Liu, W. Li et al., "Increased regional homogeneity of blood oxygen level-dependent signals in occipital cortex of early blind individuals," *NeuroReport*, vol. 22, no. 4, pp. 190–194, 2011.
- [73] J. Liu, X.-P. Gao, I. Osunde et al., "Increased regional homogeneity in internet addiction disorder: a resting state functional magnetic resonance imaging study," *Chinese Medical Journal*, vol. 123, no. 14, pp. 1904–1908, 2010.
- [74] R. Yu, M. H. Hsieh, H. L. S. Wang et al., "Frequency dependent alterations in regional homogeneity of baseline brain activity in schizophrenia," *PLoS ONE*, vol. 8, no. 3, Article ID e57516, 2013.
- [75] S. Guo, K. M. Kendrick, R. Yu, H.-L. S. Wang, and J. Feng, "Key functional circuitry altered in schizophrenia involves parietal regions associated with sense of self," *Human Brain Mapping*, vol. 35, no. 1, pp. 123–139, 2014.
- [76] S. Guo, K. M. Kendrick, J. Zhang et al., "Brain-wide functional inter-hemispheric disconnection is a potential biomarker for schizophrenia and distinguishes it from depression," *NeuroImage: Clinical*, vol. 2, pp. 818–826, 2013.
- [77] Q.-H. Zou, C.-Z. Zhu, Y. Yang et al., "An improved approach to detection of amplitude of low-frequency fluctuation (ALFF) for resting-state fMRI: fractional ALFF," *Journal of Neuroscience Methods*, vol. 172, no. 1, pp. 137–141, 2008.
- [78] X.-N. Zuo, A. Di Martino, C. Kelly et al., "The oscillating brain: complex and reliable," *NeuroImage*, vol. 49, no. 2, pp. 1432–1445, 2010.
- [79] H. Yang, X.-Y. Long, Y. Yang et al., "Amplitude of low frequency fluctuation within visual areas revealed by resting-state functional MRI," *NeuroImage*, vol. 36, no. 1, pp. 144–152, 2007.
- [80] J. Liu, L. Ren, F. Y. Womer et al., "Alterations in amplitude of low frequency fluctuation in treatment-naïve major depressive disorder measured with resting-state fMRI," *Human Brain Mapping*, vol. 35, no. 10, pp. 4979–4988, 2014.
- [81] Y.-F. Zang, Y. He, C.-Z. Zhu et al., "Altered baseline brain activity in children with ADHD revealed by resting-state functional MRI," *Brain & Development*, vol. 29, no. 2, pp. 83–91, 2007.
- [82] X. Bing, M.-G. Qiu, Z. Ye et al., "Alterations in the cortical thickness and the amplitude of low-frequency fluctuation in patients with post-traumatic stress disorder," *Brain Research*, vol. 1490, pp. 225–232, 2013.
- [83] S. Hu, H. H.-A. Chao, S. Zhang, J. S. Ide, and C.-S. R. Li, "Changes in cerebral morphometry and amplitude of low-frequency fluctuations of BOLD signals during healthy aging: correlation with inhibitory control," *Brain Structure and Function*, vol. 219, no. 3, pp. 983–994, 2014.
- [84] M. J. Hoptman, X.-N. Zuo, P. D. Butler et al., "Amplitude of low-frequency oscillations in schizophrenia: a resting state fMRI study," *Schizophrenia Research*, vol. 117, no. 1, pp. 13–20, 2010.
- [85] R. Yu, Y.-L. Chien, H.-L. S. Wang et al., "Frequency-specific alternations in the amplitude of low-frequency fluctuations in schizophrenia," *Human Brain Mapping*, vol. 35, no. 2, pp. 627–637, 2014.
- [86] X. N. Zuo, A. di Martino, C. Kelly et al., "The oscillating brain: complex and reliable," *NeuroImage*, vol. 49, no. 2, pp. 1432–1445, 2010.
- [87] K. J. Friston, C. D. Frith, P. F. Liddle, and R. S. J. Frackowiak, "Functional connectivity: the principal-component analysis of large (PET) data sets," *Journal of Cerebral Blood Flow and Metabolism*, vol. 13, no. 1, pp. 5–14, 1993.
- [88] K. Pearson, "LIII. On lines and planes of closest fit to systems of points in space," *Philosophical Magazine Series 6*, vol. 2, no. 11, pp. 559–572, 1901.
- [89] S. Wold, K. Esbensen, and P. Geladi, "Principal component analysis," *Chemometrics and Intelligent Laboratory Systems*, vol. 2, no. 1–3, pp. 37–52, 1987.
- [90] R. Viviani, G. Grön, and M. Spitzer, "Functional principal component analysis of fMRI data," *Human Brain Mapping*, vol. 24, no. 2, pp. 109–129, 2005.
- [91] H. Shen, L. Wang, Y. Liu, and D. Hu, "Discriminative analysis of resting-state functional connectivity patterns of schizophrenia using low dimensional embedding of fMRI," *NeuroImage*, vol. 49, no. 4, pp. 3110–3121, 2010.
- [92] J. Shlens, "A tutorial on principal component analysis," <http://arxiv.org/abs/1404.1100>.
- [93] M. J. McKeown and T. J. Sejnowski, "Independent component analysis of fMRI data: examining the assumptions," *Human Brain Mapping*, vol. 6, no. 5–6, pp. 368–372, 1998.
- [94] V. D. Calhoun, T. Adali, G. D. Pearlson, and J. J. Pekar, "A method for making group inferences from functional MRI data using independent component analysis," *Human Brain Mapping*, vol. 14, no. 3, pp. 140–151, 2001.
- [95] S. M. Smith, P. T. Fox, K. L. Miller et al., "Correspondence of the brain's functional architecture during activation and rest," *Proceedings of the National Academy of Sciences of the United States of America*, vol. 106, no. 31, pp. 13040–13045, 2009.
- [96] C. F. Beckmann, M. DeLuca, J. T. Devlin, and S. M. Smith, "Investigations into resting-state connectivity using independent component analysis," *Philosophical Transactions of the Royal Society B: Biological Sciences*, vol. 360, no. 1457, pp. 1001–1013, 2005.
- [97] A. Hyvärinen, J. Karhunen, and E. Oja, *Independent Component Analysis*, John Wiley & Sons, New York, NY, USA, 2004.

- [98] P. R. Bannister, C. F. Beckmann, M. Jenkinson, S. Smith, and J. M. Brady, "Motion artefact decorrelation in fMRI analysis using ICA," in *Proceedings of the 10th Annual Meeting of ISMRM*, Honolulu, Hawaii, USA, 2002.
- [99] V. Perlberg, P. Bellec, J.-L. Anton, M. Péligrini-Issac, J. Doyon, and H. Benali, "CORSICA: correction of structured noise in fMRI by automatic identification of ICA components," *Magnetic Resonance Imaging*, vol. 25, no. 1, pp. 35–46, 2007.
- [100] V. G. van de Ven, E. Formisano, D. Prvulovic, C. H. Roeder, and D. E. J. Linden, "Functional connectivity as revealed by spatial independent component analysis of fMRI measurements during rest," *Human Brain Mapping*, vol. 22, no. 3, pp. 165–178, 2004.
- [101] J. S. Damoiseaux, S. A. R. B. Rombouts, F. Barkhof et al., "Consistent resting-state networks across healthy subjects," *Proceedings of the National Academy of Sciences of the United States of America*, vol. 103, no. 37, pp. 13848–13853, 2006.
- [102] V. Schöpf, C. Windischberger, S. Robinson et al., "Model-free fMRI group analysis using FENICA," *NeuroImage*, vol. 55, no. 1, pp. 185–193, 2011.
- [103] M. Hampson, B. S. Peterson, P. Skudlarski, J. C. Gatenby, and J. C. Gore, "Detection of functional connectivity using temporal correlations in MR images," *Human Brain Mapping*, vol. 15, no. 4, pp. 247–262, 2002.
- [104] O. Sporns, "Graph theory methods for the analysis of neural connectivity patterns," in *Neuroscience Databases*, pp. 171–185, Springer, New York, NY, USA, 2003.
- [105] E. Bullmore and O. Sporns, "Complex brain networks: graph theoretical analysis of structural and functional systems," *Nature Reviews Neuroscience*, vol. 10, no. 3, pp. 186–198, 2009.
- [106] M. P. van den Heuvel and H. E. Hulshoff Pol, "Exploring the brain network: a review on resting-state fMRI functional connectivity," *European Neuropsychopharmacology*, vol. 20, no. 8, pp. 519–534, 2010.
- [107] M. P. van den Heuvel, C. J. Stam, M. Boersma, and H. E. Hulshoff Pol, "Small-world and scale-free organization of voxel-based resting-state functional connectivity in the human brain," *NeuroImage*, vol. 43, no. 3, pp. 528–539, 2008.
- [108] D. S. Bassett and E. Bullmore, "Small-world brain networks," *The Neuroscientist*, vol. 12, no. 6, pp. 512–523, 2006.
- [109] J. Wang, X. Zuo, and Y. He, "Graph-based network analysis of resting-state functional MRI," *Frontiers in Systems Neuroscience*, vol. 4, article 16, 2010.
- [110] B. C. Bernhardt, Z. Chen, Y. He, A. C. Evans, and N. Bernasconi, "Graph-theoretical analysis reveals disrupted small-world organization of cortical thickness correlation networks in temporal lobe epilepsy," *Cerebral Cortex*, vol. 21, no. 9, pp. 2147–2157, 2011.
- [111] Y. He, Z. J. Chen, and A. C. Evans, "Small-world anatomical networks in the human brain revealed by cortical thickness from MRI," *Cerebral Cortex*, vol. 17, no. 10, pp. 2407–2419, 2007.
- [112] Y. Iturria-Medina, E. J. Canales-Rodríguez, L. Melie-García et al., "Characterizing brain anatomical connections using diffusion weighted MRI and graph theory," *NeuroImage*, vol. 36, no. 3, pp. 645–660, 2007.
- [113] Y. Iturria-Medina, R. C. Sotero, E. J. Canales-Rodríguez, Y. Alemán-Gómez, and L. Melie-García, "Studying the human brain anatomical network via diffusion-weighted MRI and Graph Theory," *NeuroImage*, vol. 40, no. 3, pp. 1064–1076, 2008.
- [114] D. Meunier, S. Achard, A. Morcom, and E. Bullmore, "Age-related changes in modular organization of human brain functional networks," *NeuroImage*, vol. 44, no. 3, pp. 715–723, 2009.
- [115] G. Gong, P. Rosa-Neto, F. Carbonell, Z. J. Chen, Y. He, and A. C. Evans, "Age- and gender-related differences in the cortical anatomical network," *The Journal of Neuroscience*, vol. 29, no. 50, pp. 15684–15693, 2009.
- [116] Y. He, A. Dagher, Z. Chen et al., "Impaired small-world efficiency in structural cortical networks in multiple sclerosis associated with white matter lesion load," *Brain*, vol. 132, no. 12, pp. 3366–3379, 2009.
- [117] N. Shu, Y. Liu, K. Li et al., "Diffusion tensor tractography reveals disrupted topological efficiency in white matter structural networks in multiple sclerosis," *Cerebral Cortex*, vol. 21, no. 11, pp. 2565–2577, 2011.
- [118] R. L. Buckner, J. Sepulcre, T. Talukdar et al., "Cortical hubs revealed by intrinsic functional connectivity: mapping, assessment of stability, and relation to Alzheimer's disease," *Journal of Neuroscience*, vol. 29, no. 6, pp. 1860–1873, 2009.
- [119] E. J. Sanz-Arigita, M. M. Schoonheim, J. S. Damoiseaux et al., "Loss of 'small-world' networks in Alzheimer's disease: graph analysis of FMRI resting-state functional connectivity," *PLoS ONE*, vol. 5, no. 11, Article ID e13788, 2010.
- [120] Z. Yao, Y. Zhang, L. Lin et al., "Abnormal cortical networks in mild cognitive impairment and Alzheimer's disease," *PLoS Computational Biology*, vol. 6, no. 11, Article ID e1001006, 2010.
- [121] M. P. van den Heuvel, R. C. W. Mandl, C. J. Stam, R. S. Kahn, and H. E. Hulshoff Pol, "Aberrant frontal and temporal complex network structure in schizophrenia: a graph theoretical analysis," *The Journal of Neuroscience*, vol. 30, no. 47, pp. 15915–15926, 2010.
- [122] S. Micheloyannis, E. Pachou, C. J. Stam et al., "Small-world networks and disturbed functional connectivity in schizophrenia," *Schizophrenia Research*, vol. 87, no. 1–3, pp. 60–66, 2006.
- [123] D. S. Bassett, E. Bullmore, B. A. Verchinski, V. S. Mattay, D. R. Weinberger, and A. Meyer-Lindenberg, "Hierarchical organization of human cortical networks in health and Schizophrenia," *The Journal of Neuroscience*, vol. 28, no. 37, pp. 9239–9248, 2008.
- [124] O. Ajilore, M. Lamar, A. Leow, A. Zhang, S. Yang, and A. Kumar, "Graph theory analysis of cortical-subcortical networks in late-life depression," *The American Journal of Geriatric Psychiatry*, vol. 22, no. 2, pp. 195–206, 2014.
- [125] H. K. Lim, W. S. Jung, and H. J. Aizenstein, "Aberrant topographical organization in gray matter structural network in late life depression: a graph theoretical analysis," *International Psychogeriatrics*, vol. 25, no. 12, pp. 1929–1940, 2013.
- [126] S. C. Ponten, F. Bartolomei, and C. J. Stam, "Small-world networks and epilepsy: graph theoretical analysis of intracerebrally recorded mesial temporal lobe seizures," *Clinical Neurophysiology*, vol. 118, no. 4, pp. 918–927, 2007.

## Review Article

# Added Value of Assessing Adnexal Masses with Advanced MRI Techniques

**I. Thomassin-Naggara,<sup>1,2,3</sup> D. Balvay,<sup>1</sup> A. Rockall,<sup>4</sup> M. F. Carette,<sup>2,3</sup>  
M. Ballester,<sup>3,5</sup> E. Darai,<sup>3,5</sup> and M. Bazot<sup>2,3</sup>**

<sup>1</sup>INSERM, UMR970, Team 2, Angiogenesis Imaging, 75005 Paris, France

<sup>2</sup>AP-HP, Hôpital Tenon, Department of Radiology, 58 avenue Gambetta, 75020 Paris, France

<sup>3</sup>Sorbonne University, UPMC Univ Paris 06, IUC, 75005 Paris, France

<sup>4</sup>Imperial College London, ICTEM Building, Room 136, 1st Floor, Du Cane Road, London W12 0NN, UK

<sup>5</sup>AP-HP, Hôpital Tenon, Department of Gynaecology and Obstetrics, 4 rue de la Chine, 75020 Paris, France

Correspondence should be addressed to I. Thomassin-Naggara; [isabelle.thomassin@tnn.aphp.fr](mailto:isabelle.thomassin@tnn.aphp.fr)

Received 10 August 2014; Revised 23 November 2014; Accepted 7 December 2014

Academic Editor: Zhengchao Dong

Copyright © 2015 I. Thomassin-Naggara et al. This is an open access article distributed under the Creative Commons Attribution License, which permits unrestricted use, distribution, and reproduction in any medium, provided the original work is properly cited.

This review will present the added value of perfusion and diffusion MR sequences to characterize adnexal masses. These two functional MR techniques are readily available in routine clinical practice. We will describe the acquisition parameters and a method of analysis to optimize their added value compared with conventional images. We will then propose a model of interpretation that combines the anatomical and morphological information from conventional MRI sequences with the functional information provided by perfusion and diffusion weighted sequences.

## 1. Introduction

The clinical suspicion of an adnexal mass is one of the most frequent indications for gynecologic imaging. In this setting, the first imaging technique is ultrasonography with Doppler [1–6]. A large majority of women will not need any other imaging technique for characterization of the adnexal lesion because the lesion either has typically benign features (such as anechoic cyst) or is overtly malignant (such as the presence of peritoneal implants) [7]. In the latter case, the extent of disease will then be determined with computed tomography (CT) which is the current standard of care for preoperative staging.

However, when an echoic area is discovered at ultrasound, the question remains whether or not this represents a solid soft tissue component consistent with tumour. If the sonographer detects blood flow within the echoic area, a solid component surely exists but many benign lesions may display a solid component [8]. If no blood flow is detected in the echoic portion, the question remains without answer as solid

tissue may not display any blood flow on ultrasound [9]. Thus, when no typical signs of benignity or malignancy are present, the lesion remains indeterminate and a second line technique is needed with a frequency that depends on sonographer's experience [10, 11].

Pelvic magnetic resonance (MR) imaging has clearly been demonstrated to be the best imaging technique to characterize indeterminate or complex adnexal masses due to its excellent tissue contrast [12, 13]. Firstly, the conventional sequences (T2, T1, and T1 with fat saturation) are evaluated. MR imaging is very accurate for the identification of endometriotic or fatty masses using these sequences whereas sonography can only suggest these diagnoses in some cases [14, 15]. Moreover, conventional MR imaging readily distinguishes cystic from solid soft tissue components, as solid soft tissue enhances after gadolinium injection [16, 17]. Malignancy can only be suggested if there are enhancing solid components, such as thickened irregular septa, solid papillary projections, or a solid mass. These enhancing solid components are grouped under the name of “solid tissue” [18, 19].

TABLE 1: Acquisition parameters.

Sequences	Parameters
Sag T2 without FS	(i) <b>FOV</b> : 24 cm (ii) <b>Thickness</b> ≤6 mm (iii) +/- <b>motion correction</b> if available
Ax T2 without FS	(i) <b>FOV</b> : 30 cm, from kidney to symphysis. (ii) <b>Thickness</b> : 5 mm/1.0 spacing
Ax T1 Ax or sag T1 FS	(i) <b>Exact same location as Ax T2 without FS</b> (ii) <b>FOV</b> : 30 cm (a) <b>2D</b> thickness 5 mm/1.0 spacing (b) <b>3D</b> reconstruction thickness 3 mm/0.0 spacing
Ax DWI	(i) <b>Exact same location as Ax T2 without FS</b> (ii) <b>b value</b> : 1000–1200 with black urine (iii) <b>Thickness</b> : 6 mm/0.0 spacing or 5 mm/1.0 spacing
Ax PWI	(i) 3D T1 without FS (ii) <b>Temporal resolution</b> <15 sec (iii) <b>Spatial resolution and slice thickness</b> = 3 mm/0.0 sp (iv) <b>Size of box</b> >15 cm (v) <b>Loc. per slab</b> >50 (vi) 4 acquisitions without gadolinium (baseline) (vii) <b>Reformat good quality</b> of sagittal and coronal reconstruction +++ (viii) <b>Time duration</b> : 4 mn
Ax or sag T1 FS gadolinium	(i) Copy Ax or sag T1FS without gadolinium

Others types of solid component such as thin smooth septa or cyst wall are not considered as solid tissue and do not require any functional characterization. If solid tissue is detected within an adnexal lesion, early publications demonstrated that the T2 signal intensity of the solid tissue is useful to distinguish benign from malignant tumors [12] because some benign tumors contain fibrous material in their solid tissue and thus appear with a typically low T2 weighted signal. The accuracy of MRI interpretation to differentiate benign from malignant masses using only the conventional sequences is about 80% according to the published literature [17, 20–22]. However, Huchon et al. demonstrated that most ovarian tumors undergo surgery without any MR analysis and there is a high rate of incomplete surgery [23]. More recently, perfusion and diffusion weighted sequences were demonstrated to improve diagnostic confidence about 25% and 15%, respectively [24], allowing an accuracy of up to 94.6%. This increase in the diagnostic accuracy of MRI may help to increase the clinician's confidence in MR imaging.

This review will present these two functional techniques that are readily available in clinical routine, including acquisition parameters, method of analysis, and added value compared with conventional images. Then, we will propose a synthesis consisting of an interpretation model combining conventional and functional criteria.

## 2. Perfusion Weighted MR Sequence

Ovarian cancer is characterized by an anarchic neovascularization resulting in a wide number of immature microvessels. These vessels are characterized by a lack of coverage by pericytes and the higher expression of one of the receptors of

Vascular Endothelial Growth Factor (VEGF) named VEGFR-2 on both endothelial and epithelial cells of ovarian cystadenocarcinomas. These physiopathogenic characteristics have been demonstrated to be in line with variations of MR perfusion parameters [25].

*2.1. Technical Features.* All the parameters required to perform MRI for adnexal masses characterization are provided in Table 1.

*2.2. MR Acquisition Parameters.* For female pelvic imaging, perfusion MR technique is based on a Dynamic Contrast Enhanced (DCE) Gradient Echo (GRE) T1 weighted sequence. The main important parameters include a temporal resolution which must be lower than 15 seconds and the total sequence duration should be at least 3 minutes. External myometrium is used as an internal reference because it is enhanced to approximately the same extent as ovarian tumour tissue [26]. Ideally, an axial 3D GRE T1 sequence should be performed with high quality reformats postcontrast in the sagittal and coronal planes. If only a 2D sequence can be performed, the acquisition plane should be placed in order to cover external myometrium and the tumor, both of which need to be analyzed [27] (Figure 1).

*2.3. MR Analysis.* For perfusion data, three types of analysis exist. The first one is the time intensity curve analysis. For adnexal mass characterization, as shown in Figure 1, two regions of interest are placed on both external myometrium and solid tissue of the adnexal mass on DCE MR sequence. Then, the evolution of relative signal intensity according to time can be assessed using time intensity curves. For

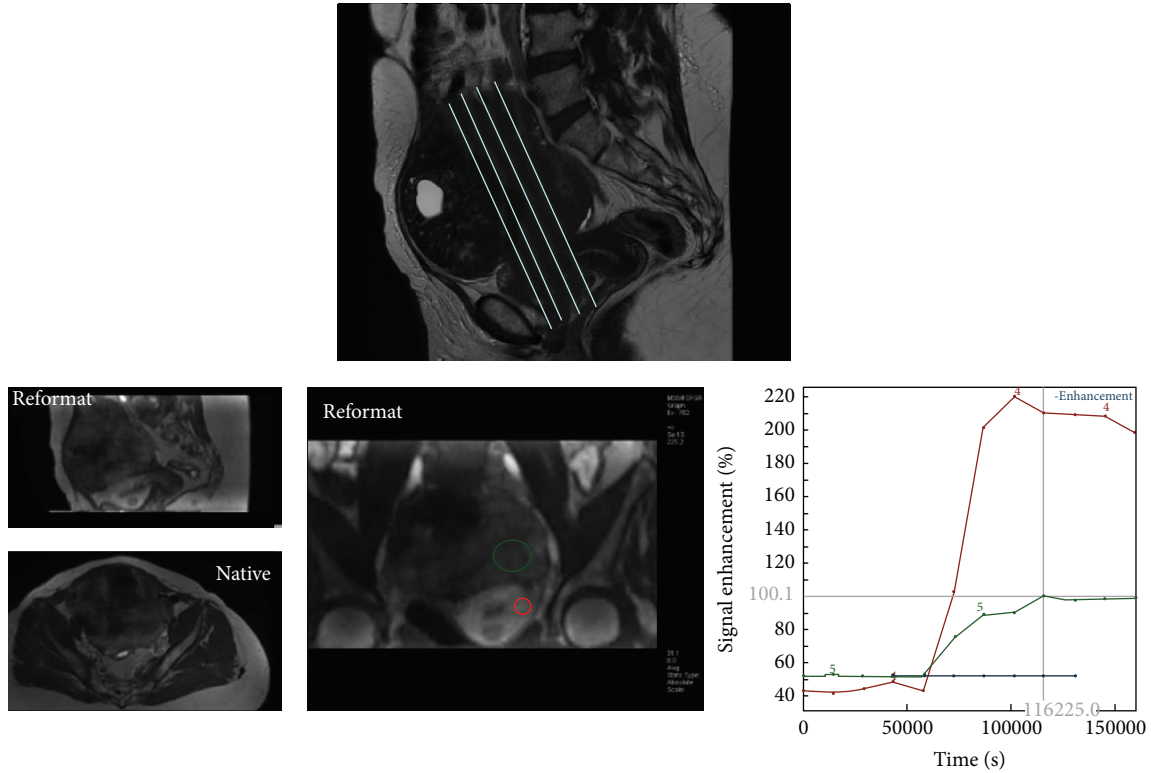


FIGURE 1: Perfusion MR acquisition. The sequence may be acquired in 2D plane in order to cover both external myometrium and the tumor or in axial 3D plane with a high quality of reformatting imaging in sagittal and coronal planes.

characterization of adnexal masses, time intensity curve of solid tissue in an adnexal mass is compared to that of external myometrium, which acts as the internal reference. The use of an internal reference overcomes to some extent the lack of reproducibility which is well known to be the main limitation of this type of postcontrast perfusion data. Thus, when solid tissue is enhanced with a weak and progressive curve in comparison to the myometrium, the curve is named “type 1.” When solid tissue is enhanced with a moderate enhancement in comparison to myometrium with a plateau, the curve is named “type 2.” Finally, when solid tissue is enhanced with a curve steeper than that of myometrium, whatever the intensity of enhancement, the curve is named “type 3” [28] (Figure 2).

The second type of analysis is named semiquantitative analysis based also on relative signal intensity of the curve as descriptive analysis. Area under the enhancing curve may be easily calculated and the initial area under the curve (before 60 sec) named Initial Area under Curve (IAUC60) has been demonstrated useful for adnexal masses characterization [28, 29]. Using different mathematic models, the time intensity curve can be fitted. With a high temporal resolution acquisition data, Thomassin-Naggara et al. determined three semiquantitative parameters by fitting with Hill equation: enhancement amplitude (EA), time of half rising (THR), and maximal slope (MS) of the curve. These parameters were demonstrated to be useful to characterize adnexal masses because a correlation was proven between enhancement amplitude and maximal slope with pericyte coverage index

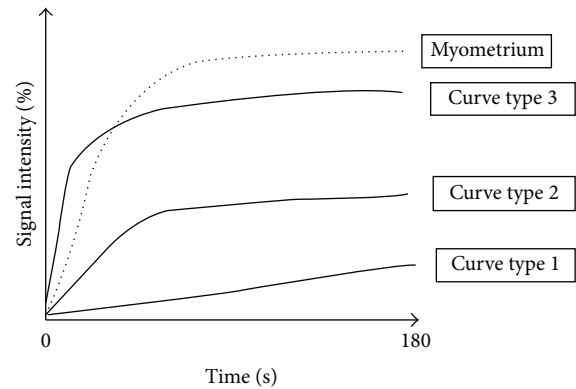


FIGURE 2: Time intensity curve.

(PCI) and high expression of VEGFR-2 on both epithelial and endothelial cells [25]. Moreover, an independent external validation of these parameters was performed later on another population studied in another center [29]. With a lower temporal resolution acquisition data of 30 seconds, Dilks et al. demonstrated the usefulness of other parameters including mean  $SI_{max}$ , a lower  $SI_{rel}$ , and a wash-in rate (WIR) that corresponds to the ratio between enhancement amplitude and time [30] (Figure 3). These authors underlined the simplicity of this technique because the software used to calculate enhancement parameters is widely available on MR imaging workstations [31].

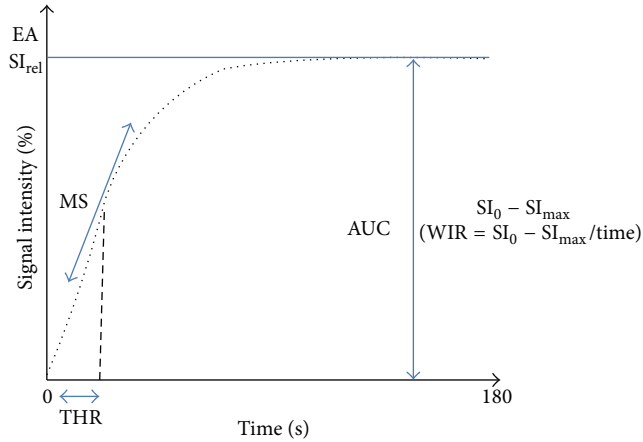


FIGURE 3: Semiquantitative analysis. Different parameters published were EA (enhancement amplitude), THR (time of half rising), maximal slope (MS),  $SI_{rel}$  (maximal relative enhancement), WIR (wash-in rate), and  $SI_{max}$ .

As we underlined before, descriptive and semiquantitative analysis are based on signal intensity evaluation. However, using MR imaging, signal intensity depends mainly on the type of acquisition parameters, such as flip angle and TR. Image contrast provided by the administration of contrast agent and linearity between signal intensity variation and contrast agent concentration are highly dependent on these parameters [32]. Thus, many authors argue that we need to obtain reproducible perfusion parameters independent of acquisition conditions. We needed to develop perfusion parameters that are not expressed according to signal intensity but to gadolinium concentration [33]. Then, a more recent approach consists in a quantitative analysis which is based on a pharmacokinetic modeling allowing conversion of signal intensity into gadolinium concentration [34, 35]. Depending on the temporal resolution of the acquisition, different pharmacokinetic models may be applied. At low temporal resolution acquisition ( $>10$  sec), Carter et al. demonstrated the usefulness of Tofts-Kety model to differentiate benign from malignant tumors using  $K_{trans}$  and  $K_{ep}$  [29]. Tofts-Kety model is the most used pharmacokinetic model in this context thanks to its good reproducibility [35]. However, the original Tofts-Kety is not a physiological model resulting in parameters with values depending on acquisition settings [36]. Moreover, descriptive and semiquantitative analysis showed that the initial part of the curve is the most informative to distinguish benign from malignant tumors which suggests that tissue blood flow would be the most informative parameter. Thus, using high temporal resolution acquisition (3 sec) [37], de Bazelaire et al. described a Brix modified model [38] that allows the determination of tissue blood flow ( $F_T$ ), blood volume fraction ( $V_b$ ), permeability-surface area product ( $P_S$ ), and interstitial volume fraction ( $V_e$ ) and this proved useful for adnexal mass characterization [39] (Figure 4).

**2.4. Added Value for Adnexal Mass Characterization.** The perfusion weighted MR sequence provides additional criteria for adnexal characterization.

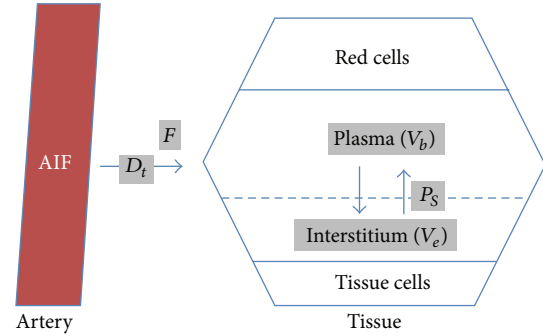


FIGURE 4: Pharmacokinetic model: Brix modified model with 4 quantitative parameters including tissue blood flow ( $F$ ), blood volumetric fraction ( $V_b$ ), the product of capillary wall permeability and surface area ( $P_S$ ), interstitial volume ( $V_e$ ), and the delay for the contrast media to reach tissue ( $D_t$ ).

Using descriptive analysis, first publications demonstrated in a population of 37 epithelial tumors that a slow, low-level enhancement pattern typical of a type 1 curve has a sensitivity of 70% and a specificity of 88.8% for benign tumor, whereas a rapid and high level of enhancement typical of a type 3 curve was only found in invasive malignant tumors with a sensitivity of 67%. A type 2 curve was mostly found in borderline tumors (sensitivity 72.4%) but with a lower specificity [28]. The added value of perfusion weighted imaging was tested in a larger population of 87 complex adnexal masses [24] and the addition of time intensity curve analysis resulted in an increase in diagnostic confidence of 25% for a senior reader in pelvic MR imaging. The diagnosis was correctly changed in 7% (3/41) of malignant masses and in 62% (10/16) of benign masses. No diagnosis was incorrectly changed. In our experience, the time intensity curve analysis is particularly interesting for benign tumors with fibrous component such as ovarian fibroma or cystadenofibroma that do not always display a low T2 signal due to oedematous areas. These lesions typically enhance with time intensity curve type 1 [40] (Figure 5). Moreover, time intensity curve analysis is also useful to differentiate borderline from invasive malignant tumors. Typically, borderline tumors display solid papillary projections whereas invasive malignant tumors display a solid mass with or without solid papillary projections. When there is no clear solid mass but grouped solid papillary projection, it can be difficult to be sure if the tumor is only a borderline tumor or an early invasive ovarian cancer. Another application of time intensity curve analysis is to help characterize a solid pelvic mass when the ovarian or uterine origin cannot be clearly identified. In menopausal women, normal ovarian parenchyma is more difficult to identify on T2 weighted sequences than in premenopausal women because follicles are usually no longer seen. The two most frequent solid pelvic masses in women are uterine leiomyoma and ovarian fibroma. When a uterine leiomyoma is pedunculated, morphological criteria are sometimes insufficient to be sure of the origin. Moreover, T2 signal intensity is not very useful to distinguish these two tumors. Time intensity curve analysis can be useful in this situation because uterine leiomyomas are typically enhanced with virtually the same time intensity

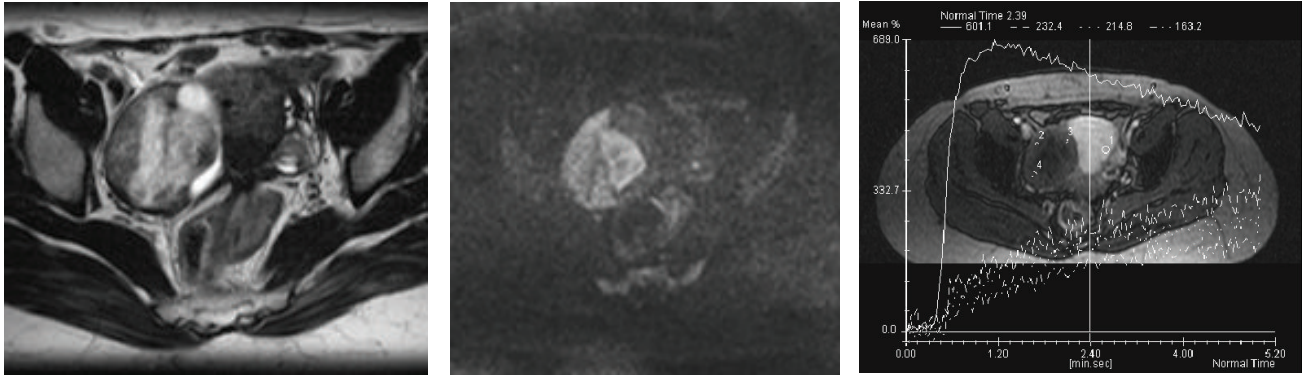


FIGURE 5: Ovarian fibroma right adnexal mixed cystic solid mass with an intermediate T2 weighted signal intensity in the solid component (A), a high DW signal (B), and a time intensity curve weak and progressive without any plateau (dotted line) in comparison with myometrial enhancement (continuous line).

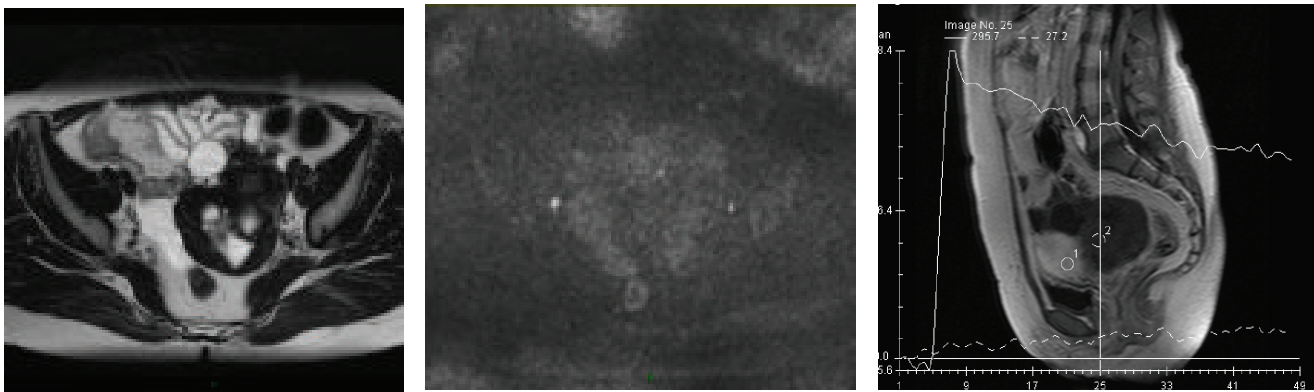


FIGURE 6: T2 “dark through” effect—cystadenofibroma. The fibrous component of this tumor was highly cellular with an ADC value lower than  $1 \cdot 10^{-3} \text{ mm}^2/\text{s}$ . However, the tumor is not bright on DW image because of its low T2 signal (T2 dark through effect).

curve as the myometrium whereas ovarian fibromas display a weak and progressive manner (type 1 curve) [41] (Figure 6).

Using semiquantitative analysis, Bernardin et al. demonstrated that benign lesions displayed a lower mean maximal signal intensity ( $SI_{max}$ ), a lower relative signal intensity ( $SI_{rel}$ ), and a lower wash-in rate (WIR) than borderline and malignant tumors [42] (Figure 3). In this study, the authors found a sensitivity of 67% and specificity of 88% in predicting borderline/invasive malignancy applying a cutoff WIR of 9.5 l/s, although there was overlap between borderline and benign lesion with a range of 2–8 l/s. Moreover, in a more recent study, the same team confirms that all benign cystadenofibroma solid tissues have a WIR less than 5.8 l/s [40]. Using myometrium as internal reference, Thomassin-Naggara et al. showed that the enhancement amplitude ratio ( $EA_{ratio}$ ), time of half rising ratio ( $THR_{ratio}$ ), and maximal slope ( $MS_{ratio}$ ) were significantly higher in invasive malignant tumors than in benign and borderline tumors. Moreover, in this last study, borderline tumors were characterized by a higher  $EA_{ratio}$  than benign tumors whereas no differences between benign and borderline tumors were found using WIR values [43]. Thus, in our experience, the use of myometrium as internal reference improves the diagnostic value of semiquantitative

parameters when viewed in combination with the descriptive parameters.

Using quantitative analysis, Thomassin-Naggara et al. demonstrated that benign tumors displayed a lower tissue blood flow ( $F_T$ ), a lower blood fraction volume ( $V_b$ ), a higher interstitial volume ( $V_e$ ), and a lower relative AUC (rAUC) than malignant tumors. Moreover, borderline tumors displayed a lower  $F_T$  and a higher  $D_t$  than invasive ovarian tumors [39]. With data acquired at lower temporal resolution, malignant tumors display a higher  $K_{ep}$  in their solid component than benign tumors ( $P < 0,001$ ) [29].

### 3. Diffusion Weighted MR Sequence

Diffusion weighted (DW) MR imaging is based on the analysis of the movement of water molecules in a tissue. In a highly cellular tissue, a restriction of the movement of water molecules (a reduction in diffusivity) exists between cells and the tissue appears as high signal intensity on high  $b$  value DW image with associated low ADC (apparent diffusion coefficient). In less cellular tissue, there is less restriction of the movement of water molecules. Thus, ADC is high

and the tissue typically appears without any high signal intensity on the high  $b$  value DW images. Indeed, depending on acquisition parameters, DW signal will be due to both cellularity (ADC values) and T2 signal.

**3.1. MR Acquisition Parameters and MR Analysis.** For adnexal mass characterization, many studies have underlined the usefulness of DW signal intensity, although the ADC analysis for solid component analysis can be unhelpful [29, 44, 45]. In fact, many benign tumors have fibrous tissue that restricts the movement of water molecules. Thus, there is a great overlap between ADC values of the solid tissue of benign and malignant tumors [29, 45]. However, as the DW signal is the combination of water diffusivity and T2 signal intensity, the typically very low T2 weighted signal intensity of fibrous tissue in these benign adnexal tumors decreases the theoretical high DW signal intensity due to the high cellularity of these tumors (T2 dark though effect) (Figure 6). Thus, the analysis of DW signal allows correct classification as benign in this group of tumors and makes such criteria accurate to distinguish benign from malignant adnexal tumors.

Then, as mainly DW signal is useful for adnexal mass characterization, we need to optimize a sequence to obtain a sequence with the lowest T2 signal effect with a maximal contrast to noise ratio. T2 signal effect decreases with the increase of  $b$  values. At  $b_0$  value, the sequence is weighted as a T2 weighted sequence. To find the optimal  $b$  value, we use urine as internal reference. As we want to suppress T2 effect, we need to obtain dark urine. In our experience, the right  $b$  value is between  $b_{1000}$  and  $b_{1200}$  depending on the manufacturer.

**3.2. Added Value for Adnexal Masses Characterization.** Many publications have studied the value of diffusion MR sequence for adnexal mass characterization. First publications studied the value of diffusion weighted MR imaging to characterize endometriotic cystic component or mature cystic teratoma [46]. The accuracy of MR imaging with conventional sequences is very high for these benign masses (up to 95%) [14, 47–49]. Thus, the added value of diffusion weighted imaging in this setting is limited and has never been statistically demonstrated. Nevertheless, in mature cystic teratoma with paucity of fat, the very low ADC value should be useful to identify keratinoid content [46, 50].

Using DWI to characterize solid tissue, many authors demonstrate that ADC values are not useful to distinguish benign from malignant tumors due to the overlap with benign fibrous tumors [44, 51]. However, thanks to “dark through” effect, the value of the absence of DW signal was demonstrated for predicting benignity (positive likelihood ratio = 10.1). Moreover, the combination of a low T2 weighted signal with a low DW signal allows a confident exclusion of malignancy. These preliminary data were confirmed in further studies that underlined the added value of diffusion weighted sequence to increase diagnostic confidence in 15% and especially for benign tumors [24]. The diagnosis was correctly changed in 8.9% (4/45) of malignant

masses and in 28% (8/28) of benign masses. One diagnosis was incorrectly changed in one case of ovarian fibroma (Figure 7).

#### 4. Combination of Functional Parameters in an Interpretation Model

Finally, some studies have evaluated the usefulness of the added combination of perfusion and diffusion weighted analysis to conventional analysis. These studies demonstrated that functional analysis is useful especially for reclassifying as benign tumors that were misclassified as malignant using conventional criteria. In our experience, that is the main issue for clinical practice. Indeed, recent trials have shown that unnecessary interventions in women with benign adnexal lesions lead to significant morbidity and mortality [52]. All women have operative and anesthetic risks, which are increased in menopausal women with additional comorbidity factors (obesity, diabetes, and hypertension). Moreover, in premenopausal women, preservation of fertility is a major issue as ovarian surgery mainly based on cystectomy is associated with the risk of ovarian reserve alteration, especially for cysts greater than 5 cm in diameter [53, 54].

Although MRI is the most accurate imaging technique to characterize adnexal masses [54, 55], a debate exists on its use among clinicians explaining why only 25% of surgeons performed MR imaging before surgery and thus the high incidence of preoperative misdiagnoses [23].

One hypothesis is the lack of standardization of the MR report and the absence of combination of conventional and functional criteria and this could in part be responsible. In this context, the first MR diagnostic score was recently built and described each complex adnexal mass according its positive predictive value of malignancy with a five categories score named  $A_{\text{DNEX}}\text{MR}_{\text{SCORING}}$  system [19] (Table 2). If the complex mass does not display any enhancing solid tissue, the classification is  $A_{\text{DNEX}}\text{MR}_{\text{SCORE}}$  2 or 3 with a PPV lower than 5%. If a complex adnexal mass displays an enhancing solid tissue, in the absence of peritoneal implants, we need to take account of the evaluation of diffusion weighted (DW) signal and time intensity curve analysis. Functional sequences are included in this score as follows: If there is a low T2 and low DW signal on the high  $b$  value image, the tumor is always benign ( $A_{\text{DNEX}}\text{MR}_{\text{SCORE}}$  2). If not, time intensity curve analysis allows differentiating probably benign masses ( $A_{\text{DNEX}}\text{MR}_{\text{SCORE}}$  3) (if the solid tissue is enhanced according to a type 1 time intensity curve), indeterminate mass ( $A_{\text{DNEX}}\text{MR}_{\text{SCORE}}$  4) (if the solid tissue is enhanced according to a type 2 time intensity), and probably malignant mass ( $A_{\text{DNEX}}\text{MR}_{\text{SCORE}}$  5) (if the solid tissue is enhanced with a type 3 time intensity curve) (Figure 8). This score was developed and validated with a very high accuracy (AUROC > 0.94). A score  $\leq 3$  has been associated with benignity with a sensitivity of 96.6% and a specificity of 93.5%. A multicentre European prospective study (the “EURAD study”) is currently in recruitment, with the aim of validating the proposed scoring system (clinical trial NCT01738789). The potential impact of

TABLE 2:  $A_{DNEX}MR_{SCORING}$  system.

$A_{DNEX}MR_{SCORE} 1$	Absence of mass	—
$A_{DNEX}MR_{SCORE} 2$	Benign mass	Purely cystic mass Purely endometriotic mass Purely fatty mass Mass without wall enhancement Low T2 and low DW signal of solid component
$A_{DNEX}MR_{SCORE} 3$	Probably benign mass	Bi- or multiloculate cyst without solid component Curve type 1 of solid component
$A_{DNEX}MR_{SCORE} 4$	Indeterminate	All others lesions (including curve type 2 of solid component)
$A_{DNEX}MR_{SCORE} 5$	Probably malignant mass	Curve type 3 of solid component Peritoneal implants

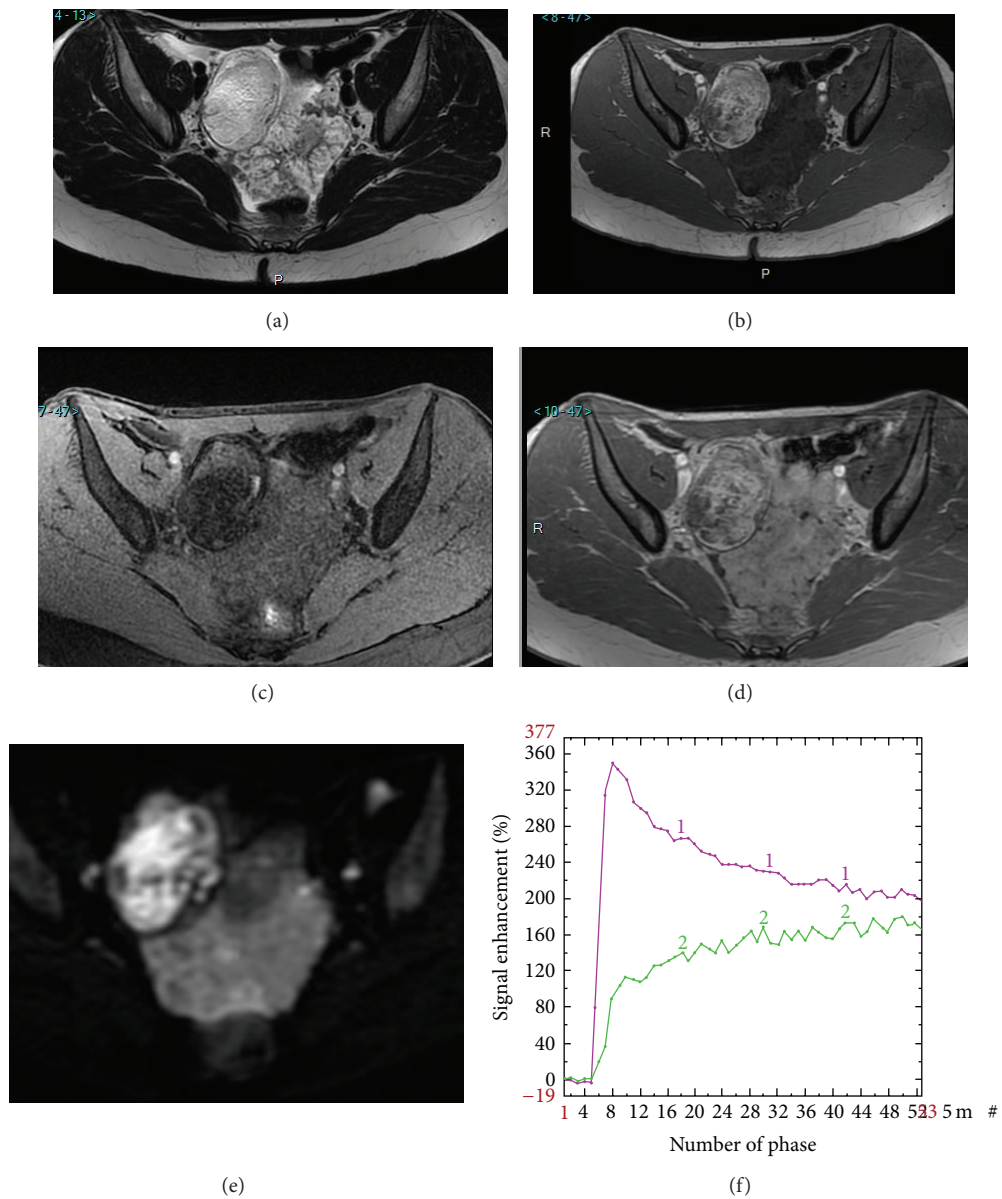


FIGURE 7: Added value of perfusion and diffusion weighted imaging. Right side: mature cystic teratoma (purely fatty mass:  $A_{DNEX}MR_{score} 2$ ). Left side: borderline serous cystadenoma (solid tissue which is bright on T2 and DW sequence and that enhances with a TIC type 2:  $A_{DNEX}MR_{score} 4$ ). T2 weighted sequence (a), T1 weighted sequence (b), T1 weighted sequence with fat saturation (c), T1 weighted sequence with gadolinium (d), DW sequence (e), and PW analysis comparing myometrial TIC (1) and tumoral TIC (2) (f).

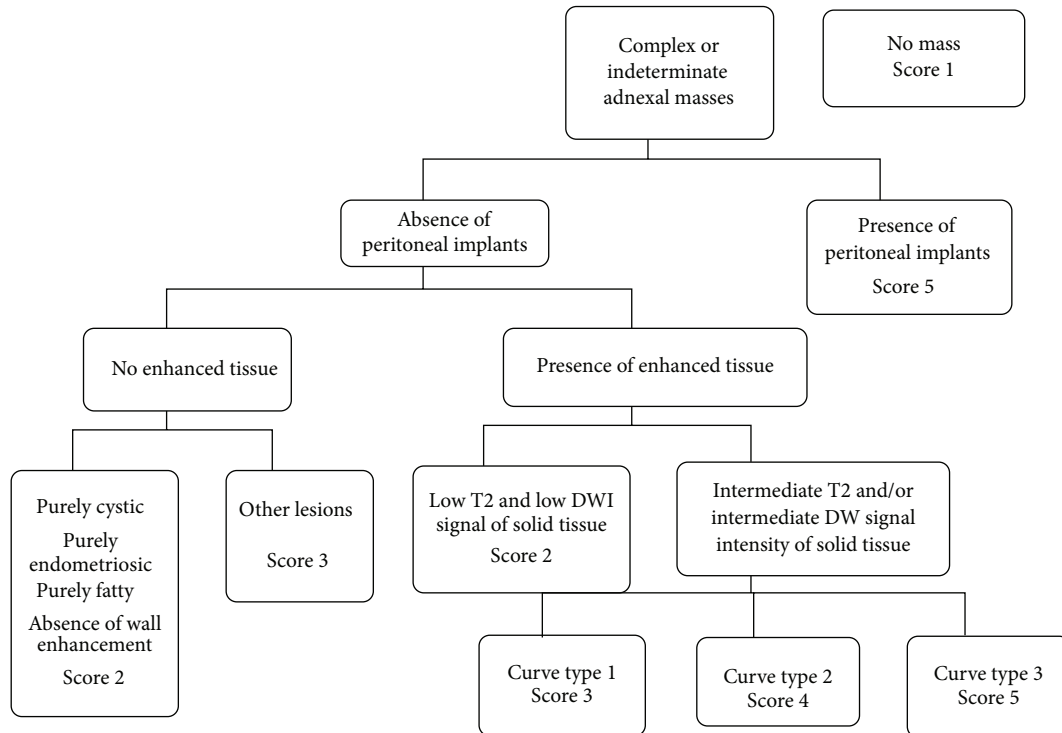


FIGURE 8:  $A_{DNEX}$  MR scoring system (19).

the score on therapeutic management will then be tested in a future trial.

In this review, we present the development of perfusion and diffusion analysis to characterize sonographically indeterminate adnexal masses. Using time intensity curve analysis and visual assessment of DW signal, functional criteria help the radiologist to improve lesion characterization especially for benign lesions and should help the clinician to avoid unnecessary surgeries. Currently, few data are available to validate in clinical routine more reproducible perfusion analysis for the characterization of adnexal masses. Very recently, new developments of DWI were reported thanks to 3T acquisition including the analysis of the heterogeneity of the tumor (ADC entropy) [51]. This method of research would be interesting in the future to find new criteria of characterization.

## 5. Key Points

- (1) Perfusion weighted and diffusion weighted MR imaging help to characterize adnexal masses.
- (2) Benign tumors with solid components typically display a low DWI signal.
- (3) Benign solid tumors are typically enhanced with a type 1 time intensity curve.
- (4)  $A_{DNEX}MR_{SCORING}$  system is helpful to relay the radiologist's suspicion of malignancy.

## Abbreviations

MR:	Magnetic resonance
VEGF:	Vascular Endothelial Growth Factor
DCE:	Dynamic Contrast Enhanced
GRE:	Gradient Echo
IAUC:	Initial Area under Curve
EA:	Enhancement amplitude
THR:	Time of half rising
MS:	Maximal slope
PCI:	Pericyte coverage index
WIR:	Wash-in rate
$F_T$ :	Tissue blood flow
$V_b$ :	Blood volume fraction
$P_s$ :	Permeability-surface area product
$V_e$ :	Interstitial volume fraction
TR:	Time of relaxation
$SI_{max}$ :	Maximum signal intensity
$EA_{ratio}$ :	Enhancement amplitude ratio
$THR_{ratio}$ :	Time of half rising ratio
$MS_{ratio}$ :	Maximal slope
ADC:	Apparent diffusion coefficient.

## Disclosure

As this paper is a review, no ethics committee approval is required. I. Thomassin-Naggara (Invited conference for General Electric, Consultant for Olea). A. Rockall (Invited conference for Guerbet).

## Conflict of Interests

The authors declare that there is no conflict of interests regarding the publication of this paper.

## References

- [1] M. Emoto, H. Iwasaki, K. Mimura, T. Kawarabayashi, and M. Kikuchi, "Differences in the angiogenesis of benign and malignant ovarian tumors, demonstrated by analyses of color Doppler ultrasound, immunohistochemistry, and microvessel density," *Cancer*, vol. 80, no. 5, pp. 899–907, 1997.
- [2] E. M. Schutter, P. Kenemans, and C. Sohn, "Diagnostic value of pelvic examination, ultrasound, and serum CA 125 in postmenopausal women with a pelvic mass. An international multicenter study," *Cancer*, vol. 74, no. 4, pp. 1398–1406, 1994.
- [3] M. H. Vuento, J. P. Pirhonen, J. I. Makinen, P. J. Laippala, M. Gronroos, and T. A. Salmi, "Evaluation of ovarian findings in asymptomatic postmenopausal women with color doppler ultrasound," *Cancer*, vol. 76, no. 7, pp. 1214–1218, 1995.
- [4] D. L. Brown, M. C. Frates, F. C. Laing et al., "Ovarian masses: can benign and malignant lesions be differentiated with color and pulsed Doppler US?" *Radiology*, vol. 190, no. 2, pp. 333–336, 1994.
- [5] D. Levine, D. L. Brown, R. F. Andreotti et al., "Management of asymptomatic ovarian and other adnexal cysts imaged at US: society of radiologists in ultrasound consensus conference statement," *Radiology*, vol. 256, no. 3, pp. 943–954, 2010.
- [6] D. Timmerman, A. C. Testa, T. Bourne et al., "Logistic regression model to distinguish between the benign and malignant adnexal mass before surgery: a multicenter study by the International Ovarian Tumor Analysis Group," *Journal of Clinical Oncology*, vol. 23, no. 34, pp. 8794–8801, 2005.
- [7] K. Kinkel, H. Hricak, Y. Lu, K. Tsuda, and R. A. Filly, "US characterization of ovarian masses: a meta-analysis," *Radiology*, vol. 217, no. 3, pp. 803–811, 2000.
- [8] Y.-Y. Jeong, E. K. Outwater, and H. K. Kang, "Imaging evaluation of ovarian masses," *Radiographics*, vol. 20, no. 5, pp. 1445–1470, 2000.
- [9] J. W. Walsh, K. J. W. Taylor, J. F. Wasson, P. E. Schwartz, and A. T. Rosenfield, "Gray-scale ultrasound in 204 proved gynecologic masses: accuracy and specific diagnostic criteria," *Radiology*, vol. 130, no. 2, pp. 391–397, 1979.
- [10] M. Bazot, E. Daraï, D. J. Biau, M. Ballester, and L. Dessolle, "Learning curve of transvaginal ultrasound for the diagnosis of endometriomas assessed by the cumulative summation test (LC-CUSUM)," *Fertility and Sterility*, vol. 95, no. 1, pp. 301–303, 2011.
- [11] J. Yazbek, S. K. Raju, J. Ben-Nagi, T. K. Holland, K. Hillaby, and D. Jurkovic, "Effect of quality of gynaecological ultrasonography on management of patients with suspected ovarian cancer: a randomised controlled trial," *The Lancet Oncology*, vol. 9, no. 2, pp. 124–131, 2008.
- [12] E. S. Siegelman and E. K. Outwater, "Tissue characterization in the female pelvis by means of MR imaging," *Radiology*, vol. 212, no. 1, pp. 5–18, 1999.
- [13] K. Kinkel, Y. Lu, A. Mehdizade, M.-F. Pelte, and H. Hricak, "Indeterminate ovarian mass at US: incremental value of second imaging test for characterization-meta-analysis and Bayesian analysis," *Radiology*, vol. 236, no. 1, pp. 85–94, 2005.
- [14] M. Bazot, E. Daraï, R. Hourani et al., "Deep pelvic endometriosis: MR imaging for diagnosis and prediction of extension of disease," *Radiology*, vol. 232, no. 2, pp. 379–389, 2004.
- [15] K. A. Jain, D. L. Friedman, T. W. Pettinger, R. Alagappan, R. B. Jeffrey Jr., and F. G. Sommer, "Adnexal masses: comparison of specificity of endovaginal US and pelvic MR imaging," *Radiology*, vol. 186, no. 3, pp. 697–704, 1993.
- [16] T. Komatsu, I. Konishi, M. Mandai et al., "Adnexal masses: transvaginal US and gadolinium-enhanced MR imaging assessment of intratumoral structure," *Radiology*, vol. 198, no. 1, pp. 109–115, 1996.
- [17] Y. Yamashita, M. Torashima, Y. Hatanaka et al., "Adnexal masses: accuracy of characterization with transvaginal US and precontrast and postcontrast MR imaging," *Radiology*, vol. 194, no. 2, pp. 557–565, 1995.
- [18] D. Timmerman, L. Valentin, T. H. Bourne, W. P. Collins, H. Verrelst, and I. Vergote, "Terms, definitions and measurements to describe the sonographic features of adnexal tumors: a consensus opinion from the International Ovarian Tumor Analysis (IOTA) group," *Ultrasound in Obstetrics & Gynecology*, vol. 16, no. 5, pp. 500–505, 2000.
- [19] I. Thomassin-Naggara, E. Aubert, A. Rockall et al., "Adnexal masses: development and preliminary validation of an MR imaging scoring system," *Radiology*, vol. 267, no. 2, pp. 432–443, 2013.
- [20] M. Bazot, D. Haouy, E. Daraï, A. Cortez, S. Dechoux-Vodovar, and I. Thomassin-Naggara, "Is MRI a useful tool to distinguish between serous and mucinous borderline ovarian tumours?" *Clinical Radiology*, vol. 68, no. 1, pp. e1–e8, 2013.
- [21] M. Bazot, J. Nassar-Slaba, I. Thomassin-Naggara, A. Cortez, S. Uzan, and E. Daraï, "MR imaging compared with intraoperative frozen-section examination for the diagnosis of adnexal tumors; correlation with final histology," *European Radiology*, vol. 16, no. 12, pp. 2687–2699, 2006.
- [22] S. A. Sohaib, A. Sahdev, P. van Trappen, I. J. Jacobs, and R. H. Reznick, "Characterization of adnexal mass lesions on MR imaging," *American Journal of Roentgenology*, vol. 180, no. 5, pp. 1297–1304, 2003.
- [23] C. Huchon, A.-S. Bats, C. Bensaïd et al., "Adnexal masses management: a prospective multicentric observational study," *Gynecologie Obstetrique Fertilité*, vol. 36, no. 11, pp. 1084–1090, 2008.
- [24] I. Thomassin-Naggara, I. Toussaint, N. Perrot et al., "Characterization of complex adnexal masses: value of adding perfusion- and diffusion-weighted MR imaging to conventional MR imaging," *Radiology*, vol. 258, no. 3, pp. 793–803, 2011.
- [25] I. Thomassin-Naggara, M. Bazot, E. Daraï, P. Callard, J. Thomassin, and C. A. Cuenod, "Epithelial ovarian tumors: value of dynamic contrast-enhanced MR imaging and correlation with tumor angiogenesis," *Radiology*, vol. 248, no. 1, pp. 148–159, 2008.
- [26] I. Thomassin-Naggara, D. Balvay, C. A. Cuenod, E. Daraï, C. Marsault, and M. Bazot, "Dynamic contrast-enhanced MR imaging to assess physiologic variations of myometrial perfusion," *European Radiology*, vol. 20, no. 4, pp. 984–994, 2010.
- [27] I. Thomassin-Naggara, C. A. Cuenod, E. Daraï, C. Marsault, and M. Bazot, "Dynamic contrast-enhanced MR imaging of ovarian neoplasms: current status and future perspectives," *Magnetic Resonance Imaging Clinics of North America*, vol. 16, no. 4, pp. 661–672, 2008.

- [28] I. Thomassin-Naggara, E. Daraï, C. A. Cuenod, R. Rouzier, P. Callard, and M. Bazot, "Dynamic contrast-enhanced magnetic resonance imaging: a useful tool for characterizing ovarian epithelial tumors," *Journal of Magnetic Resonance Imaging*, vol. 28, no. 1, pp. 111–120, 2008.
- [29] J. S. Carter, J. S. Koopmeiners, J. E. Kuehn-Hajder et al., "Quantitative multiparametric MRI of ovarian cancer," *Journal of Magnetic Resonance Imaging*, vol. 38, no. 6, pp. 1501–1509, 2013.
- [30] P. Dilks, P. Narayanan, R. Reznick, A. Sahdev, and A. Rockall, "Can quantitative dynamic contrast-enhanced MRI independently characterize an ovarian mass?" *European Radiology*, vol. 20, no. 9, pp. 2176–2183, 2010.
- [31] P. Mohaghegh and A. G. Rockall, "Imaging strategy for early ovarian cancer: characterization of adnexal masses with conventional and advanced imaging techniques," *Radiographics*, vol. 32, no. 6, pp. 1751–1773, 2012.
- [32] M. K. Ivancevic, I. Zimine, F. Lazeyras, D. Foxall, and J.-P. Valle, "FAST sequences optimization for contrast media pharmacokinetic quantification in tissue," *Journal of Magnetic Resonance Imaging*, vol. 14, no. 6, pp. 771–778, 2001.
- [33] S. M. Galbraith, M. A. Lodge, N. J. Taylor et al., "Reproducibility of dynamic contrast-enhanced MRI in human muscle and tumours: comparison of quantitative and semi-quantitative analysis," *NMR in Biomedicine*, vol. 15, no. 2, pp. 132–142, 2002.
- [34] K. Hittmair, G. Gomiscek, K. Langenberger, M. Recht, H. Imhof, and J. Kramer, "Method for the quantitative assessment of contrast agent uptake in dynamic contrast-enhanced MRI," *Magnetic Resonance in Medicine*, vol. 31, no. 5, pp. 567–571, 1994.
- [35] P. S. Tofts, "Modeling tracer kinetics in dynamic Gd-DTPA MR imaging," *Journal of Magnetic Resonance Imaging*, vol. 7, no. 1, pp. 91–101, 1997.
- [36] C. A. Cuenod, L. Fournier, D. Balvay, and J.-M. Guinebretière, "Tumor angiogenesis: pathophysiology and implications for contrast-enhanced MRI and CT assessment," *Abdominal Imaging*, vol. 31, no. 2, pp. 188–193, 2006.
- [37] J. L. Evelhoch, "Key factors in the acquisition of contrast kinetic data for oncology," *Journal of Magnetic Resonance Imaging*, vol. 10, no. 3, pp. 254–259, 1999.
- [38] C. de Bazelaire, N. Siauve, L. Fournier et al., "Comprehensive model for simultaneous MRI determination of perfusion and permeability using a blood-pool agent in rats rhabdomyosarcoma," *European Radiology*, vol. 15, no. 12, pp. 2497–2505, 2005.
- [39] I. Thomassin-Naggara, D. Balvay, E. Aubert et al., "Quantitative dynamic contrast-enhanced MR imaging analysis of complex adnexal masses: a preliminary study," *European Radiology*, vol. 22, no. 4, pp. 738–745, 2012.
- [40] Y. Z. Tang, S. Liyanage, P. Narayanan et al., "The MRI features of histologically proven ovarian cystadenofibromas—an assessment of the morphological and enhancement patterns," *European Radiology*, vol. 23, no. 1, pp. 48–56, 2013.
- [41] I. Thomassin-Naggara, E. Daraï, J. Nassar-Slaba, A. Cortez, C. Marsault, and M. Bazot, "Value of dynamic enhanced magnetic resonance imaging for distinguishing between ovarian fibroma and subserous uterine leiomyoma," *Journal of Computer Assisted Tomography*, vol. 31, no. 2, pp. 236–242, 2007.
- [42] L. Bernardin, P. Dilks, S. Liyanage, M. E. Miquel, A. Sahdev, and A. Rockall, "Effectiveness of semi-quantitative multiphase dynamic contrast-enhanced MRI as a predictor of malignancy in complex adnexal masses: radiological and pathological correlation," *European Radiology*, vol. 22, no. 4, pp. 880–890, 2012.
- [43] I. Thomassin-Naggara, E. Daraï, C. A. Cuenod, R. Rouzier, P. Callard, and M. Bazot, "Dynamic contrast-enhanced magnetic resonance imaging: a useful tool for characterizing ovarian epithelial tumors," *Journal of Magnetic Resonance Imaging*, vol. 28, no. 1, pp. 111–120, 2008.
- [44] S. Fujii, S. Kakite, K. Nishihara et al., "Diagnostic accuracy of diffusion-weighted imaging in differentiating benign from malignant ovarian lesions," *Journal of Magnetic Resonance Imaging*, vol. 28, no. 5, pp. 1149–1156, 2008.
- [45] I. Thomassin-Naggara, E. Daraï, C. A. Cuenod et al., "Contribution of diffusion-weighted MR imaging for predicting benignity of complex adnexal masses," *European Radiology*, vol. 19, no. 6, pp. 1544–1552, 2009.
- [46] T. Nakayama, K. Yoshimitsu, H. Irie et al., "Diffusion-weighted echo-planar MR imaging and ADC mapping in the differential diagnosis of ovarian cystic masses: usefulness of detecting keratinoid substances in mature cystic teratomas," *Journal of Magnetic Resonance Imaging*, vol. 22, no. 2, pp. 271–278, 2005.
- [47] M. Bazot, F. Boudghène, P. Billières, J.-M. Antoine, S. Uzan, and J.-M. Bigot, "Value of fat-suppression gradient-echo MR imaging in the diagnosis of ovarian cystic teratomas," *Clinical Imaging*, vol. 24, no. 3, pp. 146–153, 2000.
- [48] C. Guinet, J.-N. Buy, M. A. Ghossain et al., "Fat suppression techniques in MR imaging of mature ovarian teratomas: comparison with CT," *European Journal of Radiology*, vol. 17, no. 2, pp. 117–121, 1993.
- [49] C. Guinet, M. A. Ghossain, J.-N. Buy et al., "Mature cystic teratomas of the ovary: CT and MR findings," *European Journal of Radiology*, vol. 20, no. 2, pp. 137–143, 1995.
- [50] B. Chilla, N. Hauser, G. Singer, M. Trippel, J. M. Froehlich, and R. A. Kubik-Huch, "Indeterminate adnexal masses at ultrasound: effect of MRI imaging findings on diagnostic thinking and therapeutic decisions," *European Radiology*, vol. 21, no. 6, pp. 1301–1310, 2011.
- [51] A. S. Kierans, G. L. Bennett, T. C. Mussi et al., "Characterization of malignancy of adnexal lesions using ADC entropy: comparison with mean ADC and qualitative DWI assessment," *Journal of Magnetic Resonance Imaging*, vol. 37, no. 1, pp. 164–171, 2013.
- [52] S. S. Buys, E. Partridge, M. H. Greene et al., "Ovarian cancer screening in the Prostate, Lung, Colorectal and Ovarian (PLCO) cancer screening trial: findings from the initial screen of a randomized trial," *American Journal of Obstetrics & Gynecology*, vol. 193, no. 5, pp. 1630–1639, 2005.
- [53] H. Roman, M. Auber, C. Mokdad et al., "Ovarian endometrioma ablation using plasma energy versus cystectomy: a step toward better preservation of the ovarian parenchyma in women wishing to conceive," *Fertility and Sterility*, vol. 96, no. 6, pp. 1396–1400, 2011.
- [54] H. Hricak, M. Chen, F. V. Coakley et al., "Complex adnexal masses: detection and characterization with MR imaging—multivariate analysis," *Radiology*, vol. 214, no. 1, pp. 39–46, 2000.
- [55] E. K. Outwater and C. J. Dunton, "Imaging of the ovary and adnexa: clinical issues and applications of MR imaging," *Radiology*, vol. 194, no. 1, pp. 1–18, 1995.

## Research Article

# MRI Guided Brain Stimulation without the Use of a Neuronavigation System

Ehsan Vaghefi,<sup>1</sup> Peng Cai,<sup>2</sup> Fang Fang,<sup>2</sup> Winston D. Byblow,<sup>3</sup>  
Cathy M. Stinear,<sup>4</sup> and Benjamin Thompson<sup>1,5</sup>

<sup>1</sup> Department of Optometry and Vision Science, University of Auckland, Building 502, Level 4, 85 Park Road, Grafton, Auckland 1023, New Zealand

<sup>2</sup> Department of Psychology, Peking University, Haidian Road, Haidian, Beijing 100871, China

<sup>3</sup> Department of Sport and Exercise Science, University of Auckland, Symonds Street, Auckland 1023, New Zealand

<sup>4</sup> Department of Medicine, University of Auckland, Symonds Street, Auckland 1023, New Zealand

<sup>5</sup> School of Optometry and Vision Science, University of Waterloo, 200 Columbia Street W, Waterloo, ON, Canada N2L 3G1

Correspondence should be addressed to Ehsan Vaghefi; [e.vaghefi@auckland.ac.nz](mailto:e.vaghefi@auckland.ac.nz)

Received 23 June 2014; Revised 13 August 2014; Accepted 9 September 2014

Academic Editor: Zhengchao Dong

Copyright © 2015 Ehsan Vaghefi et al. This is an open access article distributed under the Creative Commons Attribution License, which permits unrestricted use, distribution, and reproduction in any medium, provided the original work is properly cited.

A key issue in the field of noninvasive brain stimulation (NIBS) is the accurate localization of scalp positions that correspond to targeted cortical areas. The current gold standard is to combine structural and functional brain imaging with a commercially available “neuronavigation” system. However, neuronavigation systems are not commonplace outside of specialized research environments. Here we describe a technique that allows for the use of participant-specific functional and structural MRI data to guide NIBS without a neuronavigation system. Surface mesh representations of the head were generated using Brain Voyager and vectors linking key anatomical landmarks were drawn on the mesh. Our technique was then used to calculate the precise distances on the scalp corresponding to these vectors. These calculations were verified using actual measurements of the head and the technique was used to identify a scalp position corresponding to a brain area localized using functional MRI.

## 1. Introduction

Noninvasive brain stimulation (NIBS) techniques such as repetitive transcranial magnetic stimulation (rTMS) and transcranial direct current stimulation (tDCS) allow for the temporary modulation of neural activity within the human brain. rTMS involves the induction of weak electrical currents within targeted regions of the cortex via brief, time-varying magnetic fields produced with a hand-held coil [1]. tDCS employs head-mounted electrodes, which allow for a weak direct current to interact with the underlying cortex [2]. NIBS can be used to investigate the role of individual brain areas in specific cognitive, behavioral, or perceptual processes [1]. In addition, these techniques are being investigated from a clinical perspective and current evidence suggests that NIBS may be applicable to the treatment of multiple neurological and psychiatric disorders [3, 4].

Studies involving the use of NIBS begin by selecting a target brain area for stimulation. This process is typically informed by evidence from brain imaging, animal neurophysiology, or studies involving neurological patients. Subsequent steps include the selection of appropriate stimulation parameters and ensuring that the stimulation is delivered to the correct brain area. This latter point is particularly important as the stimulation effects are most pronounced in close proximity to the rTMS coil and tDCS electrodes [5]. Therefore, accurate, participant-specific localization of stimulation sites on the scalp is required for optimal stimulation [6].

A number of approaches can be used to identify the correct scalp position for stimulation. Single pulse TMS can be used to activate specific regions of the primary motor cortex resulting in motor evoked potentials (MEPs) within the corresponding peripheral muscle [7]. The scalp location

that evokes the strongest MEP can then be used as the location for rTMS or tDCS. A comparable technique also exists for the visual cortex whereby single pulse TMS of the occipital pole can be used to evoke the percept of a phosphene [8]. The scalp location that induces the most robust phosphene or a phosphene in a specific visual field location can be used for visual cortex stimulation. A similar technique can be used for motion sensitive, extra-striate visual area V5 whereby TMS can be used to induce moving phosphenes [9]. It has been shown that this technique is in good agreement with localization of V5 using functional magnetic resonance imaging [10]. However, it is not possible to use this approach outside of the motor and visual cortices because most brain regions do not produce acute neurophysiological or perceptual effects in response to single pulse TMS.

An alternative technique for identifying participant-specific stimulation sites on the scalp is the 10–20-electrode system, which was originally designed for positioning EEG electrodes [11]. This approach defines a grid of positions on the scalp that are separated by 10% or 20% of the distance between anatomical landmarks such as the nasion and the inion. This approach has been used successfully in a large number of brain stimulation studies; however, the mapping of particular 10–20 system locations to specific brain areas can vary across participants [12].

Another alternative is to use structural and functional brain imaging techniques to localize specific brain areas in individuals with millimetre resolution. A number of frameless stereotactic navigation systems exist for real-time coregistration of a participant to their own MRI images. Tools such as a “pointer” or a TMS coil can also be registered within the volume. These systems typically involve ultrasound devices or infrared cameras and a number of reference targets mounted on the head and NIBS apparatus. When used in combination with structural and functional MRI images these “neuronavigation” systems allow for precise identification of the scalp position corresponding to a particular brain area [13].

The combination of brain imaging and a neuronavigation system is the current gold standard in the field of NIBS [14] and may improve the results of NIBS-based therapeutic interventions [15–20]; however, there are some disadvantages. These include difficulty in using these systems for studies of posterior brain areas that can fall outside of the neuronavigation system’s field of view and, most importantly, the high cost of these systems, which can exceed \$50,000. Techniques have been described that allow NIBS to be targeted using generic MRI datasets [21] or when structural but not functional MRI data are available for individual participants [22]. Furthermore, techniques for identifying optimal scalp locations for stimulation based on individual participant’s neuroanatomy are also available [23]. However, each of these approaches requires the use of a neuronavigation system. Here we describe a technique that allows the use of individual structural and functional MRI to guide NIBS in the absence of a neuronavigation system. The approach is based on vectors drawn on a mesh that is morphed to participant-specific MRI data. These mesh vectors are then transposed to the participant’s head by converting them to

head measurements anchored to anatomical landmarks. We report comparisons between measurements made using our technique and actual head measurements. We also give an example of how the technique can be used in combination with fMRI to localize a stimulation site for visual area V5 in a single subject. Visual area V5 was chosen for this example as it can be readily localized using fMRI and the corresponding scalp position cannot be identified based on a single anatomical landmark. Therefore, a number of measurements are required to triangulate the correct scalp location for stimulation. A MATLAB package is also provided, which allows the use of our technique in conjunction with the commercially available Brain Voyager software package or any other software platform that supports the morphing of meshes to MRI data.

## 2. Methods

*2.1. Participants.* Six healthy adult participants (5 male and 1 female, mean age 32 years) provided written informed consent and took part in this study. fMRI data were collected from one participant to provide a participant-specific example of how our technique can be used in combination with a functional localizer. All study procedures were approved by the institutional ethics review board and were in accordance with the Declaration of Helsinki.

*2.2. Magnetic Resonance Imaging.* MRI data were acquired using a 3.0 Tesla Philips Achieva scanner equipped with an 8-channel head coil. A T1-weighted 3D turbo field-echo anatomical volume (1000 ms inverted prepulse,  $1 \times 1 \times 1 \text{ mm}^3$  voxel resolution, 180 sagittal slices, 2.7 ms TE, 5.9 ms TR, and  $8^\circ$  flip angle) was acquired for each participant. For functional localization of V5, four functional scans were conducted using a T2\*-weighted gradient echo, EPI sequence (TR = 2 s, TE = 30 ms, and flip angle =  $65^\circ$ ) to acquire 160 volumes constructed from 39 axial slices covering the whole brain at voxel resolution of  $3 \times 3 \times 3 \text{ mm}$ . During the functional scans the participant viewed static and dynamic radial grating stimuli ( $10^\circ \times 20^\circ$ , 0.4 cycles per degree, 3% contrast, and 9 Hz temporal frequency when moving) presented on a mean luminance background ( $5 \text{ cd/m}^2$ ) [24]. Dynamic gratings were presented in 20-second blocks separated by 20-second blocks of stationary gratings. There were 6 dynamic blocks per scan. During each dynamic block the participant fixated centrally and performed a task whereby they judged the relative speed of two grating movements, one centripetal and one centrifugal. Each movement lasted 250 ms with an interstimulus interval of 50 ms and a behavioural response time of 1450 ms. These stimuli resulted in robust activation in area V5.

MRI data were analyzed using the commercial Brain Voyager QX package (<http://www.brainvoyager.com/>). A 3D mesh of the head was generated using the mesh functions within Brain Voyager applied to the native space T1 anatomical volume after AC-PC alignment (Figure 1). Functional data were corrected for head movement, high pass filtered, and aligned to the AC-PC aligned anatomical images using

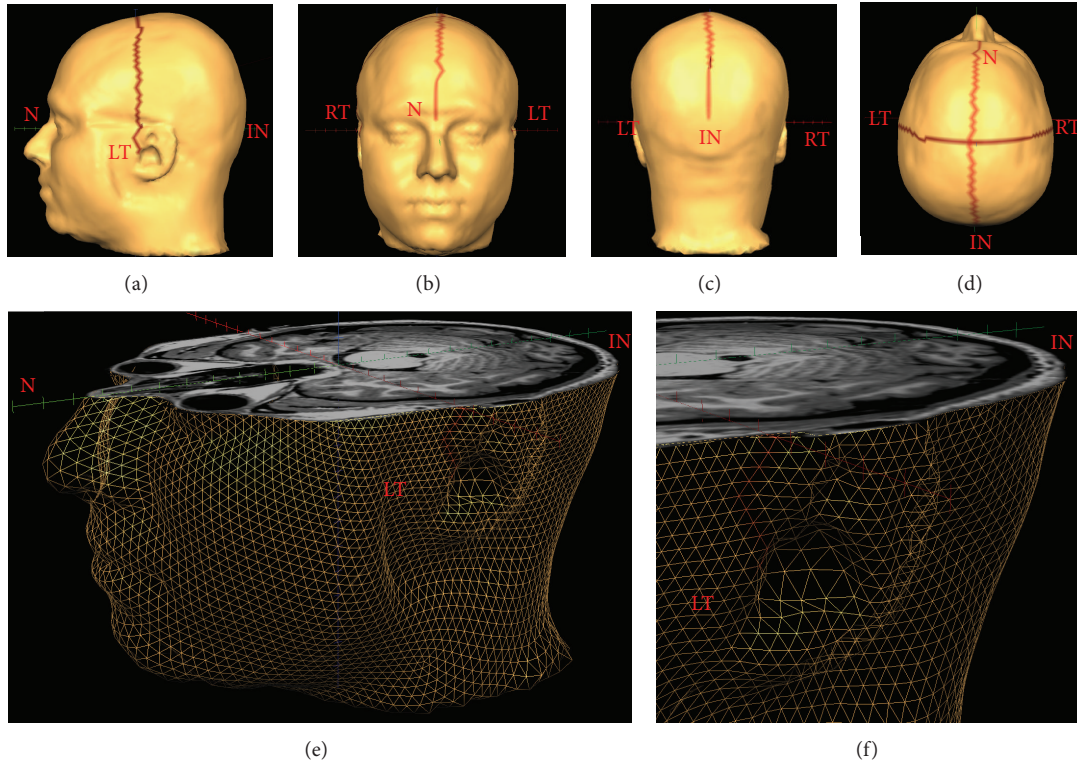


FIGURE 1: A 3D mesh morphed to the structural MRI data of a representative participant. Panels (a)–(d) show the anatomical landmarks that were used as anchor points for scalp distance calculations marked on a T1-volume surface mesh created using Brain Voyager. N: nasion, RT and LT: right and left tragi, respectively, and IN: inion. The lines connecting the anatomical landmarks are “patches of interest” (POIs) drawn in Brain Voyager that link adjacent triangles in the mesh. Panels (e) and (f) show close-up views of the mesh without the surface coloring. The mesh has been cut axially at the level of the inion. The smooth surface of the head is represented using triangular elements and each of these elements is defined by its triconers.

subroutines within Brain Voyager. A general linear analysis was conducted and the results were visualized as t-maps on the anatomical image. Area V5 was identified as a region in the appropriate anatomical location that responded significantly more strongly to dynamic than static grating stimuli (FDR corrected  $q < 0.01$ ). The precise location of V5 was defined as the location of the peak voxel within the V5 region.

**2.3. Comparison of Measurements Made on the Surface Mesh and the Head.** Four anatomical landmarks were identified on each surface mesh: the nasion, the left and right tragi, and the inion (Figures 1(a)–1(d)). The shortest paths between the nasion and inion and the left and right tragi that passed through the center point of the head (Cz) were then marked on the surface of the 3D mesh and exported as “patches of interest” (POIs) within Brain Voyager. After this, the  $x$ ,  $y$ , and  $z$  coordinates of the mesh nodes that formed the POI were exported from Brain Voyager in XLS format and read into the MATLAB analysis environment for distance calculations. The actual distances between the two tragi and the nasion and inion were also measured for each participant using a tape measure. An investigator masked to the results of the MATLAB analysis made these measurements.

**2.4. MATLAB Operations.** A Graphical User Interface was created in MATLAB to import the coordinate matrix of the POI exported from the Brain Voyager environment. Since the aim was to develop a widely applicable tool, the software does not require the use of Brian Voyager. Rather, the software is capable of reading a coordinate matrix from a text/MS-Excel file as this format is an export option in most image postprocessing software packages. The file must have three columns ( $x, y, z$ ), which conform to the following format:

$$\text{Nodal}_{\text{vector}} = (\text{Node}(n)_x, \text{Node}(n)_y, \text{Node}(n)_z). \quad (1)$$

Here,  $n$  is the index of the nodal coordinate in the vector matrix. Subscripts  $x, y$ , and  $z$  indicate the Cartesian triconordinates of the vector’s nodal points.

The MATLAB code opens the text-based input file and searches for the first line of the nodal coordinate series. Next, it reads consecutive coordinates until the pattern is broken; that is, no further coordinates are listed. The nodes of the POI/vector can then be viewed immediately in 3D (Figure 2).

There are two main issues to be addressed when calculating scalp distances from POIs measured on a surface mesh. (1) The majority of packages that provide surface meshes (Brain Voyager included) export POIs across the mesh in a proprietary format that makes it difficult to identify adjacent points along the path. (2) The use of tetrahedral elements

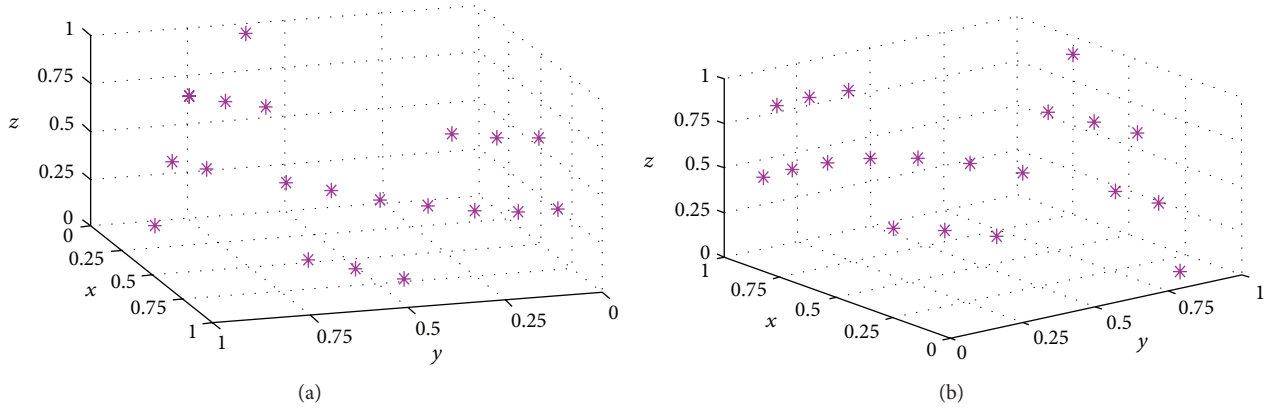


FIGURE 2: Graphical representations of the nodes making up a path along the surface of a head mesh created in Brain Voyager. (a) and (b) are two different views of the same 3D path. The axis values are 3D vector coordinates normalized to the length of the whole vector.

in the mesh produces “jagged” POIs that do not exactly represent the smooth surface of the head. These two issues were resolved using the following steps.

Having imported the coordinate matrix of the POI vector (Figure 2), the code first identifies the end points of the vector (i.e., nodal positions at the two ends of the vector). This is achieved by brute force comparison of pairs of nodal coordinates (i.e., marching along the POI vector), in order to find the outmost couple. A smoothed polynomial is then fitted to the two endpoints in 3 dimensions, which provides a reference for identifying adjacent nodal points in the vector. The nodal coordinate list is then sorted along the estimated trajectory of the POI vector (Figure 3). Finally, a second smoothed polynomial is fitted to the sorted nodal coordinate list in three dimensions, which removes the jaggedness of the path (Figure 3(c)). The length of the second fitted polynomial provides an estimate of the length of the vector on the participant’s head. After POI vector length calculation, the imported coordinate matrix and the measured pathway are plotted in the GUI.

The GUI allows multiple POIs to be imported from a single mesh and viewed simultaneously (Figure 4). The GUI also allows 3D viewing of the POI and supports 3D zooming and rotation (Figure 4).

### 3. Results

The measurements made using MATLAB were in good agreement with those made manually using a tape measure (Table 1). There were no statistically significant differences between the two sets of measurements (nasion-inion  $t(5) = 1$ ,  $P = 0.4$ ; tragus-tragus  $t(5) = 0.8$ ,  $P = 0.5$ ) and intraclass correlation (ICC) indicated that the two sets of measurements were closely related (nasion-inion ICC = 0.97,  $P < 0.001$ ; tragus-tragus ICC = 0.98,  $P < 0.001$ ).

Overall, our MATLAB application appeared to be capable of accurately measuring the length of the selected and exported POIs.

*3.1. Combination of the Technique with fMRI Data.* To assess whether the technique could be used in combination with

TABLE 1: Comparison of the manual head measurements and the MATLAB estimates.

Participant	Nasion-inion		Tragus-tragus	
	Manual (mm)	MATLAB (mm)	Manual (mm)	MATLAB (mm)
P1	390	391	390	394
P2	348	351	376	380
P3	364	361	368	365
P4	370	368	360	363
P5	352	355	355	353
P6	325	332	377	377
Mean (SD)	358 (22)	360 (20)	371 (13)	372 (15)

fMRI localization data we generated scalp measurements to localize the scalp position directly above V5 within the left hemisphere of one participant (Figure 5). The procedure was as follows.

- (1) The functional MRI data were coregistered to the anatomical MRI data and analyzed to identify V5 (see Methods section). The 3D statistical map was then visualized within the anatomical volume and a mesh was morphed to the surface of the anatomical volume using the mesh tools within Brain Voyager.
- (2) The mesh was cut along the transverse plane that contained the peak V5 voxel for the left hemisphere (as shown in Figure 5).
- (3) A POI was drawn from the nasion to the top of the cut mesh (blue POI in Figure 5).
- (4) A second POI was from the left tragus to the top of the cut mesh (white POI in Figure 5).
- (5) A third POI was drawn to connect the uppermost points of the nasion and tragus POIs (red POI in Figure 5). This POI was then extended to the scalp position that was directly above the most active voxel in the V5 (green POI in Figure 5).
- (6) The MATLAB toolbox was used to calculate the length of each POI on the participant’s head.

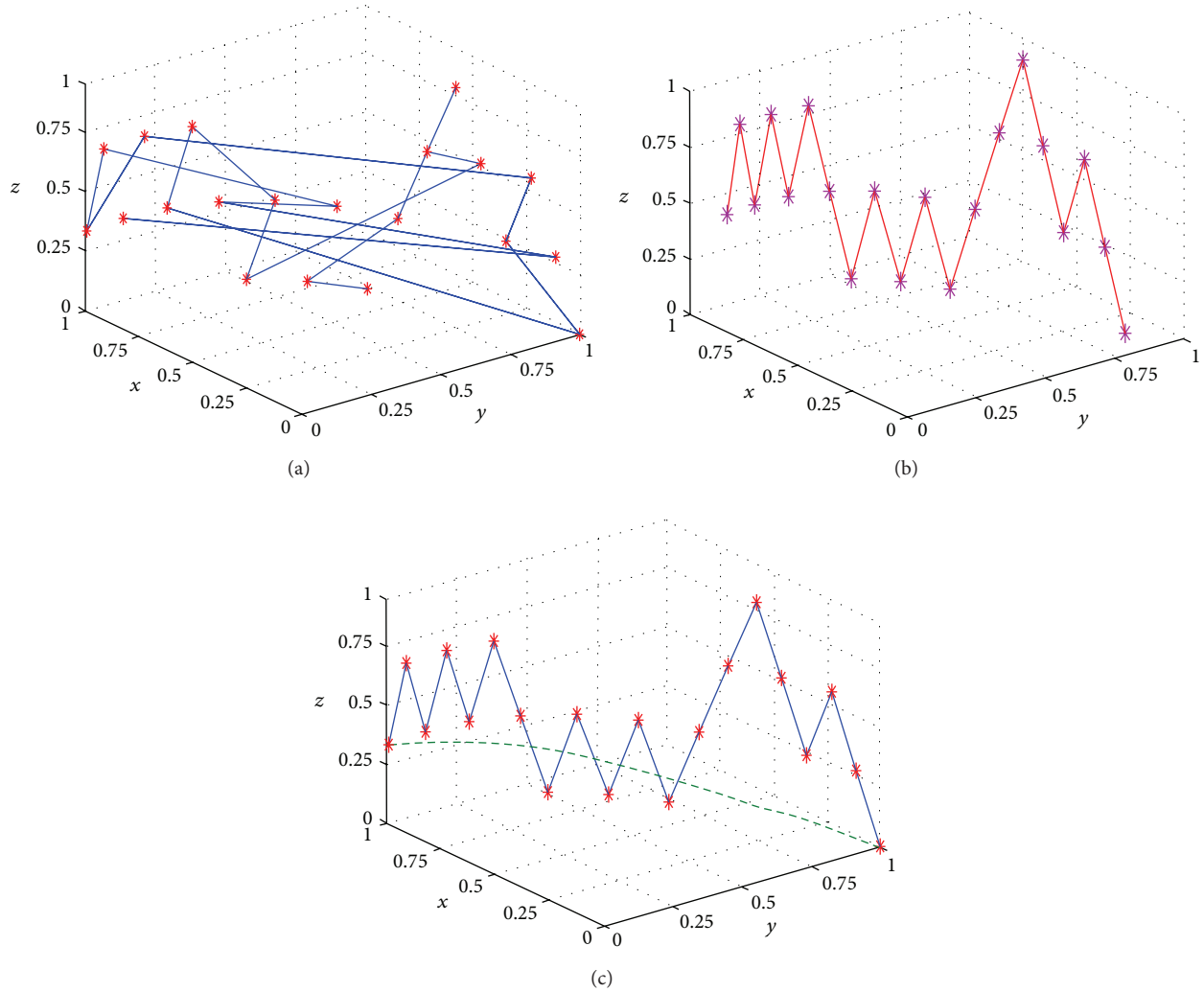


FIGURE 3: Processing of a path retrieved from a POI drawn on a surface mesh generated by Brain Voyager. (a) The randomized order of vertices provided by the Brain Voyager output. (b) The same vertices after reordering. The jagged path resulting from the triangulation of the mesh is apparent. (c) A curve fitted to the vertices (in dashed green) allows the length of the path to be accurately calculated. The axis values are normalized POI vector coordinates in 3D.

- (7) A hairnet was placed on the participant and tape was used to secure the net so that it was stretched tightly across the head. A line that was of the same length as the POI anchored to the nasion (blue in Figure 5) was then drawn vertically upwards from the participant's nasion using a tape measure and marker pen. The POI anchored to the left tragus (white in Figure 5) was transposed to the participant's head in the same way.
- (8) A line was drawn connecting the top points of the nasion and tragus POIs. The length of this line was compared to the length of the corresponding mesh POI (red in Figure 5) to ensure that the length calculations were accurate. In agreement with the data shown in Table 1, the distance between the two points on the mesh was identical to the manually measured distance on the participant's head.

- (9) The line connecting the nasion and tragus POIs was extended by the length of the corresponding mesh POI (green in Figure 5) to identify the scalp position above V5.

#### 4. Discussion

NIBS techniques such as rTMS and tDCS are becoming widely used in both basic science and clinical research. Both of these techniques are considered noninvasive because rTMS utilizes magnetic induction and tDCS uses nonpenetrating surface electrodes to induce electrical currents within superficial areas of the cortex. This means that direct access to the brain is not required as the stimulation can be delivered from the scalp. However, it also means that identifying the participant-specific scalp location that corresponds to the target brain area can be challenging. It is well established that

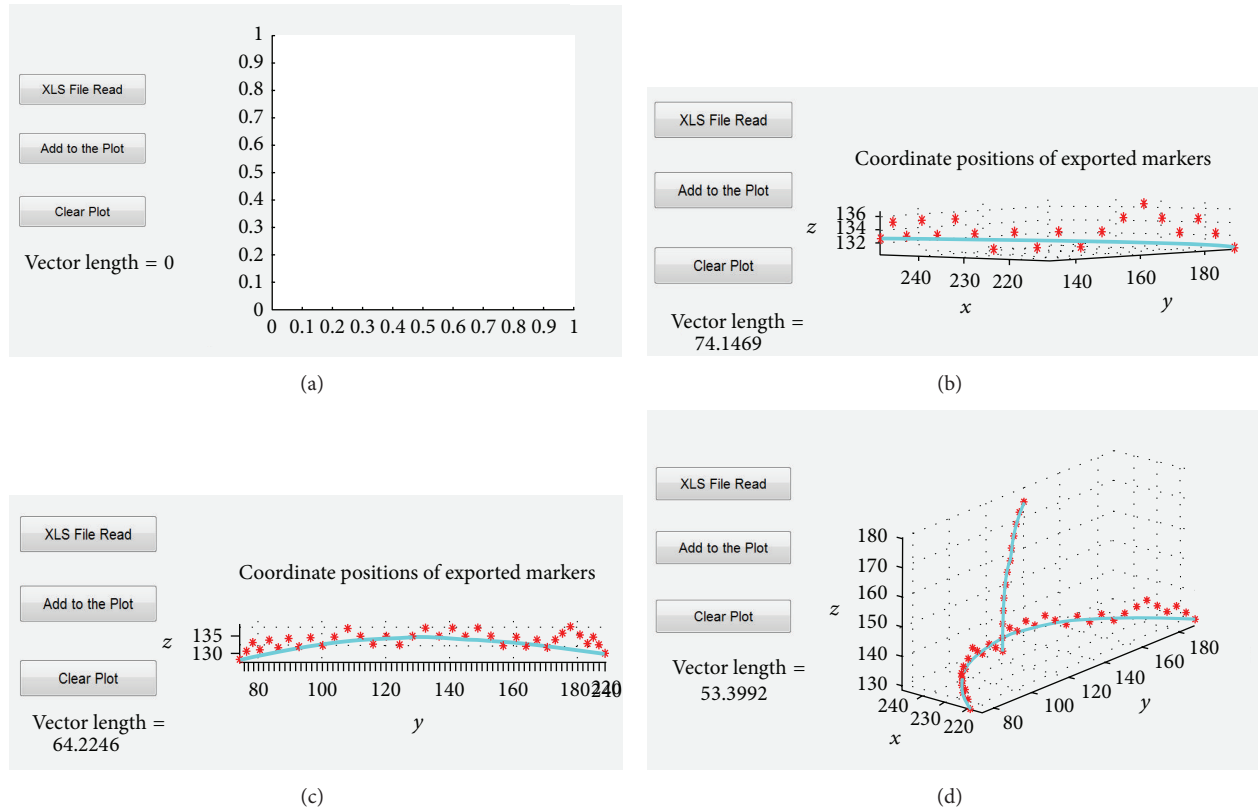


FIGURE 4: The Graphical User Interface that supports the import and plotting of POIs drawn on a surface mesh. Panel (a) shows the starting view and each consecutive panel ((b)–(d)) shows the addition of a new 3D path to the GUI. This is achieved by reading in XLS files containing the path data. The length of the most recently loaded 3D path is shown in the lower left corner of the GUI in mm.

structural and functional MRI can be used to assist in identifying the correct location for stimulation [25–28] although a specialized “neuronavigation” system is typically required to coregister the participant to their MRI data. The aim of this study was to develop a technique that would allow for MRI guided NIBS without the need for a commercially available neuronavigation system. We found that it was possible to accurately estimate scalp distances using POIs drawn on a surface mesh derived from participant-specific T1 volumes. When anchored to anatomical landmarks, these distances could be used to locate the scalp position corresponding to a specific region of neural activity identified using functional MRI.

The technique we describe here was not designed to be a replacement for neuronavigation systems that have a number of benefits. These include real-time assessment of TMS coil position, estimates of induced current flow, and the elimination of manual measurement error (although manual registration of the head and MRI data is still required). However, neuronavigation systems are not commonplace outside of specialist research environments and therefore alternative ways of utilizing MRI data to optimize NIBS are desirable.

Previous studies have calculated geodesic distances between scalp landmarks using surface mesh representations of the head in order to guide NIBS [29–32]. Our proposed

technique uses a comparable approach but unlike those used in the above studies, our tool is platform-independent and open source. Specifically, although we have implemented our technique using Brain Voyager, the principles we describe could be applied to data from any software that provides mesh vectors. It is also possible that this technique will be of use for other applications where scalp positions corresponding to specific brain areas are required. Examples include the combination of fMRI and EEG data and accurate positioning of near infrared spectroscopy apparatus. An important next step in the development of this approach will be to compare the scalp locations that are generated by our technique with those identified using commercial neuronavigation systems in a large group of participants. A comparison of MEP and phosphene induction between the two techniques will also be important.

The main advantages of our technique are its low cost and platform-independence (i.e., it can be used with any software that allows mesh morphing to MRI data). However, there are a number of limitations. For example, neuronavigation systems allow easy targeting of the same stimulation site across multiple sessions. Our technique requires remeasurement of the head for each session and this process may be prone to error. In addition, our technique allows for a stimulation site to be transposed from MRI data to the participant’s head; however the selection of the optimal stimulation site itself is

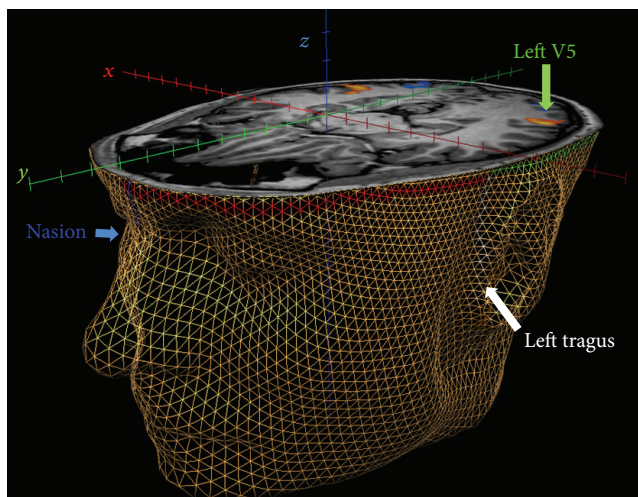


FIGURE 5: Localization of a scalp position above V5 in the left hemisphere. The axial cut through the Brain Voyager mesh was positioned to reveal the most active voxel in left V5. The lines drawn on the mesh show the POIs that were used to identify the scalp location corresponding to left V5. Blue: nasion to transverse plane, white: tragus to transverse plane, red: intersection of nasion vector and transverse plane to intersection of tragus vector and transverse plane, and green: extension of the vector to the scalp position above area V5. Orange regions indicate areas of functional activation in response to the V5 localization scans. See the main text for a detailed description of this procedure.

not supported. This issue is also relevant to the use of neuronavigation systems. Selection of the optimal stimulation site is a complex process as the electrical current generated by NIBS techniques interacts with the head and brain anatomy in ways that are unique to each participant [33–35]. A number of techniques for identifying optimal NIBS sites based on MRI data have been developed. These could be combined with our approach for transposing stimulation sites to the head to further improve the targeting of NIBS when neuronavigation systems are not available.

### Conflict of Interests

The authors declare that there is no conflict of interests regarding the publication of this paper.

### Acknowledgments

This work was supported by grants from Marsden Fund of the Royal Society of New Zealand to Ehsan Vaghefi and from the Health Research Council, University of Auckland, Faculty Development Research Fund, and Auckland Medical Research Foundation to Benjamin Thompson.

### References

[1] M. Hallett, “Transcranial magnetic stimulation: a primer,” *Neuron*, vol. 55, no. 2, pp. 187–199, 2007.

- [2] M. A. Nitsche and W. Paulus, “Excitability changes induced in the human motor cortex by weak transcranial direct current stimulation,” *Journal of Physiology*, vol. 527, no. 3, pp. 633–639, 2000.
- [3] M. C. Ridding and J. C. Rothwell, “Is there a future for therapeutic use of transcranial magnetic stimulation?” *Nature Reviews Neuroscience*, vol. 8, no. 7, pp. 559–567, 2007.
- [4] J. A. Williams, M. Imamura, and F. Fregni, “Updates of the use of non-invasive brain stimulation in physical and rehabilitation medicine,” *Journal of Rehabilitation Medicine*, vol. 41, no. 5, pp. 305–311, 2009.
- [5] M. A. Nitsche, S. Doemkes, T. Karaköse et al., “Shaping the effects of transcranial direct current stimulation of the human motor cortex,” *Journal of Neurophysiology*, vol. 97, no. 4, pp. 3109–3117, 2007.
- [6] J. Ruohonen and J. Karhu, “Navigated transcranial magnetic stimulation,” *Neurophysiologie Clinique*, vol. 40, no. 1, pp. 7–17, 2010.
- [7] A. T. Barker, R. Jalinous, and I. L. Freeston, “Non-invasive magnetic stimulation of human motor cortex,” *The Lancet*, vol. 1, no. 8437, pp. 1106–1107, 1985.
- [8] T. Kammer, “Phosphenes and transient scotomas induced by magnetic stimulation of the occipital lobe: their topographic relationship,” *Neuropsychologia*, vol. 37, no. 2, pp. 191–198, 1998.
- [9] L. M. Stewart, V. Walsh, and J. C. Rothwell, “Motor and phosphene thresholds: a transcranial magnetic stimulation correlation study,” *Neuropsychologia*, vol. 39, no. 4, pp. 415–419, 2001.
- [10] B. Thompson, C. Aaen-Stockdale, L. Koski, and R. F. Hess, “A double dissociation between striate and extrastriate visual cortex for pattern motion perception revealed using rTMS,” *Human Brain Mapping*, vol. 30, no. 10, pp. 3115–3126, 2009.
- [11] H. H. Jasper, “The ten twenty electrode system of the international federation,” *Electroencephalography and Clinical Neurophysiology*, vol. 10, pp. 371–375, 1958.
- [12] U. Herwig, P. Satrapi, and C. Schönfeldt-Lecuona, “Using the international 10-20 EEG system for positioning of transcranial magnetic stimulation,” *Brain Topography*, vol. 16, no. 2, pp. 95–99, 2003.
- [13] U. Herwig, K. Kölbel, A. P. Wunderlich et al., “Spatial congruence of neuronavigated transcranial magnetic stimulation and functional neuroimaging,” *Clinical Neurophysiology*, vol. 113, no. 4, pp. 462–468, 2002.
- [14] A. T. Sack, R. C. Kadosh, T. Schuhmann, M. Moerel, V. Walsh, and R. Goebel, “Optimizing functional accuracy of TMS in cognitive studies: a comparison of methods,” *Journal of Cognitive Neuroscience*, vol. 21, no. 2, pp. 207–221, 2009.
- [15] C. Schönfeldt-Lecuona, J.-P. Lefaucheur, L. Cardenas-Morales, R. C. Wolf, T. Kammer, and U. Herwig, “The value of neuronavigated rTMS for the treatment of depression,” *Neurophysiologie Clinique*, vol. 40, no. 1, pp. 37–43, 2010.
- [16] T. Wagner, F. Fregni, S. Fecteau, A. Grodzinsky, M. Zahn, and A. Pascual-Leone, “Transcranial direct current stimulation: a computer-based human model study,” *NeuroImage*, vol. 35, no. 3, pp. 1113–1124, 2007.
- [17] T. Wagner, A. Valero-Cabre, and A. Pascual-Leone, “Noninvasive human brain stimulation,” *Annual Review of Biomedical Engineering*, vol. 9, pp. 527–565, 2007.

- [18] A. Datta, M. Bikson, and F. Fregni, "Transcranial direct current stimulation in patients with skull defects and skull plates: high-resolution computational FEM study of factors altering cortical current flow," *NeuroImage*, vol. 52, no. 4, pp. 1268–1278, 2010.
- [19] F. Fregni and A. Pascual-Leone, "Technology insight: non-invasive brain stimulation in neurology—perspectives on the therapeutic potential of rTMS and tDCS," *Nature Clinical Practice Neurology*, vol. 3, no. 7, pp. 383–393, 2007.
- [20] P. C. Miranda, P. Faria, and M. Hallett, "What does the ratio of injected current to electrode area tell us about current density in the brain during tDCS?" *Clinical Neurophysiology*, vol. 120, no. 6, pp. 1183–1187, 2009.
- [21] F. Carducci and R. Brusco, "Accuracy of an individualized MR-based head model for navigated brain stimulation," *Psychiatry Research: Neuroimaging*, vol. 203, no. 1, pp. 105–108, 2012.
- [22] F. Duecker, M. A. Frost, T. A. de Graaf et al., "The cortex-based alignment approach to TMS coil positioning," *Journal of Cognitive Neuroscience*, vol. 26, no. 10, pp. 2321–2329, 2014.
- [23] P. M. Rusjan, M. S. Barr, F. Farzan et al., "Optimal transcranial magnetic stimulation coil placement for targeting the dorsolateral prefrontal cortex using novel magnetic resonance image-guided neuronavigation," *Human Brain Mapping*, vol. 31, no. 11, pp. 1643–1652, 2010.
- [24] B. Thompson and Z. Liu, "Learning motion discrimination with suppressed and un-suppressed MT," *Vision Research*, vol. 46, no. 13, pp. 2110–2121, 2006.
- [25] M. Nitsche, R. M. Hermann, H. Christiansen, J. Berger, and O. Pradier, "Rationale for individualized therapy in sinonasal teratocarcinoma (SNTC): case report," *Onkologie*, vol. 28, no. 12, pp. 653–656, 2005.
- [26] T. Morioka, T. Yamamoto, A. Mizushima et al., "Comparison of magnetoencephalography, functional MRI, and motor evoked potentials in the localization of the sensory-motor cortex," *Neurological Research*, vol. 17, no. 5, pp. 361–367, 1995.
- [27] E. M. Wassermann, B. Wang, T. A. Zeffiro et al., "Locating the motor cortex on the MRI with transcranial magnetic stimulation and PET," *NeuroImage*, vol. 3, no. 1, pp. 1–9, 1996.
- [28] Y. Terao, Y. Ugawa, K. Sakai et al., "Localizing the site of magnetic brain stimulation by functional MRI," *Experimental Brain Research*, vol. 121, no. 2, pp. 145–152, 1998.
- [29] M.-L. Paillère Martinot, A. Galinowski, D. Ringuenet et al., "Influence of prefrontal target region on the efficacy of repetitive transcranial magnetic stimulation in patients with medication-resistant depression: a [18F]-fluorodeoxyglucose PET and MRI study," *International Journal of Neuropsychopharmacology*, vol. 13, no. 1, pp. 45–59, 2010.
- [30] J. Andoh, E. Artiges, C. Pallier et al., "Modulation of language areas with functional MR image-guided magnetic stimulation," *NeuroImage*, vol. 29, no. 2, pp. 619–627, 2006.
- [31] C. Rynn, C. M. Wilkinson, and H. L. Peters, "Prediction of nasal morphology from the skull," *Forensic Science, Medicine, and Pathology*, vol. 6, no. 1, pp. 20–34, 2010.
- [32] A. S. Dubarry, J. M. Badier, A. Trébuchon-da Fonseca et al., "Simultaneous recording of MEG, EEG and intracerebral EEG during visual stimulation: from feasibility to single-trial analysis," *NeuroImage*, vol. 99, pp. 548–558, 2014.
- [33] Z.-D. Deng, S. H. Lisanby, and A. V. Peterchev, "Electric field strength and focality in electroconvulsive therapy and magnetic seizure therapy: a finite element simulation study," *Journal of Neural Engineering*, vol. 8, no. 1, Article ID 016007, 2011.
- [34] M. Bikson and A. Datta, "Guidelines for precise and accurate computational models of tDCS," *Brain Stimulation*, vol. 5, no. 3, pp. 430–431, 2012.
- [35] M. Bikson, A. Rahman, A. Datta, F. Fregni, and L. Merabet, "High-resolution modeling assisted design of customized and individualized transcranial direct current stimulation protocols," *Neuromodulation*, vol. 15, no. 4, pp. 306–314, 2012.

## Review Article

# Resting-State fMRI in MS: General Concepts and Brief Overview of Its Application

Emilia Sbardella,<sup>1</sup> Nikolaos Petsas,<sup>1</sup> Francesca Tona,<sup>1</sup> and Patrizia Pantano<sup>1,2</sup>

<sup>1</sup>Department of Neurology and Psychiatry, Sapienza University of Rome, Viale dell'Università 30, 00185 Rome, Italy

<sup>2</sup>IRCSS Neuromed, Via Atinense 18, 86077 Pozzilli, Italy

Correspondence should be addressed to Emilia Sbardella; [emilia.sbardella@gmail.com](mailto:emilia.sbardella@gmail.com)

Received 10 September 2014; Revised 15 January 2015; Accepted 28 January 2015

Academic Editor: Trevor Andrews

Copyright © 2015 Emilia Sbardella et al. This is an open access article distributed under the Creative Commons Attribution License, which permits unrestricted use, distribution, and reproduction in any medium, provided the original work is properly cited.

Brain functional connectivity (FC) is defined as the coherence in the activity between cerebral areas under a task or in the resting-state (RS). By applying functional magnetic resonance imaging (fMRI), RS FC shows several patterns which define RS brain networks (RSNs) involved in specific functions, because brain function is known to depend not only on the activity within individual regions, but also on the functional interaction of different areas across the whole brain. Region-of-interest analysis and independent component analysis are the two most commonly applied methods for RS investigation. Multiple sclerosis (MS) is characterized by multiple lesions mainly affecting the white matter, determining both structural and functional disconnection between various areas of the central nervous system. The study of RS FC in MS is mainly aimed at understanding alterations in the intrinsic functional architecture of the brain and their role in disease progression and clinical impairment. In this paper, we will examine the results obtained by the application of RS fMRI in different multiple sclerosis (MS) phenotypes and the correlations of FC changes with clinical features in this pathology. The knowledge of RS FC changes may represent a substantial step forward in the MS research field, both for clinical and therapeutic purposes.

## 1. Introduction

Multiple Sclerosis (MS) is an inflammatory and degenerative disease of the central nervous system (CNS). It is characterized by multiple lesions mainly affecting the white matter, with consequent structural and functional disconnection between various areas of the CNS, resulting in a wide range of signs and symptoms.

Functional magnetic resonance imaging (fMRI) during the performance of various tasks has provided a large amount of data showing functional alterations in MS patients, generally interpreted as adaptive plastic changes aimed at limiting the clinical impact of the disease [1, 2]. More recently, fMRI studies during the resting-state (RS) allowed exploring the functional connectivity (FC) of the brain. This aspect is of particular interest in MS, which is considered among the disconnection syndromes [3, 4]. The study of RS FC in MS is mainly aimed at understanding alterations in the intrinsic

functional architecture of the brain and their role in disease progression and clinical impairment. RS fMRI can be used to identify anatomically separate, though functionally connected, brain regions configuring specific RS networks [5]. Unlike fMRI during task execution, RS fMRI is not influenced by task performance, which may differ from that of healthy subjects, especially in patients with clinical disability.

In this brief review we are going to explain the physiological aspects underlying brain RS FC and to describe the methodological approaches to analyze it. We will then focus on the applications of RS fMRI in various phenotypes of MS, also considering the correlations between clinical impairment and both within- and between-network FC alterations in MS. Functional changes do not necessarily represent adaptive neuroplasticity aimed at maintaining a normal function despite widespread CNS pathological involvement; in some instances they could represent an inefficient or even worsening attempt to compensate for tissue damage, that is,

maladaptive plasticity. Correlations between changes in FC and the level of clinical impairment could help to distinguish between beneficial and nonbeneficial neuroplastic changes.

Lastly, we briefly expose some of the most promising directions for further investigation of RS FC in MS.

## 2. Resting-State fMRI: Physiological Bases

Brain activity has usually been considered as a response to external and internal stimuli, though organized activity has also been demonstrated at rest. Resting-state functional magnetic resonance imaging (RS fMRI) is used to analyze functional coherence in the activity of different brain areas, that is, functional connectivity, at rest (RS FC). This technique detects spontaneous low-frequency fluctuations (approximately in the domain of 0.01–0.1 Hz) of the blood-oxygen-level-dependent (BOLD) signal [6] that are temporally coherent across anatomically separated networks (RSNs) [7] and that represent well-organized brain activity [8]. The BOLD signal, on which fMRI is based, is due to changes in the concentration of deoxygenated hemoglobin, an endogenous paramagnetic contrast agent [9], which results in a decrease in the local magnetic field that can be detected on T2-weighted Echo-Planar imaging [6]. When a brain area is activated, cerebral blood flow and velocity increase to a greater extent than O<sub>2</sub> extraction [10, 11], thereby raising the blood oxygenation level, which in turn increases the MRI signal. The BOLD signal reflects specific biological and functional events and is believed to be due to the increased neural activity caused by a combination of biological mechanisms, including effects from neurotransmitters, ions, and other metabolites [12–14]. Nevertheless, whether BOLD signal fluctuations represent changes in brain physiology that are independent of neuronal function [15–17] or reflect neuronal baseline activity [18, 19] is not yet clear. Some studies suggest that RS fluctuations are an intrinsic property of the brain since they persist across conditions such as sleep [20], anesthesia [21], and task execution [22]. On the other hand, the neuronal origin of BOLD activity is supported by studies based on a combination of fMRI and positron emission tomography (PET), which highlighted the involvement of the grey matter (GM) alone in significant voxels [23], by studies based on a combination of fMRI and electroencephalograms, which revealed a correlation between BOLD signal and cortical electrical activity [24, 25], and by studies that highlighted RSNs changes induced by neurological disease [26].

## 3. Resting-State fMRI: Methodological Approaches

To provide the best possible setting for RS studies, subjects are usually instructed to stay awake, calm, and still in the scanner, to fix a specific point or close their eyes, and to try not to think about anything. The use of a high magnetic field is usually better, since it would allow to more easily detect signal changes, which are proportional to the main magnetic field, and to separate noise frequencies from proper RSNs more effectively due to a short relaxation time [11]. The aim

of the fMRI application is to detect different RSNs and to investigate their involvement in specific functions. The two most commonly applied methods for RS investigation are the region-of-interest (ROI) analysis and the whole brain investigation, the latter consisting mainly of the independent component analysis (ICA) [27]. The ROI analysis correlates the time course of a predefined ROI with other brain voxels [7, 8], according to the detection of coherent BOLD fluctuations. However, this approach is limited by the relative arbitrariness of the ROI selection. Conversely, ICA is a data-driven, whole-brain approach [27–29], designed to separate a multivariant signal in its sub-components, thus providing a single signal from a complex of signals. ICA is used without any *a priori* hypothesis and assuming the statistical independence of the sources and the BOLD signal is decomposed into spatially and temporally distinct maps with their own time courses. Each map may be interpreted as a network of brain regions that share similar BOLD fluctuations over time. One issue that needs to be considered when detecting RSNs, using either regional or whole brain analysis, is the presence of possible artifacts related to movement and to physiological noise, that is, cardiac and respiratory cycles [5]. Nevertheless, a frequency difference has been demonstrated between RSNs and noise, with the former being characterized by fluctuations of 0.01–0.1 Hz and the latter by fluctuations of 0.3–1 Hz [5]. Given the importance of removing confounding signals to improve the quality of the data [17, 30, 31], noise signals are now commonly monitored by means of specific software that retrospectively corrects the fMRI data [32]. Similarly, other sources of regionally specific noise, such as white matter (WM) and cerebrospinal fluid (CSF) signals, should be considered and removed during the analysis [33], as the BOLD signal in these regions is more susceptible to artifact than in cortical GM [34]. Despite all the technical issues that are involved in the collection of RS BOLD data, no consensus has yet been reached on the need for a precise experimental setting [20, 35]. Nevertheless, the detection of many neuroanatomical systems whose spontaneous activity is consistent has led to the identification of specific functional RSNs [5, 8, 36]. The best known of these systems are the default mode, sensory-motor, dorsal attention, visual, executive function, auditory, lateralized frontoparietal, salience, cerebellar, and basal ganglia networks [5, 37] (see Figure 1). Recently, changes in FC metrics over time have been also demonstrated, thus giving rise to the characterization of dynamic FC [38]. Emerging literature, by using new techniques of analyses, that is, sliding-window analysis, time-frequency coherence analysis, and flexible least squares based time-varying parameter regression strategy [38, 39], suggests that dynamic FC metrics may provide existence of changes in macroscopic neural activity patterns likely related to behavioral conditions [40]. However, limitations related to analysis and interpretation remain and it is yet unclear whether dynamic FC consists of the recurrence of multiple discrete patterns or it is a simple pattern variation along time [38].

Brain function is widely known to depend not only on the activity of individual regions, but also on the functional interaction of different areas across the whole brain through the so-called connectomes [41–43]. Connectomes are axonal

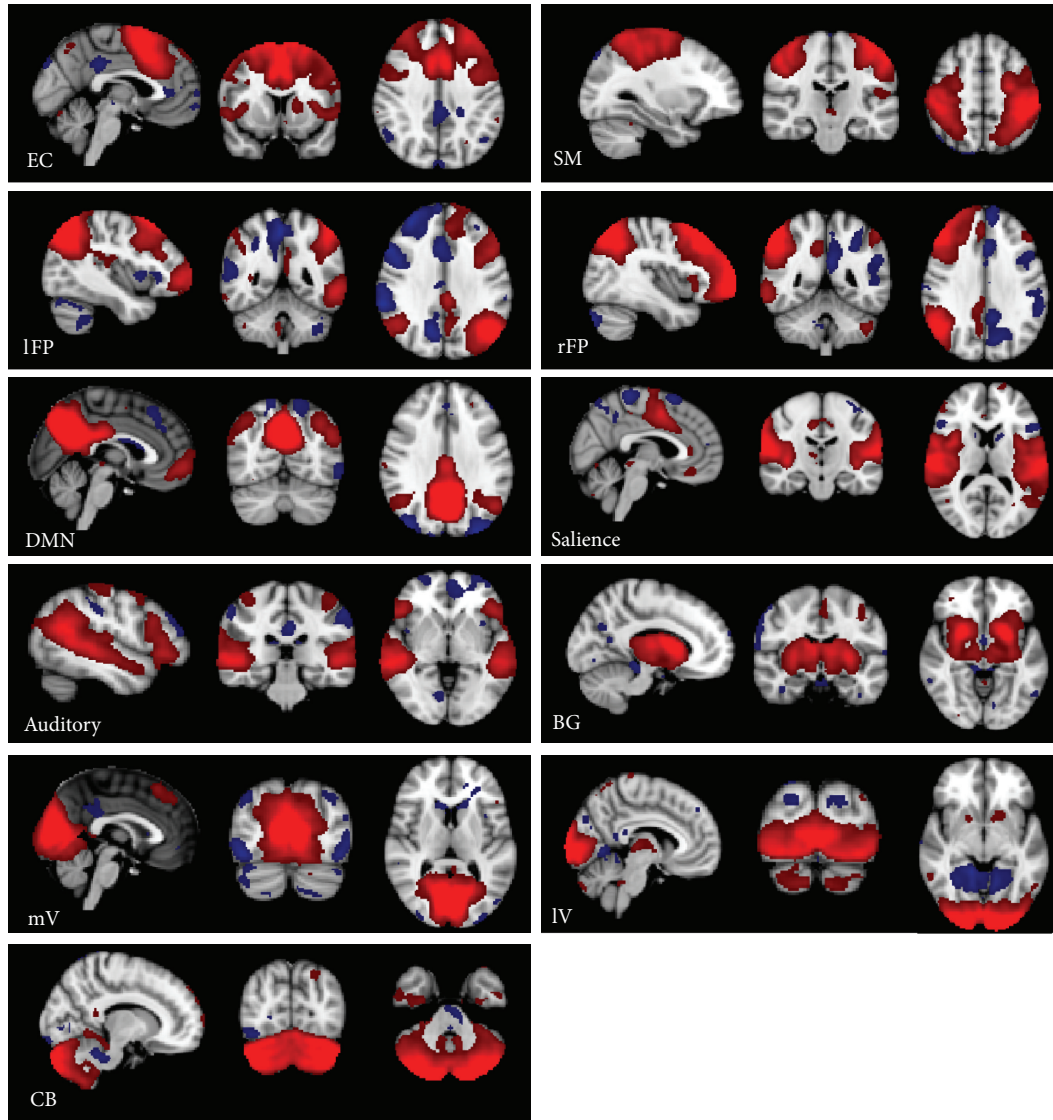


FIGURE 1: Eleven resting-state networks identified by using independent component analysis (use of MELODIC tool by FMRIB Software Library toolbox, on a cohort of 20 healthy subjects, elaboration on our data) one sample  $t$ -test, ( $P < 0.05$ , family-wise corrected). Red shows positively correlated voxels and blue shows negatively correlated voxels. fMRI results are overlaid on the MNI152, 1 mm, standard brain. Images are shown according to the radiological convention. EC: executive control; SM: sensory-motor; IFP-rFP: left and right frontoparietal; DMN: default mode network; IV: lateral visual; mV: medial visual; CB: cerebellum; BG: basal ganglia.

projections that allow functional communication between anatomically separate brain regions. Recent processing techniques enable the investigation of large-scale functional connections, thereby allowing the creation of a matrix graph of brain connectivity. Large-scale network connectivity is usually represented as a graph consisting of brain regions (nodes) that are interconnected (edges). Very briefly, after an initial definition of nodes, a matrix of functional connections between nodes is computed, though only connections higher than the setup threshold are classified as edges. Functional connectivity is provided as a statistical correlation coefficient of BOLD signal coherence between different networks [41]. The structure of a network may be designed according to

the characteristics of certain graph values, such as the clustering-coefficient, the path length, the centrality, the degree, and the modularity of a node, thereby highlighting a specific organization pattern [44]. It has been demonstrated that global brain network connectivity presents a small-world organization that is far from random, characterized by a high level of local connections between nodes and a very short path length which configure the so-called “hub” and a low presence of long connections between hubs; this network organization elevates efficiency and reduces substantially redundancy [44]. The so called “rich-club” organization has been also demonstrated, consisting in the presence of more densely connected high-order hubs [45]. The rich-club

phenomenon provides important information on the higher-order structure of a network, particularly on hierarchy and specialization [45].

Neurological pathologies may change node interactions, thereby disrupting the integration of systems and impairing their functioning.

#### 4. Resting-State fMRI: Application in Multiple Sclerosis

Advances in the comprehension of FC and the role of its alterations in the pathophysiology of human brain are given by the study of disease like MS. In fact, MS is characterized by a particularly widespread and severe damage mainly affecting the white matter that can cause FC alterations secondary to structural disconnection between RSN nodes.

RSNs abnormalities have been found in almost all multiple sclerosis (MS) phenotypes [46–57].

FC is greater in specific brain areas of many RSNs in patients with clinically isolated syndrome (CIS) than in either healthy subjects (HS) or relapsing-remitting MS (RR-MS) patients, even though GM volume and WM integrity are preserved [46]. These results suggest that the coherence of cerebral activity increases in the earliest stage of the disease, probably as a compensatory phenomenon, and is subsequently lost in the late phase of the disease as a result of structural damage progression. However, an agreement on the actual meaning of fMRI changes in early MS has not yet been reached: even if the compensatory hypothesis is still prevailing, a single study reported lower global values of temporal coherence in CIS patients [47].

Results by RS fMRI were only partially concordant when RR MS subjects were studied [46, 48–51], probably because of the wide spectrum of clinical characteristics that are peculiar to this phenotype as well as of the different methodological approaches. Widespread FC abnormalities were found in RR-MS subjects: some studies pointed to a significant increase in global connectivity levels [46, 50, 52, 53] and others reported FC decrease [49, 51]. The FC reduction is in line with results from PET and MRI perfusion studies, which have shown diffuse brain hypometabolism [58, 59] and hypoperfusion [60] in this condition, probably due to the progressive accumulation of structural damage. The FC increase instead is a more complex event; although it is generally considered as an adaptive attempt to compensate for tissue damage, any alternative hypothesis that FC increase may represent maladaptive plasticity or an epiphenomenon of the pathological process cannot be completely ruled out [46, 48, 51, 54, 61, 62]. Lastly, some studies found that specific networks, that is, the thalamic RSN and DMN, may show both significantly weaker connections with some brain regions and stronger connections with others, thus suggesting that there is a redistribution of connectivity, besides a general trend of globally increased or decreased FC in MS [51, 55].

Only few studies focused on progressive MS phenotypes [56, 57]. In a recent work that explored FC alteration in RR and secondary progressive (SP) MS, authors found an increased FC in both groups of patients; however, specific

changes in either direction were observed also between RR and SP MS groups. Interestingly, these FC changes seem to parallel patients' clinical state and capability of compensating for the severity of clinical/cognitive disabilities, supporting the compensatory role of functional reorganization [56].

In a study including patients with primary progressive (PP) and SP MS patients, compared to HS, FC was found to be decreased in some areas of the DMN in both groups of patients; FC in the anterior components of the DMN was correlated with cognitive impairment. When patients with SP and PP MS were compared, a higher FC in the anterior cingulate cortex was found in SP [57].

Taken together these results show that there is not a straightforward relationship between RSNs changes and clinical phenotype, suggesting a decisive role of specific clinical and genetic characteristics of single subjects in determining the functional response to the disease.

#### 5. fMRI Functional Connectivity Changes and Their Correlation with Clinical Disability

*5.1. Within-Network Connectivity.* Correlations of within-network FC changes with clinical MS parameters have been widely reported in MS [46, 49, 50, 52, 57–59, 63]. Although the ability of RS fMRI to detect brain functional reorganization in MS has been proved, the role of FC alterations in the pathogenesis of MS, as well as the potential relationship between resting-state network reorganization and clinical disability, remains not completely understood.

A negative correlation between FC strength and clinical impairment has been repeatedly reported [46, 49, 50, 58, 59, 63]; few studies reported a positive correlation between FC strength and clinical impairment [52, 57]. Discordant results between studies may be due not only to differences in patient populations and data analysis, but also to the clinical function considered and the specific RSNs analyzed.

Regarding the correlations between the motor network and clinical disability, a recent work revealed an association between reduced intranetwork connectivity in the motor network and higher levels of disease severity in patients with RR MS, thus pointing to the possibility that resting-state changes may serve as a biomarker of disease progression [64]. On the other hand, increased connectivity in the left premotor area was found to be associated with greater clinical disability in RR MS though not in SP MS [52]. This finding suggests that even if disease progression is related to disrupted FC within the motor network, increased FC in specific motor areas may represent an attempt to compensate for the functional impairment, at least in RR MS.

Regarding correlations between FC alterations and cognitive performance, which results from the interaction of several complex brain functions involved in cognition, that is, working memory, attention, and executive function, the interpretation of results is more complex. Increased [65, 66], decreased [50, 57], and both increased and decreased [55] FC within sustained attention networks were found to be associated with cognitive performance in MS. FC decrease in the anterior components of the DMN was found to correlate

with accumulation of cognitive deficits in patients with progressive MS [57]. Bonavita et al. [55] confirmed the anterior dysfunction of the DMN also in RR MS; moreover, they found that patients with RR MS also showed an increased FC in the posterior components of the DMN, which was more pronounced in cognitively preserved patients. A recent study on heterogeneous group of MS has shown that decreased cognitive performance is accompanied by reduced FC in all main RSNs and is also directly related to brain damage [67]. On the other hand, another study on RR MS, focused on the thalamic RSN, reported a decreased performance associated with increased FC, suggesting that neuroplastic changes are unable to fully compensate for cognitive dysfunction [51].

Taken together, these results demonstrate that RSN reorganization is closely associated with cognitive disability in MS. On the basis of this strong association, FC changes have been proposed as promising surrogate markers of disease burden [50] as well as useful tools to monitor rehabilitative strategies in MS. Indeed, cognitive rehabilitation has been shown to correlate with changes in the RS FC of brain regions subserving trained functions [68].

**5.2. Large-Scale Network Connectivity.** Studies of large-scale network connectivity have been applied in MS with the attempt to give a global view of distributed patterns of FC abnormalities also in relationship with structural damage and disability.

Abnormalities in the FC of large-scale networks have been demonstrated in MS patients, with the disconnection appearing to be proportional to the extent of the lesions and correlated with the severity of disability [69, 70]. The involvement of RSN disconnection in MS is widespread and includes motor, sensitive, visual, and cognitive network function abnormalities [41]. FC is usually decreased in the whole brain. For example, decreased FC in subcortical and cortical regions and contralateral connections has been shown to be related to lesion load and to be able to discriminate MS patients from controls with a sensitivity of 82% and specificity of 86% [63]. Furthermore, FC in attentional networks is stronger in cognitively preserved patients than in cognitively impaired patients and is correlated with lower structural damage [71]. Reduced functional integration between separate areas was also found in the early stages of MS [61]. These findings suggest that functional disconnection parallels both structural damage and clinical impairment.

By contrast, a higher degree of connectivity between RSNs associated with visual functions is correlated with higher disease burden in spite of reduced within-network connectivity in other areas [64]. This finding may be interpreted as a focused event within a framework of global reorganization of brain FC over the course of the disease. This hypothesis is supported by the finding of a widespread modularity redistribution in MS, with some RSNs displaying decreased connectivity, due in part also to lesion load and clinical impairment, and others displaying increased connectivity [72].

The large-scale connectivity analysis, when applied in patients in comparison to controls, may highlight the differences in the whole brain network functional organization

between the two groups. Accordingly, large-scale FC has been proposed as a promising tool to discriminate MS subjects from HS, to understand the functional substrate of clinical disability, and to monitor the effects of therapies. However, further studies are needed to clarify the proper meaning of these changes and whether functional modifications limit the clinical impact of the disease or, conversely, are a biomarker of disease severity.

## 6. Discussion and Future Directions

fMRI technique allows to detect brain functional connectivity across the brain. Its application in neurological pathologies, that is, MS, may provide valuable information on the neuronal changes occurring after damage, thus helping to understand the pathophysiology of the disease and the possible therapeutic approaches. Widespread connectivity abnormalities are evident both within and between RSNs in MS patients, but, unfortunately, results are not always concordant and the meaning of fMRI changes in MS is not completely clear. Additionally, RS fMRI studies are limited by the interference of noise artifacts, such as respiratory or cardiac events, which may be partially responsible of these incongruences and may also explain, at least in part, discordant fMRI results in similar MS phenotypes across different studies [5, 30, 31]. Another issue that can affect the homogeneity of the results may be ascribed to the differences among patients, that is, in terms of disease duration, within the same cohort, or between cohorts with similar disease phenotype. This problem may also influence the correlations between FC results and behavioral measures, since they do not always show the same directions. Accordingly, the significance of fMRI alterations in neurological pathology, in terms of compensatory or maladaptive mechanisms, has yet to be clarified. Despite some discrepant results, an increased FC in RSNs has been repeatedly reported and interpreted as adaptive brain reorganization; this hypothesis is supported by the fact that increased RS connectivity in MS patients usually occurs in brain areas with extensive cortical connections [53]. However, this adaptive phenomenon may be a finite process that is present in the early stages of the disease but is lost in more advanced stages, when the structural damage and the clinical impairment are too severe to be compensated for. Indeed, the increase in functional coupling between some areas of the motor network that parallels the increasing disability appears to be limited to the RR stage of the disease and is lost in the more advanced stages [52]; similarly, FC in some regions of the DMN is higher in cognitively preserved than in cognitively affected RRMS patients [55, 71].

The RS dynamics characterization [38], the graph theoretical analysis to study brain network properties [45], and the integration of RS fMRI data with other techniques, that is, transcranial magnetic stimulation and PET, could provide in the next future new insight into the pathophysiology of MS for clinical and therapeutical purposes.

## Conflict of Interests

The authors declare that there is no conflict of interests regarding the publication of this paper.

## References

- [1] P. Pantano, C. Mainero, and F. Caramia, "Functional brain reorganization in multiple sclerosis: evidence from fMRI studies," *Journal of Neuroimaging*, vol. 16, no. 2, pp. 104–114, 2006.
- [2] M. Filippi and M. A. Rocca, "Present and future of fMRI in multiple sclerosis," *Expert Review of Neurotherapeutics*, vol. 13, no. 12, pp. 27–31, 2013.
- [3] P. Calabrese and I. K. Penner, "Cognitive dysfunctions in multiple sclerosis—a 'multiple disconnection syndrome'?" *Journal of Neurology*, vol. 254, no. 2, supplement, pp. II18–II21, 2007.
- [4] R. A. Dineen, J. Vilisaar, J. Hlinka et al., "Disconnection as a mechanism for cognitive dysfunction in multiple sclerosis," *Brain*, vol. 132, no. 1, pp. 239–249, 2009.
- [5] C. F. Beckmann, M. DeLuca, J. T. Devlin, and S. M. Smith, "Investigations into resting-state connectivity using independent component analysis," *Philosophical Transactions of the Royal Society B: Biological Sciences*, vol. 360, no. 1457, pp. 1001–1013, 2005.
- [6] S. Ogawa and T.-M. Lee, "Magnetic resonance imaging of blood vessels at high fields: in vivo and in vitro measurements and image simulation," *Magnetic Resonance in Medicine*, vol. 16, no. 1, pp. 9–18, 1990.
- [7] M. D. Fox and M. E. Raichle, "Spontaneous fluctuations in brain activity observed with functional magnetic resonance imaging," *Nature Reviews Neuroscience*, vol. 8, no. 9, pp. 700–711, 2007.
- [8] B. Biswal, F. Z. Yetkin, V. M. Haughton, and J. S. Hyde, "Functional connectivity in the motor cortex of resting human brain using echo-planar MRI," *Magnetic Resonance in Medicine*, vol. 34, no. 4, pp. 537–541, 1995.
- [9] L. Pauling and C. D. Coryell, "The magnetic properties and structure of hemoglobin, oxyhemoglobin and carbonmonoxy-hemoglobin," *Proceedings of the National Academy of Sciences*, vol. 22, no. 4, pp. 210–216, 1936.
- [10] P. T. Fox and M. E. Raichle, "Focal physiological uncoupling of cerebral blood flow and oxidative metabolism during somatosensory stimulation in human subjects," *Proceedings of the National Academy of Sciences of the United States of America*, vol. 83, no. 4, pp. 1140–1144, 1986.
- [11] R. B. Buxton, *Introduction to Functional Magnetic Resonance Imaging*. Cambridge University Press, Cambridge, UK, 2009.
- [12] D. Attwell and C. Iadecola, "The neural basis of functional brain imaging signals," *Trends in Neurosciences*, vol. 25, no. 12, pp. 621–625, 2002.
- [13] M. Lauritzen, "Reading vascular changes in brain imaging: is dendritic calcium the key?" *Nature Reviews Neuroscience*, vol. 6, no. 1, pp. 77–85, 2005.
- [14] K. Uludağ, D. J. Dubowitz, E. J. Yoder, K. Restom, T. T. Liu, and R. B. Buxton, "Coupling of cerebral blood flow and oxygen consumption during physiological activation and deactivation measured with fMRI," *NeuroImage*, vol. 23, no. 1, pp. 148–155, 2004.
- [15] H. Obrig, M. Neufang, R. Wenzel et al., "Spontaneous low frequency oscillations of cerebral hemodynamics and metabolism in human adults," *NeuroImage*, vol. 12, no. 6, pp. 623–639, 2000.
- [16] R. G. Wise, K. Ide, M. J. Poulin, and I. Tracey, "Resting fluctuations in arterial carbon dioxide induce significant low frequency variations in BOLD signal," *NeuroImage*, vol. 21, no. 4, pp. 1652–1664, 2004.
- [17] R. M. Birn, J. B. Diamond, M. A. Smith, and P. A. Bandettini, "Separating respiratory-variation-related fluctuations from neuronal-activity-related fluctuations in fMRI," *NeuroImage*, vol. 31, no. 4, pp. 1536–1548, 2006.
- [18] D. A. Gusnard, E. Akbudak, G. L. Shulman, and M. E. Raichle, "Medial prefrontal cortex and self-referential mental activity: relation to a default mode of brain function," *Proceedings of the National Academy of Sciences of the United States of America*, vol. 98, no. 7, pp. 4259–4264, 2001.
- [19] S. J. Peltier and D. C. Noll, " $T_2^*$  dependence of low frequency functional connectivity," *NeuroImage*, vol. 16, no. 4, pp. 985–992, 2002.
- [20] S. G. Horowitz, M. Fukunaga, J. A. De Zwart et al., "Low frequency BOLD fluctuations during resting wakefulness and light sleep: a simultaneous EEG-fMRI study," *Human Brain Mapping*, vol. 29, no. 6, pp. 671–682, 2008.
- [21] S. J. Peltier, C. Keressens, S. B. Hamann, P. S. Sebel, M. Byas-Smith, and X. Hu, "Functional connectivity changes with concentration of sevoflurane anesthesia," *NeuroReport*, vol. 16, no. 3, pp. 285–288, 2005.
- [22] M. D. Greicius and V. Menon, "Default-mode activity during a passive sensory task: uncoupled from deactivation but impacting activation," *Journal of Cognitive Neuroscience*, vol. 16, no. 9, pp. 1484–1492, 2004.
- [23] G. L. Shulman, M. Corbetta, R. L. Buckner et al., "Common blood flow changes across visual tasks: I. Increases in subcortical structures and cerebellum but not in nonvisual cortex," *Journal of Cognitive Neuroscience*, vol. 9, no. 5, pp. 624–647, 1997.
- [24] R. I. Goldman, J. M. Stern, J. Engel Jr., and M. S. Cohen, "Simultaneous EEG and fMRI of the alpha rhythm," *NeuroReport*, vol. 13, no. 18, pp. 2487–2492, 2002.
- [25] E. Martínez-Montes, P. A. Valdés-Sosa, F. Miwakeichi, R. I. Goldman, and M. S. Cohen, "Concurrent EEG/fMRI analysis by multiway Partial Least Squares," *NeuroImage*, vol. 22, no. 3, pp. 1023–1034, 2004.
- [26] M. D. Greicius, G. Srivastava, A. L. Reiss, and V. Menon, "Default-mode network activity distinguishes Alzheimer's disease from healthy aging: evidence from functional MRI," *Proceedings of the National Academy of Sciences of the United States of America*, vol. 101, no. 13, pp. 4637–4642, 2004.
- [27] R. Sacco, S. Bonavita, F. Esposito, G. Tedeschi, and A. Gallo, "The contribution of resting state networks to the study of cortical reorganization in MS," *Multiple Sclerosis International*, vol. 2013, Article ID 857807, 7 pages, 2013.
- [28] A. J. Bell and T. J. Sejnowski, "The 'independent components' of natural scenes are edge filters," *Vision Research*, vol. 37, no. 23, pp. 3327–3338, 1997.
- [29] M. J. McKeown, S. Makeig, G. G. Brown et al., "Analysis of fMRI data by blind separation into independent spatial components," *Human Brain Mapping*, vol. 6, no. 3, pp. 160–188, 1998.
- [30] R. M. Birn, K. Murphy, and P. A. Bandettini, "The effect of respiration variations on independent component analysis results of resting state functional connectivity," *Human Brain Mapping*, vol. 29, no. 7, pp. 740–750, 2008.
- [31] K. R. A. van Dijk, T. Hedden, A. Venkataraman, K. C. Evans, S. W. Lazar, and R. L. Buckner, "Intrinsic functional connectivity as a tool for human connectomics: theory, properties, and optimization," *Journal of Neurophysiology*, vol. 103, no. 1, pp. 297–321, 2010.

- [32] G. H. Glover, T. Q. Li, and D. Ress, "Image-based method for retrospective correction of physiological motion effects in fMRI: RETROICOR," *Magnetic Resonance in Medicine*, vol. 44, no. 1, pp. 162–167, 2000.
- [33] M. D. Fox, A. Z. Snyder, J. L. Vincent, M. Corbetta, D. C. van Essen, and M. E. Raichle, "The human brain is intrinsically organized into dynamic, anticorrelated functional networks," *Proceedings of the National Academy of Sciences of the United States of America*, vol. 102, no. 27, pp. 9673–9678, 2005.
- [34] J. Tohka, K. Foerde, A. R. Aron, S. M. Tom, A. W. Toga, and R. A. Poldrack, "Automatic independent component labeling for artifact removal in fMRI," *NeuroImage*, vol. 39, no. 3, pp. 1227–1245, 2008.
- [35] M. Bianciardi, M. Fukunaga, P. van Gelderen et al., "Sources of functional magnetic resonance imaging signal fluctuations in the human brain at rest: a 7 T study," *Magnetic Resonance Imaging*, vol. 27, no. 8, pp. 1019–1029, 2009.
- [36] J. S. Damoiseaux, S. A. R. B. Rombouts, F. Barkhof et al., "Consistent resting-state networks across healthy subjects," *Proceedings of the National Academy of Sciences of the United States of America*, vol. 103, no. 37, pp. 13848–13853, 2006.
- [37] S. M. Smith, P. T. Fox, K. L. Miller et al., "Correspondence of the brain's functional architecture during activation and rest," *Proceedings of the National Academy of Sciences of the United States of America*, vol. 106, no. 31, pp. 13040–13045, 2009.
- [38] R. M. Hutchison, T. Womelsdorf, E. A. Allen et al., "Dynamic functional connectivity: promise, issues, and interpretations," *NeuroImage*, vol. 80, pp. 360–378, 2013.
- [39] W. Liao, G.-R. Wu, Q. Xu et al., "DynamicBC: a MATLAB toolbox for dynamic brain connectome analysis," *Brain Connectivity*, vol. 4, no. 10, pp. 780–790, 2014.
- [40] W. Liao, Z. Zhang, D. Mantini et al., "Dynamical intrinsic functional architecture of the brain during absence seizures," *Brain Structure and Function*, vol. 219, no. 6, pp. 2001–2015, 2014.
- [41] M. Filippi, M. P. van den Heuvel, A. Fornito et al., "Assessment of system dysfunction in the brain through MRI-based connectomics," *The Lancet Neurology*, vol. 12, no. 12, pp. 1189–1199, 2013.
- [42] O. Sporns, "Structure and function of complex brain networks," *Dialogues in Clinical Neuroscience*, vol. 15, no. 3, pp. 247–262, 2013.
- [43] O. Sporns and J. D. Zwi, "The small world of the cerebral cortex," *Neuroinformatics*, vol. 2, no. 2, pp. 145–162, 2004.
- [44] M. P. van den Heuvel and H. E. Hulshoff Pol, "Exploring the brain network: a review on resting-state fMRI functional connectivity," *European Neuropsychopharmacology*, vol. 20, no. 8, pp. 519–534, 2010.
- [45] M. P. van den Heuvel and O. Sporns, "Rich-club organization of the human connectome," *The Journal of Neuroscience*, vol. 31, no. 44, pp. 15775–15786, 2011.
- [46] S. D. Roosendaal, M. M. Schoonheim, H. E. Hulst et al., "Resting state networks change in clinically isolated syndrome," *Brain*, vol. 133, part 6, pp. 1612–1621, 2010.
- [47] Y. Liu, Y. Duan, P. Liang et al., "Baseline brain activity changes in patients with clinically isolated syndrome revealed by resting-state functional MRI," *Acta Radiologica*, vol. 53, no. 9, pp. 1073–1078, 2012.
- [48] D. J. Hawellek, J. F. Hipp, C. M. Lewis, M. Corbetta, and A. K. Engel, "Increased functional connectivity indicates the severity of cognitive impairment in multiple sclerosis," *Proceedings of the National Academy of Sciences of the United States of America*, vol. 108, no. 47, pp. 19066–19071, 2011.
- [49] M. A. Rocca, P. Valsasina, V. Martinelli et al., "Large-scale neuronal network dysfunction in relapsing-remitting multiple sclerosis," *Neurology*, vol. 79, no. 14, pp. 1449–1457, 2012.
- [50] A. Faivre, A. Rico, W. Zaaraoui et al., "Assessing brain connectivity at rest is clinically relevant in early multiple sclerosis," *Multiple Sclerosis*, vol. 18, no. 9, pp. 1251–1258, 2012.
- [51] F. Tona, N. Petsas, E. Sbardella et al., "Multiple sclerosis: altered thalamic resting-state functional connectivity and its effect on cognitive function," *Radiology*, vol. 271, no. 3, pp. 814–821, 2014.
- [52] A.-M. Dogonowski, H. R. Siebner, P. Soelberg Sørensen et al., "Resting-state connectivity of pre-motor cortex reflects disability in multiple sclerosis," *Acta Neurologica Scandinavica*, vol. 128, no. 5, pp. 328–335, 2013.
- [53] Y. Liu, P. Liang, Y. Duan et al., "Brain plasticity in relapsing-remitting multiple sclerosis: evidence from resting-state fMRI," *Journal of the Neurological Sciences*, vol. 304, no. 1-2, pp. 127–131, 2011.
- [54] M. Filippi, F. Agosta, E. G. Spinelli, and M. A. Rocca, "Imaging resting state brain function in multiple sclerosis," *Journal of Neurology*, vol. 260, no. 7, pp. 1709–1713, 2013.
- [55] S. Bonavita, A. Gallo, R. Sacco et al., "Distributed changes in default-mode resting-state connectivity in multiple sclerosis," *Multiple Sclerosis*, vol. 17, no. 4, pp. 411–422, 2011.
- [56] B. Basile, M. Castelli, F. Monteleone et al., "Functional connectivity changes within specific networks parallel the clinical evolution of multiple sclerosis," *Multiple Sclerosis Journal*, vol. 20, no. 8, pp. 1050–1057, 2014.
- [57] M. A. Rocca, P. Valsasina, M. Absinta et al., "Default-mode network dysfunction and cognitive impairment in progressive MS," *Neurology*, vol. 74, no. 16, pp. 1252–1259, 2010.
- [58] R. Bakshi, R. S. Miletrch, P. R. Kinkel, M. L. Emmet, and W. R. Kinkel, "High-resolution fluorodeoxyglucose positron emission tomography shows both global and regional cerebral hypometabolism in multiple sclerosis," *Journal of Neuroimaging*, vol. 8, no. 4, pp. 228–234, 1998.
- [59] E. Paulesu, D. Perani, F. Fazio et al., "Functional basis of memory impairment in multiple sclerosis: a [18F]FDG PET Study," *NeuroImage*, vol. 4, no. 2, pp. 87–96, 1996.
- [60] J. de Keyser, C. Steen, J. P. Mostert, and M. W. Koch, "Hypoperfusion of the cerebral white matter in multiple sclerosis: possible mechanisms and pathophysiological significance," *Journal of Cerebral Blood Flow and Metabolism*, vol. 28, no. 10, pp. 1645–1651, 2008.
- [61] O. L. Gamboa, E. Tagliazucchi, F. von Wegner et al., "Working memory performance of early MS patients correlates inversely with modularity increases in resting state functional connectivity networks," *NeuroImage*, vol. 94, pp. 385–395, 2014.
- [62] A.-M. Dogonowski, H. R. Siebner, P. S. Sørensen et al., "Expanded functional coupling of subcortical nuclei with the motor resting-state network in multiple sclerosis," *Multiple Sclerosis (Houndmills, Basingstoke, England)*, vol. 19, no. 5, pp. 559–566, 2013.
- [63] J. Richiardi, M. Gschwind, S. Simioni et al., "Classifying minimally disabled multiple sclerosis patients from resting state functional connectivity," *NeuroImage*, vol. 62, no. 3, pp. 2021–2033, 2012.
- [64] A. L. Janssen, A. Boster, B. A. Patterson, A. Abduljalil, and R. S. Prakash, "Resting-state functional connectivity in multiple sclerosis: an examination of group differences and individual differences," *Neuropsychologia*, vol. 51, no. 13, pp. 2918–2929, 2013.

- [65] M. Loitfelder, M. Filippi, M. Rocca et al., “Abnormalities of resting state functional connectivity are related to sustained attention deficits in MS,” *PLoS ONE*, vol. 7, no. 8, Article ID e42862, 2012.
- [66] M. Wojtowicz, E. L. Mazerolle, V. Bhan, and J. D. Fisk, “Altered functional connectivity and performance variability in relapsing-remitting multiple sclerosis,” *Multiple Sclerosis Journal*, vol. 20, no. 11, pp. 1453–1463, 2014.
- [67] Á. J. Cruz-Gómez, N. Ventura-Campos, A. Belenguer, C. Ávila, and C. Forn, “The link between resting-state functional connectivity and cognition in MS patients,” *Multiple Sclerosis Journal*, vol. 20, no. 3, pp. 338–348, 2014.
- [68] L. Parisi, M. A. Rocca, P. Valsasina, L. Panicari, F. Mattioli, and M. Filippi, “Cognitive rehabilitation correlates with the functional connectivity of the anterior cingulate cortex in patients with multiple sclerosis,” *Brain Imaging and Behavior*, vol. 8, no. 3, pp. 387–393, 2014.
- [69] Y. He, A. Dagher, Z. Chen et al., “Impaired small-world efficiency in structural cortical networks in multiple sclerosis associated with white matter lesion load,” *Brain*, vol. 132, no. 12, pp. 3366–3379, 2009.
- [70] M. A. Rocca, P. Valsasina, A. Meani, A. Falini, G. Comi, and M. Filippi, “Impaired functional integration in multiple sclerosis: a graph theory study,” *Brain Structure and Function*, pp. 1–17, 2014.
- [71] C. Louapre, V. Perlberg, D. García-Lorenzo et al., “Brain networks disconnection in early multiple sclerosis cognitive deficits: an anatomofunctional study,” *Human Brain Mapping*, vol. 35, no. 9, pp. 4706–4717, 2014.
- [72] M. Schoonheim, J. Geurts, O. Wiebenga et al., “Changes in functional network centrality underlie cognitive dysfunction and physical disability in multiple sclerosis,” *Multiple Sclerosis Journal*, vol. 20, no. 8, pp. 1058–1065, 2014.

## Research Article

# Evaluation of the Contribution of Signals Originating from Large Blood Vessels to Signals of Functionally Specific Brain Areas

Jun-Young Chung,<sup>1,2</sup> Yul-Wan Sung,<sup>2,3</sup> and Seiji Ogawa<sup>2,3</sup>

<sup>1</sup>Department of Biomedical Engineering, College of Health Sciences, Gachon University, 191 Hambakmoero, Yeonsu-gu, Incheon 406-799, Republic of Korea

<sup>2</sup>Neuroscience Research Institute, Gachon University, 774 Namdong-daero, Namdong-gu, Incheon 405-835, Republic of Korea

<sup>3</sup>Kansei Fukushi Research Institute, Tohoku Fukushi University, 6-149-1 Kunimigaoka, Aoba, Sendai 989-3201, Japan

Correspondence should be addressed to Yul-Wan Sung; [sung@tfu-mail.tfu.ac.jp](mailto:sung@tfu-mail.tfu.ac.jp)

Received 14 July 2014; Revised 5 September 2014; Accepted 19 September 2014

Academic Editor: Zhengchao Dong

Copyright © 2015 Jun-Young Chung et al. This is an open access article distributed under the Creative Commons Attribution License, which permits unrestricted use, distribution, and reproduction in any medium, provided the original work is properly cited.

The fusiform face area (FFA) is known to play a pivotal role in face processing. The FFA is located in the ventral region, at the base of the brain, through which large blood vessels run. The location of the FFA via functional MRI (fMRI) may be influenced by these large blood vessels. Responses of large blood vessels may not exactly correspond to neuronal activity in a target area, because they may be diluted and influenced by inflow effects. In this study, we investigated the effects of large blood vessels in the FFA, that is, whether the FFA includes large blood vessels and/or whether inflow signals contribute to fMRI signals of the FFA. For this purpose, we used susceptibility-weighted imaging (SWI) sequences to visualize large blood vessels and dual-echo gradient-echo echo-planar imaging (GE-EPI) to measure inflow effects. These results showed that the location and response signals of the FFA were not influenced by large blood vessels or inflow effects, although large blood vessels were located near the FFA. Therefore, the data from the FFA obtained by individual analysis were robust to large blood vessels but leaving a warning that the data obtained by group analysis may be prone to large blood vessels.

## 1. Introduction

Brain imaging via functional MRI is used to identify the functional sites that play specific roles in information processing in the brain. For an identified functional site, we expect that the site is as specific as possible to a function without exhibiting an overlap with other functional sites.

In BOLD imaging, on which most fMRI studies are based, the paramagnetic property of blood produces a bulk susceptibility difference between a blood vessel and the surrounding brain tissue, thus producing resonance frequency shifts in extravessel molecules. Thus, signals from oxygenation modulation can be expected in the tissues and for some distance into the venous side of the capillary bed [1]. This is, in itself, a short-range phenomenon located within a few tens of microns.

However, two factors make an undesirable contribution to BOLD-based fMRI signals, leading to an exaggeration of the spatial specificity and signal amplitude compared with those expected. One factor is the propagation of the bolus of oxygen-enriched blood by neuronal activation to the larger draining venous structures, which leads to the appearance of BOLD contrast in remote regions downstream of the actual site of neuronal activation [1, 2]. Another factor is the inflow effect. Neuronal activation alters vascular physiology, leading to increased flow both in the resistance pial arteries that feed the activated capillary beds and in the venules that drain these beds. MRI signals are inherently sensitive to inflowing fully magnetized spins; therefore, hemodynamic changes, particularly in larger blood vessels, can create signal fluctuations that are coincident with neuronal activation due to the inflow effect [3, 4].

Face recognition is important for social communication. The fusiform face area (FFA) is known to play a pivotal role in face processing [5, 6]. The measurement of responses of the FFA can provide crucial information regarding face recognition. The FFA is located in the ventral region [5, 6], at the base of the brain, through which large vessels, such as the inferior temporooccipital vein, middle temporal vein, vein of Labbé, middle temporo-basal vein, and posterior temporo-basal vein, run. The location of the FFA via fMRI varies across subjects, although the average location is almost invariant across groups of subjects. If the variation in location is dependent on large blood vessels, then the signal of the FFA can be under- or overestimated. However, this issue has not been examined. Although other functional sites also rely on individual brain structures and show variation in their location, the FFA is a special area in that it is surrounded by many large blood vessels.

In this study, we investigated the effects of large blood vessels in the FFA, that is, whether the FFA includes large blood vessels and/or whether inflow signals contribute to fMRI signals of the FFA. For this purpose, we used susceptibility-weighted imaging (SWI) sequences to visualize large blood vessels [7, 8] and dual-echo gradient-echo echo-planar imaging (GE-EPI) sequences to measure inflow signals [9, 10].

## 2. Materials and Methods

**2.1. Subjects.** Ten healthy volunteers participated in this study. After subjects were given a complete description of the study, written informed consent was obtained. This study was approved by the Institutional Review Board of Tohoku Fukushi University.

**2.2. Measurements.** All MRI experiments were performed using a Verio system (Siemens, Germany) with a standard 12-channel head matrix coil operating at 3 Tesla.

**2.2.1. Dual-Echo EPI.** The dual-echo EPI sequence was modified from the default single-shot GE-EPI of the Siemens apparatus to acquire images at the two echo times of 13 and 38 ms, which were determined as the shortest echo times possible. For functional imaging, the dual-echo GE-EPI sequence was used with a 2000 ms repetition time (TR), 90° flip angle (FA), 220 mm field of view (FOV), 64 × 64 mm matrix size, and 3.4 mm slice thickness with 0.5 mm gaps. Twenty slices parallel to the AC-PC were acquired for each volume.

**2.2.2. SWI Imaging.** An SWI 3D sequence was used with the parameters of TR of 28 ms, TE of 20 ms, FA of 15°, 294 × 320 matrix size, 220 mm FOV, and 1.13 mm thickness with 0.23 mm gaps. The orientation and center of slice positions were the same as those used in EPI. SWI image processing was performed using the Siemens default program.

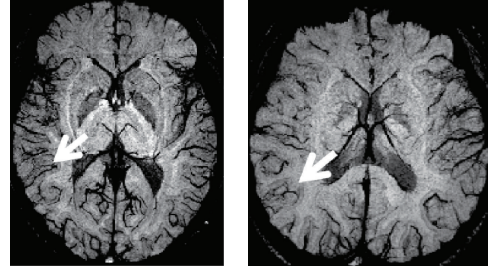


FIGURE 1: SWI-MIP images (across eight slices in sliding window mode). Image slices were from two subjects. The dark lines in the slices represent large blood vessels. The white arrows indicate some of the large blood vessels.

**2.3. Derivation of an Image for Inflow Effects.** The MRI signal evolution is, after a single RF excitation, as follows [3, 11]:

$$S(TE) = S_0(T_1) \cdot \exp\left(-\frac{TE}{T_2^*}\right), \quad (1)$$

where  $S_0$  is the initial intensity, which is dependent on the  $T_1$  of a voxel and is responsible for inflow effects;  $TE$  is the effective echo time; and  $T_2^*$  is the apparent transverse relaxation time. As reported in a previous study  $S_0$  is calculated directly using the MRI signals  $S(TE_1)$  and  $S(TE_2)$  corresponding to  $TE_1$  and  $TE_2$ . The equation that yields  $S_0$  for the corresponding voxel is as follows [4]:

$$S_0 = \exp\left[\frac{\{\log(S(TE_1)) - (TE_1/TE_2) \log(S(TE_2))\}}{(1 - TE_1/TE_2)}\right]. \quad (2)$$

**2.4. Stimulation Procedure.** Visual stimuli were images presented in the center of the visual field. An experimental run consisted of 12 event blocks of four stimulation conditions, three blocks of single stimulation for face images (SF) and scene images (SS), and three paired stimulations for face images (PF) and scene images (PS). The SF, SS, PF, and PS condition blocks were randomized at intrasubject and inter-subject levels. Single stimulation blocks (SF and SS) consisted of eight different face or scene images that were presented for 50 ms, with a 1.5-s repetition period interspersed with the control state. The paired stimulation blocks (PF and PS) consisted of eight pairs of faces or scenes, with a 1.5-s repetition period between pairs and a 150 ms interstimulus interval.

**2.5. Visual Stimulation.** Visual stimuli were grayscale images presented using a projector and displayed on a mirror mounted on the head coil (spatial resolution, 1024 × 768 pixels; refresh rate, 60 Hz; Panasonic, Japan). The images occupied 3.5° × 4°, and the crosshair occupied 0.34° × 0.34°.

**2.6. Imaging Data Analysis.** The imaging data acquired from the functional session were preprocessed using BrainVoyager QX (Brain Innovation B.V., Postbus, The Netherlands) for motion correction, scan time correction, and high-pass filtering, with a cutoff frequency of 0.005 Hz. In each functional

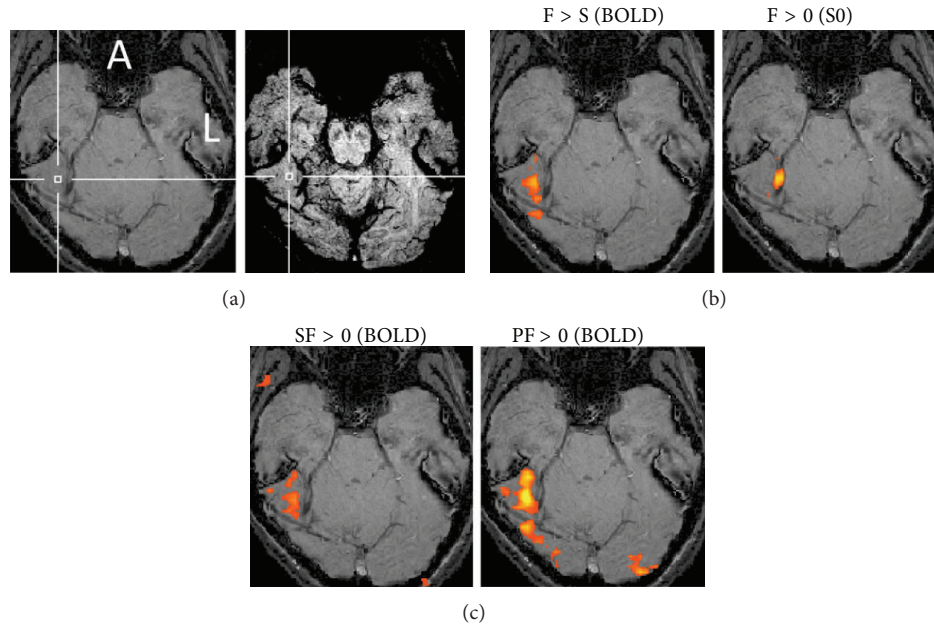


FIGURE 2: SWI images and activation maps for one subject in whom activation of BOLD and inflow signals appeared in the same image slice. The crossing of the two white lines indicates the center of the FFA. (a) SWI-noMIP (left) and SWI-MIP (right) images. (b) Activation maps on the SWI-noMIP of the FFA by BOLD signals using the contrast of the face and scene conditions ( $F > S$ ) (left) and an activation site caused by inflow ( $S_0$ ) signals using the contrast of the face and control conditions ( $F > 0$ ) (right). (c) Activation maps on the SWI image using  $SF > 0$  (left) and  $PF > 0$  (right). A: anterior; L: left.  $P < 0.005$  (uncorrected).

run, the prestimulus was discarded from the estimation. The 2D data from the functional session were converted into the 3D data via trilinear interpolation using BrainVoyager QX. For the multisubject analysis, 3D Gaussian spatial smoothing (full width at half-maximum, 5 mm) was applied to the data. Statistical analysis was performed using BrainVoyager QX with a procedure based on general linear modeling. Each experimental condition (with the exception of the control) was defined as a separate predictor. The default hemodynamic response function of BrainVoyager QX was the reference time course used as the predictor. This analysis was performed independently for the time course of each voxel for each subject. To complete this analysis, time series of the images obtained from each subject were converted into the native space and Z-normalized.

### 3. Results

SWI images were acquired with minimum intensity projection (MIP) reconstruction across eight images (SWI-MIP) and without MIP. Activation maps were overlaid on SWI images without MIP (SWI-noMIP). SWI-MIP images were used to show large blood vessels more clearly. The SWI-MIP images showed blood vessels as a dark contrast, which was similar to previous reports that proposed the SWI method (Figure 1) [7, 8].

$S_0$  images were acquired from images of two TEs of a dual-echo sequence. The activation map of  $S_0$  was acquired by contrasting the face conditions (SF and PF) to the control

condition (this contrast included the contrast of the face versus scene conditions). Five of 10 subjects exhibited activation maps of  $S_0$  in the visual ventral region, which reflects inflow effects, while another five subjects did not. Among the data from the five subjects that showed inflow effects, variation was found in the location of activation sites (Figures 2 and 3; see Supplementary Figures 1–3 of the Supplementary Material available online at <http://dx.doi.org/10.1155/2014/234345>).

The FFA was identified from images with a TE of 38 ms (BOLD signals) of the dual-echo sequence by contrasting the face conditions (SF and PF) with the scene conditions (SS and PS). The data from some subjects showed that the FFA was located near the sites that reflected inflow signals. Other data showed that the FFA was located a little bit more remotely from those sites (Figures 2 and 3; Supplementary Figures 1–3). The images acquired from other subjects are shown in the supplementary figures (Supplementary Figures 4–8).

The images presented in Figure 2 are from one of ten subjects. The FFA was located at a cortical site that did not contain large blood vessels or strong susceptibility (Figure 2(a), right, and Figure 2(b), left). The activation site that reflected inflow signals was located on the right of the FFA in the same image slice (Figure 2(b), right). However, these areas did not overlap. The activation map obtained by PF was broader and stronger compared with that obtained by single stimulation (SF) (Figure 2(c), left and right).

The images presented in Figure 3 are for another subject and show the FFA and large blood vessels or susceptibility around the FFA where sites activated by inflow signals

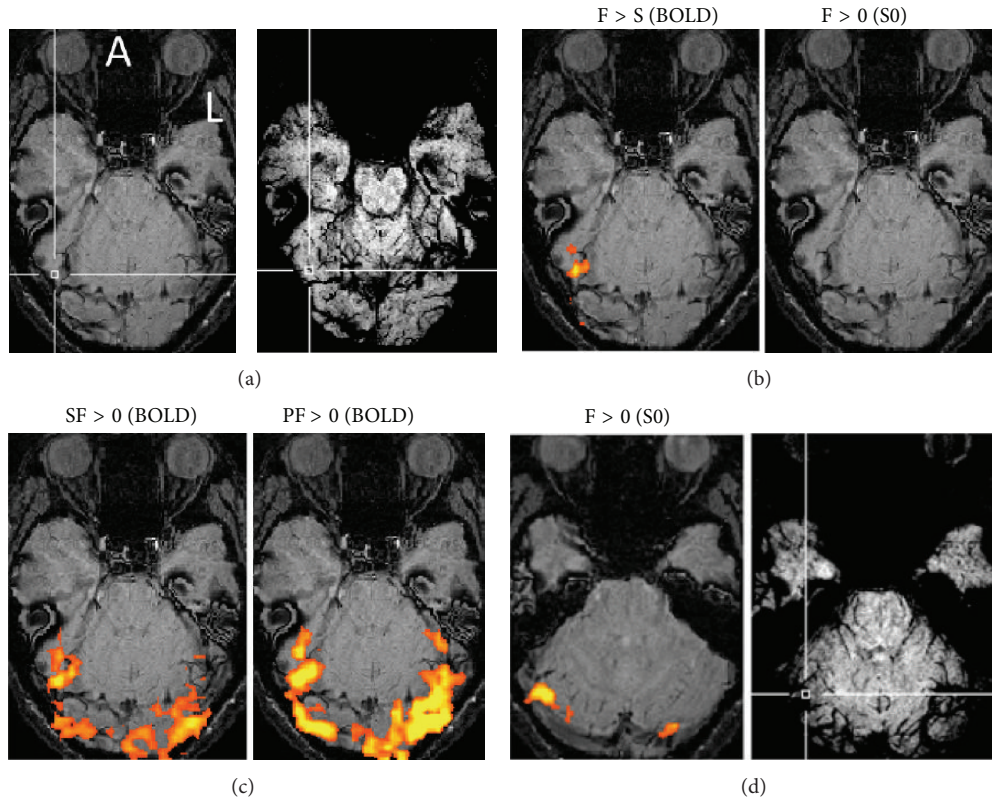


FIGURE 3: SWI images and activation maps for one subject in whom activations of BOLD and inflow signals appeared in different image slices. The crossing of the two white lines indicates the center of the FFA for (a) and the center of the S0 activation map for (d). (a) SWI-noMIP (left) and SWI-MIP (right) images. (b) Activation maps on the SWI image of the FFA were obtained by BOLD signals using the contrast of the face and scene conditions ( $F > S$ ) (left), but not by inflow (S0) signals using the contrast of the face and control conditions ( $F > 0$ ) (right). (c) Activation maps on the SWI image using  $SF > 0$  (left) and  $PF > 0$  (right). (d) Activation maps by S0 signals in a different image slice obtained by BOLD signals. A: anterior; L: left.  $P < 0.005$  (uncorrected).

are located in different image slices. The FFA appeared to be located near large blood vessels (Figure 3(a), right, and Figure 3(b), left). Activation reflecting inflow signals was not found on the same image slice as that including the FFA (Figure 3(b), right). The activation map obtained by PF was much larger than that obtained by single SF (Figure 3(c), left and right). An activation map reflecting inflow signals was found at a lower region than the FFA (Figure 3(d), right). An activation site reflecting inflow signals appeared at large blood vessels (Figure 3(d), left and right).

To assess the effect of large surrounding blood vessels in the FFA, we processed the FFA data at individual and group levels. The results of the comparison of the SF and PF conditions were different between these two analyses (Figure 4). SF and PF were not significantly different ( $P = 0.39$ ; paired  $t$ -test) but PF was larger than SF ( $P = 0.01$ ; paired  $t$ -test).

#### 4. Discussion

Our aim was to examine the contribution of large blood vessels to the fMRI response of the FFA. The data demonstrated, based on the presence of separate locations of activation sites of BOLD and S0, that fMRI responses of the FFA were not

affected by inflow signals. The data also showed that no large blood vessels were present in the FFA. This means that the FFA was not affected directly by inflow signals and that its location was not biased by large blood vessel signals.

However, the presence of large blood vessels and the activation by inflow effects around the FFA represent a warning that the evaluation of FFA responses via intersubject averaging may lead to a wrong direction, because a representative location of the FFA acquired by averaging activated sites across subjects can pick up signals that originate from large blood vessels that surround the FFA. In fact, the comparison between an averaged signal from the locations of individual subjects and a signal from a common location based on the group-averaged data yielded different results; that is, the difference between the SF and PF conditions was larger in the group analysis than in the individual subjects' analysis (Figure 4). It is considered that broader activation maps of paired stimulation reached large blood vessels and that signals from the common area contained responses originating from large blood vessels.

The contribution of signals originating from large blood vessels to BOLD activation has been reported, and several previous studies attempted to remove this contribution or identify the location of large blood vessels [12–15]. One of

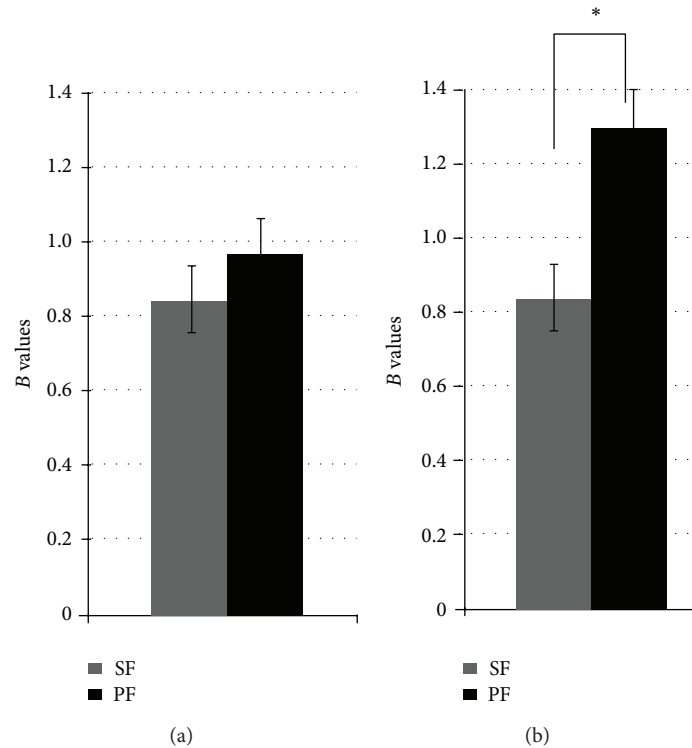


FIGURE 4: Averaged responses of the FFA in 10 subjects and estimated beta values based on BOLD signals using individual and group analyses. (a) Individual data; no significant difference was observed between SF and PF ( $P = 0.39$ , paired  $t$ -test). (b) Group data; PF was larger than SF ( $P = 0.01$ , paired  $t$ -test). Errors represent standard errors of the mean.

the ways to achieve this is to use a spin-echo (SE) EPI sequence and compare SE-EPI with GE-EPI sequences. An SE-EPI sequence with an additional gradient can remove the contribution of large blood vessels to BOLD signal, because diffusion effects are small around large blood vessels, and the velocity in the vessels is high [13, 16]. However, the disadvantages of using these methods include small signal changes, which preclude their routine use in fMRI studies of perception and cognition, although it is helpful to determine the exact components of BOLD signals. Another reason for not using these methods is that many fMRI studies are based on low spatial resolution images.

In the present study, we used SWI sequences to acquire blood vasculature information and dual-echo EPI sequences to measure inflow effects. Imaging using SWI sequences represents anatomical scanning, whereas imaging using dual-echo sequences represents functional scanning. Therefore, there was no penalty regarding scanning time for function or regarding signal intensity, because the second echo signal can be used for typical BOLD.

Signals originating from large blood vessels may lead to misinterpretation of the functional characteristics of brain areas examined using typical fMRI, particularly in high spatial resolution studies or high functional resolution studies (which deal with subtle differences between responses to similar stimuli). Therefore, the consideration of the contribution of large blood vessels in parallel with the typical functional analysis would be needed for ensuring reliability.

The present study revealed that large blood vessels do not run through the FFA and that inflow effects did not affect fMRI signals of the FFA. This assures that the fMRI data from the FFA do not include functional artifacts resulting from large blood vessels, such as the variation in the location of the FFA between subjects or the modulation of signal intensity. Conversely, information on the large vessels that surrounded the FFA provided a warning regarding group analyses. The results obtained for the FFA can also be applied to other functional areas. Therefore, it may be advisable to use SWI and dual-echo EPI sequences for high spatial resolution studies or for perception or cognitive studies that deal with subtle differences in signals [11, 17].

Our study has some limitations. Although SWI images provided a strong contrast to large blood vessels, cerebral spinal fluid (CSF) also provided a contrast of a similar level. Some additional efforts may be needed to delineate vessels if greater detail regarding the blood vasculature is required. The method used in the present study consisted of the observation of the effects of large blood vessels rather than the removal of the effects. Therefore, other methods may be used in combination with the present approach if the proposed method shows that some target areas are influenced by large blood vessels.

Taken together, the results of the present study demonstrated that the location or response signals of the FFA were not influenced by large blood vessels or inflow effects, despite large blood vessels being located near the FFA and the

variation in the location of the FFA across subjects. However, a group analysis of multiple subjects may be affected by large blood vessels. This suggests that the data from the FFA obtained by individual analysis would be robust to large blood vessels, whereas the data obtained by group analysis may be prone to large blood vessels.

## 5. Conclusions

The data from the FFA obtained by individual analysis were robust to large blood vessels but leaving a warning that the data obtained by group analysis may be prone to large blood vessels. This shows that SWI sequences and dual-echo GE-EPI sequences can be used to probe functional characteristics of brain areas.

## Conflict of Interests

The authors declare that there is no conflict of interests regarding the publication of this paper.

## Acknowledgments

This study was partly supported by MEXT-Supported Program for the Strategic Research Foundation at Private Universities (2014–2018) and the National Research Foundation of Korea (NRF) Grant funded by Korea Government (MSIP) (no. NRF-2014M3C7033998).

## References

- [1] S. Ogawa, R. S. Menon, D. W. Tank et al., “Ugurbil, Functional brain mapping by blood oxygenation level-dependent contrast magnetic resonance imaging,” *Biophysical Journal*, vol. 44, no. 3, pp. 803–812, 1993.
- [2] J. S. Gati, R. S. Menon, K. Ugurbil, and B. K. Rutt, “Experimental determination of the BOLD field strength dependence in vessels and tissue,” *Magnetic Resonance in Medicine*, vol. 38, no. 2, pp. 296–302, 1997.
- [3] J.-H. Gao, I. Miller, S. Lai, J. Xiong, and P. T. Fox, “Quantitative assessment of blood inflow effects in functional MRI signals,” *Magnetic Resonance in Medicine*, vol. 36, no. 2, pp. 314–319, 1996.
- [4] J.-H. Gao and H.-L. Liu, “Inflow effects on functional MRI,” *NeuroImage*, vol. 62, no. 2, pp. 1035–1039, 2012.
- [5] R. Epstein and N. Kanwisher, “A cortical representation of the local visual environment,” *Nature*, vol. 392, no. 6676, pp. 598–601, 1998.
- [6] N. Kanwisher, J. McDermott, and M. M. Chun, “The fusiform face area: a module in human extrastriate cortex specialized for face perception,” *The Journal of Neuroscience*, vol. 17, no. 11, pp. 4302–4311, 1997.
- [7] E. M. Haacke, Y. Xu, Y.-C. N. Cheng, and J. R. Reichenbach, “Susceptibility weighted imaging (SWI),” *Magnetic Resonance in Medicine*, vol. 52, no. 3, pp. 612–618, 2004.
- [8] E. M. Haacke and Y. Yongquan, “The role of susceptibility weighted imaging in functional MRI,” *NeuroImage*, vol. 62, no. 2, pp. 923–929, 2012.
- [9] G. H. Glover, S. K. Lemieux, M. Drangova, and J. M. Pauly, “Decomposition of inflow and blood oxygen level-dependent (BOLD) effects with dual-echo spiral gradient-recalled echo (GRE) fMRI,” *Magnetic Resonance in Medicine*, vol. 35, no. 3, pp. 299–308, 1996.
- [10] F. Beissner, S. Baudrexel, S. Volz, and R. Deichmann, “Dual-echo EPI for non-equilibrium fMRI—implications of different echo combinations and masking procedures,” *NeuroImage*, vol. 52, no. 2, pp. 524–531, 2010.
- [11] K. Grill-Spector, R. Sayres, and D. Ress, “High-resolution imaging reveals highly selective nonface clusters in the fusiform face area,” *Nature Neuroscience*, vol. 9, no. 9, pp. 1177–1185, 2006.
- [12] T. E. Conturo, R. C. McKinstry, J. A. Aronovitz, and J. J. Neil, “Diffusion MRI: precision, accuracy and flow effects,” *NMR in biomedicine*, vol. 8, no. 7-8, pp. 307–332, 1995.
- [13] T. Q. Duong, E. Yacoub, G. Adriany, X. Hu, K. Ugurbil, and S.-G. Kim, “Microvascular BOLD contribution at 4 and 7 T in the human brain: gradient-echo and spin-echo fMRI with suppression of blood effects,” *Magnetic Resonance in Medicine*, vol. 49, no. 6, pp. 1019–1027, 2003.
- [14] O. Speck and J. Hennig, “Functional imaging by I0- and T2\*-parameter mapping using multi-image EPI,” *Magnetic Resonance in Medicine*, vol. 40, no. 2, pp. 243–248, 1998.
- [15] J. Zhong, R. P. Kennan, R. K. Fulbright, and J. C. Gore, “Quantification of intravascular and extravascular contributions to BOLD effects induced by alteration in oxygenation or intravascular contrast agents,” *Magnetic Resonance in Medicine*, vol. 40, no. 4, pp. 526–536, 1998.
- [16] A. W. Song, H. Fichtenholtz, and M. Woldorff, “Bold signal compartmentalization based on the apparent diffusion coefficient,” *Magnetic Resonance Imaging*, vol. 20, no. 7, pp. 521–525, 2002.
- [17] U.-S. Choi, Y.-W. Sung, S.-H. Choi et al., “Intermixed structure of voxels with different hemispheric characteristics in the fusiform face area,” *NeuroReport*, vol. 24, no. 2, pp. 53–57, 2013.